REPORT DOCUMENTATION PAGE

Form Approved OMB No. 0704-0188

1. REPORT DATE *(DD-MM-YYYY)*	2. REPORT TYPE	3. DATES COVERED *(From – To)*
08-07-2004	Conference Proceedings	27 October 2003 - 30 October 2003

4. TITLE AND SUBTITLE

Introduction to Magneto-Fluid-Dynamics for Aerospace Applications

5a. CONTRACT NUMBER
FA8655-03-1-5075

5b. GRANT NUMBER

5c. PROGRAM ELEMENT NUMBER

6. AUTHOR(S)

Conference Committee

5d. PROJECT NUMBER

5d. TASK NUMBER

5e. WORK UNIT NUMBER

7. PERFORMING ORGANIZATION NAME(S) AND ADDRESS(ES)
von Karman Institute
72 Chaussee de Waterloo
Rhode-Saint-Genese B-1640
Belgium

8. PERFORMING ORGANIZATION REPORT NUMBER

N/A

9. SPONSORING/MONITORING AGENCY NAME(S) AND ADDRESS(ES)

EOARD
PSC 802 BOX 14
FPO 09499-0014

10. SPONSOR/MONITOR'S ACRONYM(S)

11. SPONSOR/MONITOR'S REPORT NUMBER(S)
CSP 03-5075

12. DISTRIBUTION/AVAILABILITY STATEMENT

Approved for public release; distribution is unlimited.

13. SUPPLEMENTARY NOTES

14. ABSTRACT

The Final Proceedings for Introduction to Magneto-Fluid-Dynamics for Aerospace Applications, 27 October 2003 - 30 October 2003

This is a new Lecture Series that will introduce magneto-hydro-dynamics (MHD) fundamentals and will report on the current State-of-the-Art research activities throughout Europe, Russia, and the US. Specific topics include: Electromagnetic Theory; Governing Equations; Numerical Modeling; Hypersonic Boundary Layer Interactions; Experimental Approach to Plasma ; Physical Aspects of Traditional MHD; Hypersonics and Propulsion MHD; and Plasma Flow Control for boundary Layers.

15. SUBJECT TERMS
EOARD, Magneto Hydro Dynamic (MHD), Hypersonics, Magneto Gas Dynamics (MGD)

16. SECURITY CLASSIFICATION OF:			17. LIMITATION OF ABSTRACT	18, NUMBER OF PAGES	19a. NAME OF RESPONSIBLE PERSON
a. REPORT	b. ABSTRACT	c. THIS PAGE	UL		WAYNE A. DONALDSON
UNCLAS	UNCLAS	UNCLAS			

19b. TELEPHONE NUMBER *(Include area code)*
+44 (0)20 7514 4299

Standard Form 298 (Rev. 8/98)
Prescribed by ANSI Std. Z39-18

von Karman Institute for Fluid Dynamics
Chaussee de Waterloo, 72
B – 1640 Rhode Saint Genese – Belgium

Lecture Series 2004-01

INTRODUCTION TO MAGNETO-FLUID-DYNAMICS FOR AEROSPACE APPLICATIONS

October 27-30, 2003
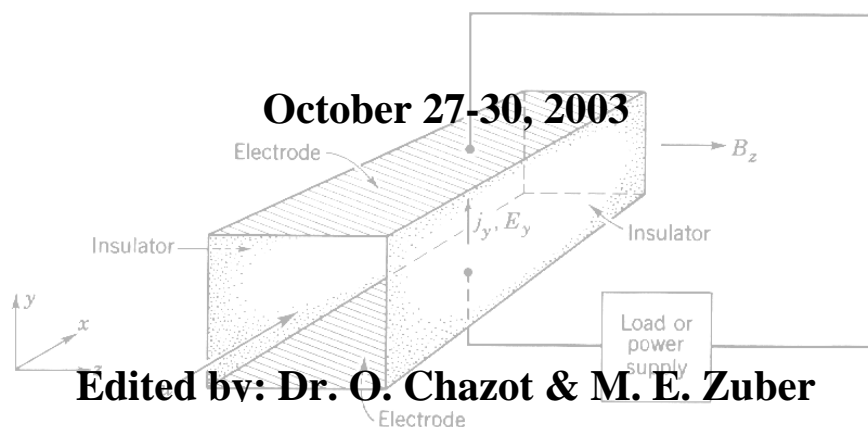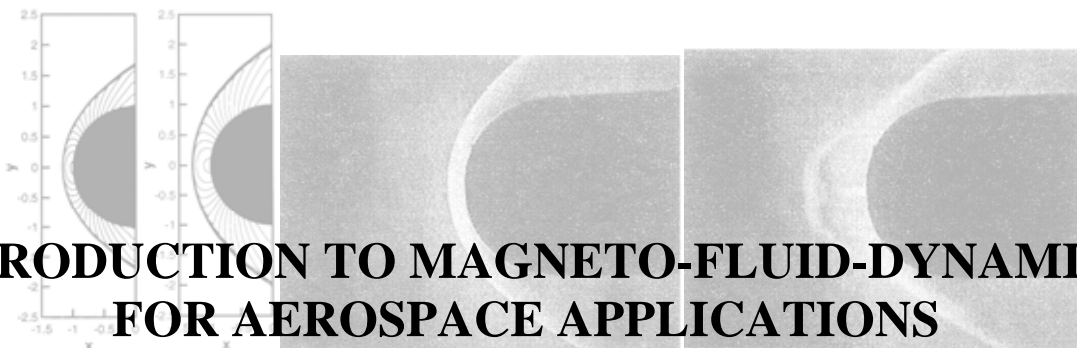
Edited by: Dr. O. Chazot & M. E. Zuber

TABLE OF CONTENTS

PREFACE

HISTORICAL PERSPECTIVE

Dr. Joseph Shang, Wright-State University, Dayton, OH, United States

MAGNETO AND ELECTROMAGNETO FLUID DYNAMICS / MAGNETOHYDRODYNAMIC WAVES

Prof. Jacques Nihoul, Liege University, Belgium

HYPERSONIC-FLOW GOVERNING EQUATIONS WITH ELECTROMAGNETIC FIELDS

Dr. Domenico Giordano, ESA/ESTEC, Netherlands

1D EQUATIONS AND ANALYSIS/CHANNEL FLOWS

Prof. Jacques Nihoul, Liege University, Belgium

COUPLING BETWEEN ELECTRO-MAGNETICS AND FLUID-DYNAMICS: PHYSICAL AND NUMERICAL ASPECTS

Prof. Domenic D'Ambrosio, Dip. di Ingegneria Aeronautica e Spaziale, Italy

UPWIND NUMERICAL METHOD FOR MAGNETO-FLUID-DYNAMICS

Prof. Maurizio Pandolfi, Dip. di Ingegneria Aeronautica e Spaziale, Italy

NUMERICAL MODELING OF ELECTROMAGNETIC CONTROL TECHNIQUES FOR HIGH-SPEED FLOW

Dr. Jon Poggie, US Air Force, United States

NUMERICAL FULLY COUPLED EXAMPLE – MHD SCRAMJET

Professor Claudio Bruno, University of Rome, Italy

EXPERIMENTAL APPROACH TO PLASMA PHYSICAL ASPECTS OF TRADITIONAL MHD

Professor Abraham Veefkind, University of Eindhoven, Netherlands

PREFACE

*"Magneto-fluid-dynamics is the science which studies the interaction between flow fields of conducting fluids and electromagnetic fields from both the macroscopic and microscopic (or particle) point of view. This new chapter of physics has attained an ever increasing importance in a large variety of fields of basic problems and hints at very promising future technological implications and developments. Especially all branches of Astronautics and Space Research will directly or indirectly influenced by the progress that will be made in this science which I have proposed to call **magneto-fluid-dynamics**."*

THEODORE VON KARMAN (1962)

Magneto-Fluid-Dynamics (MFD) has already a long history that is generally known for its cyclic technical interests. Contemporary enthusiasm must be documented for the sake of posterity. This particular progression is also linked to the fact that MFD stands at the intersection of many branches of physics, which make it a multi-domain field of investigations. It has always been widely open and has been approached by different directions and different research groups with various background and perspectives. It has also been a field of prospection, since it offers to the engineer and scientist numerous technical potentialities, as well as plenty of subtle physical features. During all these years, MFD gained a well-established theoretical and technical framework and remains full of promising applications. Considering recent experimental and computational advances, renewed interested has elicited itself as a meaningful and useful lecture series at the von Karman Institute for Fluid Dynamics with focus upon MFD for the specific aspects of aerospace applications.

The objective of this Lecture Series is to introduce the magneto-fluid-dynamics fundamentals and to report on the current state-of-the-art research for future aerospace applications. This multiphysics field has recently been rejuvenated with innovation within experimental and computational activities. MFD reveals potential to become a new technological frontier towards the improvement of aerospace vehicles and their performance. This lecture series will generally cover:

- ➢ insight into the philosophy and potential of magneto-fluid-dynamics
- ➢ understanding of the mathematical nature of the equations of motion
- ➢ experimental and numerical approaches towards MFD applications
- ➢ examples for research scientist and engineers to emulate

The lectures will begin with the fundamentals and governing equations of motion and a historical perspective on relevant MFD research and developments. Subsequent lectures will address specific numerical and experimental applications of MFD, such as flow control, propulsion, high enthalpy ground test facilities and energy management. International experts from Europe, Russia and the United States will discuss their respective activities in these areas.

We wish to thank the European Office of Aerospace Research and Development of the United States Air Force for their generous contribution towards the success and reality of this lecture series.

Dr. Olivier Chazot   Matthew E. Zuber
Lecture Series Director   Lecture Series Coordinator

Historical Perspective of Magneto-Fluid-Dynamics

J.S. Shang, Ph.D.
Department of Mechanical and Materials Engineering
Wright State University
Dayton OH, USA

Lecture outline
1. Unique Features of Plasma
    1.1 Debye shielding length
    1.2 Global neutrality
    1.3 Plasma frequency
2. Basic Assumptions of magneto-fluid-dynamics
    2.1 Continuum
    2.2 Relativistic effect, displacement current, and electrostatic force
    2.3 Governing equations system
3. Early Research findings
    3.1 Ideal MHD equations
    3.2 Resler and Sear' vision
    3.3 Theoretic and experimental finding
4. Rejuvenation in the 1980's
    4.1 Transverse magnetic waves
    4.2 Approximate Riemann formulation
    4.3 Ajax Concept Vehicle
5. Most Recent Experimental Research
    5.1 Counter-Flow plasma injection
    5.2 Remote energy deposition
    5.3 Pulsing/Microwave discharge
    5.4 Magneto-Aerodynamic interactions
6. Computational magneto-fluid-dynamics
    6.1 Eight-Wave characteristic formulation
    6.2 Drift-Diffusion theory
    6.3 Three-Dimensional MHD Scramjet energy bypass
    6.4 Return to the basics
7. Concluding Remarks

Unique Features of Plasma

In 1929, Irving Langmuir defined the plasma as a partially ionized gas and its charge separation distance, the Debye shielding length $\lambda_D = (\varepsilon \kappa T / n e^2)^{1/2}$, is small compared to all other characteristic macroscopic length scales [1]. This physical dimension defines the domain of potential energy of a very strong electrostatic force that must be balanced by the mean thermal energy of the charged particle. Therefore this physical dimension divides the small-scale particle motion from the macroscopic collective behavior of an ionized gas. As a consequence, the charge particles always move rapidly after any disturbance to reduce the potential difference and thereby restore electrical neutrality of a

partially ionized gas. This tendency of a partially ionized gas toward electrical neutrality becomes a unique feature of plasma.

A well-known and frequently investigated problem is the plasma sheath where the global neutrality of plasma breaks down in the region immediately adjacent to a solid surface. A very interesting aspect of the sheath problem is the charge disposition, and offers a significant technical challenge in engineering application. In general, the spatial extent of the plasma sheath is on the order of magnitude of few Debye lengths. This observation substantiates the fact that the plasma is self-adjusting to shield the main body from the electric field. Nevertheless, this electrically conducting medium profoundly affects the dynamics of the plasma motion in the presence of a magnetic field [2].

Another important feature of an ionized gas is the plasma frequency $\omega_p = (ne^2/\varepsilon m_e)^{1/2}$, which is also closely related to the property of electrical neutrality [3]. The plasma can be considered as a multi-component fluid with neutral particles, electrons and one or more types of ions. However, any slight displacement of plasma from the condition of electrical neutrality gives rise to large restoring forces. Consequently, oscillations of an electrostatic nature are induced. In the presence of a magnetic field, the charged particles will move in helical orbits. At a low frequency motion, even when the wavelength of the motion is comparable to the mean free path, the electrons and ions are still able to maintain local electric neutrality. Meanwhile, the charged particles drift on the average in opposite direction under the action of electric field. At higher frequencies, due to the greater difference of mass between the electrons and ions, they move independently and lead to charge separation.

In this sense, the plasma frequency is an indication of how fast the restoring forces act after a disturbance to the condition of global neutrality. From the charge conservation consideration, this frequency also measures the elapse time of charge excess to produce an electric field to impede the disturbance. This frequency becomes a controlling parameter for electromagnetic wave propagation in plasma. If the electromagnetic wave transmits from free space to plasma with lower frequencies than the plasma frequency, the incident wave will reflect from the media interface. This physical behavior can be understood as the plasma has sufficient time to rearrange and to shield its interior from the electromagnetic field. If the incident electromagnetic wave with a higher frequency than the plasma frequency, the electromagnetic wave will then propagate into the plasma with amplitude attenuation and phase shift. This behavior of plasma as a lossy medium for electromagnetic wave motion is brought out by the fact that the plasma is an electrical quasi-conductor. This dispersive characteristic of electro-magnetic wave in plasma is the fundamental cause of communication blackout in the reentry phase of space flights.

Basic Assumptions of Magneto-Fluid-Dynamics

The magneto-fluid-dynamics has traditionally been designated as Magneto-hydrodynamics MHD; this designation was partly derived from the fact that verifications of pioneering research were often obtained from experiments conducted in mercury. However, MHD had its deep roots in astrophysics and geophysics [4,5]. On the theoretical frame of reference, MHD or Magneto-Fluid-Dynamics (MFD) is a

specialization of plasma physics. The first assumption of MHD is that the continuum exists in the presence of an electromagnetic field, and the magnetization and polarization of charged particles together with the relativistic effect are negligible. Therefore all MHD phenomena are governed by the combination of the Maxwell and Navier-Stokes equations [6].

For an electrical conducting medium, the generalized Ohm's law describes the intrinsic electro-dynamic properties. This fundamental equation in MFD can be derived from kinetic theory for a group of charged particles. Because the Coulomb force acts on a short range the Enskog expansion is a reasonable approximation for collision terms. Using the facts that the plasma is globally neutral and its composition consists of electrons and positively charged ions with vast difference in mass. The generalized Ohm's law on a macroscopic scale can be given as the following:

$$\mathbf{E} = \sigma\,[\mathbf{J} + \beta\mathbf{J} \times \mathbf{B} + s\,\mathbf{B} \times (\mathbf{J} \times \mathbf{B})] \tag{1}$$

The coefficient β is related to the Hall current, and the last term in the above equation describes the ion slip phenomenon and it only exists in a partially ionized gas. The electrical conductivity σ should really be a tensor, but in most MFD analysis σ is treated as a scalar.

For an ionized gas over a wide range of collision frequencies, the Ohm's law in the simple form that relates the electric current density and the electric field is valid. At a low frequency range, the electric field generated by either a current flow or time-varying magnetic field is free from charge separation. Under this circumstance, the fluid motion can still be described as single electrically conducting fluid with the usual dependent variables of fluid motion. At low frequencies, it can be shown that the displacement current in the generalized Ampere's law is negligible up to the microwave spectrum; $\partial D/\partial t \cong O\,(\varepsilon E/t\,J) = O(\varepsilon/t\sigma) \cong O(1/t\omega)$. Another simplification based on physics is that the electrical current by transport of excess charge $\rho_e u$ is extremely small in comparison with the conduction current; $\rho_e u/\sigma E \cong O\,(\varepsilon u/\sigma L)$. Again, by the virtue of the global electrical neutrality of plasma at low frequencies, the electrostatic force can be omitted, J×B >> ρ_eE. Then the Lorentz force reduces to J×B, and the electrical field intensity E is explicitly eliminated from the Faraday induction law by Ohm's law.

Based on the aforementioned physically based assumptions, the governing equations of MFD can be given as:

$$\partial\rho/\partial t + \nabla \cdot (\rho\mathbf{U}) = 0$$
$$\partial(\rho\mathbf{U})/\partial t + \nabla \cdot [\rho\mathbf{U}\mathbf{U} - \boldsymbol{\tau} + p\,\boldsymbol{I}] = \mathbf{J} \times \mathbf{B}$$
$$\partial(\rho e)/\partial t + \nabla \cdot [\rho e\mathbf{U} + \mathbf{q} + \mathbf{U} \cdot (p\boldsymbol{I} - \boldsymbol{\tau})\,] = \mathbf{E} \cdot \mathbf{J} \tag{2}$$
$$\partial\mathbf{B}/\partial t + \nabla \times \mathbf{B} = 0$$
$$\mathbf{J} = \nabla \times \mathbf{B}/\mu_e$$
$$\mathbf{E} = \sigma\,[\mathbf{J} + \beta\mathbf{J} \times \mathbf{B} + s\,\mathbf{B} \times (\mathbf{J} \times \mathbf{B})]$$

Where
$$\boldsymbol{\tau} = \mu\,(\nabla + \nabla^*)\,\mathbf{U} + \lambda\,(\nabla \cdot \mathbf{U})\,\boldsymbol{I}$$
$$\mathbf{q} = -\kappa\,\nabla T$$

Where **B** is the magnetic flux density, **I** denotes the identity matrix, and μ_e is the magnetic permeability. The rest of dependent variables for fluid dynamics are well known. The above equations can be manipulated to closely couple the electromagnetic and fluid dynamic dependent variables to get:

$\partial \rho / \partial t + \nabla \cdot (\rho \mathbf{U}) = 0$

$\partial \mathbf{B} / \partial t + \nabla \cdot (\mathbf{UB} - \mathbf{BU}) = - \nabla \times [(\nabla \times \mathbf{B} / \mu_e)/\sigma]$

$\partial (\rho \mathbf{U}) / \partial t + \nabla \cdot [\rho \mathbf{UU} - \mathbf{BB}/\mu_e - \boldsymbol{\tau} + (p + \mathbf{B} \cdot \mathbf{B}/2\mu_e) \boldsymbol{I}] = 0$ (3)

$\partial (\rho e) / \partial t + \nabla \cdot [\rho e \mathbf{U} + \mathbf{q} + \mathbf{U} \cdot [(p + \mathbf{B} \cdot \mathbf{B}/2\mu_e)\boldsymbol{I} - \boldsymbol{\tau}] - (\mathbf{B} \cdot \mathbf{U})\mathbf{B}/\mu_e]$

$\qquad = (\nabla \times \mathbf{B}/\mu_e)^2/\sigma + [\nabla \times (\nabla \times \mathbf{B}/\mu_e)/\sigma] \cdot \mathbf{B}/\mu_e$

Now,

$e = \int C_v dT + (\mathbf{U} \cdot \mathbf{U} + \mathbf{B} \cdot \mathbf{B}/\mu_e)/2$

The associated initial and boundary conditions for the MFD governing equations can be summarized as follows. In a stationary frame of reference, this set of boundary condition for the electromagnetic field requires that the tangential components of electric field strength E, and the normal components of magnetic flux density B, are continuous across media interface. The discontinuity of the tangential components of magnetic field density B is equal to the surface current density J_s. Finally, the surface charge density ρ_s, balances the difference between normal components of the electrical field strength E across the interface. For the fluid dynamic variables the associate boundary conditions are well known. The conventional non-slip condition for velocity components, the vanishing normal pressure gradient condition, and either a prescribed surface temperature or the adiabatic condition for temperature are still applied.

Early Research Findings

The earlier research in fluid dynamics of ionized gases is almost concentrated on such outstanding problems as the interstellar gas motion, solar corona, and origin of earth magnetism in astrophysics and geophysics [4-6]. In the 1950's, interests shifted to the problem of controlled fusion, energy conversion, plasma propulsion, reentry of space flight, and microwave communication [7-9]. Pioneering efforts were also focused on the propagation of electromagnetic waves and hydrodynamic shocks [10]. Wave propagation in plasma is much more complex than the longitudinal wave in aerodynamics. First, the transverse wave like Alfven wave is independent of pressure and density, but depends on the normal component of the applied field in the direction of wave motion. The phase and group velocities of the Alfven wave are equal in magnitude but differ in direction. In addition, there are two more phase velocities that correspond to the fast and slow plasma waves [11,12].

In order to investigate the complex physics, the electrical conductivity of the medium is assumed to have an infinity value and the molecular transport properties are negligible. This approximate leads to the so-called ideal MHD equations. One consequence of this assumption is that the magnetic field must move with a perfect conductor. Another consequence is that the governing equations can degenerate into the non-convex hyperbolic system [13], for which the characteristic surface may unexpectedly incur singularities making the wave structure in plasma much more complex than in air. In

spite of that the concept of ideal MHD offers a theoretical base for analyzing the wave motion in plasma.

Four decades ago, Resler and Sears recognized the tremendous application potential of the electromagnetic effect for enhanced aerodynamic performance [14]. Their vision introduces a new physical dimension into conventional aerodynamics to enrich the fluid dynamic behavior. The added coupling of velocity and temperature by plasma through Joule heating makes some impossible flow fluid field manipulations realizable. One of the possible uses of the Lorentz force is to accelerate or decelerate plasma continuously without choking at subsonic or supersonic inlets. The flow orientation of plasma can also be altered by the intrinsic relationship of the Hall current and the helical trajectory in a magnetic field.

In practical aerodynamic applications, the air requires a rather large amount of energy to achieve the ionized state by thermal collision process and energy transfer between internal degrees of freedom [15,16]. For example, the ionization potentials for oxygen and nitrogen molecule are 5.12 and 9.26 EV respectively. However, this condition is naturally occurring in most hypersonic flights. The strong compression of bow shock wave converts nearly all kinetic energy to thermal energy. The air mixture bounded by the bow shock wave and the vehicle achieves highly excited internal energy modes. As the air temperature exceeds 5,000 K, a fraction of the dissociating molecules will shed their electrons [16]. The ionized air mixture is then characterized by a finite value of electrical conductivity, which may exceed a value of 100 mho/m depending on the flight speed and altitude. The interaction of charged particles with an applied electromagnetic field generates the Lorentz force and Joule heating as an additional mechanism to influence aerodynamic performance. These observations were strongly supported by the pioneering effort by Bush, Meyer, Ziemer and others [17-19].

In 1958, Bush led the investigation of viscous MHD hypersonic flow over a blunt body [17]. In his analysis, the magnetic field is specified in the free stream and the magnetic field at the body surface is generated by a dipole at the coordinate origin. He has found the standoff distance of the bow shock increases with the increasing electromagnetic-aerodynamic interaction parameter, $\sigma B^2 L / \rho u$. His numerical results also collaborate with the finding by Meyer that the primary mechanism that serves to reduce the heat transfer is the reduced flow field gradient normal to the surface.

Meyer recognized that if a magnetic field is applied normal to the body surface, the Lorentz force always has a component $\sigma (U \times B) \times B$, that will decelerate the flow [18]. Across the non-uniform velocity profile of a shear layer, the decelerating force increases in magnitude with distance from the solid surface. The net result is a reduction in velocity and temperature gradients in the shear layer, the diminishing velocity and temperature gradients will decrease both the heat transfer and skin friction on the surface. Under some conditions, the eddy current induced by charged particles in turbulent motion interacts with the magnetic field and tends to suppress the high frequency fluctuations. For flows in a channel, even at moderate values of Hartmann number, $LB(\sigma/\nu)^{1/2}$ the turbulent shear can be modified [3].

The most noticeable phenomenon in plasma probably is the shock wave propagation and bifurcation. Zeimer in 1959 using a co-axial solenoid generated a magnetic field of 40 kilogauss around a hemispherical blunt body in the plasma stream of a shock tube [19]. By this arrangement, the interaction parameter $\sigma B^2 L/\rho u$ of the experiment has an unusually large value, estimated to be 69. Under this condition the electromagnetic force overwhelms the aerodynamic inertia, and the standoff distance of the bow shock increases by a factor more than seven. This behavior stands in stark contrast to all calculations and experimental data of non-equilibrium flows in the absence of an external electromagnetic field. For hypersonic blunt-body flows, the shock standoff distance always decreases with an increased Mach number and non-equilibrium effect [20]. Although his experimental observation received theoretical verification from the work of Bush [17], the reason of this contradiction was understood nearly forty years later. In essence, the increase shock standoff displacement is caused by the contribution of the term $B^2/2\mu_e$ that appears as an isotropic magnetic pressure. The sum of $p + \mathbf{B} \cdot \mathbf{B}/2\mu_e$ must be balanced by hydrostatic pressure upstream the bow shock. While the magnetic field strength decays rapidly proportional to the inverse cubic power of the distance from the pole, the gas density within the shock layer is much lower than that without the external magnetic field. To satisfy the continuity condition, the bow shock must move outward to ingest the on-coming stream, see Figure 1. [20].
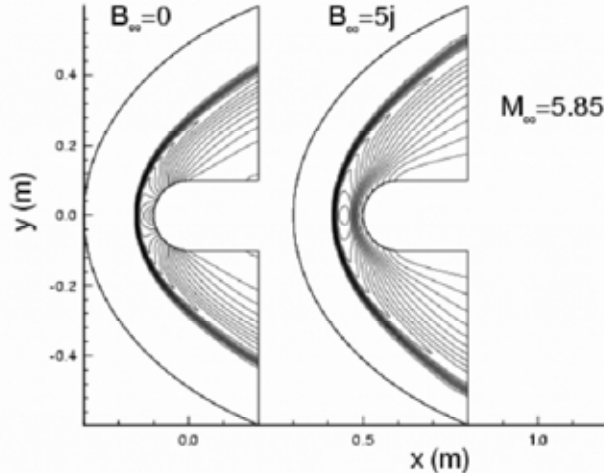
Fig. 1 Blunt body standoff distances in electromagnetic field, (Ref. 20)

The MFD research continued until the later 1960's, first into electrical power generation, microwave communication, then electrostatic propulsion but at a diminishing scale. Plasma research has always been sustained in nuclear diffusion, but the interest was focused on issue of plasma stability and ventured beyond the realm of MFD.

Rejuvenation in the Eighty's

In the field MFD, shock wave interaction with a transverse magnetic wave remains as one of the few topics that still attract research interest worldwide [21-24]. Among several interesting findings is that at high Reynolds number, for a steady-state magnetic field ahead the shock front, the field is swept along as a contact discontinuity initiated at

the moment the shock enters the field. The resultant shock wave structure is very complex including reflected shock wave [22]. The collective finding of this area of research reveals that the wave with an infinitesimal strength is substantially modified when traveling in a non-equilibrium, weakly ionized gas with an applied external magnetic field. Specifically, when a weak shock wave propagates in plasma, its strength decreases and the wave front disperses. If plasma could be introduced upstream of the bow shock of a vehicle, these newly identified physical phenomena could have revolution potential for improved high-speed flight [23-24].

The salient feature of microwave attenuation in plasma has been extensively used for plasma diagnostics [25]. In particular, the microwave attenuation was used to measure the transport property of rocket plume in missile trajectory tracking and in laboratory environments. The microwave system is also widely used in deep-space communication. Microwave attenuation in plasma is known for the famous communication blackout in the reentry phase either for an earth satellite or inter-planet flight. During the earth reentry and planetary entry, the electronic number density spans a range from 10^6 to 10^{18} per cubic centimeter, which cover a very wide spectrum of cut-off transmission frequencies. Although during this period a critical need still existed for improved applicability in this technology area, very limited investment was made.
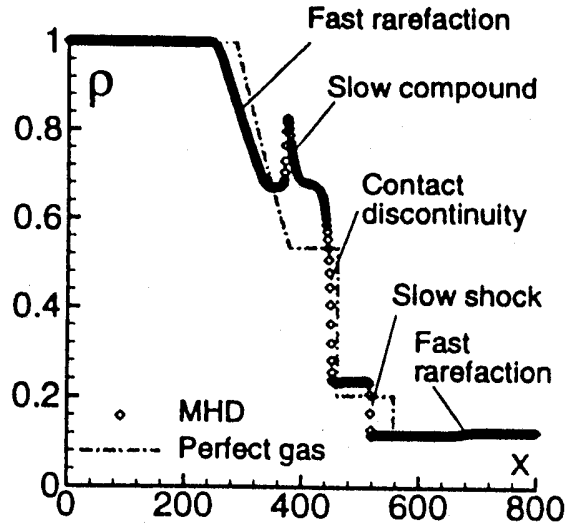
Fig. 2 Density profile in shock tube, Ref (28).

Significant progress also has been made in computational MHD using the characteristic-based formulation due to Roe [26]. Bistro and Wu in their illuminated effort solving the ideal MHD equations demonstrated for the first time several unique features of MFD [27]. A simple inviscid shock tube problem was simulated. They have shown that the fast transverse plasma wave travels ahead the acoustic wave in both the compression and expansion region of the shock tube. The plasma flow field structure is much more complex than its aerodynamic counterpart. Most importantly, the existence of a compound wave also appears in an electrically perfect conducting medium. In this aspect, the compression and expansion waves are attached to each other as degeneracy at

7

the critical point where the transverse magnetic field is changing its polarity. Unfortunately these computational results were obtained from solving the ideal MHD equations; a physical verification of their numerical results is probably unobtainable [27,28].

In the early 1990's an innovative aerodynamic design of the Ajax concept vehicle was advocated in Russia, for which the high-speed flow in a weakly ionized air was modified by electromagnetic and aerodynamic interactions [29,30]. Numerous innovations in hypersonic flow drag reduction via remote energy deposition, scramjet MHD flow bypass propulsion system, as well as enhancing mixing and combustion stirred quite a bit of interest. The basic attraction is to seek an effective application of fundamental physical principles to change the engineering paradigm. This innovation is deeply appreciated, especially after a string of unfulfilled hypersonic programs such as the Star-H in France, Saanger/Horus in Germany, Hope in Japan, Hotol in United Kingdom, NASP in US, Oryol (Raduga D-2) and Neva in the former USSR.

Drag reduction for a flying vehicle has been a goal since the days of the Wright Brothers. In most hypersonic vehicle designs, success or failure is hinged on a few percent differences between the thrust and total drag. The drag reduction by plasma injection with a powerful electrical discharge either by a counter-flow jet or by a focused directed energy beam projecting ahead the vehicle is mesmerizing. It is also perfect logical that the ionized intake air permits a MHD generator/accelerator to function. First, the electric energy is extracted from the high-speed incoming weakly ionized air and reduces the speed and entropy rise for the propulsive engine cycle. Then the extracted electricity is used to accelerate the exhaust gas after the combustor to increase the specific impulse of the propulsive system.   These novel ideas create an enormous engineering interest and in fact rejuvenate MFD research for aerodynamic applications worldwide.

Most Recent Experimental Research

Astonishing amounts of aerodynamic drag reduction via plasma injection from the stagnation point of blunt body have been reported [31,32]. The interaction of the on-coming stream and the counter-flow jet, as well as, the conspicuously absent external magnetic field were the common features of these observations. Indeed, a favorable aerodynamic performance was realized, however not all the mechanisms contributing to the performance improvement are exclusively provided by the electromagnetic force [33].   The counter-flow jet interaction, electromagnetic forces, and non-equilibrium thermodynamics were postulated as possible key mechanisms. A series of side-by-side experimental and computational research were therefore devoted this subject [33-35].

It was found that the major portion of the wave drag reduction is the consequence of the counter-flow jet and bow shock interaction. The reduced wave drag was realized by altering a single and stronger bow shock into a multiple shock structure that included the weakened bow shock, a Mach disk of the counter-flow jet and a ring shock. A shock bifurcation was also observed in the experimental effort. At the lower injection mass flow rate or the injection pressure lower than a critical state, the modified shock envelope

is conical and in a self-sustained oscillatory motion. Beyond the critical value, the displaced shock retracted to a blunt formation and the oscillatory motion ceased. This Bifurcating phenomenon is clearly illustrated by the Schlieren images presented in Figure 3. Since these photographs were taken in a long exposure, the oscillating shock wave structures appear as blurred images.

Fig. 3 Counter-flow jet shock wave bifurcation

As a further confirmation that the wave drag reduction is mostly derived from the counter-flow jet and shock interaction, a numerical solution of the time-dependent Navier-Stokes equations is presented together with the experimental data at two different testing conditions. In Figure 4, the comparison of measurements and calculations is depicted. The numerical results also reveal that the maximum wave drag reduction is reached at the shock bifurcation point.
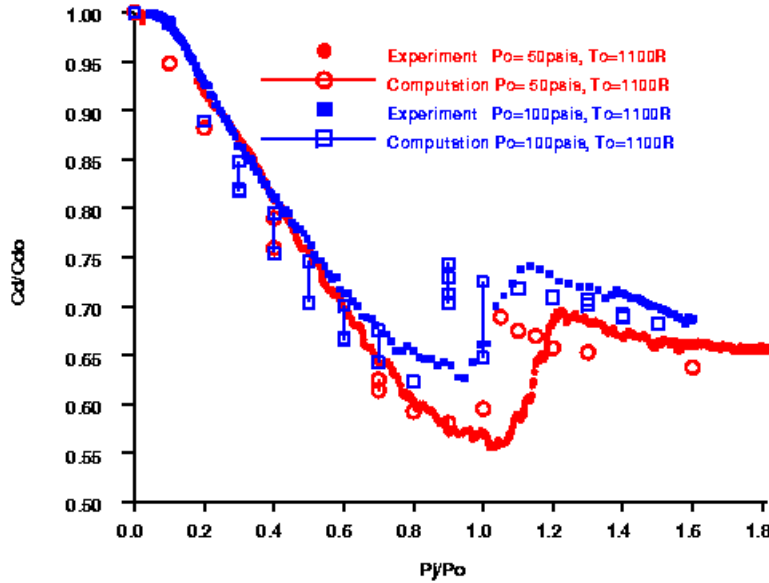
Fig. 4. Comparison of drag reduction via plasma injection

In the experimental effort, the injecting plasma can be characterized with a vibrational temperature of 4400 ± 400 K, an electron temperature and number density greater than 20,000 K and 3×10^{12} /cm^3 respectively. The advantage of plasma injection over the lower temperature air is the greater thermal energy content. However, the non-equilibrium thermodynamic and the induced electromagnetic contributions fall into the experimental data band of uncertainty [33-35]. This conclusion is just another

9

reaffirmation of classic theory that a significant magneto-aerodynamic interaction must be derived from a substantial and appropriately applied electromagnetic field. Regardless of this particular finding, the potential of utilizing electromagnetic and aerodynamics interaction for drastically improved performance of an aerospace vehicle is still unfathomable.

The idea of drag reduction or flow control using the remote energy deposition is very attractive [36-38]. The energy deposition techniques have a wide range of variety from plasma arcs, laser pulse, microwave, electron beam, glow discharge etc. The intended applications encompass an equally wide array from drag reduction, lift and moment enhancement, energetic mixing, to shock structure modification, and more. In all cases, the energy deposition into a high-speed stream attempts to induce an electromagnetic and aerodynamic interaction to acquire aerodynamic performance benefits [38]. A major portion of the experiments was conducted in Russia. Technically excellent and typical experimental efforts are represented in the works of Biturin and Kolesnichenko et al [39,40].

In some of these applications, the high-speed vehicle is immersed in the high-temperature wake of the intense energy source. In this sense the medium is ionized upstream of the bow shock contrary to all hypersonic flow environment. If the wake is supersonic, then the dispersive characteristic of wave propagation in plasma may yield an unexpected advantage for wave drag reduction. In addition, the energy deposition is self –adjusted, which means the energy deposition rate is control by the local property of the flow medium. This behavior is especially noticeable when the energy deposition is achieved by electron or laser beam [36,37].

The most active energy deposition research is conducted using the interaction of air stream with an electric discharge or a plasma formation adjacent to the vehicle [36]. Nearly all experiments have adopted a longitudinal glow discharge in a supersonic flow upstream to the body. The measurements seem to indicate that almost all voltage drop in the discharge occurs in the sheath near the electrodes. In many ways, this behavior obeys the classic theory, in that the cathode fall is the most predominant change of electric field strength in a glow discharge [41]. From the voltage and electric current characteristic of the applied discharge, the hysteresis effect is also detected. In that a single electric current can be generated at different voltages [36]. From these research results, it is recognized that energy deposition upstream of the body in high-speed flow can affect the flow field structure. The interaction is accentuated greatly by an ionized medium, because the electromagnetic energy deposition is volumetric and independent from the local gradient of field variables. To date, a complete understanding of the aerodynamic phenomena with energy deposition is still beyond our reach.

Most recently, Menart et al accomplished a first magneto-aerodynamic interaction experiment in a Mach 5 flow channel with a DC plasma discharge and an external magnetic field [42]. This research project sought the modification of the macroscopic aerodynamic structure by the application of a glow discharge and magnetic field simultaneously. In the experiment, the electric discharge is generated between two

embedded electrodes on a sharp leading edge, dielectric flat plate. The electron number density is measured by a double Langmuir probe and reaches a value as high as $10^{12}/cm^3$. The discharge current is flowing in the same direction as the hypersonic stream and the transverse magnetic field is applied perpendicular to both. This magnetic field maintains a constant strength over the plate, and the magnetic intensity has the upper limit of a Tesla. In this arrangement, the Joule heating, Lorentz force and Hall current are all active in the weakly ionized air stream. Although the glow discharge path is within the boundary layer over the plate, the electron number density still reaches its maximum value immediately adjacent to the cathode. In this region, the velocity of the neutral particles is also much slower than the external stream. Near electrodes, the interaction parameter of this interacting flow field should also attain the maximum value possible. Therefore, the magneto-aerodynamic interaction can induce an observable modification to the boundary layer. This perturbation is amplified by the viscous-inviscid interaction in the hypersonic stream.
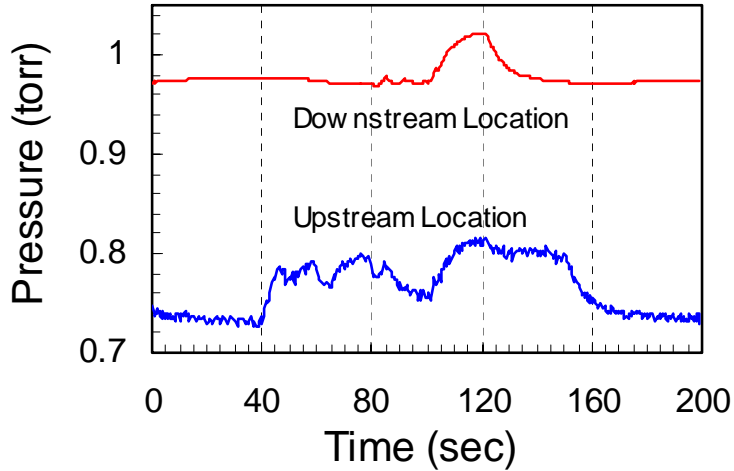

Fig. 5 Static pressure log of magneto-aerodynamic interaction Ref. [42]

The log of two pressure taps on the plate records the testing events from the ignition of the glow discharge, actuation of the transverse magnetic field, and the return to its original state. Each phase of the testing event is sustained for a period of 40 seconds. Although these data are still required additional scrutiny, there is little doubt that the Joule heating has produced a significant magneto-aerodynamic interaction. More important, the observed pressure rise over the plate is further accentuated by the sequential classic viscous-inviscid interaction. The effect of the Lorentz force and Hall current are much more difficult to discern, but the experimental evidence is clearly displayed.

Computational Magneto-Fluid-Dynamics

Computational MFD is truly an interdisciplinary science in that the electromagnetics, fluid dynamics, and chemical kinetics must be solved simultaneously to correctly describe the investigated physical phenomena. By definition the plasma that encounters MFD is classified as the ideal classic plasma according to the range of the electron temperature and electron number density [21]. In most astrophysic problems, the

electromagnetic forces dominate over the fluid dynamic inertia, and the viscous dissipation and heat transfer by conduction are negligible. In addition, if the relativistic effect is unimportant and the continuum assumption is valid, the governing equations are the simplified MFD, known as the ideal MHD equations.   This system of partial differentials equations has been used to study an expanding cometary atmosphere with the magnetized solar wind. In some analyses the effects of photoionization, electron impact ionization, recombination, and ion-neutral frictional drag were modeled [43]. Since the astrophysical phenomena are highly compressible, the solution techniques are based on approximate Riemann solvers [27,44,45].

Powell et al carried the windward formulation into an eight-wave approximate Riemann solver based on the four distinct wave mechanisms in a plasma medium; the acoustic, Alfven, slow and fast plasma waves [45]. This formulation becomes a basic building block for describing the inviscid terms of the general MFD equations. The eigenvalues of the ideal MHD equations are:

$$\lambda_1 = u \qquad \lambda_2 = u$$

$$\lambda_3 = u + \sqrt{\frac{B_n^2}{\rho\mu}} \qquad \lambda_4 = u - \sqrt{\frac{B_n^2}{\rho\mu}}$$

$$\lambda_5 = u + \sqrt{\left[C^2 + \frac{B^2}{\rho\mu} + \sqrt{(C^2 + \frac{B^2}{\rho\mu})^2 - 4C^2\frac{B_n^2}{\rho\mu}}\right]/2}$$

$$\lambda_6 = u - \sqrt{\left[C^2 + \frac{B^2}{\rho\mu} + \sqrt{(C^2 + \frac{B^2}{\rho\mu})^2 - 4C^2\frac{B_n^2}{\rho\mu}}\right]/2}$$

$$\lambda_7 = u + \sqrt{\left[C^2 + \frac{B^2}{\rho\mu} - \sqrt{(C^2 + \frac{B^2}{\rho\mu})^2 - 4C^2\frac{B_n^2}{\rho\mu}}\right]/2}$$

$$\lambda_8 = u - \sqrt{\left[C^2 + \frac{B^2}{\rho\mu} - \sqrt{(C^2 + \frac{B^2}{\rho\mu})^2 - 4C^2\frac{B_n^2}{\rho\mu}}\right]/2}$$

where $C^2 = (\partial p/\partial \rho)_s$

The other end of the MFD application spectrum is defined by the interplanetary reentry environment. In this situation, the transport property of plasma can be characterized as to have electron number density up to a value of 10^{18}/cm^3 and the electric conductivity can be around 100 mho/m. Since the weakly ionized gas is generated by thermal collision, all internal degrees of freedom of the air mixture are excited and the temperatures of the translation, rotation, vibration, and dissociation modes are on the order of 11,000 K. This environment is nearly impossible to duplicate in a ground facility, and numerical simulation becomes necessary.

 As far as the chemical kinetics of the high temperature reacting gas is concerned, the population and depletion of any quantum state can be calculated using the Master equation but not without some degree of uncertainty [16,46,47]. In a thermodynamic and chemical non-equilibrium state, the calculation of gas mixture composition is dependent on the multi-temperature models [48].   In essence, the accuracy of the thermodynamic properties of the plasma is far from certain. Fortunately, even at the higher electron

number density condition, the ionization fraction is limited to the orders of magnitude from 10^{-5} to 10^{-3} range. Therefore, the dominant mechanisms in weakly ionized gas in MFD are the added Lorentz force and Joule heating. For this reason, a major portion of MFD computations did not include the chemical kinetics and the transport properties became an input to most computational investigations.

Even if the chemical composition is obtained from the finite-rate chemical kinetics, the link between charged species concentration and the transport properties of plasma is still missing. Again in most controlled environments, the plasma generation mostly uses glow discharge or radio frequency radiation [24,26,30,36,39,40,42]. A recent development to partially remedy this shortfall is using the drift-diffusion theory by Raizer and Surzhikov to model the glow discharge electrodynamic structure [49-51]. In nearly all aspects, the modeling of a glow discharge has provided a new alternative to describe a weakly ionized gas that is suitable for computing the magneto-aerodynamic interaction.
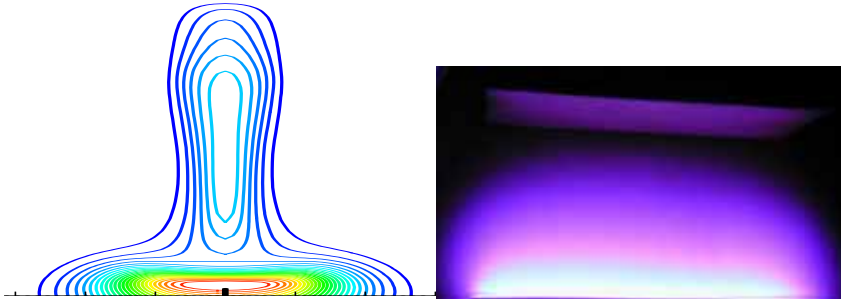

Fig. 6 Computed glow discharge and experimental results

Figure 6 depicts the computed glow discharge and experimental observation at the identical condition. The glow discharge is generated at a pressure of 5 Torr between two parallel electrodes at a distance of 5 cm apart. The applied electric field for glow discharge operation is lower than 360 volts. The values of electron number density distribution by two different approaches are similarly, in the range from 10^9 to $10^{11}/\text{cm}^3$. The electron temperatures are determined to be in the range of 100,000 K. From this numerical model the electric conductivity, current density, and electric field strength can be directly assessed.

The most impressive advancement in MFD research probably is the up-to-date capability in numerical simulations. In a short period of four years, the computing simulation capability has progressed from a stage of a rudimentary verification effort for Hartmann flow to the three-dimensional complex MFD flow control including the flow path of the MHD-bypass scramjet [28, 52-55]. For a complicated engineering analysis, the numerical result even includes the Hall current and ion slip in a convergent and divergent 3-D channel with segmented electrodes for flow control. This phenomenal achievement was built upon the shared knowledge among computational fluid dynamics (CFD) and computational electromagnetics (CEM) [56]. In essence, the accomplishments in CMD have built on the rich heritage of CFD in solving nonlinear partial differential equations for physics. This knowledge base is the essential ingredient for the plasma physics based simulations.

13

Gaitonde conducted the first ever and successful three-dimensional flow path in a MHD-Bypass scramjet – one of the highlights of the AJAX concept vehicle [53]. In this simulated configuration, the convergent inlet is connected to the divergent nozzle by a constant area combustor chamber at a flight Mach number of 8. In the inlet and nozzle coarsely segmented sidewall electrodes were mounted to provide Faraday operation. All chemical composition and plasma parameters are either specified or approximated by phenomenological relationships. The magneto-aerodynamic interaction parameter is simulated at a value of unity.
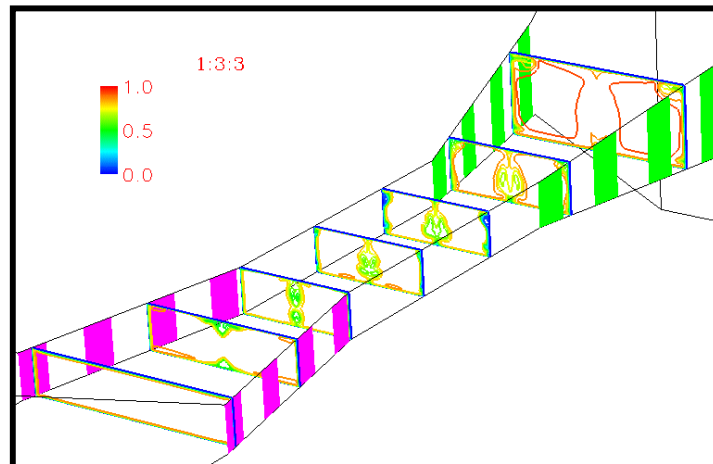
Fig. 7 Cross-flow in MHD scramjet flow path, Courtesy of Gaitonde (Ref.53)

The magnitude of the cross-flow plane velocity components is presented for the entire domain of simulation in Figure 7. To describe the flow field structure for better understanding, an aspect ratio of 1:3:3 of spatial dimensions is used in this graph. The viscous-inviscid interaction is clearly indicated. Away from the boundary-layer regions, the maximum momentum deficit occurs near the centerline of the channels, resulting in a wake-like velocity profile locally.

Fig. 8 Hall current in MHD Scramjet, Courtesy of Gaitonde (Ref. 53)

The effect of a realistic electrical conductivity described by a tensor is also simulated for this 3-D configuration. Specifically, the effectiveness of suppressing Hall current in a Faraday configuration is examined. In Figure 8, it is clearly shown that the coarse segmented electrode 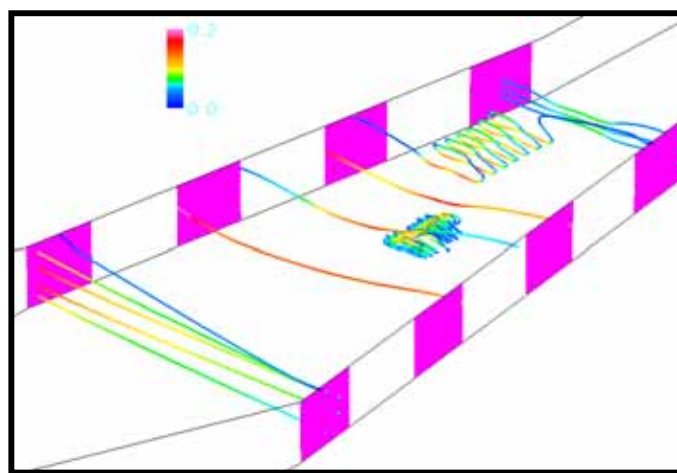arrangement is unable to annihilate this deleterious effect. In the scramjet inlet or the electric generator, the path of the electric current from the second anode downward enters the next streamwise anode. However, this behavior ceased for the fourth pair of electrodes, because the current continuity constraint. Eddy currents are stretched downstream due to the axial Hall field. A spiral pattern appears in the presentation corresponding to a complex Lorentz force field.

The numerical simulations of a MHD scramjet flow path demonstrate the present capability in analysis of a magneto-aerodynamic interacting field. For the configuration considered, the three-dimensional viscous-inviscid interaction impact strongly on the established current and Lorentz force fields. The inlet operating as a generator can indeed decelerate the flow but significantly reduces efficiency by the Joule heating. Integrated parameters reveal several anticipated tends and show that the peak magnetic forces are comparable to pressure forces and accrue a net drag penalty. More precise analysis requires additional refinement of ionization models and a fully self-consistent physical description of the constitutive relationships of the governing equations.

In numerical algorithm research for CMD, MacCormack, Gaitonde among others have made lasting contributions [52,54]. MacCormack expanded the flux vectors to preserve the homogeneous of degree one property for the MHD equations. He has found a Jacobian matrix that leads to the identical eigenvectors derived by Powell et al [45]. His effort has paved the way for applying characteristic-based schemes to CMD problems. Gaitonde's contributions to CMD have two major categories; first he has introduced all pertaining physics into this interdisciplinary endeavor [53]. The second contribution by Gaitonde is the improved numerical accuracy that is required to delineate the multiple temporal and physical scales from diffusion to shock wave. For some simulation, a spectral-like high-resolution numerical procedure is essential. To meet this requirement, he introduced a compact-differencing based algorithm to CMD and it has become one of the most effective modeling and simulation tools in CMD [52,56].

As impressive progress has been made in CMD, the working knowledge leads naturally to the basics of MFD. The most important and overlooked fact in CMD is that for most aerospace applications, the magnetic Reynolds number $R_m = uL\sigma\mu$, is much less that unity. Under this condition the induced electromagnetic field is negligible in comparison with the applied field, and the Lorentz force and Joule heating can be treated as a source term in the Navier-Stokes equations. A self-consistent electrical field must be ascertained by solving the charge conservation equation, $\partial\rho_e/\partial t + \nabla\cdot \mathbf{J} = 0$. This equation implicitly contains Gauss's law for the divergence free magnetic field strength, $\nabla\cdot \mathbf{B} = 0$. In plasma, the charge conservation law reduces to Poisson equation. Numerous techniques have been developed to solve Poisson equations for potential flow in fluid dynamics research. This physics-based simplification and understanding make all known numerical techniques that have been developed in CFD applicable for CMD.

Concluding Remarks

The maturation of a scientific discipline follows exactly the same tribulation of any human endeavor. The rate of progress and incisive understanding is strongly dependent on how knowledge is accumulated and transferred in times. The growth of magneto-fluid-dynamics is not exempt from this evolutionary pattern. A few lessons learned and shared will indeed be invaluable. In this spirit, the following observations are offered.

Magneto-Fluid-Dynamics is the last few frontiers in fluid dynamics. The difficult and urgency for turbulence research is well know and will be remained as the Achilles' heel for physics-based modeling and simulation technology. However, the development of MFD as an interdisciplinary technology to meet our future challenge in high-speed flight and access to space is equally critical.

A remarkable rate of progress has been made in magneto-fluid-dynamics both in experimental capability and numerical simulation just in the past few years. These impressive accomplishments reflect a stage of technical maturity that has reached a new horizon of understanding and attainment in plasma physics. The added dimension of magneto-aerodynamic interaction is the key ingredient for the long-sought-after enhancement to the desired aerodynamic performance.

The need to return to the basic science is absolutely essential to retain the recently grained information and to convert them into knowledge.

References

1. Langmuir, I., The interaction of Electron and Positive Ion Space Charge in Cathode Sheaths, Phys. Rev. Vol. 33, No. 6, 1929, p.954.
2. Cowling, T.G., Magnetohydrodynamics, Interscience Publishers, New York, 1957.
3. Mitchner, M. and Kruger, C.H., Partially Ionized Gas, John Wiley & Sons, New York, 1973.
4. Burgers, J.M. and van De Hulst, H.C., (ed.) Gas Dynamics of Cosmic Clouds, Interscience Publishers, New York, 1955.
5. Elsasser, W.M., Hydromagnetic Dynamo Theory, Rev. of Modern Physics, Vol. 28, April 1956, pp. 135-163.
6. Sutton, G.W. and Sherman, A., Engineering Magnetohydrodynamics, McGraw-Hill, New York, 1965.
7. Kurchatov, I.V., Thermonuclear Fusion, Gas Discharge Research in the Soviet Union, Engineering, London, Vol. 181, No. 4705, May 1956, pp.332-325.
8. Post, R.F., Control Fusion Research - An Application of the Physics of High Temperature Plasma, Rev. of Modern Physics, Vol. 28, No. 3, July 1956, pp.338-382.
9. Kantrowitz, A.A., A Survey of Physical Phenomena Occurring in Flight at Extreme Speeds, Proc. On High Speed Aerodynamics, Polytechnic Inst. Of Brooklyn, January 1955, pp. 335-339.
10. de Hoffman, F. and Teller, E., Magneto-Hydrodynamic Shocks, Phy. Rev., Vol. 80, 1950, pp. 692-703.

11. Taniuti, J.A., Non-Linear Wave Propagation, Academic Press, New York, 1964.
12. Cabannes, H., Theoretical Magnetofluiddynamics, Academic Press, New York, 1970.
13. Courant, R., Hilbert, D., Methods of Mathematical Physics, Vol. 2, New York, Interscience, 1962, pp-612-618.
14. Resler, E.L., Sears, W.R., The Prospect for Magneto-aerodynamics, J. Aero. Science 1958, Vol. 25, 1958, pp. 235-245 and 258.
15. Engel, A.V., and Steenbeck, M., Electrische Gasentladunggen, Edwards Brother inc., 1944, (Julius Springer 1932).
16. Zel'dovich, Ya. B., and Raizer, Yu. P., Physics of Shock Waves and High-Temperature Hydrodynamic Phenomena, Dover Publications, Mineola NY, 2002.
17. Bush W.B. Magnetohydrodynamics-Hypersonic Flow Past a Blunt body, J. Aero. Science, Vol.25, 1958, pp.685-690 and 728.
18. Meyer, R.C., On Reducing Aerodynamic Heat-Transfer Rates by Magneto-hydrodynamic techniques, J. Aero. Science, 1958, pp. 561-572.
19. Ziemer R.W., Experimental Investigation in magneto-Aerodynamics, Amer. Rocket Soc. J. 1959, Vol. 29, pp. 643-647.
20. Shang, J.S., Recent Research in Magneto-Aerodynamics, Progress in Aerospace Sciences, Vol. 31, 2001, pp. 1-20.
21. Panel on Physics of Plasma and Fluid, Physics Through the 1990's Plasma and Fluid, National Academy Press, Washington DC, 1986.
22. Bout, D.A. and Robert, A.G., Interaction of an Ionizing Shock Wave with a Transverse Magnetic Field, Phys. Fluids, Vol. 13, no. 6, 1970, pp. 1473- 1479.
23. Mishin, A.P., Bedin, N.I., Yushchenkova, G.E., Ryazin, A.P., Anomalous relaxation and Instability of Shock Waves in Gases. Sov. Phys. Tech. Vol. 26, 1981, pp. 1363-1368.
24. Klimov, A.I., Koblov, A.N., Mishin G.I., Serov, Yu. L., Yavor, I.P., Shock Wave Prpopagation in a glow Discharge. Sov. Tech. Physics Letter, Vol. 4, 1982, pp.192-194.
25. Heald, M.A., and Wharton, C.B., Plasma Diagnostics with Microwaves, John Wiley & Sons, 1965.
26. Roe, P.L., Characteristic –based Schemes for the Euler Equations, Annual Rev. Fluid Mechanics, Vol.18, 1986, pp. 337-365.
27. Brio M. and Wu, C.C., An upwind Differencing Scheme for the Equations of Ideal Magnetohydrodynamics, J. Comp. Physics, Vol. 75, 1988, 400-422.
28. Gaitonde, D.V., Development of a Solver for 3-D Non-ideal Magneto-gasdynamics, AIAA 99-3610, Norfolk VA, June 1999.
29. Gurijanov, E.P. and Harsha, P.T., Ajax: New Direction in hypersonic technology, AIAA Preprint 96-4609, Nov. 1996.
30. Bityurin V.A., Velikodny, V. Yu., Klimov, A.I., Leonov, S.B., Potebnya, V.G., Interaction of shock Waves with a Pulse electrical Discharge, AIAA 99-3533, June 1999.
31. Ganiev, Y.C., Gordeev, V.P., Krasilnikov, A.V. Lagutin, V.I., Otmennikov, V.N., Panasenko, A.V., Aerodynamic Drag Reduction by Plasma and Hot-Gas Injection, J. Thermo Heat Transfer, Vol. 14, No. 1, 2000, pp10-17.

32. Fomin V.M., Maslov, A.A., Malmuth N.D., Formichev V.P., Shashkin, A.P., Korotaeva, T.A., Shipyuk, A.N., Pozdnyakov, G.A., Influence of a Counterflow Plasma Jet on Supersonic Blunt-Body Pressures, AIAA J. Vol. 40, No.6, 2002, pp. 1170-1177

33. Shang, J.S., Plasma Injection for Hypersonic Blunt-Body Drag Reduction, AIAA J. Vol. 40, No. 6, 2002, pp.1178-1186.

34. Shang, J.S., Hayes, J.R., and Menart, J., Hypersonic Flow Over a Blunt Body with Plasma Injection", J.S. Shang, J.R. Hayes, and J. Menart, J. Spacecraft and Rockets Vol. 39, No. 3, May-June 2002, pp. 367-375.

35. Shang, J.S., Hayes, J., Menart, J., and Miller, J., Blunt Body in Hypersonic Electromagnetic Flow Field, J. of Aircraft, Vol. 40, No. 2, 2003, pp. 314-322.

36. Chernyi, G.G., Some Recent Results in Aerodynamic Applications of Flows with Localized Energy Addition, AIAA 99-4819, Norfolk VA, Nov. 1999.

37. Miles, R.B., Flow control by Energy Addition into High-speed Air, AIAA 2000-2324, Denver CO, June 1999.

38. Knight, D.D., Survey of Aerodynamic Flow control at High Speed by Energy Deposition, AIAA 2003-0525, Reno NV, January 2003.

39. Bityurin V.A., Velikodny, V. Yu., Klimov, A.I., Leonov, S.B., Potebnya V.G., Interaction of Shock Waves with a Pulse electrical discharge, AIAA 99-3533, Norfolk VA, June 1999.

40. Kolesnichenko, Y., Basics of Microwave Discharge Application to Supersonic Aerodynamics, AIAA 2003-3869, Orlando FL, June 2003.

41. Howatson, A.M., An Introduction to Gas Discharges, 2nd Edition, Pergamon Press, Oxford, 1975.

42. Menart, J., Shang, J.S., Kimmel, R. and Hayes, J., Effects of magnetic Fields on Plasma Generated in Mach 5 Wind Tunnel, AIAA 2003-4165, Orlando FL, June 2003.

43. Gombosi, T.I, De Zeeuw, D.L., Haberli, R.M., Powell, K., Three-dimensional Multiscale MHD Model of Cometary Plasma Environments, J. Geophysical Res., Vol. 101, No. A7, 1996, pp. 15,233-15,253.

44. Dai, W. and Woodward, P.R., A simple Finite Difference Scheme for Multi-dimensional Magnetohydrodynamical Equations, J. Comp. Phys, Vol. 142, 1998, pp. 331-369.

45. Powell, K. G., Roe, P.L., Linde, T.J., Gombsi, T.I. and De Zeeuv, D.L., A solution Adaptive Upwind Scheme for Ideal Magnetohydrodynamics, J. Comp. Phys, Vol. 154, 1999, pp. 284-309.

46. Clark, J.F. and McChesney, M., The Dynamics of Real Gases, Butterworths, Washington, DC, 1964.

47. Josyula, E., Computational Study of Vibrationally relaxing gas past Blunt body in Hypersonic Flows, J. Thermophysics, Heat Transfer, Vol. 14, 2000, pp.18-26.

48. Park, C., Nonequilibrium Hypersonic Aerothermodynamics, John Wiley and Sons, 1990.

49. Raizer, Yu. P. and Surzhikov, S.T., Two-dimensional Structure of the Normal Glow Discharge and the Role of Diffusion in Forming of Cathode and Anode Current Spots, High Temperatures, No. 3, Vol. 26, 1988.

50. Surzhikov, S.T. and Shang, J.S., Glow Discharge in Magnetic Field with Heating of Neutral Gas, AIAA 2003-3654, Orlando FL., 23-26 June 2003.

51. Surzhikov, S.T. and Shang, J.S., Supersonic Internal Flows with Gas Discharge and External Magnetic Field, AIAA 2003-3625, Orlando FL., 23-26 June 2003.

52. Gaitonde, D., Higher-Order Solution Procedure for Three-dimensional Non-ideal magnetogasdynamics, AIAA J., Vol. 39, No. 1, 2001, pp. 2111-2120.

53. Gaitonde, D., Three-Dimensional Flow through Scramjet Simulation with MGD Flow Energy-Bypass, AIAA 2003-0172, January 2003.

54. MacCormack, R.W., A Conservative Form Method for Magneto-Fluid Dynamics, AIAA 2001-0195, January 2001.

55. Dietiker, J.F. and Hoffmann, K.A., Numerical Simulation of Turbulent Magneto-hydrodynamic Flows, AIAA 2001-2737, June 2001.

56. Shang, J.S., Shared Knowledge in Computational Fluid Dynamics, Electro-magnetics, and Magneto-Aerodynamics, Progress in Aerospace Sciences, Vol. 38, 2002, pp. 449-467.

MAGNETO AND ELECTROMAGNETIC FLUID DYNAMICS

Jacques C.J. Nihoul
Liège University, Belgium

1. Electromagnetic equations

The electromagnetic field is characterized by (i) the electric field **E**, (ii) the electric "displacement" field **D**, (iii) the magnetic field **H**, (iv) the magnetic induction field **B**, (v) the density current field **J** (ampere m^{-2}), (vi) the electric charge distribution γ (coulomb m^{-3}).
The governing equations are
(i)   the Maxwell equations

$$\frac{\partial \mathbf{B}}{\partial t} = -\nabla \wedge \mathbf{E}$$

$$\frac{\partial \mathbf{D}}{\partial t} = \nabla \wedge \mathbf{H} - \mathbf{J}$$

(ii)   the charge conservation equation

$$\frac{\partial \gamma}{\partial t} + \nabla \bullet \mathbf{J} = 0$$

Considering that $\nabla \bullet (\nabla \wedge) = 0$, one can show that these equations imply

$$\nabla \bullet \mathbf{B} = 0$$

$$\nabla \bullet \mathbf{D} = \gamma$$

2. Hydrodynamic equations

The hydrodynamic field is characterized by
(i)   the velocity field **v**, (ii) the mass density ρ(kg m^{-3})
(iii)   the entropy η (m^2 s$^{-2}\kappa^{-1}$).
The governing equations are

$$\rho \frac{d\mathbf{v}}{dt} = \mathbf{F} + \mathbf{G} + \nabla \bullet \mathbf{T}$$

where **F** is the resultant electromagnetic force (per unit volume), **G** the resultant of other forces (per unit volume) and **T** is the stress tensor ($\nabla \bullet \mathbf{T}$ represent internal forces in the *deformable* fluid).

$$\frac{d\rho}{dt} + \rho \nabla \bullet \mathbf{v} = 0$$

$$\rho \frac{d\eta}{dt} = Q^{\eta} - \nabla \bullet \varphi_{\eta}$$

where Q^{η} is the rate of local production (or destruction) of entropy by viscous and Ohmic dissipations, radiation and eventual other sources and φ^{η} the molecular flux of entropy

$$\frac{d}{dt} = \frac{\partial}{\partial t} + \mathbf{v} \bullet \nabla$$

3. Magnetohydrodynamic equations

The electromagnetic and hydrodynamic equations are not sufficient to describe the electro-magneto-hydrodynamic system. The number of unknown exceeds the number of equations. To solve the problem, one must have additional equations which are called "*constitutive*" as they are based on characteristic properties of the fluid or "*state equations*" based on assumptions of the state of the fluid, although the distinction is neither easy to make nor important.

(i) It is generally assumed that $\mathbf{D}$ is a linear function of $\mathbf{E}$

$$\mathbf{D} = \varepsilon \mathbf{E}$$

where ε may be a constant ε_0 or not or even a tensor (with scalar multiplication by $\mathbf{E}$) in the case of an anisotropic material ($\varepsilon_0 \sim 8.854 \ 10^{-12}$ MKS).

(ii) Similarly, one may assume that the magnetic field is a function of the magnetic induction only, i.e.

$$\mathbf{B} = \mu \mathbf{H}$$

If one excludes ferromagnetic materials, μ can be taken as a constant μ_0

$$\mu \sim \mu_0 \sim 4\pi \ 10^{-7} \text{ MKS} = \varepsilon_0^{-1} c^{-2}$$

where c is the speed of light

$$c = 2.998 \ 10^8 \text{ ms}^{-1}$$

(iii) The electromagnetic force $\mathbf{F}$ can be written as the resultant of the action of the electric field on electric charges and of the Lorentz Force resulting from the interaction of currents and magnetic fields

$$\mathbf{F} = \gamma\mathbf{E} + \mathbf{J} \wedge \mathbf{B}$$

This formulation doesn't take into account polarization and assumes that **the fluid is not ferromagnetic**.

(iv) The current density vector $\mathbf{J}$ is a function of the electric and magnetic field. The simplest form of this function , in a solid conductor, is Ohm's law

$$\mathbf{J} = \sigma\mathbf{E}$$

where σ is the conductivity.

In a liquid conductor in motion, there is current of convection (due to the transport by the fluid of macroscopic electric charges) in addition to the current of conduction. In addition to $\mathbf{E}$, there is an induced electric field $\mathbf{v} \wedge \mathbf{B}$ produced by the motion of the conducting fluid in the magnetic field.
Hence

$$\mathbf{J} = \gamma\mathbf{v} + \sigma\left(\mathbf{E} \wedge \mathbf{B}\right)$$

The pertinence of this equation for a plasma will be discussed later.

(v) Assuming the fluid to be "Newtonian", the stress tensor is usually represented as the sum of an isotropic diagonal part and a symmetric tensor proportional to the deformation tensor $\mathbf{D}$

$$\mathbf{T} = \left(- p + \lambda\nabla \bullet \mathbf{v}\right)\mathbf{I} + 2\rho\nu\mathbf{D}$$

$$D_{ij} = \frac{1}{2}\left(\frac{\partial v_i}{\partial x_j} + \frac{\partial v_j}{\partial x_i}\right)$$

where p is the "pressure" and where ν is the kinematic viscosity.
Beside of the assumption of the fluid being *Newtonian* (i.e. $\mathbf{T}$ a linear function of $\mathbf{D}$), this formulation contains other hypotheses, assuming, for instance, that the diagonal part of the tensor is isotropic ignoring the fact that in the presence of a magnetic field, the pressure could be different in directions parallel and perpendicular to the magnetic field, and leading one to believe that the cinematic viscosity is not a function of the magnetic field.

(vi) The relation between the stress tensor $\mathbf{T}$ and the deformation tensor $\mathbf{D}$ reveals a new variable which, at best, reduces to a scalar, the "pressure" p. An additional equation is necessary to relate p to the other variables ($\rho, \eta \ldots$).
In this chapter, to emphasize the interactions between the electromagnetic field and the hydrodynamics, one shall leave out thermodynamic effects and assume that ρ is constant or a function of p only. In this case, our system of equations is closed without taking into account the evolution equation for η.

(vii) In most situations, considering typical values of ε, σ, and typical time scales and length scales, one finds

$$\gamma \mathbf{v} \ll \sigma \mathbf{E}$$

$$\frac{\partial \mathbf{D}}{\partial t} \ll \sigma \mathbf{E}$$

$$\gamma \mathbf{E} \ll \mathbf{J} \wedge \mathbf{B}$$

and one may neglect all terms containing γ and $\mathbf{D}$ from the equations.

(viii) Ohm's law revisited
If we have a plasma, and we shall assume for simplicity that it contains only positive ions and electrons, one can describe its dynamics within the framework of theoretical physics by introducing a distribution function (x standing for + or -)

$$f^x (\mathbf{r}, \mathbf{u}, t)$$

such that $f^x \, d\mathbf{r} \, d\mathbf{u}$ is the probability of finding particles of charge "x" (x = + or -) within the 6-dimensional volume element $d\mathbf{r} \, d\mathbf{u}$ centred at the point $(\mathbf{r}, \mathbf{u})$ in coordinate and velocity space. Observable properties of the plasma can be obtained from the distribution function by taking various velocity moments of f, e.g.

$$n^x (\mathbf{r}, t) = \int f^x (\mathbf{r}, \mathbf{u}, t) d\mathbf{u}$$

$$\mathbf{v}^x (\mathbf{r}, t) = \frac{1}{n^x} \int \mathbf{u} f^x (\mathbf{r}, \mathbf{u}, t) d\mathbf{u}$$
and

$$\rho^x = n^x m^x \qquad \rho = n^+ m^+ + n^- m^-$$

$$\gamma^x = n^x q^x \qquad \gamma = n^+ q^+ + n^- q^-$$

$$\rho \mathbf{v} = \rho^+ \mathbf{v}^+ + \rho^- \mathbf{v}^-$$

$$\mathbf{J} = \gamma^+ \mathbf{v}^+ + \gamma^- \mathbf{v}^-$$

By taking successive moments of the "kinetic equation" describing the space, time and velocity evolution of f, one obtains macroscopic equations for both the ion and electron gases and these can be combined to give dynamic equations of the plasma considered as a fluid.

From the definition of $\rho \mathbf{v}$ and $\mathbf{J}$ given above, it it obvious that if the equation for the velocity is a partial differential equation, so must be the equation for the current.

Writing the Ohm's law as an algebraic equation, one actually assumes immediate adaptation to initial conditions and abrupt adaptation to boundary conditions. This results in ignoring extra modes of oscillations and boundary layers conditions.
However, even if one neglects these effects and reduce the Ohm's law to an algebraic equilibrium budget, one finds that it should be written (neglecting $\gamma \mathbf{v}$)

$$\mathbf{J} = \sigma(\mathbf{E} + \mathbf{v} \wedge \mathbf{B}) - \alpha \mathbf{J} \wedge \mathbf{B}$$

σ and α may be evaluated from the kinetic theory of gases in terms of the characteristic time τ separating two collisions. One finds

$$\frac{\alpha \mathbf{J} \wedge \mathbf{B}^{\tau}}{\sigma \mathbf{v} \wedge \mathbf{B}} \sim O\left(\frac{e\mathbf{B}}{m} \tau\right) = \omega_c \tau$$

where e and m^- refer to the electron's charge and mass and ω_c is the so-called "cyclonic frequency" i.e. the characteristic frequency of rotation of a particle of charge e and mass m^- around the direction of the magnetic field. The additional term is called the "Hall effect". One can see that it is negligible if the time between collisions is small compared to the time needed for the particle to complete a rotation around the magnetic field line. In the opposite situation, however, the Hall effect is dominant.

Using the Maxwell's law and the constitutive equations (within their limits of validity), one can eliminate $\mathbf{E}, \mathbf{J}, \gamma$ … and derive a fundamental set of equations for ρ; $\mathbf{v}$ and $\mathbf{B}$ which one refers to as the *Magnetohydrodynamic Equations.*

The equation for $\mathbf{B}$ reads

$$\frac{\partial \mathbf{B}}{\partial t} + \mathbf{v} \bullet \nabla \mathbf{B} = \mathbf{B} \bullet \nabla \mathbf{v} - \mathbf{B}(\nabla \bullet \mathbf{v}) + \nu_m \nabla^2 \mathbf{B}$$

where

$$\nu_m = (\mu \sigma)^{-1}$$

is the *magnetic viscosity.*

If v and ℓ represent respectively a characteristic velocity and a characteristic length of the spatial variations of the magnetohydrodynamic fields, one defines the *magnetic Reynolds number* as

$$R_m = \frac{v\ell}{\nu_m}$$

The magnetic Reynolds number is a measure of the relative importance of the inertia terms and the dissipation term.

It is illuminating to consider two asymptotic cases

(i) $R_m \gg 1$

Neglecting dissipation, the equation for $\mathbf{B}$ can be written, using the equation of conservation of mass,

$$\frac{d}{dt}\left(\rho^{-1}\mathbf{B}\right) = \rho^{-1}\mathbf{B} \bullet \nabla\mathbf{v}$$

If we consider an element of fluid $\delta\mathbf{r}$, one can write

$$\frac{d}{dt}\left(\delta\mathbf{r}\right) = \delta\frac{d\mathbf{r}}{dt} = \delta\mathbf{v} = \delta\mathbf{r} \bullet \nabla\mathbf{v}$$

Hence the equation for $\delta\mathbf{r}$ is the same as the equation for $\rho^{-1}\mathbf{B}$.

If, at $t = 0$, the two vectors are parallel, they will remain so at ulterior times, i.e. all fluid particles which are initially on a magnetic field line remain on the field line in the motion of a perfectly conducting fluid. The magnetic field is *frozen* in the fluid.

(ii) $R_m \ll 1$

If a uniform magnetic field $\mathbf{B}_o$ is applied, the magnetic field $\mathbf{B}$ is the sum of $\mathbf{B}_o$ and an induced field $\mathbf{B}_1$ given by

$$\frac{\partial \mathbf{B}_1}{\partial t} + \mathbf{v} \bullet \nabla\mathbf{B}_1 - \mathbf{B}_1 \bullet \nabla\mathbf{v} + \mathbf{B}_1\left(\nabla \bullet \mathbf{v}\right) = \mathbf{B}_o \bullet \nabla\mathbf{v} - \mathbf{B}_o\left(\nabla \bullet \mathbf{v}\right) + \nu_m\nabla^2\mathbf{B}_1$$

One can estimate the orders of magnitude of the different terms using the characteristics velocity v and the characteristic length ℓ . With v , ℓ and ν_m , one can construct two characteristic times

$$\tau_1 = \frac{\ell^2}{\nu_m} \qquad \text{and} \qquad \tau_2 = \frac{\ell}{v}$$

The first one is the characteristic time of adaptation of the magnetic field, the second one the characteristic time of the modification of that field to the fluid's motion.
With $R_m \ll 1$, $\tau_1 \ll \tau_2$. One may thus consider that the magnetic field adapts itself quasi instantaneously to the modifications of the fluid's motion and consequently evolves with the characteristic time τ_2 of the latter.
Estimating the orders of magnitude of the different terms of the equation for the magnetic field, one can see that all the terms of the left-hand side are negligible as compared with the last term of the right-hand side. This term is of the order

$$\nu_m\frac{B_1}{\ell^2}$$

and must be balanced by the first two terms of the right-hand side, of the order of

$$\frac{B_o v}{\ell}$$

This implies

$$B_1 \sim \frac{v\ell}{v_m} B_o = R_m B_o \ll B_o$$

Hence in a weakly conducting fluid, the induced magnetic field is negligible as compared to the applied magnetic field.
The magnetic field is said to be *rigid*.

MAGNETOHYDRODYNAMIC WAVES

Jacques C.J. Nihoul
Liège University, Belgium

1. Magneto-acoustic waves

To study the waves that can propagate within a conducting fluid, we consider an infinite medium and the small perturbations of a reference state $\mathbf{v} = 0$, $\mathbf{B} = \mathbf{B}_o$, $\rho = \rho_o$, $\eta = \eta_o$.
For simplicity, we assume iso-entropic, non dissipative waves $(R \gg 1,\ R_m \gg 1)$.
We seek a solution

$$\mathbf{v} = \mathbf{u} \qquad ; \qquad \rho = \rho_0(1+\delta) \qquad ; \qquad p = p_0 + \rho_0 a^2 \delta$$

and

$$\frac{\mathbf{B}}{\sqrt{\mu\rho_0}} = \mathbf{b} = \mathbf{b}_0 + \boldsymbol{\beta}$$

where a is the sound speed.
Neglecting second order terms and eliminating δ and $\boldsymbol{\beta}$, we obtain an equation for $\mathbf{u}$

$$\frac{\partial^2 \mathbf{u}}{\partial t^2} = a^2\ \nabla(\nabla \bullet \mathbf{u}) + \left\{\nabla \wedge \left[\nabla \wedge (\mathbf{u} \wedge \mathbf{b}_0)\right]\right\} \wedge \mathbf{b}_0$$

We seek a solution of the form

$$\mathbf{u} = \mathrm{Re}\ \mathbf{U}\ e^{i(\mathbf{k}\bullet\mathbf{x}-\omega t)}$$

We may choose a system of reference such that the magnetic field is in the direction $\mathbf{e}_1$ and the wave number vector in the plane $\mathbf{e}_1, \mathbf{e}_2$

$$\mathbf{b}_0 = b_0\ \mathbf{e}_1$$

$$\mathbf{k} = k_1\mathbf{e}_1 + k_2\mathbf{e}_2 = k\cos\theta\ \mathbf{e}_1 + k\sin\theta\ \mathbf{e}_2$$

Substituting in the partial differential equation for $\mathbf{u}$, we obtain an algebraic vectorial equation for $\mathbf{U}$ which, projected on the three axes, gives

$$c^2 U_1 = a^2\left(U_1\cos\theta + U_2\sin\theta\right)\cos\theta$$

$$c^2 U_2 = a^2\left(U_1\cos\theta + U_2\sin\theta\right)\sin\theta + b_0^2 U_2$$

$$c^2 U_3 = b_0^2\cos^2\theta\,U_3 = 0$$

where $c = \dfrac{\omega}{k}$ is the "*phase velocity*".

These equations are algebraic homogenous equations for U_1, U_2, U_3. The existence of a non trivial solution requires that the determinant of the coefficients be zero. This condition gives the so-called "*dispersion equation*"

$$c^2 = b_0^2 \cos^2 \theta$$

or

$$c^4 - \left(a^2 + b_0^2\right)c^2 + a^2 b_0^2 \cos^2 \theta = 0$$

We have three solutions which we shall denote by c_a, c_ℓ, c_r $c_r^2 \geq c_\ell^2 \geq 0$

It is illuminating to consider first a few particular cases.

(i) $c = c_a = b_0 \cos\theta$
      The first dispersion relation is satisfied. The other becomes

$$b_0^4 \cos^2 \theta \left(\cos^2 \theta - 1\right) = 0$$

      and can only be satisfied if $\theta = 0$ or $\theta = \dfrac{\pi}{2}$.
      Outside these two cases

$$U_1 = U_2 = 0$$

      The vector $\mathbf{U}$ is thus perpendicular to $\mathbf{B}_0$ and $\mathbf{k}$.
      The waves are transversal waves.

(ii) If $\theta = 0$, the wave propagates in the direction of the magnetic field.
      The three roots of the dispersion equations are

      $c_a = b_0$, $c_r = a$, $c_\ell = b_0$ if $a > b_0$
      $c_a = b_0$, $c_r = b_0$, $c_\ell = a$ if $a < b_0$

      The solution $c = b_0$ satisfies both dispersion equations and the equations for U_1, U_2, U_3 reduce to

$$b_0^2 U_1 = a^2 U_1$$
$$b_0^2 U_2 = b_0^2 U_2$$
$$b_0^2 U_3 = b_0^2 U_3$$

      Hence if $b_0 \neq a$, $U_1 = 0$. The vector $\mathbf{U}$ is again perpendicular to $\mathbf{k}$ (and $\mathbf{b}_0$).
      The waves are transversal waves.

There is a second solution
$$c = a, \qquad U_2 = U_3 = 0$$

These are *longitudinal waves* ; they are *acoustic waves* propagating with the sound velocity a .

(iii) If $\theta = \dfrac{\pi}{2}$, the waves propagate perpendicularly to the magnetic field

$$c_r = \left(a^2 + b_0^2\right)^{\frac{1}{2}} \qquad c_\ell = c_a = 0$$

$$\left(a^2 + b_0^2\right) U_1 = 0$$

$$\left(a^2 + b_0^2\right) U_2 = \left(a^2 + b_0^2\right) U_2$$

$$\left(a^2 + b_0^2\right) U_3 = 0$$

The vector $\mathbf{U}$ is parallel to the direction of propagation. These waves are *longitudinal waves*. They are "sound" waves which do not propagate with the velocity of sound but with the velocity c_r .

(iv) If $b_0 = 0$

$$c_r = a \qquad\qquad c_\ell = c_a = 0$$
$$U_3 = 0 \qquad\qquad \dfrac{U_2}{U_1} = tg\,\theta$$

The vector $\mathbf{U}$ is directed along $\mathbf{k}$. These are *longitudinal waves*, the classical acoustic waves.

(v) If $\rho = \rho_0$, $\delta = 0$

$$c_r = \infty \; , \; c_a = c_\ell = b_0\cos\theta$$

On the other hand, $\delta = 0$ yields

$$\nabla \bullet \mathbf{u} = 0 \qquad \text{i.e} \quad \mathbf{k} \bullet \mathbf{U} = 0$$

These waves are *transversal waves*, propagating with the phase speed $b_0 \cos\theta$. The group speed is $\mathbf{c}_g = \mathbf{b}_0$, energy is propagated along the magnetic lines of force.
In the general case, one has three solutions

$$c_a = c_a(\theta) \quad , \qquad c_r = c_r(\theta) \quad , \qquad c_\ell = c_\ell(\theta)$$

The phase speed doesn't depend on the wave length but only on the direction of the wave number vector $\mathbf{k}$.

3

2.   Magneto-shock waves

We consider now the propagation of shock waves in a conducting fluid. These waves are characterized by extremely high gradients of the state variables (pressure; density …) at the *wave front* which can be regarded, from a mathematical point of view, as a surface of discontinuity.

In axes moving with the surface of discontinuity, the jumps of the state variables can be easily derived from the magnetohydrodynamic boundary conditions at a surface of discontinuity, a special case of the boundary conditions appropriate to magnetohydrodynamic equations.

If the subscripts 1 and 2 refer respectively to the state variables before the shock (upstream of it) and after the shock (downstream of it), introducing new variables

$$\mathbf{b} = \frac{\mathbf{B}}{\sqrt{\mu^1 \rho}} \qquad ; \qquad \pi = \frac{p}{^1\rho} \qquad ; \qquad r = \frac{^1\rho}{\rho}$$

$$u_n = \frac{\mathbf{v} \bullet \mathbf{n}}{r} \qquad ; \qquad b_n = \mathbf{b} - (\mathbf{b} \bullet \mathbf{n})\mathbf{n}$$

$$\mathbf{v}_t = \mathbf{v} - (\mathbf{v} \bullet \mathbf{n})\mathbf{n} \; ; \qquad \mathbf{b}_r = \mathbf{b} - (\mathbf{b} \bullet \mathbf{n})\mathbf{n}$$

where $\mathbf{n}$ is normal to the surface of discontinuity, one obtains (ε denoting the internal energy per unit mass and a bracket the jump from upstream to downstream values)

$$\left[\mathbf{v} b_n - \mathbf{b} r u_n \right] = 0$$

$$\left[u_n \mathbf{v} - b_n \mathbf{b} + \left(\pi + \frac{1}{2} b^2 \right)\mathbf{n} \right] = 0$$

$$\left[u_n \mathbf{v}_t - b_n \mathbf{b}_t \right] = 0$$

$$\left[u_n^2 r + \pi + \frac{1}{2} b_t^2 \right] = 0$$

$$\left[u_n^2 \left(\frac{1}{2} u_n^2 r^2 + \frac{1}{2} v_t^2 + \varepsilon + \pi r \right) - b_n \left(\mathbf{v}_t \bullet \mathbf{b}_1 \right) + u_n r b_t^2 \right] = 0$$

We can eliminate $\mathbf{v}_t$ between these equations. Noting by an over-bar the arithmetic mean of the values of a variable on both sides of the front, we obtain

$$\left[\varepsilon \right] + \bar{\pi}[r] + \frac{1}{4} \left\| [\mathbf{b}_t] \right\|^2 [r] = 0$$

This is the magnetohydrodynamic equivalent of the Rankine-Hugoniot equation of gas dynamics and it reduces to it in the absence of a magnetic field.

One can see that in a fluid of constant density $[r] = 0$ and thus $[\varepsilon] = 0$. Such a shock wave allows only discontinuities of the tangential components of the velocity and the magnetic field (with an associated surface current). These shock waves are called "Alfven shock waves".

We can choose a system of reference such that $\mathbf{e}_1$ is directed along the normal $\mathbf{n}$ of the discontinuity surface and the mean magnetic field is in the plane $\mathbf{e}_1$, $\mathbf{e}_2$.
The equations above yield six algebraic equations for $[v_1]$, $[v_2]$, $[v_3]$, $[r]$, $[b_2]$, $[b_3]$.
The system has solutions only if the determinant of the coefficients is zero. This gives the equivalent of "dispersion relations".

Setting

$$b_0 = \frac{\bar{b}}{\sqrt{\bar{r}}} \qquad , \qquad a^2 = -\frac{[\pi]}{[r]}$$

where a is the finite difference equivalent of the sound speed, the dispersion relations are identical to those obtained for the magneto-acoustic waves with u_n standing in place of the phase speed c. Solutions exist for $u_n = c_a$, $u_n = c_r$, $u_n = c_\ell$.

A similar type of analysis shows that

(i)   For $u_n = c_a$, $\theta \neq 0$, $\frac{\pi}{2}$

   $[r] = 0$, $[v_1] = 0$, $\bar{b}_2[b_2] = 0$, $[\varepsilon] = 0$, $[\eta] = 0$

   These waves are the Alfven waves mentioned above.
   For the chosen system of reference

   $$\bar{b}_2[b_2] = \mathbf{b}_t \bullet [\mathbf{b}_t] = \frac{1}{2}[b_t^2] = 0$$

   Hence the principal effect is a rotation of the tangential component of the magnetic field.

(ii)   If $\theta = 0$

   $b_2 = 0$, $c_a = c_\ell = b_0 =$, $c_r = a$ $(a > b_0)$

   For the waves corresponding to c_a or c_ℓ

   $[r] = 0$, $[v_1] = 0$, $[\varepsilon] = 0$, $[\eta] = 0$, $\bar{b}_2 = \bar{b}_3 = 0$

   These are the same waves as above.

   For the waves corresponding to $c_r = a$

$[v_2] = [v_3] = [b_2] = [b_3] = 0$

However discontinuities of v_1 and r are possible.
Since $\bar{b}_2 = \bar{b}_3 = 0$, one also has $b_2 = b_3 = 0$.
If the fluid is at rest upstream $v_2 = v_3 = 0$ and the Rankine-Hugoniot equation reduces to the classical hydrodynamic form

$$[\varepsilon] + \bar{\pi}[r] = 0$$

These waves are in fact the classical shock waves of Gas Dynamics.

(iii) If $\theta = \dfrac{\pi}{2}$

$$b_n = 0, \qquad c_a = c_\ell = 0 \qquad c_r = \sqrt{b_0^2 + a^2}$$

The waves corresponding to c_r are characterized by

$$[v_2] = [v_3] = [b_3] = 0$$

with possible discontinuities of v_1, r and $b_2 = b$.
Setting

$$\pi^* = \pi + \frac{1}{2} b^2$$

$$\varepsilon^* = \varepsilon + \frac{1}{2} r b^2$$

The Rankine-Hugoniot equation becomes

$$[\varepsilon^*] + \bar{\pi}^*[r] = 0$$

(iv) The waves corresponding to the velocities c_r and c_ℓ are called "*fast shock waves*" and "*slow shock waves*" respectively.
For these waves, $[v_3] = [b_3] = 0$ hence $b_3 = 0$ on both sides of the surface of discontinuity.
If v_3 is zero upstream, it is also zero downstream and we have a two-dimensional problem.

6

Combining the basic equations, it is easy to show that

$$\left[\tfrac{1}{2}\,b_t^2\right]=\left(a^2-u_n^2\right)[r]$$

As[1.] $T\,[r]<0$, $\|b_t\|$ increases through a fast shock and decreases through a slow shock.

One can thus imagine switch shocks : a slow shock behind which $\mathbf{b}_t = 0$ switching of the magnetic field, a fast shock before which $\mathbf{b}_t = 0$ switching on the magnetic field.

References

Ericson, W.B. and Bazar, J., (1958). *Astrophys. J.,* **129, 758.**

Ericson, W.B. and Bazar, J., (1960). *Phys. Fluids,* **3**, 631.

Friedrichs, K.O. and Kranzer, H., (1958). *Non-linear Wave Motion, Notes on Magnetohydrodynamics VIII*, New York University Report, NYO, 6486.

Jeffrey, A., (1966). *Magnetohydrodynamics*, Oliver and Boyd, Edinburgh.

Nihoul, J.C.J., (1984). *Hydrodynamique II, Magnétohydrodynamique*, E. Riga Ed., Liège, 179 pp.

Sutton, G.W. and Sherman, A., (1965). *Engineering Magnetohydrodynamics*, Mc Graw Hill, New York.

[1.] The condition $[r]>0$, $[\varepsilon]$ can be shown to be incompatible with the second principle of thermodynamics $[\eta]\geq 0$.

Hypersonic-Flow Governing Equations with Electromagnetic Fields

D. Giordano[*]

ESTEC - Aerothermodynamics Section

Keplerlaan 1, 2200 AG Noordwijk, The Netherlands

October 13, 2003

Contents

---

[*]Domenico.Giordano@esa.int

Nomenclature

$\mathbf{A}$	vector potential
$\mathcal{A}_k$	affinity of k-th chemical reaction
$\mathbf{B}$	magnetic induction
C	constant (in Arrhenius law)
c	speed of light in vacuum, 299792458 m·s^{-1}
$\mathbf{D}_{ij}$	diffusion tensors
$\mathbf{D}_i^{\mathrm{T}}$	thermodiffusion tensors
$\boldsymbol{\mathcal{D}}_{ik}$	diffusion tensors (Fick law)
$\mathbf{E}$	electric-field intensity
E_a	activation energy (in Arrhenius law)
e	electronic charge, $1.602176462 \cdot 10^{-19}$ C
e_{m}	matter energy per unit total mass
$\dot{e}_{\mathrm{m},v}$	matter-energy production
$\dot{e}_{\mathrm{em},v}$	electromagnetic-energy production
$\boldsymbol{\mathcal{F}}_i$	generalized force [Eq. (125)]
$f_{i\delta}$	Helmholtz potential of δ-th molecular degree of freedom of i-th component
G	generic extensive variable
g	generic-variable density (mass)
g_v	generic-variable density (volume)
$\dot{g}$	generic-variable production (mass)
$\dot{g}_v$	generic-variable production (volume)
h_i	enthalpy of i-th component per its unit mass
$\mathbf{J}_{\mathrm{G}}$	generic-variable diffusive flux
$\mathbf{J}_{\mathrm{Em}}$	matter-energy diffusive flux
$\mathbf{J}_{\mathrm{m}_i}$	component-mass diffusive flux
$\mathbf{J}_{\mathrm{m}_j^a}$	species-mass diffusive flux
$\mathbf{J}_{\mathrm{Q}}$	electric-charge diffusive flux or conduction-current density
$\mathbf{J}_{\mathrm{q}}$	heat flux (see text)
$\mathbf{J}_{\mathrm{U}}$	internal-energy diffusive flux
$\mathbf{J}_{\mathrm{U}_{i\delta}}$	diffusive flux of $U_{i\delta}$
$\mathbf{J}_{\mathrm{S}}$	entropy diffusive flux
$\boldsymbol{j}$	electric-current density
K_{B}	Boltzmann constant, $1.3806503 \cdot 10^{-23}$ J·K^{-1}
K_k^{c}	chemical-equilibrium constant (concentrations)
ℓ_i	number of molecular degrees of freedom of i-th component
M	gas-mixture average molar mass
M_i	component molar mass
M_j^a	species molar mass
n	number of components
N_{A}	Avogadro number, $6.02214199 \cdot 10^{23}$
$\mathcal{N}_i$	component particle number

$\mathcal{N}_j^a$	species particle number
p	pressure
p_i	partial pressure of i-th component
Q_i	component molar electric charge
q	electric charge per unit mass
R_{G}	universal gas constant, 8.314472 J·K^{-1}
r	number of chemical reactions
s	number of species
$\jmath$	entropy per unit total mass
$\jmath_i$	entropy of i-th component per its unit mass
$\dot{\jmath}_v$	entropy production
$\dot{\jmath}_{v,0,1,2}$	entropy production related to tensorial order $0, 1, 2$
T	temperature (thermal equilibrium)
$T_{i\delta}$	temperature associated with δ-th molecular degree of freedom of i-th component
t	time
$\mathbf{U}$	unit tensor
U	internal energy of the gas mixture
$U_{i\delta}$	internal energy distributed over δ-th molecular degree of freedom of i-th component
u	internal energy per unit total mass
$u_{i\delta}$	internal energy distributed over δ-th molecular degree of freedom of i-th component per unit mass of i-th component
$\dot{u}_v$	internal-energy production
$\dot{u}_{v,i\delta}$	production of $U_{i\delta}$
$\mathbf{v}$	velocity vector
$(\boldsymbol{\nabla}\mathbf{v})_{\mathrm{o}}^{\mathrm{s}}$	traceless symmetric part of velocity gradient
$(\boldsymbol{\nabla}\mathbf{v})^{\mathrm{a}}$	antisymmetric part of velocity gradient
v	specific volume
v_i	specific volume of i-th component
$\dot{v}_v$	volume production
$\mathbf{w}_i$	component diffusion velocity
x_i	molar fraction of i-th component
α_i	component mass fraction
α_j^a	species mass fraction
ε_0	dielectric constant of vacuum, $8.854187817 \cdot 10^{-12}$ F·m^{-1}
η	temperature exponent (in Arrhenius law)
$\mathcal{K}_k^{\mathrm{f}}, \mathcal{K}_k^{\mathrm{b}}$	forward, backward reaction constants
λ_{e}	scalar electrical conductivity
$\boldsymbol{\lambda}_{\mathrm{e}}$	electrical-conductivity tensor
$\boldsymbol{\lambda}_{\mathrm{e}j}^{\mathrm{p}}$	pressoelectrical-conductivity tensors
$\boldsymbol{\lambda}_{\mathrm{e}}^{\mathrm{T}}$	thermoelectrical-conductivity tensor
$\boldsymbol{\lambda}'$	thermal-conductivity tensor (see text)
μ_i	chemical potential of i-th component

μ	dynamic-viscosity tensor
μ_v	bulk-viscosity coefficient
ν_{ki}	global stoichiometric coefficients
$\nu_{ki}^{(\mathrm{r})}, \nu_{ki}^{(\mathrm{p})}$	stoichiometric coefficients of reactants, products
$\dot{\xi}_k$	chemical-reaction rate
π	normal mean stress
ρ	total-mass density
ρ_{c}	electric-charge density
ρ_i	component partial density
ρ_j^a	species partial density
σ_{ij}	formation-matrix coefficients
$\boldsymbol{\tau}$	stress tensor
$\boldsymbol{\tau}_{\mathrm{o}}^{\mathrm{s}}$	traceless symmetric part of stress tensor
$\boldsymbol{\tau}_{\mathrm{M}}$	Maxwell stress tensor
$\boldsymbol{\Phi}_{\mathrm{G}}$	generic-variable flux
ϕ	scalar potential
$\boldsymbol{\mathcal{X}}_i$	generalized force [Eq. (111)]

1   Introduction

nterest in theoretical investigations (1; 2; 3; 4; 5; 6; 7; 8; 9; 10; 11; 12; 13; 14; 15; 16; 17; 18; 19; 20; 21; 22; 23; 24; 25; 26) aimed to the understanding of the fluid dynamics and the thermodynamics of flows subjected to the action of electric and/or magnetic fields can be traced back, at least, to the first half of the past century. The main driving motivation that justifies such an interest was probably best expressed by Resler and Sears (9) in 1958: "If a fluid is a conductor of electricity, the possibility arises that an *electric body force* may be produced in it that will affect the fluid flow pattern in a significant way ... The attractive thing about the electric body force ... is that it can be controlled, insofar as the current and the magnetic field can be controlled, and perhaps made to serve useful purposes such as acceleration or deceleration of flow, prevention of separation, and the like". Since those pioneering years, the scientific/engineering discipline in question has been going through a continuous process of maturation. This process, however, has been continuously and systematically marked in time by researchers' complaints about the unsatisfactory state-of-the-art of the theory. Indeed, notwithstanding many efforts (and the voluminous literature generated by them) to confer the discipline the status of being firmly established on physically rigorous and consistent foundations freed from ad-hoc assumptions, it is the present author's opinion that the progress to achieve convergence to that goal appears today not completed yet. The study presented in this lecture was carried out in the context of a research activity motivated by renewed interest in investigating the influence that electric and/or magnetic fields might exert on the thermal power imposed on a body invested by a hypersonic flow (18; 27; 28; 29; 30; 31; 32; 33; 34). In this regard, spacecraft thermal protection during planetary reentry represented the driving engineering application.

The contents of this lecture should be considered, to a certain extent, a systematic reexamination of past work complemented with somewhat innovative ideas. The aim concentrates on the formulation of a consistent set of governing equations in open form apt to describe the physical phenomenology comprising the hypersonic flow field of an ionized gas mixture and the presence of the electromagnetic field. The discourse opens with stoichiometric considerations that are important to comprehend how specific parameters of electromagnetic nature, namely electric-charge density and conduction-current density, can be expressed in terms of variables of fluid-dynamics nature. Subsequently, the governing equations of the flow field and those of the electromagnetic field are revisited in sequence; differences or similarities with past treatments are pointed out and discussed. The equations governing the flow field hinge on the customary balance of masses, momenta and energies. The equations governing the electromagnetic field are introduced both directly in terms of the Maxwell equations and by recourse to the scalar and vector potentials. In the latter case, the convenience of adopting the Lorentz gauge, rather than the magnetostatic gauge, in order to obtain field equations with favorable mathematical symmetry and simplicity is adequately pointed out. Features, limitations and approximations implied in the open-form governing equations are explicitly addressed. Aspects associated with the necessity to assign the thermodynamic model of the gas mixture are described and discussed. The theory of linear irreversible thermodynamics

(20; 21; 23; 35; 36; 37) based on the entropy-balance equation is also examined for the purpose of obtaining, consistently with the presence of the electromagnetic field, the phenomenological relations required to bring into a mathematically closed form the governing equations. Old problems, such as, for example, the influence of medium compressibility on chemical-reaction rates or the importance of cross effects among generalized fluxes and forces, are re-discussed; additional problems, such as the necessity to take into account the tensorial nature of the transport properties because of the anisotropy introduced by the electromagnetic field, are pointed out. A non-conventional choice of first-tensorial-order generalized forces and corresponding fluxes is proposed which appears to offer more simplicity and better convenience from a conceptual point of view when compared to alternative definitions customarily used in the literature.

Polarization and magnetization have not been considered in this study. There is an important reason behind this choice. The inclusion of polarization and magnetization effects in the Maxwell equations is straightforward. That, however, would constitute only a unilateral approach to the physical phenomenology. Indeed, the important fact should not be overlooked on the fluid-dynamics side that not only body-force distributions but also torque distributions exist (21) within a polarized and magnetized medium subjected to the action of the electromagnetic field. Under these circumstances, the velocity vector is not the sole kinematic unknown that characterizes the flow field; the specific intrinsic moment (21; 23) of matter momentum may not identically vanish throughout the flow field, as it usually happens in the absence of polarization and magnetization, and must necessarily be taken into account as an additional kinematic unknown. The appearance of the corresponding balance equation in the set of the governing equations is inescapable. A non-vanishing specific intrinsic moment of matter momentum can have far reaching consequences. For example, the stress tensor loses its symmetry; its antisymmetric part, conjointly with the antisymmetric part of the velocity-vector gradient, contributes to produce entropy and the familiar Newton law does not suffice anymore to characterize the tensional state in the medium. Implications of energetic nature should also be expected because there is a *rotational* energy associated with the intrinsic moment of matter momentum; in addition, the polarization and magnetization vectors will belong to the set of the independent thermodynamic state parameters (19; 20). These and similar aspects cannot be ignored at the moment of constructing a physically rigorous theory, even if the mentioned effects may turn out to be negligible under specific flow circumstances. The complexity of the physical phenomenology in the presence of polarization and magnetization increases enormously and its study presupposes a degree of difficulty which, in the author's opinion, can be adequately tackled only after that the acquisition of a solid understanding of the coupling between fluid dynamics and pure electromagnetic field has been secured. The latter constitutes the main target of the present study and the motivation to postpone to future investigations the behavior of polarized and magnetized media.

2   Stoichiometric aspects

The chemical constituents that compose an ionized gas mixture can be subdivided in neutral components, ionized components and free electrons. The knowledge of how many and

which components intervene within a given flow problem relies on experimental evidence complemented with the judicious choice dictated by the researcher's expertise. The acquisition of such knowledge is sometimes straightforward, sometimes rather involved; in any case, it constitutes a problem of its own. When the n components are identified then it is possible to recognize the s ($s \leq n$) chemical elements that participate in their formation. These chemical elements will be hereinafter referred to with the term *species*. There is, obviously, a certain arbitrariness in the qualification of the species. For example, either the molecule N_2 can be considered formed by putting together two N atoms or, vice versa, the atom N can be considered formed by breaking the N_2 molecule; the role of species is played by N or N_2 in the former or latter case, respectively. For reasons of convenience, monoatomic elements are chosen by convention as species and they are enumerated in such a way that the first $(s-1)$ are the true atoms $A^1, A^2, ..., A^{s-1}$ and the last one A^s is the electron 'e' responsible for building the electric charge carried by the ionized components (if any). The formation concept is formalized in the chemical formula $A^1_{\sigma_{i1}} A^2_{\sigma_{i2}} \cdots A^s_{\sigma_{is}}$ of the generic component. The coefficient σ_{ij} represents the number of A^j atoms required to form the i-th chemical component; if $\sigma_{ij} = 0$ then the j-th species does not intervene in the formation of the i-th component and the corresponding symbol (A^j) is dropped from the chemical formula. The non-vanishing coefficients σ_{ij} $(j = 1, \ldots, s-1)$ are necessarily positive integers. For a neutral component, the coefficient σ_{is} is identically zero. For an ionized component, the coefficient σ_{is} is positive or negative for exceeding or missing electrons and its opposite gives the electric charge carried by the component molecule as an integer multiple of the electronic charge. In a more common formalism, $A^s_{\sigma_{is}}$ is replaced by superscripting the chemical formula with '+' signs, if $\sigma_{is} < 0$, or '−' signs, if $\sigma_{is} > 0$, in number equal to $|\sigma_{is}|$. The coefficients σ_{ij} can be grouped together to compose the $n \times s$ formation matrix

$$
\begin{array}{c|cccc}
 & A^1 & A^2 & \cdots & \text{e} \\
\hline
\text{CF}_1 & \sigma_{11} & \sigma_{12} & \cdots & \sigma_{1s} \\
\text{CF}_2 & \sigma_{21} & \sigma_{22} & \cdots & \sigma_{2s} \\
\vdots & & & \vdots & \\
\text{CF}_n & \sigma_{n1} & \sigma_{n2} & \cdots & \sigma_{ns}
\end{array}
\tag{1}
$$

In the matrix representation (1), CF_i stands for the chemical formula $A^1_{\sigma_{i1}} A^2_{\sigma_{i2}} \cdots A^s_{\sigma_{is}}$ and the rightmost column is the electric-charge column which appears and acquires significance exclusively when ionized components are present in the mixture. The coefficients σ_{ij} permit to express the molar masses M_i of the components as linear combinations

$$
M_i = \sum_{j=1}^{s} \sigma_{ij} M_j^a
\tag{2}
$$

of the molar masses M_j^a of the species ($M_s^a = 5.48579911 \cdot 10^{-7}$ kg is the mass of one mole of electrons) intervening in their formation. The molar electric charges Q_i require only the coefficients in the electric-charge column

$$
Q_i = -\sigma_{is} e N_A
\tag{3}
$$

An explicit example of formation matrix relative to the seven-component high-temperature air mixture would read

	N	O	e
N	1	0	0
O	0	1	0
e^-	0	0	1
NO	1	1	0
N_2	2	0	0
O_2	0	2	0
NO^+	1	1	-1

In this case, there are $n = 7$ components formed by $s = 3$ species.

Another important construct is the stoichiometric matrix connected with the r chemical reactions

$$\sum_{i=1}^{n} \nu_{ki}^{(r)} \, CF_i \rightleftharpoons \sum_{i=1}^{n} \nu_{ki}^{(p)} \, CF_i \qquad k = 1, 2, \cdots, r \tag{4}$$

that can occur in the gas mixture. The processes formalized in Eq. (4) are subjected to component-mass conservation

$$\sum_{i=1}^{n} \nu_{ki}^{(r)} M_i = \sum_{i=1}^{n} \nu_{ki}^{(p)} M_i \tag{5}$$

After defining the stoichiometric coefficients $\nu_{ki} = \nu_{ki}^{(p)} - \nu_{ki}^{(r)}$, Eq. (5) can be recast into the form

$$\sum_{i=1}^{n} \nu_{ki} M_i = 0 \tag{6}$$

The coefficients ν_{ki} are also integer numbers that can be conveniently assembled in the $(r \times n)$ stoichiometric matrix

k	CF_1	CF_2	$\cdots$	CF_n
1	ν_{11}	ν_{12}	$\cdots$	ν_{1n}
2	ν_{21}	ν_{22}	$\cdots$	ν_{2n}
$\vdots$			$\vdots$	
r	ν_{r1}	ν_{r2}	$\cdots$	ν_{rn}

$$\tag{7}$$

The combination of the formation concept embodied in Eq. (2) and the component-mass conservation enforced by Eq. (6) allows to obtain important conditions to which formation and stoichiometric matrices are subjected and that express physically the species-mass conservation. The substitution of Eq. (2) into Eq. (6) and the permutation of the sum operators yields

$$\sum_{j=1}^{s} M_j^a \sum_{i=1}^{n} \nu_{ki} \sigma_{ij} = 0 \tag{8}$$

Given the (mathematical) arbitrariness of the molar masses M_j^a, the solution

$$\sum_{i=1}^{n} \nu_{ki} \sigma_{ij} = 0 \qquad j = 1, \cdots, s \tag{9}$$

is the sole possibility left to have Eq. (8) identically satisfied. It is interesting to notice that when $j = s$, and taking in account Eq. (3), Eq. (9) yields the electric-charge conservation

$$\sum_{i=1}^{n} \nu_{ki} Q_i = 0 \tag{10}$$

across the given chemical reaction. The conservation of the electric charge is, therefore, not an independent statement but follows from the mass conservation relative to the electron species.

The formation matrix (1) permits to express composition parameters, and their properties, related to the species in terms of those related to the components. The basic relation, in this regard, is the one that connects particle number of the species with particle number of the components

$$\mathcal{N}_j^a = \sum_{i=1}^{n} \mathcal{N}_i \sigma_{ij} \tag{11}$$

From Eq. (11), for example, one obtains similar expressions for mass fractions

$$\alpha_j^a = \sum_{i=1}^{n} \frac{\alpha_i}{M_i} \sigma_{ij} M_j^a \qquad j = 1, \cdots, s \tag{12}$$

and partial densities

$$\rho_j^a = \sum_{i=1}^{n} \frac{\rho_i}{M_i} \sigma_{ij} M_j^a \qquad j = 1, \cdots, s \tag{13}$$

The electric charge per unit mass also follows from Eq. (11) after setting $j = s$ and multiplying by $-e$; it reads

$$q = -e N_{\mathrm{A}} \frac{\alpha_s^a}{M_s^a} = -e N_{\mathrm{A}} \sum_{i=1}^{n} \frac{\alpha_i}{M_i} \sigma_{is} \tag{14}$$

In turn, multiplication of Eq. (14) by the total-mass density ρ provides the expression for the electric-charge density

$$\rho_{\mathrm{c}} = \rho q = -e N_{\mathrm{A}} \frac{\rho_s^a}{M_s^a} = -e N_{\mathrm{A}} \sum_{i=1}^{n} \frac{\rho_i}{M_i} \sigma_{is} \tag{15}$$

Equation (15) is an important relation. It establishes a first necessary link between the electromagnetic side (ρ_{c}) of the physical phenomenology and its fluid-dynamics counterpart (ρ_s^a or all ρ_i). It also endorses the idea that the electric-charge density should not be looked at as a basic field unknown because it can be straightforwardly calculated once the gas mixture composition has been determined.

3   Physical significance of the balance equations

In view of the analysis which will be carried out in the following sections, it appears appropriate to dwell preliminarily upon an important aspect related to the physical significance of the balance equations which becomes manifest when the presence of the electromagnetic field has to be considered.

It is a recurrent occurrence in the mechanics of continuous media that important equations governing the dynamic evolution of a system, namely the portion of the medium contained in a specified control volume, are developed from the idea of balancing the variations of the extensive properties (mass, momentum, energy, etc.) that characterize the macroscopic state of the system. The typical balance equation

$$\frac{\partial g_v}{\partial t} = -\boldsymbol{\nabla} \cdot \boldsymbol{\Phi}_{\mathrm{G}} + \dot{g}_v \tag{16}$$

is the translation in mathematical language of the basic principle (35; 36; 38) affirming that any generic extensive variable G owned by the system can vary only for two specific reasons: a) an exchange with the external environment and b) an internal production. Equation (16) constitutes the local formulation of such a principle and establishes a formal link between the density g_v, the flux $\boldsymbol{\Phi}_{\mathrm{G}}$ and the production $\dot{g}_v$ of the variable G. Density and production in Eq. (16) carry the subscript v to emphasize that they are referred to unit volume. Feynman (39) provided a very interesting disquisition in his famous lectures concerning the physics behind Eq. (16); his reasoning, although expounded in didactic style, is certainly one of the most lucid accounts the present author ever had the opportunity to read. The aspect related to Eq. (16) that is meant to be pointed out here regards the possibility for the quantities $g_v, \boldsymbol{\Phi}_{\mathrm{G}}$ and $\dot{g}_v$ of being attached directly to space instead of being associated with the matter occupying that same space. Such an occurrence is somewhat *forgotten* in traditional fluid dynamics because the physical variables are all associated with matter in that case. Indeed, customary practice proceeds one step further from Eq. (16) by introducing density $g = g_v/\rho$ and production $\dot{g} = \dot{g}_v/\rho$ referred to unit mass and by separating the flux

$$\boldsymbol{\Phi}_{\mathrm{G}} = \rho \mathbf{v} g + \mathbf{J}_{\mathrm{G}} \tag{17}$$

in a convective part that takes care of the transport associated with the macroscopic motion of matter and a diffusive part which takes care of everything else. Accordingly, Eq. (16) becomes

$$\frac{\partial \rho g}{\partial t} + \boldsymbol{\nabla} \cdot (\rho \mathbf{v} g) = -\boldsymbol{\nabla} \cdot \mathbf{J}_{\mathrm{G}} + \rho \dot{g} \tag{18}$$

Equation (18) is the stencil that embeds all the governing equations belonging to traditional fluid dynamics. It comes to no surprise, therefore, that the mathematical structure of Eq. (18) has stood as the starting point in computational fluid dynamics (CFD) from which all efforts towards the development of numerical algorithms have originated. In this sense, Eq. (18) has undoubtedly contributed to forging the way of thinking in the CFD community. Yet, things may be looked at from a different perspective in the presence of the electromagnetic field. Obviously, the applicability of the convection-diffusion separation [Eq. (17)], pertaining to the flux $\boldsymbol{\Phi}_{\mathrm{G}}$, and of Eq. (18) still survives when the fluid-dynamics field and the electromagnetic field have to be dealt with simultaneously.

However, Eq. (16) can also be made to play a role if the definition of global variables, namely momentum and energy, are adequately generalized in a manner that relaxes the unnecessary conceptual habit of matter association; then the ensuing equations become statements of conservation ($\dot{g}_v = 0$) and, in so doing, they assume a mathematical structure that, in principle, may favorably lend itself to a more simplified numerical analysis.

In the following sections, the formal balance-equation concept will be explicited in relation to the fundamental physical quantities mass, momentum and energy in order to formulate a consistent set of governing equations. Concerning the latter two quantities, the programme will be carried out in a comparative fashion by confronting the fluid-dynamics habitual approach with the novel perspective just discussed and brought to surface by the presence of the electromagnetic field.

4   Mass-balance equations

The standard equations

$$\frac{\partial \rho_i}{\partial t} + \boldsymbol{\nabla} \cdot (\rho_i \mathbf{v}) = -\boldsymbol{\nabla} \cdot \mathbf{J}_{\mathrm{m}_i} + \sum_{k=1}^{r} \dot{\xi}_k \nu_{ki} M_i \quad i = 1, \cdots, n \qquad (19)$$

balancing the component masses are available for the determination of the gas-mixture composition. The component-mass diffusive fluxes $\mathbf{J}_{\mathrm{m}_i}$ and the chemical-reaction rates $\dot{\xi}_k$ require the assignment of phenomenological relations (Secs. 8 and 9). Other variables with same prerogative will be encountered in the following sections. Such variables should be viewed as *windows* through which physical models manifest their influence on the open-form governing equations. The component-mass diffusive fluxes are linked to the corresponding diffusion velocities

$$\mathbf{J}_{\mathrm{m}_i} = \rho_i \mathbf{w}_i \qquad (20)$$

and are subjected to the condition

$$\sum_{i=1}^{n} \mathbf{J}_{\mathrm{m}_i} = \sum_{i=1}^{n} \rho_i \mathbf{w}_i = 0 \qquad (21)$$

Equation (21) enforces the physical fact that total mass cannot diffuse. In other words, there are only $n-1$ independent diffusive fluxes or diffusion velocities. Taking into account Eq. (6), Eq. (21) and mass additivity

$$\rho = \sum_{i=1}^{n} \rho_i \qquad (22)$$

the continuity equation

$$\frac{\partial \rho}{\partial t} + \boldsymbol{\nabla} \cdot (\rho \mathbf{v}) = 0 \qquad (23)$$

follows from the summation of Eq. (19) on the subscript i. There are two options for the determination of the $n+1$ unknowns ρ_i, ρ. The most straightforward way would seem to consist in the selection of Eqs. (19) and (22) because the use of a very simple algebraic

equation, as Eq. (22) is, is appealing, of course. There is, however, a risk in doing so because potential inconsistencies carried into Eq. (19) by phenomenological relations for component-mass diffusive fluxes and chemical-reaction rates would produce inaccurate partial densities which, in turn, would pass on their inaccuracy to the total-mass density via Eq. (22). The alternative way to proceed could be to replace Eq. (22) with Eq. (23). In this manner, the effect of the previously mentioned inconsistencies is somewhat contained because neither partial densities nor phenomenological relations are explicitly required in Eq. (23). As a matter of fact, Eq. (22) could be used aside, once the unknowns ρ_i, ρ have been obtained, as a sort of error verifier. The drawback of this approach consists in the necessity to solve an additional differential equation [Eq. (23)].

The chemical-reaction rates are known to be numerically stiff properties to deal with. It is, therefore, desirable to make them appear as sparingly as possible in the governing equations. To this aim, simplification can be achieved if the composition parameters relative to the species are brought into the picture. Taking into account the definition of species partial densities [Eq. (13)], the balance equations of the species masses are obtained by multiplying Eq. (19) by $\sigma_{ij} M_j^a / M_i$ and summing on the subscript i; they read

$$\frac{\partial \rho_j^a}{\partial t} + \boldsymbol{\nabla} \cdot (\rho_j^a \mathbf{v}) = -\boldsymbol{\nabla} \cdot \mathbf{J}_{\mathrm{m}_j^a} \qquad j = 1, \cdots, s \qquad (24)$$

The species-mass diffusive flux in Eq. (24) turns out to be expressed in terms of the component-mass diffusive fluxes as

$$\mathbf{J}_{\mathrm{m}_j^a} = \sum_{i=1}^{n} \frac{1}{M_i} \mathbf{J}_{\mathrm{m}_i} \sigma_{ij} M_j^a \qquad j = 1, \cdots, s \qquad (25)$$

The production term is absent in Eq. (24) because Eq. (9) makes it vanish identically. Thus, the species masses are conservative: they cannot be either created or destroyed, regardless of the reactive mechanisms at work in the gas mixture. This occurrence suggests an advantageous manoeuvre to limit the appearance of the chemical-reaction rates. The idea is to relinquish as unknowns the last s partial densities ρ_i and replace them with the partial densities ρ_j^a; at the same time, the last s equations of the set (19) are replaced with the set (24). In this way, the number of differential equations is unchanged but the chemical-reaction rates appear only in $n - s$ equations. The s relinquished partial densities ρ_i can be expressed in terms of the first $n - s$ partial densities ρ_i and of the s partial densities ρ_j^a from Eq. (13) after expanding

$$\rho_j^a = \sum_{i=1}^{n-s} \frac{\rho_i}{M_i} \sigma_{ij} M_j^a + \sum_{i=n-s+1}^{n} \frac{\rho_i}{M_i} \sigma_{ij} M_j^a \qquad j = 1, \cdots, s \qquad (26)$$

and re-arranging

$$\sum_{i=n-s+1}^{n} \frac{\rho_i}{M_i} \sigma_{ij} M_j^a = \rho_j^a - \sum_{i=1}^{n-s} \frac{\rho_i}{M_i} \sigma_{ij} M_j^a \qquad j = 1, \cdots, s \qquad (27)$$

Equation (27) represents an algebraic system of s equations for the s relinquished partial densities ρ_i. It can be formally solved in the following manner. First, introduce for brevity

the $(s \times s)$ coefficient matrix

$$\hat{\sigma}_{ij} = \sigma_{ij} \frac{M_j^a}{M_i} \tag{28}$$

$$i = n - s + 1, \cdots, n; \; j = 1, \cdots, s$$

and the $(1 \times s)$ known-term array

$$\hat{\rho}_j^a = \rho_j^a - \sum_{i=1}^{n-s} \frac{\rho_i}{M_i} \sigma_{ij} M_j^a \qquad j = 1, \cdots, s \tag{29}$$

so that Eq. (27) can be recast in the standard form

$$\sum_{i=n-s+1}^{n} \rho_i \hat{\sigma}_{ij} = \hat{\rho}_j^a \qquad j = 1, \cdots, s \tag{30}$$

The matrix $\hat{\sigma}_{ij}$ can be inverted once and forever when the formation matrix (1) and the species molar masses are known. Then, the formal solution of Eq. (30) is

$$\rho_i = \sum_{j=1}^{s} \hat{\rho}_j^a \; \hat{\sigma}_{ji}^{-1} \qquad i = n - s + 1, \cdots, n \tag{31}$$

Another important aspect to look at in connection with the species is the balancing of the electric charge. The electric-charge balance equation is not an independent statement but is embedded in Eq. (24) when particularized to the case of the electron species. Indeed, setting $j = s$ in Eq. (24) and multiplying it by $-eN_A/M_s^a$ [see Eq. (15)] yields the fluid-dynamics styled equation

$$\frac{\partial \rho_c}{\partial t} + \boldsymbol{\nabla} \cdot (\rho_c \mathbf{v}) = -\boldsymbol{\nabla} \cdot \mathbf{J}_Q \tag{32}$$

in which, taking into account Eq. (25) with $j = s$, the electric-charge diffusive flux turns out to be expressed by the following linear combination

$$\mathbf{J}_Q = -eN_A \mathbf{J}_{m_s^a} \frac{1}{M_s^a} = -eN_A \sum_{i=1}^{n} \frac{1}{M_i} \mathbf{J}_{m_i} \sigma_{is} \tag{33}$$

of the component-mass diffusive fluxes. Equations (32) and (33) warn against any presumptive imposition of charge neutrality ($\rho_c = 0$) throughout the flow field; even if there are zones in which the gas mixture is electrically neutral, the mass diffusion of ionized component and free electrons works towards the removal of such a condition. Rephrasing Eq. (32) in electromagnetic-theory style

$$\frac{\partial \rho_c}{\partial t} + \boldsymbol{\nabla} \cdot (\rho_c \mathbf{v} + \mathbf{J}_Q) = 0 \tag{34}$$

leads to the identification of, in the corresponding parlance, the electric-current density

$$\boldsymbol{j} = \rho_c \mathbf{v} + \mathbf{J}_Q \tag{35}$$

and to the recognition of its separability in convection-current ($\rho_\text{c}\mathbf{v}$) and conduction-current ($\mathbf{J}_\text{Q}$) densities. These are the sole contributions that need to be accounted for in the absence of polarization and magnetization. Equation (33) represents the other important relation that establishes a second, and final, necessary link between electromagnetism ($\mathbf{J}_\text{Q}$) and fluid dynamics (all $\mathbf{J}_{\text{m}_i}$). Both Eq. (15) and Eq. (33) converge into the definition provided by Eq. (35) and, in so doing, enforce the unambiguous assertion that the electric-current density is specified entirely in terms of variables of fluid-dynamics nature. Also, the dependence expressed in Eq. (33) clearly shows that it is not necessary to pursue an independent phenomenological relation for the conduction-current density because the latter descends naturally from the knowledge of the phenomenological relations for the component-mass diffusive fluxes. It will be seen in Sec. 9.4 how the famous Ohm law and additional effects of thermodynamic origin arise naturally in this way.

5   Electromagnetic-field equations

The essence of electromagnetism finds its deepest representation in the differential equations that govern the electromagnetic field, namely the well known Maxwell equations. The body of didactic literature on this subject matter is enormous and the theory can very well be considered consolidated on solid foundations if the phenomenology of matter polarization and magnetization is left out. The contents of this section took advantage mainly from Feynman's lectures (39); Maxwell's fundamental treatise (40) together with the textbooks written by Møller (41), Lorrain and Colson (42), Persico (43), Tolman (44), and Pauli (45) were also helpful. Notwithstanding the satisfactory state-of-the-art of the theory, there is one peculiar aspect of electromagnetism that always deserves extreme care and attention: the choice of the physical units. The issue is not trivial. As a consequence of (unfortunate) human decision, equations and formulae assume different mathematical forms in the CGS and MKS systems. Although only slight, the differences are nevertheless sufficient enough to generate confusion in formal manipulations and numerical calculations. In order to comply with modern standards, SI units have been adopted throughout this lecture. With this choice, and in the absence of polarization and magnetization, the Maxwell equations read

$$\boldsymbol{\nabla}\cdot\mathbf{E} \;=\; \frac{\rho_\text{c}}{\varepsilon_0} \tag{36}$$

$$\boldsymbol{\nabla}\cdot\mathbf{B} \;=\; 0 \tag{37}$$

$$\boldsymbol{\nabla}\times\mathbf{E} \;=\; -\frac{\partial\mathbf{B}}{\partial t} \tag{38}$$

$$\varepsilon_0 c^2\boldsymbol{\nabla}\times\mathbf{B} \;=\; \boldsymbol{j} + \varepsilon_0\frac{\partial\mathbf{E}}{\partial t} \tag{39}$$

The presence of ρ_c and $\boldsymbol{j}$ in these equations confers them the role of *channels* through which the coupling between fluid-dynamics field and electromagnetic field becomes manifest [recall Eq. (15), Eq. (33) and Eq. (35)]. In principle, Eqs. (38) and (39) are all that is required to associate with the fluid-dynamics equations in order to determine simultaneously electric-field intensity and magnetic induction. However, their mathematical

structure is substantially distinct from the habitual fluid-dynamics stencil [Eq. (18)]. A widespread practice (34; 46; 47; 48; 49; 50; 51; 52; 53) that aims to derive and use an equation with more suitable mathematical form is based on the adaptation of Eq. (38) following the neglect of the displacement-current density ($\varepsilon_0 \partial \mathbf{E}/\partial t$) in Eq. (39) and the assumed validity of the generalized Ohm law

$$\mathbf{J}_\mathrm{Q} = \lambda_\mathrm{e}\left(\mathbf{E} + \mathbf{v}\times\mathbf{B}\right) \tag{40}$$

although with a scalar electrical conductivity. The method leads to the so-called magnetic-induction equation

$$\frac{\partial\mathbf{B}}{\partial t} + \boldsymbol{\nabla}\cdot(\mathbf{v}\mathbf{B}) = \boldsymbol{\nabla}\cdot(\mathbf{B}\mathbf{v}) + \frac{\varepsilon_0 c^2}{\lambda_\mathrm{e}}\nabla^2\mathbf{B} + \frac{\varepsilon_0 c^2}{\lambda_\mathrm{e}{}^2}\boldsymbol{\nabla}\lambda_\mathrm{e}\times(\boldsymbol{\nabla}\times\mathbf{B}) \;+ $$
$$+\frac{\rho_\mathrm{c}}{\lambda_\mathrm{e}}\boldsymbol{\nabla}\times\mathbf{v} - \mathbf{v}\times\boldsymbol{\nabla}\left(\frac{\rho_\mathrm{c}}{\lambda_\mathrm{e}}\right) \tag{41}$$

The details of the derivation of Eq. (41) are given in appendix A. Further simplified forms in the event of electric-charge neutrality ($\rho_\mathrm{c} \simeq 0$) or uniform electrical conductivity ($\lambda_\mathrm{e} \simeq$ const) are easily deduced. Equation (41) looks certainly attractive from a numerical point of view because its structure reflects perfectly that of Eq. (18). In this way, the solution of the electromagnetic field is brought within the reach of familiar algorithms in CFD. At the same time, the idea of magnetic-field *convection* is favored to find its way into the picture of the physical phenomenology. The computational fluid dynamicist is most likely satisfied with this situation because he is provided with an additional instrument [Eq. (41)] which features the same mathematical characteristics of familiar tools, namely the flow-field equations without the electromagnetic field. He can, then, proceed to calculate. Seen from the perspective of the hard efforts and time invested in the development of numerical schemes, this attitude is comprehensible. Yet, the theoretical fluid dynamicist would feel concerned about the same situation because Eq. (41) and its associated interpretation are very much in contrast with the physical fact that the electromagnetic field is attached to space regardless of the matter flowing through that same space. In this regard, he may ponder about the physical significance of Eq. (41), asking important questions such as: can the vector $\mathbf{B}$ be interpreted as the volume density of some extensive property of the matter moving in the space occupied by the electromagnetic field? If there is such a property then can the diadic tensor $\mathbf{B}\mathbf{v}$ and the remaining terms on the right-hand side of Eq. (41) be interpreted as, respectively, its diffusive flux and production? The difficulty in finding convincing answers suggests a critical scrutiny of the assumptions on which Eq. (41) is built. The neglect of the displacement-current density is justifiable in circumstances of not rapidly varying electric field but it is still an undesirable limitation at the moment of constructing a general theory. The generalized Ohm law [Eq. (40)] is more prone to criticism. Concern about its applicability is not a novelty and was explicitly raised long time ago (11; 16; 18; 21). The major hurdle to accept is the fact that the applicability of Eq. (41), which is a governing equation, is subjugated to the validity of Eq. (40), which is a phenomenological relation. This levies a serious toll on the generality of the ensuing theory because the latter becomes medium-dependent. Equation (19), for example, is medium-independent because it remains applicable regardless of the phenomenological relations assumed for the component-mass diffusive fluxes

and chemical-reaction rates. This is not the case for Eq. (41). What happens if the tensorial nature of the electrical conductivity, a feature already discussed by Maxwell (40) in 1873, cannot be neglected or, worst, if the medium does not comply with Eq. (40)? These arguments may appear irrelevant to the computational fluid dynamicist who is interested mainly in numerical algorithms but for the theoretical fluid dynamicist they are strong reasons of concern that originate from the awareness of having at disposition a theory whose solidity may be compromised in particular and unforeseeable situations.

Another exploitable method takes advantage of the scalar and vector potentials often used in electromagnetism. The knowledge of the potentials implies that of electric-field intensity and magnetic induction because the latter vectors follow from the definitions

$$\mathbf{E} = -\boldsymbol{\nabla}\phi - \frac{\partial \mathbf{A}}{\partial t} \tag{42}$$

$$\mathbf{B} = \boldsymbol{\nabla} \times \mathbf{A} \tag{43}$$

The substitution of Eqs. (42) and (43) into Eqs. (38) and (39) leads to the following nicely symmetrical field equations

$$\frac{1}{c^2}\frac{\partial^2 \phi}{\partial t^2} = \nabla^2 \phi + \frac{\rho_{\mathrm{c}}}{\varepsilon_0} \tag{44}$$

$$\frac{1}{c^2}\frac{\partial^2 \mathbf{A}}{\partial t^2} = \nabla^2 \mathbf{A} + \frac{1}{\varepsilon_0 c^2}\, \boldsymbol{j} \tag{45}$$

The details of the derivation are provided in appendix B. The mathematical symmetry of Eqs. (44) and (45) is strongly dependent on the gauge condition

$$\frac{1}{c^2}\frac{\partial \phi}{\partial t} + \boldsymbol{\nabla} \cdot \mathbf{A} = 0 \tag{46}$$

known as Lorentz gauge (39; 45). A similar approach was already pursued by Burgers (14) and Pai (18) who, however, opted for the typical magnetostatic gauge

$$\boldsymbol{\nabla} \cdot \mathbf{A} = 0 \tag{47}$$

Instead of Eqs. (44) and (45), they obtained two much more complicated highly cross-coupled field equations in which terms involving ϕ and $\mathbf{A}$ appear simultaneously in both equations.

Equations (44) and (45) indicate explicitly the wave-like evolution taking place in the electromagnetic field and how that is influenced by the presence of matter through the electric-charge and electric-current densities. The equations reduce to the Poisson equation in steady-state circumstances. It may be asked what is the gain of using Eqs. (44) and (45) rather than Eqs. (38) and (39) or Eq. (41). First of all, Eqs. (44) and (45) are four scalar differential equations instead of the six represented by Eqs. (38) and (39). Moreover, they are general and independent of the medium in so far as they are unaffected by arguments related to importance or disregard of the displacement-current density and as they need no appeal to any phenomenological relation to provide reason for their existence. It is true that, once again, Eqs. (44) and (45) do not reflect the structure of Eq. (18) and, therefore, they presuppose the necessity to develop new numerical algorithms for their

simultaneous solution with the fluid-dynamics equations. On the other hand, they are equations of the mathematical physics which have been studied numerically since long time and for whose properties a huge body of knowledge and understanding has been accumulated.

6   Momentum-balance equations

The determination of the velocity-vector field occurs via the equation balancing the momentum associated with the matter flowing in the control volume. For reasons that will appear evident soon, it is appropriate to emphasize the association to matter by systematically referring to this quantity with the term *matter momentum*. In the presence of the electromagnetic field, its balance equation assumes the form

$$\frac{\partial \rho \mathbf{v}}{\partial t} + \boldsymbol{\nabla} \cdot (\rho \mathbf{v}\,\mathbf{v}) = \boldsymbol{\nabla} \cdot \boldsymbol{\tau} + \rho_\mathrm{c}\mathbf{E} + \boldsymbol{j} \times \mathbf{B} \tag{48}$$

As in traditional fluid dynamics, the matter-momentum diffusion is characterized by the stress tensor which, as anticipated in Sec. 1, preserves its feature of being a symmetrical tensor in the absence of polarization and magnetization. The gravitational contribution to the body force on the right-hand side of Eq. (48) has been omitted not only for compatibility with the typical circumstances settling in in hypersonic regime that presuppose the negligibility of gravitational effects with respect to those due to the tensional state of the medium but also for reasons of simplicity. As a matter of fact, the inclusion in the discourse of a (Newtonian) gravitational field is conceptually straightforward because the gravitational body-force term can be treated similarly to the electric counterpart ($\rho_\mathrm{c}\mathbf{E}$) and made fit smoothly in the equation framework described in the sequel. On the other hand, the emphasis of the present context addresses the importance of the electromagnetic field; the presence of a gravitational field would only burden the equations with unnecessary additional terms whose inclusion would not change at all the considerations that will follow and the conclusions that will be drawn.

The electromagnetic field produces matter momentum through the body force

$$\dot{\mathbf{g}}_v = \rho_\mathrm{c}\mathbf{E} + \boldsymbol{j} \times \mathbf{B} \tag{49}$$

This is the term to which the statement of Resler and Sears (9) quoted in the introduction refers to and that is responsible for a variety of new effects substantially inimaginable in traditional fluid dynamics. Under the action of the electromagnetic field, for example, the mass diffusion of the electrically charged components takes an active role in affecting the motion of the fluid particles because it enters explicitly into the equation of their motion [Eq. (48)] via the electric-current density [see Eqs. (33) and (35)]. Without the electromagnetic field, mass diffusion produces only an indirect effect on the dynamics of the flow field through a thermodynamic pathway that involves the gas-mixture composition and, subsequently, the pressure distribution; the latter, in turn, represents a substantial contribution to the build-up of the stress tensor.

Equation (48) is a necessary and sufficient equation qualified for inclusion in the governing set; one could be satisfied with its availability. Nevertheless, there are more interesting features of the physical phenomenology that await to be unravelled. Whether it

may, perhaps, appear a somewhat fortuitous circumstance or it could be looked at as the manifestation of something of deep physical significance, it is certainly interesting that the Maxwell equations [Eqs. (36) and (39)] allow a very useful transformation (41; 43; 44; 45) of the electromagnetic body force [Eq. (49)]. In a single stroke, this transformation provides evidence of the existence of momentum associated with the electromagnetic field, namely the *electromagnetic momentum*, and leads to the formulation of its balance equation. The mathematical details are given in appendix C. The final outcome from the mentioned transformation provides the electromagnetic body force in the form

$$\rho_{\mathrm{c}}\mathbf{E} + \boldsymbol{j} \times \mathbf{B} = \boldsymbol{\nabla} \cdot \boldsymbol{\tau}_{\mathrm{M}} - \frac{\partial}{\partial t}(\varepsilon_0 \mathbf{E} \times \mathbf{B}) \tag{50}$$

In Eq. (50), the tensor $\boldsymbol{\tau}_{\mathrm{M}}$ represents the following combination of electric-field intensity and magnetic induction

$$\boldsymbol{\tau}_{\mathrm{M}} = \varepsilon_0(\mathbf{EE} - \frac{1}{2}E^2\mathbf{U}) + \varepsilon_0 c^2(\mathbf{BB} - \frac{1}{2}B^2\mathbf{U}) \tag{51}$$

It is, therefore, a symmetric tensor. Equation (50) can be simply overturned as

$$\frac{\partial}{\partial t}(\varepsilon_0 \mathbf{E} \times \mathbf{B}) = \boldsymbol{\nabla} \cdot \boldsymbol{\tau}_{\mathrm{M}} - (\rho_{\mathrm{c}}\mathbf{E} + \boldsymbol{j} \times \mathbf{B}) \tag{52}$$

to match exactly the structure of Eq. (16). Hence, Eq. (52) is a balance equation. It shows unequivocally the existence of electromagnetic momentum distributed in space with density $\varepsilon_0 \mathbf{E} \times \mathbf{B}$ and transported through space with flux $-\boldsymbol{\tau}_{\mathrm{M}}$. The symmetric tensor $\boldsymbol{\tau}_{\mathrm{M}}$ plays in Eq. (52) the same role fulfilled by the stress tensor in Eq. (48) and, for this reason, it is suggestively named as *Maxwell stress tensor*. Equation (52) highlights in an evident manner also that the transport of electromagnetic momentum takes place through space exclusively in consequence of the presence of the electromagnetic field and bears no relation whatsoever with the matter transported through that same space. It is important to keep in mind that, although very useful, Eq. (52) is not a new independent equation. In principle, it can replace one of Eqs. (38) and (39) but it does not say anything more that is not already contained in the Maxwell equations. The nice features of Eq. (52) consist of its balance-equation structure and that it fulfills the task of permitting a deep insight towards the understanding of the existence of important properties of the electromagnetic field that are not immediately recognizable from the equations of electromagnetism as given by Maxwell.

Another aspect worth of attention is that all the electromagnetic momentum that disappears locally turns out to reappear as matter momentum or viceversa. This is the obvious conclusion ensuing from the appearance of the electromagnetic body force both in Eq. (48) and, with changed sign, in Eq. (52). In other words, the sum of the two forms of momentum cannot be produced (created or destroyed). Thus, the global momentum $\rho\mathbf{v} + \varepsilon_0 \mathbf{E} \times \mathbf{B}$ is a conservative property of the physical system composed by the conjoint fluid-dynamics and electromagnetic fields. This profound characteristic of the physical phenomenology is brought to surface by summing together Eqs. (48) and (52) to obtain the balance equation of total momentum

$$\frac{\partial}{\partial t}(\rho\mathbf{v} + \varepsilon_0 \mathbf{E} \times \mathbf{B}) = -\boldsymbol{\nabla} \cdot (\rho\mathbf{v}\,\mathbf{v} - \boldsymbol{\tau} - \boldsymbol{\tau}_{\mathrm{M}}) \tag{53}$$

Equation (53) is equivalent to Eq. (48) and constitutes a valid and, perhaps, more convenient alternative at the moment of performing numerical calculations because it is not burdened by the presence of any production term.

7   Energy-balance equations

7.1   Preliminary considerations

The prerequisite steps in the formulation of balance equations related to the concept of energy, in its entirety and in its variety of kinds, are the identification of the forms that play a role within a specific physical phenomenology and the recognition of the sum of those forms as the total energy. In turn, the subduing of the latter to the famous principle of conservation ($\dot{e}_v = 0$) leads to the deduction and, at the same time, to the physical interpretation of interesting and important features related to the possible mechanisms of energy conversion.

In the absence of electromagnetic fields, the typical forms of energy that intervene in hypersonic regime are the kinetic energy possessed by the fluid particles as a consequence of their macroscopic motion and the internal energies distributed over the molecular degrees of freedom of the components. Energy ascribed to intermolecular interactions is systematically neglected. Gravitational energy is not admitted in the picture for the same reasons adduced in Sec. 6 to justify the omission of the gravitational-field contribution to the body force on the right-hand side of Eq. (48). Under the assumed circumstances, the sum of kinetic energy and internal energies constitutes the total energy and, as such, that sum acquires the prerogative of being conservative. The situation changes drastically in the presence of the electromagnetic field. The kinetic energy and the internal energies associated with matter are still part of the scene but their sum, which will be referred to as *matter energy* for consistency with the terminology introduced in Sec. 6 when dealing with momentum, does not exhaust the totality of forms. The electromagnetic field possesses energy in the same way as it does for momentum. It turns out, therefore, that there is a further kind of energy to account for: the *electromagnetic energy*. It is the sum of matter energy and electromagnetic energy to provide the total energy in this case and to be characterized by a vanishing production. It will be shown in the sequel that, once again, the Maxwell equations [Eqs. (38) and (39)] and their adequately manipulated blend with the balance equations of kinetic energy and internal energies play a fundamental role in the achievement of the outlined understanding of the physical situation.

7.2   Kinetic energy

The kinetic-energy balance equation

$$\frac{\partial}{\partial t}(\rho \frac{\mathbf{v}^2}{2}) + \boldsymbol{\nabla} \cdot (\rho \frac{\mathbf{v}^2}{2}\mathbf{v}) = \boldsymbol{\nabla} \cdot (\boldsymbol{\tau} \cdot \mathbf{v}) - \boldsymbol{\tau} : \boldsymbol{\nabla}\mathbf{v} \; +$$
$$+ \; \rho_c\mathbf{v} \cdot \mathbf{E} - \mathbf{J}_Q \cdot \mathbf{v} \times \mathbf{B} \tag{54}$$

descends straightforwardly from that of matter momentum simply by scalar-multiplying both sides of Eq. (48) by the velocity vector and by rearranging the resulting right-hand

side to reflect the structure of Eq. (18). Inspection of Eq. (54) indicates at once kinetic-energy diffusive flux and production. The latter comprises the habitual contribution that includes the combined action of medium deformation and tensional state, and a contribution originating from the existence of the electromagnetic field. With regard to this additional contribution, the magnetic part contains only the conduction-current density. This is the obvious consequence of the orthogonality $[\mathbf{v}\cdot(\rho_c\mathbf{v}\times\mathbf{B}) = 0]$ between the velocity vector and the part of the body force in Eq. (49) containing the convection-current density that appears explicitly after expanding the electric-current density according to Eq. (35). Equation (54) is, clearly, not an independent equation; it merely represents the projection of Eq. (48) along the local direction of the instantaneous streamlines of the flow field.

7.3   Internal energy

From a thermodynamic point of view, the ionized gas mixture of interest in the present context has to be considered as a composite system whose subsystems, represented by the molecular degrees of freedom possessed by the components, are in disequilibrium with respect to mass exchanges (chemical reactions) and energy exchanges (thermal relaxations) (38). In other words, the internal energies distributed over the molecular degrees of each component must be introduced and accounted for separately. In general, the i-th component owns ℓ_i independent molecular degrees of freedom ($\delta = 1, \cdots, \ell_i$) and the δ-th degree of freedom features its private internal energy $U_{i\delta}$. It appears worthwhile, in this regard, to mention that the problem of the explicit separation of the molecular degrees of freedom in independent entities at the level of the internal Schrödinger equation of the molecules is still an open issue in demand of satisfactory resolution and is systematically glossed over by making recourse to the poor, and incorrect, classical separation in rotational, vibrational, electronic (and etc.) molecular degrees of freedom. This is certainly a gap that calls for enhancement of basic understanding achievable only through advanced research. This limitation, however, does not prevent the development of a formal equation framework. The independence of the degrees of freedom implies the additivity of the internal energies

$$U = \sum_{i=1}^{n} \sum_{\delta=1}^{\ell_i} U_{i\delta} \tag{55}$$

Equation (55) can be conveniently rephrased in terms of specific quantities as

$$\rho u = \sum_{i=1}^{n} \sum_{\delta=1}^{\ell_i} \rho_i u_{i\delta} \tag{56}$$

The specificity of $u_{i\delta}$ refers to the unit mass of the i-th component while the specificity of u refers to the unit total mass. On the fluid-dynamics side, the $\sum_{i=1}^{n} \ell_i$ specific internal energies $u_{i\delta}$ are unknowns of the flow field and their determination can be achieved through

the following $\sum_{i=1}^{n} \ell_i$ balance equations

$$\frac{\partial \rho_i u_{i\delta}}{\partial t} + \boldsymbol{\nabla} \cdot (\rho_i u_{i\delta} \mathbf{v}) = -\boldsymbol{\nabla} \cdot \mathbf{J}_{\mathrm{U}_{i\delta}} + \dot{u}_{v,i\delta} \tag{57}$$

$$\delta = 1, \cdots, \ell_i; i = 1, \cdots, n$$

The diffusive fluxes and productions appearing on the right-hand side of Eq. (57) require the assignment of phenomenological relations. With regard to the productions, it will be shown in Sec. 7.4 that only $\sum_{i=1}^{n} \ell_i - 1$ of them are independent in consequence of the principle of total-energy conservation. On the thermodynamics side, the specific internal energies $u_{i\delta}$ are linked to the Helmholtz potentials $f_{i\delta}(T_{i\delta}, v_i)$ that describe the thermodynamic behaviour of the molecular degrees of freedom. The link takes the form

$$u_{i\delta} = -T_{i\delta}^2 \left(\frac{\partial f_{i\delta}/T_{i\delta}}{\partial T_{i\delta}} \right)_{v_i} = u_{i\delta}(T_{i\delta}, v_i) \tag{58}$$

$$\delta = 1, \cdots, \ell_i; i = 1, \cdots, n$$

Each of the $\sum_{i=1}^{n} \ell_i$ thermodynamic relations (58) provides the functional dependence to obtain the temperature $T_{i\delta}$ for prescribed specific internal energy $u_{i\delta}$ and specific volume ($v_i = 1/\rho_i$) of the i-th component. The ensemble of the functions $f_{i\delta}(T_{i\delta}, v_i)$ characterizes the global thermodynamic model (38) of the gas mixture. Their explicit determination presupposes the knowledge of appropriate partition functions (54; 55) whose construction, in turn, belongs to the domain of statistical thermodynamics [see Refs. (54; 55; 56; 57) and references therein]. It ought to be remarked that the described equation scheme is founded on the assumption that the population distributions over the quantum energy states associated with the molecular degrees of freedom can be represented in analytical form, the Boltzmann distribution being a particular case. This assumption is critical for the effectiveness of Eq. (57) and the validity of Eq. (58). Circumstances cannot be excluded in which this assumption becomes untenable. In that case, a deeper characterization of the thermal relaxations, with repercussions on the chemical kinetics of the gas mixture, becomes necessary because the quantum-state populations are themselves unknowns subjected to balance equations that deal with state-to-state exchanges of energy and mass. A substantial body of works [see Refs. (58; 59; 60; 61; 62) and references therein] addressing the state-to-state phenomenology has been growing recently but the methods elaborated so far are not yet completely free from difficulties of conceptual and computational nature. However, these difficulties notwithstanding, experimental and computational evidence [see Refs. (63; 64) and references therein] of the existence of non-analytical distributions of the quantum-state populations points towards the conclusion that the avenue of state-to-state thermal kinetics certainly deserves to be explored with vigorous effort for reasons of both scientific and engineering interest. This topic will not be elaborated further here because it is beyond the scope of the present context. Interested readers are referred to the cited literature.

Taking into account the additivity [Eq. (56)] of the internal energies, the balance equation of the gas-mixture internal energy

$$\frac{\partial \rho u}{\partial t} + \boldsymbol{\nabla} \cdot (\rho u \mathbf{v}) = -\boldsymbol{\nabla} \cdot \mathbf{J}_{\mathrm{U}} + \dot{u}_v \tag{59}$$

is easily deduced from the summation of Eq. (57) on the subscripts i, δ. The internal-energy diffusive flux and production in Eq. (59) read respectively

$$\mathbf{J}_{\mathrm{U}} = \sum_{i=1}^{n} \sum_{\delta=1}^{\ell_i} \mathbf{J}_{\mathrm{U}_{i\delta}} \tag{60}$$

$$\dot{u}_v = \sum_{i=1}^{n} \sum_{\delta=1}^{\ell_i} \dot{u}_{v,i\delta} \tag{61}$$

Equation (59) is not in its final form. There is more to say about the internal-energy production in consequence of the principle of total-energy conservation. The completion will be done in Sec. 7.4.

Thermal equilibrium prevails when all temperatures $T_{i\delta}$ equalize to a common temperature T. This situation should arise as a particular solution of the multi-temperature scheme embodied in Eqs. (57) and (58), assuming that the component internal-energy diffusive fluxes and productions are correctly prescribed. An alternative approach, possible when there is sufficient (experimental) evidence that supports the idea as a useful approximation accurate enough to reflect realism, consists in the presumptive imposition of thermal equilibrium as a shortcut to spare the numerical costs of dealing with the mathematical complexity of Eqs. (57) and (58). In this manner, the details associated with Eq. (57) are given up and Eq. (59) is used directly for the determination of the gas-mixture specific internal energy with the provision that, now, a phenomenological relation is needed for the internal-energy diffusive flux appearing on the left-hand side of Eq. (60). A phenomenological relation for the internal-energy production appearing on the left-hand side of Eq. (61) is not needed because its expression is fixed by the imposition of total-energy conservation (see Sec. 7.4). Obviously, the thermodynamic relations (58) are still applicable with $T_{i\delta} = T$; thus, the temperature of the gas mixture follows from the resolution of

$$\rho u = \sum_{i=1}^{n} \sum_{\delta=1}^{\ell_i} \rho_i u_{i\delta}(T, v_i) \tag{62}$$

7.4   Matter energy

According to the considerations of Sec. 7.1, specific matter energy is defined as the sum

$$e_{\mathrm{m}} = u + \frac{\mathbf{v}^2}{2} \tag{63}$$

of kinetic energy and gas-mixture internal energy. The corresponding balance equation

$$\frac{\partial \rho e_{\mathrm{m}}}{\partial t} + \boldsymbol{\nabla} \cdot (\rho e_{\mathrm{m}} \mathbf{v}) = -\boldsymbol{\nabla} \cdot (\mathbf{J}_{\mathrm{U}} - \boldsymbol{\tau} \cdot \mathbf{v}) + \dot{u}_v \ - $$
$$- \boldsymbol{\tau} : \boldsymbol{\nabla}\mathbf{v} + \rho_c \mathbf{v} \cdot \mathbf{E} - \mathbf{J}_{\mathrm{Q}} \cdot \mathbf{v} \times \mathbf{B} \tag{64}$$

follows, therefore, from the sum of Eqs. (54) and (59). The inspection of the right-hand side of Eq. (64) provides the matter-energy diffusive flux

$$\mathbf{J}_{\text{Em}} = \mathbf{J}_{\text{U}} - \boldsymbol{\tau} \cdot \mathbf{v} \tag{65}$$

and production

$$\dot{e}_{\text{m},v} = \dot{u}_v - \boldsymbol{\tau} : \boldsymbol{\nabla}\mathbf{v} + \rho_{\text{c}}\mathbf{v} \cdot \mathbf{E} - \mathbf{J}_{\text{Q}} \cdot \mathbf{v} \times \mathbf{B} \tag{66}$$

In the presence of the electromagnetic field, one is not entitled to assume the matter-energy production as unconditionally vanishing. The further addendum to account for is the production of the electromagnetic energy

$$\dot{e}_{\text{em},v} = -\boldsymbol{j} \cdot \mathbf{E} \tag{67}$$

Its expression derives from arguments related to the work done by the electromagnetic field when electric charges are displaced within it (39). So, for consistency with the physical phenomenology, the principle of total-energy conservation must be enforced as

$$\dot{e}_{\text{m},v} + \dot{e}_{\text{em},v} = 0 \tag{68}$$

The substitution of Eqs. (66) and (67), the latter expanded according to Eq. (35), into Eq. (68) leads to the following important, full of physical significance, expression of the internal-energy production

$$\dot{u}_v = \boldsymbol{\tau} : \boldsymbol{\nabla}\mathbf{v} + \mathbf{J}_{\text{Q}} \cdot (\mathbf{E} + \mathbf{v} \times \mathbf{B}) \tag{69}$$

The *Joule effect* appears naturally in Eq. (69) and is represented by the electromagnetic term linked exclusively to the conduction-current density. With regard to this point, it seems worth mentioning that sometimes the electromagnetic term on the right-hand side of Eq. (67) is erroneously confused as being responsible for the Joule effect. An important conclusion to be drawn from Eq. (69), with a view to Eq. (61), is that not only the combined action of medium deformation and tensional state but also the flowing of a conduction current through the electromagnetic field concurs to induce non-equilibrium excitation of the molecular degrees of freedom. How the repartition of the converted amount of energy takes place among the molecular degrees of freedom can be ascertained only when the expressions of the productions $\dot{u}_{v,i\delta}$ are explicitly known. In any case, Eqs. (61) and (69) together indicate that in multi-temperature circumstances, only $\sum_{i=1}^{n} \ell_i - 1$ productions need the assignment of phenomenological relations, and that such a necessity does not exist in the event of thermal equilibrium.

The availability of Eq. (69) leads to recast Eq. (64) into the final form

$$\frac{\partial \rho e_{\text{m}}}{\partial t} + \boldsymbol{\nabla} \cdot (\rho e_{\text{m}}\mathbf{v}) = -\boldsymbol{\nabla} \cdot (\mathbf{J}_{\text{U}} - \boldsymbol{\tau} \cdot \mathbf{v}) + \boldsymbol{j} \cdot \mathbf{E} \tag{70}$$

and to the completion of the balance equation [Eq. (59)] of the gas-mixture internal energy which now reads

$$\frac{\partial \rho u}{\partial t} + \boldsymbol{\nabla} \cdot (\rho u \mathbf{v}) = -\boldsymbol{\nabla} \cdot \mathbf{J}_{\text{U}} + \boldsymbol{\tau} : \boldsymbol{\nabla}\mathbf{v} + \mathbf{J}_{\text{Q}} \cdot (\mathbf{E} + \mathbf{v} \times \mathbf{B}) \tag{71}$$

Equation (70) or Eq. (71) can replace anyone of Eq. (57) in the set of the governing equations.

7.5   Electromagnetic energy

The recognition of the existence of the electromagnetic energy and the derivation of its associated balance equation are achieved by following a procedure very similar to the one worked out for the electromagnetic momentum, that is, through a skillful transformation (39; 41; 44; 45) of the electromagnetic-energy production [Eq. (67)] by taking advantage of the Maxwell equations [Eqs. (38) and (39)]. Appendix D provides the mathematical details. The final result already cast in accordance with Eq. (16) reads

$$\frac{\partial}{\partial t}[\frac{\varepsilon_0}{2}(E^2 + c^2 B^2)] = -\boldsymbol{\nabla} \cdot (\varepsilon_0 c^2 \mathbf{E} \times \mathbf{B}) - \boldsymbol{j} \cdot \mathbf{E} \tag{72}$$

Equation (72) indicates explicitly that the electromagnetic field contains energy distributed in space with density $\frac{\varepsilon_0}{2}(E^2 + c^2 B^2)$, transported through space with flux given by the Poynting vector $\varepsilon_0 c^2 \mathbf{E} \times \mathbf{B}$, and exchanged with the energy of matter with the production rate $-\boldsymbol{j} \cdot \mathbf{E}$. Once again, Eq. (72) is not an independent equation; there is no new physical information in it that is not already contained in the Maxwell equations. The considerations made in this regard with respect to the balance equation of electromagnetic momentum [Eq. (52)] apply here unvaried.

Equation (72) reflects the structure of Eq. (16) but there have been attempts (13; 14) to adapt it for the purpose of fitting the structure of Eq. (18). The adaptation is based on the transformation of electric-field intensity and magnetic induction between two reference systems in the non-relativistic approximation

$$\mathbf{E}' \;=\; \mathbf{E} + \mathbf{v} \times \mathbf{B} \tag{73}$$

$$\mathbf{B}' \;=\; \mathbf{B} - \frac{1}{c^2}\mathbf{v} \times \mathbf{E} \tag{74}$$

The primed reference system is identified with the one attached to the generic fluid particle during its motion. The basic step is the evaluation of the Poynting vector in the primed reference system (13; 14; 20)

$$\varepsilon_0 c^2 \mathbf{E}' \times \mathbf{B}' = \varepsilon_0 c^2 \mathbf{E} \times \mathbf{B} - \frac{\varepsilon_0}{2}(E^2 + c^2 B^2)\mathbf{v} + \boldsymbol{\tau}_{\mathrm{M}} \cdot \mathbf{v} \tag{75}$$

by taking advantage of the transformations (73) and (74). Appendix E contains the mathematical details. It is then a simple matter to solve Eq. (75) for $\varepsilon_0 c^2 \mathbf{E} \times \mathbf{B}$ and to substitute the resulting expression into Eq. (72) to obtain an alternative balance equation of the electromagnetic energy

$$\frac{\partial}{\partial t}\left[\frac{\varepsilon_0}{2}(E^2 + c^2 B^2)\right] + \boldsymbol{\nabla} \cdot \left[\frac{\varepsilon_0}{2}(E^2 + c^2 B^2)\mathbf{v}\right] \;=$$
$$=\; -\boldsymbol{\nabla} \cdot (\varepsilon_0 c^2 \mathbf{E}' \times \mathbf{B}' - \boldsymbol{\tau}_{\mathrm{M}} \cdot \mathbf{v}) - \boldsymbol{j} \cdot \mathbf{E} \tag{76}$$

Equation (76) reflects the structure of Eq. (18) and shows a remarkable similarity with Eq. (70). From its perspective, electromagnetic energy is *convected* with matter and diffused with flux $\varepsilon_0 c^2 \mathbf{E}' \times \mathbf{B}' - \boldsymbol{\tau}_{\mathrm{M}} \cdot \mathbf{v}$. This viewpoint shares many analogies with the one discussed in Sec. 5 in relation to the magnetic-induction equation [Eq. (41)]. In this case

also, there is a conceptual objection, already hinted at by Napolitano (16), that obscures the appeal of this adaptation and of its consequent interpretation. The transformations (73) and (74) are rigorously valid only between two reference systems in uniform rectilinear motion with respect to each other. Thus, they are not complete if the primed reference system is attached to the generic fluid particle because the latter is accelerated ($\mathbf{a} = \partial\mathbf{v}/\partial t + \mathbf{v} \cdot \boldsymbol{\nabla}\mathbf{v}$). As explicitly emphasized by Feynman (39), transformations of electric-field intensity and magnetic induction between two reference systems in relative accelerated motion do depend on the acceleration. One may wonder whether or not the terms connected with acceleration that should appear in Eqs. (73) and (74) are negligible in the non-relativistic approximation. Besides the fact that general transformations including acceleration seem to be found nowhere in the literature, the question appears to be a moot argument not worth grappling with because even if a positive answer is found, one cannot reconcile Eq. (76) with the physical fact that the electromagnetic field and its properties momentum and energy are attached to space.

7.6   Total energy

According to Eq. (68), all the electromagnetic energy that disappears locally reappears as matter energy or viceversa, exactly in the same guise of what happens to momentum. The sum of Eqs. (70) and (72), therefore, provides the balance equation of total energy

$$\frac{\partial}{\partial t}[\rho e_{\mathrm{m}} + \frac{\varepsilon_0}{2}(E^2 + c^2 B^2)] \;\; =$$
$$= -\boldsymbol{\nabla} \cdot (\rho\mathbf{v}e_{\mathrm{m}} + \mathbf{J}_{\mathrm{U}} - \boldsymbol{\tau} \cdot \mathbf{v} + \varepsilon_0 c^2 \mathbf{E} \times \mathbf{B}) \qquad (77)$$

For the purpose of numerical calculations, Eq. (77) is perfectly equivalent to either Eq. (70) or Eq. (71) but, on the contrary of the latter equations, it does not present any burdensome production term.

7.7   Mechanisms of energy conversion

A summary of the productions relative to kinetic energy, internal energy and electromagnetic energy is illustrated in Table 1. The electromagnetic-energy production [Eq. (67)] has been expanded according to Eq. (35). The tabulation gives a visual representation of the possible mechanisms of energy conversion. Thus, electromagnetic energy is converted partly in kinetic energy ($\rho_{\mathrm{c}}\mathbf{v} \cdot \mathbf{E}$) through the action of the electric field on the convection current and partly in internal energy ($\mathbf{J}_{\mathrm{Q}} \cdot \mathbf{E}$) through the action of the electric field on the conduction current. In turn, kinetic energy is converted in internal energy via the interplay between medium deformation and tensional state ($\boldsymbol{\tau} : \boldsymbol{\nabla}\mathbf{v}$), and through the combined action of the conduction current and the magnetic induction ($\mathbf{J}_{\mathrm{Q}} \cdot \mathbf{v} \times \mathbf{B}$). The Joule effect [$\mathbf{J}_{\mathrm{Q}} \cdot (\mathbf{E} + \mathbf{v} \times \mathbf{B})$] is the conjoint manifestation of two different conversion mechanisms of, respectively, electromagnetic and kinetic nature. A more complete characterization of the energy-conversion schematism illustrated in Table 1 covering aspects of reversibility and irreversibility presupposes the explicit knowledge of the entropy production. By definition, the latter identifies the irreversible processes and, being subdued to the second law of thermodynamics that guarantees its non-negativity, imposes an inviolable direction arrow

on some of the conversion pathways existing among the corresponding terms in Table 1. The entropy production will be dealt with in Sec. 9.2.

8   Remarks on the governing equations in open form

The governing equations in open form surveyed in the preceeding sections embrace the physical phenomenology comprising the hypersonic flow field of an ionized, but not polarized and magnetized, gas mixture and the presence of the electromagnetic field. For quick reference, they are summarized in Tables 2–5 according to several alternative but physically equivalent options. Regardless of the selected option, the set of equations is not operative yet because it contains the unknown variables requiring the assignment of phenomenological relations. These unknowns identify the fundamental disciplines that converge into the foundational framework on which hypersonics rests, namely thermodynamics ($f_{i\delta}$), chemical kinetics ($\dot{\xi}_k$), thermal kinetics ($\dot{u}_{v,i\delta}$), diffusion theory ($\mathbf{J}_{m_i}, \boldsymbol{\tau}, \mathbf{J}_{U_{i\delta}}$), and call for the selection of models apt to represent in an as accurate as possible manner the physical behavior shown by a given real medium under the specific circumstances characteristic of a given application. The latter requirement materializes through the assignment of the thermodynamic model (all $f_{i\delta}$) for the gas mixture and of the phenomenological relations establishing the link between the unknowns $\dot{\xi}_k$, $\dot{u}_{v,i\delta}$, $\mathbf{J}_{m_i}$, $\boldsymbol{\tau}$, $\mathbf{J}_{U_{i\delta}}$ and the basic unknowns, and/or their gradients, of the flow field. Only then, the equations in the governing set acquire the prerequisite closed form necessary to proceed towards the achievement of their mathematical solution. It seems appropriate at this point to emphasize that the seemingly *incomplete* character of the governing set in open form should not hinder at all the development of algorithms for the numerical solution of the differential equations that belong to the set. On the contrary, such a development is highly desirable. As a matter of fact, it will never be stressed enough how much convenient it is for the efficient resolution of the flow field that algorithm-development studies would concentrate on the governing set in open form as main target. This is a proposition that certainly implies an ambitious programme but the prospective benefits are too appealing to be ignored and the idea to be hurriedly dismissed. If such a programme succeeds then the phenomenological relations become relegated to the role of *subroutines*, interchangeable according to the specific necessities of a given application, and the architecture of the numerical kernel will feature the extraordinary useful flexibility of being generally applicable and independent from the specific physical behavior of the real medium.

The construction of the thermodynamic model is a task belonging to the realm of statistical thermodynamics (see Sec. 7.3). There are a few options available concerning the derivation of the phenomenological relations for the unknown productions and diffusive fluxes. One can seek recourse to irreversible thermodynamics (20; 21; 22; 23; 24; 35; 36; 37; 65; 66; 67; 68), to the more sophisticated kinetic theory of gases (69; 70; 71; 72; 73; 74; 75) or to experimental investigation. In practice, the phenomenological relations emerge as the outcome of a concerted effort involving all three options exploited to different degrees of depth. The approach relying on irreversible thermodynamics is preferable *to get started* in the derivation endeavor because, although its findings may have sometimes narrow limits of validity from a *quantitative* point of view, it proceeds in a conceptually straightforward manner from the exploitation of the entropy production and of the

second law of thermodynamics, it is not affected (not to the same extent, at least) by the overwhelming mathematical cumbersomeness and complexity of the detailed kinetic theories and, above all, it offers a depth of insight that goes a long way in the direction of understanding the transport processes at work in the flow field and of recognizing the associated driving forces.

9 Linear irreversible thermodynamics

9.1 Preliminary remarks

The linear theory of irreversible thermodynamics will be revisited in the following sections in conformity with the prescription of thermal equilibrium. The assumption that thermal equilibrium prevails among the molecular degrees of freedom of the components is a recurrent characteristic shared by authors that follow the irreversible-thermodynamics approach. Some (23; 37) even go further and assume mechanical equilibrium. Thermal equilibrium implies the possibility of dealing with one single temperature and, obviously, brings in great simplification; on the other hand, it restricts the applicability domain of the ensuing phenomenological relations. The sole attempts the present author is aware of that ventured into a thermal-disequilibrium analysis were made by Woods (22), Napolitano (35; 36), and Morro and Romeo (76; 77; 78). However, the treatments proposed by Woods and by Napolitano share similarities that contain elements, bearing on the definition of the driving forces connected with the occurrence of multiple temperatures, apparently not yet completely freed from conceptual objections. Similarly, Morro and Romeo did not consider the internal structure of the molecules; in other words, they implicitly assumed for each component the thermal equilibrium among its molecular degrees of freedom. More work is certainly needed to improve knowledge in this department of irreversible thermodynamics. The motivation justifying the choice adopted here resides mainly in the intention to put the emphasis on the peculiarities of the physical phenomenology connected with the existence of the electromagnetic field and, for that purpose, to keep the mathematical analysis relieved from tangential or, even, unnecessary complexity. Nevertheless, the multitemperature phenomenology is quantitatively important in hypersonic applications and should not be disregarded.

9.2 Entropy-balance equation and entropy production

The thermodynamics of the irreversible processes hinges on the entropy balance equation

$$\frac{\partial \rho s}{\partial t} + \boldsymbol{\nabla} \cdot (\rho \mathbf{v} s) = -\boldsymbol{\nabla} \cdot \mathbf{J}_s + \dot{s}_v \tag{78}$$

Equation (78) represents a formal balance and acquires operational character only after that the entropy diffusive flux and production are given more explicit expressions. This is achieved by taking advantage of the thermodynamic fundamental relation (24; 38; 66; 79) of the gas mixture in the entropic formulation which, under the assumption of thermal equilibrium, reads formally

$$s = s(u, v, \alpha_1, \alpha_2, \dots, \alpha_n) \tag{79}$$

In view of the forthcoming analysis, it is appropriate to recall that the first derivatives of the function (79) represent the state equations in the entropic scheme and define, respectively, temperature, pressure and chemical potentials

$$\frac{1}{T} = \left(\frac{\partial s}{\partial u}\right)_{v,\alpha} \tag{80}$$

$$\frac{p}{T} = \left(\frac{\partial s}{\partial v}\right)_{s,\alpha} \tag{81}$$

$$-\frac{\mu_i}{T} = \left(\frac{\partial s}{\partial \alpha_i}\right)_{u,v,\alpha_{j\neq i}} \quad i = 1, \cdots, n \tag{82}$$

of the gas mixture. Also, for reasons of simplicity in the notation, it is convenient to work out the mathematical details with the aid of the substantial-derivative operator $D/Dt = \partial/\partial t + \mathbf{v} \cdot \boldsymbol{\nabla}$, whose intervention in the balance equations stems from the equivalence [recall also Eq. (18)]

$$\frac{\partial \rho g}{\partial t} + \boldsymbol{\nabla} \cdot (\rho \mathbf{v} g) = \rho \frac{Dg}{Dt} \tag{83}$$

Equation (83) is a direct consequence of total-mass conservation [Eq. (23)]. Taking into account the definitions (80)–(82), the application of the substantial-derivative operator to the function (79) leads to

$$\rho \frac{Ds}{Dt} = \frac{1}{T}\rho \frac{Du}{Dt} + \frac{p}{T}\rho \frac{Dv}{Dt} - \sum_{i=1}^{n} \frac{\mu_i}{T}\rho \frac{D\alpha_i}{Dt} \tag{84}$$

The steps to achieve the explicit form of the entropy-balance equation appear now evident. The first step consists in obtaining the volume-balance equation. The quickest way is to set $g \equiv v$ in Eq. (83) and to take into account that $\rho v = 1$; hence

$$\rho \frac{Dv}{Dt} = \boldsymbol{\nabla} \cdot \mathbf{v} \tag{85}$$

Counterintuitively as it may appear at first sight, the term on the right-hand side of Eq. (85) does not represent the divergence of the diffusive flux of volume because, by its very definition, a diffusive flux cannot depend on the velocity vector [see Eq. (17)]; this inescapable requirement suggests that a volume-production ($\dot{v}_v = \boldsymbol{\nabla} \cdot \mathbf{v}$) interpretation is the sole possible for the term in question. An alternative explanation reaching the same conclusion can be found in Ref. (19). The second step involves the substitution of the component-mass balance equations [Eq. (19)], the internal-energy balance equation [Eq. (71)] and the volume balance equation [Eq. (85)] into Eq. (84), and the consequent rearrangement to reflect the structure of Eq. (78). This brings to the identification of the entropy diffusive flux

$$\mathbf{J}_{\mathrm{S}} = \frac{1}{T}\mathbf{J}_{\mathrm{U}} - \sum_{i=1}^{n} \frac{\mu_i}{T}\mathbf{J}_{\mathrm{m}_i} \tag{86}$$

and of the entropy production

$$\dot{s}_v = \quad \frac{1}{T}\boldsymbol{\tau} : \boldsymbol{\nabla}\mathbf{v} \quad -$$
$$- \quad \frac{1}{T^2}(\mathbf{J}_{\mathrm{U}} - \sum_{i=1}^{n} \mu_i \mathbf{J}_{\mathrm{m}_i}) \cdot \boldsymbol{\nabla}T - \frac{1}{T}\sum_{i=1}^{n} \mathbf{J}_{\mathrm{m}_i} \cdot \boldsymbol{\nabla}\mu_i \quad +$$
$$+ \quad \frac{1}{T}\mathbf{J}_{\mathrm{Q}} \cdot (\mathbf{E} + \mathbf{v} \times \mathbf{B}) + \frac{p}{T}\boldsymbol{\nabla} \cdot \mathbf{v} - \frac{1}{T}\sum_{k=1}^{r} \dot{\xi}_k \mathcal{A}_k \tag{87}$$

The affinities of the chemical reactions are defined as linear combinations

$$\mathcal{A}_k = \sum_{i=1}^{n} \nu_{ki} M_i \mu_i \qquad k = 1, \cdots, r \tag{88}$$

of the chemical potentials. The entropy production [Eq. (87)] is not in its final form but must be furtherly refined for the purpose of the present context. The refinement consists in performing the standard expansion of the stress and velocity-gradient tensors to bring forth their isotropic, traceless-symmetric (or deviatoric) and antisymmetric parts. This operation presupposes some familiarity with tensor analysis; extensive help, in this regard, is provided in Refs. (22; 23; 37; 72). The stress tensor separates in the sum

$$\boldsymbol{\tau} = \pi\mathbf{U} + \boldsymbol{\tau}_{\mathrm{o}}^{\mathrm{s}} \tag{89}$$

of the isotropic part, which contains the (scalar) normal mean stress built as the arithmetic average ($\pi = 1/3\,\boldsymbol{\tau} : \mathbf{U}$) of the diagonal terms of the stress tensor, and of the traceless-symmetric part. The antisymmetric part vanishes identically because the stress tensor remains symmetric in the absence of polarization and magnetization. The same expansion performed on the velocity gradient yields

$$\boldsymbol{\nabla}\mathbf{v} = \frac{1}{3}(\boldsymbol{\nabla} \cdot \mathbf{v})\mathbf{U} + (\boldsymbol{\nabla}\mathbf{v})_{\mathrm{o}}^{\mathrm{s}} + (\boldsymbol{\nabla}\mathbf{v})^{\mathrm{a}} \tag{90}$$

With the help of relatively simple tensor algebra, it can be shown that, taking into account Eqs. (89) and (90), the first term on the right-hand side of Eq. (87) becomes

$$\boldsymbol{\tau} : \boldsymbol{\nabla}\mathbf{v} = \pi(\boldsymbol{\nabla} \cdot \mathbf{v}) + \boldsymbol{\tau}_{\mathrm{o}}^{\mathrm{s}} : (\boldsymbol{\nabla}\mathbf{v})_{\mathrm{o}}^{\mathrm{s}} \tag{91}$$

The substitution of Eq. (91) and of the expression of the conduction-current density in terms of the component-mass diffusive fluxes [Eq. (33)] into Eq. (87) leads to the desired final form of the entropy production

$$\dot{s}_v = \quad \frac{1}{T}\boldsymbol{\tau}_{\mathrm{o}}^{\mathrm{s}} : (\boldsymbol{\nabla}\mathbf{v})_{\mathrm{o}}^{\mathrm{s}} \quad -$$
$$- \quad \frac{1}{T^2}(\mathbf{J}_{\mathrm{U}} - \sum_{i=1}^{n} \mu_i \mathbf{J}_{\mathrm{m}_i}) \cdot \boldsymbol{\nabla}T \quad -$$
$$- \quad \frac{1}{T}\sum_{i=1}^{n} \mathbf{J}_{\mathrm{m}_i} \cdot [\boldsymbol{\nabla}\mu_i + eN_{\mathrm{A}}\frac{\sigma_{is}}{M_i}(\mathbf{E} + \mathbf{v} \times \mathbf{B})] \quad -$$
$$- \quad \frac{1}{T}[-(\pi + p)]\boldsymbol{\nabla} \cdot \mathbf{v} - \frac{1}{T}\sum_{k=1}^{r} \dot{\xi}_k \mathcal{A}_k \tag{92}$$

Equation (92) shows, in irreversible-thermodynamics parlance, the *generalized fluxes* and the *generalized forces* that produce entropy and, in so doing, identifies the processes responsible for promoting irreversibility in the flow field. In addition to the habitual effects, namely shape $[(\boldsymbol{\nabla}\mathbf{v})_{\mathrm{o}}^{\mathrm{s}}]$ and volume $(\boldsymbol{\nabla}\cdot\mathbf{v})$ deformation of the medium, nonequilibrium chemical reactions $(\mathcal{A}_k \neq 0)$, thermal $(\boldsymbol{\nabla}T)$ and chemical-potential $(\boldsymbol{\nabla}\mu_i)$ disuniformities, also the electromagnetic field enlists in the category of the irreversible processes through contributions that add to the chemical-potential gradients and connect to the mass diffusive fluxes of the electrically charged components. Generalized fluxes and forces are summarized in Table 6. The core of irreversible thermodynamics is the exploitation of the entropy production [Eq. (92)] and of the second law of thermodynamics

$$\dot{\delta}_v \geq 0 \tag{93}$$

which endorses its unconditional non-negativity as an ineluctable fact of nature, for the purpose of obtaining suitable expressions of the generalized fluxes in terms of the generalized forces. In this regard, the validity of the Curie postulate is assumed here. The postulate affirms that generalized fluxes of a given tensorial order can depend only on generalized forces of the same tensorial order. This is a simplification because the postulate is rigorously applicable only for isotropic media; that is not the case in the presence of the electromagnetic field because the existence of the magnetic induction removes the medium isotropy. Thus, the assumption of the postulate validity implies the negligibility of the couplings among each generalized flux and all the generalized forces of different tensorial order. The motivation behind this choice is the same adduced at the end of Sec. 9.1 to justify the assumption of thermal equilibrium, namely the intention to emphasize the essential characteristics due to the presence of the electromagnetic field and, at the same time, minimize mathematical complexity. Readers interested in the general case that includes the neglected cross effects are referred to the specialized literature mentioned in Sec. 8 [see Refs. (22; 23) in particular]. To compensate to some extent for the limitations ensuing from the Curie postulate, the anisotropy imposed on the medium by the magnetic induction will be taken into account in the tensorial nature of the transport coefficients (22; 23; 69; 72; 73; 75; 80; 81; 82; 83; 84; 85; 86; 87; 88).

In compliance with the invoked Curie postulate, it is convenient to emphasize the subdivision of the entropy-production terms with same tensorial order by rephrasing Eq. (92) as

$$\dot{\delta}_v = \dot{\delta}_{v,2} + \dot{\delta}_{v,1} + \dot{\delta}_{v,0} \tag{94}$$

in which

$$\dot{\delta}_{v,2} = \frac{1}{T}\boldsymbol{\tau}_{\mathrm{o}}^{\mathrm{s}} : (\boldsymbol{\nabla}\mathbf{v})_{\mathrm{o}}^{\mathrm{s}} \tag{95}$$

$$\dot{\delta}_{v,1} = -\frac{1}{T^2}(\mathbf{J}_{\mathrm{U}} - \sum_{i=1}^{n} \mu_i \mathbf{J}_{\mathrm{m}_i}) \cdot \boldsymbol{\nabla}T \ -$$
$$-\frac{1}{T}\sum_{i=1}^{n} \mathbf{J}_{\mathrm{m}_i} \cdot [\boldsymbol{\nabla}\mu_i + eN_{\mathrm{A}}\frac{\sigma_{is}}{M_i}(\mathbf{E} + \mathbf{v}\times\mathbf{B})] \tag{96}$$

$$\dot{\delta}_{v,0} = -\frac{1}{T}[-(\pi + p)]\boldsymbol{\nabla}\cdot\mathbf{v} - \frac{1}{T}\sum_{k=1}^{r} \dot{\xi}_k \mathcal{A}_k \tag{97}$$

Given the independence of the three groups (95), (96) and (97), the non-negativity property of the entropy production [Eq. (93)] is passed on to each of them. They will be dealt with separately in the following sections.

9.3   Tensorial (second-order) generalized force

The traceless symmetric part of the velocity gradient is the sole generalized force of second tensorial order that, conjointly with the traceless symmetric part of the stress tensor, participates in the entropy production [Eq. (95)]

$$\dot{\mathcal{A}}_{v,2} = \frac{1}{T}\boldsymbol{\tau}_{\circ}^{s} : (\boldsymbol{\nabla}\mathbf{v})_{\circ}^{s} \geq 0 \tag{98}$$

The application of the Curie postulate leads to the relatively simple phenomenological relation (22; 23)

$$\boldsymbol{\tau}_{\circ}^{s} = 2\,\boldsymbol{\mu} : (\boldsymbol{\nabla}\mathbf{v})_{\circ}^{s} \tag{99}$$

that resembles the more familiar Newton law. The dynamic viscosity in Eq. (99) is a fourth-order tensor due to the anisotropy introduced by the magnetic induction. Its determination is beyond the reach of irreversible thermodynamics and it must be considered an import either from the kinetic theory of gases or from experiments. A thorough analysis of the dynamic-viscosity tensor is beyond the purpose of the present context. Here, it is sufficient to recall that most of the 81 scalar coefficients required to compose the tensor turn out to vanish and that its complete characterization is limited to the knowledge of only five scalar coefficients. The sign of some of them must be necessarily positive for compliance with the non-negativity of $\dot{\mathcal{A}}_{v,2}$. References (22; 23) provide detailed descriptions of structure and properties of the dynamic-viscosity tensor.

9.4   Vectorial generalized forces

Phenomenological relations for vectorial generalized forces arise from the entropy production related to the first tensorial order

$$\dot{\mathcal{A}}_{v,1} = -\frac{1}{T^2}(\mathbf{J}_{\mathrm{U}} - \sum_{i=1}^{n}\mu_i\mathbf{J}_{\mathrm{m}_i})\cdot\boldsymbol{\nabla}T \; -$$
$$-\frac{1}{T}\sum_{i=1}^{n}\mathbf{J}_{\mathrm{m}_i}\cdot[\boldsymbol{\nabla}\mu_i + eN_{\mathrm{A}}\frac{\sigma_{is}}{M_i}(\mathbf{E} + \mathbf{v}\times\mathbf{B})] \geq 0 \tag{100}$$

In this regard, one has to confront a multifaceted situation because the combination of generalized fluxes and forces appearing in Eq. (100) is not unique. Different, although equivalent, forms of $\dot{\mathcal{A}}_{v,1}$ exist in consequence of transformations to which fluxes and forces can be subjected, a peculiarity due to the occurrence of mass diffusion and recognized long time ago. The equivalence of the several forms stems from the expectable, and provable, invariance of the phenomenological relations for internal-energy diffusive flux and component-mass diffusive fluxes with respect to the mentioned transformations. On the other hand, the multiplicity of forms implies the non-uniqueness of the heat-flux definition. This fact should not come as a surprise or be perceived as the manifestation of some inconsistency in the theory because, as appropriately remarked by Napolitano

(35; 36) in 1969, the "...arbitrariness in the definition of heat flux stems from the fact that any time there is a flux of matter ...there is also a flux of energy ...and it is only a matter of convention (or of convenience) to single out one or more of these fluxes of energy and call them heat flux. ...Any possible definition obviously leaves all physical results unchanged and one should only pay attention in using it consistently, i.e. in associating to it the pertinent expression for the entropy production ...". For a given selection of generalized forces, the heat flux is identified with the generalized flux associated with the temperature gradient. Thus, the definition compatible with the generalized forces appearing in Eq. (100) reads

$$\mathbf{J}'_{\mathrm{q}} = \mathbf{J}_{\mathrm{U}} - \sum_{i=1}^{n} \mu_i \mathbf{J}_{\mathrm{m}_i} = T\mathbf{J}_{\mathrm{S}} \tag{101}$$

Equation (101) is somewhat reminiscent of the classical-thermodynamics relation $dQ = TdS$ but it has received scant attention and its implications on the derivation of the phenomenological relations have rarely been pursued in detail (23; 24; 66). Another form of $\dot{s}_{v,1}$ sometimes encountered in the literature (21; 35; 36; 23; 37) is obtained by contracting the terms with the component-mass diffusive fluxes

$$\frac{\mu_i}{T^2}\mathbf{J}_{\mathrm{m}_i} \cdot \boldsymbol{\nabla}T - \frac{1}{T}\mathbf{J}_{\mathrm{m}_i} \cdot \boldsymbol{\nabla}\mu_i = -\mathbf{J}_{\mathrm{m}_i} \cdot \boldsymbol{\nabla}\frac{\mu_i}{T} \tag{102}$$

in Eq. (100). In this way, the latter becomes

$$\dot{s}_{v,1} = -\frac{1}{T^2}\mathbf{J}_{\mathrm{U}} \cdot \boldsymbol{\nabla}T \; - $$
$$- \frac{1}{T}\sum_{i=1}^{n}\mathbf{J}_{\mathrm{m}_i} \cdot [T\boldsymbol{\nabla}\frac{\mu_i}{T} + eN_{\mathrm{A}}\frac{\sigma_{is}}{M_i}(\mathbf{E} + \mathbf{v} \times \mathbf{B})] \tag{103}$$

and yields the heat-flux definition

$$\mathbf{J}''_{\mathrm{q}} = \mathbf{J}_{\mathrm{U}} = T\mathbf{J}_{\mathrm{S}} + \sum_{i=1}^{n} \mu_i \mathbf{J}_{\mathrm{m}_i} \tag{104}$$

The overwhelmingly preferred form (23; 35; 36; 37) of $\dot{s}_{v,1}$, however, is the one arrived at from the assumption according to which the components of the gas mixture behave as perfect gases. Indeed, in this case

$$\mu_i = h_i - T s_i \tag{105}$$

and

$$\boldsymbol{\nabla}\mu_i = -s_i\boldsymbol{\nabla}T + v_i\boldsymbol{\nabla}p_i \tag{106}$$

The substitution of Eqs. (105) and (106) into Eq. (100) leads to the form

$$\dot{s}_{v,1} = -\frac{1}{T^2}(\mathbf{J}_{\mathrm{U}} - \sum_{i=1}^{n} h_i\mathbf{J}_{\mathrm{m}_i}) \cdot \boldsymbol{\nabla}T \; - $$
$$- \frac{1}{T}\sum_{i=1}^{n}\mathbf{J}_{\mathrm{m}_i} \cdot [v_i\boldsymbol{\nabla}p_i + eN_{\mathrm{A}}\frac{\sigma_{is}}{M_i}(\mathbf{E} + \mathbf{v} \times \mathbf{B})] \tag{107}$$

with the corresponding heat-flux definition

$$\mathbf{J}_{\mathrm{q}}^{'''} = \mathbf{J}_{\mathrm{U}} - \sum_{i=1}^{n} h_i \mathbf{J}_{\mathrm{m}_i} = T\mathbf{J}_{\mathrm{S}} - T\sum_{i=1}^{n} s_i \mathbf{J}_{\mathrm{m}_i} \tag{108}$$

The instances considered so far by no means exhaust the list of possibilities. Other choices (37) of the generalized fluxes and forces, together with the identification of the correspondig heat flux, are possible. On the other hand, it is neither necessary nor intended in the present context to embark in an exhaustive survey. The three described forms of $\dot{s}_{v,1}$ suffice to portray the manifoldness of the heat-flux concept. The irrelevance of its arbitrariness, pointed out in Napolitano's remark, becomes mathematically evident and comprehensible by overturning Eq. (101), Eq. (104) and Eq. (108) as

$$
\begin{aligned}
\mathbf{J}_{\mathrm{U}} &= \mathbf{J}_{\mathrm{q}}^{'} + \sum_{i=1}^{n} \mu_i \mathbf{J}_{\mathrm{m}_i} \\
&= \mathbf{J}_{\mathrm{q}}^{''} \\
&= \mathbf{J}_{\mathrm{q}}^{'''} + \sum_{i=1}^{n} h_i \mathbf{J}_{\mathrm{m}_i}
\end{aligned}
\tag{109}
$$

and by keeping in mind that the internal-energy diffusive flux is invariant with respect to any possible selection of generalized fluxes, forces and corresponding heat-flux definition. Indeed, it is the internal-energy diffusive flux to be the physical flux that really matters in order to evaluate the thermal energy transferred from the flow field into a body or viceversa.

The derivation of the phenomenological relations of first tensorial order pursued here differs from the habitual treatments found in the literature. It proceeds along a pathway that, starting from a slight adaptation of Eq. (107), establishes a strong parallelism with the Chapman-Enskog theory (69; 70; 71; 72; 73; 74; 75; 80; 82; 83; 84; 85; 86) and enormously facilitates the import of the transport coefficients provided by that theory. The transformation that takes care of bringing $\dot{s}_{v,1}$ into the appropriate form presupposes the temporary replacement of the component-mass diffusive flux in the term

$$\mathbf{J}_{\mathrm{m}_i} \cdot [v_i \boldsymbol{\nabla} p_i + eN_{\mathrm{A}} \frac{\sigma_{is}}{M_i}(\mathbf{E} + \mathbf{v} \times \mathbf{B})] \tag{110}$$

with the intermediate appearance of the diffusion velocity defined in Eq. (20). After substituting the latter into Eq. (110), taking into account that $\rho_i v_i = 1$, and setting for brevity

$$\boldsymbol{\mathcal{X}}_i = \boldsymbol{\nabla} p_i + eN_{\mathrm{A}} \rho_i \frac{\sigma_{is}}{M_i}(\mathbf{E} + \mathbf{v} \times \mathbf{B}) \qquad i = 1, \cdots, n \tag{111}$$

Eq. (107) can be rephrased as

$$T\dot{s}_{v,1} = -(\mathbf{J}_{\mathrm{U}} - \sum_{i=1}^{n} h_i \mathbf{J}_{\mathrm{m}_i}) \cdot \boldsymbol{\nabla} \ln T - \sum_{i=1}^{n} \mathbf{w}_i \cdot \boldsymbol{\mathcal{X}}_i \tag{112}$$

The advantage of using Eq. (112) rather than Eq. (107) is that the former leads to operate with the central ingredients (69), namely the vectors $\mathbf{w}_i, \boldsymbol{\mathcal{X}}_i$ and $\boldsymbol{\nabla} \ln T$, of the

Chapman-Enskog theory. The application of the Curie postulate to Eq. (112) provides the phenomenological relations

$$\mathbf{w}_i = -\sum_{j=1}^{n} \mathbf{L}_{ij} \cdot \mathcal{X}_j - \mathbf{L}_{i\mathrm{T}} \cdot \boldsymbol{\nabla} \ln T \tag{113}$$

$$\mathbf{J}_{\mathrm{U}} - \sum_{i=1}^{n} h_i \mathbf{J}_{\mathrm{m}_i} = -\sum_{i=1}^{n} \mathbf{L}_{\mathrm{T}i} \cdot \mathcal{X}_i - \mathbf{L}_{\mathrm{TT}} \cdot \boldsymbol{\nabla} \ln T \tag{114}$$

in which the phenomenological coefficients $\mathbf{L}_{ij}, \mathbf{L}_{i\mathrm{T}}, \mathbf{L}_{\mathrm{T}i}$ and $\mathbf{L}_{\mathrm{TT}}$ are second-order tensors due to the presence of the magnetic induction. Equations (113) and (114) mirror exactly the expressions intervening in the Chapman-Enskog theory and, in consequence of that, the tensors $\mathbf{L}_{ij}, \mathbf{L}_{i\mathrm{T}}, \mathbf{L}_{\mathrm{T}i}$ and $\mathbf{L}_{\mathrm{TT}}$ can be directly and explicitly related as

$$\mathbf{L}_{ij} = -\frac{1}{p}\frac{\rho}{\rho_i}\frac{M_i M_j}{M^2}\mathbf{D}_{ij} \tag{115}$$

$$\mathbf{L}_{i\mathrm{T}} = \frac{1}{\rho_i}\mathbf{D}_i^{\mathrm{T}} \tag{116}$$

$$\mathbf{L}_{\mathrm{T}i} = \tilde{\mathbf{D}}_i^{\mathrm{T}}(-\mathbf{B}) \tag{117}$$

$$\mathbf{L}_{\mathrm{TT}} = T\varkappa' \tag{118}$$

to the tensors of diffusion, thermal diffusion and thermal conductivity provided by that theory. The latter tensors are consistent with the (scalar) formalism of Hirschfelder, Curtiss and Bird (70). In Eq. (115), M is the average molar mass

$$M = \left(\sum_{i=1}^{n} \frac{\alpha_i}{M_i}\right)^{-1} = \sum_{i=1}^{n} M_i x_i \tag{119}$$

of the gas mixture. Equation (117) is an Onsager reciprocal relation. The tilde indicates matrix transposition and the attached functional dependence reminds the necessary inversion of the sign of the magnetic induction. Similar reciprocal relations apply also to the diffusion and thermal-conductivity tensors. However, although important, reciprocity details are not of specific relevance in the present context; interested readers are referred to the specialized literature, particularly the textbooks by Woods (22) and De Groot and Mazur (23). The prime attached to the thermal-conductivity tensor in Eq. (118) is important; following Hirschfelder, Curtiss and Bird's convention, it represents the definition of thermal conductivity consistent with the scalar one that *does not* include the thermodiffusion ratios (69; 70).

The phenomenological relations

$$\mathbf{J}_{\mathrm{m}_i} = \frac{\rho}{p}\frac{M_i}{M}\sum_{j=1}^{n} \frac{M_j}{M}\mathbf{D}_{ij} \cdot \mathcal{X}_j - \frac{1}{T}\mathbf{D}_i^{\mathrm{T}} \cdot \boldsymbol{\nabla} T \quad i = 1, \cdots, n \tag{120}$$

for the component-mass diffusive fluxes follow from the substitution of Eqs. (115) and (116) into Eq. (113) and of the resulting diffusion velocities into Eq. (20). The kinetic-theory result

$$\sum_{i=1}^{n} M_i \mathbf{D}_{ij} \;=\; 0 \tag{121}$$

$$\sum_{i=1}^{n} \mathbf{D}_i^{\mathrm{T}} \;=\; 0 \tag{122}$$

makes the condition (21) identically satisfied. In the same guise, the substitution of Eqs. (117) and (118) into Eq. (114) yields the phenomenological relation for the internal-energy diffusive flux

$$\mathbf{J}_{\mathrm{U}} = \sum_{i=1}^{n} h_i \mathbf{J}_{\mathrm{m}_i} - \sum_{i=1}^{n} \tilde{\mathbf{D}}_i^{\mathrm{T}} \cdot \boldsymbol{\mathcal{X}}_i - \lambda' \cdot \boldsymbol{\nabla} T \tag{123}$$

In Eq. (123), the functional dependence $(-\mathbf{B})$ has been dropped from the transposed thermal-diffusion tensor in order to simplify the notation; nevertheless, this peculiarity should always be kept in mind.

In order to derive phenomenological relations analogous to Eqs. (120) and (123), several authors (23; 35; 36; 37) follow an alternative procedure starting directly from Eq. (107). In their analyses, the term $v_i \boldsymbol{\nabla} p_i$ appears as the *isothermal* gradient of the chemical potential whose definition descends from the following rearrangement

$$v_i \boldsymbol{\nabla} p_i = \boldsymbol{\nabla} \mu_i + \mathcal{s}_i \boldsymbol{\nabla} T = \boldsymbol{\nabla}_{\mathrm{T}} \mu_i \tag{124}$$

of Eq. (106). Then, the generalized forces associated with the component-mass diffusive fluxes in Eq. (107) appear as

$$\boldsymbol{\mathcal{F}}_i = \boldsymbol{\nabla}_{\mathrm{T}} \mu_i + e N_{\mathrm{A}} \frac{\sigma_{is}}{M_i} (\mathbf{E} + \mathbf{v} \times \mathbf{B}) \tag{125}$$

The ensuing phenomenological relations for the component-mass diffusive fluxes and the internal-energy diffusive flux are further manipulated to bring forth the gradients of mass fractions (Fick law) and pressure. The drawback of this procedure resides in the fact that the intervening tensorial phenomenological coefficients, say $\mathbf{L}'_{ij}, \mathbf{L}'_{i\mathrm{T}}, \mathbf{L}'_{\mathrm{T}i}, \mathbf{L}'_{\mathrm{TT}}$, are not expressible in terms of the kinetic-theory tensors $\mathbf{D}_{ij}, \mathbf{D}_i^{\mathrm{T}}, \lambda'$ as simply as in Eqs. (115)–(118) but, in order to obtain the required correlation, necessitate an elaborate manipulation involving the resolution of cumbersome algebraic systems of equations.

The phenomenological relations (120) and (123) are operational equations that, together with Eq. (111) and with adequate input from the kinetic theory, qualify to complement the set of governing equations in open form for the purpose of numerical calculations. However, noticeable insight towards the understanding of the transport processes can be gained if the role played by the contributions composing the generalized force $\boldsymbol{\mathcal{X}}_i$ is made explicit. The substitution of Eq. (111) into Eq. (120) yields

$$\mathbf{J}_{\mathrm{m}_i} = \frac{\rho}{p} \frac{M_i}{M} \sum_{j=1}^{n} \frac{M_j}{M} \mathbf{D}_{ij} \cdot \boldsymbol{\nabla} p_j + \mathbf{F}_i^{\mathrm{m}} \cdot (\mathbf{E} + \mathbf{v} \times \mathbf{B}) \;-$$

$$-\frac{1}{T} \mathbf{D}_i^{\mathrm{T}} \cdot \boldsymbol{\nabla} T \tag{126}$$

with the tensorial coefficients

$$\mathbf{F}_i^{\mathrm{m}} = e N_{\mathrm{A}} \frac{\rho}{p} \frac{M_i}{M^2} \sum_{j=1}^{n} \mathbf{D}_{ij} \rho_j \sigma_{js} \tag{127}$$

Equation (126) shows explicitly how the electromagnetic field participates to the build-up of the component-mass diffusive fluxes at the same footing of the partial-pressure and temperature gradients. The appearance of the mass-fraction gradients is one step away from Eq. (126) and is produced by expanding the partial pressures with the aid of the perfect-gas relations $p_i = x_i p$ and $x_i = \alpha_i M_i / M$. Accordingly, Eq. (126) becomes

$$\mathbf{J}_{\mathrm{m}_i} = - \sum_{k=1}^{n-1} \boldsymbol{\mathfrak{D}}_{ik} \cdot \boldsymbol{\nabla} \alpha_k + \mathbf{P}_i^{\mathrm{m}} \cdot \boldsymbol{\nabla} p \ +$$

$$+ \ \mathbf{F}_i^{\mathrm{m}} \cdot (\mathbf{E} + \mathbf{v} \times \mathbf{B}) - \frac{1}{T} \mathbf{D}_i^{\mathrm{T}} \cdot \boldsymbol{\nabla} T \tag{128}$$

with the tensorial coefficients

$$\boldsymbol{\mathfrak{D}}_{ik} = \left(\frac{M_i}{M_k} - \frac{M_i}{M_n} \right) \left(\sum_{j=1}^{n} \mathbf{D}_{ij} \rho_j \right) - \rho \frac{M_i}{M} (\mathbf{D}_{ik} - \mathbf{D}_{in}) \tag{129}$$

$$\mathbf{P}_i^{\mathrm{m}} = \frac{1}{p} \frac{M_i}{M} \sum_{j=1}^{n} \mathbf{D}_{ij} \rho_j \tag{130}$$

Equation (128) warns against the uncareful practice of limiting the expressions of the component-mass diffusive fluxes to the sole Fick law, namely the first term on the right-hand side. Even in the event of negligible thermodiffusion and vanishing electromagnetic field, that widely assumed law may not be sufficient to characterize completely the component-mass diffusive fluxes because the tensorial coefficients $\mathbf{P}_i^{\mathrm{m}}$, being constructed according to combinations of the diffusion tensors very similar to those that appear in Eq. (129), could have magnitudes comparable to the tensorial coefficients $\boldsymbol{\mathfrak{D}}_{ik}$. Thus, it seems safer not to discard *a priori* the pressure-gradient contribution in Eq. (128) but to let its negligibility, if any, arise spontaneously during the course of numerical simulations.

The substitution of Eq. (126) into Eq. (33) leads to a more explicit and meaningful expression of the conduction-current density

$$\mathbf{J}_{\mathrm{Q}} = \sum_{j=1}^{n} \boldsymbol{\lambda}_{\mathrm{e}j}^{\mathrm{p}} \cdot \boldsymbol{\nabla} p_j + \boldsymbol{\lambda}_{\mathrm{e}} \cdot (\mathbf{E} + \mathbf{v} \times \mathbf{B}) + \boldsymbol{\lambda}_{\mathrm{e}}^{\mathrm{T}} \cdot \boldsymbol{\nabla} T \tag{131}$$

and to the recognition of the *pressoelectrical*-conductivity tensors

$$\boldsymbol{\lambda}_{\mathrm{e}j}^{\mathrm{p}} = -e N_{\mathrm{A}} \frac{\rho}{p} \frac{M_j}{M^2} \sum_{i=1}^{n} \sigma_{is} \mathbf{D}_{ij} \tag{132}$$

the electrical-conductivity tensor

$$\boldsymbol{\lambda}_{\mathrm{e}} = -(e N_{\mathrm{A}})^2 \frac{\rho}{p M^2} \sum_{i=1}^{n} \sum_{j=1}^{n} \sigma_{is} \mathbf{D}_{ij} \rho_j \sigma_{js} \tag{133}$$

in rigorous agreement with the expression derived by Chapman and Cowling (69), and the thermoelectrical-conductivity tensor

$$\lambda_{\mathrm{e}}^{\mathrm{T}} = e N_{\mathrm{A}} \frac{1}{T} \sum_{i=1}^{n} \frac{\sigma_{is}}{M_i} \mathbf{D}_i^{\mathrm{T}} \tag{134}$$

Equation (131) evidences unambiguously that the generalized Ohm law alone may not be sufficient to characterize the conduction-current density in an ionized gas mixture because, even in the event of negligible thermodiffusion, the contributions associated with the partial-pressure gradients may not be negligible with respect to the diffusion promoted by the electromagnetic field. These considerations have a negative impact on the applicability of the magnetic-induction equation discussed in Sec. 5. At the same time, Eq. (133) casts skepticism about the physical meaningfulness of (actually, it severely admonishes against) undertaking flow-field simulations in the presence of the electromagnetic field in which the gas mixture is assimilated to a perfect gas without electrically charged carriers but still with a finite (scalar) electrical conductivity. This is a flagrant infringement of physical coherence because the electrically-conductivity tensor vanishes identically in the absence of electrically charged components, as Eq. (133) unconditionally indicates ($\sigma_{is} = \sigma_{js} = 0$).

An expression structured in the same style of Eq. (126) can be obtained also for the internal-energy diffusive flux by substituting Eqs. (111) and (126) into Eq. (123); the final outcome reads

$$\mathbf{J}_{\mathrm{U}} = \sum_{j=1}^{n} \mathbf{P}_j^{\mathrm{u}} \cdot \boldsymbol{\nabla} p_j + \mathbf{F}^{\mathrm{u}} \cdot (\mathbf{E} + \mathbf{v} \times \mathbf{B}) - \lambda_{\mathrm{T}}^{\mathrm{u}} \cdot \boldsymbol{\nabla} T \tag{135}$$

with the tensorial coefficients

$$\mathbf{P}_j^{\mathrm{u}} = \sum_{i=1}^{n} (\delta_{ij} \tilde{\mathbf{D}}_j^{\mathrm{T}} + \frac{\rho}{p} h_i \frac{M_i M_j}{M^2} \mathbf{D}_{ij}) \tag{136}$$

$$\mathbf{F}^{\mathrm{u}} = e N_{\mathrm{A}} \sum_{i=1}^{n} \left(\tilde{\mathbf{D}}_i^{\mathrm{T}} \rho_i \frac{\sigma_{is}}{M_i} + \frac{\rho}{p} h_i \frac{M_i}{M^2} \sum_{j=1}^{n} \mathbf{D}_{ij} \rho_j \sigma_{js} \right) \tag{137}$$

$$\lambda_{\mathrm{T}}^{\mathrm{u}} = \lambda' + \frac{1}{T} \sum_{i=1}^{n} h_i \mathbf{D}_i^{\mathrm{T}} \tag{138}$$

There are two aspects related to Eq. (135), not encountered in hypersonic-flow theory when the electromagnetic field is absent, that may have implications for spacecraft thermal protection during planetary reentry. As clearly shown in Eq. (135), there is a direct contribution arising just from the mere existence of the electromagnetic field. In particular, the influence of the magnetic induction disappears on the wall ($\mathbf{v} = 0$) of a reentry body but the influence of the electric field could still play a role. Moreover, Eq. (135) indicates also that, on the contrary of the widespread habitude acquired within the realm of a scalar transport theory, the component of $\mathbf{J}_{\mathrm{U}}$ normal to the wall of a reentry body depends not only on the normal gradients of partial pressures and temperature but also on their tangential gradients (23). With the goal in mind of achieving a controlled mitigation of the internal-energy diffusive flux, this occurrence gives cause for the necessity to produce an accurate assessment of the importance of the off-diagonal terms in the

transport tensors. More specifically, a thorough understanding of the anisotropic character of the transport tensors under the influence of the electromagnetic field appears to be a worthwhile target. Chapman and Cowling (69) pioneered the study of this subject but the cases they considered were subdued to simplifications (steady states, slight or full ionization, binary mixtures, absence of chemical reactions, mixtures macroscopically at rest, and the like) which appear (sometimes very) restrictive when looked at from the perspective of hypersonics applications. Chapman and Cowling's findings and conclusions have reverberated throughout the literature (11; 22; 72); unfortunately, the accompanying simplifications seem to have been somehow *diluted* during the reverberation process. Thus, central issues are still in demand of attention. For example, it is important to identify the circumstances according to which the anisotropy possessed by the transport tensors is or is not negligible, to recognize if the anisotropy works against or in favor of the sought mitigation, to investigate the existence of potential ways to enhance the anisotropy effects and drive them towards the sought mitigation. In the present author's opinion, the work already done (69; 72; 73; 75; 80; 81; 82; 83; 84; 85; 86; 87; 88) requires improvement in the generality of the findings and, if necessary, in their adaptation to routine use in numerical calculations.

9.5   Scalar generalized forces

The derivation of the phenomenological relations relative to the scalar generalized forces is based on the entropy production related to the zero tensorial order

$$\dot{s}_{v,0} = -\frac{1}{T}[-(\pi + p)]\boldsymbol{\nabla} \cdot \mathbf{v} - \frac{1}{T}\sum_{k=1}^{r}\dot{\xi}_{k}\mathcal{A}_{k} \geq 0 \tag{139}$$

The application of the Curie postulate to Eq. (139) provides the phenomenological relations

$$-(\pi + p) = -\sum_{k=1}^{r}l_{vk}\mathcal{A}_{k} - l_{vv}\boldsymbol{\nabla} \cdot \mathbf{v} \tag{140}$$

$$\dot{\xi}_{k} = -\sum_{j=1}^{r}l_{kj}\mathcal{A}_{j} - l_{kv}\boldsymbol{\nabla} \cdot \mathbf{v} \tag{141}$$

The scalar phenomenological coefficients $l_{vk}, l_{vv}, l_{kj}, l_{kv}$ form an $[(r + 1) \times (r + 1)]$ matrix which must be positive definite in order to have the inequality (139) identically satisfied. Onsager reciprocal relations exist also for these coefficients but they will not be considered here for the same reason mentioned in Sec. 9.4; plenty of information is available in the specialized literature. The scalar phenomenological coefficients appearing in Eqs. (140) and (141) have not been investigated with the same attention devoted to the kinetic-theory tensors encountered in Secs. 9.3 and 9.4 because it was soon recognized (23; 35; 36; 67) that the linear combinations of the affinities in Eqs. (140) and (141) have very narrow limits of validity. The coefficient l_{vv} is better known as the bulk-viscosity coefficient

$$l_{vv} = \mu_{v} \tag{142}$$

and is the only one which has received attention because it characterizes the direct effect of the medium compressibility ($\boldsymbol{\nabla} \cdot \mathbf{v}$) on the generation of normal stresses. Even with the limitation imposed by their restricted applicability, Eqs. (140) and (141) retain importance from a theoretical point of view because they reveal unambiguously the existence of cross effects between chemical reactions and medium compressibility (21; 35; 36; 37). This aspect has been systematically ignored by authors concerned with CFD applications. Notwithstanding a few daring attempts (89; 90; 91) towards theoretical progress on the subject matter, the concern expressed by Napolitano (35; 36) in 1969 that "Not much is known nor is done ... to ascertain the order of magnitude of this type of coupling" is, unfortunately, still applicable today.

The disregard of cross effects brings Eq. (140) into the simplified form

$$\pi = -p + \mu_v \boldsymbol{\nabla} \cdot \mathbf{v} \tag{143}$$

which finds widespread used in the applications, most often accompanied by the ulterior approximation of vanishing bulk viscosity ($\mu_v = 0$). In the same guise, Eq. (141) would become

$$\dot{\xi}_k = -l_{kk} \mathcal{A}_k \tag{144}$$

However, chemical-reactions rates are never used in the form (144) but, rather, in the non-linear form

$$\dot{\xi}_k = \mathcal{K}_k^{\mathrm{f}} \prod_{i=1}^n \left(\frac{\rho_i}{M_i}\right)^{\nu_{ki}^{(\mathrm{r})}} - \mathcal{K}_k^{\mathrm{b}} \prod_{i=1}^n \left(\frac{\rho_i}{M_i}\right)^{\nu_{ki}^{(\mathrm{p})}} \tag{145}$$

that features explicit dependence on the component partial densities and that sometimes is referred to as the law of mass action (23; 35; 36). Equation (145) arises from a blend of theoretical considerations and (mainly) experimental evidence (74; 92; 93; 94; 95; 96; 97). The reaction *constants* $\mathcal{K}_k^{\mathrm{f}}, \mathcal{K}_k^{\mathrm{b}}$ are in reality functions of the temperature, customarily assumed in accordance with a modified version

$$\mathcal{K}^{\mathrm{f,b}} = C T^\eta e^{-E_a/K_{\mathrm{B}} T} \tag{146}$$

of the Arrhenius law, and are related to each other through the chemical-equilibrium constant defined in terms of the component concentrations

$$\frac{\mathcal{K}_k^{\mathrm{f}}}{\mathcal{K}_k^{\mathrm{b}}} = K_k^{\mathrm{c}}(T) \tag{147}$$

A theoretical justification for Eq. (146) can be produced only in particularly simple cases. In practice, the parameters C, η, E_a are derived by utilizing that expression as an interpolation formula constructed on experimentally determined data and, then, collected in databases (98; 99) readily available to serve the needs of the applications. The reliability of Eq. (146) becomes weak in the high-temperature range due to serious difficulties encountered in carrying out accurate measurements. The uncertainties of the reaction constants at high temperatures is a well known and long standing problem in demand of resolution. In the chemical-equilibrium limit $[(\mathcal{A}_k \to 0) \Rightarrow \mathcal{A}_k/R_{\mathrm{G}} T \ll 1]$, Eq. (145) reduces (35; 36; 37; 67) to Eq. (144) with the phenomenological coefficient given by

$$l_{kk} = \frac{\mathcal{K}_k^{\mathrm{f}}}{R_{\mathrm{G}} T} \prod_{i=1}^n \left(\frac{\rho_i^{\mathrm{e}}}{M_i}\right)^{\nu_{ki}^{(\mathrm{r})}} = \frac{\mathcal{K}_k^{\mathrm{b}}}{R_{\mathrm{G}} T} \prod_{i=1}^n \left(\frac{\rho_i^{\mathrm{e}}}{M_i}\right)^{\nu_{ki}^{(\mathrm{p})}} \tag{148}$$

The subscript "e" attached to the partial densities in Eq. (148) indicates their chemical-equilibrium values corresponding to the local couple of thermodynamic parameters $[(T, v)$ or $(T, p)]$.

Notwithstanding the widespread use of Eq. (145) in CFD, it is important to keep in mind that the premises on which it is constructed reflect the chemical kinetics of a perfect-gas mixture contained in a constant volume, macroscopically at rest, without spatial disuniformities, and whose population distributions over the quantum energy states associated with the molecular degrees of freedom can still be sufficiently assimilated to a Boltzmann distribution (35; 36). The chemical-kinetics phenomenology described by Eq. (145) is, therefore, substantially simpler than the more complex one accompanying hypersonics situations. For example, some unresolved, but of extreme relevance, issues are the failure of Eq. (145) to bring into account the influence of the medium compressibility, the intrinsic difficulty to adapt it to multitemperature situations, and its incompatibility with quantum-state populations that do not follow a Boltzmann distribution.

10   Conclusions

The understanding of the coupling between the hypersonic flow field of an ionized gas mixture and the electromagnetic field is conceptually straightforward in the absence of polarization and magnetization effects. The recognition of the weaknesses affecting the assumptions on which the derivation of the largely used magnetic-induction equation is based indicates that the adoption of either directly the Maxwell equations [Eqs. (38) and (39)] or the field equations for the electromagnetic scalar and vectorial potentials represents a better choice reflecting a more consistent physical description of the electromagnetic field. The cost to pay is the development of appropriate numerical algorithms that, especially in the case in which the field equations of the potentials are chosen, may turn out to be substantially different from those in use since many years in computational fluid dynamics. Obviously, the coverage of the physical phenomenology relative to polarization and magnetization is desirable for reasons of both scientific interest and engineering necessity. Thus, the open-form governing equations should be extended for that purpose. The extension should be accomplished in a bilateral manner, that is, not only by using the appropriate Maxwell equations but also by introducing the required ingredients on the fluid-dynamics side such as, for example, the intrinsic moment of matter momentum, its associated energy, their respective balance equations, and so on. Subsequently, the formalization of state-to-state thermal kinetics and radiation together with their integration in the open-form governing equations represent a wishful endeavor towards completion.

The open-form governing equations must be complemented with phenomenological relations. In this respect, the method of irreversible thermodynamics, based on the analysis of the entropy production, proves useful to recognize generalized fluxes and generalized forces at work in the flow, achieves deep insight into the physics of their cross couplings, and provides linear phenomenological relations that, although with the exception of the chemical-reaction rates, go rather far in satisfying the needs of engineering applications. The method straightforwardly reveals how the influence exerted by the electromagnetic field on the diffusion of (electrically-charged) component masses and internal energy becomes manifest. There is a novelty with respect to more habitual fluid-dynamics situa-

tions without electromagnetic field: the presence of the magnetic induction destroys the isotropy of the flow. The introduced anisotropy calls for particular attention to the possibility of cross coupling between generalized fluxes and forces of different tensorial order and to understand the importance of the tensorial nature of the transport coefficients with the goal in mind of exercising control over the distributions of internal-energy diffusive flux imposed on the surfaces of a body during planetary reentry. Multitemperature circumstances should not be underestimated. There have been efforts to bring the multitemperature phenomenology within the reach of irreversible thermodynamics but the actual status of the theory demands further improvements. This appears a mandatory task to pursue in order to incorporate correctly the effects originating from the thermal disequilibrium among the molecular degrees of freedom of the components.

The final goal of the theoretical fluid dynamicist is the construction of an adequate mathematical apparatus with the *proper* physics built in it. According to the previous considerations, there is plenty of work in the theoretical arena awaiting investigation and understanding. New problems join old ones, some of which were identified and formulated long time ago but are still unresolved today. In this respect, it can be safely maintained that two antithetical approaches emerge. The *minimalist* approach consists in throwing into the equations a simplified physics, most of the times even stretched beyond its domain of applicability, and rushing to the computer in the hope that the discarded physics is unimportant and that either numerically predicted flows match experimental evidence within an acceptable approximation or sensitivity analyses produce conservative results. This is a risky approach. For one thing, accurate experimental evidence in hypersonic regime may be difficult to gather; in addition, the necessity imposed by engineering applications to produce results within awfully short time limits induces to yield at the temptation of *numerically* fine-tuning the physical models, an exercise that sometimes is camouflaged under the epithet of validation. The *maximalist* approach is characterized by an attitude of thoroughness towards the physics translated into the equations; conceptual difficulties are not avoided but are confronted without hesitation in order to push further ahead the comprehension of the phenomenology dealt with. This is a lengthy approach, certainly incompatible with the shortness of the time limits mentioned above. On the other hand, it is inescapable when the minimalist approach leads into a situation of stagnating failure. The choice between the two approaches is a matter of personal taste. The last years have seen an unquestionable unbalance towards the former approach sponsored by an unjustified rush to computational fluid dynamics. Probably, the most convenient way to go about is the one that takes advantage of both. When dealing with new physical complexities, the minimalist approach is acceptable to start with but resources should also be allocated to promote a parallel line of development following the maximalist-approach philosophy. In the author's opinion, the latter is a *sine qua non* condition to achieve progress in such a complex discipline as hypersonics is.

Acknowledgments

The author wishes to thank F. Ongaro (ESA/SER-A) for the funding support provided to this research activity in the context of the ESA General Studies Programme.

References

[1] E. Guggenheim, On Magnetic and Electrostatic Energy, Proc. R. Soc. London **A155**, 49–70 (1936).

[2] E. Guggenheim, The Thermodynamics of Magnetization, Proc. R. Soc. London **A155**, 70–101 (1936).

[3] J. Hartmann, Hg-Dynamics I. Theory of the Laminar Flow of an Electrically Conductive Liquid in a Homogeneous Magnetic Field, Kgl Danske Vidensk. Selskab **XV**, 3–28 (1937).

[4] E. Guggenheim, *Thermodynamics* (North Holland Publ. Co., Amsterdam, 1950).

[5] P. Mazur and I. Prigogine, Contribution à la Thermodynamique de la Matière dans un Champ Électromagnétique, Mem. Acad. Roy. Belg. (Cl. Sc.) **23**, 1–56 (1952).

[6] S.-I. Pai, Energy Equation of Magneto-Gas Dynamics, Phys. Rev. **105**, 1424–1426 (1957).

[7] T. Cowling, *Magnetohydrodynamics* (Interscience Publishers, London, 1957).

[8] V. Rossow, On Flow of Electrically Conducting Fluids over a Flat Plate in the Presence of a Transverse Magnetic Field, NACA Technical Report No. 1358, 1958.

[9] E. Resler and W. Sears, The Prospects for Magneto-Aerodynamics, J. Aeron. Sciences **25**, 235–245/258 (1958).

[10] W. Bush, Magnetohydrodynamic-Hypersonic Flow past a Blunt Body, J. Aero/Space Sciences **25**, 685–690/728 (1958).

[11] L. Napolitano, Contributo alla Magnetofluidodinamica, Missili **1**,15–34 (1959).

[12] W. Sears, Magnetohydrodynamic Effects in Aerodynamic Flows, Amer. Rocket Soc. J., June, 397–406 (1959).

[13] B.-T. Chu, Thermodynamics of Electrically Conducting Fluids, Phys. Fluids **2**, 473–484 (1959).

[14] S. Goldstein, *Lectures on Fluid Mechanics* (Interscience Publishers Ltd, London, 1960).

[15] B. Finzi, Principio d'Azione Stazionaria nell'Elettrodinamica dei Fluidi, Ann. Matem. Pura e Appl. **50**, 321–339 (1960).

[16] L. Napolitano, La Magnetofluidodinamica dal Punto di Vista Fenomenologico, in *Atti del Simposio sulla Magnetofluidodinamica, 1961* (Oderisi Editrice, Gubbio, Italy, 1962), p. 235.

[17] L. Spitzer *Physics of Fully Ionized Gases* (Interscience Publishers, London, 1962).

[18] S.-I. Pai, *Magnetogasdynamics and Plasma Dynamics* (Springer Verlag, Wien, 1962).

[19] L. Napolitano, Equazioni Macroscopiche della Magnetofluidodinamica, in *Atti del Convegno sulla Fisica del Plasma, 1963,* (Consiglio Nazionale delle Ricerche, Rome, 1965), p. 5.

[20] L. Napolitano, Electrofluid Dynamics, Inst. of Aerodynamics (Univ. of Naples, Italy) Report No. 140, January 1969.

[21] L. Sedov, *Mécanique des Milieux Continus. Tome I.* (Éditions MIR, Moscou, 1975).

[22] L. Woods, *The Thermodynamics of Fluid Systems* (Clarendon Press, Oxford, 1975).

[23] S. De Groot and P. Mazur, *Non-Equilibrium Thermodynamics* (Dover Publications, New York, 1984).

[24] H. Robertson, *Statistical Thermophysics* (Prentice-Hall, Englewood Cliffs NJ, 1993).

[25] A. Castellanos, *Electrohydrodynamics* (Springer Verlag, Wien, 1998).

[26] R. Peterkin and P. Turchi, Magnetohydrodynamic Theory for Hypersonic Plasma Flow: What's Important and What's Not, in *31st Plasmadynamics and Lasers Conference*, 19–22 June 2000, Denver CO, (American Institute of Aeronautics and Astronautics). AIAA 2000-2257.

[27] N. Kemp, On Hypersonic Blunt-Body Flow with a Magnetic Field, J. Aeron. Sciences **25**, 405–407 (1958).

[28] R. Meyer, On Reducing Aerodynamic Heat-Transfer Rates by Magnetohydrodynamics Techniques, J. Aerod. Sciences **?**, 561–566/572 (1958) or preprint no. 816, Institute of the Aeronautical Sciences, January, 1958.

[29] R. Goulard, Optimum Magnetic field for Stagnation Heat Transfer Reduction at Hypersonic Velocities, Amer. Rocket Soc. J., August, 604–605 (1959).

[30] R. Phillips, Effect of Magnetic Drag on Re-Entry Body Heating, Amer. Rocket Soc. J., May, 672–674 (1961).

[31] M. Romig, The Influence of Electric and Magnetic Fields on Heat Transfer to Electrically Conducting Fluids, in *Advances in Heat Transfer, Vol. 1,* edited by T. Irvine and J. Hartnett (Academic Press, New York, 1964), p. 267.

[32] R. Nowak and M. Yuen, Heat Transfer to a Hemispherical Body in a Supersonic Argon Plasma, AIAA J. **11**, 1463–1464 (1973).

[33] J. Lineberry, R. Rosa, V. Bityurin, A. Botcharov and V. Potebnya, Prospects of MHD Flow Control for Hypersonics, in *35th Intersociety Energy Conversion Engineering Conference*, 24–28 July 2000, Las Vegas NV, (American Institute of Aeronautics and Astronautics). AIAA 2000-3057.

[34] J. Poggie and D. Gaitonde, Computational Studies of Magnetic Flow Control in Hypersonic Flow, in *39th Aerospace Sciences Meeting & Exhibit*, 8–11 January 2001, Reno NV, (American Institute of Aeronautics and Astronautics). AIAA 2001-0196.

[35] L. Napolitano, Derivation of the Basic Equations for Non-Equilibrium Boundary Layers, AGARD-VKI Lecture Series on "Hypersonic Boundary Layers", February 1969.

[36] L. Napolitano and O. Belotserkovski, *Computational Gasdynamics* (Springer Verlag, Wien, 1975).

[37] S. Wiśniewski, B. Staniszewski and R. Szymanik, *Thermodynamics of Nonequilibrium Processes* (Reidel Publishing Company, Dordrecht, Holland, 1976).

[38] L. Napolitano, *Thermodynamique des Systèmes Composites en Équilibre ou Hors d'Équilibre* (Gauthier-Villars Éditeurs, Paris, 1971).

[39] R. Feynman, R. Leighton and M. Sands, *The Feynman Lectures on Physics. Vol. II.* (Addison-Wesley Publish. Co., Reading MA, 1989). Commemorative issue.

[40] J. Maxwell, *A Treatise on Electricity and Magnetism* (Dover Publications, New York, 1954).

[41] C. Møller, *The Theory of Relativity* (Oxford University Press, Oxford, 1969).

[42] P. Lorrain and D. Colson, *Electromagnetic Fields and Waves* (Freeman and Co., San Francisco, 1970).

[43] E. Persico, *Introduzione alla Fisica Matematica* (Zanichelli Editrice, Bologna, 1971).

[44] R. Tolman, *Relativity Thermodynamics and Cosmology* (Dover Publications, New York, 1987).

[45] W. Pauli, *Electrodynamics* (Dover Publications, New York, 2000).

[46] J. Augustinus, K. Hoffmann and S. Harada, Effect of Magnetic Field on the Structure of High-Speed Flows, J. of Spacecraft and Rockets **35**, 639–646 (1998).

[47] K. Hoffmann, H-M. Damevin and J-F. Dietiker, Numerical Simulation of Hypersonic Magnetohydrodynamic Flows, in *31th Plasmadynamics and Lasers Conference*, 19–22 June 2000, Denver CO, (American Institute of Aeronautics and Astronautics). AIAA 2000-2259.

[48] P. Deb and R. Agarwal, Numerical Study of MHD-Bypass Scramjet Inlets with Finite Rate Chemistry, in *39th Aerospace Sciences Meeting & Exhibit*, 8–11 January 2001, Reno NV, (American Institute of Aeronautics and Astronautics). AIAA 2001-0794.

[49] R. Munipalli and V. Shankar, Development of Computational Capabilities in Real gas MHD, in *39th Aerospace Sciences Meeting & Exhibit*, 8–11 January 2001, Reno NV, (American Institute of Aeronautics and Astronautics). AIAA 2001-0198.

[50] J. Shang, Shared Knowledge in Computational Fluid Dynamics, Electromagnetic, and Magneto-Aerodynamics, in *15th Computational Fluid Dynamics Conference*, 11–14 June 2001, Anaheim CA, (American Institute of Aeronautics and Astronautics). AIAA 2001-2522.

[51] U. Shumlak and B. Udrea, An Approximate Riemann Solver for MHD Computations on Parallel Architectures, in *15th Computational Fluid Dynamics Conference*, 11–14 June 2001, Anaheim CA, (American Institute of Aeronautics and Astronautics). AIAA 2001-2591.

[52] R. MacCormack, A Computational Method for Magnetofluid Dynamics, in *32nd Plasmadynamics and Lasers Conference*, 11–14 June 2001, Anaheim CA, (American Institute of Aeronautics and Astronautics). AIAA 2001-2735.

[53] H-M. Damevin and K. Hoffmann, Numerical Magnetogasdynamics Simulations of Hypersonic Chemically Reacting Flows, in *32nd Plasmadynamics and Lasers Conference*, 11–14 June 2001, Anaheim CA, (American Institute of Aeronautics and Astronautics). AIAA 2001-2746.

[54] T. Eddy and K. Cho, A Multitemperature Model for Plasmas in Chemical Equilibrium, in *HTD, Vol. 161: Heat Transfer in Thermal Plasma Processing*, edited by K. Etemadi and J. Mostaghimi (American Society of Mechanical Engineers, New York, 1991)

[55] D. Giordano, On the Statistical Thermodynamics of Multi-Temperature Systems, European Space Research & Technology Centre, ESA STM-251, November 1993.

[56] R. Jaffe, The Calculation of High-Temperature Equilibrium and Nonequilibrium Specific Heat Data for N_2, O_2 and NO, in *22nd Thermophysics Conference*, 8–10 June 1987, Honolulu HI, (American Institute of Aeronautics and Astronautics). AIAA 87-1633.

[57] M. Capitelli, G. Colonna, C. Gorse and D. Giordano, Survey of Methods of Calculating High-Temperature Thermodynamic Properties of Air Species, European Space Research & Technology Centre, ESA STR-236, December 1994.

[58] D. Giordano, V. Bellucci, G. Colonna, M. Capitelli, I. Armenise, and C. Bruno, Vibrationally Relaxing Flow of N_2 past an Infinite Cylinder According to State-to-State Vibrational Kinetics and to the Harmonic-Oscillator Model, in *30th Thermophysics Conference*, 19–22 June 1995, San Diego CA, (American Institute of Aeronautics and Astronautics). AIAA 95-2072.

[59] M. Capitelli, C. Gorse and I. Armenise, State to State Approach in the Kinetics of Air Components under Reentry Conditions, in *27th Fluid Dynamics Conference*, 17–20 June 1996, New Orleans LA, (American Institute of Aeronautics and Astronautics). AIAA 96-1985.

[60] E. Josyula, Computationally Study of Vibrationally Relaxing Gas past Blunt Body in Hypersonic Flows, J. of Thermophysics and Heat Transfer **14**, 18–26 (2000).

[61] E. Josyula and W. Bailey, Vibration-Dissociation Coupling Using Master Equations in Nonequilibrium Hypersonic Blunt-Body Flow, J. of Thermophysics and Heat Transfer **15**, 157–167 (2001).

[62] G. Colonna, State to State Electron and Vibrational Kinetics in Supersonic Nozzle Air Expansion: An Improved Model, in *33rd Plasmadynamics and Lasers Conference*, 20–23 May 2002, Maui HI, (American Institute of Aeronautics and Astronautics). AIAA 2002-2163.

[63] D. Giordano, Influence of Non-Boltzmann Distributions on the Thermodynamic Properties of Gaseous Species, J. of Thermophysics and Heat Transfer **11**, 273–279 (1997).

[64] M. Capitelli, C. Ferreira, B. Gordiets and A. Osipov, *Plasma Kinetics in Atmospheric Gases* (Springer Verlag, Berlin, 2000).

[65] K. Denbigh, *The Thermodynamics of the Steady State* (Methuen & Co. LTD., London, 1951).

[66] H. Callen *Thermodynamics and an Introduction to Thermostatistics* (John Wiley & Sons, New York, 1985).

[67] I. Prigogine, *Introduction à la Thermodynamique des Processus Irréversibles* (Éditions Jacques Gabay, Paris, 1996).

[68] L. Woods, *Thermodynamic Inequalities in Gases and Magnetoplasmas* (John Wiley & Sons, New York, 1996).

[69] S. Chapman and T. Cowling, *The Mathematical Theory of Non-Uniform Gases* (Cambridge University Press, Cambridge UK, 1990).

[70] J. Hirschfelder, C. Curtiss and R. Bird, *Molecular Theory of Gases and Liquids* (John Wiley & Sons, New York, 1954).

[71] A. Hochstim, ed., *Kinetic Processes in Gases and Plasmas* (Academic Press, New York, 1969).

[72] J. Ferziger and H. Kaper, *Mathematical Theory of Transport Processes in Gases* (North Holland, Amsterdam, 1972).

[73] M. Mitchner and C. Kruger, *Partially Ionized Gases* (John Wiley & Sons, New York, 1973).

[74] W. Vincenti and C. Kruger, *Introduction to Physical Gas Dynamics* (John Wiley & Sons, New York, 1975).

[75] F. McCourt, J. Beenakker, W. Kohler and I. Kuscer, *Nonequilibrium Phenomena in Polyatomic Gases* (Clarendon Press, Oxford, 1990).

[76] A. Morro and M. Romeo, On the Law of Mass Action in Fluid Mixtures with Several Temperatures, Nuovo Cimento **7 D**, 539–550 (1986).

[77] A. Morro and M. Romeo, Thermodynamic Derivation of Saha's Equation for a Multi-Temperature Plasma, J. Plasma Phys. **39**, 41–51 (1988).

[78] A. Morro and M. Romeo, The Law of Mass Action for Fluid Mixtures with Several Temperatures and Velocities, J. Noneq. Thermodyn. **13**, 339–353 (1988).

[79] L. Tisza, *Generalized Thermodynamics* (The M.I.T. Press, Cambridge MA, 1977).

[80] R. Devoto, Transport Properties of Ionized Monatomic Gases, Phys. Fluids **9**, 1230–1240 (1966).

[81] J. Korving, The Influence of a Magnetic Field on the Transport Properties of Gases of Polyatomic Molecules, Doctoral Thesis, Rijksuniversiteit Leiden, 1967.

[82] S. Schweitzer and M. Mitchner, Electrical Conductivity of a Partially Ionized Gas in a Magnetic Field, Phys. Fluids **10**, 799–806 (1967).

[83] R. Chmieleski and J. Ferziger, Transport Properties of a Nonequilibrium Partially Ionized Gas in a Magnetic Field, Phys. Fluids **10**, 2520–2530 (1967).

[84] U. Daybelge, Transport Properties of Two-Temperature Partially Ionized Plasmas, Institute for Plasma Research, Stanford University, SU-IPR Report No. 263, December 1968.

[85] R. Devoto, Heat and Diffusion Fluxes in a Multicomponent Ionized Gas in a Magnetic Field, Z. Naturforsch. **24a**, 967–976 (1969).

[86] A. Hochstim and G. Massel, Calculations of Transport Coefficients in Ionized Gases, in *Kinetic Processes in Gases and Plasmas*, edited by A. Hochstim (Academic Press, New York, 1969), p. 141.

[87] L. Hermans, The Heat Conductivity of Polyatomic Gases in Magnetic Fields, Doctoral Thesis, Rijksuniversiteit Leiden, 1970.

[88] G. 'T Hooft, Thermal Diffusion and Dufour Effect for Gases in External Fields, Doctoral Thesis, Rijksuniversiteit Leiden, 1978.

[89] G. Gerasimov and E. Kolesnichenko, Transport Phenomena in a Nonequilibrium Dissociating Gas, Mekhanika Zhidkosti i Gaza (Izvestiya Akademii Nauk SSSR) **5**, 159–166 (1983). English translation.

[90] N. Makashev, The Effect of Gas Motion on the Reaction Kinetics of Vibrationally Excited Molecules, Mekhanika Zhidkosti i Gaza (Izvestiya Akademii Nauk SSSR) **6**, 100–105 (1984). English translation.

[91] A. Viviani, Coupling between Flow Velocity and Non-Equilibrium Internal Processes in Hypersonic Flow Aerothermochemistry, in *Proceedings of the IUTAM Symposium on Aerothermochemistry of Spacecraft and Associated Hypersonic Flows*, 1–4 September 1992, Marseille, (International Union of Theoretical and Applied Mechanics), pp. 137–142.

[92] S. Glasstone, K. Laidler and H. Eyring, *The Theory of Rate Processes* (McGraw-Hill, New York, 1941).

[93] S. Benson, *The Foundations of Chemical Kinetics* (McGraw-Hill, New York, 1960).

[94] S. Bauer, Chemical Kinetics: a General Introduction, in *Hypersonic Flow Research*, edited by F. Riddell (Academic Press, New York, 1962).

[95] J. Clarke and M. McChesney, *The Dynamics of Real Gases* (Butterworths, London, 1964).

[96] C. Hansen, Rate Processes in Gas Phase, National Aeronautics and Space Administration, NASA RP-1090, 1983.

[97] J. Anderson, *Hypersonic and High Temperature Gas Dynamics* (McGraw-Hill, New York, 1989).

[98] C. Park, *Nonequilibrium Hypersonic Aerothermodynamics* (John Wiley & Sons, New York, 1990).

[99] J. William, Étude des Processus Physico-Chimiques dans les Ecoulements Détendus à Haute Enthalpie, Doctoral Thesis, Université de Provence, Marseille, 1999.

A   Magnetic-induction equation

Neglecting the displacement-current density $\varepsilon_0 \partial \mathbf{E}/\partial t$, Eq. (39) becomes

$$\boldsymbol{j} = \varepsilon_0 c^2 \boldsymbol{\nabla} \times \mathbf{B} \tag{149}$$

Expanding the electric-current density in Eq. (149) according to Eq. (35) gives the conduction-current density

$$\mathbf{J}_{\mathrm{Q}} = \varepsilon_0 c^2 \boldsymbol{\nabla} \times \mathbf{B} - \rho_{\mathrm{c}} \mathbf{v} \tag{150}$$

The presumed applicability of the generalized Ohm law [Eq. (40)] brings Eq. (150) into the form

$$\lambda_{\mathrm{e}} \left(\mathbf{E} + \mathbf{v} \times \mathbf{B} \right) = \varepsilon_0 c^2 \boldsymbol{\nabla} \times \mathbf{B} - \rho_{\mathrm{c}} \mathbf{v} \tag{151}$$

from which the electric field

$$\mathbf{E} = \frac{\varepsilon_0 c^2}{\lambda_{\mathrm{e}}} \boldsymbol{\nabla} \times \mathbf{B} - \frac{\rho_{\mathrm{c}}}{\lambda_{\mathrm{e}}} \mathbf{v} - \mathbf{v} \times \mathbf{B} \tag{152}$$

can be obtained. The substitution of Eq. (152) into Eq. (38) and the subsequent expansion of the terms affected by the curl operator leads to Eq. (41).

B Field equations for scalar and vector potentials

Taking into account that the divergence of a curl and the curl of a gradient give always a null result, Eq. (37) implies that the magnetic induction can be expressed in terms of a vector potential and of an arbitrary function of space and time as

$$\mathbf{B} = \boldsymbol{\nabla} \times (\mathbf{A}' + \boldsymbol{\nabla}\psi) \tag{153}$$

The replacement of three scalar quantities, namely the components of the vector $\mathbf{B}$, with four scalar quantities, namely the components of the vector $\mathbf{A}'$ and the scalar function ψ, introduces an arbitrariness about the vector potential $\mathbf{A} = \mathbf{A}' + \boldsymbol{\nabla}\psi$ which, in order to be resolved, requires the assignment of a conveniently chosen scalar condition. With this provision, Eq. (153) can be simply rephrased as

$$\mathbf{B} = \boldsymbol{\nabla} \times \mathbf{A} \tag{154}$$

The field equation for the vector potential derives from Eq. (39). Performing the curl on both sides of Eq. (154) yields

$$\boldsymbol{\nabla} \times \mathbf{B} = \boldsymbol{\nabla} \times (\boldsymbol{\nabla} \times \mathbf{A}) = \boldsymbol{\nabla}(\boldsymbol{\nabla} \cdot \mathbf{A}) - \nabla^2 \mathbf{A} \tag{155}$$

The substitution of Eq. (154) into Eq. (38) provides the form

$$\boldsymbol{\nabla} \times \mathbf{E} + \frac{\partial}{\partial t}\boldsymbol{\nabla} \times \mathbf{A} = 0 \tag{156}$$

which, after permutation of the time derivative with the gradient operator, turns into

$$\boldsymbol{\nabla} \times (\mathbf{E} + \frac{\partial \mathbf{A}}{\partial t}) = 0 \tag{157}$$

The quantity in brackets is, thus, irrotational and can be expressed as the gradient of a scalar potential

$$\mathbf{E} + \frac{\partial \mathbf{A}}{\partial t} = -\boldsymbol{\nabla}\phi \tag{158}$$

From Eq. (158), the electric-field intensity is obtained in terms of the potentials as

$$\mathbf{E} = -\boldsymbol{\nabla}\phi - \frac{\partial \mathbf{A}}{\partial t} \tag{159}$$

The substitution of Eqs. (155) and (159) into Eq. (39) leads to

$$\varepsilon_0 c^2 [\boldsymbol{\nabla}(\boldsymbol{\nabla} \cdot \mathbf{A}) - \nabla^2 \mathbf{A}] = \boldsymbol{j} - \varepsilon_0 \frac{\partial}{\partial t}(\boldsymbol{\nabla}\phi + \frac{\partial \mathbf{A}}{\partial t}) \tag{160}$$

which can be rearranged as

$$\frac{1}{c^2}\frac{\partial^2 \mathbf{A}}{\partial t^2} - \nabla^2 \mathbf{A} + \boldsymbol{\nabla}(\boldsymbol{\nabla} \cdot \mathbf{A} + \frac{1}{c^2}\frac{\partial \phi}{\partial t}) = \frac{1}{\varepsilon_0 c^2}\boldsymbol{j} \tag{161}$$

Inspection of Eq. (161) suggests that the gauge transformation

$$\frac{1}{c^2}\frac{\partial \phi}{\partial t} + \boldsymbol{\nabla} \cdot \mathbf{A} = 0 \tag{162}$$

rather than the gauge $\boldsymbol{\nabla} \cdot \mathbf{A} = 0$, customarily imposed in magnetostatics, is the most convenient choice to resolve the arbitrariness about $\mathbf{A}$. The condition (162) is known as the Lorentz gauge (39; 45). Following it, Eq. (161) reduces to the simpler Eq. (45).

The field equation for the scalar potential derives from Eq. (36). The substitution of Eq. (159) into Eq. (36) gives

$$-\boldsymbol{\nabla} \cdot (\boldsymbol{\nabla}\phi) - \boldsymbol{\nabla} \cdot \frac{\partial \mathbf{A}}{\partial t} = \frac{\rho_\mathrm{c}}{\varepsilon_0} \tag{163}$$

Equation (163) is equivalent to

$$-\nabla^2\phi - \frac{\partial}{\partial t}\boldsymbol{\nabla} \cdot \mathbf{A} = \frac{\rho_\mathrm{c}}{\varepsilon_0} \tag{164}$$

The term $\boldsymbol{\nabla} \cdot \mathbf{A}$ is obtained from the Lorentz gauge [Eq. (162)]

$$\boldsymbol{\nabla} \cdot \mathbf{A} = -\frac{1}{c^2}\frac{\partial\phi}{\partial t} \tag{165}$$

and substituted into Eq. (164) to obtain Eq. (44).

C Transformation of the electromagnetic body force and derivation of the balance equation of electromagnetic momentum

The electric-charge density and the electric-current density can be obtained from Eqs. (36) and (39) as

$$\rho_{\mathrm{c}} = \varepsilon_0 \boldsymbol{\nabla} \cdot \mathbf{E} \tag{166}$$

$$\boldsymbol{j} = \varepsilon_0 c^2 \boldsymbol{\nabla} \times \mathbf{B} - \varepsilon_0 \frac{\partial \mathbf{E}}{\partial t} \tag{167}$$

and substituted into Eq. (49) to yield

$$\dot{\mathbf{g}}_v = \varepsilon_0 \mathbf{E} \boldsymbol{\nabla} \cdot \mathbf{E} + \varepsilon_0 c^2 (\boldsymbol{\nabla} \times \mathbf{B}) \times \mathbf{B} - \varepsilon_0 \frac{\partial \mathbf{E}}{\partial t} \times \mathbf{B} \tag{168}$$

At the same time, one can take advantage of Eqs. (37) and (38) to construct the identity

$$0 = \varepsilon_0 c^2 \mathbf{B} \boldsymbol{\nabla} \cdot \mathbf{B} + \varepsilon_0 (\boldsymbol{\nabla} \times \mathbf{E} + \frac{\partial \mathbf{B}}{\partial t}) \times \mathbf{E} \tag{169}$$

and to expand it into the expression

$$0 = \varepsilon_0 c^2 \mathbf{B} \boldsymbol{\nabla} \cdot \mathbf{B} + \varepsilon_0 (\boldsymbol{\nabla} \times \mathbf{E}) \times \mathbf{E} + \varepsilon_0 \frac{\partial \mathbf{B}}{\partial t} \times \mathbf{E} \tag{170}$$

somewhat symmetrical with respect to Eq. (168). The sum of Eqs. (168) and (170) yields

$$\dot{\mathbf{g}}_v = \varepsilon_0 c^2 [\mathbf{B} \boldsymbol{\nabla} \cdot \mathbf{B} + (\boldsymbol{\nabla} \times \mathbf{B}) \times \mathbf{B}] \; +$$
$$+ \; \varepsilon_0 [\mathbf{E} \boldsymbol{\nabla} \cdot \mathbf{E} + (\boldsymbol{\nabla} \times \mathbf{E}) \times \mathbf{E}] - \frac{\partial}{\partial t} (\varepsilon_0 \mathbf{E} \times \mathbf{B}) \tag{171}$$

Taking into account that the terms in squared brackets can be contracted as

$$\mathbf{B} \boldsymbol{\nabla} \cdot \mathbf{B} + (\boldsymbol{\nabla} \times \mathbf{B}) \times \mathbf{B} = \boldsymbol{\nabla} \cdot (\mathbf{B}\mathbf{B} - \frac{1}{2} B^2 \mathbf{U}) \tag{172}$$

$$\mathbf{E} \boldsymbol{\nabla} \cdot \mathbf{E} + (\boldsymbol{\nabla} \times \mathbf{E}) \times \mathbf{E} = \boldsymbol{\nabla} \cdot (\mathbf{E}\mathbf{E} - \frac{1}{2} E^2 \mathbf{U}) \tag{173}$$

Eq. (171) can be rephrased in the final form

$$\dot{\mathbf{g}}_v = \boldsymbol{\nabla} \cdot [\varepsilon_0 c^2 (\mathbf{B}\mathbf{B} - \frac{1}{2} B^2 \mathbf{U}) + \varepsilon_0 (\mathbf{E}\mathbf{E} - \frac{1}{2} E^2 \mathbf{U})] \; -$$
$$- \frac{\partial}{\partial t} (\varepsilon_0 \mathbf{E} \times \mathbf{B}) \tag{174}$$

which, considering the definitions (49) and (51), coincides with Eq. (50).

D Transformation of the electromagnetic-energy production and derivation of the balance equation of electromagnetic energy

Equation (39) can be resolved to express the electric-current density as

$$\boldsymbol{j} = \varepsilon_0 c^2 \boldsymbol{\nabla} \times \mathbf{B} - \varepsilon_0 \frac{\partial \mathbf{E}}{\partial t} \tag{175}$$

Taking into account Eq. (175), the electromagnetic energy production becomes

$$
\begin{aligned}
\boldsymbol{j} \cdot \mathbf{E} &= \varepsilon_0 c^2 \mathbf{E} \cdot \boldsymbol{\nabla} \times \mathbf{B} - \varepsilon_0 \mathbf{E} \cdot \frac{\partial \mathbf{E}}{\partial t} = \\
&= \varepsilon_0 c^2 \mathbf{E} \cdot \boldsymbol{\nabla} \times \mathbf{B} - \varepsilon_0 \frac{\partial E^2/2}{\partial t} \tag{176}
\end{aligned}
$$

The first term on the right-hand side of Eq. (176) can be easily transformed

$$\mathbf{E} \cdot \boldsymbol{\nabla} \times \mathbf{B} = -\boldsymbol{\nabla} \cdot (\mathbf{E} \times \mathbf{B}) + \mathbf{B} \cdot \boldsymbol{\nabla} \times \mathbf{E} \tag{177}$$

to bring forth the curl of the electric-field intensity. The substitution of Eq. (38) into Eq. (177) yields

$$
\begin{aligned}
\mathbf{E} \cdot \boldsymbol{\nabla} \times \mathbf{B} &= -\boldsymbol{\nabla} \cdot (\mathbf{E} \times \mathbf{B}) - \mathbf{B} \cdot \frac{\partial \mathbf{B}}{\partial t} = \\
&= -\boldsymbol{\nabla} \cdot (\mathbf{E} \times \mathbf{B}) - \frac{\partial B^2/2}{\partial t} \tag{178}
\end{aligned}
$$

so that Eq. (176) finally takes the form

$$\boldsymbol{j} \cdot \mathbf{E} = -\boldsymbol{\nabla} \cdot (\varepsilon_0 c^2 \mathbf{E} \times \mathbf{B}) - \frac{\partial}{\partial t}\left[\frac{\varepsilon_0}{2}(E^2 + c^2 B^2)\right] \tag{179}$$

that coincides with Eq. (72).

E Poynting-vector transformation

From Eqs. (73) and (74), the vector product between $\mathbf{E}'$ and $\mathbf{B}'$ can be expanded as follows

$$\mathbf{E}' \times \mathbf{B}' = \mathbf{E} \times \mathbf{B} - \frac{1}{c^2}\mathbf{E} \times (\mathbf{v} \times \mathbf{E}) -$$
$$- \mathbf{B} \times (\mathbf{v} \times \mathbf{B}) - \frac{1}{c^2}(\mathbf{v} \times \mathbf{B}) \times (\mathbf{v} \times \mathbf{E}) \tag{180}$$

The second term on the right-hand side of Eq. (180) expands as

$$
\begin{aligned}
\mathbf{E} \times (\mathbf{v} \times \mathbf{E}) &= (\mathbf{E} \cdot \mathbf{E})\mathbf{v} - (\mathbf{E} \cdot \mathbf{v})\mathbf{E} \\[2mm]
&= (E^2\mathbf{U} - \mathbf{EE}) \cdot \mathbf{v} \\[2mm]
&= \frac{E^2}{2}\mathbf{v} + (\frac{E^2}{2}\mathbf{U} - \mathbf{EE}) \cdot \mathbf{v}
\end{aligned}
\tag{181}
$$

Similarly, the third term on the right-hand side of Eq. (180) expands into

$$\mathbf{B} \times (\mathbf{v} \times \mathbf{B}) = \frac{B^2}{2}\mathbf{v} + (\frac{B^2}{2}\mathbf{U} - \mathbf{BB}) \cdot \mathbf{v} \tag{182}$$

The fourth term on the right-hand side of Eq. (180) is a little bit more complicated. It expands as

$$
\begin{aligned}
(\mathbf{v} \times \mathbf{B}) \times (\mathbf{v} \times \mathbf{E}) &= (\mathbf{v} \times \mathbf{B}) \cdot \mathbf{E}\mathbf{v} \\[2mm]
&= \mathbf{E} \cdot (\mathbf{v} \times \mathbf{B})\mathbf{v} \\[2mm]
&= \mathbf{v} \cdot (\mathbf{B} \times \mathbf{E})\mathbf{v} \\[2mm]
&= -\mathbf{v} \cdot (\mathbf{E} \times \mathbf{B})\mathbf{v}
\end{aligned}
\tag{183}
$$

In the non-relativistic approximation, therefore, the term

$$\frac{1}{c^2}(\mathbf{v} \times \mathbf{B}) \times (\mathbf{v} \times \mathbf{E}) = -\frac{1}{c^2}\mathbf{v} \cdot (\mathbf{E} \times \mathbf{B})\mathbf{v} \tag{184}$$

is negligible with respect to $\mathbf{E} \times \mathbf{B}$ and can be disregarded in Eq. (180). Taking into account the definition [Eq. (51)] of the Maxwell stress tensor, the substitution of Eqs. (181) and (182) into Eq. (180) and the subsequent multiplication by the factor $\varepsilon_0 c^2$ leads to Eq. (75).

Table 1: Mechanisms of energy conversion.

energy form	production		
kinetic	$-\boldsymbol{\tau} : \boldsymbol{\nabla}\mathbf{v}$ $\quad +\rho_{\mathrm{c}}\mathbf{v}\cdot\mathbf{E}$		$-\mathbf{J}_{\mathrm{Q}}\cdot\mathbf{v}\times\mathbf{B}$
internal	$+\boldsymbol{\tau} : \boldsymbol{\nabla}\mathbf{v}$	$+\mathbf{J}_{\mathrm{Q}}\cdot\mathbf{E}$	$+\mathbf{J}_{\mathrm{Q}}\cdot\mathbf{v}\times\mathbf{B}$
electromagnetic	$-\rho_{\mathrm{c}}\mathbf{v}\cdot\mathbf{E}$ $\quad -\mathbf{J}_{\mathrm{Q}}\cdot\mathbf{E}$		

Table 2: Governing equations relative to gas-mixture composition

equations	Eq.	unk.s	number of equations or subscript range
$\dfrac{\partial\rho_i}{\partial t} + \boldsymbol{\nabla}\cdot(\rho_i\mathbf{v}) = -\boldsymbol{\nabla}\cdot\mathbf{J}_{\mathrm{m}_i} + \displaystyle\sum_{k=1}^{r}\dot\xi_k\nu_{ki}M_i$	(19)	ρ_i	$i = 1,\cdots,n-s$
$\dfrac{\partial\rho_j^a}{\partial t} + \boldsymbol{\nabla}\cdot(\rho_j^a\mathbf{v}) = -\boldsymbol{\nabla}\cdot\mathbf{J}_{\mathrm{m}_j^a}$	(24)	ρ_j^a	$j = 1,\cdots,s$
$\mathbf{J}_{\mathrm{m}_j^a} = \displaystyle\sum_{i=1}^{n}\dfrac{1}{M_i}\mathbf{J}_{\mathrm{m}_i}\sigma_{ij}M_j^a$	(25)	$\mathbf{J}_{\mathrm{m}_j^a}$	$j = 1,\cdots,s$
$\hat\rho_j^a = \rho_j^a - \displaystyle\sum_{i=1}^{n-s}\dfrac{\rho_i}{M_i}\sigma_{ij}M_j^a$	(29)	$\hat\rho_j^a$	$j = 1,\cdots,s$
$\rho_i = \displaystyle\sum_{j=1}^{s}\hat\rho_j^a\,\hat\sigma_{ji}^{-1}$	(31)	ρ_i	$i = n-s+1,\cdots,n$
$\dfrac{\partial\rho}{\partial t} + \boldsymbol{\nabla}\cdot(\rho\mathbf{v}) = 0$	(23)	ρ	1
$\rho_{\mathrm{c}} = -eN_{\mathrm{A}}\displaystyle\sum_{i=1}^{n}\dfrac{\rho_i}{M_i}\sigma_{is}$	(15)	ρ_{c}	1
$\mathbf{J}_{\mathrm{Q}} = -eN_{\mathrm{A}}\displaystyle\sum_{i=1}^{n}\dfrac{1}{M_i}\mathbf{J}_{\mathrm{m}_i}\sigma_{is}$	(33)	$\mathbf{J}_{\mathrm{Q}}$	3
$\boldsymbol{j} = \rho_{\mathrm{c}}\mathbf{v} + \mathbf{J}_{\mathrm{Q}}$	(35)	$\boldsymbol{j}$	3

Table 3: Governing equations relative to momentum

equations	Eq.	unk.s	number of equations
$\dfrac{\partial \rho \mathbf{v}}{\partial t} + \boldsymbol{\nabla} \cdot (\rho \mathbf{v}\, \mathbf{v}) = \boldsymbol{\nabla} \cdot \boldsymbol{\tau} + \rho_{\mathrm{c}} \mathbf{E} + \boldsymbol{j} \times \mathbf{B}$	(48)	$\mathbf{v}$	3
or			
$\dfrac{\partial}{\partial t}(\rho \mathbf{v} + \varepsilon_0 \mathbf{E} \times \mathbf{B}) = -\boldsymbol{\nabla} \cdot (\rho \mathbf{v}\, \mathbf{v} - \boldsymbol{\tau} - \boldsymbol{\tau}_{\mathrm{M}})$	(53)	$\mathbf{v}$	3
$\boldsymbol{\tau}_{\mathrm{M}} = \varepsilon_0(\mathbf{E}\mathbf{E} - \dfrac{1}{2}E^2\mathbf{U}) + \varepsilon_0 c^2(\mathbf{B}\mathbf{B} - \dfrac{1}{2}B^2\mathbf{U})$	(51)	$\boldsymbol{\tau}_{\mathrm{M}}$	6

Table 4: Governing equations relative to energy

equations	Eq.	unk.s	no. of eq.s or sub. range
$\dfrac{\partial \rho_i u_{i\delta}}{\partial t} + \boldsymbol{\nabla} \cdot (\rho_i u_{i\delta} \mathbf{v}) = -\boldsymbol{\nabla} \cdot \mathbf{J}_{\mathrm{U}_{i\delta}} + \dot{u}_{v,i\delta}$	(57)	$u_{i\delta}$	$\delta = 1, \cdots, \ell_i$ $i = 1, \cdots, n$
$u_{i\delta} = -T_{i\delta}^2 \left(\dfrac{\partial f_{i\delta}/T_{i\delta}}{\partial T_{i\delta}} \right)_{v_i} = u_{i\delta}(T_{i\delta}, v_i)$	(58)	$T_{i\delta}$	$\delta = 1, \cdots, \ell_i$ $i = 1, \cdots, n$
$v_i = 1/\rho_i$		v_i	$i = 1, \cdots, n$
$\rho u = \displaystyle\sum_{i=1}^{n} \sum_{\delta=1}^{\ell_i} \rho_i u_{i\delta}$	(56)	u	1
$e_{\mathrm{m}} = u + \dfrac{\mathrm{v}^2}{2}$	(63)	e_{m}	1
or			
$\dfrac{\partial \rho u}{\partial t} + \boldsymbol{\nabla} \cdot (\rho u \mathbf{v}) =$ $\quad = -\boldsymbol{\nabla} \cdot \mathbf{J}_{\mathrm{U}} + \boldsymbol{\tau} : \boldsymbol{\nabla} \mathbf{v} + \mathbf{J}_{\mathrm{Q}} \cdot (\mathbf{E} + \mathbf{v} \times \mathbf{B})$	(71)	u	1
$\mathbf{J}_{\mathrm{U}} = \displaystyle\sum_{i=1}^{n} \sum_{\delta=1}^{\ell_i} \mathbf{J}_{\mathrm{U}_{i\delta}}$	(60)	$\mathbf{J}_{\mathrm{U}}$	3
$\dfrac{\partial \rho_i u_{i\delta}}{\partial t} + \boldsymbol{\nabla} \cdot (\rho_i u_{i\delta} \mathbf{v}) = -\boldsymbol{\nabla} \cdot \mathbf{J}_{\mathrm{U}_{i\delta}} + \dot{u}_{v,i\delta}$	(57)	$u_{i\delta}$	$\displaystyle\sum_{i=1}^{n} \ell_i - 1$
$\rho u = \displaystyle\sum_{i=1}^{n} \sum_{\delta=1}^{\ell_i} \rho_i u_{i\delta}$	(56)	$u_{i\delta}$	1
$u_{i\delta} = -T_{i\delta}^2 \left(\dfrac{\partial f_{i\delta}/T_{i\delta}}{\partial T_{i\delta}} \right)_{v_i} = u_{i\delta}(T_{i\delta}, v_i)$	(58)	$T_{i\delta}$	$\delta = 1, \cdots, \ell_i$ $i = 1, \cdots, n$
$v_i = 1/\rho_i$		v_i	$i = 1, \cdots, n$
$e_{\mathrm{m}} = u + \dfrac{\mathrm{v}^2}{2}$	(63)	e_{m}	1

Table 4: Continued

equations	Eq.	un.s	no. of eq.s or sub. range
or			
$\dfrac{\partial \rho e_{\mathrm{m}}}{\partial t} + \boldsymbol{\nabla} \cdot (\rho e_{\mathrm{m}} \mathbf{v}) = -\boldsymbol{\nabla} \cdot (\mathbf{J}_{\mathrm{U}} - \boldsymbol{\tau} \cdot \mathbf{v}) + \boldsymbol{j} \cdot \mathbf{E}$	(70)	e_{m}	1
$\mathbf{J}_{\mathrm{U}} = \sum\limits_{i=1}^{n} \sum\limits_{\delta=1}^{\ell_i} \mathbf{J}_{\mathrm{U}_{i\delta}}$	(60)	$\mathbf{J}_{\mathrm{U}}$	3
$\dfrac{\partial \rho_i u_{i\delta}}{\partial t} + \boldsymbol{\nabla} \cdot (\rho_i u_{i\delta} \mathbf{v}) = -\boldsymbol{\nabla} \cdot \mathbf{J}_{\mathrm{U}_{i\delta}} + \dot{u}_{v,i\delta}$	(57)	$u_{i\delta}$	$\sum\limits_{i=1}^{n} \ell_i - 1$
$\rho u = \sum\limits_{i=1}^{n} \sum\limits_{\delta=1}^{\ell_i} \rho_i u_{i\delta}$	(56)	$u_{i\delta}$	1
$u_{i\delta} = -T_{i\delta}^2 \left(\dfrac{\partial f_{i\delta}/T_{i\delta}}{\partial T_{i\delta}} \right)_{v_i} = u_{i\delta}(T_{i\delta}, v_i)$	(58)	$T_{i\delta}$	$\delta = 1, \cdots, \ell_i$ $i = 1, \cdots, n$
$v_i = 1/\rho_i$		v_i	$i = 1, \cdots, n$
$e_{\mathrm{m}} = u + \dfrac{\mathbf{v}^2}{2}$	(63)	u	1
or			
$\dfrac{\partial}{\partial t}[\rho e_{\mathrm{m}} + \dfrac{\varepsilon_0}{2}(E^2 + c^2 B^2)] =$ $\quad = -\boldsymbol{\nabla} \cdot (\rho \mathbf{v} e_{\mathrm{m}} + \mathbf{J}_{\mathrm{U}} - \boldsymbol{\tau} \cdot \mathbf{v} + \varepsilon_0 c^2 \mathbf{E} \times \mathbf{B})$	(77)	e_{m}	1
$\mathbf{J}_{\mathrm{U}} = \sum\limits_{i=1}^{n} \sum\limits_{\delta=1}^{\ell_i} \mathbf{J}_{\mathrm{U}_{i\delta}}$	(60)	$\mathbf{J}_{\mathrm{U}}$	3
$\dfrac{\partial \rho_i u_{i\delta}}{\partial t} + \boldsymbol{\nabla} \cdot (\rho_i u_{i\delta} \mathbf{v}) = -\boldsymbol{\nabla} \cdot \mathbf{J}_{\mathrm{U}_{i\delta}} + \dot{u}_{v,i\delta}$	(57)	$u_{i\delta}$	$\sum\limits_{i=1}^{n} \ell_i - 1$
$\rho u = \sum\limits_{i=1}^{n} \sum\limits_{\delta=1}^{\ell_i} \rho_i u_{i\delta}$	(56)	$u_{i\delta}$	1
$u_{i\delta} = -T_{i\delta}^2 \left(\dfrac{\partial f_{i\delta}/T_{i\delta}}{\partial T_{i\delta}} \right)_{v_i} = u_{i\delta}(T_{i\delta}, v_i)$	(58)	$T_{i\delta}$	$\delta = 1, \cdots, \ell_i$ $i = 1, \cdots, n$
$v_i = 1/\rho_i$		v_i	$i = 1, \cdots, n$
$e_{\mathrm{m}} = u + \dfrac{\mathbf{v}^2}{2}$	(63)	u	1

Table 5: Governing equations relative to the electromagnetic field

equations	Eq.	unk.s	no. of eq.s
$\dfrac{\partial \mathbf{B}}{\partial t} + \boldsymbol{\nabla} \times \mathbf{E} = 0$	(38)	$\mathbf{B}$	3
$\varepsilon_0 \dfrac{\partial \mathbf{E}}{\partial t} - \varepsilon_0 c^2 \boldsymbol{\nabla} \times \mathbf{B} = -\boldsymbol{j}$	(39)	$\mathbf{E}$	3
or			
$\dfrac{1}{c^2}\dfrac{\partial^2 \phi}{\partial t^2} = \nabla^2 \phi + \dfrac{\rho_{\mathrm{c}}}{\varepsilon_0}$	(44)	ϕ	1
$\dfrac{1}{c^2}\dfrac{\partial^2 \mathbf{A}}{\partial t^2} = \nabla^2 \mathbf{A} + \dfrac{1}{\varepsilon_0 c^2}\boldsymbol{j}$	(45)	$\mathbf{A}$	3
$\mathbf{B} = \boldsymbol{\nabla} \times \mathbf{A}$	(43)	$\mathbf{B}$	3
$\mathbf{E} = -\boldsymbol{\nabla}\phi - \dfrac{\partial \mathbf{A}}{\partial t}$	(42)	$\mathbf{E}$	3

Table 6: Generalized fluxes and forces contributing to the entropy production [Eq. (92)]

flux	force	tensorial order	subscript range
$\boldsymbol{\tau}_{\mathrm{o}}^{\mathrm{s}}$	$(\boldsymbol{\nabla}\mathbf{v})_{\mathrm{o}}^{\mathrm{s}}$	2	
$\dfrac{1}{T}\left(\mathbf{J}_{\mathrm{U}} - \sum\limits_{i=1}^{n} \mu_i \mathbf{J}_{\mathrm{m}_i}\right)$	$\boldsymbol{\nabla}T$	1	
$\mathbf{J}_{\mathrm{m}_i}$	$\boldsymbol{\nabla}\mu_i + eN_{\mathrm{A}}\dfrac{\sigma_{is}}{M_i}(\mathbf{E} + \mathbf{v} \times \mathbf{B})$	1	$i = 1, \cdots, n$
$-(\pi + p)$	$\boldsymbol{\nabla} \cdot \mathbf{v}$	0	
$\dot{\xi}_k$	$\mathcal{A}_k$	0	$k = 1, \cdots, r$

1D EQUATIONS AND ANALYSIS/CHANNEL FLOWS

Jacques C.J. Nihoul
Liège, University, Belgium

1. Hartman flow

The flow of conducting fluids in channels, i.e. between rigid walls, provides an illustrative example of application of the magnetohydrodynamic equations and a simple introduction to the important question of energy conversion and the principles of MHD generators and propellers.

We shall first assume the fluid density constant and the Hall effect negligible.

We consider the steady flow of a conducting fluid between two infinite horizontal parallel plates with a uniform magnetic field perpendicular to the plates.

This problem must be regarded as an idealized version of a channel of rectangular cross section the length and width of which are much larger than the height.

The hypothesis of a channel infinitely long and infinitely large justifies the assumption that the variables $\mathbf{v}$, $\mathbf{B}$, … only depend on the x_3 coordinate. However, one cannot ignore completely that the channel has a finite width as the longitudinal flow induces transversal currents and the solution of the problem depends on the boundary conditions imposed on the lateral walls. (The upper and lower boundaries are assumed insulators).

For a fluid of constant density, the magnetohydrodynamic equations can be written

$$\nabla \bullet \mathbf{v} = 0 \qquad \nabla \bullet \mathbf{b} = 0$$

$$\frac{\partial \mathbf{v}}{\partial t} + \mathbf{v} \bullet \nabla \mathbf{v} = -\nabla q + \mathbf{b} \bullet \nabla \mathbf{b} + \nu \nabla^2 \mathbf{v}$$

$$\frac{\partial \mathbf{b}}{\partial t} + \mathbf{v} \bullet \nabla \mathbf{b} = \mathbf{b} \bullet \nabla \mathbf{v} + \nu_m \nabla^2 \mathbf{b}$$

$$\frac{\partial \mathbf{b}}{\partial t} = -\nabla \wedge \mathbf{e}$$

$$\mathbf{j} = \nabla \wedge \mathbf{b} = \nu_m^{-1} \left(\mathbf{e} + \mathbf{v} \wedge \mathbf{b} \right)$$

$$W_e = \mathbf{e} \bullet \mathbf{j} = \nu_m \mathbf{j}^2 + \mathbf{v} \bullet \left(\mathbf{j} \wedge \mathbf{b} \right)$$

$$q = \frac{p + \xi}{\rho} + \frac{1}{2} b^2$$

$$\mathbf{b} = \frac{\mathbf{B}}{\sqrt{\mu\rho}} \qquad \mathbf{e} = \frac{\mathbf{E}}{\sqrt{\mu\rho}}$$

e₃

e₁

e₂

b₀

Isolants

Electrode

Electrode

2ℓ

v   **j** →

2L

Conduite   **b₀**   Isolant

Electrode

→ **j**

Résistance
ou
source de puissance

$$\mathbf{j} = \sqrt{\frac{\mu}{\rho}}\,\mathbf{J}$$

Assuming a steady state, the time derivative can be dropped and taking into account the geometry and symmetry of the system, we may look for a solution where the velocity $\mathbf{v}$ and the induced magnetic field $\mathbf{h}$ are directed along the channel axis ($\mathbf{e}_1$) and depend only on x_3, the electric field and the current are directed along $\mathbf{e}_2$.

Introducing non-dimensional variables

$$u = \bar{u}u \qquad\qquad \bar{u} = \frac{1}{2\ell}\int_{-\ell}^{\ell} u\,dx_3$$

$$x_3 = \ell z \qquad\qquad \frac{\partial q}{\partial x_1} = \frac{\nu\bar{u}}{\ell^2}\,\chi_p \qquad\qquad h = \frac{b_o\bar{u}\ell}{\nu_m}\,h$$

and the Hartman number m

$$m^2 = \frac{b_o^2\ell^2}{\nu\nu_m}$$

and substituting in the equations, one finds that

χ_e and χ_p are constants

$$\chi_e - \frac{\chi_p}{m^2} = \frac{\operatorname{ch} m}{\operatorname{ch} m - \dfrac{\operatorname{sh} m}{m}}$$

$$u = \frac{\operatorname{ch} m - \operatorname{ch} m\,z}{\operatorname{ch} m - \dfrac{\operatorname{sh} m}{m}}$$

$$h = (\chi_e - 1)z + \frac{\operatorname{sh} m\,z - z\operatorname{sh} m}{m\operatorname{ch} m - \operatorname{sh} m}$$

$$j = \frac{b_o\bar{u}}{\nu_m}(\chi_e - u) \qquad ; \qquad \bar{j} = \frac{b_o\bar{u}}{\nu_m}(\chi_e - 1)$$

$$\overline{\mathbf{e}\bullet\mathbf{j}} = \frac{b_o^2\bar{u}^2}{\nu_m}\chi_e(\chi_e - 1)$$

3
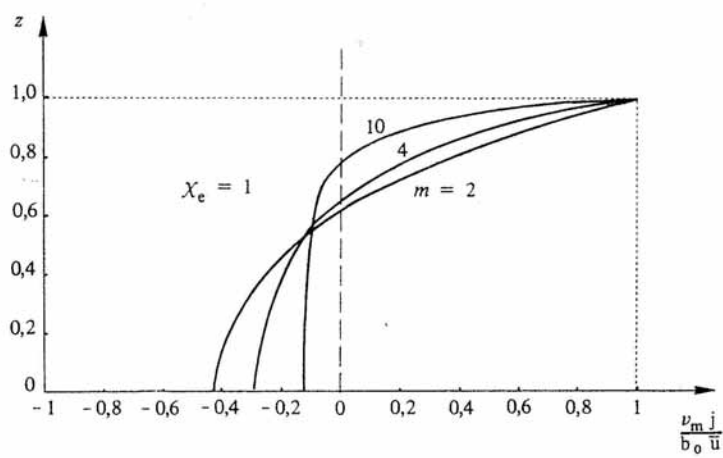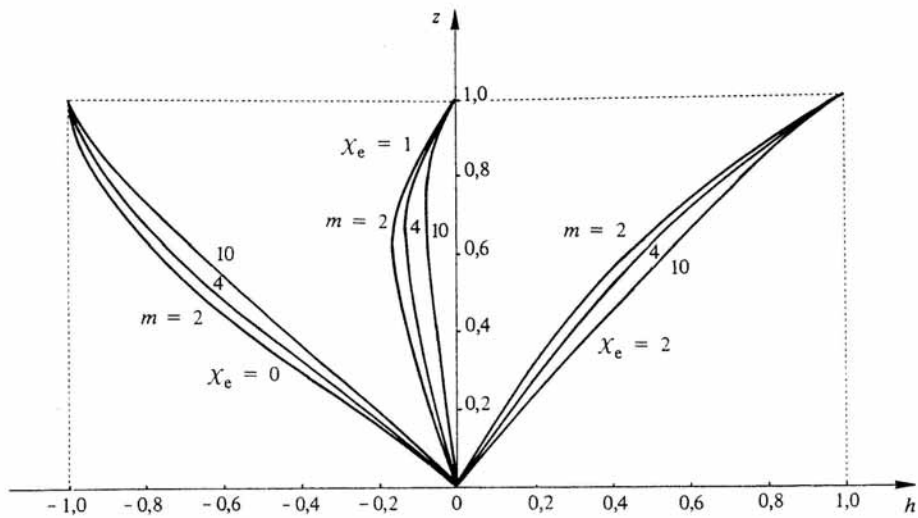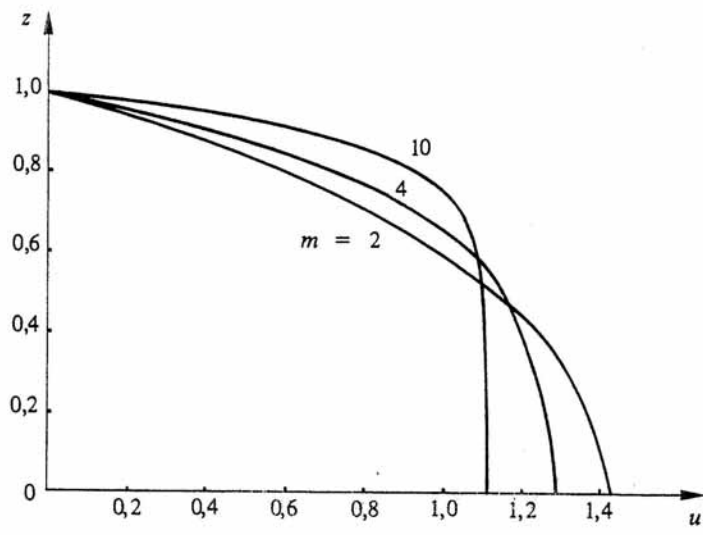
It is illuminating to consider two asymptotic cases

a) $m \ll 1$ $u = \dfrac{3}{2}\overline{u}\left(1 - z^2\right)$ $h = 0$

b) $m \gg 1$ $u = \overline{u}\left[1 - e^{-m(1-z)} - e^{-m(1+z)}\right]$

$$h = \dfrac{\overline{u}\,\ell}{\nu_m} b_o\left(\chi_e - 1\right)z$$

In the first case, we find the well-known Poiseuille Flow.
In the second case, we find a flat profile with narrow regions of transition near the boundaries where the profile adjust itself to the boundary condition $u = 0$.
The thickness of the boundary layers is of the order

$$\delta = \dfrac{\ell}{m}$$

The particular case $\chi_e = 1$ is interesting. In this case, $\overline{j} = 0$. Each boundary layer is the seat of a current $\sim \dfrac{b_o \overline{u}}{\nu_m}$ and the core of the fluid is the seat of a current of opposite sign

$$\sim \dfrac{b_o \overline{u}}{m\,\nu_m} \quad .$$

The total contribution of the boundary layers is of the order of

$$2\delta\dfrac{b_o \overline{u}}{\nu_m} = 2\ell\dfrac{b_o \overline{u}}{m\,\nu_m}$$

the contribution of the core is

$$-2\ell\dfrac{b_o \overline{u}}{m\,\nu_m}$$

The power supplied to the system $\overline{\mathbf{e}\bullet\mathbf{j}}$ is zero for $\chi_e = 0$ (zero electric field, external connection in short circuit) and $\chi_e = 1$ (zero mean current, insulating lateral walls). More generally

	> 0	$\chi_e > 1$	or	$\chi_e < 0$
$\overline{\mathbf{e}\bullet\mathbf{j}}$	$= 0$	$\chi_e = 1$	or	$\chi_e = 0$
	< 0	$1 > \chi_e > 0$		

5

$$\frac{\partial p}{\partial x_1} < 0 \qquad\qquad \frac{\partial p}{\partial x_1} > 0$$

Le système reçoit de l'énergie hydraulique   Le système fournit de l'énergie hydraulique

Le système reçoit de l'énergie électrique   Le système fournit de l'énergie électrique   Le système reçoit de l'énergie électrique

①   ②   ③   ④ ⑤   ⑥

Générateur MHD   Pompe MHD

0   1 X_e^* X_e

Frein   Débitmètre
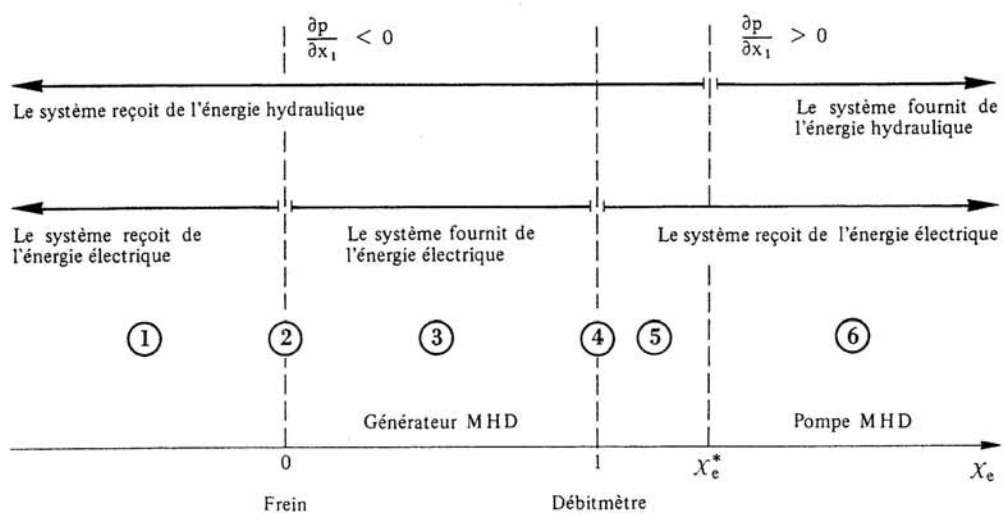
On the other hand, the pressure gradient changes sign for

$$\chi_e = \chi_e^* = \frac{ch\,m}{ch\,m - \dfrac{sh\,m}{m}} > 1$$

For values of $\chi_e > \chi_e^*$, the pressure gradient is positive, the pressure increases in the direction of the flow. The system receives electric energy and supplies hydraulic energy. It works as an *magnetohydrodynamic pump*. On the other hand for $0 < \chi_e < 1$, the system receives hydraulic energy ($-\dfrac{\partial p}{\partial x_1} > 0$) and supplies electric energy.

Regions 1 and 5 correspond to useless regimes. Both electric and hydraulic energies are supplied to the system where they are dissipated.

Region 3 corresponds to the magnetohydrodynamic generator and region 6 to the magnetohydrodynamic pump (or propulser).

At point 2, the system works as a brake (the electrical energy is zero, the induced currents dissipate the kinetic energy).

At point 4, the electrical energy is also zero as the mean current $\bar{j}$, the electric field and consequently the difference of potential at the lateral terminals is proportional to the mean velocity $\bar{u}$ and the device can be used as a flow meter.

2. Hartman-Hall flow

In the presence of a significant Hall effect, the Ohm's law must be modified as follows

$$\mathbf{j} = \nabla \wedge \mathbf{b} = \nu_m^{-1}\left(\mathbf{e} + \mathbf{v} \wedge \mathbf{b}\right) - \alpha\sqrt{\mu\rho}\;\mathbf{j} \wedge \mathbf{b}$$

The last term in the right-hand side does not allow to seek solutions of such a simple symmetry as in the pure Hartman flow. One has to consider the possibility of an axial component of the current j_1 , of a transversal velocity u_2 , of a transversal induced magnetic field h_2, … .

To take this into account, we introduce *complex* non-dimensional variables

$$u_1 + iu_2 = \bar{u}u$$

$$h_1 + ih_2 = \frac{b_o\bar{u}\ell}{\nu_m}\;\frac{1 + in}{1 + n^2}h$$

$$\chi_2 - i\chi_1 = \chi_e$$

$$\frac{\partial q}{\partial x_1} + i\frac{\partial q}{\partial x_2} = \frac{\nu\bar{u}}{\ell^2}\,\chi_p$$

$$\tilde{m}^2 = m^2\,\frac{1 + in}{1 + n^2}$$

7
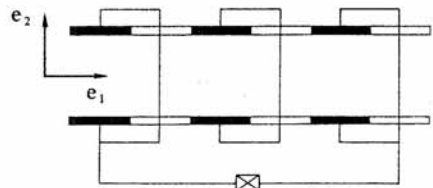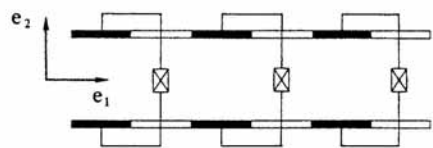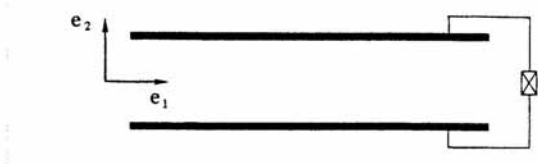
Then the equations reduce to the equations for the Hartman flow and the solutions are formerly the same.

To determine χ_e and then χ_p, one has to specify the boundary conditions on the lateral walls but also at the entry and exit of the channel.

When the lateral electrodes are short-circuited $\chi_2 = 0$, when the entry and exit electrodes are short-circuited (it is the case when the lateral electrodes are continuous) $\chi_1 = 0$.

In general, the constants χ_1 and χ_2 are given by conditions of the type

$$\frac{1}{2}\int_{-1}^{1} j_1 \, dz = I_1 \qquad\qquad \frac{1}{2}\int_{-1}^{1} j_2 \, dz = I_2$$

Energy conversion with Hall effect

The electric power supplied to the system is equal to

$$\mathbf{e} \bullet \mathbf{j} = b_o \overline{u}(\chi_1 j_1 + \chi_2 j_2)$$

i.e.

$$\mathbf{e} \bullet \mathbf{j} = \frac{b_o^2 \overline{u}^2}{\nu_m(1+n^2)}\left[\chi_2(\chi_2 - 1) + \chi_1(\chi_1 + n)\right]$$

The power $\mathbf{e} \bullet \mathbf{j}$ is negative inside the circle

$$\left(\chi_2 - \frac{1}{2}\right)^2 + \left(\chi_1 + \frac{n}{2}\right)^2 = \frac{1+n^2}{4}$$

The longitudinal pressure gradient is given by

$$\frac{\partial}{\partial x_1}\left(\frac{p}{\rho}\right) = \frac{\nu \overline{u}}{\ell^2} \operatorname{Re} \chi_p$$

$$= \frac{\nu \overline{u}\, m^2}{\ell^2(1+n^2)}\left(n\chi_1 + \chi_2 - a\right)$$

when

$$a = \operatorname{Re}\left[\frac{(1+in)\operatorname{ch}\tilde{m}}{\operatorname{ch}\tilde{m} - \dfrac{\operatorname{sh}\tilde{m}}{\tilde{m}}}\right] \geq 1$$

The system functions as a generator for values of χ_1 and χ_2 inside the circle and as a pump for values of χ_1 and χ_2 situated to the right of the line $\operatorname{Re} \chi_p = 0$.

9
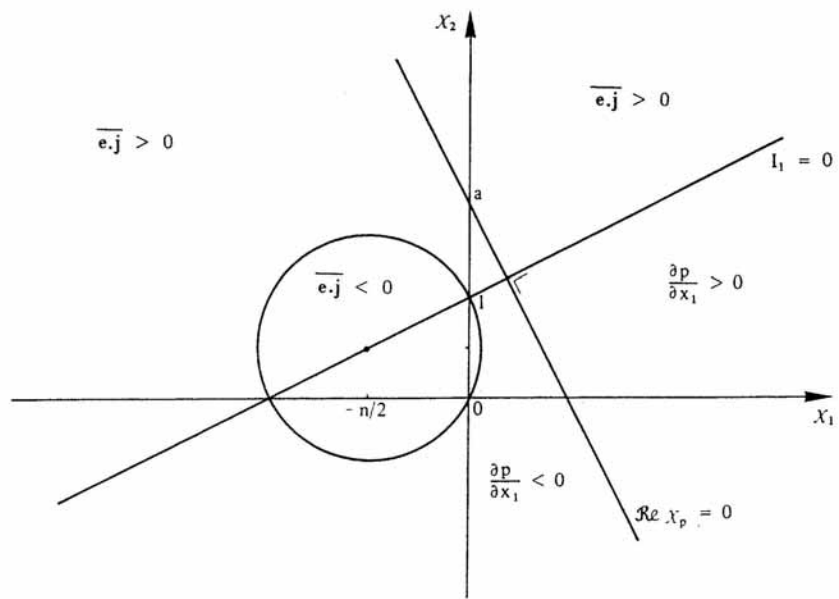
In the three cases considered before

(a) $\chi_1 = 0$ χ_2 imposed

$$\mathbf{e} \bullet \mathbf{j} = \frac{\overline{u}^2 b_o^2}{v_m (1 + n^2)} \chi_2 (\chi_2 - 1)$$

(b) $I_1 = 0$ i.e. $\chi_1 = n(\chi_2 - 1)$
       χ_2 imposed

$$\mathbf{e} \bullet \mathbf{j} = \frac{\overline{u}^2 b_o^2}{v_m} \chi_2 (\chi_2 - 1)$$

(c) $\chi_2 = 0$ $\chi_1 =$ imposed

$$\mathbf{e} \bullet \mathbf{j} = \frac{\overline{u}^2 b_o^2}{v_m (1 + n^2)} \chi_1 (\chi_1 + n)$$

One can see, in case a, that the existence of a Hall current decreases the energy exchange.
On the other hand, if one suppresses the Hall current using segmented electrodes with the circuit open between the electrodes at the channel's entry and exit, the convertible power is the same as in the classical Hartman flow (case b).
Once can imagine, on the contrary, to exploit the Hall current (case c), the convertible power is then a function of n.

$m = 10$

$n = 0$ 1 4 10 100

1.5

$u_1 = u_1/\bar{u}$

$n = 0$

100

1

10

4

$m = 10$

$- 0.5$ 0 0.5

$u_2 = u_2/\bar{u}$

12

$(m = 10, X_1 = 1, X_2 = 0)$

13

$(m = 10, \; X_1 = 0, \; X_2 = 1)$

$(m = 10, \; X_1 = 0, \; X_2 = 0.5)$

14

$$(m = 10 \, , \, X_1 = 1 \, , \, X_2 = 0)$$

15
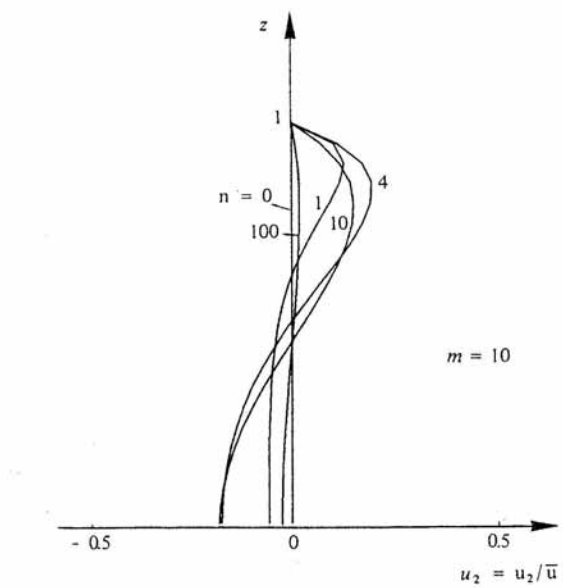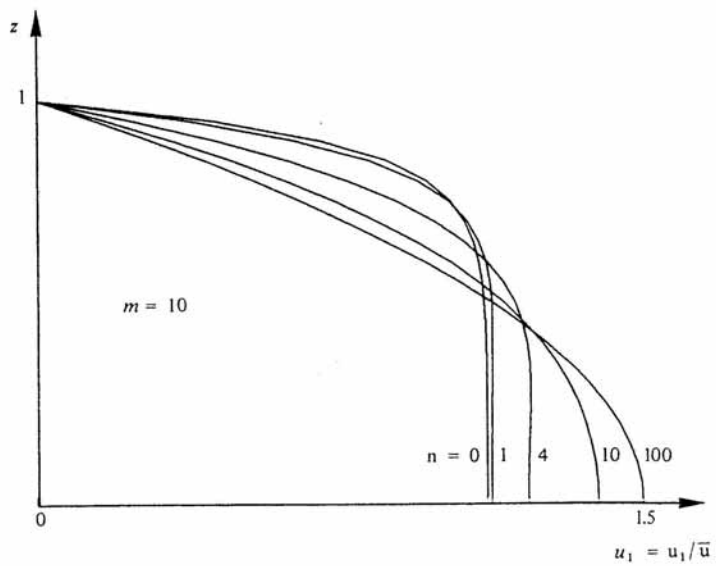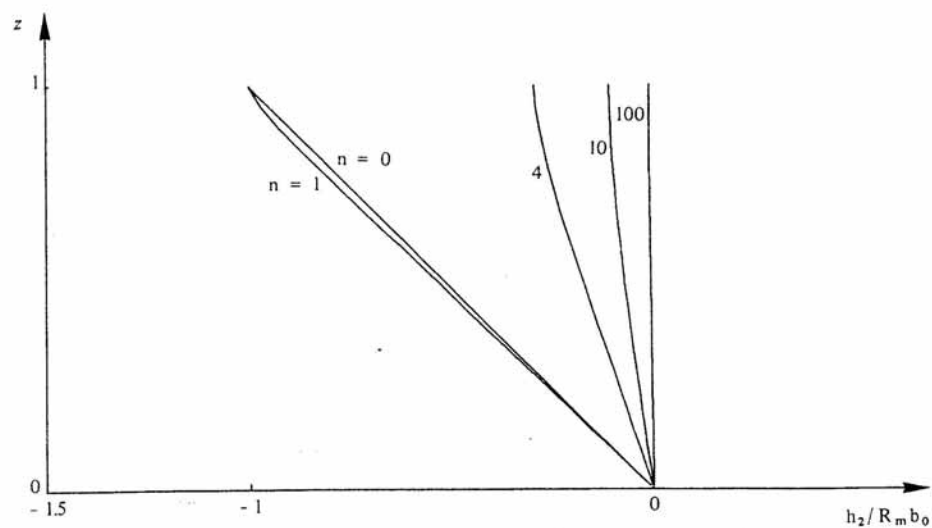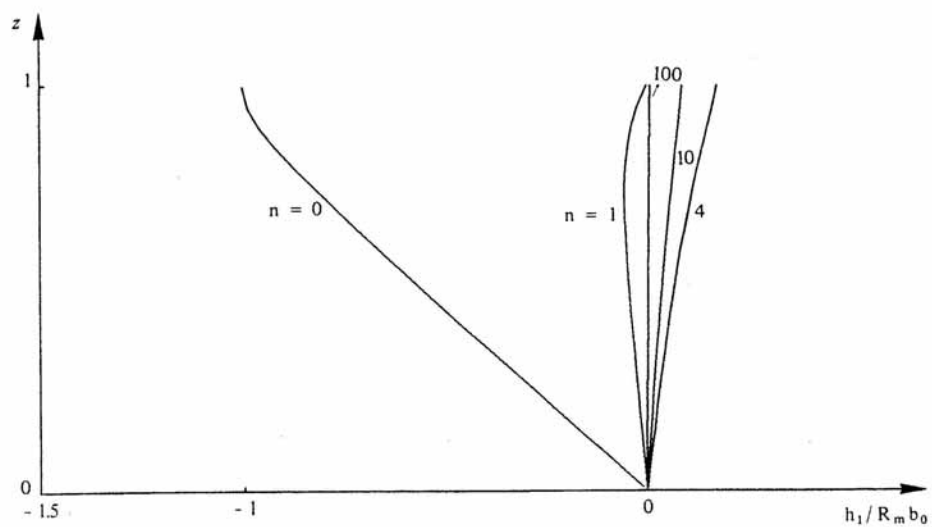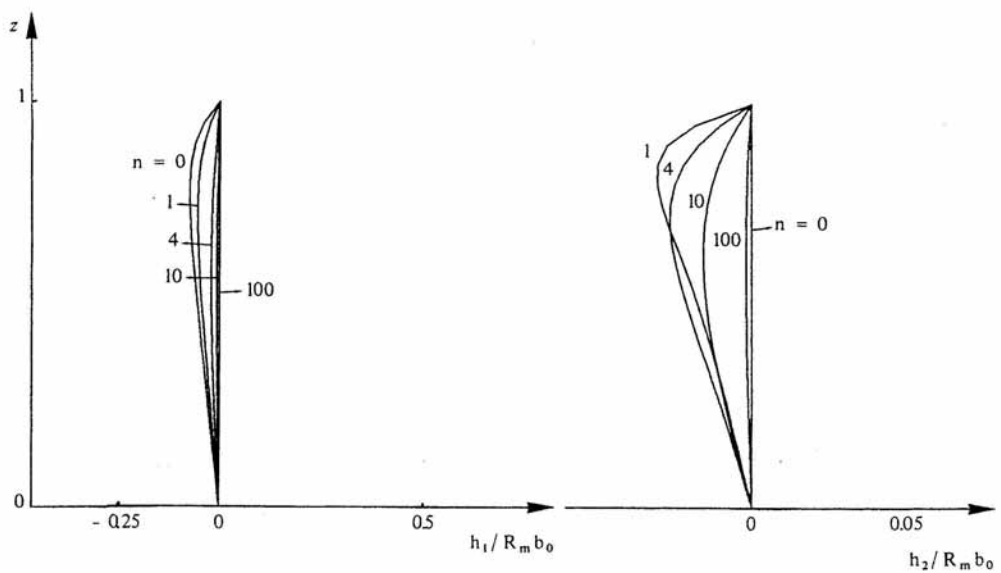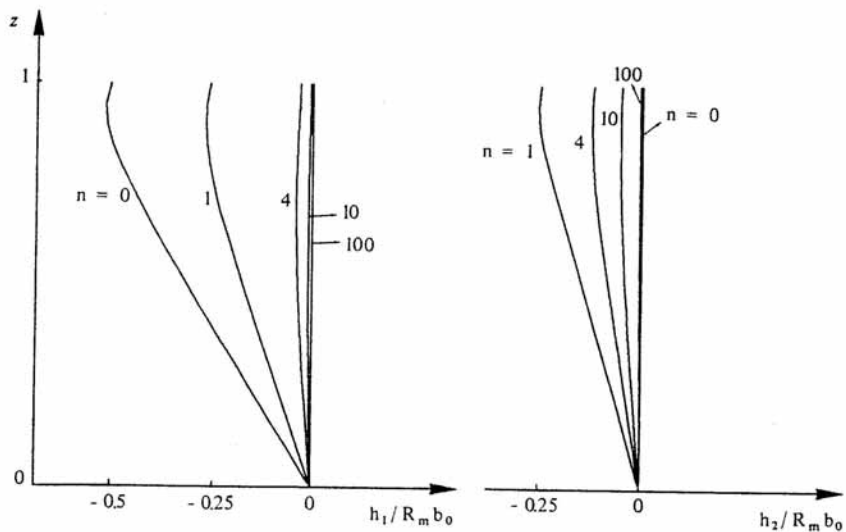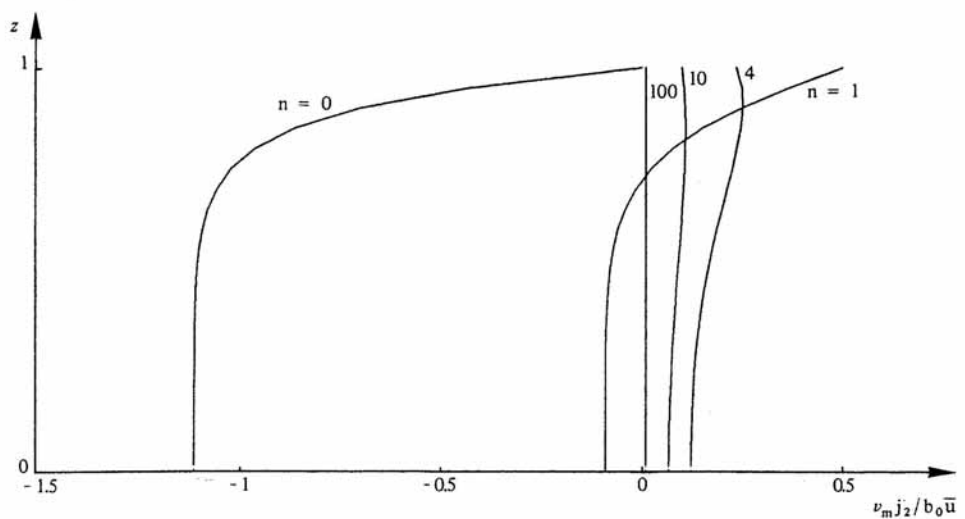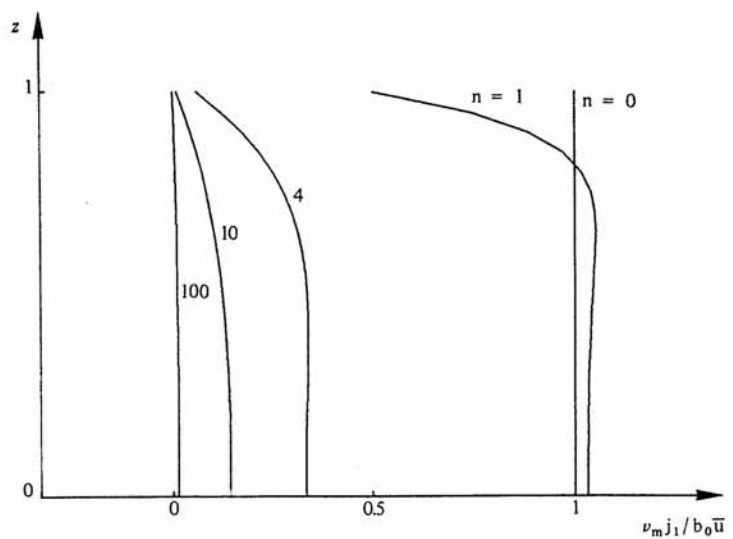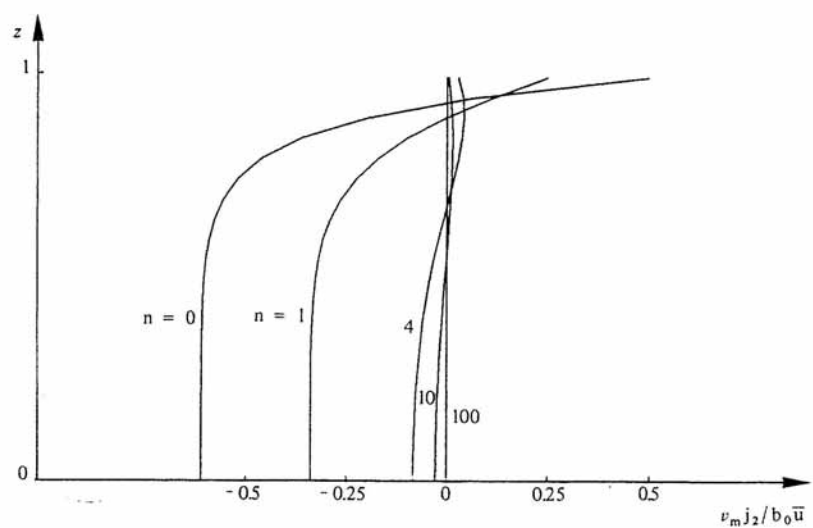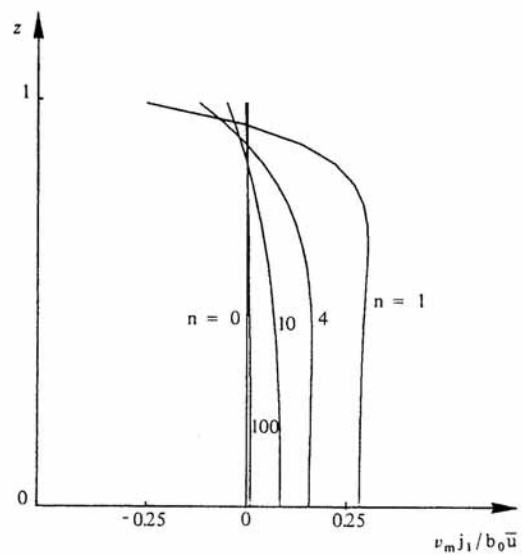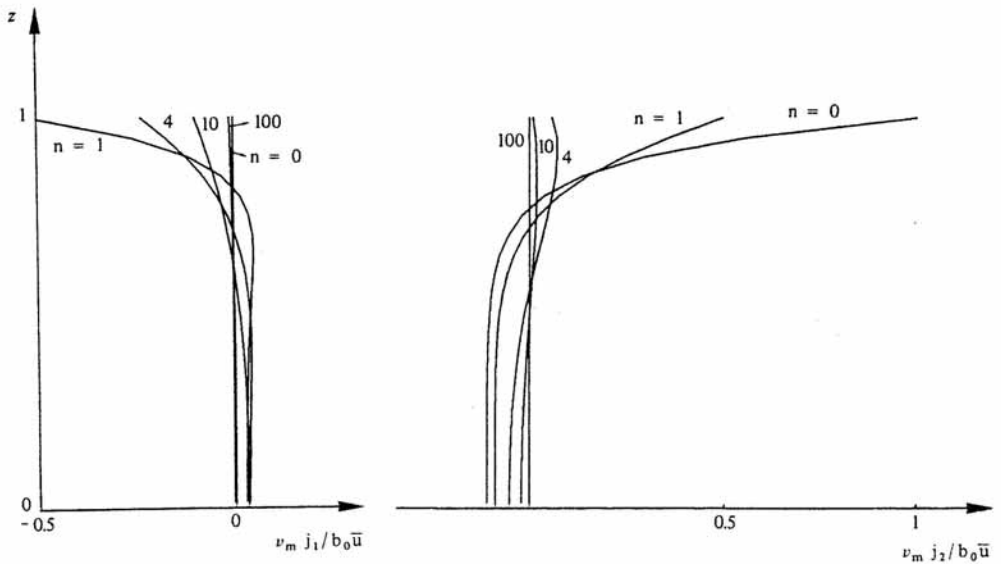
$(m = 10 \, , \; \chi_1 = 0 \, , \; \chi_2 = 0.5)$

$(m = 10 , X_1 = 0 , X_2 = 1)$

Reference

Nihoul J.C.J., (1984). Hydrodynamique II, Magnétohydrodynamique,
    E. Riga Editeur, Liège, 179 pp.

COUPLING BETWEEN ELECTRO-MAGNETICS AND FLUID-DYNAMICS: PHYSICAL AND NUMERICAL ASPECTS.

D. D'Ambrosio

Politecnico di Torino - Dip. di Ingegneria Aeronautica e Spaziale

Corso Duca degli Abruzzi, 24, 10129 Torino, Italy

`domenic.dambrosio@polito.it`

1. Introduction

The aim of this paper is to provide the reader with a comprehensive view of the physical and mathematical models that are used nowadays in the simulation of magneto-fluid dynamic problems, especially in the framework of aerospace applications. As a starting point, the full magneto-fluid dynamics equations, resulting from the coupling of the fluid dynamics balance equations with the Maxwell's equations, will be presented. Then, the approximations that are usually adopted in practical applications will be discussed and applied. The limitations introduced by the simplifying hypotheses in the resulting set of reduced magneto-fluid dynamics equations will be put in evidence. Through the definition of the similarity parameters usually adopted in MFD, the special limiting cases of overwhelming convection or of overwhelming magnetic diffusion will be considered. Finally, the reader will be introduced to the methodologies that are more frequently considered for the numerical simulation of high-speed magneto-fluid dynamics.

2. Full magneto-fluid dynamics equations

In a flow which is able to conduct electricity, a mutual interaction establishes between the flow field and the electromagnetic field. The necessary link between the two is the presence of charged particles in the fluid. Such particles, namely electrons and ions, are subject to the influence of the electromagnetic field through the Lorentz force and, on its side, the electromagnetic field intensity can be modified by the electromagnetic induction effect due to presence of moving charged particles. In the following, the three principal players participating in the magneto-fluid dynamics game will be presented in sequence, with particular attention to focusing the coupling mechanisms embedded in the governing equations.

2.1. Electric charge and electric currents

In magneto-fluid dynamics, the conservative variable related to the net electric charge is the *electric charge density*, ρ_c. The latter is obtained summing up the electric charge per unit volume carried by each charged component of the gas mixture:

$$\rho_c = -e N_A \sum_{i=1}^{n} \frac{\rho_i}{\mathcal{M}_i} \sigma_{is} \qquad (1)$$

where σ_{is} is equal to (+1) for electrons, to (-1) for ions and (0) elsewhere. Clearly, the electric charge density depends on the chemical composition of the gas mixture, which, in chemical non-equilibrium conditions, is governed by the *components mass balance equation*

$$\frac{\partial \rho_i}{\partial t} + \nabla \cdot (\rho_i \mathbf{v}) + \nabla \cdot \mathbf{J}_{m_i} = \Omega_i \qquad i = 1, n \tag{2}$$

where $\mathbf{J}_{m_i}$ are the components mass diffusive fluxes and Ω_i represents the production rate of the i-th chemical component per unit volume.

Summing up the n equations enclosed in Eq. (2) according to the rule defined in Eq. (1), one obtains the *electric charge balance equation*

$$\frac{\partial \rho_c}{\partial t} + \nabla \cdot (\rho_c \mathbf{v}) + \nabla \cdot \mathbf{J}_Q = 0 \tag{3}$$

The term $\rho_c \mathbf{v}$ is the flux of electric charge density due to convection, also referred to as *"convection current"*. The term $\mathbf{J}_Q$ is the flux of electric charge density due to diffusion and it is frequently called *"conduction current"*. In fluid dynamics, species diffusion phenomena are typically related, from a macroscopical point of view, to the gradients of concentration and (though to a lesser extent) of pressure and temperature also, through some *"diffusion coefficient"*. In magneto-fluid dynamics, however, the motion of charged particles is also controlled, at the microscopic level, by the electromagnetic field via the Lorentz force. The consequence is that, at the macroscopic level, mass diffusion depends on the electromagnetic field also through a particular diffusion coefficient. Thus, the components diffusive flux $\mathbf{J}_{m_i}$ can be written as

$$\mathbf{J}_{m_i} = \frac{\rho}{p} \frac{\mathcal{M}_i}{\mathcal{M}^2} \sum_{j=1}^{n} \mathcal{M}_j \mathbf{D}_{ij} \cdot \nabla p_j + \mathbf{F}_i^m \cdot (\mathbf{E} + \mathbf{v} \times \mathbf{B}) - \frac{1}{T} \mathbf{D}_i^T \cdot \nabla T \tag{4}$$

Since the electric charge density is an appropriate linear combination of the mass densities of charged mixture components, electric charge diffusion will follow diffusion mechanisms that are analogous to those of charged particles mass diffusion. Thus, following the approach of Ref. 1, the expression for $\mathbf{J}_Q$ reads like

$$\mathbf{J}_Q = \sum_{j=1}^{n} \overline{\boldsymbol{\lambda}}_{e_j}^p \cdot \nabla p_j + \overline{\boldsymbol{\lambda}}_e \cdot (\mathbf{E} + \mathbf{v} \times \mathbf{B}) + \overline{\boldsymbol{\lambda}}_e^T \cdot \nabla T \tag{5}$$

The first and the third addenda are the fluxes of electric charge due to classical transport phenomena and coefficients $\overline{\boldsymbol{\lambda}}_{e_j}^p$ and $\overline{\boldsymbol{\lambda}}_e^T$ are called, respectively, the *presso-electrical* and the *thermo-electrical* conductivity tensor. In the second addendum, instead, we find the fluxes of electric charge due to the presence of the electromagnetic field, which are proportional to the Lorentz force through the tensorial coefficient $\overline{\boldsymbol{\lambda}}_e$, called *electrical conductivity*. In general, conductivities are local properties of the gas mixture that depend on the local composition and thermodynamic conditions.

The sum of convection and conduction currents is defined as the *electric current density*, $\mathbf{j}$:

$$\mathbf{j} = \rho_c \mathbf{v} + \mathbf{J}_Q \tag{6}$$

Using the definition of $\mathbf{j}$, the electric charge balance equation [Eq. (1)] can be re-written as

$$\frac{\partial \rho_c}{\partial t} + \nabla \cdot \mathbf{j} = 0 \tag{7}$$

2.2. Flow-field governing equations

In classical fluid dynamics, the equations that govern the flow-field reflect three basic principles of physics: the conservation of mass, Newton's first law and the First Principle of Thermodynamics. Of course, these principles maintain their validity in the presence of an electromagnetic field also. The difference with respect to classical fluid dynamics is found in the fact that, if the fluid is electrically conductive, electromagnetic forces will come into play when writing the Newton's first law and, in addition, the work done by electromagnetic forces and the diffusion of energy due to electromagnetic effects will have to be accounted for when writing the First Principle of Thermodynamics.

As a consequence of the above mentioned remarks, the conservation laws applicable to electrically conducting flows take the following form:

$$\frac{\partial \rho}{\partial t} + \nabla \cdot (\rho \mathbf{v}) = 0 \tag{8}$$

total mass balance (continuity)   [mass is conserved]

$$\frac{\partial \rho \mathbf{v}}{\partial t} + \nabla \cdot (\rho \mathbf{v} \mathbf{v} + p \mathbf{I}) - \nabla \cdot \overline{\boldsymbol{\tau}} = \rho_c \mathbf{E} + \mathbf{j} \times \mathbf{B} \tag{9}$$

momentum balance   [descending from Newton's First Law]

$$\frac{\partial (\rho e_m)}{\partial t} + \nabla \cdot (\rho e_m \mathbf{v}) + \nabla \cdot (\mathbf{J}_U - \overline{\boldsymbol{\tau}} \cdot \mathbf{v}) = \mathbf{j} \cdot \mathbf{E} \tag{10}$$

matter energy balance   [descending from the First Principle of Thermodynamics]

The right-hand sides in Eqs. (9)–(10) express the influence of the electromagnetic field on the fluid dynamic field through the electric charge density and the electric current density. In particular, the right-hand side of Eq. (9) is the Lorentz force per unit volume, while the right-hand side of Eq. (10) represents the rate of conversion of electromagnetic energy $\frac{\varepsilon_0}{2} \left(E^2 + c^2 B^2 \right)$ into matter energy ρe_m (consult Refs. 1, 2 for a description of the mechanisms of energy conversion).

In addition, electromagnetic effects are also embedded in the internal energy diffusive flux $\mathbf{J}_U$, that reads like

$$\mathbf{J}_U = \sum_{j=1}^{n} \overline{\mathbf{P}}_j^u \cdot \nabla p_j + \overline{\mathbf{F}}^u \cdot (\mathbf{E} + \mathbf{v} \times \mathbf{B}) - \overline{\boldsymbol{\lambda}}_T^u \cdot \nabla T \tag{11}$$

where $\overline{\mathbf{P}}_j^u$, $\overline{\mathbf{F}}^u$ and $\overline{\boldsymbol{\lambda}}_T^u$ are tensorial energy diffusion coefficients (Ref. 1).

2.3. Electromagnetic field governing equations

In the absence of polarization and magnetization, the Maxwell equations (in SI units) read like

$$\nabla \cdot \mathbf{E} = \frac{\rho_c}{\varepsilon_0} \tag{12}$$

Gauss' law for electricity

$$\nabla \cdot \mathbf{B} = 0 \tag{13}$$

Gauss' law for magnetism

3

$$\nabla \times \mathbf{E} = -\frac{\partial \mathbf{B}}{\partial t} \tag{14}$$

Faraday's law of induction

$$\varepsilon_0 c^2 \nabla \times \mathbf{B} = \mathbf{j} + \varepsilon_0 \frac{\partial \mathbf{E}}{\partial t} \tag{15}$$

Ampère's law

In fact, only Equations (14) and (15) are necessary to determine the evolution of the electric field and magnetic induction, while Equations (12) and (13) can be used to check the obtained results. Again, the role of the electric current density, **j**, as a bridging element between fluid dynamics and electromagnetism is well evident in the equations.

2.4. Bringing all together: the full system

At this stage, it is worthwhile to gather the equations written in the previous subsections to have a comprehensive view of the magneto-fluid dynamic system. For a three dimensional problem, $(12 + n)$ partial differential equations are available, where n is the number of the mixture components:

$$\frac{\partial \rho_i}{\partial t} + \nabla \cdot (\rho_i \mathbf{v}) + \nabla \cdot \mathbf{J}_{m_i} = \Omega_i \qquad i = 1, n \tag{2}$$

$$\frac{\partial \rho_c}{\partial t} + \nabla \cdot \mathbf{j} = 0 \tag{7}$$

$$\frac{\partial \rho}{\partial t} + \nabla \cdot (\rho \mathbf{v}) = 0 \tag{8}$$

$$\frac{\partial \rho \mathbf{v}}{\partial t} + \nabla \cdot (\rho \mathbf{v} \mathbf{v} + p \mathbf{I}) - \nabla \cdot \overline{\overline{\tau}} = \rho_c \mathbf{E} + \mathbf{j} \times \mathbf{B} \tag{9}$$

$$\frac{\partial (\rho e_m)}{\partial t} + \nabla \cdot (\rho e_m \mathbf{v}) + \nabla \cdot (\mathbf{J}_U - \overline{\overline{\tau}} \cdot \mathbf{v}) = \mathbf{j} \cdot \mathbf{E} \tag{10}$$

$$\nabla \times \mathbf{E} = -\frac{\partial \mathbf{B}}{\partial t} \tag{14}$$

$$\varepsilon_0 c^2 \nabla \times \mathbf{B} = \mathbf{j} + \varepsilon_0 \frac{\partial \mathbf{E}}{\partial t} \tag{15}$$

Nevertheless, the number of partial differential equations to be solved is $(10 + n)$, because one can choose not to solve two between Eqs.(2), (7) and (8) and to obtain the two remaining unknown using the algebraic relations:

$$\rho_c = -eN_A \sum_{i=1}^{n} \frac{\rho_i}{\mathcal{M}_i} \sigma_{is} \tag{1}$$

$$\rho = \sum_{i=1}^{n} \rho_i \tag{16}$$

In addition, there is a number of auxiliary algebraic equations to be used, such as, for instance

$$\mathbf{j} = \rho_c \mathbf{v} + \mathbf{J}_Q \tag{6}$$

$$\mathbf{J}_{m_i} = \frac{\rho}{p} \frac{\mathcal{M}_i}{\mathcal{M}^2} \sum_{j=1}^{n} \mathcal{M}_j \mathbf{D}_{ij} \cdot \nabla p_j + \mathbf{F}_i^m \cdot (\mathbf{E} + \mathbf{v} \times \mathbf{B}) - \frac{1}{T} \mathbf{D}_i^T \cdot \nabla T \tag{4}$$

$$\mathbf{J}_Q = \sum_{j=1}^{n} \overline{\boldsymbol{\lambda}}_{e_j}^p \cdot \nabla p_j + \overline{\boldsymbol{\lambda}}_e \cdot (\mathbf{E} + \mathbf{v} \times \mathbf{B}) + \overline{\boldsymbol{\lambda}}_e^T \cdot \nabla T \tag{5}$$

$$\mathbf{J}_U = \sum_{j=1}^{n} \overline{\mathbf{P}}_j^u \cdot \nabla p_j + \overline{\mathbf{F}}^u \cdot (\mathbf{E} + \mathbf{v} \times \mathbf{B}) - \overline{\boldsymbol{\lambda}}_T^u \cdot \nabla T \tag{11}$$

$$p = \rho \frac{R_G}{\mathcal{M}} T \tag{17}$$

plus additional thermodynamic relations linking the mixture internal energy and the various diffusion coefficients to the mixture composition and to thermodynamic variables.

The full magneto-fluid dynamics system appears very complex and cumbersome, but the major difficulty in its solution does not reside in the number and intricacy of the equations, but rather on the different time scales that are involved in it. In particular, electromagnetic waves propagate with the speed of light, while acoustic waves, typical of the fluid dynamics system, propagate with the speed of sound. In mathematical parlance, thus, the magneto-fluid dynamics system is a very stiff one and requires particular numerical strategies for its solution. This point will be the subject of a following section.

3. Simplified magneto-fluid dynamics equations

Magneto-fluid dynamics equations are usually simplified on the basis of engineering considerations in order to reduce their complexity. The whole of hypotheses on whose basis the simplification is made is usually called the *"magnetohydrodynamic approximation"*.

The first hypothesis consists in neglecting the so-called *"displacement current density"*, that is the term $(\epsilon_0 \partial \mathbf{E}/\partial t)$ in the Ampère's law [Eq. (15)]. The argument for such an approximation is that the displacement current density is small with respect to the other terms appearing in Eq. (15), unless the electric field varies with extremely high frequency (Ref. 3). In typical engineering applications, the assumption is in general valid even at microwaves frequencies, but one cannot exclude a priori local situations where its validity may break up.

If the displacement current density is removed from the Ampère's equation [Eq. (15)], then the latter is reduced to

$$\epsilon_0 c^2 \nabla \times \mathbf{B} = \mathbf{j} \tag{18}$$

If we now apply the divergence operator to Eq. (18), we immediately obtain that

$$\nabla \cdot \mathbf{j} = 0 \tag{19}$$

This is an important result, because, when applied to the electric charge balance equation [Eq. (7)], it shows that, within the magnetohydrodynamic approximation, the electric charge density, ρ_c, cannot change in time. This fact implies that, in numerical simulations that adopt the simplified magneto-fluid dynamics equations, the electric charge density will always maintain its initial distribution. The mechanism that guarantees the time-invariance of the electric charge density is based on the role that

the electric field, $\mathbf{E}$, takes up in simplified magneto-fluid dynamics. In fact, when the time derivative of $\mathbf{E}$ is neglected in the Ampère's equation, the electric field ceases to be an independent variable of the mathematical system and becomes a dependent variable, that can be decoded from the definition of the current density, $\mathbf{j}$, and using Equation (18):

$$\mathbf{E} = \left[\overline{\boldsymbol{\lambda}}_e\right]^{-1} \cdot \left(\epsilon_0 c^2 \nabla \times \mathbf{B} - \rho_c \mathbf{v} - \sum_{j=1}^{n} \overline{\boldsymbol{\lambda}}_{e_j}^{p} \cdot \nabla p_j - \overline{\boldsymbol{\lambda}}_e^{T} \cdot \nabla T\right) - \mathbf{v} \times \mathbf{B} \tag{20}$$

It is trivial to see that the definition of $\mathbf{E}$ given by Eq. (20) satisfies the condition $\nabla \cdot \mathbf{j} = 0$. Indeed, the electric field changes in time according to Eq. (20) in such a way that the divergence of $\mathbf{j}$ remains equal to zero. In fact, $\mathbf{E}$ is no more a significative variable, except for the fact that it has to be used to compute the diffusion term of the components mass balance equation [Eq. (2)]. The substitution of the definition of the electric field given by Eq. (20) in Eq. (4) ensures that the value of the electric charge density, ρ_c, will not change in time. Equation (7) can thus be disregarded and substituted by the algebraic relation

$$\rho_c = \rho_c\left(x, y, z\right) \tag{21}$$

In the following, it will be assumed that ρ_c be equal to zero everywhere at the initial instant, so that Eq. (21) becomes

$$\rho_c = 0 \tag{22}$$

in our further discussion. This is in accordance with the second hypothesis of the MHD approximation, that states that the convection current is small with respect to the conduction current. This assumption is justified by considerations about the order of magnitude of those terms containing $\rho_c \mathbf{v}$, but is also consistently consequent on the fact that, in a model that is not capable of determining the time evolution of a certain variable, that variable itself must be unimportant. Notice that electric charge neutrality does not implies that the electrical conductivity $\overline{\boldsymbol{\lambda}}_e$ is equal to zero, because the latter depends on the concentration of electrons and ions, which can be present even though the net electrical charge is zero. An immediate consequence of Eq. (22) is that

$$\mathbf{j} = \mathbf{J}_Q \tag{23}$$

A third important hypothesis that is frequently adopted in simplified magneto-fluid dynamics is that the conduction-current density, $\mathbf{J}_Q$, can be expressed using the so-called *generalized Ohm law*, which differs from Eq. (5) in the fact that the presso-electrical and the thermo-electrical conductivity terms are neglected:

$$\mathbf{J}_Q = \overline{\boldsymbol{\lambda}}_e \left(\mathbf{E} + \mathbf{v} \times \mathbf{B}\right) \tag{24}$$

Note that the electrical conductivity is maintained in its original tensorial form to account for the so-called *Hall effect*, which produces important effects in hypersonic magneto-fluid dynamics (Ref. 4). The hypothesis contained in Eq. (24) simplifies the system, but in principle it doesn't change the mathematical nature of the equation set and could be retained with a minimum effort.

Substituting Eq. (24) in Eq. (18) and reminding that $\rho_c = 0$, one obtains

$$\epsilon_0 c^2 \nabla \times \mathbf{B} = \overline{\boldsymbol{\lambda}}_e \left(\mathbf{E} + \mathbf{v} \times \mathbf{B}\right) \tag{25}$$

At this point, the electric field $\mathbf{E}$ is extracted from Eq. (25), obtaining

$$\mathbf{E} = \epsilon_0 c^2 \overline{\boldsymbol{\lambda}}_e^{-1} (\nabla \times \mathbf{B}) - \mathbf{v} \times \mathbf{B} \qquad (26)$$

Again, it must be underlined that, within the magnetohydrodynamic approximation, the electric field, $\mathbf{E}$, is not an independent variable. Indeed, it depends on the magnetic flux density, $\mathbf{B}$, and on the velocity vector, $\mathbf{v}$, in such a way that $\nabla \cdot \mathbf{j} = 0$. Now, if the curl operator is applied to Eq. (26), the Faraday's law [Eq. (14)] becomes a partial differential equation in $\mathbf{B}$ where only the magnetic flux density vector and the velocity vector are present. Such an equation is called the *magnetic induction equation* and it reads:

$$\frac{\partial \mathbf{B}}{\partial t} + \mathbf{B} (\nabla \cdot \mathbf{v}) + (\mathbf{v} \cdot \nabla) \mathbf{B} - \mathbf{v} (\nabla \cdot \mathbf{B}) - (\mathbf{B} \cdot \nabla) \mathbf{v} = -\epsilon_0 c^2 \nabla \times \left[\overline{\boldsymbol{\lambda}}_e^{-1} (\nabla \times \mathbf{B}) \right] \qquad (27)$$

If the electrical conductivity, $\overline{\boldsymbol{\lambda}}_e$, is considered as a constant in Eq. (27), then the right hand side can be written as:

$$\frac{\partial \mathbf{B}}{\partial t} + \mathbf{B} (\nabla \cdot \mathbf{v}) + (\mathbf{v} \cdot \nabla) \mathbf{B} - \mathbf{v} (\nabla \cdot \mathbf{B}) - (\mathbf{B} \cdot \nabla) \mathbf{v} = \epsilon_0 c^2 \left[\overline{\boldsymbol{\lambda}}_e \right]^{-1} \cdot \nabla^2 \mathbf{B} \qquad (28)$$

Also the momentum balance and the energy balance equations can now be re-written in the light of Eqs. (22)–(24) and (26). In particular, the momentum balance equation takes the form

$$\frac{\partial \rho \mathbf{v}}{\partial t} + \nabla \cdot (\rho \mathbf{v}\mathbf{v} + p\mathbf{I}) - \nabla \cdot \overline{\boldsymbol{\tau}} = \mathbf{j} \times \mathbf{B} = \epsilon_0 c^2 (\nabla \times \mathbf{B}) \times \mathbf{B} \qquad (29)$$

Now, since

$$(\nabla \times \mathbf{B}) \times \mathbf{B} = \nabla \cdot \left(\mathbf{B}\mathbf{B} - \frac{1}{2} B^2 \mathbf{I} \right) - \mathbf{B} \nabla \cdot \mathbf{B} \qquad (30)$$

but $\nabla \cdot \mathbf{B} = 0$, it is possible to write that

$$\mathbf{j} \times \mathbf{B} = \epsilon_0 c^2 \nabla \cdot \left(\mathbf{B}\mathbf{B} - \frac{1}{2} B^2 \mathbf{I} \right) \qquad (31)$$

Thus, the momentum balance equation becomes

$$\frac{\partial \rho \mathbf{v}}{\partial t} + \nabla \cdot \left[\left(p + \frac{\epsilon_0 c^2}{2} B^2 \right) \mathbf{I} + \rho \mathbf{v}\mathbf{v} - \epsilon_0 c^2 \mathbf{B}\mathbf{B} \right] = \nabla \cdot \overline{\boldsymbol{\tau}} \qquad (32)$$

The term $\dfrac{\epsilon_0 c^2}{2} B^2$ can be interpreted as an isotropic pressure stress and it is frequently defined as the *magnetic pressure*. In addition, term $\epsilon_0 c^2 \mathbf{B}\mathbf{B}$ can be regarded as a a fictitious *magnetic stress* system (for instance, $\sigma_{xx}^M = \epsilon_0 c^2 B_x^2$, $\sigma_{xy}^M = \epsilon_0 c^2 B_x B_y$, etc.). The sum of the magnetic pressure stress and the magnetic stresses is called the *Maxwell stress tensor*. Note that the electrical conductivity does not appear in Eq. (32). Nevertheless, in case of vanishing electrical conductivity, the magnetic force force $\mathbf{j} \times \mathbf{B}$ must vanish identically, despite the Maxwell stresses do not go to zero individually (Ref. 2).

Let's now consider the energy balance equation. In the framework of the magnetohydrodynamic approximation, it can be rearranged in the form:

$$\frac{\partial (\rho e_m)}{\partial t} + \nabla \cdot (\rho e_m \mathbf{v}) + \nabla \cdot (\mathbf{J}_U - \overline{\boldsymbol{\tau}} \cdot \mathbf{v}) = \mathbf{j} \cdot \mathbf{E}$$

$$= \left[\epsilon_0 c^2 \nabla \times \mathbf{B} \right] \cdot \left[\epsilon_0 c^2 \left[\overline{\boldsymbol{\lambda}}_e \right]^{-1} \cdot \nabla \times \mathbf{B} - \mathbf{v} \times \mathbf{B} \right] \qquad (33)$$

After some manipulation, the following relation is obtained:

$$\frac{\partial E_t}{\partial t} + \nabla \cdot \left[\left(p + E_t + \frac{\epsilon_0 c^2}{2} B^2 \right) \mathbf{v} - \epsilon_0 c^2 \left(\mathbf{v} \cdot \mathbf{B} \right) \mathbf{B} \right] = \nabla \cdot [\overline{\boldsymbol{\tau}} \cdot \mathbf{v} - \mathbf{J}_U]$$
$$- \nabla \cdot \left[\left(\epsilon_0 c^2 \right)^2 \left[\overline{\boldsymbol{\lambda}}_e \right]^{-1} \cdot (\nabla \times \mathbf{B}) \times \mathbf{B} \right] \tag{34}$$

with

$$E_t = \left(\rho e_m + \frac{\epsilon_0 c^2}{2} B^2 \right) \tag{35}$$

Rearranging the last addendum of its right-hand side, Eq. (34) can also be written as

$$\frac{\partial E_t}{\partial t} + \nabla \cdot \left[\left(p + E_t + \frac{\epsilon_0 c^2}{2} B^2 \right) \mathbf{v} - \epsilon_0 c^2 \left(\mathbf{v} \cdot \mathbf{B} \right) \mathbf{B} \right] = \nabla \cdot [\overline{\boldsymbol{\tau}} \cdot \mathbf{v} - \mathbf{J}_U] +$$
$$+ \left(\epsilon_0 c^2 \right)^2 \left[\left[\overline{\boldsymbol{\lambda}}_e \right]^{-1} (\nabla \times \mathbf{B}) \right] \cdot (\nabla \times \mathbf{B}) - \tag{36}$$
$$- \left(\epsilon_0 c^2 \right)^2 \mathbf{B} \cdot \nabla \times \left[\left[\overline{\boldsymbol{\lambda}}_e \right]^{-1} (\nabla \times \mathbf{B}) \right]$$

In case of constant and scalar electrical conductivity, the final form is:

$$\frac{\partial E_t}{\partial t} + \nabla \cdot \left[\left(p + E_t + \frac{\epsilon_0 c^2}{2} B^2 \right) \mathbf{v} - \epsilon_0 c^2 \left(\mathbf{v} \cdot \mathbf{B} \right) \mathbf{B} \right] = \nabla \cdot [\overline{\boldsymbol{\tau}} \cdot \mathbf{v} - \mathbf{J}_U] +$$
$$+ \frac{\left(\epsilon_0 c^2 \right)^2}{\lambda_e} \left[(\nabla \times \mathbf{B})^2 + \mathbf{B} \cdot \nabla^2 \mathbf{B} \right] \tag{37}$$

In compact vector form, the *simplified magneto-fluid dynamics equations*, to whom we will refer in the future as to the *SMFD* equations, can be expressed as:

$$\frac{\partial}{\partial t} \begin{bmatrix} \rho_i \\ \rho \\ \rho\mathbf{v} \\ \mathbf{B} \\ E_t \end{bmatrix} + \nabla \cdot \begin{bmatrix} \rho_i \mathbf{v} \\ \rho\mathbf{v} \\ \left(p + \epsilon_0 c^2 \frac{B^2}{2} \right) \overline{\mathbf{I}} + \rho\mathbf{v}\mathbf{v} - \epsilon_0 c^2 \mathbf{B}\mathbf{B} \\ \mathbf{v}\mathbf{B} - \mathbf{B}\mathbf{v} \\ \left(E_t + p + \frac{\epsilon_0 c^2}{2} B^2 \right) \mathbf{v} - \epsilon_0 c^2 \left(\mathbf{v} \cdot \mathbf{B} \right) \mathbf{B} \end{bmatrix} =$$
$$= \begin{bmatrix} -\nabla \cdot \mathbf{J}_{m_i} \\ 0 \\ \nabla \cdot \overline{\boldsymbol{\tau}} \\ 0 \\ \nabla \cdot (\overline{\boldsymbol{\tau}} \cdot \mathbf{v}) - \nabla \cdot \mathbf{q} \end{bmatrix} + \begin{bmatrix} \Omega_i \\ 0 \\ 0 \\ -\epsilon_0 c^2 \nabla \times \left[\overline{\boldsymbol{\lambda}}_e^{-1} (\nabla \times \mathbf{B}) \right] \\ \left(\epsilon_0 c^2 \right)^2 \left\{ \left[\left[\overline{\boldsymbol{\lambda}}_e \right]^{-1} (\nabla \times \mathbf{B}) \right] \cdot (\nabla \times \mathbf{B}) - \mathbf{B} \cdot \nabla \times \left[\left[\overline{\boldsymbol{\lambda}}_e \right]^{-1} (\nabla \times \mathbf{B}) \right] \right\} \end{bmatrix}$$
$$\tag{38}$$

with

$$E_t = \left(\rho u + \frac{1}{2} \rho v^2 + \frac{\epsilon_0 c^2}{2} B^2 \right)$$

For the sake of simplicity, non-equilibrium thermochemical kinetics will be neglected in the following and the electrical conductivity will be considered as a constant scalar value. With these simplifications, that will not significantly affect the essence of the discussed subjects, the system will

read:

$$\frac{\partial}{\partial t}\begin{bmatrix} \rho \\ \rho\mathbf{v} \\ \mathbf{B} \\ E_t \end{bmatrix} + \nabla \cdot \begin{bmatrix} \rho\mathbf{v} \\ \left(p + \epsilon_0 c^2 \dfrac{B^2}{2}\right)\overline{\mathbf{I}} + \rho\mathbf{vv} - \epsilon_0 c^2 \mathbf{BB} \\ \mathbf{vB} - \mathbf{Bv} \\ \left(E_t + p + \dfrac{\epsilon_0 c^2}{2}B^2\right)\mathbf{v} - \epsilon_0 c^2\left(\mathbf{v}\cdot\mathbf{B}\right)\mathbf{B} \end{bmatrix} =$$

$$= \begin{bmatrix} 0 \\ \nabla\cdot\overline{\boldsymbol{\tau}} \\ 0 \\ \nabla\cdot(\overline{\boldsymbol{\tau}}\cdot\mathbf{v}) - \nabla\cdot\mathbf{q} \end{bmatrix} + \begin{bmatrix} 0 \\ 0 \\ \dfrac{\epsilon_0 c^2}{\lambda_e}\nabla^2\mathbf{B} \\ \dfrac{(\epsilon_0 c^2)^2}{\lambda_e}\left[(\nabla\times\mathbf{B})^2 + \mathbf{B}\cdot\nabla^2\mathbf{B}\right] \end{bmatrix} \tag{39}$$

In the next section, the system represented by Eq. (39) will be written in normalized form and the similarity parameters that are typical of magneto-fluid dynamics will be put in evidence.

4. Non-dimensional magneto-fluid dynamics equations

4.1. Similarity parameters in MFD

In order to assess the relative importance of the terms appearing in the magneto-fluid dynamics equations, it is convenient to introduce some similarity parameters. Indicating with the subscript '0' the reference magneto-fluid dynamics variables and with L the reference length, one can define:

$$Re = \frac{\rho_0 V_0 L}{\mu_0} \qquad\qquad \text{Reynolds number} \tag{40}$$

$$M = \frac{V_0}{\sqrt{\gamma p_0/\rho_0}} \qquad\qquad \text{Mach number} \tag{41}$$

$$Re_m = \frac{\lambda_{e_0} V_0 L}{\epsilon_0 c^2} \qquad\qquad \text{Magnetic Reynods number} \tag{42}$$

$$S = \frac{\epsilon_0 c^2 B_0^2}{\rho_0 V_0^2} \qquad\qquad \text{Magnetic force number} \tag{43}$$

where Re_m and S are given as a dowry by magnetism.

The *magnetic Reynolds number*, Re_m, is a measure of how easily the fluid slips through the magnetic field. In fact, the group $\dfrac{\epsilon_0 c^2}{\lambda_{e_0}}$ has the same dimensions of the kinematic viscosity ($[m^2/s]$) and represents the *magnetic diffusivity* of the plasma. Thus, the magnetic Reynolds number quantifies the ratio between convection and magnetic diffusion effects. If Re_m is very large, then magnetic diffusion is negligible, $\mathbf{E} + \mathbf{v}\times\mathbf{B}$ tends to be very small and a large induced magnetic field is created. If Re_m is very small, magnetic diffusion dominates and the *imposed magnetic field*, $\mathbf{B}_0$, is only slightly perturbed by the magnetic induction effects generated by the fluid motion.

The *magnetic force number*, S, can be thought as the ratio of the magnetic body force to the inertia force. When it is small, the magnetic field is ineffectual in perturbing the flow field. On the other hand, if it is of the order of 1 or larger, large magnetic effects can be expected.

9

4.2. Normalized full MFD equations

The non-dimensional form of the full magneto-fluid dynamics equations is given by

$$\frac{\partial \rho_c}{\partial t} + \nabla \cdot (\rho_c \mathbf{v}) + \frac{c^2}{V_0^2} \sqrt{\gamma} M \, Re_m \, \nabla \cdot [\lambda_e \, (\mathbf{E} + \mathbf{v} \times \mathbf{B})] = 0 \tag{44}$$

$$\frac{\partial \rho}{\partial t} + \nabla \cdot (\rho \mathbf{v}) = 0 \tag{45}$$

$$\frac{\partial \rho \mathbf{v}}{\partial t} + \nabla \cdot (\rho \mathbf{v} \mathbf{v} + p\mathbf{I}) - \frac{\sqrt{\gamma} M}{Re} \nabla \cdot \overline{\boldsymbol{\tau}} = \frac{V_0^2}{c^2} S \, \rho_c \mathbf{E} + \frac{V_0^2}{c^2} S \, \rho_c \mathbf{v} \times \mathbf{B} + \sqrt{\gamma} M \, S \, Re_m \, \mathbf{J}_Q \times \mathbf{B} \tag{46}$$

$$\frac{\partial (\rho e_m)}{\partial t} + \nabla \cdot (\rho e_m \mathbf{v}) + \frac{\sqrt{\gamma} M}{Re} \nabla \cdot (\mathbf{J}_U - \overline{\boldsymbol{\tau}} \cdot \mathbf{v}) = \frac{V_0^2}{c^2} S \, \rho_c \mathbf{v} \cdot \mathbf{E} + \sqrt{\gamma} M \, S \, Re_m \, \mathbf{J}_Q \cdot \mathbf{E} \tag{47}$$

$$\frac{\partial \mathbf{B}}{\partial t} + \nabla \times \mathbf{E} = 0 \tag{48}$$

$$\frac{\partial \mathbf{E}}{\partial t} - \frac{c^2}{V_0^2} \gamma M^2 \, \nabla \times \mathbf{B} = -\frac{c^2}{V_0^2} \sqrt{\gamma} \, M \, Re_m \, \mathbf{j} \tag{49}$$

where, for simplicity, only diffusion due to the Lorentz force has been considered in $\mathbf{J}_Q$:

$$\mathbf{J}_Q = \overline{\boldsymbol{\lambda}}_e \cdot (\mathbf{E} + \mathbf{v} \times \mathbf{B}) \tag{50}$$

The presence of the term γM^2 (or of its square root) in the dimensionless equations is due to the fact the the reference speed has been taken equal to $\sqrt{RT_0}$.

Considering Eqs. (44)–(49), it is interesting to note that all terms involving the conduction current, $\rho_c \mathbf{v}$, are multiplied by the factor V_0^2/c^2, which is very small in normal applications, also in the case of hypersonic flows. In addition, the displacement current is very small with respect to the other terms in the Ampère's law [Eq. (49)], which are multiplied by c^2/V_0^2. Finally, $\nabla \cdot \mathbf{J}_Q$ is very large with respect to the remaining elements of the electric charge balance equation [Eq. (44)]. All these facts represent the argument for neglecting the displacement current and the convection current in the full magneto-fluid dynamics equations. Nevertheless, the validity of considerations based on the order of magnitude should always be checked for each specific problem.

4.3. Normalized simplified MFD equations

If we re-write the simplified magnetogasdynamics equations in terms of dimensionless variables, we obtain:

$$
\frac{\partial}{\partial t}
\begin{bmatrix}
\rho \\
\rho\mathbf{v} \\
\mathbf{B} \\
E_t
\end{bmatrix}
+ \nabla \cdot
\begin{bmatrix}
\rho\mathbf{v} \\
\rho\mathbf{v}\mathbf{v} + \left(p + \gamma M^2 S \dfrac{B^2}{2}\right)\bar{\mathbf{I}} - \gamma M^2 S\,\mathbf{B}\mathbf{B} \\
\mathbf{v}\mathbf{B} - \mathbf{B}\mathbf{v} \\
\left(E_t + p + \gamma M^2 S \dfrac{B^2}{2}\right)\mathbf{v} - \gamma M^2 S\,(\mathbf{v}\cdot\mathbf{B})\,\mathbf{B}
\end{bmatrix}
=
$$

$$
=
\begin{bmatrix}
0 \\[4pt]
\dfrac{\sqrt{\gamma}M}{Re}\nabla\cdot\bar{\boldsymbol{\tau}} \\[8pt]
-\dfrac{\sqrt{\gamma}M}{Re_m}\nabla\times\left(\dfrac{\nabla\times\mathbf{B}}{\lambda_e}\right) \\[8pt]
\dfrac{\sqrt{\gamma}M}{Re}\left[\nabla\cdot\left(\bar{\boldsymbol{\tau}}\cdot\mathbf{v} - \dfrac{\gamma}{(\gamma-1)Pr}\mathbf{q}\right)\right] + \dfrac{\sqrt{\gamma}M}{Re_m}\gamma M^2 S\dfrac{1}{\lambda_e}\left[(\nabla\times\mathbf{B})^2 + \mathbf{B}\cdot\nabla^2\mathbf{B}\right]
\end{bmatrix}
\tag{51}
$$

with

$$
E_t = \left(\rho e_m + \gamma M^2 S \frac{B^2}{2}\right)
$$

Again, the presence of the term γM^2 (or of its square root) in the dimensionless equations is due to the fact the the reference speed has been taken equal to $\sqrt{RT_0}$.

4.3.1. Limiting case # 1: small magnetic force number

This is a trivial case. When $S \to 0$, the MFD equations reduce to the Navier-Stokes equations:

$$
\frac{\partial}{\partial t}
\begin{bmatrix}
\rho \\
\rho\mathbf{v} \\
\mathbf{B} \\
\rho e_m
\end{bmatrix}
+ \nabla \cdot
\begin{bmatrix}
\rho\mathbf{v} \\
\rho\mathbf{v}\mathbf{v} + p\bar{\mathbf{I}} \\
\mathbf{v}\mathbf{B} - \mathbf{B}\mathbf{v} \\
(\rho e_m + p)\,\mathbf{v}
\end{bmatrix}
=
\begin{bmatrix}
0 \\[4pt]
\dfrac{\sqrt{\gamma}M}{Re}\nabla\cdot\bar{\boldsymbol{\tau}} \\[8pt]
-\dfrac{\sqrt{\gamma}M}{Re_m}\nabla\times\left(\dfrac{\nabla\times\mathbf{B}}{\lambda_e}\right) \\[8pt]
\dfrac{\sqrt{\gamma}M}{Re}\left[\nabla\cdot\left(\bar{\boldsymbol{\tau}}\cdot\mathbf{v} - \dfrac{\gamma}{(\gamma-1)Pr}\mathbf{q}\right)\right]
\end{bmatrix}
\tag{52}
$$

The magnetic induction equation is still present, but it is not coupled with the fluid dynamics equations. The magnetic field is not sufficiently strong to produce any effect on fluid dynamics: it just varies according to the kinematic field.

4.3.2. Limiting case #2: small magnetic Reynolds number

When $Re_m \to 0$, the applied magnetic field is practically undisturbed by the flow. In this case, the magneto-fluid dynamics equations can be further simplified. In fact, the magnetic induction equation [Eq. (27)] reduces to

$$
\nabla\times\left[\bar{\boldsymbol{\lambda}}_e^{-1}(\nabla\times\mathbf{B})\right] = 0
\tag{53}
$$

11

or, assuming a scalar and constant electrical conductivity, to

$$\nabla^2 \mathbf{B} = 0 \tag{54}$$

The substitution of Eq. (27) with Eq. (53) means that, in the limit as $Re_m \rightarrow 0$, the induced magnetic field becomes negligible and the applied magnetic field is undisturbed by the flow. There is not an *induced magnetic field*, $\mathbf{B}$, that is the magnetic field due to induced currents, but only the *imposed magnetic field*, $\mathbf{B}_0$, that, given the boundary conditions, varies in space according to Eq.(53).

The other governing equations do not change. What is important, is that the magnetic field, $\mathbf{B} = \mathbf{B}_0$, is no more an unknown. It is not bi-univocally coupled with the fluid dynamics field, but it univocally influences the latter through source terms. In order to avoid the numerical difficulty of treating terms containing $1/Re_m$, the momentum and energy balance equations are written in the original form used for the full magneto-fluid dynamics system [Eqs. (9) and (10)].

Thus, in the case of a small magnetic Reynolds number, the magnetic induction equation is dropped and the new resulting system is just composed of the Navier-Stokes equations, amended with source terms representing the effect of the magnetic diffusion.

$$\frac{\partial}{\partial t}\begin{bmatrix} \rho \\ \rho\mathbf{v} \\ \rho e_m \end{bmatrix} + \nabla \cdot \begin{bmatrix} \rho\mathbf{v} \\ \rho\mathbf{v}\mathbf{v} + p\bar{\mathbf{I}} \\ (\rho e_m + p)\,\mathbf{v} \end{bmatrix} = \begin{bmatrix} 0 \\ \dfrac{\sqrt{\gamma}M}{Re}\nabla\cdot\overline{\boldsymbol{\tau}} \\ \dfrac{\sqrt{\gamma}M}{Re}\left[\nabla\cdot\left(\overline{\boldsymbol{\tau}}\cdot\mathbf{v} - \dfrac{\gamma}{(\gamma-1)\,Pr}\mathbf{q}\right)\right] \end{bmatrix} +$$

$$+ \begin{bmatrix} 0 \\ \sqrt{\gamma}MSRe_m\,\mathbf{j}\times\mathbf{B} \\ \sqrt{\gamma}MSRe_m\,\mathbf{j}\cdot\mathbf{E} \end{bmatrix} \tag{55}$$

4.3.3. Limiting case #3: very large magnetic Reynolds number

When $Re_m \rightarrow \infty$, then convection is overwhelming with respect to magnetic diffusion. In this case, the magnetic field and the fluid dynamics field are strongly coupled and they react instantaneously to their reciprocal variations. Fluid and magnetic field are "frozen" together (Ref. 2), as if the induced currents would inhibit any relative motion of the fluid and the field.

Those terms containing Re_m disappear from the dimensionless simplified MFD equations, which take the form:

$$\frac{\partial}{\partial t}\begin{bmatrix} \rho \\ \rho\mathbf{v} \\ \mathbf{B} \\ E_t \end{bmatrix} + \nabla \cdot \begin{bmatrix} \rho\mathbf{v} \\ \rho\mathbf{v}\mathbf{v} + \left(p + \gamma M^2 S\dfrac{B^2}{2}\right)\bar{\mathbf{I}} - \gamma M^2 S\,\mathbf{B}\mathbf{B} \\ \mathbf{v}\mathbf{B} - \mathbf{B}\mathbf{v} \\ \left(E_t + p + \gamma M^2 S\dfrac{B^2}{2}\right)\mathbf{v} - \gamma M^2 S\,(\mathbf{v}\cdot\mathbf{B})\,\mathbf{B} \end{bmatrix} =$$

$$= \begin{bmatrix} 0 \\ \dfrac{\sqrt{\gamma}M}{Re}\nabla\cdot\overline{\boldsymbol{\tau}} \\ 0 \\ \dfrac{\sqrt{\gamma}M}{Re}\left[\nabla\cdot\left(\overline{\boldsymbol{\tau}}\cdot\mathbf{v} - \dfrac{\gamma}{(\gamma-1)\,Pr}\mathbf{q}\right)\right] + 0 \end{bmatrix} \tag{56}$$

with

$$E_t = \left(\rho e_m + \gamma M^2 S \frac{B^2}{2} \right)$$

5. MFD physical models for hypersonic applications: resumé

In summary, we can identify the physical models that are normally used in magneto-fluid dynamics as follows.

- At the highest level, we find the full magneto-fluid dynamics equations, that are composed of the Maxwell equations coupled with the mass, momentum and balance equations for a conducting fluid in the presence of an electromagnetic field. The latter are the Navier-Stokes equations, with the addition of source terms that account for the presence of electromagnetic forces and energies that enter in the balances. In the full system, the electric field and the electric charge density belong to the set of the independent variables.

  – At a lower level, there are the simplified magneto-fluid dynamics equations, where the hypotheses of a negligible displacement-current and of a negligible convection current are made. In the SMFD equations, the Maxwell equations are replaced by the magnetic induction equation, which is still coupled to the Navier-Stokes equations. It is possible to write the equations system in divergence form with the addition of *magnetic* source terms that appear only in the magnetic induction and energy equations and that depend on the electrical conductivity. Those fluxes that appear under the divergence operator and that are not related to momentum and energy diffusion are composed of a fluid dynamics part and of a part related to the magnetic field. Thus, there can be in general a very strict coupling between the flow field and the magnetic field. The mutual adaptation of the one to the other is controlled by the ratio between convection and magnetic diffusion effects, which is represented by the magnitude of the *magnetic Reynolds number*.

    * A limiting situation exists when the magnetic Reynolds number, whose inverse multiplies the magnetic source terms, is very large. In this case, that is when the plasma is close to be a perfect electricity conductor, the *induced* magnetic field becomes predominant and the *magnetic* source terms disappear from the SMFD equations. The coupling between fluid dynamics and the magnetic field is very strong: the effect of one on the other is instantaneous.

    * If, conversely, the magnetic Reynolds number is small, then the dimensions of the problem can be reduced. Indeed, in this situation, the magnetic field induced by the motion of electric charges, prompt by fluid dynamics, is negligible with respect to the applied magnetic field. Therefore, it is only necessary to take into account the latter for the coupling with fluid dynamics. The magnetic induction equation is no more necessary and the SMFD equations reduce to the Navier-Stokes equations, with the addition of source terms that account for the contribution of the magnetic forces and energies due to the *applied* magnetic field only.

    * Another limiting situation, though a less interesting one, arises when the magnitude of the *magnetic force number*, S, is considered. In case the latter is large enough, than

magnetic forces are comparable with inertia forces and a electrically conductive flow is affected by the presence of a magnetic field. Yet, if the magnetic force number is very small, then the magnetic field is unable to significantly perturb fluid dynamics and the simplified MFD equations simply reduce to the Navier-Stokes equations.

The above depicted classification is schematized in Fig.1. In principle, the simplified MFD model
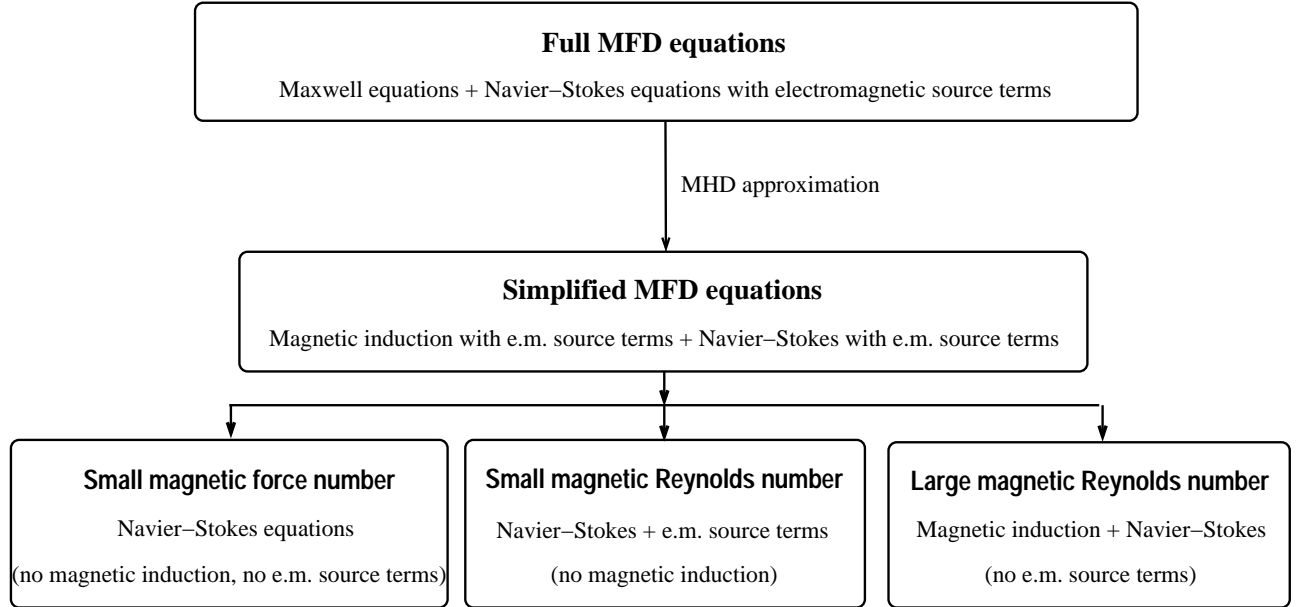
Fig. 1   Schematic view of the MFD physical models.

and its limiting cases should be coupled with thermochemical non-equilibrium models to account for variable transport coefficients that depend on the nature of the ionized gas. In the present section, this aspect was omitted to simplify the discussion.

6.   Numerical approaches to magneto-fluid dynamics

The recent interest in magneto-fluid dynamics for aerospace applications as a mean to control the flow during atmospheric re-entry or hypersonic flight induced a number of members of the Computational Fluid Dynamics (CFD) community to undertake research work in Computational Magneto-Fluid Dynamics (CMFD). The experience of these scientists in the field of CFD has provided a rich heritage of knowledge for CMFD, as noted in Ref. 5. Most numerical methods for CMFD were developed following the guidelines coming from CFD methods, as it is demonstrated by the large number of published papers on numerical simulation of MFD flows where the numerical schemes belong to CFD methods families (Refs. 6–18 can be cited as examples, though they represent only a subset of the amount of work done in the field).

6.1.   Numerical approaches to the full magneto-fluid dynamics equations

To the author's knowledge, no paper has ever been published describing the attempt to simulate MFD flows using the full magneto-fluid dynamics equations. This fact can be partly explained noting that,

in general, the magnetohydrodynamic approximation is reasonable in most engineering applications, included those related to hypersonic motion. However, as implicitly noted in Ref. 1, there could be regions of the flow where those effects neglected using the simplified MFD equations could important. An example is the fact that SMFD is not capable of simulating flows with local accumulation of electric charge density, while in the real world this effect could be expected. Presently, however, an attempt to identify numerical difficulties and potentialities in using the full MFD equations is carried out by the authors of Ref. 19 in the framework of research activities commissioned by the European Space Agency under the impulse of the author of Ref. 1.

The major problem in the numerical simulation of the full magneto-fluid dynamics equations resides in the fact that signals propagation speeds typical of fluid dynamics differ orders of magnitude from the signal propagation speeds typical of electromagnetism. The former are of the order of the speed of sound, or at most one order of magnitude larger (flying at Mach 20 at high altitude, the fastest propagation speed has an order of magnitude of 7000 m/s), while the latter are as fast as the speed of light (that is about $3 \cdot 10^8$ m/s). Since there are at least 5 orders of magnitude separating signal propagation speeds in fluid dynamics and in electromagnetism, the resulting coupled system is a very stiff one, and requires a special treatment.

Let's imagine that one wishes to solve both the Maxwell and the Navier-Stokes equations (Eqs. (44) and (49)) using, for instance, a finite volume scheme and a time-dependent method. Solution methods for the two systems, when considered separately, are well known (Ref. 5). However, the coupling requires that the two systems are solved simultaneously. Stability considerations will request that, using explicit schemes, the common time step be very small, namely of the order of $\Delta x/c$. This is definitely a too small time step for fluid dynamics. The way to overcome such an obstacle is to solve the Maxwell equations using implicit schemes, that allow for very large computational times step as they are nominally unconditionally stable. Thanks to the constancy of the speed of light, the homogeneous electromagnetic system is linear, so that the application of implicit schemes to the Maxwell equations allows for very large time steps (relative to the Maxwell system). Thus, one can march the Navier-Stokes system for one iteration using the values of the electromagnetic field variables frozen at the beginning of the time step, and then march the Maxwell system in time for a couple of iterations until the same time value of the companion fluid dynamics step is reached. In this case, one could decide to use the flow-field values frozen at the beginning of the time step, or those at the end, or an average. Clearly, such a way of proceeding does not possess the time resolution necessary to resolve electromagnetic phenomena that evolve with very high frequency.

Further difficulties arise when the source terms that are present in the coupled system become large. In fact, it is well known that the numerical solution of hyperbolic equations becomes very hard when stiff source terms are present. Such a problem is typical, for instance, of the numerical simulation of chemically reacting flows. In the full MFD equations, source terms become stiff when the magnetic Reynolds number is large. In order to increase the value of Re_m above which the numerical method fails, the classical strategy of treating implicitly those source terms that appear in the Navier-Stokes equations can be used (in fact, the source term appearing in the Faraday's equation is always treated implicitly). Other approaches could be borrowed from numerical analysis studies on hyperbolic equations with stiff source terms.

6.2. Numerical approaches to the simplified magneto-fluid dynamics equations

The magnetohydrodynamic approximation completely changes the mathematical nature of the MFD equations. The propagation of electromagnetic signals with the speed of light is completed removed (in fact, the electric field is no more a significative variable). The homogenous SMFD system (that is in the limit of infinite viscous and magnetic Reynolds numbers) is characterized by eigenvalues and eigenvectors that correspond to seven different signals with the respective propagation speeds. Details on the subject are given in Ref. 19 and are widely reported in the literature (see, for instance, Refs. 3, 20, 21).

Numerical methods for the simplified MFD equations can be very different depending on the magnetic Reynolds number of the application. In fact, the system contained in Eq. (51) presents source terms that become large for small values of Re_m. In the following two subsections, the approaches usually followed for the two cases will be discussed.

6.2.1. Moderate and large magnetic Reynolds number

For large or not too small magnetic Reynolds numbers, most part of the numerical methods used to solve the SMFD equations for aerospace applications adopt upwind schemes originally developed for one-dimensional *ideal magnetohydrodynamics (MHD)* equations, that is the SMFD equation for inviscid flows and in the limit of an infinite magnetic Reynolds number. The approach replicates the one followed by numerical methods for compressible flows: first upwind schemes were developed for the Euler equations in one-dimension and then extended to two and three-dimensions and to Navier-Stokes. Upwind methods developed to solve the ideal MHD equations belong to the Roe family (Refs. 8–10), to the flux-vector splitting family (Ref. 11), to the HLLE family (Refs. 12, 13), to the gas-kinetics theory based flux-splitting family (Ref. 14), to the PPM family (Ref. 15), to the Lax-Friedrichs family (Ref. 16) and to the Osher family (Ref. 19). With the exception of the gas-kinetic FVS method, all the above cited upwind methods follow the Godunov approach and thus necessitate knowledge of the eigenvectors and eigenvalues system that characterize the one-dimensional ideal MHD equations. Other numerical methods for MHD adopt the TVD scheme (Ref. 17) or a combination of compact-difference for space derivatives and the classical Runge-Kutta method for time derivatives (Ref. 18).

When these methods are extended to more than one dimension, special procedures must be adopted in order to enforce the $\nabla \cdot \mathbf{B} = 0$ constraint in the integration of the discretized equations (Refs. 11, 22–24).

6.2.2. Small magnetic Reynolds number

As previously reported, in the limit of a small magnetic Reynolds number, the SMFD equations are reduced to the Navier-Stokes equations with the addition of source terms. In this case, standard numerical methods for compressible fluid dynamics with source terms can be used, coupled with the solution of an additional equation that is used to evaluate the electric field, $\mathbf{E}$, via the electric potential, ϕ. Indeed, in case of small magnetic Reynolds number, the use of Eq. (20) or Eq. (26) to obtain the value of $\mathbf{E}$ could lead to inaccurate evaluations. Thus, the condition that $\nabla \cdot \mathbf{j} = 0$ is enforced, leading

to the equation:

$$\nabla \cdot \mathbf{j} = \nabla \cdot \left[\overline{\boldsymbol{\lambda}}_e \cdot (\mathbf{E} + \mathbf{v} \times \mathbf{B}) \right] = 0 \tag{57}$$

Reminding that

$$\mathbf{E} = -\nabla \phi \tag{58}$$

the final equation to be solved is

$$\nabla \cdot \left(\overline{\boldsymbol{\lambda}}_e \nabla \phi \right) = \nabla \cdot \left[\overline{\boldsymbol{\lambda}}_e \left(\mathbf{v} \times \mathbf{B} \right) \right] \tag{59}$$

Nomenclature

$\mathbf{B}$	magnetic flux density
c	speed of light
$\mathbf{D}_{ij}$	diffusion tensors
$\mathbf{D}_i^T$	thermo-diffusion tensors
$\mathbf{E}$	electric field
E_t	total energy
e	electric charge
e_m	matter energy per unit mass
$\mathbf{F}_i^m$	electro-diffusion tensors
$\overline{\mathbf{F}}^u$	internal energy electro-diffusion tensor
$\mathbf{J}_{m_i}$	i-th component mass diffusive flux
$\mathbf{J}_Q$	conduction-current density
$\mathbf{J}_U$	internal energy diffusive flux
$\mathbf{j}$	electric current density
M	Mach number
$\mathcal{M}$	mixture molar mass
$\mathcal{M}_i$	i-th component molar mass
N_A	Avogadro number
n	number of chemical components
$\overline{\mathbf{P}}_j^u$	internal energy presso-diffusion tensor
p	pressure
p_i	partial pressure
R	gas mixture constant
Re	Reynolds number
Re_m	magnetic Reynolds number
R_G	universal gas constant
S	magnetic force number
T	temperature
t	time
u	internal energy
$\mathbf{v}$	velocity vector
ε_0	permittivity of vacuum

$\overline{\boldsymbol{\lambda}}_e$	electrical conductivity tensor
$\overline{\boldsymbol{\lambda}}_{e_j}^p$	presso-electrical conductivity tensor
$\overline{\boldsymbol{\lambda}}_e^T$	thermo-electrical conductivity tensor
$\overline{\boldsymbol{\lambda}}_T^u$	internal energy thermo-diffusion tensor
ρ	density
ρ_c	electric charge density
ρ_i	i-th component partial density
$\overline{\boldsymbol{\tau}}$	stress tensor
Ω_i	i-th chemical component production rate

,

References

[1] D. Giordano, "Hypersonic-Flow Governing Equations with Electromagnetic Fields," AIAA Paper 2002-2165, May 2002.

[2] J. A. Shercliff, *A Textbook of Magnetohydrodynamics*. Oxford: Pergamon Press Ltd., 1965.

[3] G. W. Sutton and A. Sherman, *Engineering Magnetohydrodynamics*. New York: McGraw-Hill, 1965.

[4] C. A. Borghi, M. R. Carraro, and A. Cristofolini, "An Analysis of MHD Interaction in the Boundary Layer of Hypersonic Blunt Body," AIAA-2003-3761, June 2003.

[5] J. S. Shang, "Shared Knowledge in Computational Fluid Dynamics, Electromagnetics, and Magneto-Aerodynamics," *Progress in Aerospace Sciences*, vol. 38, pp. 449–467, 2002.

[6] H.-M. Damevin and K. A. Hoffmann, "Numerical Simulations of Hypersonic Magnetogasdynamics Flows over Blunt Bodies," AIAA-2002-0201, January 2002.

[7] D. V. Gaitonde and J. Poggie, "Elements of a Numerical Procedure for 3-D MGD Flow Control Analysis," AIAA-2002-198, January 2002.

[8] M. Brio and C. C. Wu, "An Upwind Differencing Scheme for the Equations of Ideal Magnetohydrodynamics," *Journal of Computational Physics*, vol. 75, pp. 400–422, 1988.

[9] K. G. Powell, P. L. Roe, R. S. Myong, T. Gombosi, and D. L. D. Zeeuw, "An Upwind Scheme for Magnetohydrodynamics," AIAA-95-1704-CP, 1995.

[10] R. S. Myong and P. L. Roe, "On Gudonov-Type Schemes for Magnetohydrodynamics," *Journal of Computational Physics*, vol. 147, pp. 545–567, 1998.

[11] R. W. MacCormack, "An Upwind Conservation Form Method for the Ideal Magnetohydrodynamics Equations," AIAA 99-3609, June 1999.

[12] T. J. Linde, *A Three-Dimensional Adaptive Multifluid MHD Model for the Heliosphere*. PhD thesis, Univ. of Michigan, 1998.

[13] P. Janhunen, "A positive conservative method for magnetohydrodynamics based on HLL and Roe methods," *Journal of Computational Physics*, vol. 160, pp. 649–661, 2000.

[14] K. Xu, "Gas-kinetic Theory Based Flux Splitting Method for Ideal Magnetohydrodynamics," ICASE Report 98-53, November 1998.

[15] W. Dai and P. R. Woodward, "A High-Order Godunov-type Scheme for Shock Interactions in Ideal Magnetohydrodynamics," *SIAM J. Sci. Comput.*, vol. 18, no. 4, pp. 957–981, 1997.

[16] H. D. Sterk, A. Csíc, D. V. Abeele, S. Poedts, and H. Deconinck, "Stationary Two-Dimensional Magnetohydrodynamics Flows with Shocks: Characteristic Analysis and Grid Convergence Study," *Journal of Computational Physics*, vol. 166, pp. 28–62, 2001.

[17] J. Augustinus, K. A. Hoffmann, and S. Harada, "Effect of Magnetic Field on the Structure of High-Speed Flows," *J. Spacecraft and Rockets*, vol. 35, no. 5, pp. 639–646, 1998.

[18] D. V. Gaitonde, "High-Order Solution Procedure for Three-Dimensional Nonideal Magnetogasdynamics," *AIAA Journal*, vol. 39, no. 11, pp. 2111–2120, 2001.

[19] M. Pandolfi and D. D'Ambrosio, "Upwind Numerical Methods for Magneto-Fluid Dynamics," in *Introduction to Magneto-Fluid Dynamics for Aerospace Applications*, VKI-LS 2003-2004, October 2003.

[20] A. Jeffrey and T. Taniuti, *Non-linear wave propagation: with applications to physics and magnetohydrodynamics*. New York: Academic Press, 1964.

[21] R. S. Myong and P. L. Roe, "Shock Waves and Rarefaction Waves in Magnetohydrodynamics. Part 2. The MHD System," *Journal of Plasma Physics*, vol. 58, pp. 521–552, 1997.

[22] K. G. Powell, P. L. Roe, T. J. Linde, T. I. Gombosi, and D. L. D. Zeeuw, "A Solution-Adaptive Upwind Scheme for Ideal Magnetohydrodynamics," *Journal of Computational Physics*, vol. 154, pp. 284–309, 1999.

[23] A. Dedner, F. Kemm, D. Kröner, C.-D. Munz, T. Schnitzer, and M. Wesenberg, "Hyperbolic Divergence Cleaning for the MHD Equations," *Journal of Computational Physics*, vol. 175, pp. 645–673, 2002.

[24] G. Tóth and P. L. Roe, "Divergence- and Curl-Preserving Prolongation and Restriction Formulas," *Journal of Computational Physics*, vol. 180, pp. 736–750, 2002.

UPWIND NUMERICAL METHODS FOR MAGNETO-FLUID-DYNAMICS

M. Pandolfi and D. D'Ambrosio

Politecnico di Torino - Dip. di Ingegneria Aeronautica e Spaziale

Corso Duca degli Abruzzi, 24, 10129 Torino, Italy

{maurizio.pandolfi,domenic.dambrosio}@polito.it

1. Introduction

The magneto-fluid-dynamics (MFD) flows we are here interested refer to aerospace applications in the high speed regime, where upwind methods are very efficient and highly appreciated. These procedures require a well founded knowledge of wave propagation phenomena since the relevant algorithms strongly incorporate their features.

For this reason, the present lecture is divided in three parts, addressed to the following points:

1. **wave propagation in 1D MFD**, where the basic aspects of unsteady flows are presented;

2. **discontinuities in the planar 1D MFD**, where different possible discontinuities are **predicted** and **their admissibility** is discussed; moreover, **some numerical results** on their evolution are presented that contribute to the understanding of the generation of complex and unexpected wave structures;

3. an **upwind numerical method** and an approximate solver for the Riemann problem for MFD.

In the following we will always refer to the MFD model which results from the merging of Maxwell and Euler equations in the often called *ideal MHD* form which is obtained under the main hypothesis of (i) negligible displacement current density, (ii) negligible density charge and (iii) infinite electrical conductivity of the gas.

2. Wave Propagation in 1D MFD

We consider the wave propagation in the 1D MFD model (Fig.1) where $\frac{\delta(\cdot)}{\delta y} = 0$ and $\frac{\delta(\cdot)}{\delta z} = 0$. We define:

the velocity: $\vec{q} = u\vec{\imath} + v\vec{\jmath} + w\vec{k}$

the magnetic field intensity: $\vec{B} = B_x\vec{\imath} + B_y\vec{\jmath} + B_z\vec{k}$

and its transversal component $\vec{B_t} = B_y\vec{\jmath} + B_z\vec{k}$

In the following, we examine:

- the **Euler flow equations**;

- the **MFD equations**, within the frame of the above three hypothesis;

- **particular cases of the 1D MFD model**: the planar model and the limiting cases for $B_x = 0$, or $B_t = 0$, or both null.

2.1. Euler flow equations

We remind the classical 1D wave propagation for the Euler equations:

$$
\begin{aligned}
\rho_t + u\rho_x + \rho u_x &= 0 \\
u_t + uu_x + \frac{p_x}{\rho} &= 0 \\
v_t + uv_x &= 0 \\
w_t + uw_x &= 0 \\
p_t + up_x + \gamma p u_x &= 0
\end{aligned}
$$

The characteristics directions are defined as (Fig.2) :

$$
\lambda_1 = u - a \;\; ; \;\; \lambda_2 = u \;\; ; \;\; \lambda_3 = u \;\; ; \;\; \lambda_4 = u \;\; ; \;\; \lambda_5 = u + a
$$

where $a^2 = \dfrac{\gamma p}{\rho}$. Note the multiplicity of characteristics $\lambda_2 = \lambda_3 = \lambda_4$. The compatibility equations $(i = 1, 2, 3, 4, 5)$ are:

$$
R_{it} + \lambda_i R_{ix} = 0
$$

The signals that propagate along the characteristic rays are defined as:

$$
\begin{aligned}
dR_1 &= dp - \rho a\, du \\
dR_2 &= dv \\
dR_3 &= d\rho - \frac{dp}{a^2} \\
dR_4 &= dw \\
dR_5 &= dp + \rho a\, du
\end{aligned}
$$

2.2. MFD equations

In the general case of 1D MFD, with $B_x \neq 0$, $B_y \neq 0$, $B_z \neq 0$, the system of the governing equations is the following:

$$
\rho_t + u\rho_x + \rho u_x = 0
$$

$$
u_t + uu_x + \frac{p_x}{\rho} + \frac{B_y}{\rho}(B_y)_x + \frac{B_z}{\rho}(B_z)_x = 0
$$

$$
v_t + uv_x - \frac{B_x}{\rho}(B_y)_x = 0
$$

$$
w_t + uw_x - \frac{B_x}{\rho}(B_z)_x = 0
$$

$$
p_t + up_x + \gamma p u_x = 0
$$

$$
(B_y)_t + u(B_y)_x + B_y\, u_x - B_x\, v_x = 0
$$

$$
(B_z)_t + u(B_z)_x + B_z\, u_x - B_x\, w_x = 0
$$

Note that B_x is constant because $\nabla \cdot \vec{B} = 0$. Now, there are seven distinct characteristic directions (Fig.3a):

$$\lambda_1 = u - c_f \quad ; \quad \lambda_2 = u - c_A \quad ; \quad \lambda_3 = u - c_s$$
$$\lambda_4 = u$$
$$\lambda_5 = u + c_s \quad ; \quad \lambda_6 = u + c_A \quad ; \quad \lambda_7 = u + c_f$$

The characteristics λ_1 and λ_7 are path of propagation of the *fast magnetoacoustic* waves, λ_2 and λ_6 refer to the *Alfvén* waves , λ_3 and λ_5 are related to the *slow magnetoacoustic* waves. The contact surface (discontinuity of thermodynamic properties, pressure excluded) propagates along λ_4.

The fast magnetoacoustic speed (c_f), the Alfvén speed (c_A) and the slow magnetoacoustic speed (c_s) are defined as:

$$c_f = \sqrt{\frac{1}{2}\sqrt{a^2 + c_A^2 + \frac{B_t^2}{\rho} + \sqrt{(a^2 + c_A^2 + \frac{B_t^2}{\rho})^2 - 4a^2 c_A^2}}}$$

$$c_A = \frac{B_x}{\sqrt{\rho}}$$

$$c_s = \sqrt{\frac{1}{2}\sqrt{a^2 + c_A^2 + \frac{B_t^2}{\rho} - \sqrt{(a^2 + c_A^2 + \frac{B_t^2}{\rho})^2 - 4a^2 c_A^2}}}$$

where $a^2 = \dfrac{\gamma p}{\rho}$ and $B_t^2 = B_y^2 + B_z^2$.

It can be seen that:

$$c_f > c_A > c_s$$
$$c_f \cdot c_s = a \cdot c_A$$
$$(c_f^2 - c_A^2)(c_s^2 - c_A^2) = -c_A^2 \frac{B_t^2}{\rho}$$

The compatibility equations have always the same form ($i = 1, 2, 3, 4, 5, 6, 7$):

$$R_{it} + \lambda_i R_{ix} = 0$$

where now the signals are:

$$
\begin{aligned}
dR_1 &= dp - \rho c_f \, du + \beta_f B_x B_y \, dv + \beta_f B_x B_z \, dw + c_f \beta_f B_y \, dB_y + c_f \beta_f B_z \, dB_z \\
dR_2 &= -B_z \, dv + B_y \, dw - \frac{1}{\sqrt{\rho}} B_z \, dB_y + \frac{1}{\sqrt{\rho}} B_y \, dB_z \\
dR_3 &= dp - \rho c_s \, du + \beta_s B_x B_y \, dv + \beta_s B_x B_z \, dw + c_s \beta_s B_y \, dB_y + c_s \beta_s B_z \, dB_z \\
dR_4 &= d\rho - \frac{dp}{a^2} \\
dR_5 &= dp + \rho c_s \, du - \beta_s B_x B_y \, dv - \beta_s B_x B_z \, dw + c_s \beta_s B_y \, dB_y + c_s \beta_s B_z \, dB_z \\
dR_6 &= -B_z \, dv + B_y \, dw + \frac{1}{\sqrt{\rho}} B_z \, dB_y - \frac{1}{\sqrt{\rho}} B_y \, dB_z \\
dR_7 &= dp + \rho c_f \, du - \beta_f B_x B_y \, dv - \beta_f B_x B_z \, dw + c_f \beta_f B_y \, dB_y + c_f \beta_f B_z \, dB_z
\end{aligned}
\tag{1}
$$

The coefficients β_f and β_s are respectively:

$$\beta_f = \frac{c_f}{(c_f^2 - c_A^2)} \quad ; \quad \beta_s = \frac{c_s}{(c_s^2 - c_A^2)}$$

2.3. Particular cases of the 1D MFD model

There are some particular cases where the seven waves propagation model is reduced.

2.3.1. Planar model

In this case there are no components of the velocity and magnetic field intensity along one transversal coordinate. If, for example, $w = 0$ and $B_z = 0$, the previous general case does not include the equations for w and B_z. Even if the Alfvén speed c_A is important for defining the magnetoacoustic speeds c_f and c_s, the equations of compatibility related to the Alfvén waves drop down, as well as the relevant signals.

The governing equations become:

$$\rho_t + u\rho_x + \rho u_x \qquad\qquad = 0$$

$$u_t + uu_x + \frac{p_x}{\rho} + \frac{B_y}{\rho}(B_y)_x \qquad = 0$$

$$v_t + uv_x - \frac{B_x}{\rho}(B_y)_x \qquad\qquad = 0$$

$$p_t + up_x + \gamma pu_x \qquad\qquad = 0$$

$$(B_y)_t + u(B_y)_x + B_y u_x - B_x v_x = 0$$

The corresponding characteristics are distinct and defined as (Fig.3b):

$$\lambda_1 = u - c_f \;\; ; \;\; \lambda_2 = u - c_s \;\; ; \;\; \lambda_3 = u \;\; ; \;\; \lambda_4 = u + c_s \;\; ; \;\; \lambda_5 = u + c_f$$

The compatibility equations have the usual form ($i = 1, 2, 3, 4, 5$):

$$R_{it} + \lambda_i R_{ix} = 0$$

and the signals are given by:

$$
\begin{aligned}
dR_1 &= dp - \rho c_f \, du + \beta_f B_x B_y \, dv + c_f \beta_f B_y \, dB_y \\
dR_2 &= dp - \rho c_s \, du + \beta_s B_x B_y \, dv + c_s \beta_s B_y \, dB_y \\
dR_3 &= d\rho - \frac{dp}{a^2} \\
dR_4 &= dp + \rho c_s \, du - \beta_s B_x B_y \, dv + c_s \beta_s B_y \, dB_y \\
dR_5 &= dp + \rho c_f \, du - \beta_f B_x B_y \, dv + c_f \beta_f B_y \, dB_y
\end{aligned}
$$

2.3.2. Limiting case for $B_x = 0$, $B_y = 0$, $B_z = 0$

Since the magnetic field intensity does not play any role, this case is the already considered Euler flow.

2.3.3. Limiting case for $B_x = 0$, but $B_t \neq 0$

In this case only the transversal component of the magnetic field intensity exists. Because all terms with B_x disappear, the previously general case with seven equations reduces to one system of five equations and to a second one with two equations. The first system is:

$$\rho_t + u\rho_x + \rho u_x = 0$$

$$u_t + uu_x + \frac{p_x}{\rho} + \frac{B_y}{\rho}(B_y)_x + \frac{B_z}{\rho}(B_z)_x = 0$$

$$p_t + up_x + \gamma p u_x = 0$$

$$(B_y)_t + u(B_y)_x + B_y\, u_x = 0$$

$$(B_z)_t + u(B_z)_x + B_z\, u_x = 0$$

and the second one is:

$$v_t + uv_x = 0$$
$$w_t + uw_x = 0$$

The fast magnetoacoustic speed reduces to:

$$c_f = a^* = \sqrt{a^2 + \frac{B_t^2}{\rho}}$$

and the Alfvén speed, as well as the slow magnetoacoustic speed, go to zero:

$$c_A = 0 \quad ; \quad c_s = 0$$

From the first system we obtain five characteristics:

$$\lambda_1 = u - a^* \quad ; \quad \lambda_2 = u \quad ; \quad \lambda_4 = u \quad ; \quad \lambda_6 = u \quad ; \quad \lambda_7 = u + a^*$$

and from the second one, two other characteristics:

$$\lambda_3 = u \quad ; \quad \lambda_5 = u$$

In Fig.3c, we note the multiplicity of five characteristics: $\lambda_2 = \lambda_3 = \lambda_4 = \lambda_5 = \lambda_6$. The compatibility equations ($i = 1, 2, 4, 6, 7$ and $i = 3, 5$) present the usual form:

$$R_{it} + \lambda_i R_{ix} = 0$$

and the relevant signals become:

$$
\begin{aligned}
dR_1 &= dp - \rho a^*\, du + B_y\, dB_y + B_z\, dB_z \\
dR_2 &= dB_y - \frac{B_y}{\gamma p}\, dp \\
dR_3 &= dv \\
dR_4 &= d\rho - \frac{dp}{a^2} \\
dR_5 &= dw \\
dR_6 &= dB_z - \frac{B_z}{\gamma p}\, dp \\
dR_7 &= dp + \rho a^*\, du + B_y\, dB_y + B_z\, dB_z
\end{aligned}
$$

2.3.4. Limiting case for $B_x \neq 0$, but $B_t = 0$

This case seems to be symmetric of the previous one, but it is rather different. The transversal intensity drops down ($B_t = 0$), while its axial component remains finite ($B_x \neq 0$).

The original system of seven equations reduces now to three systems. The first one is merely related to fluid dynamics, with the only x-component of the velocity:

$$
\begin{aligned}
\rho_t + u\rho_x + \rho u_x &= 0 \\
u_t + uu_x + \frac{p_x}{\rho} &= 0 \\
p_t + up_x + \gamma p u_x &= 0
\end{aligned}
$$

The second system refers to the y-components of velocity and magnetic field intensity:

$$
\begin{aligned}
v_t + uv_x + \frac{B_x}{\rho}(B_y)_x &= 0 \\
(B_y)_t + u(B_y)_x - B_x v_x &= 0
\end{aligned}
$$

and the third one refers to the z-components:

$$
\begin{aligned}
w_t + uw_x + \frac{B_x}{\rho}(B_z)_x &= 0 \\
(B_z)_t + u(B_z)_x - B_x w_x &= 0
\end{aligned}
$$

Note that the initial condition of $B_t = 0$ does not prevent the generation of B_t itself, through finite values of $(B_y)_t$ or $(B_z)_t$, if $v_x \neq 0$ or $w_x \neq 0$.

In the compatibility equations ($i = 1, 4, 7$, $i = 2, 6$ and $i = 3, 5$):

$$
R_{it} + \lambda_i R_{ix} = 0
$$

the corresponding signals are:

$$
\begin{aligned}
dR_1 &= dp - \rho a\, du \\
dR_2 &= dv + \frac{dB_y}{\sqrt{\rho}} \\
dR_3 &= dw + \frac{dB_z}{\sqrt{\rho}} \\
dR_4 &= d\rho - \frac{dp}{a^2} \\
dR_5 &= dw - \frac{dB_z}{\sqrt{\rho}} \\
dR_6 &= dv - \frac{dB_y}{\sqrt{\rho}} \\
dR_7 &= dp + \rho a\, du
\end{aligned}
$$

Depending on the magnitude of the Alfvén speed $c_A = \dfrac{B_x}{\sqrt{\rho}}$ with respect to the sound speed $a = \sqrt{\gamma \dfrac{p}{\rho}}$, we have different definitions of the characteristics.

If $B_x < \sqrt{\gamma p}$, and therefore $c_A < a$, from the first system we have:

$$
\lambda_1 = u - a \quad ; \quad \lambda_4 = u \quad ; \quad \lambda_7 = u + a
$$

from the second one:

$$\lambda_2 = u - c_A \quad ; \quad \lambda_6 = u + c_A$$

and from the third one:

$$\lambda_3 = u - c_A \quad ; \quad \lambda_5 = u + c_A$$

In this case we have a double multiplicity, where λ_2 coincides with λ_3 and λ_6 with λ_5, as evident in Fig.3d.

If $B_x > \sqrt{\gamma p}$, and therefore $c_A > a$, we have the same set of characteristics, with the same multiplicity, but now the characteristic pattern is slightly different, as shown in Fig.3e.

Finally, when $B_x = \sqrt{\gamma p}$, that is $c_A = a$, the multiplicity is still double, but higher (Fig.3f):

$$\lambda_1 = \lambda_2 = \lambda_3 = u - a \quad ; \quad \lambda_4 = u \quad ; \quad \lambda_5 = \lambda_6 = \lambda_7 = u + a$$

3. Discontinuities in the planar 1D MFD

Here, we develop the **prediction of possible discontinuities**, we discuss considerations on the **admissibility of discontinuities** and we present **some numerical results** on their evolution. We restrict our analysis to the planar 1D problem where $w = 0$ and $B_z = 0$.

3.1. Prediction of possible discontinuities

The laws of conservation are:

$$\frac{d}{dt} \int_{x_1}^{x_2} W \, dx = -(F_2 - F_1)$$

where:

$$W = \begin{vmatrix} \rho \\ \rho u \\ \rho v \\ B_y \\ e + \dfrac{B_y{}^2}{2} \end{vmatrix} \quad ; \quad F = \begin{vmatrix} \rho u \\ p + \rho u^2 + \dfrac{B_y{}^2}{2} \\ \rho u v - B_x B_y \\ u B_y - v B_x \\ u(p + e) + u B_y{}^2 - v B_x B_y \end{vmatrix}$$

and

$$e = \frac{p}{(\gamma - 1)} + \frac{\rho}{2}(u^2 + v^2)$$

For a discontinuity **at rest**, the flux at its left (L) and right (R) sides is conserved:

$$F_R = F_L$$

By denoting the mass flux $m = \rho u$, the **jump conditions** through a possible discontinuity are given by:

$$
\begin{array}{rcl}
m[1/\rho] - [u] & = & 0 \\
m[u] + [p] + \overline{B}_y[B_y] & = & 0 \\
m[v] - B_x[B_y] & = & 0 \\
m(\overline{1/\rho})[B_y] + \overline{B}_y[u] - B_x[v] & = & 0 \\
m[\dfrac{e}{\rho} + \dfrac{B_y{}^2}{2}] + [u(p + \dfrac{B_y{}^2}{2})] - B_x[vB_y] & = & 0
\end{array}
\tag{2}
$$

where :

$$
\overline{(\cdot)} = \frac{1}{2}\left((\cdot)_R + (\cdot)_L\right) \qquad \text{and} \qquad [(\cdot)] = ((\cdot)_R - (\cdot)_L)
$$

For $\mathbf{m} = \mathbf{0}$ (no mass flux through the discontinuity) and $\mathbf{B_x} \neq \mathbf{0}$, the discontinuity is represented by a contact surface where $[u] = 0$, $[B_y] = 0$, $[p] = 0$, $[v] = 0$ and $[\rho] \neq 0$.

For $\mathbf{m} \neq \mathbf{0}$, we have discontinuities permeable to the gas flow. Hereafter, we follow the approach proposed in Refs. 1–3. By properly rearranging the jump conditions of Eqs.2, we obtain an equation where the jump of the pressure $[p]$ is related to the jump of the transversal magnetic field intensity $[B_y]$:

$$
\frac{(\gamma - 1)}{4}\overline{B}_y[B_y]^4 + \frac{(\gamma - 1)}{4}[p][B_y]^3 + \gamma\overline{p}\,\overline{B}_y[B_y]^2 +
$$
$$
+(\gamma\overline{p} - B_x{}^2 - \overline{B}_y{}^2)[p][B_y] - \overline{B}_y[p]^2 = 0
$$

By normalizing pressure and transversal magnetic field intensity as:

$$
U = \frac{\gamma p}{B_x{}^2} \qquad ; \qquad V = \frac{B_y}{B_x}
$$

the above equation can be written as:

$$
([U] + \gamma\overline{V}[V])\left\{\gamma(\gamma - 1)[V]^3 + 4\gamma\overline{U}[V] - 4\overline{V}[U]\right\} - 4\gamma[U][V] = 0
$$

Since

$$
\overline{(\cdot)} = \frac{1}{2}\left((\cdot)_R + (\cdot)_L\right) = (\cdot)_L + \frac{1}{2}[(\cdot)]
$$

we obtain a simple second degree algebraic equation for the unknown $[U]$:

$$
\tilde{\alpha}[U]^2 + \tilde{\beta}[U] + \tilde{\gamma} = 0
\tag{3}
$$

where:

$$
\tilde{\alpha} = (\tilde{d} - \frac{\tilde{c}}{2}) \;\; ; \;\; \tilde{\beta} = (\tilde{b} + \tilde{c}U_L - \tilde{c} + \tilde{a}\tilde{d} - \frac{\tilde{a}\tilde{c}}{2}) \;\; ; \;\; \tilde{\gamma} = \tilde{a}(\tilde{b} + \tilde{c}U_L)
$$

and

$$
\tilde{a} = \gamma\overline{V}[V] \;\; ; \;\; \tilde{b} = \gamma(\gamma - 1)[V]^3 \;\; ; \;\; \tilde{c} = 4\gamma[V] \;\; ; \;\; \tilde{d} = 4\overline{V}
$$

The coefficients $\tilde{\alpha}, \tilde{\beta}, \tilde{\gamma}$ (and $\tilde{a}, \tilde{b}, \tilde{c}, \tilde{d}$) are known once:

- the values of γ and B_x are given,

- the values of pressure p_L and transversal magnetic field intensity B_{yL} on the left side L are given (therefore also U_L and V_L are know) and

- a value of the transversal magnetic field intensity B_{yR} on the right side R is prescribed, so that both $[V] = \dfrac{B_{yR} - B_{yL}}{B_x}$ and $\overline{V} = \dfrac{B_{yR} + B_{yL}}{2B_x}$ are known.

Provided that the prescribed value of B_{yR} gives a positive radical $(\tilde{\beta}^2 - 4\tilde{\alpha}\ \tilde{\gamma})$, then Eq. 3 presents two real solutions for $[U]$ and therefore for p_R:

$$p_R = p_L + [U]\frac{B_x{}^2}{\gamma}$$

For any solution $[U]$, the density ratio can be found:

$$\frac{\rho_L}{\rho_R} = \frac{4\gamma\overline{U} + \gamma(\gamma - 1)[V]^2 - 2[U]}{4\gamma\overline{U} + \gamma(\gamma - 1)[V]^2 + 2[U]}$$

where $\overline{U} = U_L + \dfrac{1}{2}[U]$. The density ρ_L (or ρ_R) can be prescribed and ρ_R (or ρ_L) follows. From the first and second of Eqs. 2, the mass flux m can be evaluated:

$$|m| = \left(\frac{[p] + \overline{B}_y[B_y]}{(1/\rho_L)(1 - \rho_L/\rho_R)}\right)^{\frac{1}{2}}$$

and the axial velocity components u_L and u_R are obtained:

$$u_L = \frac{|m|}{\rho_L} \quad ; \quad u_R = \frac{|m|}{\rho_R}$$

The transversal velocity component v_L (or v_R) can be also prescribed and the value of v_R (or v_L) follows from:

$$v_R - v_L = \frac{B_x}{|m|}(B_{yR} + B_{yL})$$

The jump conditions for a couple of prescribed left values (p_L, B_{yL}) and the corresponding right values (p_R, B_{yR}) that satisfy Eqs.2 can be represented on a curve shaped like a **curl**, as the ones reported in Figs.4a,4b. The ordinate refers to the normalized transversal magnetic field intensity component V and the abscissa to the normalized pressure U. The point L on each curve represents the prescribed left values $(V_L = B_{yL}/B_x; U_L = (\gamma p_L)/B_x{}^2)$ which characterize the curl itself. Any point of the curl represents a couple of right values $(V_R = B_{yR}/B_x; U_R = (\gamma p_R)/B_x{}^2)$ that satisfy Eqs.2.

Note that the complete knowledge of the flow properties on the two sides of the discontinuity needs, in addition, one prescribed value for the density $(\rho_L$ or $\rho_R)$ and one for the transversal velocity $(v_L$ or $v_R)$. Moreover, we observe that flow properties at side L are prescribed in terms of p_L, B_{yL}, but all other properties at L will vary, depending on the point R selected on the curl.

We consider these discontinuities permeable to the gas flow that moves from right to left. Therefore,

9

they will be related to the characteristics of the families $\lambda_f = u + c_f$ (fast) and $\lambda_s = u + c_s$ (slow).
It is convenient to classify each point on a curl curve by looking at the sign of the characteristics λ_f and λ_s, on both the sides of the discontinuity. In principle, we should expect 16 possible configurations for the combinations of sign of the four values of $(\lambda_f)_{L,R}$ and $(\lambda_s)_{L,R}$. However, because $c_f > c_s$ (and therefore $\lambda_f > \lambda_s$) at both L and R, only 9 of them will be possible. They are shown in Fig.5 and identified as it follows:

- fast shock (FS) discontinuity, when $\lambda_{fL} > 0$ and $\lambda_{fR} < 0$ while $\lambda_{sL} < 0$ and $\lambda_{sR} < 0$;

- slow shock (SS) discontinuity, when $\lambda_{sL} > 0$ and $\lambda_{sR} < 0$ while $\lambda_{fL} > 0$ and $\lambda_{fR} > 0$;

- fast expansion (FE) discontinuity, when $\lambda_{fL} < 0$ and $\lambda_{fR} > 0$ while $\lambda_{sL} < 0$ and $\lambda_{sR} < 0$;

- slow expansion (SE) discontinuity, when $\lambda_{sL} < 0$ and $\lambda_{sR} > 0$ while $\lambda_{fL} > 0$ and $\lambda_{fR} > 0$;

- overcompression (OC) discontinuity, where all the characteristics converge on the discontinuity: $\lambda_{fL} > 0$, $\lambda_{sL} > 0$ and $\lambda_{fR} < 0$, $\lambda_{sR} < 0$;

- overexpansion (OE) discontinuity, where all the characteristics diverge from the discontinuity: $\lambda_{fL} < 0$, $\lambda_{sL} < 0$ and $\lambda_{fR} > 0$, $\lambda_{sR} > 0$;

- undercompression (UC) discontinuity, where the fast characteristics move rightwards ($\lambda_{fL} > 0$, $\lambda_{fR} > 0$) and the slow ones move leftwards ($\lambda_{sL} < 0$, $\lambda_{sR} < 0$);

- left transport (LT) discontinuity , where all the characteristics move leftwards ($\lambda_{fL} < 0$, $\lambda_{fR} < 0$, $\lambda_{sL} < 0$, $\lambda_{sR} < 0$);

- right transport (RT) discontinuity , where all the characteristics move rightwards ($\lambda_{fL} > 0$, $\lambda_{fR} > 0$, $\lambda_{sL} > 0$, $\lambda_{sR} > 0$).

These configurations can be found along curl curves, as the ones of Figs.4a,4b.
The upper branch that moves, from the point L, leftwards (or rightwards) refer to SS (or FE) discontinuities.
The lower branches, below the point L, represent, along a limited extension, respectively FS discontinuities on the left and SE discontinuities on the right.
The remaining portion of the curl loop, between the SE and FS portions, can refer to one or more different configurations. However, the sequence from SE to FS should be ordered in a such way that the transition from one to a neighboring configuration presents the change in sign of only one characteristic.
Note, that as also reported in Ref. 2, possible configurations LT and RT never appeared on curl curves. Therefore, our attention will be addressed only to the first 7 configurations.

3.2. Admissibility of discontinuities

A wide debate appears in the literature on the admissibility of the different discontinuities that satisfy the jump conditions of Eqs.2. Hereafter we would like to present our contribution to this debate.
We assume **admissible** any discontinuity that shows up and remains stable in numerical simulations

of the flow described by the planar 1D MFD model. In particular we look at the solutions of those Riemann problems (RP), where the initial data are given by couples of conditions identified on curl curves, with points L and R.

Our numerical simulations are obtained with a code based on the method that will be shown in the third part of this presentation. We report now on some of our numerical experiences on the admissibility.

When we take, as initial data for the RP, points of the curl curves representing FS or SS discontinuities, the numerical result shows a transition from the initial prescribed discontinuity to a sharply captured one that represents respectively a fast or slow shock. The captured shock is perfectly at rest. No other waves are generated in the RP, so that the upstream and downstream conditions for the captured shock are just the R and L conditions selected on the curl (in fact the above transition generates very small disturbances, only due to the numerics, that go away through the boundaries without any influence on the upstream and downstream conditions of the shock). We consider the FS and SS discontinuities identified on the curl as admissible discontinuities.

When we take, as initial data for the RP, points FE on the upper right branch of the curl, the discontinuity collapses be generating a fast rarefaction fan, with a sonic point, and some other waves, not negligible and not only due to the numerics, but *physically* needed to match the fast rarefaction fan to the prescribed L and R initial conditions. We call *matching* waves these other waves and we note that they always appear when the discontinuity is not admissible.

A similar picture is found at SE points located on the lower right branch of the curl provided that the value of B_{y_R} has the same sign of B_{y_L}. If we move further on this SE branch, with B_{y_R} changing its sign, then a new kind of wave shows up (in fact this does not occur exactly at the change of sign of B_{y_R} because of the effects generated on B_y by the matching waves). Such a new kind of wave has been called in the literature **compound wave**(CW) and we will comment on it in the following. We have also found CWs at FE points located on the loop of the curl, as in Fig.4a. Discontinuities of the kind of FE or SE are not admissible since they collapse as rarefaction fans or CW, beside matching waves.

When the loop of the curl shows points with OC configurations, we observe that this OC portion is embedded between FS and SS configurations (Fig.4b). For OC points close to FS or SS configurations, our numerical experiences show that very clean structures of captured shocks are generated, without the formation of matching waves. The captured shocks are enclosed by the initially converging characteristics $\lambda_{f_L} > 0$, $\lambda_{s_L} > 0$ and $\lambda_{f_R} < 0$, $\lambda_{s_R} < 0$. If the selected OC points are located close to the FS portion, the fast λ_{f_L} and λ_{f_R} characteristics converge strongly on the discontinuity, while the slow one λ_{s_L} is only moderately positive and weakly converging. The resulting captured shock is the result of fast and slow magnetoacoustic waves, with the fast one that appears predominant. The contrary happens for OC points close to the SS portion. Now the slow characteristics converge strongly and the fast λ_{f_R} converges weakly and is only moderately negative. In the captured shock, the role of the slow wave appears now predominant. We define *overcompressive* these shocks

that result from OC discontinuities.

Finally, we have to mention that at points OC located in the middle of the overcompressive portion of the curl, our numerical experiments fail because of instabilities in the computations. We have not been able up to now to identify clearly the reason for such failures, but we think that our code presents a well defined deficiency in the RP solver, as it will be discussed later.

Beside the disappointing failure in our numerics at some of the OC points, we consider OC discontinuities as admissible.

Very interesting appears the collapse of initial OE discontinuities, that corresponds to points located on a portion of the loop embedded between SE and FE configurations (Fig.4a). From our numerical experiences, we note that OE discontinuities collapse by generating rarefaction fans and CWs, as it will be discussed later. Matching waves with remarkable intensity appear also. We consider OE discontinuities as not admissible.

As the UC discontinuities are concerned, we have to recognize that also in this case our numerical experiences are unsatisfactory. The UC configurations are embedded between FE and FS (Fig.4a) or between SE and SS (Fig.4b) portions and show a compression branch ($p_L > p_R$) and an expansion one ($p_L < p_R$). When the initial discontinuity is close to FS or SS configurations, a numerical shock, respectively fast or slow, is generated. However, the structure of such a shock is not clean and nice as we should expect from the upwind method we use (a moderate overshoot behind the shock, without intermediate points). When the UC discontinuity is close to FE or SE configurations, we have clear and nice examples of CWs, but, in some cases, we have also a disappointing stable expansion discontinuity. Once more, we are convinced that these unsatisfactory results have to be ascribed to a deficiency in our RP solver.

At this point it is convenient to define the **compound wave**. A CW is formed by a rarefaction fan and a shock of the same family. Therefore, we can have fast compound waves (FCW) and slow compound waves (SCW). The fan and the shock are attached each other. For a FCW the fan is positioned ahead of the shock, on its low pressure side, while for a SCW the fan follows the shock, on its high pressure side. These are the fan-shock wave structures we have identified in our experiences up to now. Because of the attachment fan-shock, it follows that the characteristic of the fan, on the shock side, propagates at the same speed of the shock itself.

As far as the authors are aware, the only CW presented in the literature is the one originally identified in Ref. 10 and reproduced, as a test case, by many other authors: it is a SCW (of the characteristics family $u - c_s$) that propagates leftwards as the result of a particular RP. Possible FCWs are envisaged in Ref. 1, but no relevant numerical results are reported there.

In conclusion, we would like to summarize our analysis on admissibility in the following points:

- the possible discontinuities indicated by the curl curves satisfy the jump conditions of Eqs.2, but there are no reasons why they should exist in the unsteady flow model;

- the possible discontinuities can be used as initial conditions for a RP, the solution of which can provide criteria for their admissibility;

- if a discontinuity results admissible, the configuration shown in Fig.5 is certainly meaningful; when it is not admissible, the characteristics configuration indicates only the starting of its collapse and the formation of waves very different from the initial discontinuity;

- in the 1D classical gasdynamics (Euler eqs.), any disturbance, small or large, propagates as a shock or a rarefaction fan (of course we refer only to *acoustic* perturbations, permeable to the gas flow, not to entropy or transversal velocity waves). In the planar 1D MFD, not only fast or slow shocks and rarefaction fans occur, but numerical experiments on the solution of RPs show that CWs and OC shocks can exist. A CW can be fast or slow, but it is always related to one family of characteristics, fast or slow (only in a very particular limiting case we find a CW with a shock embedded between a fast and a slow fan, as we show later). On the contrary, the OC shocks can not be identified as fast shock or a slow shock, since both the fast and the slow characteristics contribute to it.

3.3. Some numerical results on Riemann Problem solutions

The numerical results we report here are obtained with a code based on the numerical method presented in the next section 4. We solve RPs with initial conditions taken on the curl curves of Figs.4a,4b, and labeled as case B and case C because they come from the original Figs.1b,1c reported in Ref. 2. The following twelve examples are selected among several numerical experiments we have carried out in investigating discontinuities admissibility. Each example refers to a point well identified on the curl curves of Figs.4a,4b.

The values of the normalized values of pressure and transversal magnetic field intensity at the point L are:

$$
\begin{array}{llll}
\text{case B} & U_L = 0.352 & V_L = 0.300 \\
\text{case C} & U_L = 1.490 & V_L = 0.380
\end{array}
$$

being $\gamma = 1.667$ and $B_x = 1.0$. We have assumed $\rho_L = 1.0$ and $v_L = 0.0$. In the following Figs.6 and 7 we show results on RP solutions. The values of U and V are indicated between parenthesis in the captions of these figures , as $(U, V)_L$ or $(U, V)_R$.

case C, point FS_1; $U_R = 0.847$; $V_R = 0.100$ This is a typical FS configuration. The pressure distribution along x, once the RP has been solved, is reported in Fig.6a and looks exactly and nicely as the pressure distribution through a classical gasdynamic shock.

case C, point SS_1; $U_R = 0.855$; $V_R = 0.700$ A similar pressure distribution for an initial SS discontinuity is shown in Fig.6b.

case B, point FE_4; $U_R = 0.740$; $V_R = 0.920$ The pressure distribution that results from the collapse of a FE discontinuity is shown in Fig.6c. Note the fast rarefaction fan and the leftwards moving matching wave, a slow rarefaction fan.

case B, point SE_2; $U_R = 1.033$; $V_R = 0.100$ A similar collapse for a SE discontinuity is shown in Fig.6d. The matching wave is now a fast one and moves rightwards as a rarefaction fan.

case C, point OC_1; $U_R = 0.308$; $V_R = -0.470$ Fig.6e shows a typical unsatisfactory result for a OC discontinuity; the resulting shock shows a slight overshoot we ascribe to a deficiency of the RP solver.

case C, point OC_3; $U_R = 0.460$; $V_R = -0.180$ Fig.6f shows a much better result for a OC discontinuity; the shock is captured very nicely; no matching waves are generated and the upstream and downstream conditions coincide with the L and R initial data; it is an overcompressive shock, with all the four characteristics converging on it.

case C, point UC_1; $U_R = 1.698$; $V_R = -0.210$ The collapse of this UC discontinuity, close to SE points of the curl and presenting opposite signs of B_{y_L} and B_{y_R}, generate a nice example of SCW, as shown in Fig.7a : note the fast matching wave on the right, a rarefaction fan.

case C, point SE_3; $U_R = 1.771$; $V_R = -0.050$ Again a SCW, but with a much weaker shock, is found for a SE point, with a very small negative value of B_{y_R}, as reported in Fig.7b.

case C, point SE_2; $U_R = 1.765$; $V_R = 0.050$ The value of B_{y_R} is now slightly positive and we have a simple slow rarefaction fan (Fig.7c); the matching wave on the right is a fast rarefaction fan with a small intensity.

case B, point SE_5; $U_R = 1.385$; $V_R = -0.080$ This point on the loop refers to an SE configuration, but is very close to the OE portion. In Fig.7d we note the generation of a SCW, with a very small shock, on the left and the fast matching wave on the right, much stronger than in the previous case and very close to the slow wave.

case B, point OE_3; $U_R = 1.528$; $V_R = -0.280$ This point is located in the middle of the OE portion of the loop. We note the fully developed SCW, but also the fast rarefaction fan, very strong and more and more closer to the SCW (Fig.7e).

case B, point OE_4; $U_R = 1.522$; $V_R = -0.330$ For this point, very close to the previous one and displaced towards the FE portion, Fig.7f shows a very different picture: the shock disappears from the previous SCW that reduces to a classical slow rarefaction fan, while the previous fast rarefaction wave becomes now a well developed FCW.

We can envisage a transition point between the two ones just seen (OE_3 and OE_4 in Figs.7e,7f), where the shock is attached to the slow fan on its high pressure side and to the fast fan on the low pressure side. Unfortunately, we have not been able to reproduced numerically such a configuration, probably for the same deficiencies already mentioned. Note that this double-face CWD, formed with the contribution of fast and slow waves can be found in only one point of the OE portion of the loop in Fig.4a, whereas the OC shocks, formed with the contribution of both fast and slow characteristics can be found over a continuous range of initial data in Fig.4b. Proceeding further along the OE and the following FE portions of the loop, the new FCW separates from the slow rarefaction fan that decreases and moves more and more to the left.

In concluding this short review of numerical experiences, we would like to point out the not only different slow compound waves (SCW) are here identified, but also fast compound waves (FCW) and overcompressive shocks, that, as far as the present authors are aware, are not reported in the literature.

4. An upwind numerical method for MFD

Codes used for the prediction of high speed flows are mostly based on upwind methods because of their capability in dealing with strong shock waves. The need of describing MFD problems, where in addition complex wave structures are expected, suggests to extend to them the past experience on upwind methods achieved in classical gasdynamics.

In the 1D MFD model, the governing system of conservation laws (CLs) is given by:

$$\frac{d}{dt} \int_{x_1}^{x_2} W \, dx = -(F_2 - F_1)$$

where:

$$W = \begin{vmatrix} \rho \\ \rho u \\ \rho v \\ \rho w \\ B_y \\ B_z \\ e + \dfrac{B_t^2}{2} \end{vmatrix} \quad ; \quad F = \begin{vmatrix} \rho u \\ p + \rho u^2 + \dfrac{B_t^2}{2} \\ \rho uv - B_x B_y \\ \rho uw - B_x B_z \\ u B_y - v B_x \\ u B_z - w B_x \\ u(p + e) + u B_t^2 - v B_x B_y - w B_x B_z \end{vmatrix}$$

and

$$e = \frac{p}{(\gamma - 1)} + \frac{\rho}{2}(u^2 + v^2 + w^2) \quad ; \quad B_t^2 = B_x^2 + B_y^2$$

According to the finite volume discretization, the integration in time of the CLs is given by:

$$W_N^{K+1} = W_N^K - \frac{Dt}{Dx}(F_{N+1/2} - F_{N-1/2})$$

where N is the index of the cell (finite volume), Dx its length, K the integration step, Dt the integration time interval, and W_N^{K+1} and W_N^K are average values of the conservative variable over the cell N, at the integration steps $K + 1$ and K. Since we focus here our attention to the first order of accuracy integration scheme, the flux $F_{N+1/2}$ (or $F_{N-1/2}$) at the interface $N + 1/2$ (or $N - 1/2$) will be evaluated on the basis of the initial values F_{N+1} and F_N (or F_N and F_{N-1}). The procedure for estimating the flux at the interfaces is the basic feature that characterizes numerical methods. In performing these estimates, upwind methods take into account, in different ways depending on each upwind method, the wave propagation phenomenology. Several upwind methods have been proposed in the literature for the classical gasdynamics (Euler equations); they are quite different each others and can present very different numerical performances. We would like to address the readers to two papers (Refs. 8, 9) where the present authors discuss upwinding themes.

Some of the upwind methods used for classical gasdynamics have been also extended to the predictions of flowfields described by MFD equations. Among these methods, we remind the flux-difference splitting (FDS) with an approximate solver of the Riemann problem (Ref. 4), the flux-vector splitting (Ref. 5), the HLLE method (Ref. 6).

The upwind numerical method we propose here is a FDS procedure with an approximate RP solver conceived as an extension of a classical gasdynamic solver used fruitfully and successfully for almost twenty years in a large variety of high speed flows problems (Ref. 7).

Before showing the features of this method it is convenient to remind how a FDS procedure works. From the solution provided by a RP solver, on the base of the initial data F_{N+1} and F_N (or F_N and F_{N-1}), we identify waves that propagate leftwards and rightwards. In particular, with reference to the cell N, we predict the waves generated in the evolution of the RP at $N + 1/2$ (or $N - 1/2$) that moves leftwards (or rightwards). We indicate the related difference of the flux as $\overleftarrow{D_N}F$ (or $\overrightarrow{D_{N-1}}F$). Note that:

$$
\begin{aligned}
\overleftarrow{D_N}F + \overrightarrow{D_N}F &= (F_{N+1} - F_N) \\
(\text{or} \quad \overleftarrow{D_{N-1}}F + \overrightarrow{D_{N-1}}F &= (F_N - F_{N-1}))
\end{aligned}
$$

We define the flux at the interface $N + 1/2$ (or $N - 1/2$) as:

$$
\begin{aligned}
F_{N+1/2} &= F_N + \overleftarrow{D_N}F \\
(\text{or} \quad F_{N-1/2} &= F_N - \overrightarrow{D_{N-1}}F)
\end{aligned}
$$

Therefore, the integration of the CLs gives:

$$
W_N{}^{K+1} = W_N{}^K - \frac{Dt}{Dx} \ (\overrightarrow{D_{N-1}}F + \overleftarrow{D_N}F)
$$

At this point we show how the gasdynamic approximate solver of Ref. 7 can be extended to the MFD area. The solver is approximate because the evolution through fast and slow waves is considered isentropic, even if these waves are shocks. From the collapse of the initial discontinuity at the interface $N + 1/2$, seven waves are generated which separate eight regions, as shown in Fig.8:

$$
\begin{aligned}
\lambda_1 &= u - c_f \quad ; \quad \lambda_2 = u - c_A \quad ; \quad \lambda_3 = u - c_s \\
\lambda_4 &= u \\
\lambda_5 &= u + c_s \quad ; \quad \lambda_6 = u + c_A \quad ; \quad \lambda_7 = u + c_f
\end{aligned}
$$

Properties in the regions a and b are known, since they coincide with those at N and $N + 1$. The properties in the six regions c, d, e, f, g, h are unknown and are evaluated as it follows.

We introduce a second approximation by taking all the coefficients in the differential form of the signals dR_i ($i = 1, 2, 3, 4, 5, 6, 7$) (Eqs.1) as constant and based on the arithmetic average of the primitive variables in regions a and b. Let us denote these constant coefficients with a bar. We write

the following finite approximations of the signals:

$$
\begin{aligned}
R_1 &= p - \overline{\rho}\,\overline{c_f}\,u + \overline{\beta_f}\,B_x\,\overline{B_y}\,v + \overline{\beta_f}\,B_x\,\overline{B_z}\,w + \overline{c_f}\,\overline{\beta_f}\,\overline{B_y}\,B_y + \overline{c_f}\,\overline{\beta_f}\,\overline{B_z}\,B_z \\
R_2 &= -\overline{B_z}\,v + \overline{B_y}\,w - \frac{1}{\sqrt{\overline{\rho}}}\,\overline{B_z}\,B_y + \frac{1}{\sqrt{\overline{\rho}}}\,\overline{B_y}\,B_z \\
R_3 &= p - \overline{\rho}\,\overline{c_s}\,u + \overline{\beta_s}\,B_x\,\overline{B_y}\,v + \overline{\beta_s}\,B_x\,\overline{B_z}\,w + \overline{c_s}\,\overline{\beta_s}\,\overline{B_y}\,B_y + \overline{c_s}\,\overline{\beta_s}\,\overline{B_z}\,B_z \\
R_4 &= \rho - \frac{p}{\overline{a^2}} \\
R_5 &= p + \overline{\rho}\,\overline{c_s}\,u - \overline{\beta_s}\,B_x\,\overline{B_y}\,v - \overline{\beta_s}\,B_x\,\overline{B_z}\,w + \overline{c_s}\,\overline{\beta_s}\,\overline{B_y}\,B_y + \overline{c_s}\,\overline{\beta_s}\,\overline{B_z}\,B_z \\
R_6 &= -\overline{B_z}\,v + \overline{B_y}\,w + \frac{1}{\sqrt{\overline{\rho}}}\,\overline{B_z}\,B_y - \frac{1}{\sqrt{\overline{\rho}}}\,\overline{B_y}\,B_z \\
R_7 &= p + \overline{\rho}\,\overline{c_f}\,u - \overline{\beta_f}\,B_x\,\overline{B_y}\,v - \overline{\beta_f}\,B_x\,\overline{B_z}\,w + \overline{c_f}\,\overline{\beta_f}\,\overline{B_y}\,B_y + \overline{c_f}\,\overline{\beta_f}\,\overline{B_z}\,B_z
\end{aligned}
$$

The value of any R_i $(i = 1, 2, 3, 4, 5, 6, 7)$ in a j region $(j = c, d, e, f, g, h)$ is given by:

$$
(R_i)_j = (R_i)_a \quad \text{or} \quad R_{i\,j} = (R_i)_b
$$

depending from which initial region (a or b), the characteristic λ_i arriving in the region j has been originated.

The following table defines the values of the approximate signals R_i:

Region	R_1	R_2	R_3	R_4	R_5	R_6	R_7
c	$(R_1)_b$	$(R_2)_a$	$(R_3)_a$	$(R_4)_a$	$(R_5)_a$	$(R_6)_a$	$(R_7)_a$
d	$(R_1)_b$	$(R_2)_b$	$(R_3)_a$	$(R_4)_a$	$(R_5)_a$	$(R_6)_a$	$(R_7)_a$
e	$(R_1)_b$	$(R_2)_b$	$(R_3)_b$	$(R_4)_a$	$(R_5)_a$	$(R_6)_a$	$(R_7)_a$
f	$(R_1)_b$	$(R_2)_b$	$(R_3)_b$	$(R_4)_b$	$(R_5)_a$	$(R_6)_a$	$(R_7)_a$
g	$(R_1)_b$	$(R_2)_b$	$(R_3)_b$	$(R_4)_b$	$(R_5)_b$	$(R_6)_a$	$(R_7)_a$
h	$(R_1)_b$	$(R_2)_b$	$(R_3)_b$	$(R_4)_b$	$(R_5)_b$	$(R_6)_b$	$(R_7)_a$

The primitive variables in the j region are evaluated on the basis of the above values of R_i:

$$p = \frac{\overline{c_s}\,\overline{\beta_s}\,(R_7 + R_1) - \overline{c_f}\,\overline{\beta_f}\,(R_5 + R_3)}{2(\overline{c_s}\,\overline{\beta_s} - \overline{c_f}\,\overline{\beta_f})}$$

$$u = \frac{\overline{\beta_s}\,(R_7 - R_1) - \overline{\beta_f}\,(R_5 - R_3)}{2\overline{\rho}\,(\overline{c_s}\,\overline{\beta_f} - \overline{c_s}\,\overline{\beta_f})}$$

$$v = \frac{1}{2B_t{}^2}\left(\frac{B_y}{B_x}\frac{\overline{c_s}\,(R_7 - R_1) - \overline{c_f}\,(R_5 - R_3)}{(\overline{c_s}\,\overline{\beta_f} - \overline{c_s}\,\overline{\beta_f})} - \overline{B_z}\,(R_6 + R_2)\right)$$

$$w = \frac{1}{2B_t{}^2}\left(\frac{B_z}{B_x}\frac{\overline{c_s}\,(R_7 - R_1) - \overline{c_f}\,(R_5 - R_3)}{(\overline{c_s}\,\overline{\beta_f} - \overline{c_s}\,\overline{\beta_f})} - \overline{B_y}\,(R_6 + R_2)\right)$$

$$\rho = R_4 + \frac{p}{\overline{a^2}}$$

$$B_y = \frac{1}{2B_t{}^2}\left(B_y\frac{-(R_7 + R_1) + (R_5 + R_3)}{(\overline{c_s}\,\overline{\beta_s} - \overline{c_f}\,\overline{\beta_f})} + \overline{\sqrt{\rho}}\,\overline{B_z}\,(R_6 - R_2)\right)$$

$$B_z = \frac{1}{2B_t{}^2}\left(B_z\frac{-(R_7 + R_1) + (R_5 + R_3)}{(\overline{c_s}\,\overline{\beta_s} - \overline{c_f}\,\overline{\beta_f})} - \overline{\sqrt{\rho}}\,\overline{B_y}\,(R_6 - R_2)\right)$$

This procedure applies when the characteristics λ_i in the two regions that confine the wave i present the same sign. Therefore, there is no uncertainty in determining to which of the two terms $\overleftarrow{D_N F}$ or $\overrightarrow{D_N F}$ the wave i contributes with its the flux difference. However, in the case the characteristics change the sign across the relative wave (this is the case of a sonic transition across a shock or a rarefaction fan), the difference of the flux across this wave has to be split in two parts that partly contribute to both $\overleftarrow{D_N F}$ or to $\overrightarrow{D_N F}$. In these cases the procedure follows the guidelines as in the classical gasdynamics Ref. 7 which allow for the correct collapse of expansion shocks and the robust and sharp capturing of compression shocks.

For the limiting cases where multiple definitions of characteristics occur, this approximate solver has to be slightly modified.

A second order of accuracy integration scheme can be constructed, by incorporating features of the ENO schemes Ref. 11. The results of the above numerical experiments on the solutions of RPs with initial data given by possible discontinuities are obtained with the second order scheme.

At this point we would like to emphasize the importance of describing the pattern of characteristics and the structures of waves, at the most accurate level. Such a requirement becomes imperative in dealing with complex wave structures as compound waves and with particular shocks. We are convinced that the previous second approximation introduced in our solver for the solution of the RP, by taking the coefficients that appear in the definition of the signals constant all over the waves generated in the RP evolution, is responsible for some of the deficiencies we have reported in some of our numerical experiences. Presently, we are working on a more accurate solver, where the above coefficients are allowed to vary from region to region and are assumed constant only through each singular wave. We are confident that this implementation will fix most of our unsatisfactory results.

Nonetheless, the actual code seems to be accurate enough to allow for the identification of compound waves not yet predicted numerically in the literature.

References

[1] R.S.Myong and P.L.Roe,"Shock waves and rarefaction waves in magnetohydrodynamics. Part1. A model system", *Journal of Computational Physics*, vol.58, part 3, pp.485-519, 1997.

[2] R.S.Myong and P.L.Roe,"Shock waves and rarefaction waves in magnetohydrodynamics. Part2. The MHD system", *Journal of Computational Physics*, vol.58, part 3, pp.521-552, 1997.

[3] R.S.Myong,"Analytical results on MHD intermediate shocks", *Geophysical Research Letters*, vol.24, No.22, pp.2929-2932, 1997.

[4] K.G.Powell, P.L.Roe, T.J.Linde, T.I.Gombosi and D.L.De Zeeuw,"A solution-adaptive upwind scheme for ideal Magnetohydrodynamics", *Journal of Computational Physics*, vol.154, pp.284-309, 1999.

[5] R.W.MacCormack, "An upwind conservation form method for the ideal magnetohydrodynamics equations", AIAA 99-3609, June 1999.

[6] P.Janhunen,"A positive conservative method for magnetohydrodynamicsbased on HLL and Roe methods", *Journal of Computational Physics*, vol.160, pp.649-661, 2000.

[7] M.Pandolfi, "A contribution to the numerical prediction of unsteady flows", *AIAA Journal*, vol.22, No.5, pp.602-610,1983.

[8] M.Pandolfi and D.D'Ambrosio, "Numerical instabilities in upwind methods: analysis and cures for the carbuncle phenomenon", *Journal of Computational Physics*, vol.166, pp.271-301, 2001.

[9] M.Pandolfi and D.D'Ambrosio, "Performances of upwind methods in predicting shear-like flows", *Computers and Fluids*, vol.31, pp.725-744, 2002.

[10] M.Brio and C.C.Wu, "An upwind differencing scheme for the equations of ideal magnetohydrodynamics", *Journal of Computational Physics*, vol.75, pp.400-422, 1988.

[11] A.Harten, B.Engquist, S.Osher and S.R.Chakravarthy, "Uniformly high order accurate essentially non-oscillatory schemes, III", *Journal of Computational Physics*, vol.71, pp.231-303, 1987.
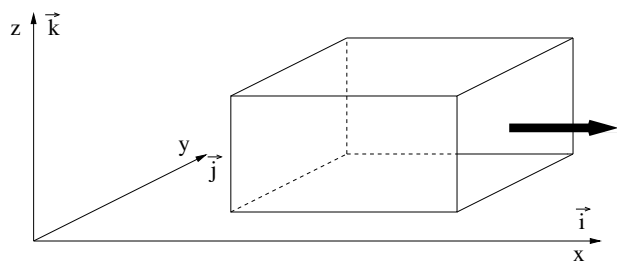
Fig. 1   One-dimensional MFD model.
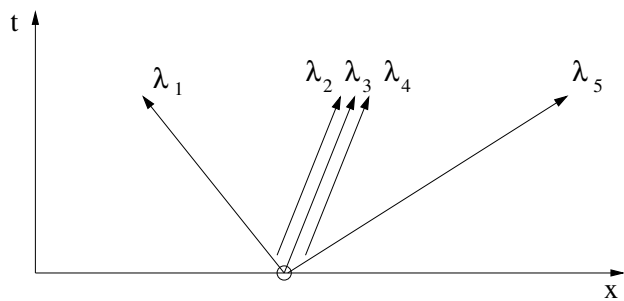
Fig. 2   Characteristics pattern for the 1D Euler flow.
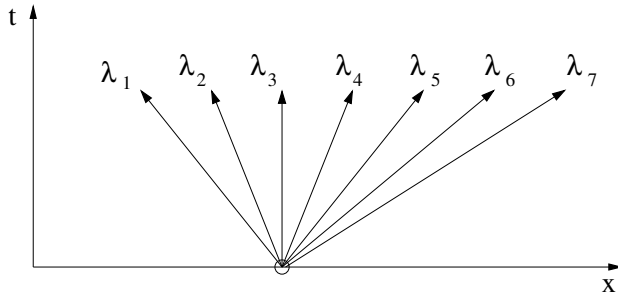
a) Characteristics pattern for the general 1D MFD flow.
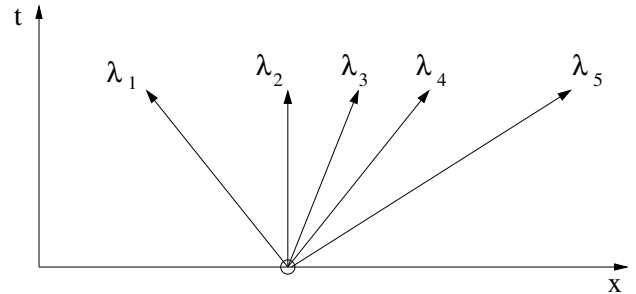
b) Characteristics pattern for the planar 1D MFD flow.
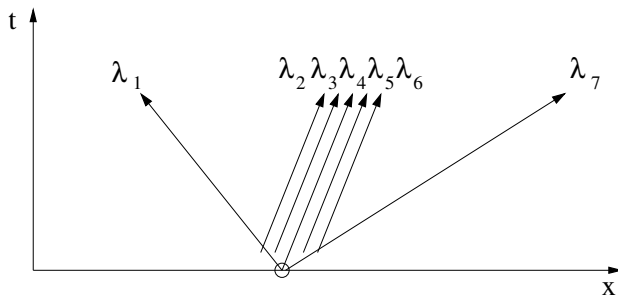
c) Characteristics pattern for the 1D MFD flow with $B_x = 0$ and $B_t \neq 0$.
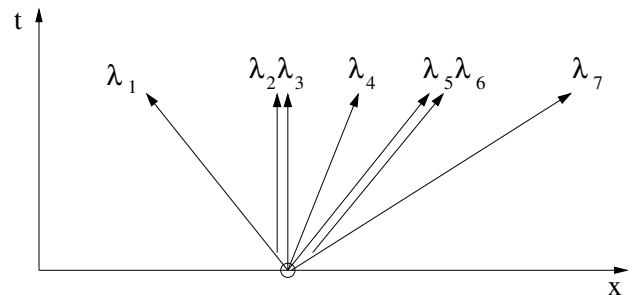
d) Characteristics pattern for the 1D MFD flow with $B_x < \sqrt{\gamma p}$ and $B_t = 0$.
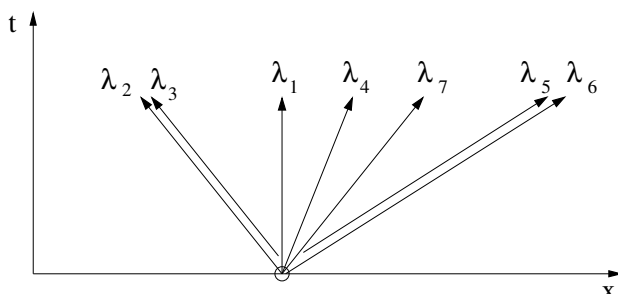
e) Characteristics pattern for the 1D MFD flow with $B_x > \sqrt{\gamma p}$ and $B_t = 0$.
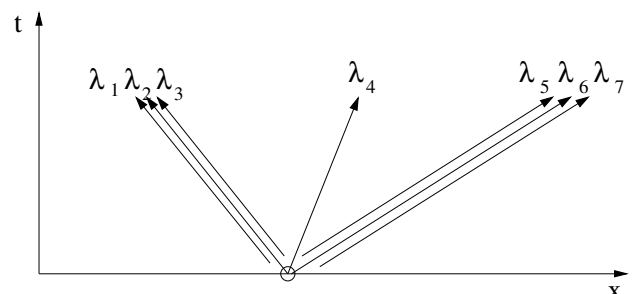
f) Characteristics pattern for the 1D MFD flow with $B_x = \sqrt{\gamma p}$ and $B_t = 0$.

Fig. 3 Characteristic patterns for the 1D MFD flow.
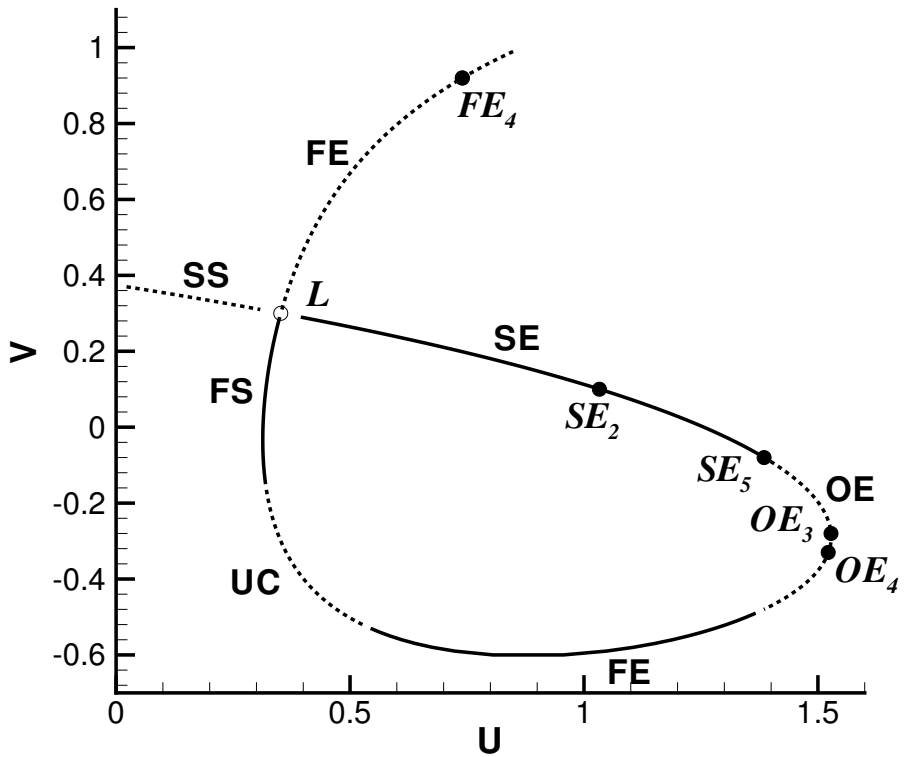
a) Curl-shaped curve for the case B: $U_L = 0.352$ **and** $V_L = 0.300$.
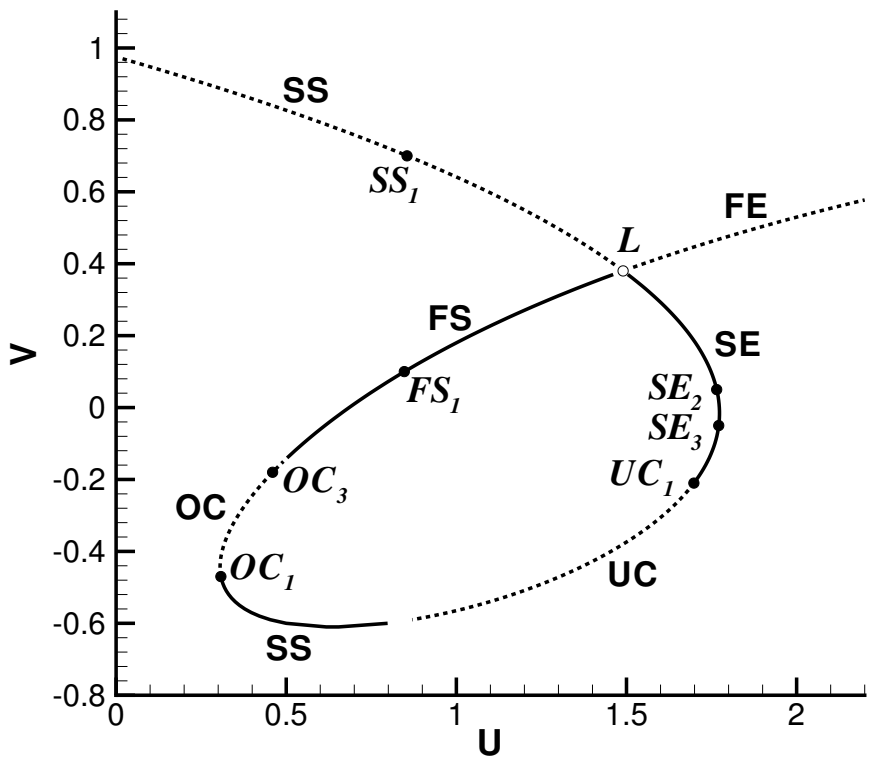
b) Curl-shaped curve for the case C: $U_L = 1.490$ **and** $V_L = 0.380$.

Fig. 4   Curl-shaped curves for cases B and C.

fast shock (FS)   slow shock (SS)   fast expansion (FE)   slow expansion (SE)

overcompression (OC)   overexpansion (OE)   undercompression (UC)

left transport (LT)   right transport (RT)
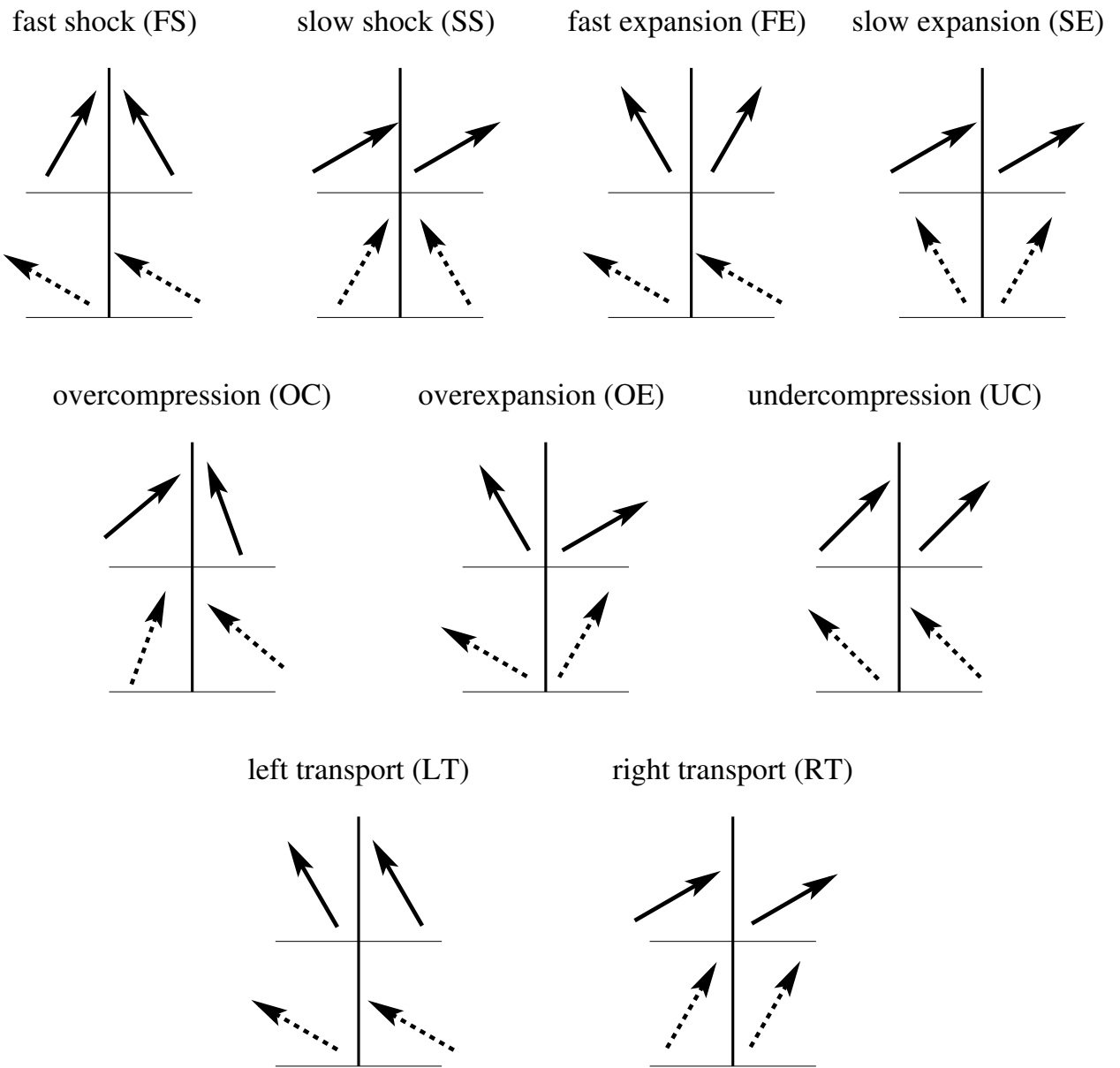
Fig. 5   Different characteristic configurations for planar 1D MFD discontinuities.
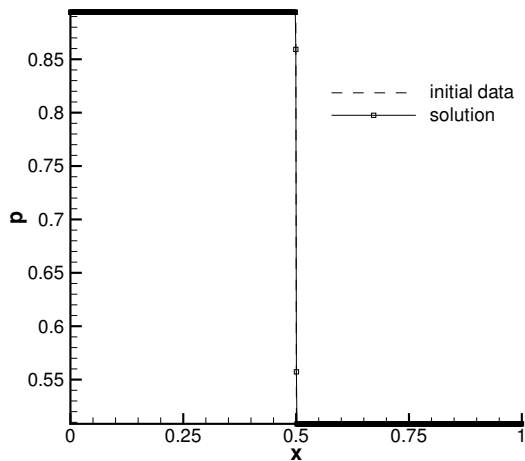
a) **case C, point** $FS_1(0.847;0.100)_R$.
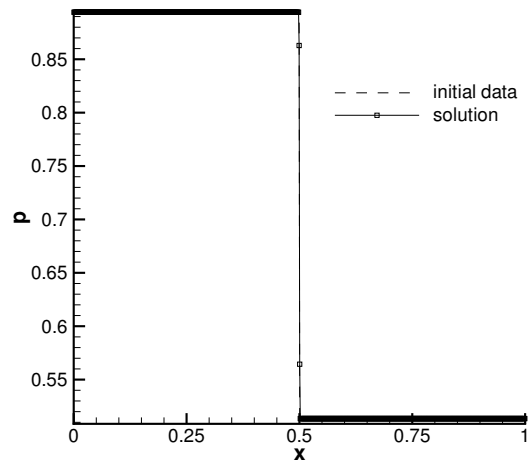
b) **case C, point** $SS_1(0.855;0.700)_R$.
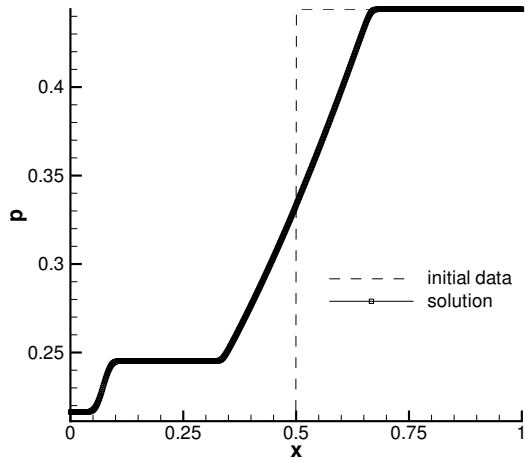
c) **case B, point** $FE_4(0.740;0.920)_R$.
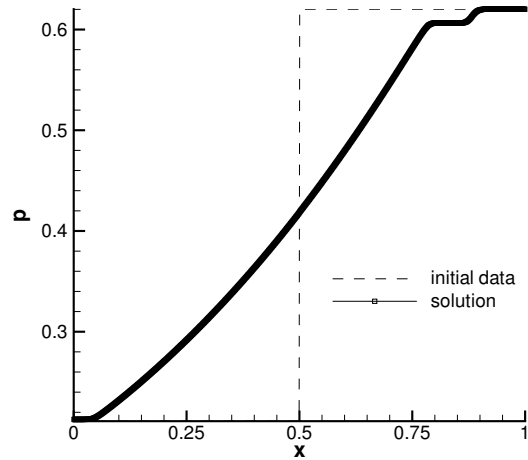
d) **case B, point** $SE_2(1.033;0.100)_R$.
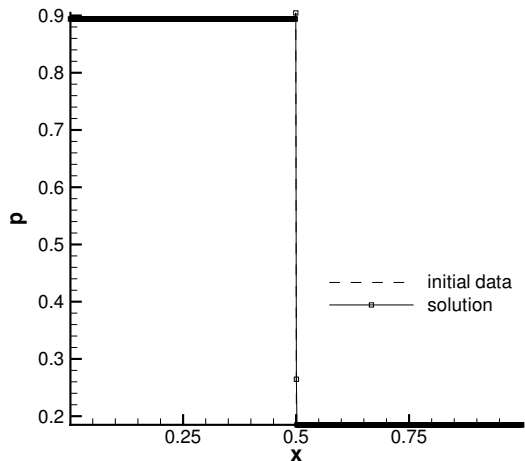
e) **case C, point** $OC_1(0.308;-0.470)_R$.
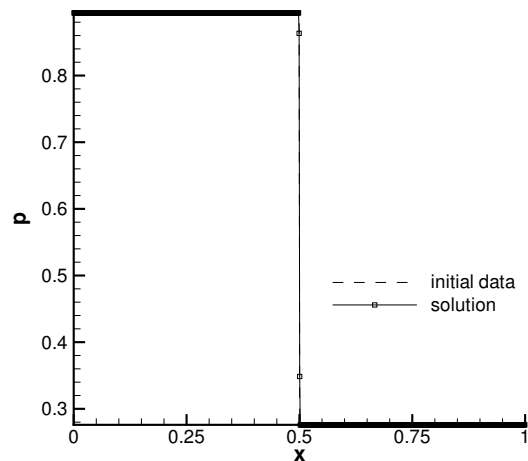
f) **case C, point** $OC_3(0.460;-0.180)_R$.

Fig. 6   Riemann problems solutions for cases B $(0.352;0.300)_L$ and C $(1.490;0.380)_L$.
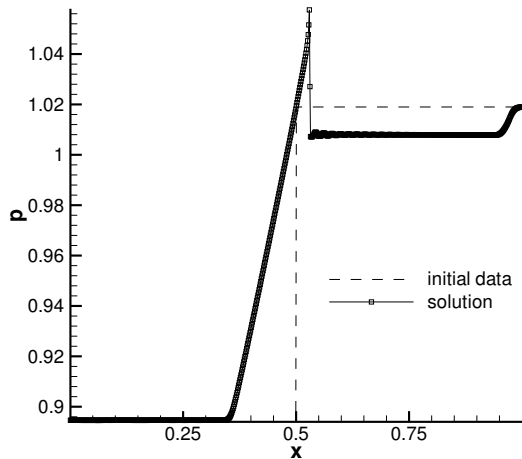
a) **case C, point** $UC_1(1.698; -0.210)_R$.
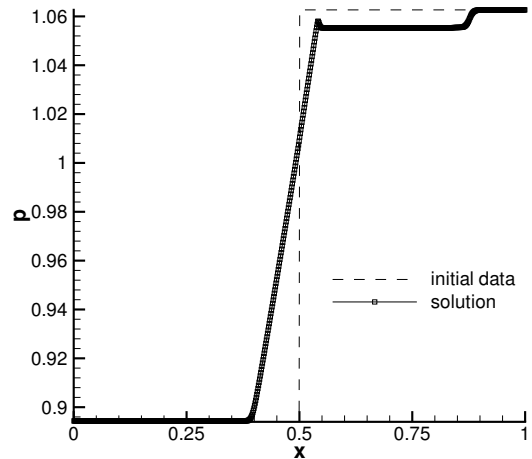
b) **case C, point** $SE_3(1.771; -0.050)_R$.
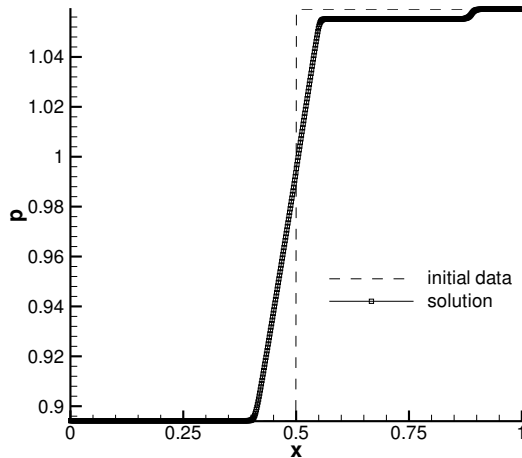
c) **case C, point** $SE_2(1.765; 0.050)_R$.
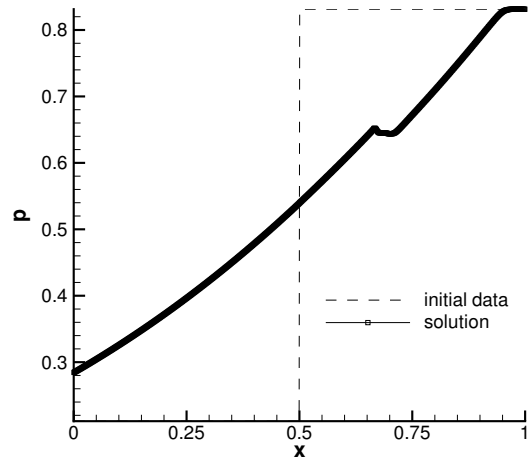
d) **case B, point** $SE_5(1.385; -0.080)_R$.
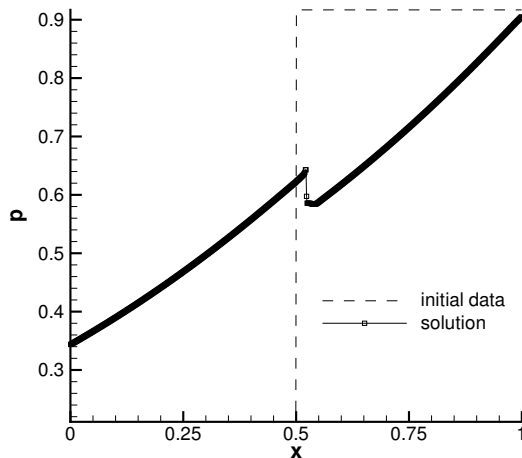
e) **case B, point** $OE_3(1.528; -0.280)_R$.
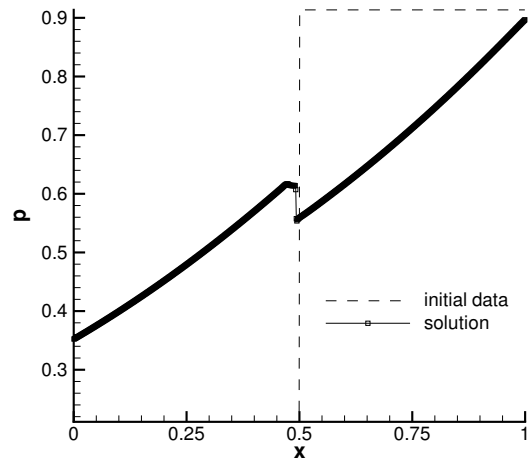
f) **case B, point** $OE_4(1.522; -0.330)_R$.

Fig. 7   Riemann problems solutions for cases B $(0.352; 0.300)_L$ and C $(1.490; 0.380)_L$.
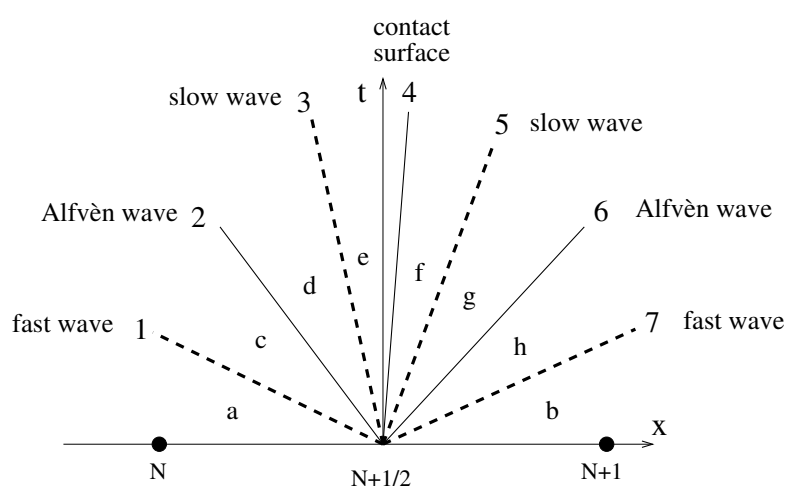
Fig. 8　Riemann problem for the MFD system.

Numerical Modeling of Electromagnetic Control Techniques for High-Speed Flow

Jonathan Poggie
Air Force Research Laboratory
Wright-Patterson Air Force Base, USA

Electromagnetic control for high-speed flow was first suggested in the mid-1950's [1], and was pursued with enthusiasm up to about 1970. After lying dormant for a number of years, the field began a resurgence in the 1990's with the disclosure of the Russian Ajax vehicle concept [2] and independent interest by a few research groups [3, 4]. Although practical applications of this technology remain elusive, plausible control systems have been proposed in the literature.

Over the past few years, the Computational Sciences Center at the United States Air Force Research Laboratory has been developing a set of computational tools to investigate the feasibility of electromagnetic flow control. In particular, two codes that solve the coupled fluid and electromagnetic equations are under development: a magnetogasdynamics code `FDL3DI-mhd` and a plasma sheath code `PS3D`. (For related work on thermochemical nonequilibrium carried out by our research group, see, for example, Ref. [5].) The present paper will discuss applications of the magnetogasdynamics code carried out by the author, and go on to describe the development of the sheath code.

First, the governing equations solved by the various versions of each code will be discussed in §1. Then application of the magnetogasdynamic code to blunt body heat transfer mitigation will be explored in §2. Finally, calculations using the plasma sheath code will be discussed in §3, with a preview of ongoing work on glow discharges in §4. A few concluding remarks are made in §5.

1   Governing Equations

Computation of weakly ionized flow can be approached from several levels of modeling [6–8]. These range, at the very fundamental level, from computing the motion of a collection of independent particles using Particle-in-Cell Monte Carlo Collision (PIC-MCC) methods, to solutions of the Boltzmann equation for the particle distribution function. Here we pursue a somewhat higher and less computationally expensive level of modeling: the conservation laws for mass (or particle identity), momentum, and energy, derived from moments of the Boltzmann equation [8–10], are solved using techniques from computational fluid dynamics.

The conservation equations of mass, momentum, and energy for the overall fluid are

expressed as:

$$\frac{\partial \rho}{\partial t} + \nabla \cdot (\rho \boldsymbol{u}) = 0, \tag{1}$$

$$\frac{\partial}{\partial t}(\rho \boldsymbol{u}) + \nabla \cdot (\rho \boldsymbol{u}\boldsymbol{u} - \boldsymbol{\Sigma}) = \boldsymbol{f}, \tag{2}$$

$$\frac{\partial \mathcal{E}}{\partial t} + \nabla \cdot (\boldsymbol{u}\mathcal{E} - \boldsymbol{\Sigma} \cdot \boldsymbol{u} + \boldsymbol{Q}) = P. \tag{3}$$

Here the dependent variables are the mass density $\rho = \Sigma_s m_s n_s$, where m_s is the particle mass and n_s is the number density for species-s, the bulk fluid velocity $\boldsymbol{u}$, and the total energy $\mathcal{E} = \rho(\epsilon + u^2/2)$, where ϵ is the internal energy. The independent variables are time t and position $\boldsymbol{x}$. The total stress tensor is $\boldsymbol{\Sigma}$ and the heat flux is $\boldsymbol{Q}$. The source terms on the right hand side are the electromagnetic body force $\boldsymbol{f}$ and the total power delivered to the fluid by electromagnetic effects P.

In the present work, we will neglect magnetization and polarization of the fluid. Maxwell's equations can be expressed as follows using SI units:

$$\epsilon_0 \nabla \cdot \boldsymbol{E} = \zeta, \tag{4}$$

$$\nabla \cdot \boldsymbol{B} = 0, \tag{5}$$

$$\nabla \times \boldsymbol{E} = -\frac{\partial \boldsymbol{B}}{\partial t}, \tag{6}$$

$$\nabla \times \boldsymbol{B}/\mu_0 = \boldsymbol{j} + \epsilon_0 \frac{\partial \boldsymbol{E}}{\partial t}, \tag{7}$$

where Eqs. (4)-(7) are, respectively, Gauss's law, conservation of magnetic flux, Faraday's law, and the Ampère-Maxwell law. The charge conservation equation

$$\frac{\partial \zeta}{\partial t} + \nabla \cdot \boldsymbol{j} = 0 \tag{8}$$

can be derived from Maxwell's equations.

In the present notation, ϵ_0 is the vacuum permittivity and μ_0 is the vacuum permeability, $\boldsymbol{E}$ is the electric field, and $\boldsymbol{B}$ is the magnetic field. The total charge density is $\zeta = \Sigma_s q_s n_s$, where q_s is the charge per particle of species-s. The total electric current is $\boldsymbol{j} = \Sigma_s q_s n_s \boldsymbol{u}_s$, and we define the conduction current as $\boldsymbol{J} = \boldsymbol{j} - \zeta \boldsymbol{u}$. The force per unit volume of matter is $\boldsymbol{f} = \zeta \boldsymbol{E} + \boldsymbol{j} \times \boldsymbol{B}$, and the power delivered to matter by the field is $P = \boldsymbol{E} \cdot \boldsymbol{j}$.

In the applications discussed in §2, we will consider the case where typical flow length scales are much larger than the Debye length, flow time scales are larger than the reciprocal of the plasma frequency, and flow velocities are much less than the speed of light. Under these conditions, a simplified magnetogasdynamic model is applicable. The displacement current $\epsilon_0 \partial \boldsymbol{E}/\partial t$ and the convected charge $\zeta \boldsymbol{u}$ are neglected as small compared to the conduction current $\boldsymbol{J}$. Since charge separation is small, the force due to the electric field and the unsteady term in Eq. (8) are also neglected. With these assumptions, Maxwell's

equations can be reduced to:

$$\nabla \cdot \boldsymbol{J} = 0, \tag{9}$$

$$\nabla \cdot \boldsymbol{B} = 0, \tag{10}$$

$$\nabla \times \boldsymbol{E} = -\partial \boldsymbol{B}/\partial t, \tag{11}$$

$$\nabla \times \boldsymbol{B}/\mu_0 = \boldsymbol{J}. \tag{12}$$

The force on the fluid is $\boldsymbol{f} = \boldsymbol{J} \times \boldsymbol{B}$ and the power delivered to the fluid is $P = \boldsymbol{E} \cdot \boldsymbol{J}$. (The force and power terms can be rewritten to eliminate $\boldsymbol{E}$. For example, see Ref. [11].)

For simplicity, we assume in the present work that the current is given by Ohm's law:

$$\boldsymbol{J} = \boldsymbol{\sigma} \cdot (\boldsymbol{E} + \boldsymbol{u} \times \boldsymbol{B}), \tag{13}$$

where $\boldsymbol{\sigma}$ is the electrical conductivity tensor. The electrical conductivity can be approximated by a scalar value if the collision frequency is much greater than the cyclotron (gyro) frequency, as in a relatively dense gas. Equations (9)-(13) can be combined to give the magnetic induction equation:

$$\frac{\partial \boldsymbol{B}}{\partial t} = \nabla \times \left(\boldsymbol{u} \times \boldsymbol{B} - \boldsymbol{\eta} \cdot \nabla \times \boldsymbol{B} \right), \tag{14}$$

where $\boldsymbol{\eta} = (\mu_0 \boldsymbol{\sigma})^{-1}$ is the magnetic diffusivity tensor.

An order of magnitude analysis of the terms in Eq. (14) reveals that the ratio of the magnitudes of the convective and diffusive terms is given by the magnetic Reynolds number $\text{Re}_m = \sigma \mu_0 V L$. This quantity is small in many aerospace applications; typically $\text{Re}_m \lesssim 1$.

For small magnetic Reynolds numbers, the distortion of the magnetic field by the flow can be neglected, and only the imposed field has a significant influence on the flow. The imposed magnetic field is specified or computed beforehand, and the electric field is found from the current continuity equation:

$$\nabla \cdot [\boldsymbol{\sigma} \cdot (\boldsymbol{E} + \boldsymbol{u} \times \boldsymbol{B})] = 0. \tag{15}$$

The current version of our magnetogasdynamic code `FDL3DI-mhd` includes options to solve either the general model consisting of Eqs. (1)-(3), and (14) or the low magnetic Reynolds number model consisting of Eqs. (1)-(3), and (15). The total stress tensor $\boldsymbol{\Sigma}$ is given by the usual constitutive equation for a Newtonian fluid and the heat flux $\boldsymbol{Q}$ follows Fourier's heat conduction law. The fluid is assumed to be an ideal gas.

In §3 we investigate applications in which typical length scales are on the order of the Debye length, so that the assumption of quasi-neutrality is not appropriate. Assuming a weakly-ionized gas, the particle conservation and momentum conservation equations for each species are:

$$\frac{\partial n_s}{\partial t} + \nabla \cdot (n_s \boldsymbol{u}_s) = \omega_s, \tag{16}$$

$$\frac{\partial}{\partial t}(n_s m_s \boldsymbol{u}_s) + \nabla \cdot (n_s m_s \boldsymbol{u}_s \boldsymbol{u}_s + p_s \boldsymbol{I}) = q_s n_s (\boldsymbol{E} + \boldsymbol{u}_s \times \boldsymbol{B}) + \boldsymbol{F}_s. \tag{17}$$

The heavy particle temperature is assumed to be the same as that of the neutral gas, so that $p_s = n_s k_B T$. The rate of production of particles of species s is ω_s. The frictional force $\boldsymbol{F}_s$ is due to collisions between the ions and the neutral background gas. The detailed expressions for these terms will be discussed later.

The electric potential is determined by a Poisson equation:

$$\nabla^2 \phi = -\zeta/\epsilon_0, \tag{18}$$

where ϵ_0 is the permittivity of free space, and $\boldsymbol{E} = -\nabla\phi$. The Poisson equation is derived from Eqs. (4) and (6), assuming that the magnetic field varies slowly with time.

A further level of simplification is possible if the inertia of the particles can be neglected. Neglecting acceleration terms and temperature gradients, and defining the diffusion velocity and flux as $\boldsymbol{w}_s = \boldsymbol{u}_s - \boldsymbol{u}$ and $\boldsymbol{\Gamma}_s = n_s \boldsymbol{w}_s$, respectively, the particle and momentum conservation equations for each species are:

$$\frac{\partial n_s}{\partial t} + \nabla \cdot (n_s \boldsymbol{u} + \boldsymbol{\Gamma}_s) = \omega_s, \tag{19}$$

$$\boldsymbol{\Gamma}_s - s_s \mu_s \boldsymbol{\Gamma}_s \times \boldsymbol{B} = -D_s \nabla n_s + s_s n_s \mu_s (\boldsymbol{E} + \boldsymbol{u} \times \boldsymbol{B}), \tag{20}$$

where s is the sign of q, μ is the mobility, and D is the diffusion coefficient.

We define the tensor:

$$M_{ij}^s = \frac{1}{1 + \mu_s^2 B^2}(\delta_{ij} + \mu_s^2 B_i B_j + s_s \mu_s \epsilon_{ijk} B_k). \tag{21}$$

Taking the dot product of $\boldsymbol{M}^s$ with both sides of (20), we find:

$$\boldsymbol{\Gamma}_s = \boldsymbol{M}^s \cdot [-D_s \nabla n_s + s_s n_s \mu_s (\boldsymbol{E} + \boldsymbol{u} \times \boldsymbol{B})], \tag{22}$$

where the dot product corresponds to summation on the second index of M_{ij}. Using $\boldsymbol{E} = -\nabla\phi$, substituting into (19), and rearranging:

$$\frac{\partial n_s}{\partial t} + \nabla \cdot [n_s (\boldsymbol{u} + s_s \mu_s \boldsymbol{M}^s \cdot \boldsymbol{u} \times \boldsymbol{B})] = \nabla \cdot [\boldsymbol{M}^s \cdot (n_s s_s \mu_s \nabla\phi + D_s \nabla n_s)] + \omega_s. \tag{23}$$

Equation (23) is the basic drift-diffusion equation.

The current version of our plasma sheath and glow discharge code PS3D includes options to solve either Eqs. (1)-(3) with Eqs. (16)-(17), and (18), or Eqs. (1)-(3) with Eqs. (18) and (23).

2 Magnetogasdynamic Heat Transfer Mitigation

The extremely high temperatures in the shock layer at the blunt nose of a hypersonic vehicle remain one of the prime impediments to routine trans-atmospheric flight. Given the ionization associated with these high temperatures, it is natural to consider electromagnetic control as a means of heat transfer mitigation. Since the ponderomotive force tends to oppose fluid motion across magnetic field lines, a magnetic field applied to the conductive shock layer would tend to slow the flow near the surface of the body, and thus reduce surface heat transfer.

The origin of this idea dates to the late 1950's [12–14]. Various system concepts included both local flow control for stagnation point heat transfer reduction and large-scale, self-powered magnetogasdynamic systems [13, 15, 16]. Enthusiasm for the practical application of these ideas waned by the mid-1960's, however, and publication on the subject tapered off after that decade. The idea was eventually abandoned because it was not believed to be competitive in terms of weight with other means of thermal protection [17]. Nearly five decades have elapsed since the first suggestion of electromagnetic control of hypersonic flight, and considerable progress has been made in the technologies of magnet construction and plasma generation. It is now appropriate to reconsider the technique.

To examine the possibility of heat transfer mitigation through magnetic deceleration, magnetogasdynamic computations were carried out in the low magnetic Reynolds number regime [11, 18, 19]. The problem was solved using the `FDL3DI-mhd` code. The Hall effect was neglected and the imposed magnetic field was taken to be a dipole centered at the origin. It can be shown [20] that axial symmetry and negligible Hall effect require that $\mathbf{E} = 0$, so that Eq. (15) is reduced to an identity.

The case of a Mach 5, ideal gas flow over a hemisphere was chosen to match the inviscid computations of Coakley and Porter [21]. The results were compared to these early computations and to the inviscid theory of Bush [20]. (The Bush theory solves Eqs. (1)-(3),(14); here we took $\mathrm{Re}_m = 0$ for comparison with the numerical solution. Additional consideration will be given to Eq. (14) at the end of this section.) Viscous calculations were also carried out to examine the influence of magnetic control on the heat transfer in the vicinity of the stagnation point, and were compared to Bush's boundary layer theory [22].

The freestream conditions were $M = 5$ and $\gamma = 1.4$. The inviscid computations were carried out on an axisymmetric grid of $60 \times 40 \times 5$ points distributed, respectively, in the directions along the body surface, normal to the body, and in the circumferential direction.

The basic flow structure is illustrated in Fig. 1, which shows the pressure field predicted by the numerical computations for two cases: $Q = 0$ and $Q = 6$, where $Q = \sigma B_0^2 R / \rho_\infty V_\infty$ is the magnetic interaction parameter based on the body radius R. With the application of a strong magnetic field, there is a dramatic increase in the shock standoff, but little qualitative change in the flow structure.

The increase in shock standoff with interaction parameter is quantified in Fig. 2. The predictions of Bush's theory [20], Coakley and Porter's computations [21], and the correlation of Ambrosio and Wortman [23] are shown for comparison with the results of the present computations. As expected for a constant-density calculation, the prediction of the Bush theory tends to be too low for the non-magnetic case, whereas the results from Coakley and Porter and the present computations are close to the empirical correlation. Although all methods predict higher standoff with increasing interaction parameter, the present computations show a more rapid rise.

A corresponding set of viscous computations was carried out for $\mathrm{Re}_R = 80000$ and $T_w/T_\infty = 3$. Two grids were used: a baseline case with $60 \times 80 \times 5$ points, and a finer grid of $120 \times 160 \times 5$ points. Figure 3 shows boundary layer profiles of velocity and temperature for a station close to the centerline. The circular and square symbols show, respectively, the results from the coarse and fine grid computations. The solid lines indicate the predictions of Bush's similarity solution [22], with the edge conditions from

5

(a) $Q = 0$ (b) $Q = 6$
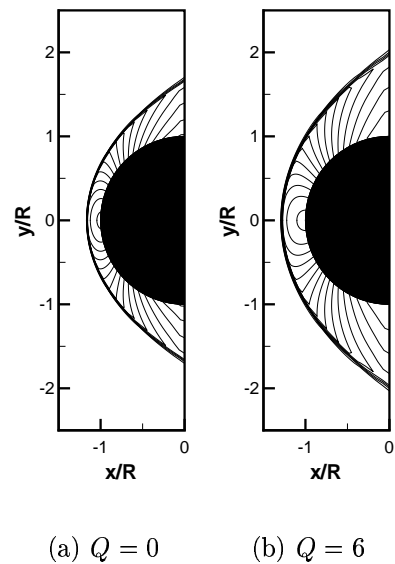
Figure 1: Pressure field p/p_∞ for inviscid flow (contour interval 2).
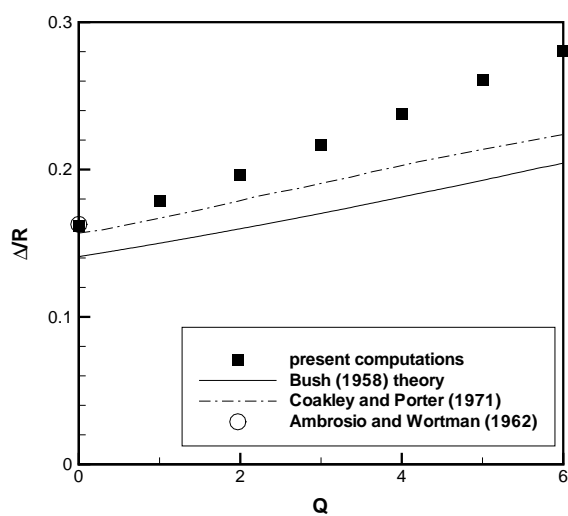
Figure 2: Effect of applied magnetic field on shock standoff.
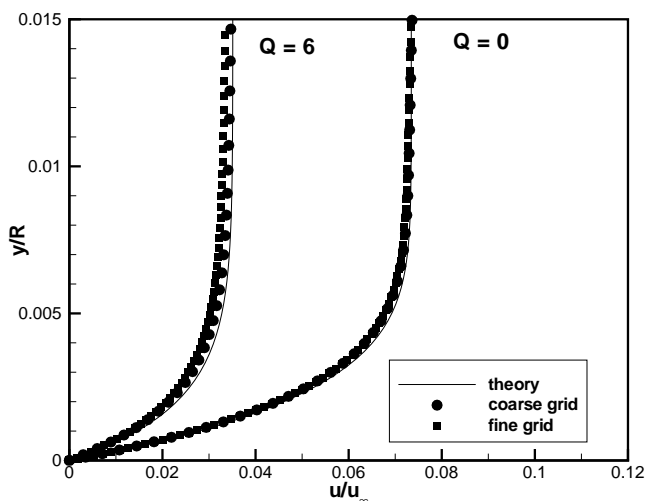
(a) Velocity Profiles.
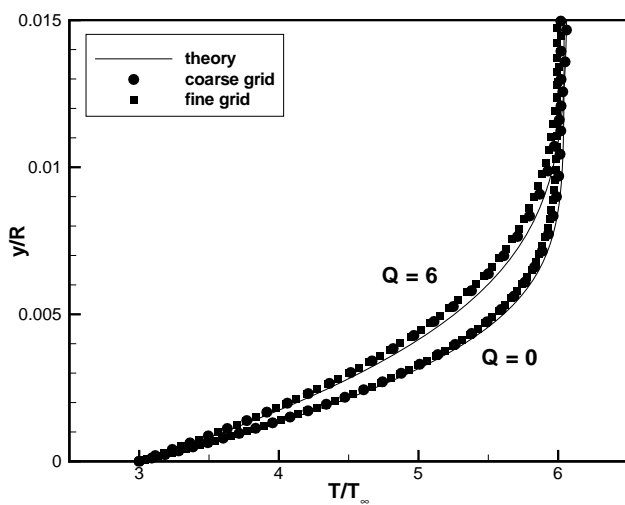
(b) Temperature profiles.

Figure 3: Boundary layer profiles, 6.6° off centerline.
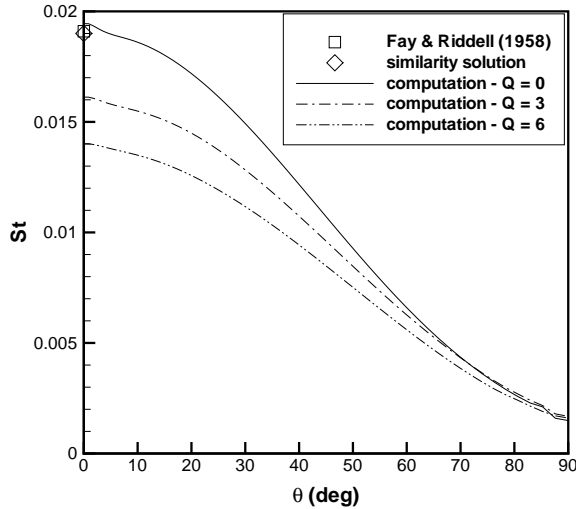
Figure 4: Effect of applied magnetic field on surface heat transfer profile.

the inviscid, numerical solution used as input for the similarity solution. Excellent overall agreement is obtained between theory and computation, and it is evident that results of the computations are practically mesh-independent. With the application of a strong magnetic field, the magnetic force effectively counteracts the favorable pressure gradient, decelerating the freestream and strongly reducing the velocity gradient at the wall. A similar trend is seen in the temperature profiles. The applied magnetic field causes a reduction in the temperature gradient at the wall, with a corresponding reduction in the wall heat flux.

Figure 4 shows the computed Stanton number profile around the body surface. The lines indicate the computational results (coarse grid) for different values of the interaction parameter, whereas the symbols indicate the stagnation point value computed using the Fay-Riddell [24] correlation and using a similarity solution of the non-magnetic boundary layer equations. An applied magnetic field is seen, in the computations, to reduce the level of heat transfer over the major portion of the hemisphere, with the greatest reductions in the vicinity of the stagnation point ($\theta = 0°$). The heat transfer does not change near $\theta = 90°$ because the velocity vector and magnetic field vector are nearly collinear in that part of the flow, and thus the electric current, Eq. (13), becomes small.

Figure 5 shows the Stanton number at the stagnation point as a function of the interaction parameter. The solid line represents the predictions of the combined constant density and boundary layer theories of Bush, the filled symbols are the results of the coarse-grid computations, and the open symbols represent the Fay-Riddell correlation and corresponding non-magnetic similarity solution. In the non-magnetic case, the computations are in good agreement with the latter heat transfer theories, whereas the prediction of Bush's theory is somewhat high. Both theory and numerical computation predict a significant decrease in the heat transfer rate with increasing strength of the applied field, and there is good agreement between the two models in the fractional change in heat transfer. The overall higher value predicted by Bush's theory is probably due to an overestimate of the velocity gradient at the boundary layer edge.

8
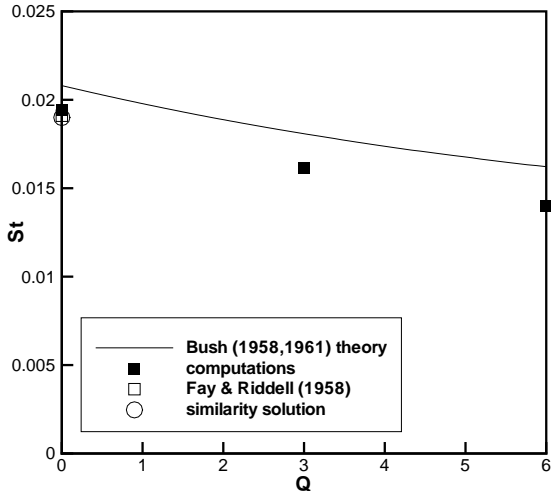
Figure 5: Effect of applied magnetic field on stagnation point heat transfer.

In the preceding numerical solutions, the distortion of the magnetic field was neglected because the magnetic Reynolds number is believed to be small in practical applications. Additional calculations were carried out using the Bush theory to examine the influence of this parameter. The calculations considered a sphere immersed in a Mach 25 freestream flow at 180 Pa and 250 K. These conditions correspond to a velocity of 8 km/s and a shock density ratio of $K = 15.8$ for equilibrium air. The electrical conductivity was taken to be $\sigma = 300\ \mho/\text{m}$. Two values of the sphere radius were considered: 1 m and 2 m, corresponding to magnetic Reynolds numbers of $\text{Re}_m = 3.01$ and $\text{Re}_m = 6.02$, respectively.

The shock standoff predicted by the inviscid-flow theory is shown in Fig. 6. The effectiveness of magnetic control is seen to be reduced for increased values of the magnetic Reynolds number. This occurs because currents set up in the fluid generate an induced field that tends to oppose the applied field.

Figure 7 shows the ratio of the total magnetic field to the applied field at the nose of the body. With increasing magnetic Reynolds number, the induced field becomes stronger, reducing the overall field and thus the effectiveness of magnetic control.

The magnetic Reynolds numbers encountered in aerodynamic applications will almost certainly be in the range $\text{Re}_m \lesssim 1$, and probably much less than one. The low magnetic Reynolds number approximation, Eqs. (1)-(3) and (15), is thus well-justified.

An applied magnetic field is seen, in principle, to reduce the stagnation point heat flux. Additional work is needed to evaluate the Hall effect (e.g., see Refs. [25, 26]).

3   Plasma Sheaths

In order to examine the role of plasma sheaths in flow control and plasma generation, computations [27–29] were carried for a relatively low density regime in which ion inertia is significant. Equations (16)-(17) were solved for the ions, the electric potential was
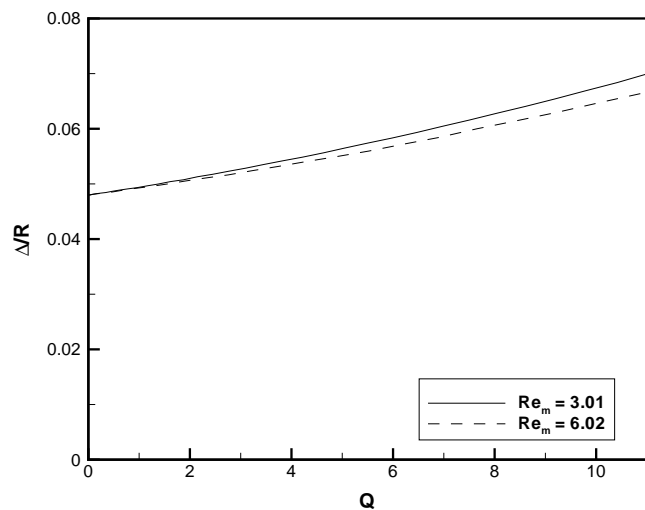
Figure 6: Effect of varying magnetic field strength on shock standoff at $M = 25$.
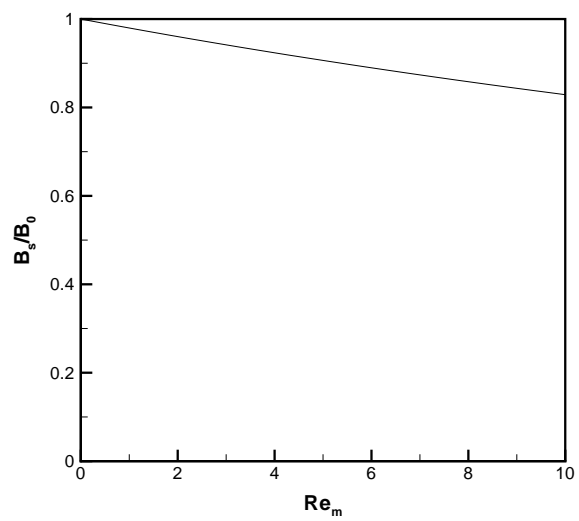
Figure 7: Effect of magnetic Reynolds number for $M = 25$ and $Q = 11.4$.

found from Eq. (18), and the electrons were assumed to be in Boltzmann equilibrium:

$$n_e = n_0 \exp(e\phi/k_B T_e), \tag{24}$$

where n_0 is the reference number density corresponding to $\phi = 0$. The electron temperature was fixed at $T_e = 11600$ K (1 eV). The frictional force due to charge-exchange collisions between the ions and the neutral background gas was taken to have the form:

$$\mathbf{F}_k = -\frac{\pi |\mathbf{u}_k - \mathbf{u}|}{2\lambda_i} n_k m_k (\mathbf{u}_k - \mathbf{u}), \tag{25}$$

where λ_i is the ion mean free path.

3.1 Verification and Validation

For the purpose of code verification, we consider here a one-dimensional problem in which an ionized gas is confined between a pair of electrodes a distance $2R$ apart. The electrodes are assumed to be maintained at a constant negative potential, and to draw a current which is maintained by ionization in the bulk plasma. Charged particles were assumed to be produced by 'direct' ionization $\omega_k = z n_e$, where z is the constant ionization frequency necessary to achieve a steady state.

Approximate analytical solutions can be obtained in the case of a non-magnetic, collisionless plasma sheath [30, 31]. We introduce the following dimensionless variables, known in the literature as the plasma coordinates:

$$
\begin{array}{ll}
\hat{x} = xz/u_B & \eta(\hat{x}) = -e\phi(x)/k_B T_e \\
y(\hat{x}) = n_i(x)/n_0 & y_e(\hat{x}) = n_e(x)/n_0 \\
\hat{\mathbf{u}}(\hat{x}) = \mathbf{u}_i(x)/u_B &
\end{array} \tag{26}
$$

Note that x is the direction normal to the electrode surface, or wall. The coordinate $\hat{x} = 0$ corresponds to the plasma center, whereas $\hat{x} = \hat{R} = zR/u_B$ corresponds to the position of the wall. The velocity scale $u_B = \sqrt{k_B T_e/m_i}$ is the Bohm velocity.

An outer, or plasma solution, can be obtained by assuming quasi-neutrality:

$$
\begin{array}{rcl}
\hat{x} & = & 2\arctan(\hat{u}) - \hat{u} \\
y & = & 1/(1 + \hat{u}^2) \\
\eta & = & \ln(1 + \hat{u}^2)
\end{array} \tag{27}
$$

where $0 \leq \hat{u} < 1$. An inner, or sheath solution, can be obtained assuming that the electron number density near the electrode is negligible. If the values of the independent variables at the wall are assumed to be known, then the solution has the form:

$$
\begin{array}{rcl}
\hat{x} & = & \frac{1}{3A^2} \left(2A\hat{u} + B\right)^{1/2} \left(A\hat{u} - B\right) - C \\
y & = & \hat{u}_w y_w/\hat{u} \\
\eta & = & (\hat{u}^2 - \hat{u}_w^2)/2 + \eta_w
\end{array} \tag{28}
$$

where,

$$
\begin{array}{rcl}
A & = & \hat{u}_w y_w/(q_0 \hat{R})^2 \\
B & = & \left(\eta_w'\right)^2 - 2A\hat{u}_w \\
C & = & \frac{1}{6A^2} \left(\eta_w'\right)^3 - \frac{B}{2A^2}\eta_w' - \hat{x}_w
\end{array} \tag{29}
$$
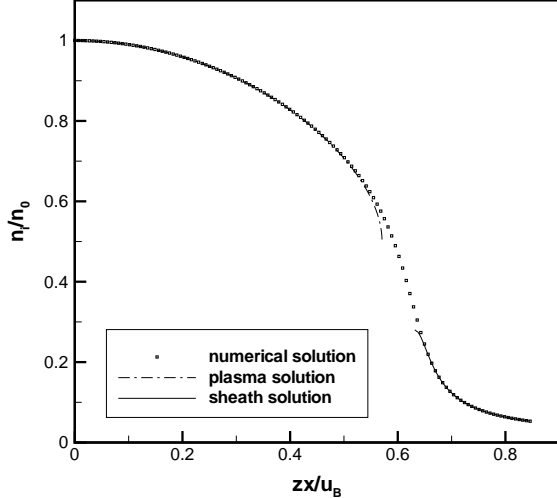
Figure 8: Ion number density predicted by analytical and numerical methods. Every fourth computational point shown. Neither analytical approximation is valid in the gap near $\hat{x} \approx 0.6$.

	Case A	Case B
p (mTorr)	0.44	1.00
T_e (eV)	2.4	0.5
n_0 (m^{-3})	9.8×10^{13}	4.4×10^{14}
ϕ_w (V)	-32.6	-32.1
λ_i (mm)	70	30

Table 1: Test conditions in the experiments of Oksuz and Hershkowitz.

and $-B/2A \leq \hat{u} \leq \hat{u}_w$.

Figure 8 compares the numerical solution obtained with PS3D with the inner and outer analytical solutions. The plasma (outer) solution is seen to be in excellent agreement with the full numerical solution over much of the domain. As the wall is approached from the plasma center, however, a region ($\hat{x} \lesssim 0.6$) is reached where quasi-neutrality is no longer a good approximation, and the plasma solution deviates from the numerical solution. Proceeding farther toward the wall, a singularity in the electric field for the plasma solution is reached at $\hat{u} = 1$.

An analogous situation occurs for the sheath (inner) solution. Near the wall, there is excellent agreement between the analytical and numerical solutions. Sufficiently far from the wall, however, a region ($\hat{x} \gtrsim 0.6$) is reached where the electron number density is no longer negligible. There the sheath solution begins to deviate from the full numerical solution. The electric field in the sheath solution becomes undefined closer to the center, where $\hat{u} < -B/2A$.

To validate the mathematical model, the computations were compared to a set of experiments carried out by Oksuz and Hershkowitz [32] in a multi-dipole argon plasma

generated by DC-biased hot filaments. The cylindrical test chamber was 350 mm in diameter and 400 mm in height. A 75 mm diameter stainless steel disk was positioned within the uniform portion of the plasma (about 190 mm in diameter and 330 mm high), at a location 100 mm from the sidewalls and 160 mm from the top of the test chamber. The plate was maintained at -30 V with respect to the grounded chamber walls. An emissive probe was traversed along the axis of the disk electrode to measure the plasma potential. Data were obtained at several working pressures; two cases that displayed a wide variation in relative length scales were selected for comparison with the computations. The corresponding experimental conditions are given in Table 1.

Figure 9 compares computational results with experimental data for the plasma potential. The reference potential has been shifted so that $\phi = 0$ at the plasma center, and the coordinate system has been selected so that $x = 0$ at the electrode surface and $x = R$ at the plasma center. There is some ambiguity in determining the location of the plasma center in the experiment: here we have taken $R = 125$ mm.

The agreement between computation and experiment is seen to be excellent in both cases. The sheath thickness is larger in Case A, corresponding to the larger Debye length in that case. Despite this close agreement, the details of the mathematical model need to be explored carefully in future work. In particular, three-dimensional inflow of ions from the far-field may be a more important source of ions in the presheath than direct ionization. Nevertheless, there is an excellent match between computation, theory, and experiment for this problem. It is fair to conclude that the computer code correctly implements the mathematical model, and that the mathematical model is a good fit to the experimental data.

3.2 Wind Tunnel Probe

A preliminary calculation was made of a case that combined bulk fluid flow, ion diffusion, and varying electric potential in a three-dimensional geometry. The test article selected was a small hemispherical body, intended to represent a probe mounted in a hypersonic wind tunnel.

The flow conditions were selected to correspond to recent experiments with plasma generation in a Mach 5 wind tunnel [33, 34]. In this facility, a typical stagnation pressure and temperature are $p_0 = 45$ kPa and $T_0 = 300$ K. For Mach 5 flow in the test section, the corresponding static pressure and temperature are about $p_\infty = 86$ Pa (0.65 torr) and $T_\infty = 50$ K. The probe diameter was taken to be 6 mm, with a corresponding Reynolds number of about $\mathrm{Re}_D = 4 \times 10^3$. Adiabatic wall conditions were assumed.

For the present calculations, the source terms in Eqs. (2)-(3) were turned off, so that the bulk flow affected the sheath, but the sheath did not affect the bulk flow. Although the code is designed to allow an arbitrary number of species, only one ion species (N_2^+) was assumed to be present, and the electrons were taken to be in Boltzmann equilibrium with the electric field. Frozen chemistry was also assumed. (These simplifications were used due to time constraints; they do not represent inherent limitations in the code.) All other features of the computer code were exercised in fully three-dimensional form, including viscosity, heat conduction, ion motion, electric forces, and ion-neutral collisions.

The computation was accomplished in two stages. First, the bulk gas flow only was computed, and the code was run until the flowfield converged. Next, the computed bulk
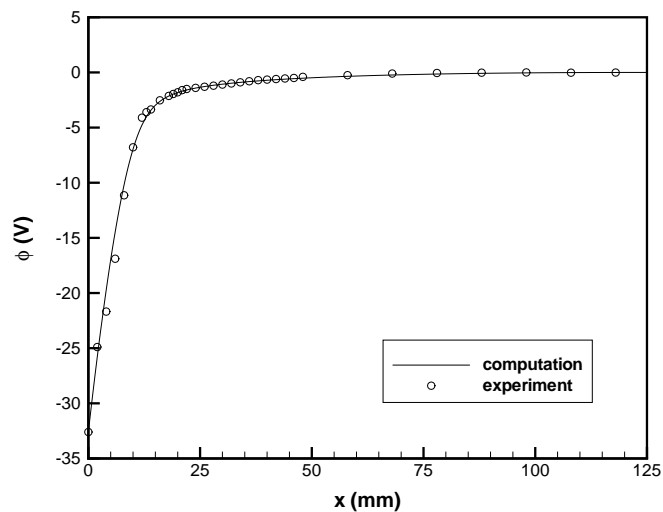
(a) Case A: $p = 0.44$ mTorr.
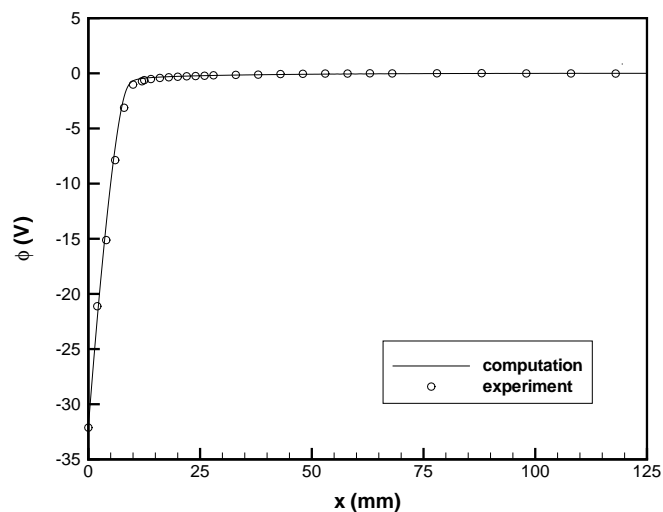
(b) Case B: $p = 1.0$ mTorr.

Figure 9: Comparison of computation and experiment.

(a) Computational mesh.　　　　　　　　(b) Density field.
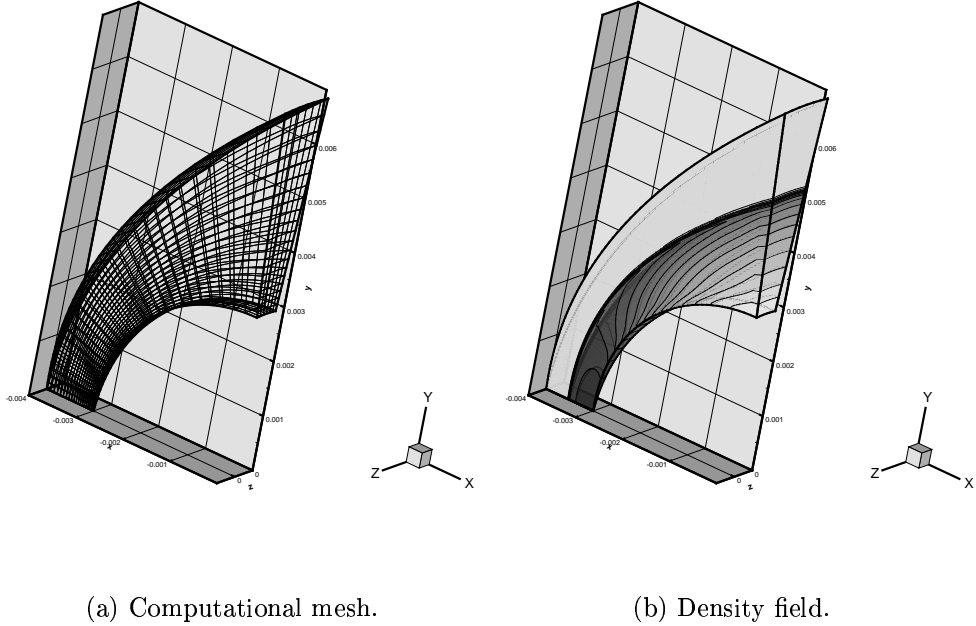
Figure 10: Numerical solution in three dimensions.

gas flow was taken as frozen, and the potential and ion diffusion equations were solved. The body surface was maintained at a potential of -50 V, with the freestream at ground (0 V). The freestream ion density was taken as $n_\infty = 1 \times 10^{17}$ m^{-3}, and the electron temperature was $T_e = 11600$ K (1 eV).

The computational mesh is shown in Fig. 10a, and a view of the three-dimensional density field for the bulk gas flow is shown in Fig. 10b. Every other grid line is shown along the streamwise direction and every fourth line along the wall-normal direction. The resolution was $61 \times 81 \times 7$ points along the streamwise, wall-normal, and circumferential directions ($i \times j \times k$), respectively. Exponential stretching was applied along the i- and j-directions, and the k-direction consisted of a 10° 'pie slice.'

The basic flow structure in the center plane is shown in Fig. 11. Figure 11a shows the pressure field. The results display the features of a typical hypersonic blunt body flow. The bow shock is evident as a sharp pressure upstream of the hemisphere. Due to the strong compression at Mach 5, the bow shock lies close to the body surface. The shock standoff at the centerline of $\Delta_s/R = 0.16$ corresponds closely to a standard correlation [23] for air flows, and the shock shape lies closely on a hyperbola fit to experimental data [35]. The viscous boundary layer is apparent near the body surface in the form of an alignment of the pressure contours along the wall-normal direction.

The corresponding electric potential field is shown in Fig. 11b. The potential varies significantly only in a thin layer near the body (electrode) surface; this layer corresponds to the plasma sheath. The sheath thickness is seen to grow around the circumference of the hemisphere in a manner similar to that of the fluid dynamic boundary layer.

15

(a) Pressure field. Contour interval 200 Pa.

(b) Electric potential. Contour interval 5 V.
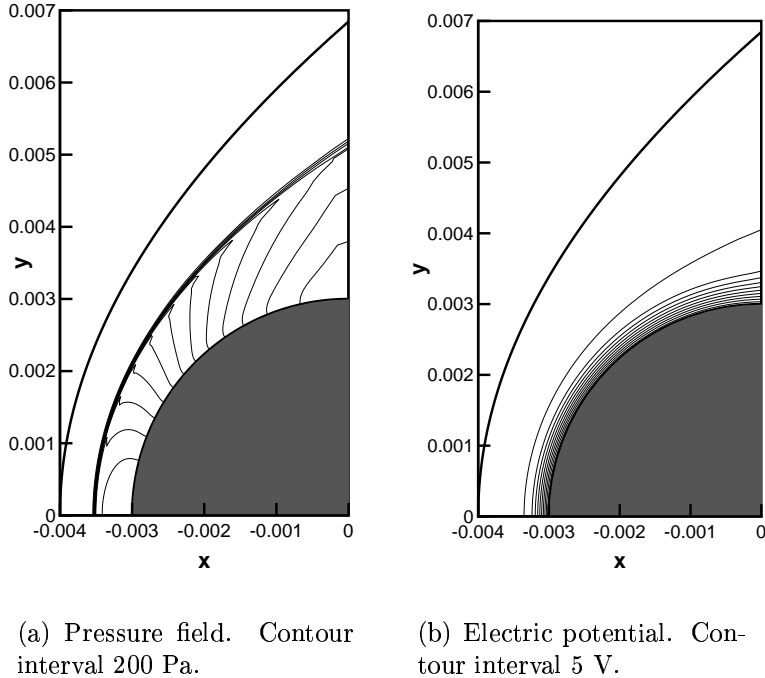
Figure 11: Numerical solution in center plane.

4   Glow Discharge

Many aerospace applications occur at relatively high density, and the model including ion inertia considered in §3 involves unnecessary computational expense. Under higher density conditions, ion inertia is negligible, and we apply a drift-diffusion model, using Eqs. (18) and (23). As an initial verification and exploration exercise, a set of calculations was carried out for a glow discharge in nitrogen. Fluid property data (mobility, diffusion coefficient, Townsend ionization coefficient, recombination coefficient) were obtained from Ref. [36]. A grid of $201 \times 3 \times 3$ points, clustered near the boundaries, was used. For these calculations, the pressure was fixed at 67 Pa (0.5 torr) and the temperature at 300 K everywhere, and a no-flow condition was imposed over the whole domain. The ion number density was taken to be zero on the anode, and the electron number density on the cathode was found from the relation $\Gamma_e = -\gamma \Gamma_i$, where $\gamma = 0.1$ is the secondary emission coefficient. The potential at the anode was taken to be zero, and the cathode potential was specified. Other quantities at the boundaries were determined by extrapolation. Uniformity was imposed in the y- and z-directions for all variables.

Figure 4 shows profiles of the number densities and potential for several cases: $V_c = -300$ V, -500 V, and -1000 V. The cathode is at the left and the anode is at the right. In each case, the cathode sheath is apparent on the left as a region relatively free of electrons, but with a high ion concentration. In the center is the quasi-neutral ($n_i \approx n_e$) positive column. At right is the anode sheath, which, in contrast to the cathode sheath, is distinguished by a depletion of ions relative to electrons. With increasing applied potential, the sheaths on both electrodes are seen to become thinner, and the maximum

16
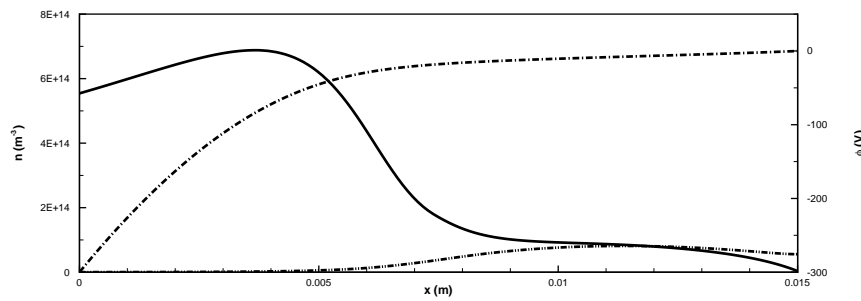
(a) Applied potential 300 V.
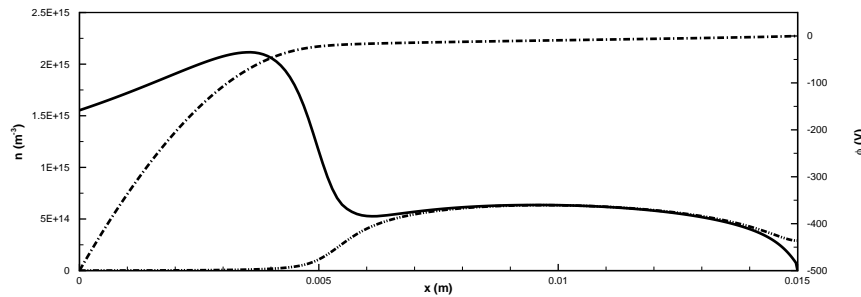
(b) Applied potential 500 V.
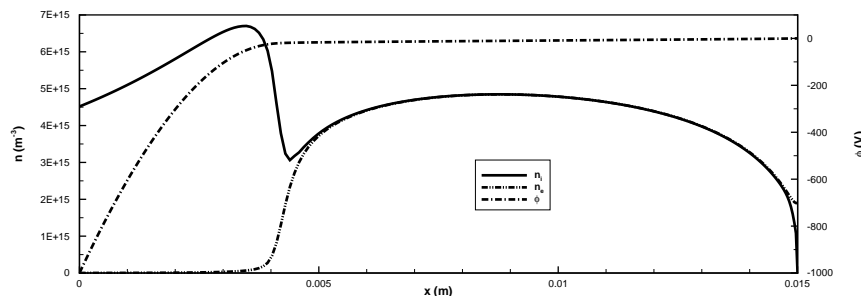
(c) Applied potential 1000 V.

Figure 12: Glow discharge solution for 0.5 Torr nitrogen.

in the ion concentration becomes higher with the corresponding increase in electric field strength in the cathode sheath.

In ongoing work, calculations are being performed for two-dimensional cases with an external circuit boundary condition. Gas heating is also being modeled.

5   Concluding Remarks

Over the past few years, we have developed two computer codes in order to investigate the feasibility of electromagnetic flow control. The magnetogasdynamics code `FDL3DI-mhd` solves the conservation laws for fluid flow in conjunction with a quasi-neutral model for electromagnetic effects, whereas the plasma sheath code `PS3D` includes the effects of significant charge separation.

The magnetogasdynamics code includes options for both a high and low magnetic Reynolds number model. Although the higher Reynolds number regime is interesting from a scientific perspective, magnetic field distortion is expected to be small for most aerospace applications. For practical problems, it is probably not worth the computational expense of solving the magnetic induction equation. It may, however, be of interest to estimate field distortion from a converged low magnetic Reynolds number solution.

The plasma sheath code `PS3D` also includes options for different physical models for high and low pressure regimes. The higher pressure, diffusion model is more appropriate for flow control applications because only weak aerodynamic forces can be generated at low pressure. The low pressure model is primarily of interest for modeling plasma generation and probe response.

We have carried out extensive code verification of `FDL3DI-mhd` against available analytical solutions. Detailed experimental data are needed before acceptable code validation can be completed. The sheath code is less well developed, but preliminary validation and verification work has been carried out.

In ongoing work, we are endeavoring to improve the fidelity of the physical model incorporated into the various versions of the two codes, and to explore electromagnetic flow control techniques that have potential aerospace applications. In particular, work is focused on incorporating finite rate chemistry and an accurate electrical conductivity model.

6   Acknowledgments

References

[1] A. R. Kantrowitz. A survey of physical phenomena occurring in flight at extreme speeds. In A. Ferri, N. J. Hoff, and P. A. Libby, editors, *Proceedings of the Conference on High-Speed Aeronautics*, pages 335–339. Polytechnic Institute of Brooklyn, New York, 1955.

[2] E. P. Gurijanov and P. T. Harsha. Ajax: New directions in hypersonic technology. AIAA Paper 96-4609, American Institute of Aeronautics and Astronautics, November 1996.

[3] G. Palmer. Magnetic field effects on the computed flow over a Mars return aerobrake. *Journal of Thermophysics and Heat Transfer*, 7(2):294–301, 1993.

[4] J. H. Mullen, R. J. Kashuba, J. D. Kelley, P. Vogel, P. Smereczniak, and K. Chadwick. Recent progress in plasma aerodynamics. In W. L. Bain, editor, *Proceedings of the 2nd Workshop on Weakly Ionized Gases*, pages 233–251. American Institute of Aeronautics and Astronautics, Reston, VA, 1998.

[5] E. Josyula and W. Bailey. Vibrational population enhancement in nonequilibrium hypersonic flows. AIAA Paper 2003-3778, American Institute of Aeronautics and Astronautics, Reston, VA, 2003.

[6] M. A. Lieberman and A. J. Lichtenberg. *Principles of Plasma Discharges and Materials Processing*. J. Wiley, New York, 1994.

[7] J.-P. Boeuf and A. Merad. Fluid and hybrid models of non equilibrium discharges. In P. F. Williams, editor, *Plasma Processing of Semiconductors*, pages 291–319. Kluwer, Dordrecht, the Netherlands, 1997.

[8] A. R. Choudhuri. *The Physics of Fluids and Plasmas: An Introduction for Astrophysicists*. Cambridge University Press, Cambridge, 1998.

[9] E. H. Holt and R. E. Haskell. *Foundations of Plasma Dynamics*. Macmillan, New York, 1965.

[10] S. R. Seshadri. *Fundamentals of Plasma Physics*. Elsevier, New York, 1973.

[11] J. Poggie and D. V. Gaitonde. Magnetic control of hypersonic blunt body flow. AIAA Paper 2000-0452, American Institute of Aeronautics and Astronautics, Reston, VA, January 2000.

[12] V. J. Rossow. On flow of electrically conducting fluids over a flat plate in the presence of a transverse magnetic field. NACA Report 1358, National Advisory Committee for Aeronautics, Washington, DC, March 1957.

[13] E. L. Resler and W. R. Sears. The prospects for magneto-aerodynamics. *Journal of the Aeronautical Sciences*, 25(4):235–245,258, 1958.

[14] R. W. Ziemer and W. B. Bush. Magnetic field effects on bow shock stand-off distance. *Physical Review Letters*, 1(2):58–59, 1958.

[15] C. du P. Donaldson and M. J. Brunner. Discussion of a self-powered MHD control for re-entry vehicle application. In N. W. Mather and G. W. Sutton, editors, *Engineering Aspects of Magnetohydrodynamics: Proceedings, 3rd Symposium*, pages 559–577. Gordon and Breach Science Publishers, New York, 1964.

[16] S. Kranc, R. W. Porter, and A. B. Cambel. Electrodeless magnetogasdynamic power during entry. *Journal of Spacecraft and Rockets*, 4(6):813–815, 1967.

[17] M. F. Romig. The influence of electric and magnetic fields on heat transfer to electrically conducting fluids. In T. F. Irvine and J. P. Hartnett, editors, *Advances in Heat Transfer*, volume 1, pages 267–354. Academic Press, New York, 1964.

[18] J. Poggie and D. V. Gaitonde. Computational studies of magnetic control in hypersonic flow. AIAA Paper 2001-0196, American Institute of Aeronautics and Astronautics, January 2001.

[19] J. Poggie and D. V. Gaitonde. Magnetic control of flow past a blunt body: Numerical validation and exploration. *Physics of Fluids*, 14(5):1720–1731, 2002.

[20] W. B. Bush. Magnetohydrodynamic-hypersonic flow past a blunt body. *Journal of the Aero/Space Sciences*, 25(11):685–690,728, 1958.

[21] J. F. Coakley and R. W. Porter. Time-dependent numerical analysis of MHD blunt body problem. *AIAA Journal*, 9(8):1624–1626, 1971.

[22] W. B. Bush. The stagnation-point boundary layer in the presence of an applied magnetic field. *Journal of the Aerospace Sciences*, 28(8):610–611,630, 1961.

[23] A. Ambrosio and A. Wortman. Stagnation point shock detachment distance for flow around spheres and cylinders. *ARS Journal*, 32(2):281, 1962.

[24] J. A. Fay and F. R. Riddell. Theory of stagnation point heat transfer in dissociated air. *Journal of the Aeronautical Sciences*, 25(2):73–85,121, 1958.

[25] R. W. Porter and A. B. Cambel. Hall effect in flight magnetogasdynamics. *AIAA Journal*, 5(12):2208–2213, 1967.

[26] J. T. Lineberry, V. A. Bityurin, and A. N. Bocharov. MHD flow control studies: Analytical study of MHD flow interaction around a right circular cylinder in transverse hypersonic flow. AIAA Paper 2002-2112, American Institute of Aeronautics and Astronautics, Reston, VA, May 2002.

[27] J. Poggie and D. V. Gaitonde. Electrode boundary conditions in magnetogasdynamic flow control. AIAA Paper 2002-0199, American Institute of Aeronautics and Astronautics, January 2002.

[28] J. Poggie, D. V. Gaitonde, and N. Sternberg. Numerical simulation of plasma sheaths in aerodynamic applications. AIAA Paper 2002-2166, American Institute of Aeronautics and Astronautics, May 2002.

[29] J. Poggie and N. Sternberg. Numerical simulation of electrode sheaths in a magnetized plasma. AIAA Paper 2003-0359, American Institute of Aeronautics and Astronautics, January 2003.

[30] V. A. Godyak and N. Sternberg. Smooth plasm-sheath transition in a hydrodynamic model. *IEEE Transactions on Plasma Science*, 18(1):159–168, 1990.

[31] N. Sternberg and V. A. Godyak. Approximation of the bounded plasma problem by the plasma and the sheath models. *Physica D*, 97:498–508, 1996.

[32] L. Oksuz and N. Hershkowitz. First experimental measurements of the plasma potential throughout the presheath and sheath at a boundary in a weakly collisional plasma. *Physical Review Letters*, 89(14):145001–1–145001–3, 2002.

[33] J. A. Menart, J. Shang, S. Henderson, A. Kurpik, R. L. Kimmel, and J. R. Hayes. Survey of plasmas generated in a mach 5 wind tunnel. AIAA Paper 2003-1194, American Institute of Aeronautics and Astronautics, January 2003.

[34] J. S. Shang, R. L. Kimmel, J. R. Hayes, and C. Tyler. Performance of a low-density hypersonic magneto-aerodynamic facility. AIAA Paper 2003-0329, American Institute of Aeronautics and Astronautics, January 2003.

[35] F. S. Billig. Shock-wave shapes around spherical- and cylindrical-nosed bodies. *Journal of Spacecraft and Rockets*, 4(6):822–823, 1967.

[36] S. T. Surzhikov and J. S. Shang. Glow discharge in magnetic field. AIAA Paper 2003-1054, American Institute of Aeronautics and Astronautics, 2003.

NUMERICAL FULLY COUPLED EXAMPLE-MHD SCRAMJET

H. Bottini*, <u>C. Bruno</u>**
* Aerospace Engineer, Department of Mechanics and Aeronautics, University of Rome "La Sapienza", Rome, Italy
e-mail:hbottini@libero.it
** Associate Professor, Department of Mechanics and Aeronautics, University of Rome "La Sapienza", Rome, Italy
e-mail:bruno@dma.ing.uniroma1.it

1.   Introduction

Beginning in the '90s, in the Russian and Ukrainian literature, articles appeared about a new long-range aircraft cruising at hypersonic speeds, named AYAKS (AJAX). Its propulsion system employed a Magneto-Hydrodynamic scramjet engine (MHD scramjet) that significantly increased the performance of and decreased the size of this hypersonic vehicle.
The article "Space wings of Russia and the Ukraine", in the September 1990 magazine *Echoes of the planet/Aerospace*, states that the project originates in the State Hypersonic System Scientific Research Enterprise (GNIPGS) in Saint Petersburg, headed by Vladimir Freistadt.
The article goes on to state that the AJAX project be carried on by cooperation of industrial enterprises, Technical Institutes, the VPK (Military Industrial Commission) and the RAN (Russian Academy of Sciences).
It is clear in the literature that AJAX is primarily a global range hypersonic cruise vehicle with the potential as a space launcher.
Through these articles and discussions with individuals, the following elements were identified to constitute the AJAX system:

- Reduction of the vehicle total drag by the injection of cold plasma at the vehicle nose
- Increase in the combustion volume and efficiency within the engine by means related to plasma injection of material ahead of the fuel injection struts.
- Reforming of hydrocarbon fuel and water into gaseous hydrogen and carbon monoxide

and, finally,

- Bypass of a portion of the free stream kinetic energy around the combustion chamber to reduce the entropy rise of air diffusion and combustion process via a coupled MHD generator-accelerator system
- Ionization of the flow entering the engine to permit the MHD generator-accelerator system to function with realistic magnetic field intensities and flow velocities present within the engine module.

The propulsion system of AJAX consists in a Magnetoplasma-chemical scramjet (in short, MHD scramjet).
The literature identifies four aircraft of this type: NEVA-25 and NEVA-26 Hypersonic Airplanes, with ranges 4800 to 11000 Km distant, and NEVA-23 and NEVA-24 Hypersonic Airplanes, with ranges 10000 to 19000 Km.
From this brief historical introduction, it should be evident the degree of the technologies involved in this propulsive solution, such as plasma, nuclear, and aerospace technology, and also the substantial interest for military purposes stemming from this propulsion system. Hence, in

the end, the scarcity or even the lack of details about many aspects of this engine in its following description is understandable. Some of the earlier attempt at understanding how AYAKS might work are in….

The energy bypass of a magneto-hydrodynamic flow passing through an electromagnetic field consists in extracting part of the total enthalpy from the airflow ahead of the combustor in order to achieve efficient and practical combustion. The same amount of extracted total enthalpy is put back into the flow just downward the combustor, so that combustion can take place and the flow does not lose [the extracted amount of] its total enthalpy.

Since extraction of the total enthalpy will result in production of electromagnetic energy, the device in which this extraction takes place is called MHD-generator or, shortly, generator. Similarly, the device where the energy is put back is called MHD-accelerator or, shortly, accelerator.

Figure 1 shows a simplified scheme of the MHD scramjet as conceptually outlined in the present work (i.e., using a 1-D approximation); **D**E_e is the energy bypassed.

The main tasks of such MHD scramjet design are:

- Providing airflow ionization to permit an appreciable MHD effect
- Providing an effective electromagnetic field strength
- Managing the amount of bypassed energy

The purpose of this lecture is to try to predict the performance of a MHD SCRJ by implementing modeling that couples thermodynamics and electromagnetic (e.m.) theory in as rigorous manner as possible, given the status of our present knowledge. Attempts, even recent [Riggins, ref. [5], have focused on classical thermodynamic approaches; in these, for instance, e.m. energy is not considered in the total energy conservation equation. It is hoped that this lecture may be a step toward reaching the ultimate goal of developing a fully coupled thermodynamic and e.m. SCRJ model.

Some conceptual solutions and technical approaches to the three main aspect of a MHD SCRJ will be now briefly presented.

1.1. Airflow ionization

Suggestion on how to ionize inlet air to a sufficiently high electric conductivity (σ= 40- 100 mho/m) are all based on collisions with high energy particles, including neutron[8], electrons[9], and alpha.

Seeding the air with alkaline metals is also possible[10], but is also impractical in hypersonics because of the extra mass to be carried on board and possible unwanted effects in the stratosphere.

Neutron sources exist (e.g. in Russia) that can be triggered in such a way as to reach neutron fluxes comparable with those in a nuclear reactor [Preles,1997, personal communication]. Neutron energy may be realistically assumed to be about 2 MeV average, with a rather broad energy spectrum. Neutron case ionizes air via four main mechanism: 1, elastic collision with O_2 and N_2, where electrons are stripped off due to the neutron energy>>ionization potential, the nuclei recoiling with energy $\approx$ 0(KeV); 2, inelastic collision; 3, inelastic transmutation of O_2 and N_2 nuclei into a different nucleus (emitting an electron, deuteron or other neutron); and, 4, inelastic collisions with a second nucleus, followed by absorption of the neutron by the nucleus and release of a **g** photon with energy $\approx$ O(1 MeV) (this mechanism takes place using slow neutrons).

The most likely mechanism are the first and fourth; the **g** rays released can ionize atoms and molecules by the photoelectric effect, by Compton effect and by forming e^--e^+ pairs [Ref.: Segre, E. (1977), "Nuclei and Particles", The Benjamin/Cummings Publ. Co., Inc., Menlo Park, pp 54-55].

Ionization by electron beams has also been investigated by the research team at Princeton University[9]. This strategy is somewhat difficult to implement in hypersonics, and operates at much lower particle energy, but its performance is still interesting.

The third ionization mechanism is based on alpha particles (doubly charged Helium nuclei) emitted by available industrial isotopes[11,12]. Conceptually, a $O(10^{-3}$ mm) layer of an isotope producing alpha particles of energy 4-5 MeV (e.g. Curium-244) may coat the surface(s) of the air inlet. The alpha particles released isotropically collide with O_2 and N_2 in the air producing electrons that will increase electric conductivity. As in the case of neutrons, there are also here several mechanisms at work.

1.2. Electromagnetic field strength

In order to produce the magnetic induction required, the choice of cryogenic superconducting magnets seems to be the only effective one. Cryogenic cooling by liquid hydrogen stored in the vehicle as fuel for the scramjet, or by other cryofluid appears feasible, for instance. Using High Temperature Super Conduction (HTSC) materials such as BSCCO 2212, the total (generator +accelerator) magnet weight was estimated[7] to be 1310 Kg.

About the electrode design little is known: the electrodes material is reported to be a ceramic composite material (maybe a perovskite).

1.3. Management and use of the energy bypassed

Details of the energy bypass system are not known, but there is ground to suppose that the energy produced within the generator does more than simply accelerate the exhaust flow: it is supposed also to drive directed energy devices.

2. Equations set for the MHD Scramjet model

The set of equations constituting the simplified engine model is now illustrated. The equations are the product of a systematic reexamination by Giordano[1] of past work about magneto-hydrodynamics, completed with some personal innovative ideas. This study was carried out in the context of a research activity initially motivated by renewed interest in magneto-hydrodynamics applied to spacecraft thermal protection systems during LEO (and planetary) reentry. The aim of this Section is to formulate a consistent set of governing equations in open form, apt to describe the physics of hypersonic, ionized gas mixture in the presence of electromagnetic fields.

Polarization and magnetization are not considered in this study. In fact, the inclusion of polarization and magnetization effects in the Maxwell's equations is straightforward, but heavy complications on the fluid-dynamics side arise. According to Giordano[1], it is best to avoid these complications at this stage of investigation, and face them after reaching a solid understanding of the coupling between fluid-dynamics and the pure (imposed) electromagnetic field. Hence, the assumption of no medium polarization and magnetization.

To be true, this assumption mat turn out to be realistic on physical grounds, since the medium polarization and magnetization consist in the orienting of the gas molecules, in the fashion of electric and magnetic dipoles, respectively; molecular collisions could hinder it, or even make it negligible. Therefore, a comparison between the mean collision frequency and the polarization and magnetization time should be made to check the physical validity of this assumption. This, among others, is an open question arising from the fact that electromagnetic properties of gases have not yet been studied with the same attention as solid state electromagnetic properties, for which abounds literature.

Radiative heat transfer (RHT) is also neglected. In principle, RHT <u>could</u> be implicit in the treatment in [1], provided the properties of continuum were replaced, or complemented, by those of atoms and molecules, so that the bound-bound, free-bound, and free-free electron- matter contributions to RHT could be accounted for.

Finally, it must be noted that the 1-D topology does away with the need of implementing BCs, that still need to be rigorously formulated.

The equations in [1] are:

$$\frac{\partial \rho}{\partial t} + \nabla \cdot (\rho \underline{V}) = 0 \qquad (1)$$

$$\frac{\partial (\varepsilon_0 \underline{E} \times \underline{B} + \rho \underline{V})}{\partial t} = -\nabla \cdot \left(\rho \underline{V}\underline{V} - \underline{\underline{\tau}} - \underline{\underline{\tau}}_M \right) \quad (2)$$

$$\frac{\partial \left(\frac{\rho V^2}{2} \right)}{\partial t} + \nabla \left(\frac{\rho V^2}{2} \underline{V} \right) = \nabla \cdot \left(\underline{\underline{\tau}} \cdot \underline{V} \right) - \underline{\underline{\tau}} : \nabla \underline{V} + \rho_c \underline{V} \cdot \underline{E} - \underline{J}_Q \cdot \left(\underline{V} \times \underline{B} \right) \quad (3)$$

$$\frac{\partial}{\partial t} \left[\frac{\varepsilon_0}{2} \left(E^2 + c^2 B^2 \right) \right] = -\nabla \cdot \left(\varepsilon_0 c^2 \underline{E} \times \underline{B} \right) - \underline{J} \cdot \underline{E} \quad (4)$$

$$\frac{\partial}{\partial t} \left[\rho e_m + \frac{\varepsilon_0}{2} \left(E^2 + c^2 B^2 \right) \right] = -\nabla \cdot \left[\rho e_m \underline{V} + \underline{J}_U - \underline{\underline{\tau}} \cdot \underline{V} + \varepsilon_0 c^2 \underline{E} \times \underline{B} \right] \quad (5)$$

Equation (1) is the well-known mass conservation equation.

To the extent that the electromagnetic field is attached to space and not to matter (i.e. air), the formulation of its governing equations and of the equations governing matter can be carried on independently. The results of both these formulations are then combined to achieve the set of equations describing the coupling between matter and electromagnetic field (equations (2) to (5)).

Equation (2) is the total momentum balance equation. The total momentum $\left(\varepsilon_0 \underline{E} \times \underline{B} + \rho \underline{V} \right)$ is the sum of the matter-momentum $\left(\rho \underline{V} \right)$ and the electromagnetic-momentum $\left(\varepsilon_0 \underline{E} \times \underline{B} \right)$. $\underline{\underline{\tau}}$ is the Navier-Stokes stress tensor, while

$$\underline{\underline{\tau}}_M = \varepsilon_0 \left[\underline{E}\underline{E} - \frac{E^2}{2} I \right] + \varepsilon_0 c^2 \left[\underline{B}\underline{B} - \frac{B^2}{2} I \right]$$

is the Maxwell stress tensor, with the underlined terms standing for dyads and *I* for the unit tensor.

Equation (3) is the kinetic-energy conservation equation, which is not independent since it is derived from equation (2). ρ_c is the electric-charge density , and $\underline{J_Q}$ is the conduction-current density vector[1].

Equation (4) is the electromagnetic energy conservation equation, where ε_0 is the dielectric constant of vacuum (remember no polarization neither magnetization are accounted for), c is the light speed in vacuum, and $\underline{J}$ is the current density vector.

Finally, equation (5) is the total energy $\left(\rho e_m + \dfrac{\varepsilon_0}{2}\left(E^2 + c^2 B^2\right)\right)$ conservation equation, where $e_m = u_{en} + V^2/2$ is the specific energy of matter (i.e. associated with the mass), and $\underline{J_U}$ the diffusive flux comprised of all the diffusive effects on the total energy.

At this point, the set of equations above will be simplified to a form apt to model the MHD scramjet under analysis. The aim is to produce a simple engine model, i.e. a model that does not need [yet] computational fluid-dynamics, but it is described just by algebraic equations. This model can be seen as a 1-D engineering tool to help in preliminarily designing the MHD-influenced portions of a scramjet. Hence, the following assumptions have been made:

- 1-D flow
- Isentropic inlet and nozzle
- Constant thermodynamic properties
- Energy extracted in the MHD generator completely put back in the flow inside the MHD accelerator
- Frictionless flow within the MHD devices
- Shockless flow

This idealized MHD scramjet model is presented in Figure 1.
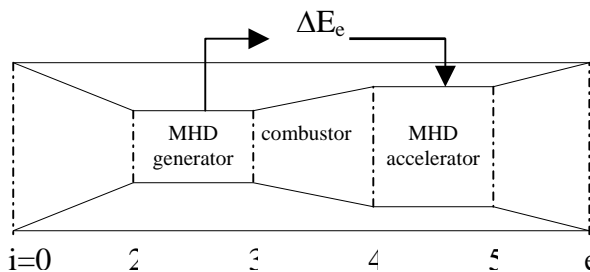
Figure 1

With the above assumptions equations (1) to (5) reduce to:

$$\frac{d(\rho u)}{dx} = 0 \tag{6}$$

$$\frac{d}{dx}\left(\rho u^2 + p + \frac{\varepsilon_0}{2}(E_y^2 + c^2 B_z^2) \right) = 0 \tag{7}$$

$$\rho u \frac{d}{dx}\left(\frac{u^2}{2} \right) = -u \frac{dp}{dx} + J_{Qy} u B_z \tag{8}$$

$$J_{Qy}E_y = -\frac{d}{dx}\left(\varepsilon_0 c^2 E_y B_z\right) \qquad (9)$$

$$\frac{d}{dx}\left(\rho u h_t + \varepsilon_0 c^2 E_y B_z\right) = 0 \qquad (10)$$

with

$$\underline{J}_Q = \sigma\left[E_y - uB_z\right]\hat{j} = J_{Qy}\hat{j} \qquad (11)$$

and
$$p \cong \rho R T \qquad (12)$$

Equation (10) is derived from equation (5) by introducing the definition of total enthalpy.
Equation (11) is the equation for the conduction-current density vector which, with the assumptions made, reduces to its component on the y-axis. The set is completed by the entropy balance equation

$$\rho u \frac{ds}{dx} = \frac{J_{Qy}}{T}\left(E_y - uB_z\right) \qquad (13)$$

stemming from the following general entropy transport equation for a fluid

$$\frac{\partial(\rho s)}{\partial t} + \nabla \cdot \left(\rho s \underline{V}\right) = -\nabla \cdot \underline{J}_S + \dot{s}_V \qquad (14)$$

where $\underline{J}_S$ is the entropy diffusive flux, and $\dot{s}_V$ is the entropy-production rate.

Equation (13) states that, with the assumptions made, in the presence of an electro-magnetic field the entropy is not constant, but it increases because of the Joule effect represented by the conduction-current density J_Q.

Note from equations (7),(9), and (10) that, if E_y and B_z were both constant along x, there would be no electromagnetic effect on the flow.

The E_y and B_z variables are the <u>total</u> electric field and the <u>total</u> magnetic field, respectively i.e., the <u>sum</u> of the electromagnetic field applied to the flow inside the MHD devices (B_{app}, E_{app}) and of the electromagnetic field produced by the electrically charged flow itself (B_p, E_p, where the subscript p stands for plasma). In other words,

$$\underline{B}_z = \underline{B}_{tot} = \underline{B}_{app} + \underline{B}_p \quad (15)$$
$$\underline{E}_y = \underline{E}_{tot} = \underline{E}_{app} + \underline{E}_p \quad (16)$$

Solving the Maxwell's equations <u>just</u> for the plasma electromagnetic field inside both the MHD generator and accelerator one can obtain B_p and E_p, and, from equation (16) and (15), also B_{app} and E_{app}. These are the electromagnetic field quantities to impose on the cold plasma to drive an effective MHD interaction, hence are the most important values from the designer point of view.

As shown in [7],this approach yields the conclusion that the plasma is globally neutral. The set of equations allows a certain freedom in choosing, for instance, B_{app}, and E_{app}. This fact can be exploited as shown ion Section 3.2 and 3.3.

The trends of the total, applied, and plasma magnetic induction within the MHD generator and MHD accelerator will be presented in the following.

To simplify the present analysis, it will be assumed from now on that the plasma-generated magnetic induction as well as the total electromagnetic field is zero outside the MHD devices[2].

An interesting aspect of the interaction between the MHD SCRJ flowfield and its electromagnetic field can be already seen by introducing in (7) the following sum

$$\bar{p} = p + \frac{\rho u^2}{2}$$

Equation (7) can be rearranged as

$$\frac{d}{dx}\left(\frac{\rho u^2}{2} + \bar{p} + \frac{\varepsilon_0}{2}(E_y^2 + c^2 B_z^2) \right) = 0 \qquad (17)$$

where $\frac{\rho u^2}{2}$ is the flow kinetic energy <u>per unit volume</u>, and $\frac{\varepsilon_0}{2}(E_y^2 + c^2 B_z^2)$ is the electromagnetic energy <u>per unit volume</u>. Since the purpose of MHD devices is to convert electromagnetic energy into kinetic energy and vice versa, the first differential term and the third differential term in (7) cancel each other yielding to the conclusion that the sum of static pressure and kinetic energy per unit volume <u>is constant within the MHD devices</u>. In other words, if we consider that static pressure describes the macroscopic effects of the motion of the molecules constituting the gas, the interaction between the MHD flow and the electromagnetic field transfers <u>completely</u> kinetic energy ($\rho u^2/2$) into internal energy and, ultimately, increases pressure. Numerical calculations of the flow inside the MHD generator and accelerator models confirm this conclusion [6].

3. MHD Scramjet model

In this Section, first, the electric conductivity evaluation is presented, and then the MHD generator, combustor, and MHD accelerator models are illustrated. For brevity's sake and also because of other considerations, the MHD generator and accelerator models do not include the detailed derivation, from Section 1 set of equations, of the expressions for the fluid-dynamic and electromagnetic variables(see ref.[6]). Their trends, instead, are shown by Figures 7 to 12, typifying the potentialities of both devices. These Figures are commented and complemented by the basic assumptions made for the models, by constraints on the electromagnetic variables also due to the nature of the model electromagnetic equations, and, finally, by the results. Remember that inlet and nozzle are assumed to be isentropic devices with zero electromagnetic field, hence the flowfield within both of them are solved by the customary isentropic flow equations.

Following the MHD scramjet model in Figure 1, the inlet entrance area is assumed $=0.6$ m^2, the inlet exit to entrance area ratio (A_2/A_i) $=1/20$[3], and the engine overall exit to entrance area ratio is assumed $=1.2$.

To analyse the MHD generator and accelerator, it is useful to introduce the parameter η:

$$\eta = \frac{uB_z}{E_y} \qquad\qquad (17)$$

In (17) uB_z is the induced electric field, i.e. the electric field produced by the Lorentz force, which pulls the positive and negative charged particles away from each other creating an electrostatic potential in the space between them, i. e., an electric field.

The denominator E_y, is the electric field produced by the charged particles constituting the cold plasma plus the electric field applied to the plasma itself. Since in the present analysis the plasma is globally neutral, E_y coincides with the applied electric field.

In conclusion, with the assumptions made, the electric field within the MHD generator and accelerator is the vector sum of the applied electric field and the induced electric field, as sketched in Figure 2 in the next page. This Figure shows the MHD device model as assumed in the present analysis, that is, a simple constant-section duct with a negative electrode as upper surface, and a positive electrode as lower surface. Between these two surfaces the applied electric field (E_y) acts on the cold plasma flowing-through. This flow of charged particles, perpendicular to the magnetic induction, produces the induced electric field (uB_z).
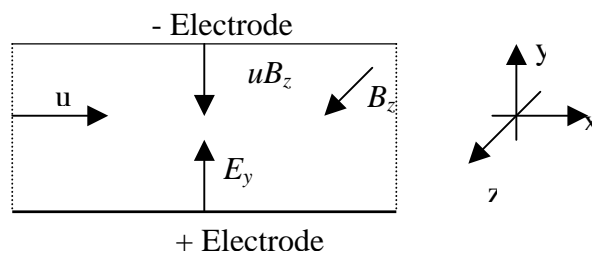
Figure 2 Sketch of a MHD device

3.1. Electric conductivity evaluation

The electric conductivity (σ) needed depends also on the possibility of getting combustor entrance Mach number and temperature enabling an effective combustion.

The maximum allowable values for the combustor entrance Mach number and temperature are assumed to be $M_{3max}= 0.38 \cdot M_0$ and $T_{3max} \in [1440\text{-}1670]K^{[4]}$.

Figure 3 shows the temperature at the MHD generator exit (i.e. at the combustor entrance) as a function of the electric conductivity (σ) for three flight Mach numbers.
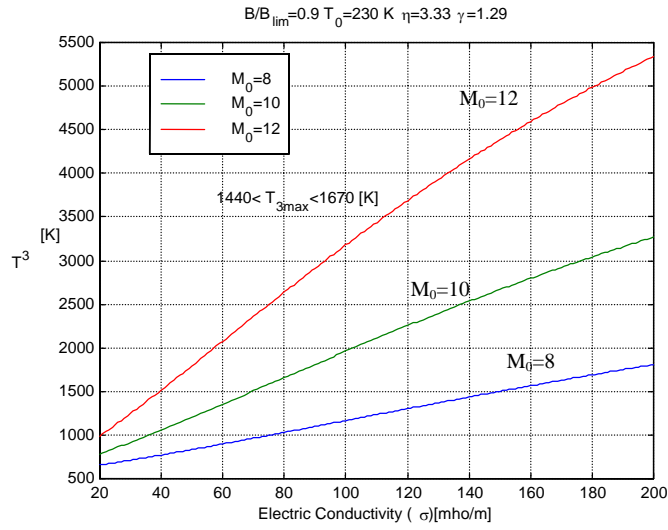
Figure 3

Next page Figure 4 shows the Mach number at the MHD generator exit as a function of the electric conductivity (σ) for three flight Mach numbers.
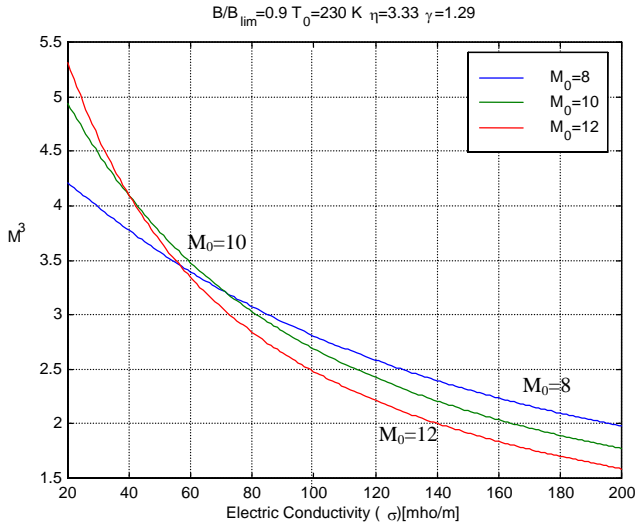
Figure 4

Provided that the highest allowable combustor entrance Mach number is $M_{3max}= 3$ for $M_0=8$, $M_{3max}=3.8$ for $M_0=10$, and $M_{3max}=4.56$ for $M_0=12$, and the maximum allowable temperature is in the range above mentioned, comparison between Figures 3 and 4 provides the following ranges for σ:

$$M_0=8 \quad 85<\sigma<180 \text{ mho/m}$$
$$M_0=10 \quad 50<\sigma<80 \text{ mho/m}$$
$$M_0=12 \quad 35<\sigma<45 \text{ mho/m}$$

Since high electric conductivity is purportedly difficult to achieve in real conditions, here low σ values chosen to perform the calculations are those in the lower range:

$$M_0=8 \quad \sigma=90 \text{ mho/m}$$
$$M_0=10 \quad \sigma=60 \text{ mho/m}$$
$$M_0=12 \quad \sigma=40 \text{ mho/m}$$

Note that the range of usable electric conductivity values narrows with the flight Mach number. This is due to the fact that the combustor entrance Mach number sets the lower limit of the σ range, decreasing with the flight Mach number, and thus reducing also the lower limit. The upper limit is set by the maximum allowable temperature, which decreases with the flight Mach number M_0 faster than M_3, since T_3 increases rapidly with M_0.

3.2. MHD generator model

Introduce now the parameter η_g of (17) (the subscript 'g' stands for generator) in the kinetic-energy balance equation (8), and in the electromagnetic energy balance equation (9). Then the condition for which equation (8) shows a decrease of kinetic energy, and equation (9) an increase of electromagnetic energy, is

$$1-\eta_g=(E_y-uB_z)/E_y<0,$$

hence $\eta_g>1$ to meet this condition.

The parameter η_g is assumed constant within the MHD generator and equal to 3.33 as in [2]. The reason is that a constant η_g obtains simple algebraic expressions from the set of differential equations used to describe the MHD scramjet: this is why it has been assumed constant.

Assume also the following trend of the total magnetic induction within the MHD generator:

$$B_z = \frac{Bu_2}{u} \qquad (18)$$

where B is the magnetic induction amplitude and u_2 is the speed at the exit of the inlet. It follows

$$E_y = \frac{u}{\eta_g}\frac{Bu_2}{u} = \frac{Bu_2}{\eta_g} = const$$

From the above assumption the expressions for speed, density, pressure, temperature, and total enthalpy are derived.

Within the MHD generator the flow speed decreases, since kinetic energy is transformed in electromagnetic energy. Pressure, instead, increases, since the Joule effect raises the internal energy. Imposing

$$\frac{dp}{dx} > 0$$

the following condition for the magnetic induction amplitude B must be met:

$$B < \sqrt{\frac{(\rho u)u_2}{\varepsilon_0 c^2 \left(1-\alpha L_g\right)^3}} = B_{\text{lim}}$$

showing that B depends on flight conditions (ρu), on the geometry inlet (u_2), electric conductivity (σ), and on MHD generator length (L_g).

Figure 5 shows the flow speed non-dimensionalized using the MHD generator entrance speed value (u_2), vs. the x distance along the generator.
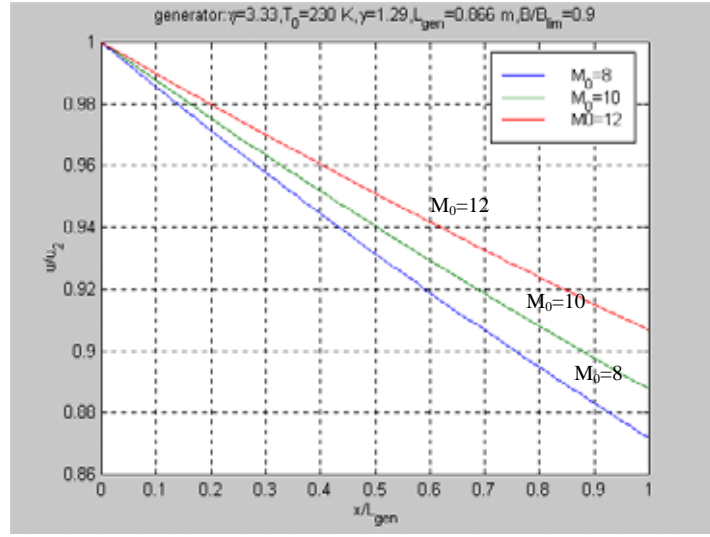
Figure 5

The speed decreases by 9 to 13 percent of the MHD generator entrance speed. This decrease is inversely proportional to the flight Mach number.

Figure 6 shows the density non-dimensionalized using the MHD generator entrance density. At the MHD generator exit the density rises by 10 to 15 percent. This ratio is also inversely proportional to the flight Mach number.
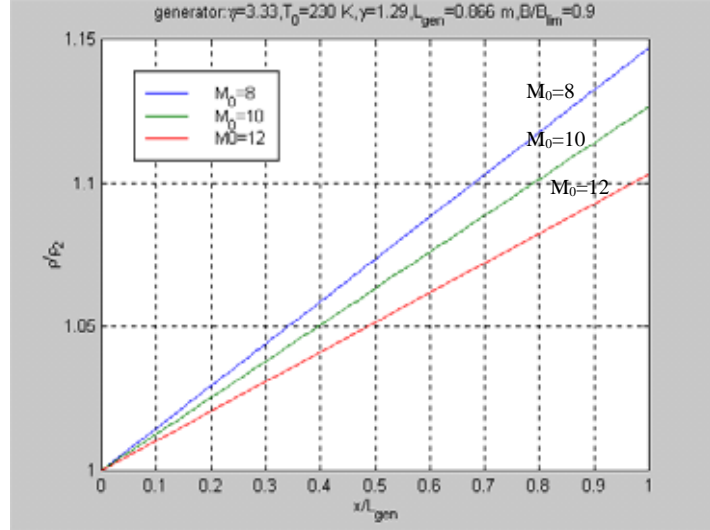
Figure 6

Figure 7 shows the pressure trend within the MHD generator.
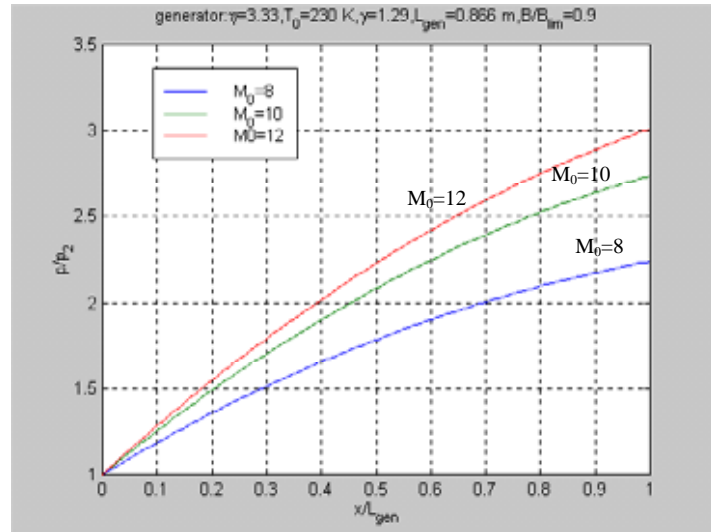
Figure 7

The pressure at the MHD generator exit is at least 2.2 times that at the MHD generator entrance; the ratio p/p_2 increases with flight Mach number at fixed x/L_{gen}.
Finally, Figure 8 illustrates the temperature trend within the MHD generator.
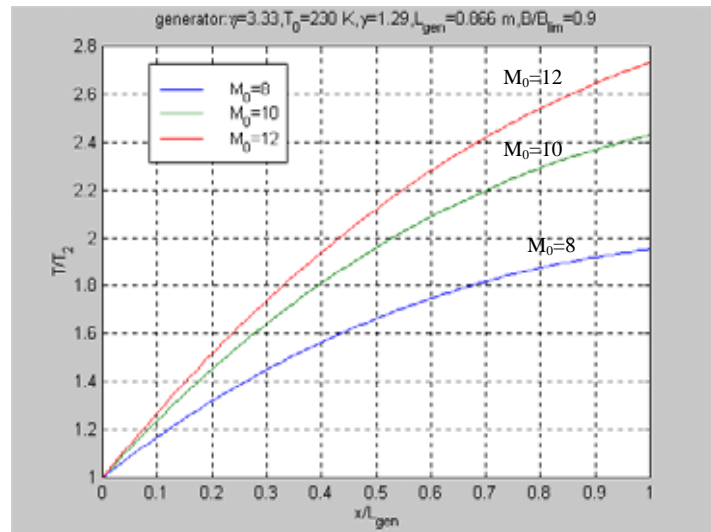
Figure 8

This temperature ratio also increases with flight Mach number.

Variables at the MHD generator exit are summarized in Table 1, as functions of the flight Mach number.

M_0	u_3 [m/s]	ρ_3 [kg/m^3]	p_3 [Pa]	T_3 [K]	β	M_3
8	1870.2	0.289	$9.1 \cdot 10^4$	1097	0.036	2.93
10	2460	0.275	10^5	1353	0.036	3.6
12	3065.7	0.264	$1.15 \cdot 10^5$	1515.4	0.033	4.1

Table 1

Table 1 shows that the MHD generator provides temperature and Mach number at the combustor entrance conducive to effective combustion. Note that the amount of total enthalpy to be extracted from the flow (β) to get this performance is not as high as (probably) expected.

The numbers in Table 1 are comparable with those resulting from the 2-D simulations of viscous flow within a MHD generator in [2]. 2-D simulations in [2] assume a viscous MHD flow, with and without Hall effect, within a MHD generator with walls kept at constant temperature ($T=T_2$) equal to the flow temperature at the MHD generator entrance, where the Mach number (M_2) is equal to 5.

Actually, in the present MHD scramjet model, a slightly different MHD generator entrance Mach number of 4.7 corresponds to a flight Mach number $M_0= 8$. The comparison between the present results for $M_0= 8$ and the results of the Vathazin and Kopchenov MHD generator model in [2] is still proposed to validate (numerically) the present model.

In fact, Table 2 shows the 2-D simulation results of [2] for laminar and turbulent flows, including Hall effect, and the present results for the MHD generator (with $M_2=4.7$).

	p_3/p_2	T_3/T_2	M_3	β
2-D simulation laminar	2.27	1.88	3.02	0.0434
2-D simulation turbulent	2.88	2.28	2.62	0.0618
Present analysis	2.24	1.95	2.93	0.036

Table 2

Table 2 shows that the results of the present analysis are close to those from the 2-D simulations. The laminar case is closer to the 1-D model of the present analysis than the turbulent case.

Figure 9 shows the magnetic fields within the MHD generator. The $M_0=12$ case requires the highest magnetic induction, but is representative also of trends at $M_0=8$ and 10. The magnetic field intensity is the only variable depending on x, since the total electric field is constant along x, in compliance with the assumption of η_g constant within the MHD generator. Furthermore,

the electric field produced by the plasma is nil (remember that the plasma is globally neutral), hence the E presented in the following is meant to be the applied electric field.
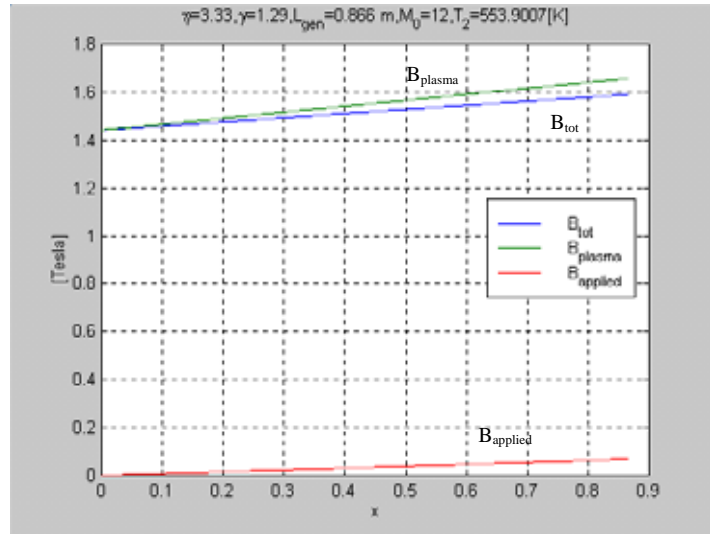
Figure 9

In Figure 9 $B_{applied}$ must be subtracted to B_{plasma} to obtain B_{tot}, since equation (15) is a vector sum with the B_{plasma} direction chosen as positive.

Table 6 summarizes the results about the MHD generator electromagnetic variables.

M_0	B [T]	E [V/m]	ΔE_{em} [MW]
8	0.88	570	1.77
10	1.5	961	3.36
12	1.44	1465.5	5.19

Table 6

where B is the magnetic induction amplitude, E is the applied electric field, and ΔE_{em} is the electrical power produced by the MHD generator to be put back into the flow within the MHD accelerator. Note that, by the very definition of η_g, (fixed) E increases with M_0 through the increase of the MHD generator entrance speed (u_2). Nevertheless, E has values technically feasible at all the three flight Mach number.

Finally, Figure 9 shows that the B needed is about one order of magnitude less than the ones so far presented in literature. However, this result is dependent also on the range of σ chosen and on its previously discussed feasibility.

3.3. MHD accelerator model

Within the MHD accelerator electromagnetic forces accelerate the flow, hence the electromagnetic term in equation (8) must be positive. This implies that the left side of equation (9) is negative, so that electromagnetic energy is transformed in flow-kinetic energy.

With $\eta_a = \dfrac{uB_{za}}{E_{ya}}$, it follows

$$E_{ya} - uB_{za} = E_{ya}\left(1 - \eta_a\right) > 0$$

hence $\eta_a < 1$

It has been assumed that the electromagnetic energy extracted by the MHD generator is entirely put back into the flow inside the MHD accelerator. This is also the electromagnetic energy available for acceleration, i.e., from equation (9) applied to the MHD generator:

$$\Delta E_{em} = \int_0^{L_g} \varepsilon_0 c^2\, \frac{B^2 u_2}{\eta}\, d\left(1 - \alpha x\right) = \varepsilon_0 c^2\, \frac{B^2 u_2}{\eta}\left(-\alpha L_g\right) \quad (19)$$

Assume, as done for the generator,

$$B_{za} = u_4 B_a / u$$

where u_4 is the flow speed at the accelerator entrance, and B_a is the magnetic induction amplitude, and assume also η_a constant along x

$$\eta_a = u\, B_{za}/E_{ya} = u_4 B_a / E_{ya}$$

hence, as for the MHD generator,

$$E_{ya} = E_a = const.$$

From equation (9), with equation (19), the expression of E_a as function of ΔE_{em} can be derived as

$$\Delta E_{em} = \sigma E_a\left(E_a - u_4 B_a\right)L_a \qquad (20)$$

Equation (20) is a second order algebraic equation for E_a; its negative solution has no physical meaning and must be discarded. This equation is the link between the MHD generator energy-extraction process and the MHD accelerator energy-addition process; this link relies on the amplitude of the electric field E_a within the MHD accelerator.

To obtain physical validity in the expressions for u and p, these expressions must return positive values. This leads to the following condition for the magnetic induction amplitude B_a:

$$B_a = \sqrt{\frac{\left(\rho u\right)u_4}{\varepsilon_0 c^2}}$$

With this value for B_a, E_a is calculated from equation (20), and, then, η_a from its definition. Hence, for the MHD accelerator η_a does not depend on x but is a function of u_4.

Next, the trends of this MHD accelerator model are presented and analyzed.

As in the MHD generator the parameter $\eta_a = u_4 B_a / E_a$ is assumed constant along x ('a' is short for accelerator), but, since $u_4 \propto M_0$, η_a changes with M_0.

Table 4 shows η_a as function of the flight Mach number:

M_0	B_a [T]	E_a [V/m]	η_a
8	0.6	1520	0.67
10	0.8	2643	0.69
12	1	4074	0.7

Table 4

Table 4 shows that η_a is almost constant with M_0 and close to unity. <u>When the η_a is unity, no electromagnetic energy is added to the flow</u>. As stated by the equation (8) recalled below

$$\rho u \frac{d}{dx}\left(\frac{u^2}{2}\right) = -u \frac{dp}{dx} + \sigma\left(E_{ya} - uB_{za}\right)uB_{za} \quad (8)$$

where $(E_{ya} - uB_{za}) = E_{ya}(1 - \eta_a)$, $\eta_a = uB_{za}/E_{ya} = u_4 B_a / E_a$ and $B_{za} = u_4 B_a/u$. <u>When $\eta_a = 1$ the MHD accelerator does not work.</u>

The magnetic field amplitude (B_a) depends only on the fluid-dynamic variables (ρ_4, u_4). E_a, instead, depends on the fluid-dynamic variables (ρ_4, u_4), the electromagnetic variables ($\sigma, \Delta E_{em}$), and the geometric variable L_{acc}.

To reduce η_a and thus to improve the MHD accelerator performance, one must either to lower $u_4 B_a$ or/and increase E_a. The first option brings in a decrease of the speed at the MHD accelerator exit, since B_a depends on u_4, and it can be debatable whether the flow acceleration due to a better performing MHD accelerator can compensate for the flow deceleration needed to achieve it. Furthermore, decreasing u_4 implies the combustor exit temperature increases, probably an unwanted effect.

The second option, i.e. increasing E_a, would imply extracting more energy within the MHD generator. Energy extraction raises the temperature at the combustor entrance, possibly above the maximum allowable. The η_a shown in Table 4 can complement the result from Figure 10 that follows.

accelerator T_0=230 K, γ=1.29, B/B$_{lim}$=0.9, L$_{acc}$=0.866 m
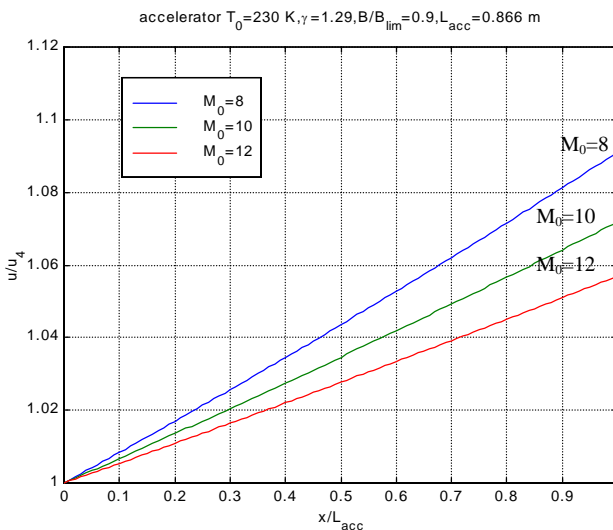
Figure 10

Figure 10 shows that the flow accelerates throughout the MHD accelerator, hence this device accomplishes its goal. Moreover, the speed increase is at best 9% of the speed at the device entry.

Before analyzing the temperature trend within the MHD accelerator, it must be pointed out that the flow acceleration inside this device is achieved in a way different from the one expected and (perhaps) evoked by the device name.

Recall the conservation equations for the three forms of energy considered in the present analysis:

$$\rho u \frac{d}{dx}\left(\frac{u^2}{2}\right) = -u\frac{dp}{dx} + J_{Qy} u B_z \qquad (8)$$

$$J_{Qy} E_y = -\frac{d}{dx}\left(\varepsilon_0 c^2 E_y B_z\right) \qquad (9)$$

$$\rho u \frac{du_{en}}{dx} = p\frac{du}{dx} + J_{Qy}(E_y - u B_z) $$

where the last equation is the internal-energy conservation equation, derived from the total-enthalpy conservation equation.

The electromagnetic-energy balance equation (9) has no term in common with the kinetic-energy balance equation (8), hence the direct transformation of electromagnetic energy into flow kinetic energy is impossible. The electromagnetic energy can be only transformed in flow internal energy by the Joule effect via the term $J_{Qy}E_y$. This means that the MHD accelerator does not work as a particle accelerator, wherein the Coulomb and Lorentz forces accelerate directly the charged particles. The MHD accelerator works, in fact, as a sort of "electromagnetic afterburner" in which the internal energy is increased by the Joule effect instead of the heat release by chemical reactions.

The above conclusion is supported by Figure 11, where the temperature rises within the MHD accelerator.

accelerator T_0=230 K, γ=1.29, B/B$_{lim}$=0.9, L$_{acc}$=0.866 m
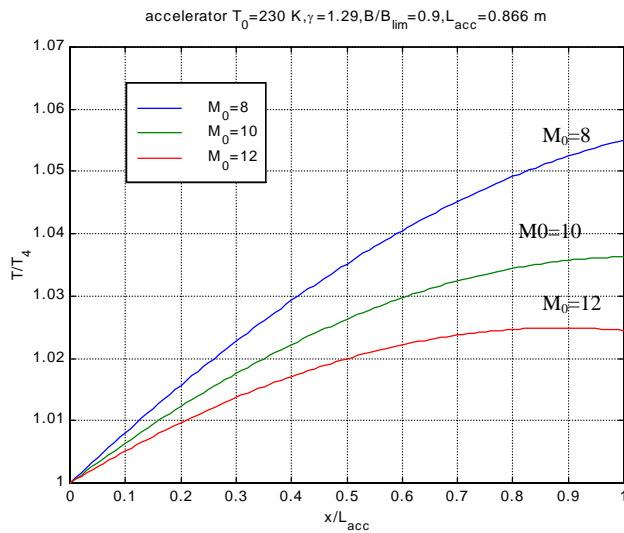
Figure 11

Figure 11 shows that if the MHD accelerator is long enough the temperature reaches a maximum and then decreases. This trend is different from the continuous decrease expected if the MHD accelerator provided acceleration throughout its entire length.

Finally, Figure 12 in the next page shows the magnetic fields intensities at M_0= 12.

accelerator $\gamma=1.29, M_0=12, L_{acc}=0.866$ m
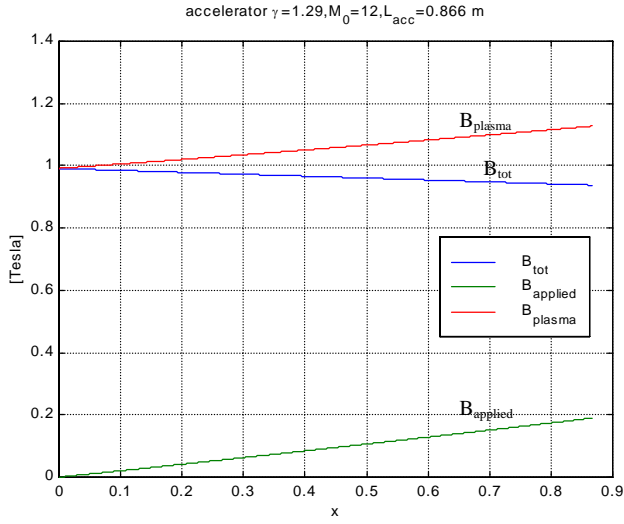
Figure 12

Note that the total magnetic field intensity (B_{tot}) is practically constant along the accelerator length. Recalling that $B_{tot}=B_z=B_a u_4/u$, and looking at u/u_4 of Figure 10, the explanation of B_{tot} constant is straightforward. The magnetic induction needed by the MHD accelerator is technically feasible, as for the MHD generator.

In conclusion, the MHD accelerator, as modelled in the present analysis, increases the flow speed of only about *160 m/s* at all the M_0 considered.

In fact, the main problem of the MHD accelerator is the high flow speed (u_4) through it. This high speed implies an high induced electric field ($u_4 B_z$), contrasting almost completely the applied electric field ($E_a=E_y$, see Figure (2)), and yielding a <u>total</u> electric field too small to produce very large effects on the ionized flow.

High speeds (u_4) are common in Scramjets, hence high pure-MHD accelerator effectiveness seems unlikely to be expected in such an engine, at least, under the assumptions made,.

3.4. MHD scramjet performance

Finally, the performance of the MHD scramjet modeled is presented in Table 5 and commented [7].

Table 5 shows the MHD scramjet performance at three flight Mach numbers.

Remember that the H_2-air ratio has been assumed stoichiometric, f_{stoi} is *0.029*.

M_0	T_{SP} [m/s]	I_{SP} [s]
8	810	2847
10	684.5	2406
12	579	2034

Table 5

Table 5 shows the specific thrust (T_{SP}) and the specific impulse (I_{SP}) decrease with M_0. However, the I_{SP} calculated are still remarkable in the range of flight Mach numbers considered.

Table 6 shows the entropy rise within both MHD devices and the combustor, since inlet and nozzle are assumed isentropic.

The entropy rise within both MHD generator and accelerator has been calculated by solving numerically the entropy equations by a MATLAB code. In the present analysis, the entropy rise within both MHD components is due only to the Joule effect.

Note that the MHD accelerator results support the results presented in Section 3.3 about the low performance of the MHD accelerator.

M_0	ΔS_{gen} [J/KgK]	ΔS_{acc} [J/KgK]	ΔS_{comb} [J/KgK]	ΔS_{tot} [J/KgK]
8	292.15	33.6	1483	1809
10	391	39.3	1314	1745
12	475.3	44.5	1211	1431

Table 6

3.5 Total pressure in MHD flows

Total pressure is a key parameter to analyze high-speed air-breathing engines, in fact, it is representative of the mechanical energy per unit volume, and its trends are not shown here because it must be redefined with respect to classical gasdynamics, when an e.m. field is present. Indeed, to define total conditions it is assumed that the flow is adiabatic and that <u>body forces are negligible</u>[13]. From these assumptions it follows that total enthalpy is constant along a streamline; then assuming also that the flow is stagnated <u>isentropically</u> to zero speed, expressions for total pressure and total density are derived using total temperature expression and isentropic flow relationships[13]. In MHD flow, instead, body forces <u>are</u> the main player in determining flow properties and cannot be neglected.

However, if we assume an MHD adiabatic flow and use eq.(5) to obtain an expression for the total enthalpy, the result is that total enthalpy <u>is not constant</u> along a streamline precisely because of flow-electromagnetic field interaction. This fact prevents obtaining the classical expression for total temperature, especially for real gases. Furthermore the isentropic assumption for an MHD flow means no Joule effect (see eq.13), i.e. no kinetic-electromagnetic energy transformation (eqs. (2) and (3) are decoupled): in the end, if the flow is isentropic no MHD device can work.

These few considerations lead to the conclusion that the expressions so far used in compressible gasdynamics cannot be extended to MHD-flow analysis automatically, and that, perhaps, the meaning of total quantities (if any) has to be rethought for MHD flows.

This interesting aspect is actually being investigated and results will be presented in the future.

4. Conclusion

The purpose of the MHD scramjet model presented in this lecture was to investigate the interactions between the cold plasma flow and the electro-magnetic field, that is, the essence of this new propulsion system, with suitable theoretical tools. These tools have been provided by the rigorous theoretical analysis of MHD flows by Giordano in reference [1].

The governing equation set developed in the Section 2 have been, at least partially, validated by comparing them with the equation set presented by Vathazin and Kopchenov in their paper [2].

The results indicate that the MHD generator is effective in providing the conditions required for practical supersonic combustion. Clearly distinguishing between the plasma electromagnetic field and the electromagnetic field applied has pointed out that the electromagnetic field to be applied may be lower than the one so far expected: an interesting result, considering the technical difficulty in producing high intensity magnetic fields on board.

The order of magnitude of the fluid-dynamic variables in the MHD generator model is also confirmed by the comparison with the CFD results in [2].

The MHD accelerator, at least as modeled here, seems to have instead intrinsic limitations in accomplishing its nominal task. The high speed, common through the scramjet flowpath, seems to affect substantially the effectiveness of this device, as described by the parameter η_a.

In conclusion, within the [many] assumptions made, the analysis performed shows that the MHD energy bypass is a promising solution for enlarging the range of applicability of the scramjet engine for hypersonic applications. Hence, further work on the MHD physics is recommended not only for drag-reduction applications, but also for propulsion applications.

References

[1] D. Giordano "*Hypersonic-flow governing equations with electro-magnetic fields*", 2002, Paper AIAA 2002-2165

[2] A. B. Vathazin, V.I. Kopchenov "*Problem of hypersonic flow deceleration by magnetic field*" in E.T. Curran and S.N.B. Murthy, editors "Scramjets propulsion", Progress in Astronautics and Aeronautics, Vol. 189, (2000), Chapter 5 AIAA, Reston VA

[3] C. Bruno, P.A. Czysz " *An electro-magnetic-chemical propulsion system*", AIAA, Reston VA

[4] W.D. Heiser, D.T. Pratt ''*Hypersonic air-breathing propulsion*", page 177, AIAA Education Series, AIAA, Reston VA

[5] D. W. Riggins "*Analysis of the Magneto-hydrodynamic (MHD) Energy Bypass Engine for High-Speed Air-Breathing Propulsion*", 2002 CPIA

[6] H. Bottini " *Thermodynamic Analysis of Energy bypass in SCRJ*", Master work, University of Rome "La Sapienza", Engineering Faculty, 2003

[7] H. Bottini, C. Bruno, P.A. Czysz "*Is The MHD Scramjet Really An Advantage?*", 2003, paper AIAA 2003-5046

[8] C. Bruno, P.A. Czysz "*Scramjet/MHD Aeropropulsion System*", paper AIAA 98-1582

[9] Macheret S.O., Schneider M.N., Miles R.B. "*Magnetohydrodynamic and electrodynamic control of hypersonic flow of weakly ionized plasmas*", paper AIAA 2002

[10] D. W. Bogdanoff, U. B. Mehta "*Experimental Demonstration of Magneto-Hydro-Dynamic (MHD) Acceleration*", paper AIAA 2003-4285

[11] M. Rosa-Clot, C. Bruno "*α Emission Thruster for deep Space Missions*", paper AIAA 94-2940

[12] C. Bruno, M. Rosa-Clot "*Curium-244 α Emission for a Nano- and Micro-Newton Thruster*", Acta Astronautica, Vol. 38, No 4-8, pp 231-234

[13] J.D. Anderson Jr. "*Fundamentals of Aerodynamics*", McGraw-Hill International Editors

EXPERIMENTAL APPROACH TO PLASMA PHYSICAL ASPECTS OF TRADITIONAL MHD

Abraham Veefkind

Retired from Eindhoven University of Technology,
Willem Alexanderpark 17, 2202 XW, Noordwijk, The Netherlands,
e-mail: a.veefkind@planet.nl

EXECUTIVE SUMMARY

A number of experiments is discussed, which were carried out to investigate the plasma characteristics of closed cycle MHD generators. Electron temperature elevation and corresponding increase of the electron density were non-equilibrium properties of importance for the power generation.

The desired non-equilibrium properties appeared to occur indeed, but plasma instability and the corresponding plasma non-uniformity formed serious complications. The experimental studies, which will be discussed, are carried out roughly between 1960 and 2000. They all deal with the effect of instability and non-uniformity on plasma properties or MHD performance capability. The basic characteristics of the involved experimental facilities and diagnostics will be presented. The investigations are subdivided in the following topics:
- observation of fluctuations in electron temperature, electron density and electro-dynamic quantities,
- streamers as the nonlinear appearance of the ionization instability,
- inlet relaxation,
- fully ionized seed as a means to suppress the ionization instability,
- closed cycle MHD generator performance.

TABLE OF CONTENTS

1   INTRODUCTION

The title of the lecture contains the following elements:
- traditional MHD,
- plasma physical aspects,
- experimental approach.

With "traditional MHD" is meant the reference to research in the past on behalf of electrical power generation, i.e. the conversion of internal energy of a plasma into electrical energy. The basic configuration (seed Appendix C) is a plasma channel flow across a magnetic field. The induced field $u \times B$ (with u the flow velocity and B the magnetic induction) is loaded by means of electrodes in opposite side walls of the channel. Often also a Hall electric field appears, directed opposite to the flow direction. By using suitable electrode configurations, this field can also be exploited for power generation.

Restricting the topic to "plasma physical aspects" implies that we shall deal with so-called closed cycle MHD, i.e. MHD generators with alkali seeded *noble gases* as a medium. Seeded combustion gases appear to be mostly in thermodynamic equilibrium. This means that the thermodynamic state completely defines the plasma properties, particularly the degree of ionization. As we shall learn, this is different in noble gasses. They are in a non-equilibrium condition. Their plasma characteristics are not only determined by the thermodynamic properties of the gas, but e.g. also by the current density.

The third limitation is the "experimental approach". Theories will not be discussed in this lecture. Theoretical results, however, will be mentioned and compared with experimental ones.

2 ELECTRON TEMPERATURE ELEVATION

Kerrebrock [1] did an experiment in an argon-potassium flow to measure the electrical conductivity as a function of the current density. The installation is presented in Fig.1. A stationary argon flow of 2 g/s at a temperature near 4000 K is produced with an arc heater. Potassium vapor is mixed into the flow and the mixture is fed into a test channel. Two electrodes provide for an electric field across the flow. Typical voltages are between 0 and 12 V and corresponding electric fields between 0 and 20 V/cm.
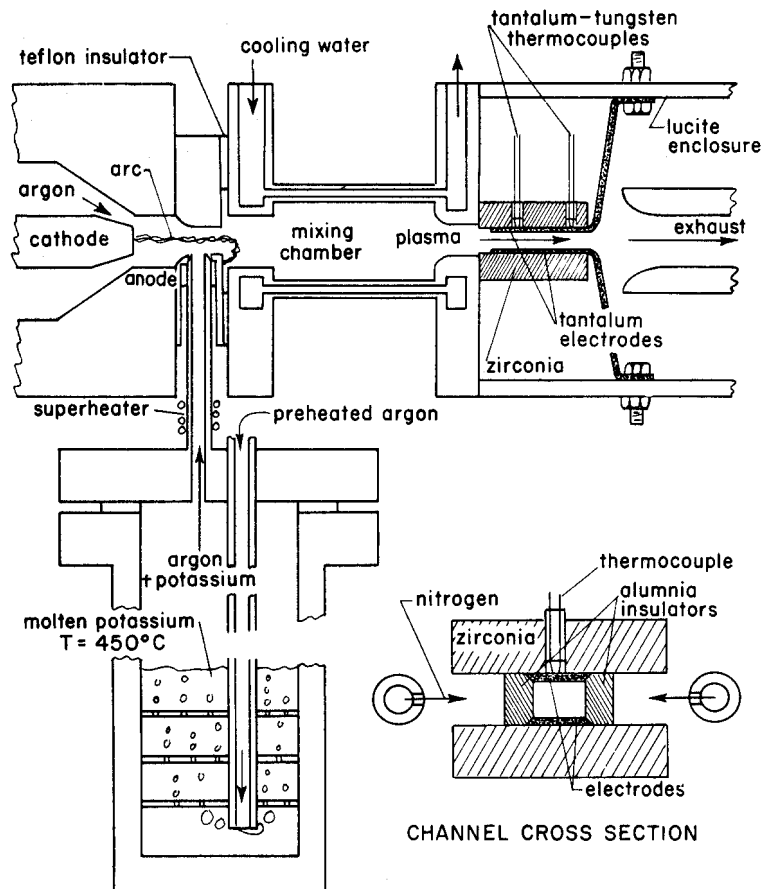
Fig. 1. From [1]. Experiment to demonstrate electron temperature elevation.

The result of the experiment is shown in Fig.2. The dependency between the conductivity and the current density has to be explained by an increase of the ionization degree with the current density: electrons gain energy in the field and ionize neutral potassium atoms. Because the energy that can be gained by an electron in the field between two collisions is too small to ionize an atom, a thermal ionization mechanism was assumed in a two-temperature plasma. In the model electrons and heavy particles (ions as well as neutrals) have Maxwell distributions but the temperature of the electrons is higher than that of the heavy particles. Moreover, the electron density is assumed to obey the Saha equilibrium relationship, but at
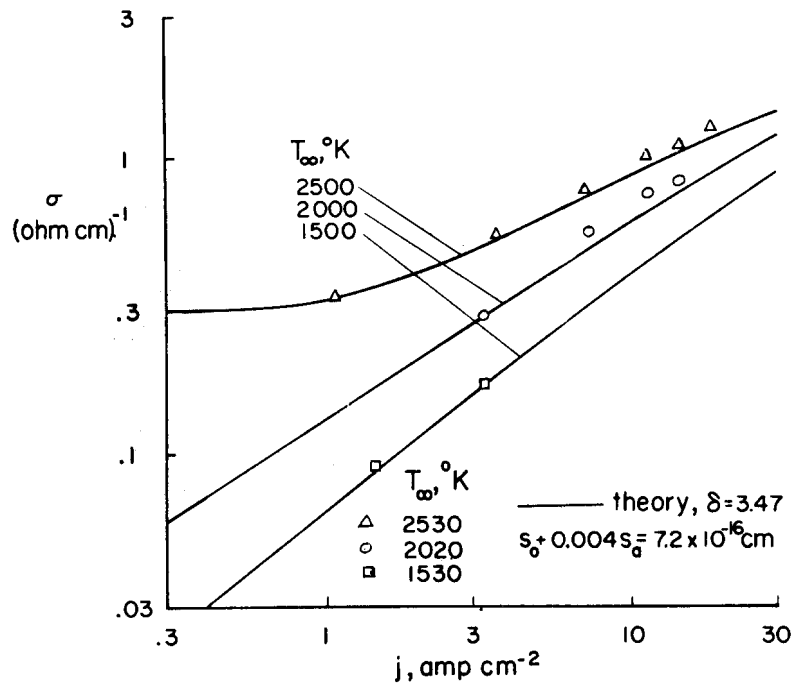
Fig. 2. From [1].Electrical conductivity vs. current density, demonstrating the effect of electron temperature elevation.

the electron temperature. The value of electron temperature and density is given by the electron energy equation and the Saha equation. Kerrebrock used the following equations:

$$eEu_e - \delta(m_e / m_a)(U_e - U_a)v_c = 0$$

$$j = en_e u_e$$

$$\sigma = \frac{n_e e^2}{m_e v_c}$$

$$\frac{U_e}{U_a} = 1 + \frac{m_a}{\delta U_a}\left(\frac{j}{n_e e}\right)^2$$

$$U_e = \frac{3}{2}kT_e$$

$$U_a = \frac{3}{2}kT_a$$

$$\frac{n_e^2}{n_a - n_e} = K_{SAHA}(T_e)$$

e: electronic charge
E: electric field
u_e: electron velocity
δ: elastic loss factor
m: mass
U: energy

3

v_c: collision frequency
j: current density
σ: electrical conductivity
T: temperature
K_{SAHA}: Saha function
Index e: electron
Index a: heavy particle

The crucial assumption is that the electron energy U_e can be interpreted as an *internal* energy. The loss factor δ was used to fit the data to the theoretical results (Fig.2). The theoretical value of δ is 2. The deviation was attributed to molecular impurities, which increase the energy transfer between electrons and heavy particles through vibrational-rotational excitations.

Under conditions as in the experiment electron temperature elevation can only be obtained in noble gas plasmas because there the collision frequency is small enough (see e.g. [2]) to inhibit the collisional energy loss sufficiently.

The conclusion that the electrical conductivity can be enhanced through electron temperature elevation was important for MHD energy conversion, because in this way it was possible to convert energy also at comparatively low gas temperatures. For this reason a number of experiments followed to demonstrate the effect with induced electrical fields.

3 FACILITIES AND DIAGNOSTICS

3.1 Facilities

The following categories of facilities were used to study non-equilibrium MHD generator plasmas:
- arc heater experiments,
- shock tube experiments,
- blow down experiments,
- closed loop systems.

They are distinguished by their plasma production.

An example of an arc heater experiment has already been given in Fig.1. An electric arc is used to heat up the working gas. These experiments are usually rather small with mass flows of the order g/s and consequently channels with cross-sections of the order 1 cm^2 and lengths of the order 10 cm.

A schematic representation of a shock tube experiment is given in Fig.3. Here the plasma is produced by fast (nearly adiabatic) compression of the later working gas in a shock tube to obtain desirable stagnation temperatures and pressures. Since these conditions exist only for short times, shock tube experiments are by definition pulsed experiments, with test times of the order ms. Mass flows obtained are of the order kg/s and thermal energy inputs of the order MW. Order of magnitude channel sizes are 10×10 cm^2 cross-section and 1 m length.
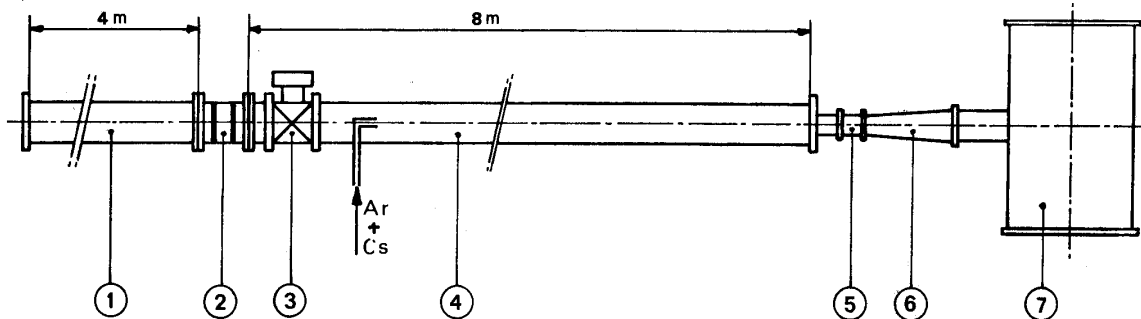
Fig. 3. From [3]. Schematic of shock tube facility. 1) driver section 2) diaphragm section 3) ball valve 4) test section 5) preionizer 6) generator 7) vacuum tank.

Blow down facilities were constructed to approach real MHD energy conversion conditions. Usually an important objective was to demonstrate a sufficiently large electrical power output. Already in the 1960's a blow down facility was constructed CNEN, Italy in Frascati. A schematic is shown Fig.4. Blow down experiments use storage heaters consisting of ceramic material, which is heated up electrically or by fuel combustion. Due to the finite heat storage test times are limited to typically 10 s. Mass flows up to order kg/s are possible and consequently thermal power inputs up to MW. Most blow down facilities use cryogenic or super-conducting magnets to obtain magnetic inductions of typically 5 T.

5
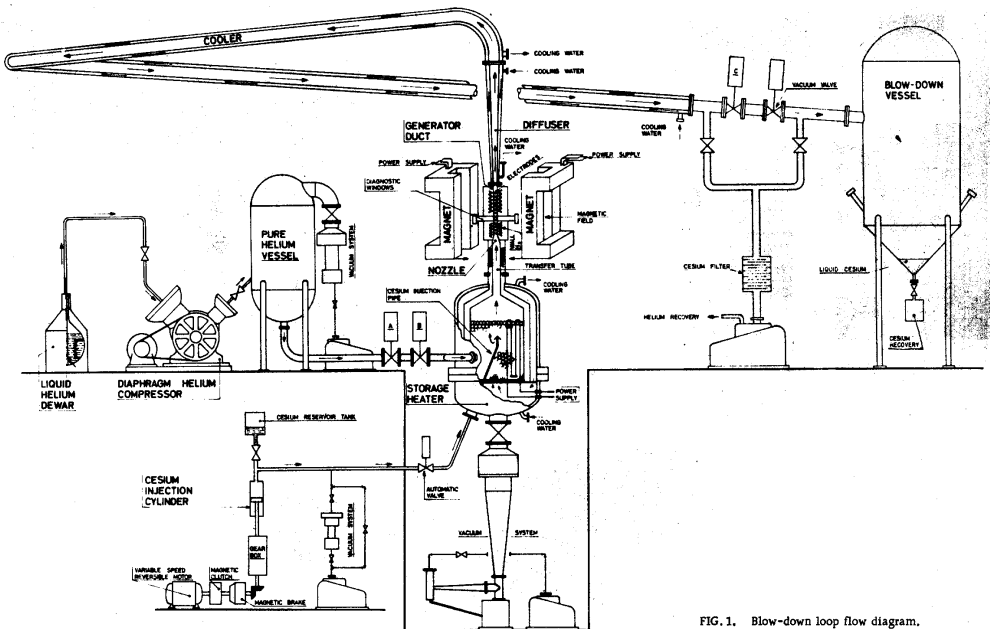
FIG. 1.   Blow-down loop flow diagram.

Fig. 4. From [4]. CNEN blow down facility.
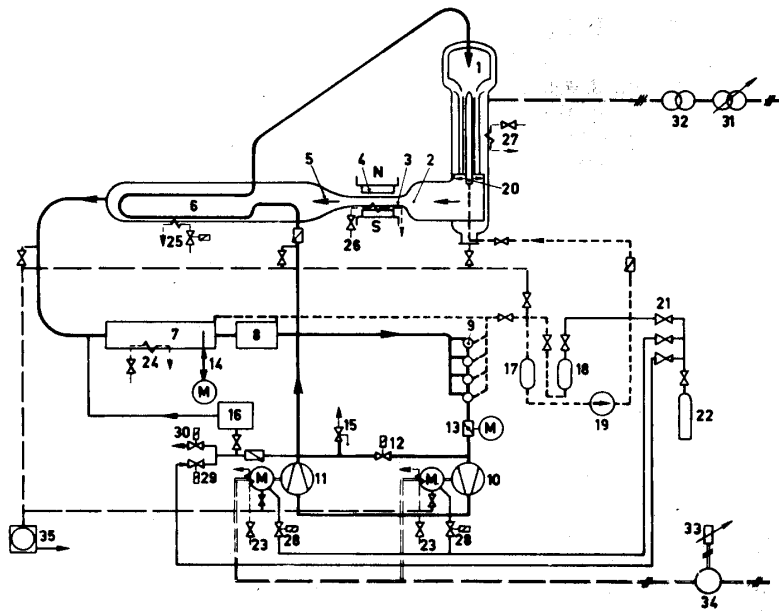
FIG. 1.   Functional scheme of the ARGAS-test facility: Cross section = 50 cm ; M_{max} = 0.85 Mach;
T_{max} = 1800°K; $\dot{m}_{gas}$ = 4.5 kg/s, $P_{tot.}$ = 1-8.5 bar; B = 2 tesla

1. 3-phase gas heater	13. Suction throttle	25. Emergency cooling heat ex-
2. Nozzle	14. Pipe assembly cover of aftercooler	changer
3. MHD duct	15. Burst disc	26. External cooling channel section
4. Magnet	16. Gas cleaning	27. External cooling heater
5. Diffuser	17. Caesium collector	28. Gas bearing - pressurized gas
6. Recuperative heat exchanger	18. Caesium reservoir	supply
7. Aftercooler	19. Caesium-MHD pump	29. Argon inlet valve
8. Gravity separator	20. Caesium injection	30. Argon outlet valve
9. Cyclone separator (4 stage)	21. Argon pressure reducer	31. 3-phase regulating transformer
10. Bearing gas compressor 1	22. Argon reservoir	32. 3-phase matching transformer
11. Bearing gas compressor 2	23. Compressor motor cooling	33. Rotor theostat
12. By-pass	24. Water cooling for aftercooling	34. Frequency changer
		35. Vacuum pump

Fig. 5. From [5] Closed loop facility ARGAS, KFA Jülich, Germany.

Fig. 5 shows as an example the closed loop facility ARGAS constructed in the 1960's by KFA in Jülich, Germany. Plasma was produced by heating argon in a 1.5 MW electric heater. The mass flow was 4.5 kg/s at a stagnation temperature of 1800 K at maximum.

3.2 Diagnostics

The mostly used diagnostics for the investigation of plasma physical aspects are
- measurement of electrical quantities,
- measurement of line reversal,
- measurement of continuum radiation,
- fast photography.

A typical arrangement for measurement of electrical quantities in an MHD channel is shown in Fig. 6. Electrode currents are collected and/or applied parallel as well as perpendicular to the flow direction by segmented electrodes. The advantage of applying current additional to collecting current from the MHD conversion is that the current density can be made an independent variable, as we will see later. Electric fields are measured by floating voltage probes. They have the disadvantage that they are located in the boundary layer.
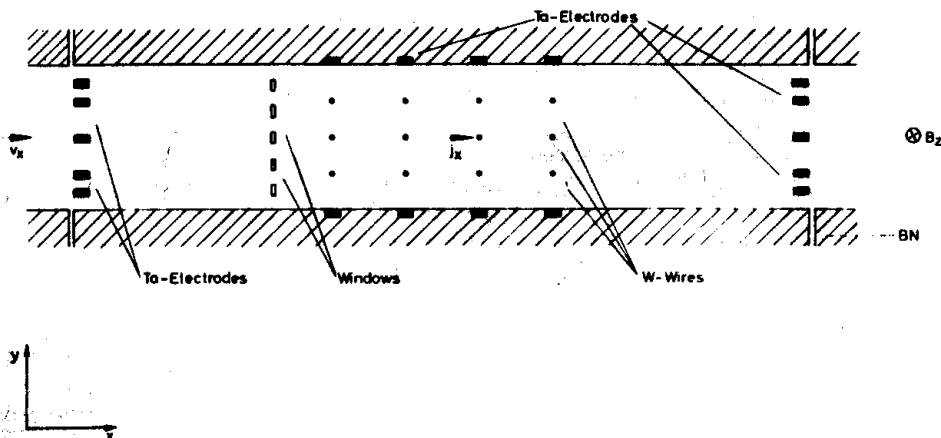
Fig. 6. From[6]. Arrangement of diagnostics in an experimental MHD channel. The wires are used as voltage probes. The channel is 100 mm long, 20 mm high and 15 mm wide. Tungsten wires were 0.5 mm in diameter

Since the electron temperature elevation is the key phenomenon in non-equilibrium MHD plasmas, its direct measurement is extremely important. The line reversal method, usually applied to the resonance lines of the seed material is most widely used to determine the electron temperature. The only assumption that has to be made is that the population of the excited states is governed by the electron temperature. A typical set-up is shown in Fig. 7. The calibrated light source is a tungsten ribbon lamp. In other experiments Xe lamps are used as well. A typical result is shown in Fig.7 too. There it can be seen that the measurement has to be carried out in the line wing in order to be out of the range of the self-absorption.
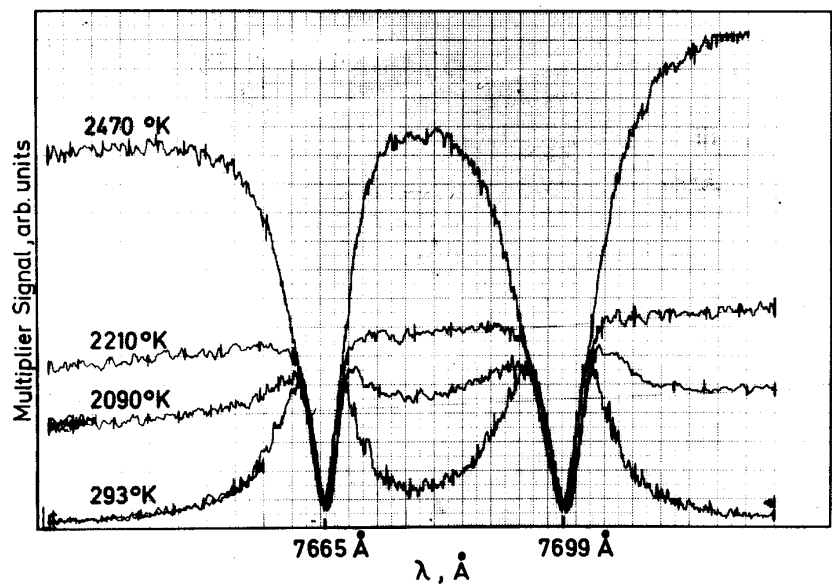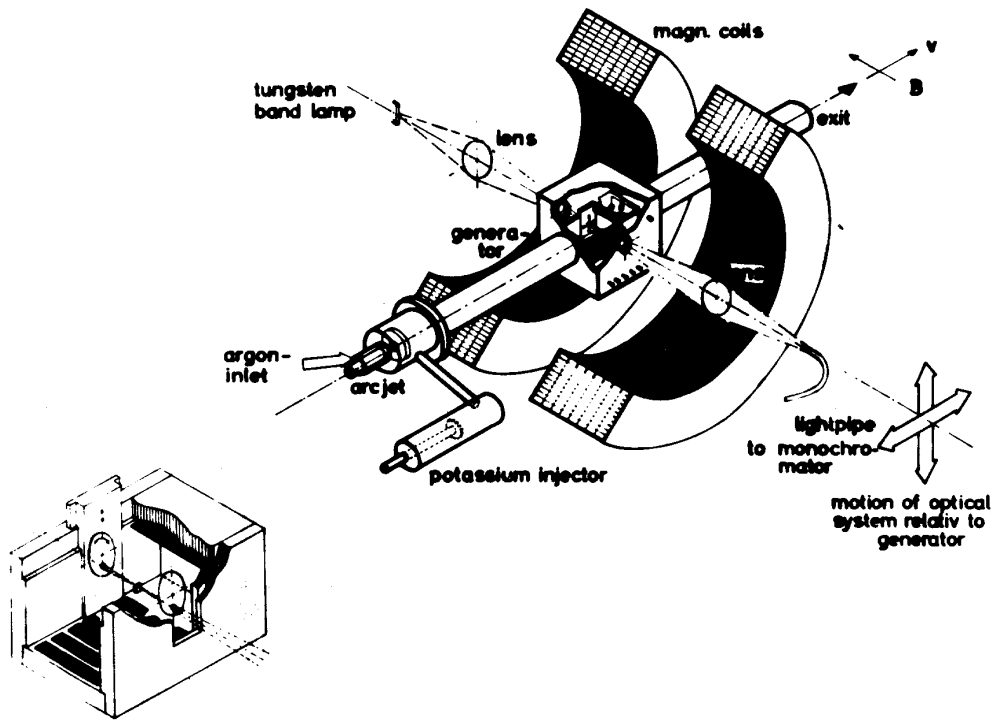
Fig. 7. From [7]. Line reversal measurement set-up and result.

The electron density is the other important plasma characteristic to be measured directly. This has usually been done by measuring the recombination radiation. Part of the recombinations in the plasma occur as two-body recombinations: an electron collides with an ion causing a

recombination with an excited atom and a photon as products. The process and its energy balance are given below.

$$e^- + A^+ \rightarrow A_j^* + photon$$
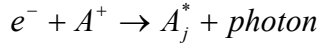
$$\frac{hc}{\lambda} = \frac{hc}{\lambda_j} + \frac{1}{2}m_e v_e^2$$

$e^- : electron$

$A^+ : ion$

$\dfrac{hc}{\lambda} : photon\ energy$

$\dfrac{hc}{\lambda_j} : binding\ energy\ of\ atomic\ state\ j$

$\dfrac{1}{2}m_e v_e^2 : electron\ kinetic\ energy$

Since the kinetic energy of the electrons is continuously distributed, the released photons contribute to a continuous spectrum, reflecting the energy distribution of the electrons. The amplitude of this spectrum is proportional to n_e^2. Further details of this method can be found in Appendix A. When the spectrum is measured at two wavelengths, electron temperature and density can be measured under the assumption of a Maxwellian electron energy distribution function. A typical experimental set-up is shown in Fig.8.
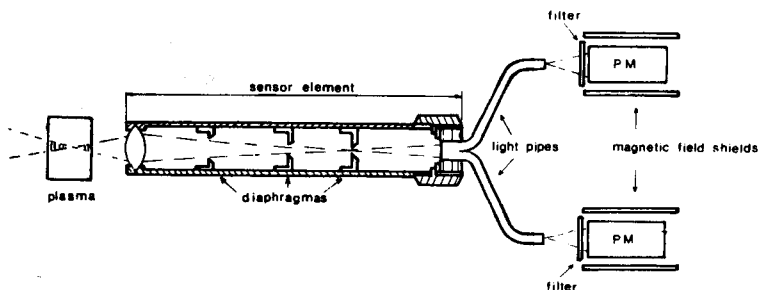
Fig. 8. From[8]. Set-up for recombination radiation measurement.

4 FLUCTUATIONS AND NON-UNIFORMITY

4.1 Non-equilibrium in induced fields

Following the idea of electron temperature elevation a number of experiments was carried out to demonstrate the enhancement of the electrical conductivity for MHD generator conditions, i.e. in induced electric fields. Particularly in the Max Planck Institute in Garching, Germany many investigations on this topic were carried out. In the set-up of Fig. 6 electric fields were measured with voltage probes, current density was determined from the currents through a number of segmented electrode circuits, electron temperature was measured by line reversal and electron density by recombination radiation. Currents were applied as well as collected from MHD conversion, so that the current density was independent from e.g. the magnetic induction. Figs. 9, 10 and 11 result from the experiments. Fig. 9 shows that the electron temperature increases with the current density independent from the value of the magnetic induction. This behavior is in agreement with the conception of Kerrebrock [1], where the electron temperature elevation results from the Ohmic heating j^2/σ irrespective the cause of the current. In Figs. 10 and 11, however, it is shown that the electrical conductivity and Hall parameter behave differently: they do not only depend on the current density, but also on the magnetic field. It has to be noted that the conductivity and the Hall parameter in Figs. 10 and 11 are determined from the electrical measurements and not from their microscopic values (see next section). The explanation of the reduction of electrical conductivity and Hall parameter was that due to the magnetic field a stationary and (quasi-)uniform distribution of electron temperature and density was no longer stable. The instability was called *electro-thermal instability* or *ionization instability*. Linear theory predicted that the instability appears when the Hall parameter becomes higher than a critical value, in most cases around 2.
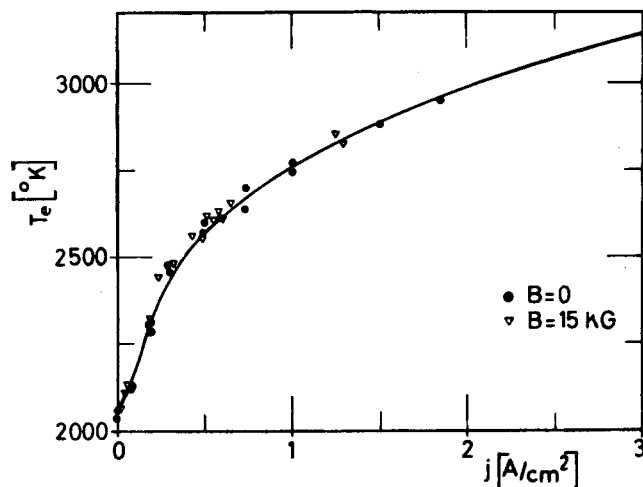
Fig. 9 From [6]. Electron temperature vs. current density with and without magnetic field.
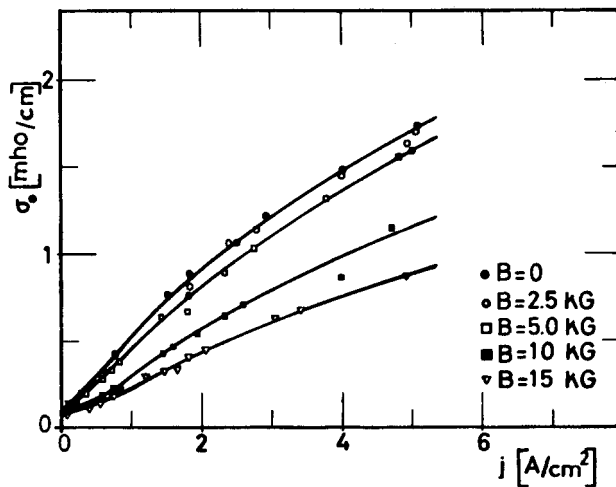
Fig. 10. From [6]. Electrical conductivity vs. current density for several values of magnetic induction.
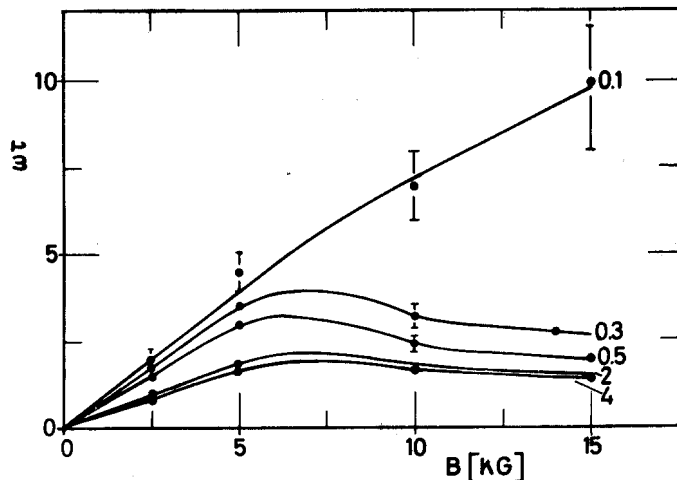
Fig. 11. From [6]. Hall parameter vs. magnetic induction for several values of current density [A/cm²]

4.2 Apparent quantities (averaged Ohm's law)

The consequence of a non-stationary and non-uniform plasma state is that the measured quantities, such as the electron temperature, current density and electric field in the previous section have to be interpreted as averages and the practical question is how these averages are related to each other.

The local Ohm's law reads

$$J + J \times \omega\tau = \sigma(E + u \times B)$$

11

With J the current density, E the electric field, u the gas velocity and B the magnetic induction. $\omega\tau$ is the vector representation of the Hall parameter equal to $\omega\tau.B/B$ with $\omega\tau$ the scalar value of the Hall parameter. σ is the electrical conductivity. In the expression above $\omega\tau$ and σ are equal to their microscopic values: $\omega\tau = eB/(m_e v_c)$ and $\sigma = n_e e^2/(m_e v_c)$ with e the electronic charge, m_e the electronic mass and v_c the electron collision frequency.

In the situation of an unstable plasma, the quantities J, E, σ and $\omega\tau$ are non-uniform and fluctuating. In this case it is assumed that the averaged quantities can be related in the same way as the local quantities, but with apparent values of the conductivity and Hall parameter, no longer equal to the microscopic values:

$$<J> +<J> \times \omega\tau_{app} = \sigma_{app}(<E> + u \times B)$$

Adopting the plasma instability as the explanation of the figures 10 and 11, the plotted values of the electrical conductivity and the Hall parameter have to be interpreted as *apparent*. Note that the apparent values of $\omega\tau$ and σ are not equal to their averaged values.

4.3   Experimental observation of fluctuations

Some experiments were carried out to investigate fluctuations of the plasma quantities directly. As an example some results of [9] will be presented here. In a shock tube MHD generator, experiments have been carried out at high stagnation temperatures, typically 3500 K. Electron temperature and electron density are determined both from recombination radiation, which was collected at two different wavelengths. The signals are shown in Fig. 12.
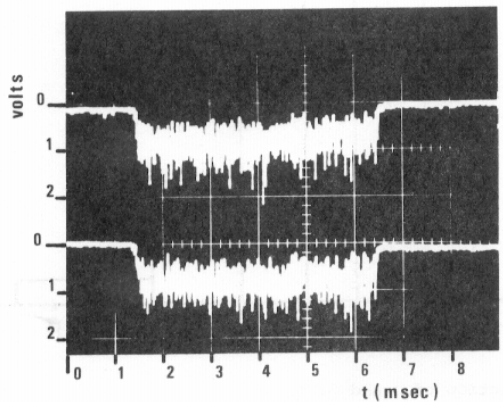
4.3.1.1   Fig. 12. From [9]. Time resolved recombination radiation signals

 From the strong cross-correlation between the signals it can be concluded that the fluctuations originate from the plasma. The spectrum of the fluctuations shows mainly frequencies between 10 and 40 kHz. Probability distribution functions of electron temperature and density are derived from the measured radiation (Fig. 13). As expected the fluctuation amplitude of the electron temperature is considerably smaller than that of the electron density. Fluctuations of the microscopic values of electrical conductivity and Hall parameter mainly depend on the electron density fluctuations. Their PDF's are presented in Fig. 14. By comparing these results with the electrical measurements, it can be concluded, that the apparent values of σ and $\omega\tau$ are smaller than their averaged values.
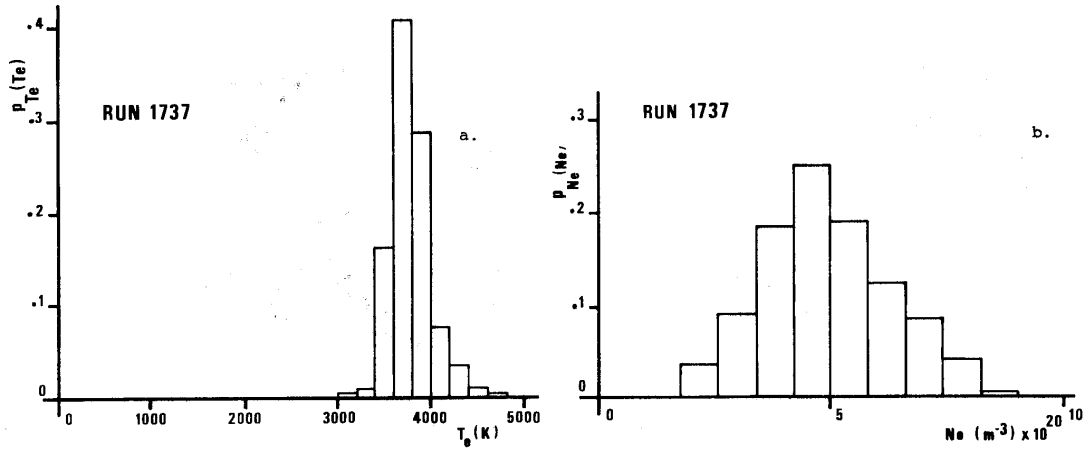
Fig. 13. From [9]. Probability distribution functions of electron temperature and electron density.
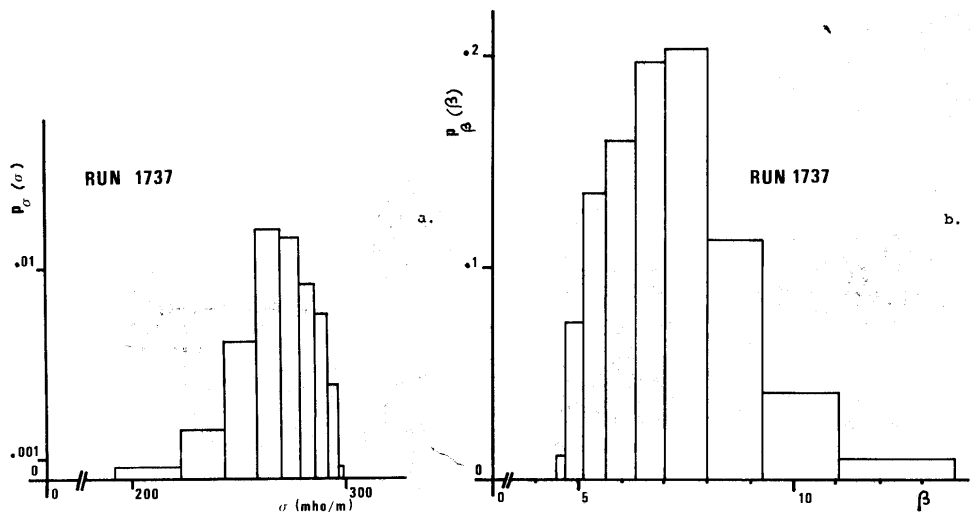
Fig. 14. From [9]. Probability distribution functions of electrical conductivity and Hall parameter.

Cross-correlation between the currents of the segmented electrode generator reveals the propagation velocity of the instabilities (Fig. 15). It turns out that this velocity is very close to the gas velocity.
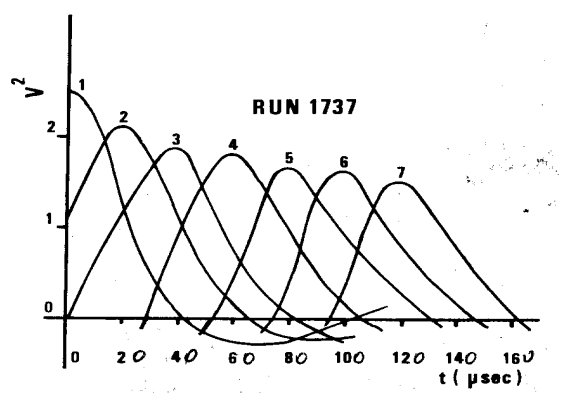
Fig. 15. From [9]. Cross correlation between electrode currents.

14

5 STREAMERS

Fast photography in non-equilibrium MHD flows revealed strong non-uniformities. An example is given in Fig. 16. Apparently there exists a strong non-uniform distribution of the degree of ionization. Furthermore, the pictures suggest that the high ionization regions form current paths. Streamers were interpreted as the result of non-linear growth of ionization instability.
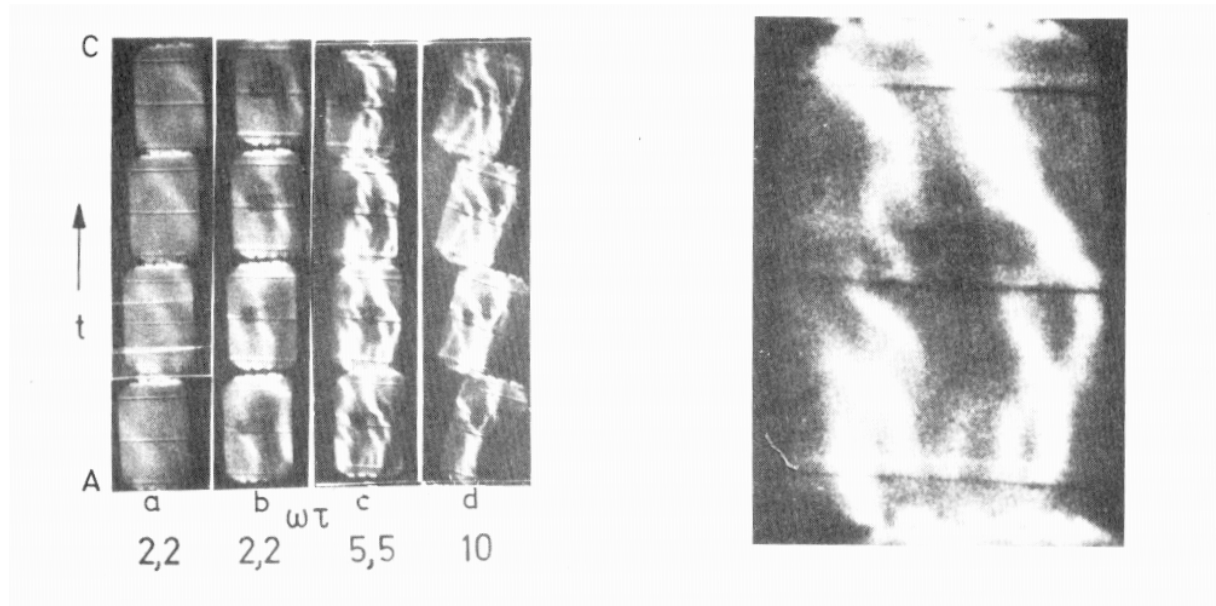
Fig. 16. From [10]. Image converter pictures of streamers.
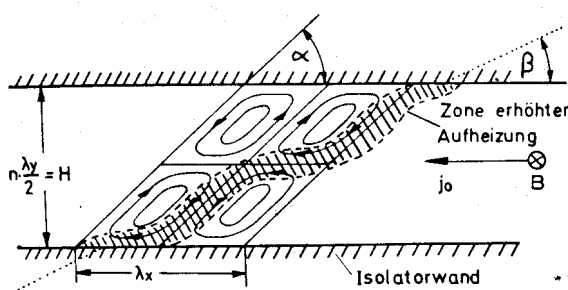
Fig. 17. From [11]. Current distribution of the ionization instability as a result of a linear calculation for a channel with insulating walls.

 A point of discussion is the fine structure of the streamers. The authors of [10] emphasize that although the fine structures look like helical current paths, they are layers of high and low ionization inside the streamers. According to this interpretation the layer structure is already predicted by the linear analysis, when boundary conditions are included. In Fig. 17 a calculated current distribution is presented in a channel with insulating walls. The layer of high ionization degree has been indicated.

Under conditions of strong magnetic interaction, as realized in shock tube experiments, very similar streamer structures are observed as those of Fig. 16. An example is given in Fig. 18.
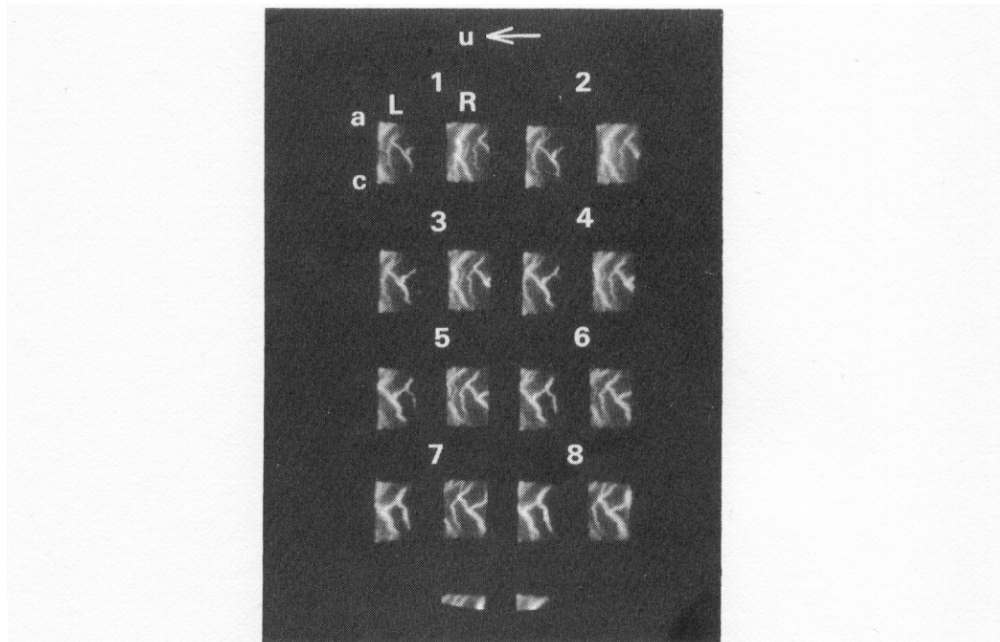
Fig.4a. Framing picture of run 3410 taken 2.1 ms after the pressure
step at the end of the shock tube. Experimental conditions:
T_s = 3536 K, p_s = 7.73 atm, B = 2.61 T,
loading: electrode pairs 1 - 10 R_L = ∞
        electrode pairs 11 - 32 R_L = 1 Ω
no external voltage,
no pre-ionizer.
Frame number 6 is used for reconstruction.

Fig. 18. From [12]. Streamers in a shock tube MHD generator. Two pictures L and R are simultaneously taken from different view points under an angle of 26.4^0.

In the experiment of [12] an attempt was made to observe the 3D structure of the streamers by taking 2 simultaneous pictures from different view angles. In contrast with [10], it was concluded from these observations that the fine structure is helical, so that streamers can be considered as a bunch of current paths.

Another aspect of streamers, which is different from the linear representation of ionization instabilities, is the propagation velocity. The linear theory predicts a phase velocity that is different from the gas velocity. The expected difference between phase velocity and gas velocity is of order 100 m/s, but depends strongly on plasma conditions and the orientation of the wave vector with respect to the main current. In [13] an experiment was carried out to compare gas velocity and streamer velocity directly. In a shock tube MHD generator, a spark

16

was produced by an optical discharge from a ruby laser. Assuming that the spark is entrained by the gas flow, fast photography shows the velocities of both gas and streamers (Fig. 19).
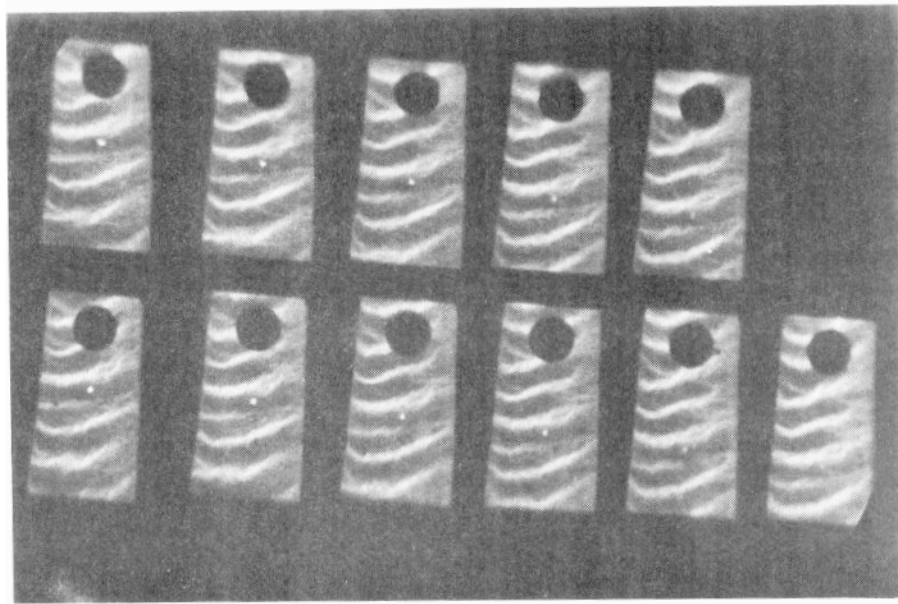
Fig. 19. From [13]. Framing photograph showing a spark surrounded by streamers. In the picture the flow velocity points vertically down. Exposure time of each frame: 1 μs. Inter-frame time 5 μs. Approximate size of the window: 10×20 cm^2. Time sequence of the pictures: first from top to bottom, then from left to right.

The result of these observations was that streamers move on average with the gas velocity, but there is a rather large (say 100 m/s) scatter of velocities of individual streamers.

6 INLET RELAXATION

When the plasma enters the MHD channel, it is originally in thermodynamic equilibrium. In practice this means that the electron temperature is equal to the gas temperature and the electron density can be calculated from the Saha equation. Directly downstream of the entrance, due to the current density produced by the MHD action, the electron temperature will rise to the value where the electron energy balance is in equilibrium and the electron density will rise to a value where the ionization balance is in equilibrium. It can be estimated that the characteristic equilibration time for the electron energy is of order 1 µs and the characteristic ionization time of order 10 µs. Taking into account a convection velocity of 1000 m/s this implies that the latter process determines the length of the inlet relaxation region to be of order 1 cm. Numerical calculations were carried out by [14]. Results are shown in Fig. 20.
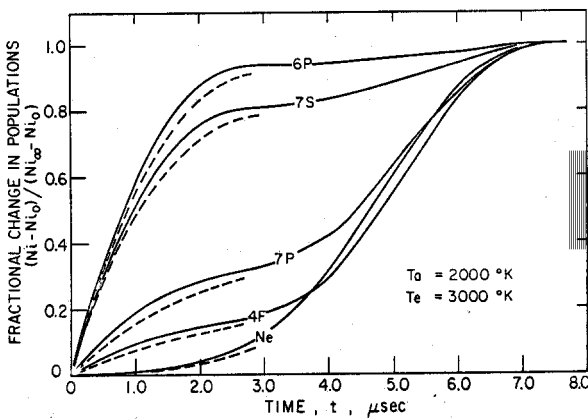
Fig. 20. From [14]. Time development of electron density and populations of excited states of cesium following a stepwise increase of the electron temperature from 2000 to 3000 K.

The figure refers to a calculation of the increase of the populations of excited states of cesium and the electron density following a stepwise increase of the electron temperature from 2000 to 3000 K. See for the energy level diagram Appendix A. The figure suggests a strong coupling between the 7P and 4F levels with the electron density in contrast with the 6P and 7S levels.

In shock tube experiments it was found that the region of reduced MHD activity at the inlet was much larger than expected from 1D calculations as in [14]. An example is shown in Fig. 21 [15]. Currents rise in these experiments over distances between 10 and 40 cm[1] depending on the stagnation temperature, which was varied from 2560 to 3060 K. The reason is that the non-uniformity must be considered. This is demonstrated in Fig. 22. There it can be seen that the inlet relaxation length is determined by the development of streamers. Fig. 22 is a streak picture, which can be interpreted as an x,t diagram of the steamer motion. The distance in the generator corresponds to the vertical direction of the picture and the time with the horizontal direction. For more details, see Appendix D. Fig. 22 demonstrates that at lower stagnation temperatures streamers start to develop further downstream and that also the streamer density

---

[1] The electrode segmentation length in these experiments was 2.5 cm.

is initially lower. The qualitative interpretation can be seen from Fig. 23 [16]. The figure shows that streamers are bent in the downstream direction because of their motion with the gas in the main flow on one hand and their attachment to the electrodes on the other hand. The figure also shows that new streamers are produced by break-downs. If at a certain location in the inlet region the electron density is too low for break-down, the corresponding electrode pair will not participate in the current production[2].
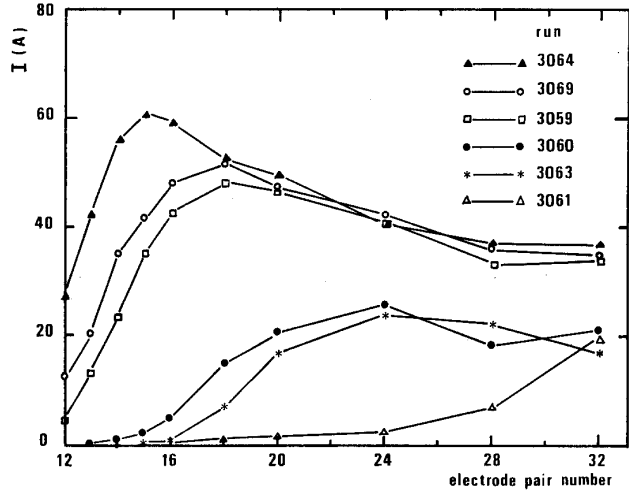
Fig. 21. From [15]. Inlet relaxation effect on current distribution. Runs represent different stagnation temperatures, increasing from 2560 K (run 3061) to 3370 K (run 3064).
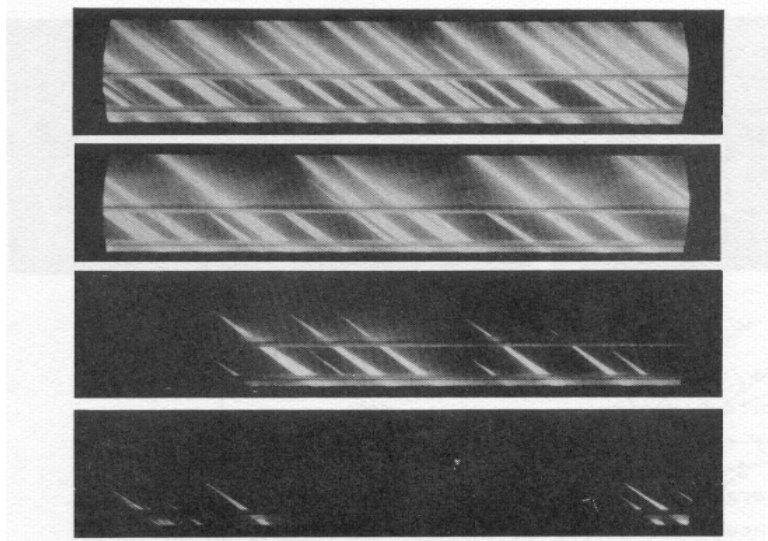
Fig. 22. From [15]. Streamer development for different stagnation temperatures, from top to bottom 3370, 3080, 2800 and 2580 K.

---

[2] In disk generators a complete azimuthal current path must be created to make MHD action possible. In these generators one often sees a region of reversed electric field in the entrance region where the plasma conductivity is insufficient.
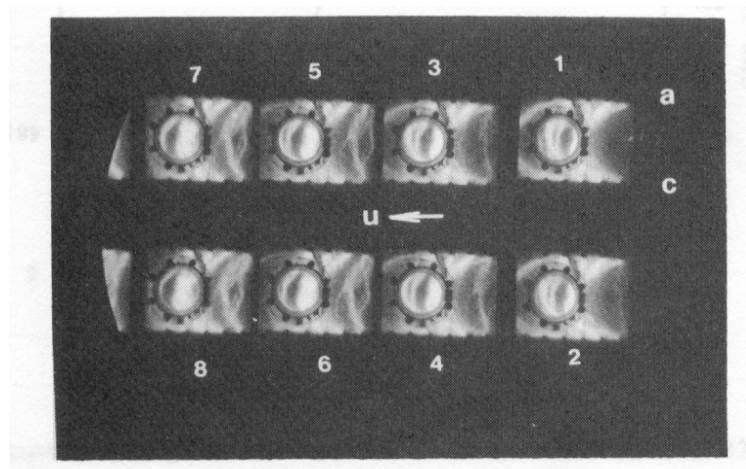
Fig. 23. From [16]. Framing pictures of the inlet relaxation region, showing initial break-down.

7 FULLY IONIZED SEED

In order to suppress ionization instabilities Nakamura [18,19] introduced the concept of fully ionized seed (FIS). Qualitatively the idea is as follows. When the ionizable material is fully ionized, fluctuations in the electron temperature will not result in fluctuations in the electron density. Consequently the electrical conductivity and the Ohmic heating of the electron gas will not be influenced, so that there is no amplification of the fluctuations anymore. The condition of fully ionized seed can in practice be obtained by applying a low seed fraction. In that case FIS occurs at electron temperatures (4000 – 5000 K), which can be reached in MHD generators.
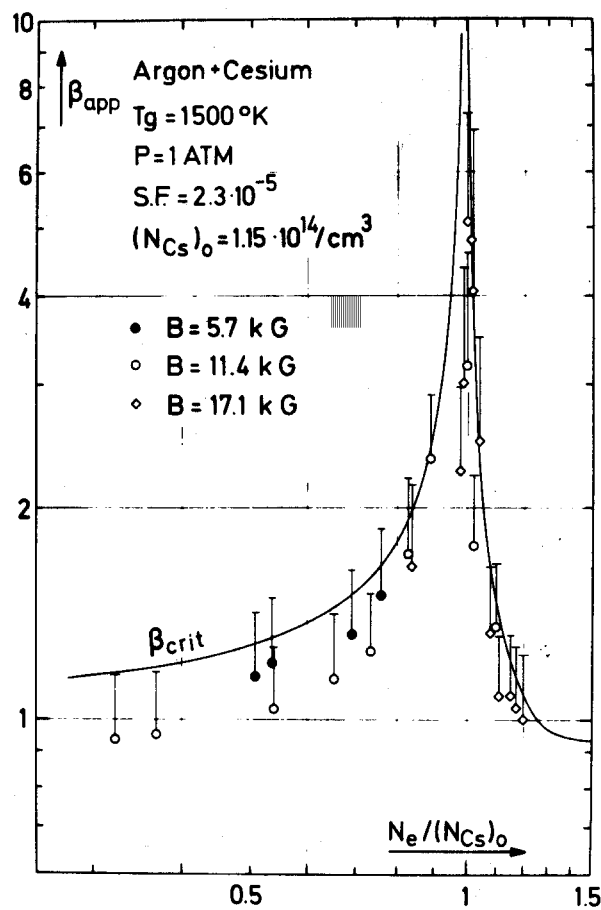
Fig. 24. From [19]. Effect of fully ionized seed on Hall parameter.

In Fig. 24 theoretical and experimental results are compared. In the figure experimental values of apparent Hall parameters are compared with critical Hall parameters as found from the linear theory (see Appendix B). In Fig. 24 the Hall parameters are plotted against the seed fraction. Electron temperature and electron density were obtained by measuring the recombination radiation. The peak in Fig. 24 shows the stability of the plasma when the

ionization degree of the seed is approximately 1^3. When higher values of the electron density occur due to partial ionization of the inert gas, the plasma becomes unstable again.

Length between anode and cathode.

L=5.6 cm

Electrode width.

D=0.4 cm

Channel height.(constant cross section)

H=0.75 cm

at outer electrode
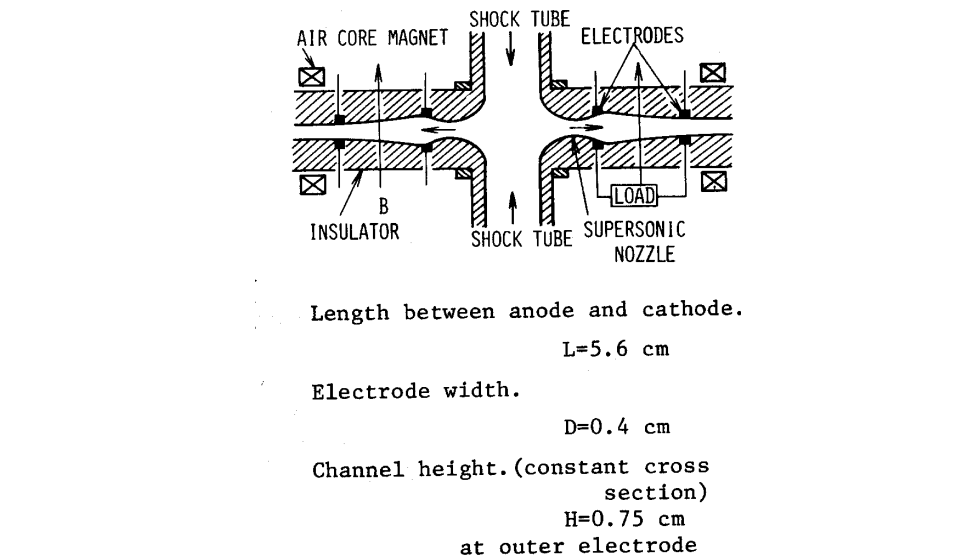
Fig. 25. From [20]. Disk Hall channel configuration.
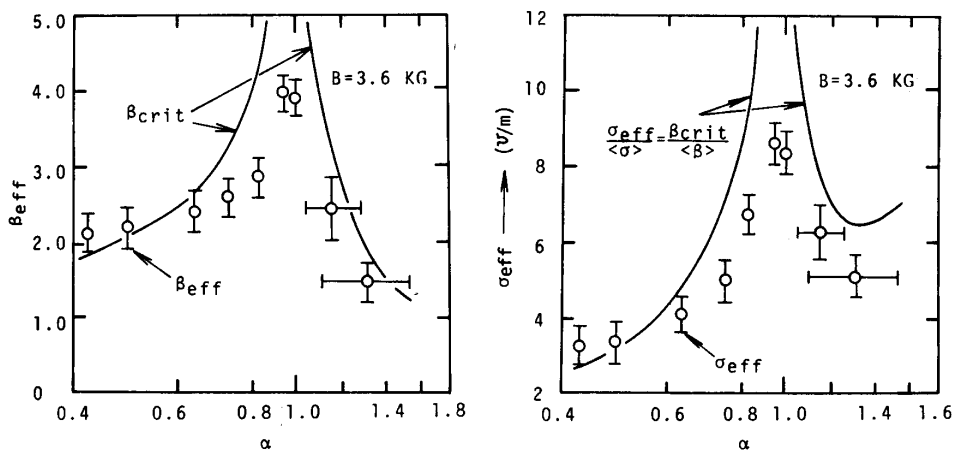
Fig. 26. From [20]. Effect of fully ionized seed on Hall parameter and electrical conductivity. Magnetic field was 3.6 Tesla.

FIS became a trademark for the MHD investigations carried out at Tokyo Institute of Technology. An early shock tube experiment is presented in [20]. Like many of the TIT experiments it is carried out in a disk Hall channel (Fig.25). The plasma flow is radially outward. The plasma is short circuited in the azimuthal direction. Concentric electrode rings are used to load the Hall field. In Fig. 25 the shock tube flow is supplied from two sides to the disk center. In later versions the disk channel was integrated with the shock tube end plate

---

[3] The peak was later called "Mount Fuji" and was the inspiration for the name of the MHD facilities of Tokyo Institute of Technology.

(see Appendix C). Results the shock tube experiment of [20] are shown in Fig. 26. As in Fig. 24 experimentally found apparent Hall parameters[4] are compared with critical Hall parameters found from the linear theory using the ionization degree as independent variable. In Fig. 26 the effect on the apparent electrical conductivity is shown as well. The electron temperature in the channel was measured through recombination radiation. The electron density was determined by the phase shift of an 8 mm microwave. From the measured T_e and n_e the values of $<\sigma>$ and $<\beta>$ can be determined. The advantage of FIS was demonstrated in many experiments following the one of [20], particularly in shock tube and blow-down experiments involving large electrical power outputs of order 1 MW. A very direct demonstration was presented in [21]. During an experiment with the blow-down facility of the Tokyo Institute of Technology Fuji-1, the seed fraction was varied and the (space averaged) electron temperature measured. The result is shown in Fig. 27. When the seed fraction is low enough[5], FIS can occur and the electron temperature rises accordingly. The effect on the electrical power output of the generator is presented in Fig. 28. Here it appears that a seed fraction of 2×10^{-4} is an optimum value. At larger values the seed is only partially ionized and at lower values the inert gas ionization starts to be significant.
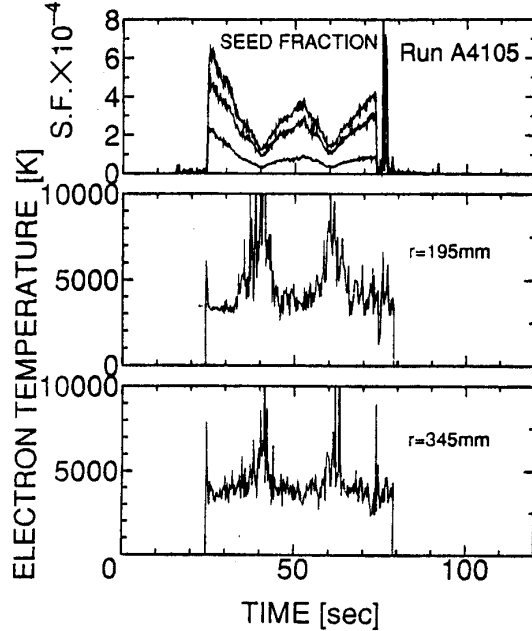
Fig. 27. From [21]. Variation of seed fraction and electron temperature during a blow-down run

---

[4] The expression "effective Hall parameter" is equivalent to "apparent Hall parameter".
[5] Note that the value of the seed fraction corresponding to FIS is an order of magnitude larger than in [19].
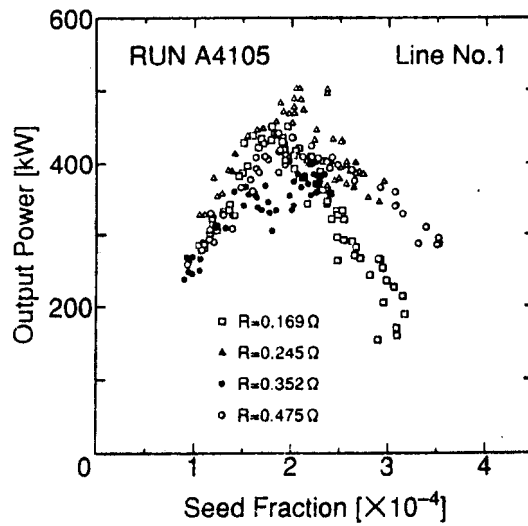
Fig. 28. From [21]. Electrical output vs. seed fraction in a non-equilibrium disk generator.

The performance of an inert gas MHD generator can be numerically predicted, taking the effect of ionization instability into account by a 2D,t computation including the basic equations of electrons (see Appendix B). Such a calculation has been carried out for a large disk generator (thermal input power 29.84 MW) [22]. The calculated current to voltage characteristic is given in Fig. 29. It shows a maximum power output at load resistances between 0.15 and 0.25 Ω. The stability of the plasma can e.g. be observed from the electron density space distribution. It is shown for various load resistances in Fig. 30. From that figure it can be seen that at a load resistance of 0.15 Ω the electron density distribution is uniform, thus demonstrating that also a *nonlinear* analysis predicts that the maximum power output corresponds to plasma stability.
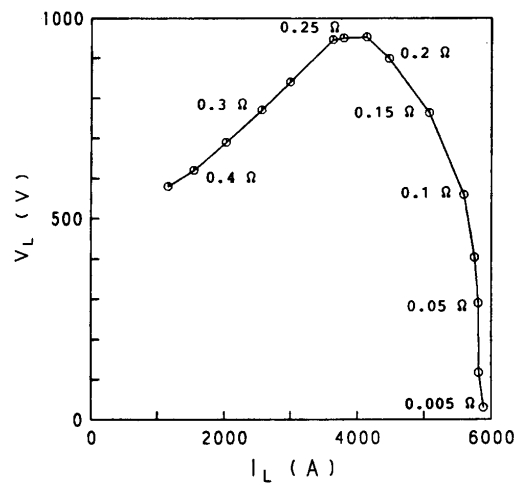
Fig. 29. From [22]. Current to voltage characteristic of non-equilibrium disk Hall generator.

24
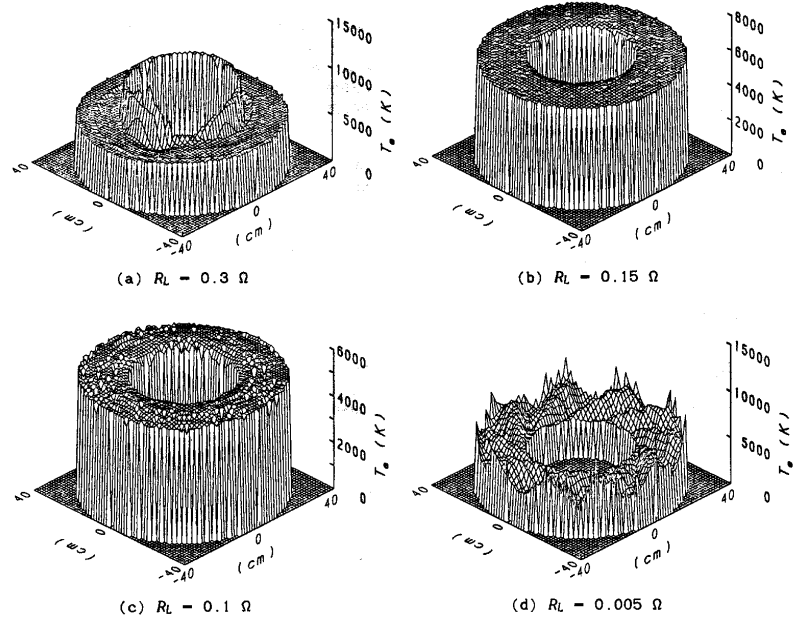
Fig. 30. From [22]. Electron density distribution in a non-equilibrium disk hall generator.

8 PERFORMANCE

One can wonder whether non-equilibrium MHD generators do have a significant electrical power output. The answer is affirmative. Enthalpy extractions over 20% have been obtained in experimental generators. An overview of the Japanese results of both shock tube and blow-down experiments is given in Fig. 31 [25]. In Fig. 32 worldwide obtained results are collected of both combustion and non-equilibrium generators. It has, however, to be noted that the minimum stagnation temperature at which the energy conversion occurs in the reported experiments is not below 1800 K. According to the theory, much lower temperatures must still correspond to sufficient electrical conductivity, if the plasma is stationary and uniform. The reason why the ideal conditions cannot be obtained at low temperatures is not well understood.
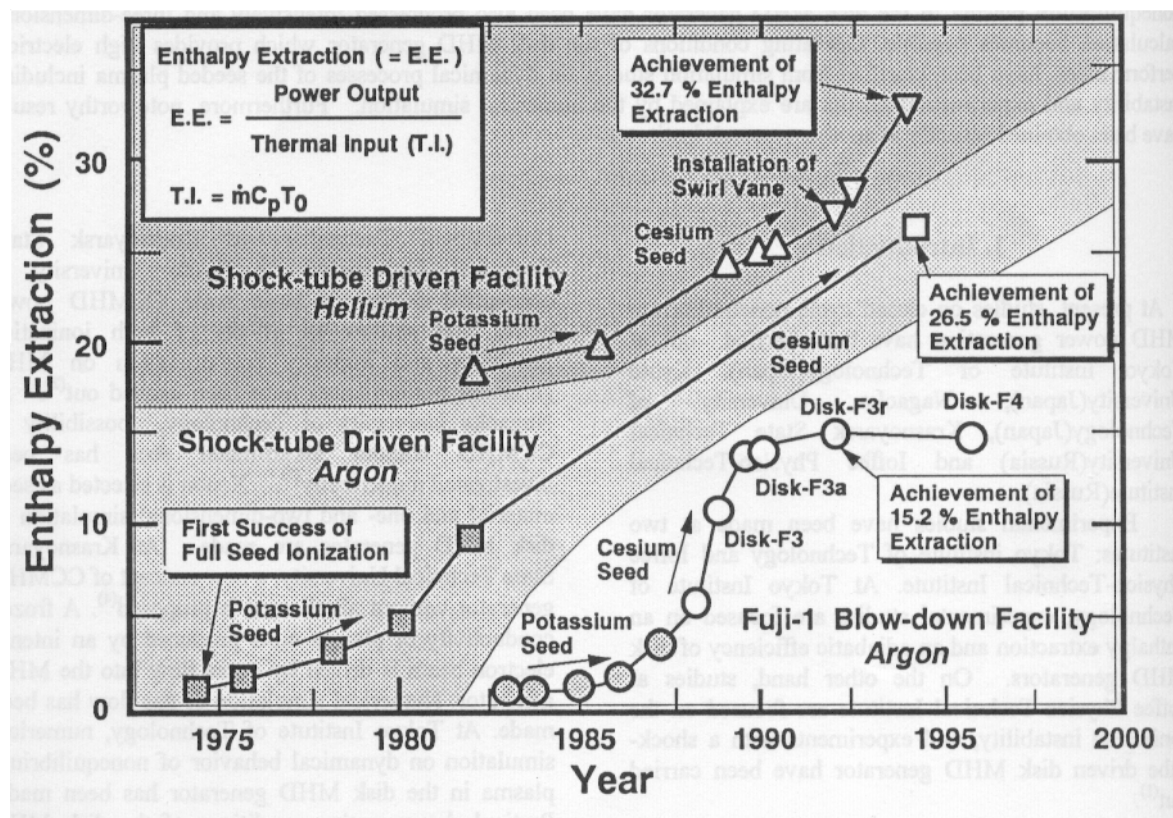
Fig. 31. From [25]. Performance of non-equilibrium generator experiments at Tokyo Institute of Technology, mostly with FIS.
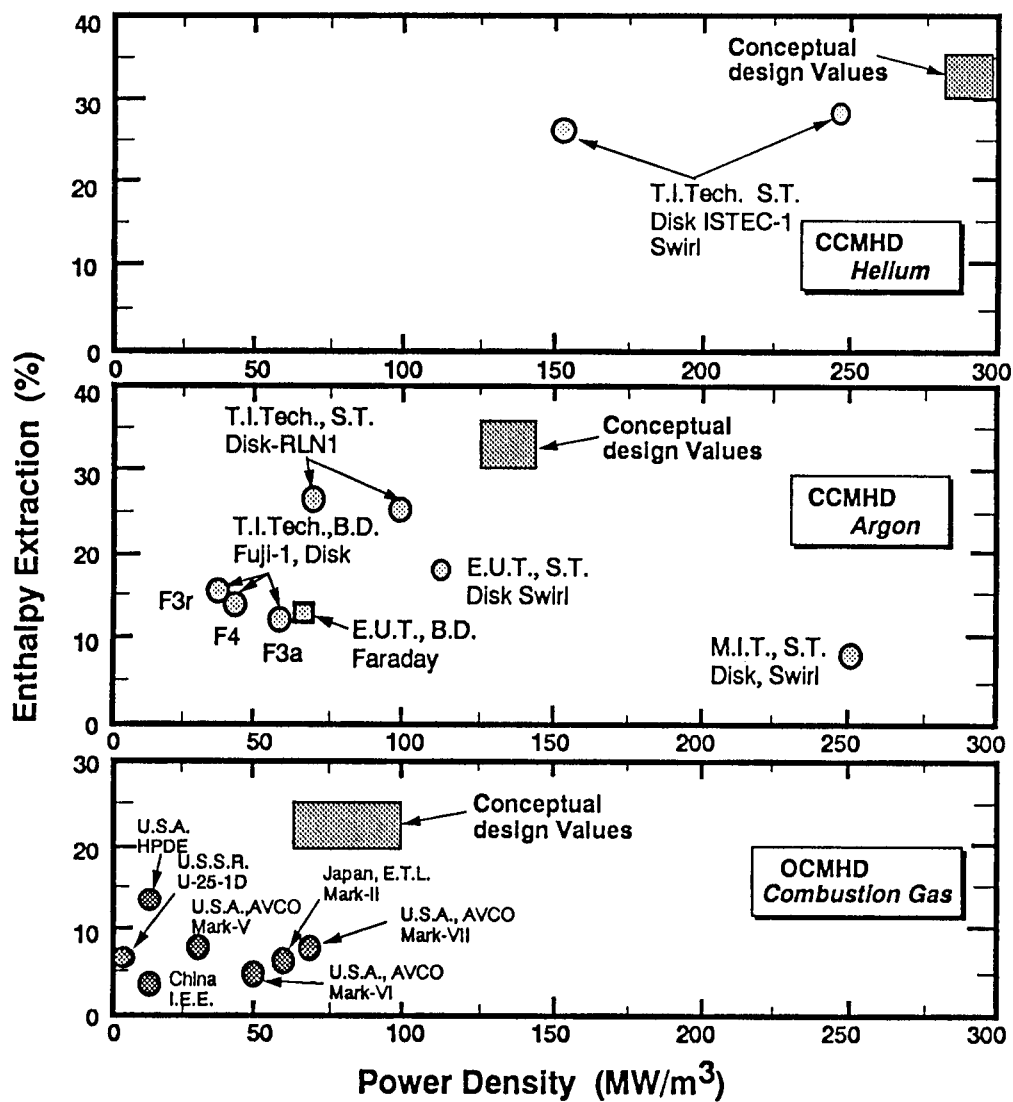
Fig. 32. From [25]. Worldwide overview of MHD generator performances.

27

References

1. J.L.Kerrebrock, "Conduction in Gases with Elevated Electron Temperatures", Proc. 2nd SEAM, p.327, Philadelphia, 1961.
2. M.Nitchner and C.H.Kruger, "Partially Ionized Gases", Wiley, NY, !973.
3. J.H.Blom, J.W.M.A.Houben and L.H.Th. Rietjens, "First Results of the Eindhoven Shocktunnel,Experiment", Proc. 13th SEAM, I.6, Stanford University, 1973.
4. E.Bertolini, et al. , "The CNEN Helium-Caesium Blow-down MPD facility and Experimentswith a Proto-type Duct", Proc. 3rd Int. Conf. on MHD Electrical Power Generation, II,473, Salzburg, 1966.
5. T.Bohn, et al., "The Closed Loop. Argas", Proc. 3rd Int. Conf. on MHD Electrical Power Generation, II,525, Salzburg, 1966.
6. G.Brederlow, W.Feneberg and R.Hodgon, "The Non-equilibrium Conductivity in an Argon-Potassium Plasma in Crossed Electric and Magnetic Fields", Proc. 3rd Int. Conf. on MHD Electrical Power Generation, II,29, Salzburg, 1966.
7. D.Dodel, "Simultaneous Measurements of the Electron Density and Electron Temperature Distribution in a Simulated Faraday-type MHD Generator", Proc. 5th Int. Conf. on MHD Electrical Power Generation, II,127, Munich, 1971.
8. J.W.M.A.Houben, "Loss Mechanisms in an MHD Generator", Ph.D. Thesis, Eindhoven University of Technology, 1972.
9. W.M.Hellebrekers, A.Veefkind and L.H.Th. Rietjens, "Experimental Fluctuation Analysis in a Noble Gas MHD Generator", Proc. 16th SEAM, II.3, Pittsburgh, 1977.
10. G.Brederlow, H. Zinko and K. –J. Witte, "Performance of the IPP Noble-gas Alkali MHD Generator and Investigation of the "Streamers"in the Generator Duct", Proc. 5th Int. Conf. on MHD Power Gen. Vol. 2, p. 387, Munich, 1971.
11. W. Riedmüller, "Experimental and Theoretical Studies of the Influence of Boundary Conditions on the Development of Ionization Instability", Proc. 11th SEAM, p. 199, Pasadena, 1970.
12. A.F.C.Sens et al., "Investigations on the Gasdynamical Effects of a Non-Uniform Supersonic Flow with Streamers in a Noble Gas MHD Generator", Proc. 20th SEAM, 10.6, Irvine 1982.
13. J.C.N.Bosma, "Gasdynamic Effects in Linear MHD Generators", PhD. Thesis, Eindhoven University of Technology, 1987.
14. T.Takeshita and L.M.Grossman, "Excitation and Ionization Processes in Non-equilibrium MHD Plasmas", 4th Int. Conf. on MHD Electr. Power Generation, Vol. 1, p. 191, Warsaw, 1968.
15. C.A.Borghi, "Onset of the Non-Equilibrium Regime in a Noble Gas MHD Generator", 8th Int. Conf. on MHD Electr. Power Generation", Vol. 4, p. 126, Moscow, 1983.
16. V.A.Bityurin, A.F.C.Sens and A.Veefkind, "Gas-Dynamical Effects of Non-Uniform Flow, Shocks and Streamers in a Noble Gas MHD Generator", SMP Internal Report 81/15, Eindhoven University of Technology, 1981.
17. C.A.Borghi, "Discharges in the Inlet Region of a Noble Gas MHD Generator", Ph.D. Thesis, Eindhoven University of Technology, 1982.
18. T. Nakamura and W. Riedmüller, "Investigations of a Nonequilibrium MHD Plasma under the Conditions of Fully Ionized Seed", Proc. 5th Int. Conf. 0n MHD Electr. Power Generation, Vol. 2, p.291, Munich, 1971.
19. T. Nakamura, Stability of the Nonequilibrium MHD Plasma in the Regime of Fully Ionized Seed", Proc. 12th SEAM, V.3, Argonne, 1972.
20. S.Shioda and H.Yamasaki, "Generation Experiments with a Disk MHD Generator

under the Conditions of Fully Ionized Seed", Proc. 6th Int. Conf. on MHD Electr. Power Generation", Vol. 2, p. 105, Washington, 1975.

21. Y.Okuno, et al., "Recent Activities on CCMHD Power Generation Studies with Fuji-1 Blow-down Facility", 33rd SEAM, II.1, UTSI, 1995.
22. Y. Inui, et. al., "Preliminary Study of Performance Characteristics of Pilot Plant Scale Nonequilibrium Disk Type MHD Generator", Proc. 26th SEAM, 7.5, Nashville, 1988.
23. S.Shioda, et al., "Power generation Experiments and Prospects of Closed Cycle MHD with Fully Ionized Seed", Proc. 7th Int. Conf. on MHD Electr. Power Generation, Vol. 2, p. 685, Cambridge, 1980.
24. G.W.Sutton and A.Sherman, Ëngineering Magnetohydrodynamics", McGraw-Hill, NY, 1965.
25. S.Kabashima and H.Yamasaki, "Recent Progress in Closed Cycle Nonequilibrium MHD Power Generation", Proc. 12th Int. Conf on MHD Electr. Power Generation, Vol. 1, p.1, Yokohama, 1996.

APPENDIX A

Recombination Radiation [8]

The recombination radiation rate as distributed over the wavelength is given by

$$Q_j(\lambda)d\lambda = n_e n_i v_e \sigma_j(v_e) f(v_e) dv_e$$

$Q_j(\lambda)d\lambda$: *photon emission rate in wavelength range $d\lambda$ corresponding to electron velocity range dv_e*
for radiative recombination to state j

n_e, n_i : *electron, ion density*

v_e : *electron velocity*

$\sigma_j(v_e)$: *radiative recombination cross $-$ sec tion for electrons with velocity v_e to state j*

$f(v_e)dv_e$: *fraction of electrons in the velocity range dv_e*

The relevant transitions for Cesium are those to the 6P, 5D, 6D and 7P levels, see Fig. A1
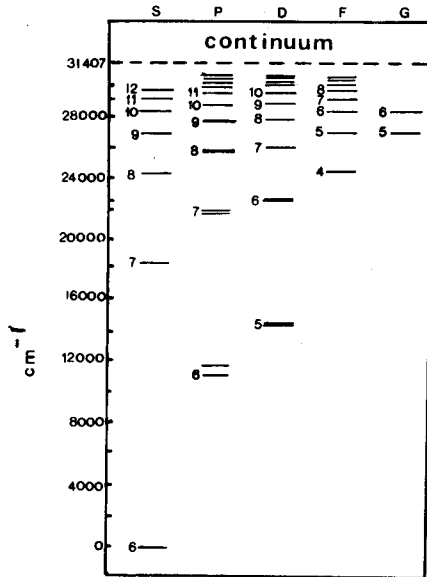
Fig. VI.6. The cesium energy level diagram.

Fig. A1. From [8]. Cesium energy level diagram.

APPENDIX B

LINEAR ANALYSIS OF IONIZATION INSTABILITIES

B1. BASIC EQUATIONS

Under reasonable assumptions the electron energy equation and continuity equation can be written as follows:

$$\frac{3}{2}kn_e\frac{\partial T_e}{\partial t} + \frac{5}{2}k(n_e\underline{u} - \underline{j})\cdot\nabla T_e = \frac{j^2}{\sigma} - 3n_e m_e k(T_e - T)v_c - (I - R)E_i$$

$$\frac{\partial n_e}{\partial t} + \nabla\cdot(n_e\underline{u}) = I - R$$

When electron inertia and electron pressure gradient are neglected the electron momentum equation can be replaced by Ohm's law

$$\underline{j} + \underline{j}\times\frac{e}{m_e v_c}\underline{B} = \frac{n_e e^2}{m_e v_c}(\underline{E} + \underline{u}\times\underline{B})$$

The usual electro-dynamic assumptions yield

$$\nabla\cdot\underline{j} = 0$$

$$\nabla\times\underline{E} = 0$$

B2. LINEARIZATION

The dependent variables are written as the sum of a stationary term (solution of the stationary basic equations) and a small space and time dependent term.

$$T_e(\underline{r},t) = T_{e0}(\underline{r}) + T_{e1}(\underline{r},t)$$
$$n_e(\underline{r},t) = n_{e0}(\underline{r}) + n_{e1}(\underline{r},t)$$
$$\underline{j}\{\underline{r},t) = \underline{j}_0(\underline{r}) + \underline{j}_1(\underline{r},t)$$
$$\underline{E}(\underline{r},t) = \underline{E}_0(\underline{r}) + \underline{E}_1(\underline{r},t)$$

B3. PLANE WAVE SOLUTIONS

First order terms are written as

$$X(\underline{r},t) = \hat{X}\exp[i(\underline{K}\cdot\underline{r} - \omega t)]$$

B4. PROCEDURE

- Introduce the linearization and the plane wave representation. Subtract the zero-order equations. The result is a set of homogeneous linear equations in the first order amplitudes.
- The set can only be solved, if the main determinant is equal to 0. This condition yields the dispersion relation, a relationship between ω and $\underline{K}$.
- The dispersion relation can be written as an expression of ω as a function of $\underline{K}$ and zero-order quantities. Since ω is a complex number such an expression can be found for its real as well as imaginary part.
- The imaginary part of ω describes the growth of the amplitude. A negative ω_i represents a growing instability. Often ω_i is expressed as a function of $\omega\tau$ with other zeroth order quantities constant. Onset of the instability occurs at the value of $\omega\tau$ for which ωi is equal to 0. This value of $\omega\tau$ is called the *critical Hall parameter*.

B5. NOMENCLATURE

Quantities
k	Boltzmann's constant
n	number density
T_e	electron temperature
T	gas temperature
$\underline{u}$	gas velocity
$\underline{j}$	current density
m	mass
I	ionization rate
R	recombination rate
E_i	ionization energy
e	electronic charge
$\underline{B}$	magnetic induction
$\underline{r}$	space co-ordinate
t	time
X	arbitrary quantity
$\underline{K}$	wave vector
ω	complex frequency

Sub- and superscripts
$\wedge$	amplitude
e	electron
0	zeroth order
1	first order
i	imaginary part

APPENDIX C

MHD Generator configurations

The general configuration of an MHD generator channel is schematically drawn in Fig. C1.
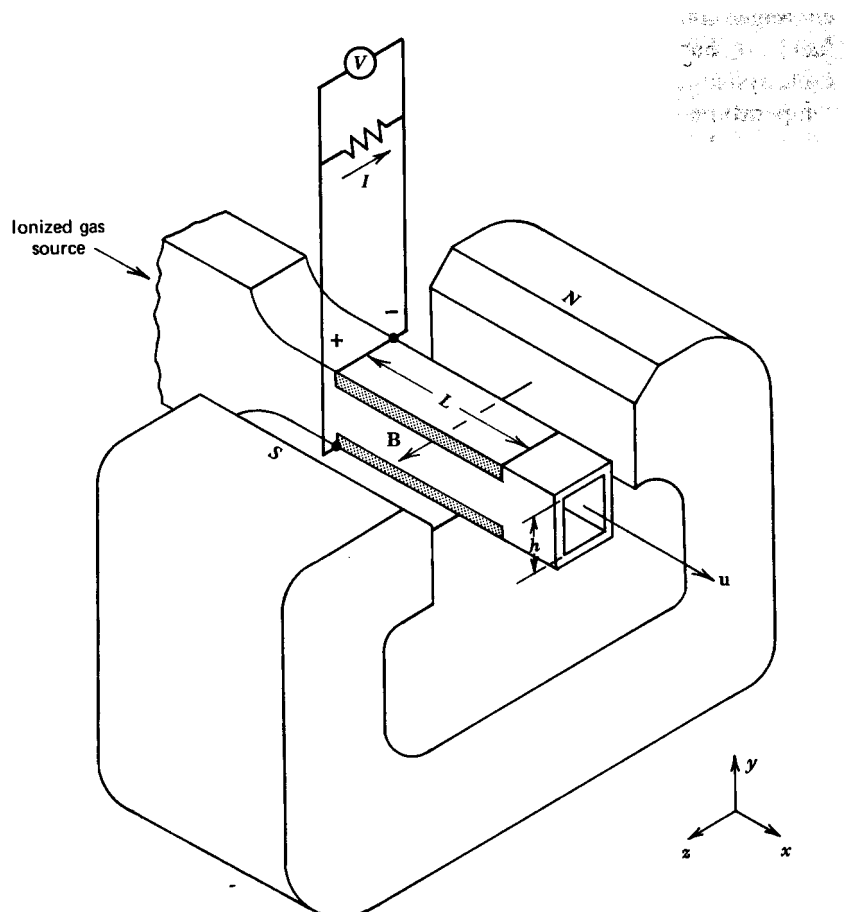
Fig. C1. From [2]. Schematic of the general MHD generator configuration.

The channel flow is directed perpendicular to the magnetic field and by means of electrodes, mounted in the walls, the induced $u \times B$ field can be loaded by an external circuit. Segmented electrodes can be applied to prevent short circuiting of the Hall field (see Fig. C2). When the load resistances are connected perpendicular to the flow we deal with a segmented Faraday generator and when they load the Hall field (parallel to the flow) we deal with a Hall generator.
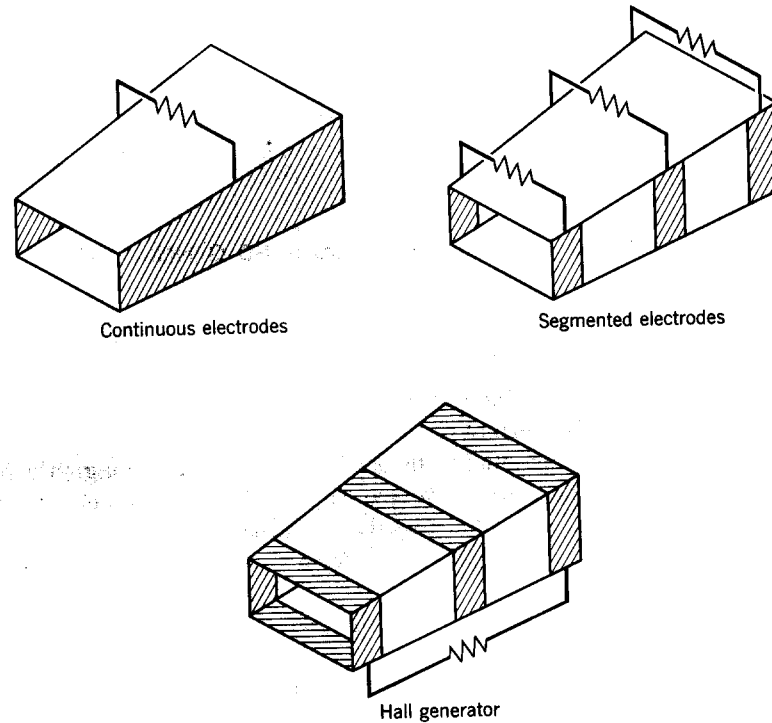
Fig. C2. From [24]. Common electrode configurations in linear channels.

Fig. C3 shows the Hall disk geometry. Here the flow is directed radially, away from the center. The magnetic field is in the axial direction. Since the azimuthal direction is short circuited the generator is operated as a Hall generator. The Hall field is loaded by resistors connected to electrode rings at the upstream and downstream end of the channel.
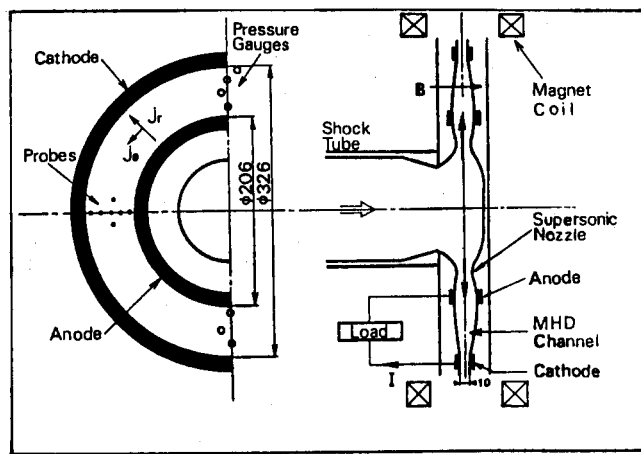
Fig. C3. From [23]. Hall disk geometry.

34

APPENDIX D

Streak photography

Fig. D1 shows the set-up of streak photography as it is applied for Fig. 22. A slit is projected on the channel wall, in the direction of the flow. During an exposure time of typically 400 μs the plasma is observed through the slit, while at the same time the photographic image is moved along the phosphor screen of the camera with a constant streak velocity. Fig. 22 is the result of this procedure. Since at a particular instant the streamer is seen as a dot, the complete picture can be interpreted as an *x,t* diagram of the streamer motion.
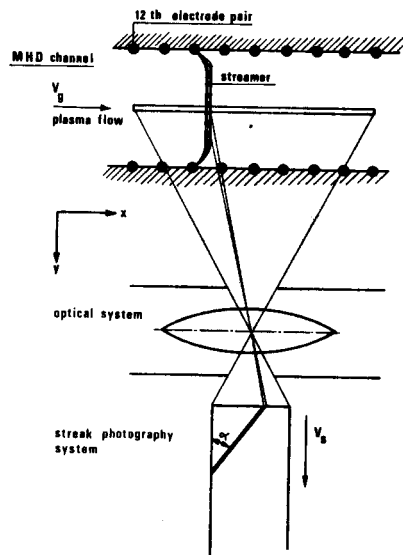
Fig. D1. From [17]. Set-up for streak photography.

PROSPECTIVE OF MHD INTERACTION IN HYPERSONIC & PROPULSION TECHNOLOGIES

V.A.Bityurin

Director of Division, Institute of High Temperatures of Russian Academy of Sciences,
Moscow, Russia

Abstract. In this paper three main potential applications of MHD interaction for advanced hypersonic and propulsion technologies are discussed. They are: (1) MHD flow/flight control; (2) MHD assisted mixing, ignition and combustion control in co-flow streams; (3) on-board MHD electrical power generation and flow acceleration. The first one seems to be very promising for hypersonic vehicles moving with high speed (3 -7 km/sec) through upper atmosphere that is typically related to re-entry missions. In such a situation the properly organized MHD interaction can help to reduce significantly the peak heat fluxes. Besides of this the MHD body force induced in the vicinity of the vehicle can control the trajectory parameters as well.

The recently formulated problem of using MHD interaction in internal flows (in particularly, in flow train of high-speed combustors) is studied now rather intensively. The anticipated effects of MHD interaction here are to stimulate the fuel/air mixing in co-flow streams by the additional vortex generation, to reduce the ignition time by the additional energy release and to control flame development.

The third, very traditional MHD application is the momentum and energy conversion in external and internal flows.

The status and physical and technical problems arisen in practical application development are also briefly discussed.

1.   Introduction

A new MHD role for aerospace applications was formulated at fiftieth [1]when the re-entry problem became real and critically important. Several proposals have been developed to reduce heat flux strength at critical point by means of magnetic field created by an on-board system. At the same time two new areas were formed where the MHD effects are the primary importance – MHD electrical power generation as a direct heat energy conversion into electricity and thermonuclear reactors with magnetic sustain of active matter –hot high temperature plasma.

A number of successful demonstration of MHD interaction stimulated research and development a numerous applications and particularly for space. One of the practically developed branches is the development of so called MHD low thrust accelerators for long term interplanetary journey. Another example of the successful development of a large-scale MHD system is pulse MHD generator in power output range from 1MWe till 100MWe for special applications in defense systems.

Since 50th considerable attention has been paid to the flows around blunt body in the presence of external magnetic field. At high magnetic Reynolds number the fluid deforms the magnetic field, rather than passes through it. As a result liquid free cavities are produced near the body, which prevents to appearing of large heat flux into the body surface [2]. The application problems of author's interest are those in which magnetic Reynolds number values are of order of unit or even much less. In this case the feasibility of MHD flow control relies on another principles and should be investigated in more details. The incompressible MHD flows around bodies including cylindrical that were

vastly studied in 60th (see, for example, [3]). Many exact and approximate analytical methods were developed for solving problems on the MHD flow over bodies of different shape. The bibliography of earlier studies on the finite conductivity MHD flows can be found in [4]. In one of the first work on the supersonic MHD flow around a body [4] it was shown that increasing MHD interaction factor leads to increasing of the bow-shock stand-off distance. Many fundamental features of MHD flows have been revealed in works of Bush [6,7] and Bleviss [8]. From recent studies on MHD flows around bodies note the works [9-13]. In papers [9-12] the Hall effect was neglected. In [10] the effects of chemistry on the MHD flow around a blunt body were evaluated. In [13] the two-dimensional analysis of the Scramjet inlet has been carried out.

Later a number of papers are published at AIAA Aerospace Science meetings (USA), Weakly Ionized Gas Workshop (AF,USA) , Moscow Workshop on Magneto-Aerodynamics for Aerospace Applications (RAS/EOARD) and at others forums.

In hypersonic low-pressure air flows (M>10) the electrical conductivity behind the bow-shock may become sufficient for the strong MHD interaction to appear in the presence of magnetic field of order of one Tesla.

The primary conditions for the implementation of any on-board MHD technology are the first - to provide a sufficient level of electrical conductivity of airflow and, the second – to make proper design of the magnetic system, which is known to be a weight critical component. In this respect, the physical background of flow parameters modification and the magnetic system assessments are discussed further in this Section. The magnet size and weight must be gauged against the gain that can be obtained in terms of flow optimization. Some general relationships are obtained in this Section which should be useful for the development of a systematic approach to this problem.

The MHD flow/flight control is one of the clearest options of MHD technology applications in this field. However in literature there are not so many good examples of such a suggestion. Typically the MHD flow control is the natural component of another suggestion including MHD interaction such as, for example, MHD scramjet in-take optimization.

The latter is included in one of the most intrigue cases of MHD application in aerospace so-called AJAX concept proposed more than ten years ago in Russia. The basic idea is to use MHD energy conversion cycle to provide more desirable flow conditions inside of scramjet flow train from in-take up to the nozzle exit. The results of estimation for this type of system, based on a simplified analysis, are discussed herein.

One of the most promising fields for MHD applications is MHD control of the bow shock characteristics. In particular, optimization of the drag to thrust ratio and/or a significant reduction in vehicle heat stress can be expected. Theoretical estimations and numerical simulation have shown that the bow shock configuration changes significantly when in the presence of an externally applied magnetic field. On the other hand, the reliable flow parameters prediction is still problematic due to very complicated phenomena that occur in the vicinity of a hypersonic vehicle nose.

2. Background

The motion of spacecraft in the upper atmosphere occurs with hypersonic velocity and for these reason results in a strong shock wave creation. The strong shock waves form highly non-uniform flow field. The velocity of spacecraft between 7 and 11km/s corresponds to temperature elevation just behind the shock up to 10000-20000K. Due to relaxation phenomena the air temperature decreases to the level of 5000-10000K at the vehicle surface. High heat fluxes in the vicinity of critical points of spacecraft limit the acceptable trajectories of different kinds of spacecraft and need to optimize the flow around the hypervelocity vehicle. Traditional gas dynamics approach is based on the vehicle shape and trajectory optimization. The potential of the condition optimization can be increased significantly by involving additional physical phenomena influencing on the flow field. In the case under consideration when one of the main peculiarities of the process is the ionization phenomena in shock layer on the vehicle surface the magnetohydrodynamic (MHD) interaction can be used to extend the optimizing flow control.

Generally speaking the MHD interaction is characterized by the local momentum and energy conversion and their redistribution over the flow field. The ponderomotive force

$$\mathbf{F} = \int \mathbf{j} \times \mathbf{B} dV \tag{2.1}$$

integrated over whole external flow has provided the reaction $\mathbf{R} = -\mathbf{F}$ and, probably, the moment

$$\mathbf{K} = \int \mathbf{r} \times (\mathbf{j} \times \mathbf{B}) dV . \tag{2.2}$$

These two body force integral values in combination with conventional gasdynamics force and moment

$$\mathbf{F}_{gd} = -\int \mathbf{p}_n dS \quad , \quad \mathbf{K} = -\int \mathbf{r} \times \mathbf{p}_n dS \tag{2.3}$$

define the motion of the aircraft in atmosphere. It is important to note that electrodynamics ponderomotive force $\mathbf{f} = \mathbf{j} \times \mathbf{B}$ and energy source $\mathbf{jE}$ modifies the flow field and, consequently indirectly change the gasdynamics values $\mathbf{F}_{gd}$ and $\mathbf{K}_{gd}$.

Thus, the magnetohydrodynamics interaction between the external flow and electrical and magnetic fields can be used as an additional flight control system influencing on the external flow in some vicinity of the vehicle. The flow region affected by such a control system is independent directly upon Mach number distribution.

The MHD interaction intensity is characterized by the value of so-called MHD interaction parameters (or Steward number) equal to the ratio of the electromagnetic body force $|\mathbf{j} \times \mathbf{B}|$ times characteristics length l to the dynamics pressure gradient

$$S = |\mathbf{j} \times \mathbf{B}| l / \mathbf{r} u^2 \approx \mathbf{s} B^2 l / \mathbf{r} u \quad , \tag{2.4}$$

where $\mathbf{j}$ is the electrical current density, $\mathbf{B}$ is the magnetic induction, and l represents a characteristics length (a deceleration distance). It should be noted that the second definition of the Steward number is based on an implicit assumption that the electrical

current is self-generated. The current is produce by the mechanical work done by the flow against body force $\mathbf{j} \times \mathbf{B}$. In an on-board MHF flow/flight control system the electrical current can be defined by externally applied electrical field, which could be much higher as compared with the characteristic value of induced field $\mathbf{u} \times \mathbf{B}$. In such cases the actual MHD interaction could be correspondingly much higher than the classical MHD estimation. One of the examples is a MHD accelerator providing significant increase of the jet impulse.

Electrical current density $\mathbf{j}$ is defined by the generalized Ohm's law, one of the it's simplest form including so-called Hall effect is

$$\mathbf{j} + wt/B \mathbf{j} \times \mathbf{B} = s(\mathbf{E} + \mathbf{u} \times \mathbf{B}), \tag{2.5}$$

where s is electrical conductivity and wt Hall parameter. The electrical conductivity can be estimated by formula $s = n_e e^2 t / m_e$, where n_e is electron number density and t is a free path time. Consequently in the same approximation the Hall parameter is

$$wt = eB/m_e t \quad \text{or} \quad wt = sB/n_e e.$$

It is clear that there are two key values needed for actual MHD interaction: electrical conductivity and magnetic field. The magnetic field can be in principle created with a proper on-board magnetic system. The electrical conductivity needs the presence of free charges in the gas flow – in practice it should be electrons. Taking as an example the conditions of upper atmospheric hypersonic flight: velocity 3000m/s, temperature 250K, pressure 1kPa, gas density .01kg/m^3 one can find the current density required for effective MHD interaction $(S \sim 1)$ $j \sim \rho u^2/Bl \sim 10^4$ - 10^5A/m^2 for B=1T and l~1m.

Thus, the required level of the electrical conductivity is from several Siemens till several tens of Siemens. In the pure air such a level of electrical conductivity corresponds under thermal equilibrium conditions to the temperature above 6000-7000K. This level is reached in the hypersonic viscous shock layer formed behind bow shock in hypersonic flight.

Another possibility to provide the conductivity is an artificially created a rather high ionization degree. The latter can be estimated as

$$a \approx s \frac{m_e Q_{ea}}{e^2} \sqrt{\frac{3kT_e}{m_e}} \approx 10^{-3}\text{-}10^{-2}. \tag{2.6}$$

From the other hand the MHD interaction parameter based on an induced current density as a characteristic value can presented in the following form:

$$S_u \approx \frac{sB^2 l}{ru} = \frac{n_e e^2 t}{m_e} \frac{B^2 l}{ru} = \dots = a \frac{t}{t} \frac{m_e}{m_a} (wt)^2 \ , \tag{2.7}$$

where t is a residence time in working volume.

In the case of externally applied electric field the similar estimation gives

$$S_p \approx \frac{\boldsymbol{s}EBl}{p} = \frac{n_e e^2 \boldsymbol{t}}{m_e} \frac{EBl}{n_a k T_a} = \ldots = \boldsymbol{a} \boldsymbol{w} \boldsymbol{t} \frac{eV}{k T_a} \quad . \qquad (2.8)$$

In this expression V represents an external voltage applied over the whole interaction area.

In high Mach number supersonic flow it is important to note that two different definition of MHD interaction parameter – by momentum S_u and by pressure S_p are connected as following: $\qquad\qquad\qquad S_u \approx S_p \boldsymbol{g} \mathrm{M}^2$

One of the most important meaning of the Hall parameter is to indicate when the scalar ('conventional') character of the plasma conductivity in external magnetic field ($\boldsymbol{wt} \ll 1$) changes to the tensor character of the conductivity ($\boldsymbol{wt}^3 1$). The tensor character of the conductivity results, in particular, in the fact that the directions of electrical field and current density vectors are significant different. Furthermore the effective plasma impedance becomes higher along with the value of $(1 + \boldsymbol{wt}^2)$. It is known however that the effective conductivity of plasma in magnetic field can be recovered in principle with special configuration of electric field. Unfortunately under realistic conditions of more or less significant non-uniformity of electrical conductivity in flow such an electrical field re-configuration becomes not effective – the effective plasma impedance is estimated as $r = G / \langle \boldsymbol{s} \rangle$, where so-called G-factor firstly introduced by R.Rosa [14] is defined as

$$G = (\boldsymbol{k} - 1)(\boldsymbol{wt})^2 + \boldsymbol{k},$$
$$\boldsymbol{k} = \langle \boldsymbol{s} \rangle \langle 1/\boldsymbol{s} \rangle \quad \text{where} \quad \boldsymbol{k} \geq 1$$

(2.9)

Furthermore, under conditions when the Hall current leakage is allowed the G-factor should be modified as

$$G_x = (\boldsymbol{k} - k_x)(\boldsymbol{wt})^2 + \boldsymbol{k}, \text{ where } k_x \leq 1.$$

(2.10)

Substitution of (2.10) into (2.7) and (2.8) results in

$$S_u \approx \frac{\boldsymbol{s}B^2 l}{\boldsymbol{ru}G_x} = \frac{n_e e^2 \boldsymbol{t}}{m_e} \frac{B^2 l}{\boldsymbol{ru}G_x} = \ldots = \boldsymbol{a} \frac{t}{t} \frac{m_e}{m_a} \frac{\boldsymbol{wt}^2}{G_x} \to \boldsymbol{a} \frac{t}{t} \frac{m_e}{m_a} \frac{1}{(\boldsymbol{k} - k_x)} \text{ when } \boldsymbol{wt} \to \infty$$

(2.11)

Thus, MHD interaction parameter for non-uniform non-perfectly insulated plasma formation saturates at some level with $\boldsymbol{wt}^2 \circledR \yen$ (magnetic field strength!). For this reason the operation under high Hall parameter condition ($\omega\tau > 1$) is rather undesirable because results in much more complexity of on-board MHD system. Then the relationships presented above can be used to estimate the value of governing parameters when the Hall parameter is limited.

As it will be shown later the typical values of the parameters in MHD interaction parameter formula for the conditions of hypervelocity flight in upper atmosphere are as follows: $\boldsymbol{s} \sim 200 \mathrm{S/m}$, $\boldsymbol{ru} \sim 1$, and for the characteristics length the shock wave distant can

be used $l\sim0.1$m. So for effective MHD interaction the magnetic induction needed is about $B\geq0.2$T that is the routine electromechanical level. However, the discussed above Hall effect limits the effectiveness significantly.

In calculating the hypersonic flow over blunt body one should take into account the radiation transfer from the high temperature region. Also note that factor M^2/Re (M is the Mach number and Re is the Reynolds number) becomes of order of one, which leads to smearing of the shock wave.

Under conditions mentioned above the MHD flow is described by the following set of the governing parameters:

$$\rho_\infty, p_\infty, v_\infty, r, c_p, \boldsymbol{m}\ \boldsymbol{l}, \boldsymbol{g}, T_w, q_R, T, B^*, E_z$$
(2.12)

In (2.12) c_p is the heat capacity at constant pressure, γ is the ratio of heat capacities, q_R is the characteristic radiation power, or the value of divergence of radiative heat flux, $\boldsymbol{m}=\boldsymbol{w_e}\boldsymbol{t_e}/B$, $\boldsymbol{w_e}\boldsymbol{t_e}$ is the Hall parameter.

According to the theory of similarity and dimensionality (see, for example [15]), any dimensionless flow characteristics is the function of the set of the following parameters

$$\Gamma = \{M, Re, \gamma, Pr, \bar{T}_w, \bar{q}_R ; S, K, \beta, Re_m\},$$
(2.13)

Here M is the Mach number, Re is the Reynolds number, Pr is the Prandtl number, $\bar{T}_w$ is the temperature factor, the ratio of surface temperature and the free-stream stagnation temperature. $\bar{q}_R$ is the characteristic radiation power. S and K are MHD interaction factor and electric load coefficient, respectively. β is the Hall parameter, Re_m is the magnetic Reynolds number. These magnitudes are defined as follows:

$$M^2 = \frac{u_\infty^2 \rho_\infty}{\gamma p_\infty}, \quad Re = \frac{\boldsymbol{r}_\infty u_\infty r}{\boldsymbol{m}}, \quad Pr = \frac{c_p \boldsymbol{m}}{\boldsymbol{l}}, \quad S = \frac{\sigma B_*^2 r}{\rho_\infty u_\infty},$$

$$K = \frac{E_z}{u_\infty B_*}, \quad \boldsymbol{b} = \frac{e\boldsymbol{t}B_*}{m}, \quad Re_m = u_\infty r \boldsymbol{s}\boldsymbol{m}_0 \qquad (2.14)$$

(μ_0 is the magnetic permeability of vacuum). Variety of flow regimes is determined by first six gasdynamics parameters and by four electrodynamics ones.

It is notable that under hypersonic flight conditions the non-equilibrium and finite rate kinetics effects play an important role. Thus, for the full characterization of the hypersonic flow over a body the Damkoeler number Da$=\boldsymbol{t}_{ch}u_\yen/L$ is to be introduced into the expression (2.14). Moreover, taking into account the low pressure at high altitude and the rather limited size of the bodies considered the Knudsen number Kn $= l_f /L$ is to be added into the right hand part of the symbolic expression (2.12). It can be easily shown that the Knudsen number is naturally appeared in expressions (2.7), (2.8), and (2.11) in

place of **t**/t ratio. This fact seems to be very important saying that the fundamental linear scale for MHD aerospace applications is the free path length of electron.

Typical Trajectories

The minimum velocity of a spacecraft on stationary orbit of the Earth satellite is defined by the balance between centrifugal force and gravitation force $v = \sqrt{gR}$ =7.92 km/s ,which corresponds to the first space velocity. The maximal velocity on a stationary orbit of the Earth satellite is defined by the balance of kinetic energy and potential energy of spacecraft in gravitational field of the Earth $v = \sqrt{2gR}$ =11.2 km/s , which corresponds to the second space velocity.
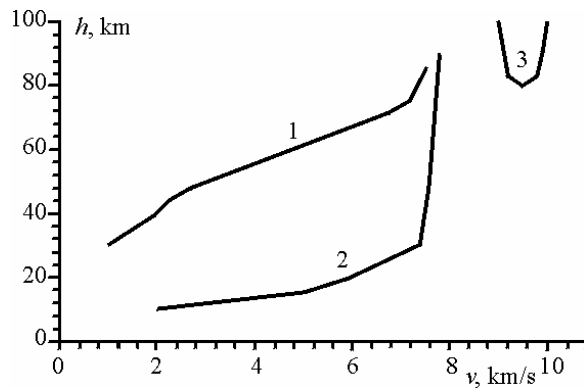
Figure 1 Typical Spacecraft Trajectories.

The Earth is covered by the gaseous layer atmosphere. The thickness of the atmosphere is about 700km. Thus, during re-entering or penetrating maneuver spacecraft or hypervelocity vehicle has to pass through the atmosphere. At this path the vehicle is affected strongly by aerodynamics forces and heating. The initial velocity of the vehicle at atmospheric path depends on the kind of trajectory and lies in interval between the first and the second space velocities. The typical trajectories corresponding to [16,17] are presented in Fig. 1 and represents (1) the gliding losing height with aerodynamics control by lift and tangent forces, (2) ballistic trajectories with no control, and (3) inter orbit maneuvers with reflection.

Parameters of Atmosphere

The parameters of the Earth atmosphere are defined as the standard atmosphere

Figure 2 Atmosphere Parameters vs Altitude
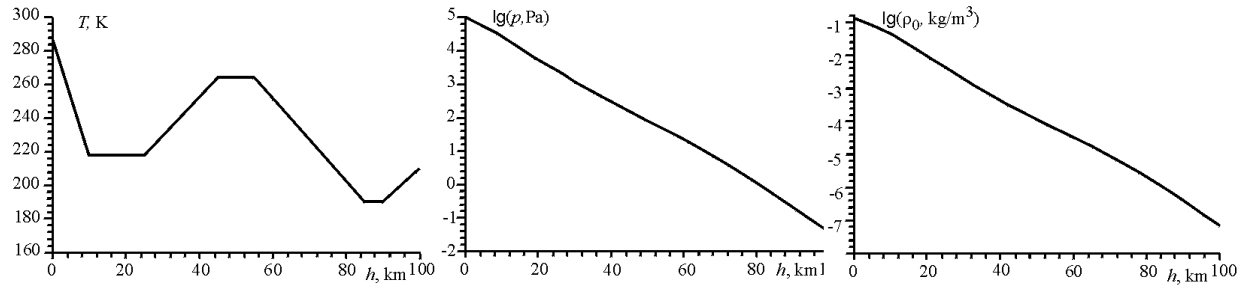
[18] averaged on year period. The atmosphere is characterized by the exponential pressure and density drops with altitude (Fig.2). The Knudsen number calculated within boundary layer thickness shows that at the altitude grater then 100km the aerodynamics influence on the spacecraft motion is practically negligible.

Aerodynamics conditions

The typical flow parameters in external flow around the spacecraft are presented in Fig.3. Due to strong deceleration at the critical point the air just behind the (normal) shock wave is heated up to 20000K when Mach number is 25. The dissociation and ionization occurred under such high temperature conditions results in decreasing the temperature in shock layer till to 5000K.
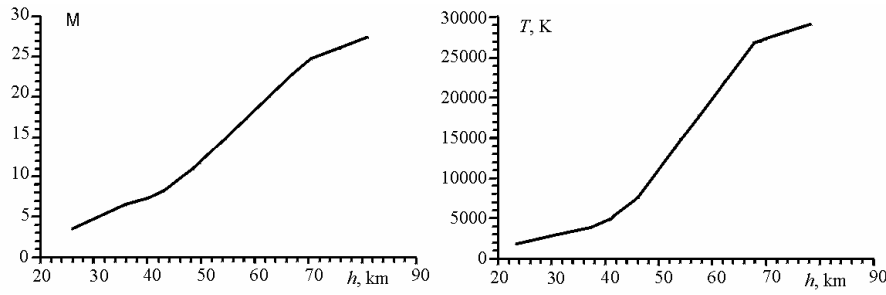
Figure 3 Mach Number and Temperature behind the Shock Wave along the Gliding Trajectory.

The ionized air becomes electrical conductive. This natural electrical conductivity in shock layer can be used to change the thermal and dynamics effects on spacecraft [1,19] (see also the critical review presented in paper [20]). As it was mentioned above the most critical parameters for effective utilization of the MHD interaction to optimize spacecraft flight conditions is conductivity. The analysis of complex plasma-chemical processes performed in [21,22] has shown that the «natural» electrical conductivity along the trajectory has a maximum in the altitude interval from 60 to 80km.

The analysis of the flow parameters in the shock layer performed in [21,22] for different type of spacecraft (1— gliding spacecraft trajectory of Shuttle and Buran type, 2— trajectory with reflecting maneuvering, 3— re-entering hypervelocity space craft). The schematic of the spacecraft considered is presented in Fig..4 and nominal conditions are presented in the Table 1.

Table.1.

	R, cm	$\varphi,°$	S/R	h, km	v, km/s	σ, S	δ, cm	S_b
gliding trajectory				60	5.5	2	4	0.1
gliding trajectory	10	10	40	70	7	16	7	30
gliding trajectory				80	7.8	6	10	40
maneuver with reflection	40	70	10	80	10	60	15	3000
hypervelocity entry	40	10	10	80	10	200	15	1000
hypervelocity entry		45				350	15	1700
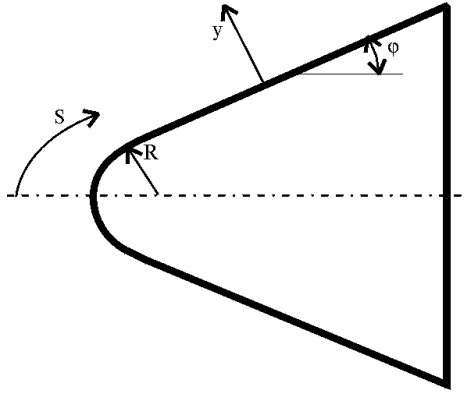
Figure 4. Schematic spacecraft geometry considered and parameter definition

S_b is calculated for B=1T.

The numerical analysis of the flow around the vehicle by V.A.Gorelov et
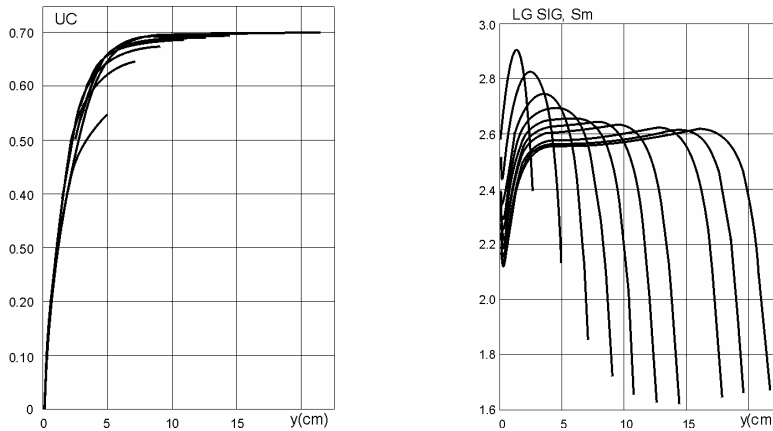
Figure 6. Relative Velocity Profile and Electrical Conductivity across Shock Layer for 10 Different Location along Streamline. Conditions: U=10km/s, H=80km, φ =45°, R=0.4m.

al…[21,22] was based on a model of continuous media with sliding at the surface. The gas flow including the endothermic dissociation and recombination reactions is described by the full set of equations for the viscous shock layer. As an example of calculation in Figs.6 the relative velocity and log of conductivity across the viscous shock layer for the case 3 are presented for ten different locations along the flow direction. Just behind the shock wave the parameters are defined by generalized Renkine-Gugonout relationships. After that the dissociation and ionization region occupies approximately 25% of the layer. The temperature decreases here in 2-3 times. Below this an equilibrium region with approximately constant temperature and mixture composition occupies another 50% of the layer. Near the wall the gas temperature decreases due to heat transfer resulting in a back recombination reactions. The wall temperature is defined by the convective and radiative heat fluxes and equal approximately to 1200K.

In the Table 1 the characteristic values of conductivity, the thickness of the constant conductivity layer along the sidewall of the vehicle and MHD interaction parameter for the conditions considered are presented also. The conclusion derived from the Table 1 is that the MHD interaction is rather high and can be used effectively to control the external flow parameters and the spacecraft trajectory. It is important to note that the maximum heat fluxes occurred also in the altitude interval from 60 to 80km for gliding trajectories.

At the same time the natural conductivity in shock layer is not high enough to utilize the MHD interaction for the purposes indicated for the lower altitude and for aircraft flying with lower velocities. In this case to extend the MHD application for lower altitude and lower velocities different pre-ionizing technique are considered: microwave [20], pulse corona [23], seeding the flow with low ionization potential material [20],
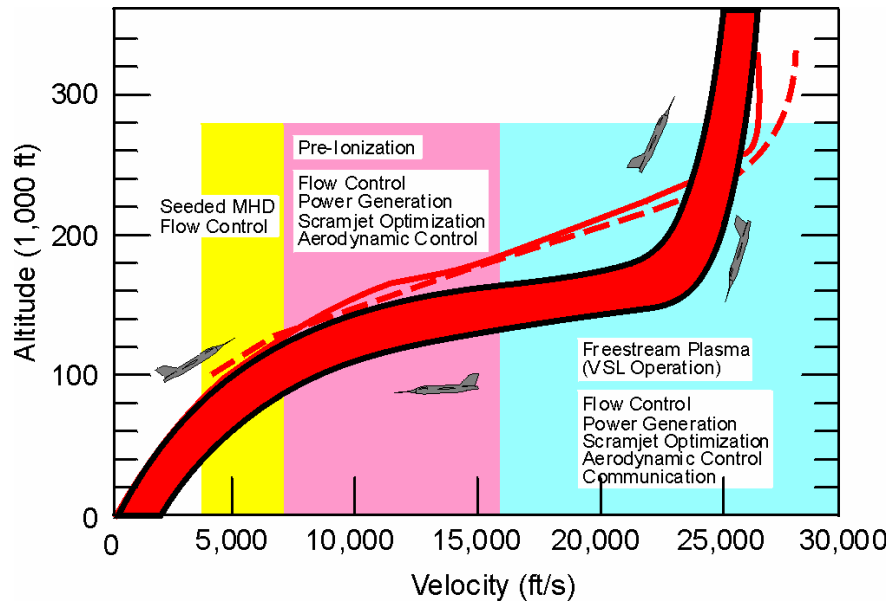
Figure 7 MHD Application Map

special organization of the MHD interacting flow [22,24,25], e-beam utilization [26-28].

On this base the summarized MHD application operational map is presented [29] in Fig.7.

3.   MHD Flow Control

3.1 Flow Field Modification

A body moving through atmosphere with hypersonic velocity creates a system of strong shock waves. The shock waves formed are mainly responsible for a dramatic increasing in drag and huge heat flux into the body surface. These effects are significant technical problems that must be addressed for practical implementation of the hypersonic technologies [30,31].

Because of MHD as a conventional electromagnetic device is reversible the MHD system discussed above can be used also to control the flight by the creation the drag, lift and tangent forces as well as controlling moment. The advantages of MHD flight control are associated with the extended interaction region including the gas dynamically undisturbed upstream flow. One of the promising features of MHD control system is a principle possibility to influence on the external flow structure including the shock wave formation.

Various aspects of the MHD flow control have been discussed in papers [1,5-13,19-30,33-37]. The MHD flow control system (MHDFCS) under consideration consists of two main components: a magnet system that provides a desirable level of magnetic induction in the interaction region; and, an MHD generator/accelerator represented by an electrode system installed on vehicle upstream surface. A proper load control subsystem is assumed to be available and its design and operation are outside of the scope of this paper but within current technology grasp.

The cost of such an MHD provided advantage in energy resources on a spacecraft board is the weight of the whole MHD system consisting of magnet, MHD channel, the MHD generator control system and so on. For rough estimation one can refer to the results of transportable MHD system optimization by weight to the power installed. In the papers [36,38-40] a transportable MHD generator of 10MWe was proposed. It was found that specific weight was expected as high as 0.02-0.04kg/kW. This figure is comparable with the typical transportable power supplying systems.

An MHDFCS affects the flow in the hypersonic viscous shock layer by means of three field parameters defined by the three integral characteristics: integral electromagnetic body force $\mathbf{F}$ acting in the flow and its corresponding reaction force $\mathbf{R} = -\mathbf{F} = -\int_{flow} \mathbf{j} \times \mathbf{B} dV$;

the integral moment, $\mathbf{K} = \int_{vehicle} \mathbf{r} \times \mathbf{f} dV$;

and, the integral electrical power source/sink $Q = \int_{flow} \mathbf{jE} \, dV$.

Besides the aforementioned impacts MHD effects have on the flow, the MHDFCS influence is implicit through the flowfield modification caused by the local body force $\mathbf{f}=\mathbf{j}\times\mathbf{B}$ and local energy source/sink $\mathbf{q}=\mathbf{j}\times\mathbf{E}$.

In the concept considered the magnetic system is assumed to be simulated by one- or two-wind coils zigzag, shaped (see Fig.2.5.3.1 and Fig.2.5.3.2). This winding system provides a multipole magnetic induction distribution. The depth of the significant magnetic field penetration into the flow in normal-to-surface direction is defined by, the period size of the winding in azimuthal direction.

Considering the hypersonic viscous shock layer as the most probable field for MHD influence, one can hypothesize that the most preferable winding configuration is that in which the characteristics thickness of the HVSL is used as the estimation for the half period size. It is assumed implicitly that the flow direction size of the winding considered is typically much greater than the azimuth period.

Two typical MHD interaction patterns might be considered. The first is when the

Figure 8 The schematic of the multipole magnetic system installed on a hypersonic spacecraft.

interaction occurs in the vicinity of a flow directed portion of the winding. (no even/odd difference). (Because of aforementioned remarks on size ratio this case is much more important.) The second pattern is when the flow in the vicinity of an azimuthal portion of the winding. Both are considered in analysis of following sections.

Assuming for simplicity all flow parameters are constant and that the magnetic system is infinitely long in the flow direction, one can derive the following expressions for governing parameters

$$\mathbf{B} = (0,0,B) \ , \ \ B = B_0 \frac{r_0}{r} \ , \ \ B_0 = \frac{n I_m}{2 p r_0} \ ,$$

$$\mathbf{j} = (0, j, 0) \ , \ \ \mathbf{E} = (0, E, 0) \ , \ \ j = s(E - uB) \ , \ \ j = j^0 \frac{r_0}{r} \ ,$$

$$i = \int_0^p jr \, d\mathbf{q} = \text{const} \ .$$

(A cylindrical reference frame is used with the x-axis in the flow and magnetic inductor current direction, r-axis in direction perpendicular to the magnetic inductor axis, and θ-axis as the azimuth direction.) In the above expressions, I_m is magnet current, r_0 is an apparent winding radius, u is x-component of the flow velocity, B is the θ-component of the magnetic induction, E is the r-component of the electrical field strength, i is specific electrode current (per unit length).

For the short circuit case (E=0), the specific current is expressible as: $i = R_m^1 I_m$, where R_m^1 is the magnetic Reynolds number for a 1.0 meter characteristics

length. The integral electromagnetic force integrated on the one-meter domain can be estimated as

$$F_i = R_m^1 \boldsymbol{m}_m^2 \boldsymbol{z}/G \; , \;\; \boldsymbol{z} = \frac{1}{2\boldsymbol{p}} \ln \frac{r^*}{r_0} \; , \;\; P_{i,\max} F_{i,\max} \, u/4 \; .$$

where r^* is the characteristics thickness of the interaction region and μ is the magnetic permeability. The condition required such that the MHD system is self sustained, e.g., the power consumed by the flight control systems is less than the power produced by MHD generator, is

$$\boldsymbol{x} = \frac{P_{MHD}}{P_{mag}} = \frac{\boldsymbol{s}_{mag}}{\boldsymbol{s}_{flow}} \operatorname{Re}_m^2 \frac{\boldsymbol{p}}{16G} \ln^2 \frac{r^*}{r_0} > 1 \; , \;\; \operatorname{Re}_m = \boldsymbol{s}\boldsymbol{m}u r_0 \; ,$$

where G is so called G-factor modified for the considered configuration. (Note, G-factor
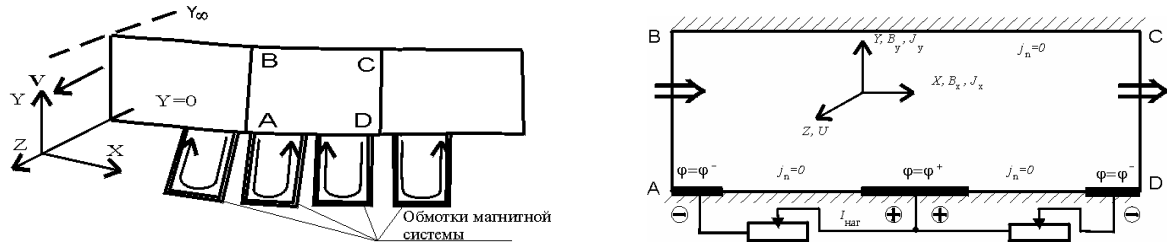
Figure 9 Geometry of MHD Generator, Numerical Simulation Domain and Boundary Conditions used in Numerical Simulation.
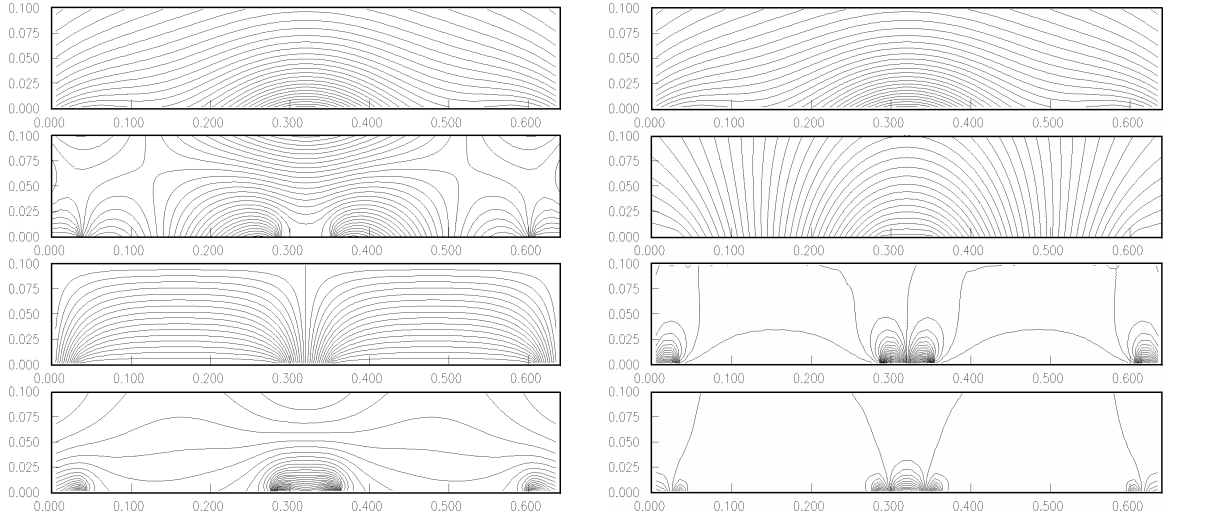
Figure 10. Magnetic Field Strength Lines, Electrical Potential, Electrical Current Stream lines (, and Body Force Distributions.
Open Circuit Condition (left) and Short Circuit Condition (right).

is a measure of plasma non-uniformity used in MHD power technology.)

The schematic of MHD converter utilizing the ionized gas flow in the viscous shock layer (VSL) is presented in Fig.9. A multipole magnetic system similar to configuration used in MHD-Submarine Propulsion System has been proposed. In the case

considered the efficiency of such a configuration can be high enough in comparison with submarine case dealing with uniform conductivity in the flow. In Fig.10 an example of magnetic field and induced electrical current structure are plotted.

In the Fig.11 the controlling force generating by one-section of MHD system is also indicated.

From the preceding expressions it is clear that interaction intensity is dependent on the magnetic system characteristics (total length of winding and inducting current I_m) and the flow parameters in the interaction region (typically in the HVSL). At the lower flight altitudes and for lower flight Mach number the ionization degree and, consequently electrical conductivity behind of the bow shock in viscous shock layer are not high
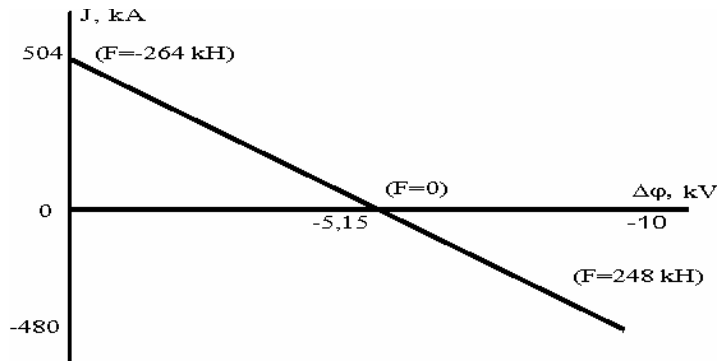
Figure 11. Loading Characteristics of a Single Section of MHD Converter.

enough to provide the effective MHD interaction.

One of the possible approaches solving the incoming flow conductivity problem was firstly proposed by V.Derevyanko, Latyev et al [41] to use non-uniform flow MHD interaction. Such a scheme was originally developed for MHD electrical power generation to avoid any seed injection. The high temperature plasma formation: T-layer programmable created at the entrance into the MHD device channel should be
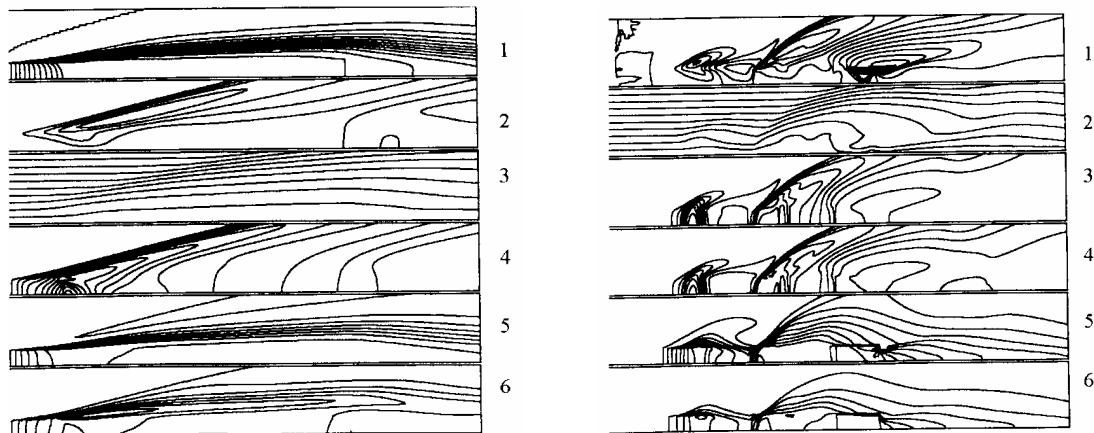
Figure 12. Flow Field Numerical Simulation Results . "Shock free case".(left) "Multi Shock case".(right).
Level lines: 1— u, 2— v, 3— color, 4— relative density, 5— relative stagnation enthalpy, 6— Mach number.

responsible for effective interaction of the floe with the magnetic field. Many others schemes of such a type were discussed later [36,42,43]. In the paper [36] a simplified analysis was conducted to estimate potential of non-uniform flow concept.

In Figs.12 as example of some results of flow fields modification with MHD simulating interaction are plotted. Two cases are presented: The first demonstrates a practically free shock wave deceleration of the flow from 3000m/s to 500m/s, and the second demonstrates the flow parameters distributions with a series of weak shocks. In both cases a quasi periodic interaction was implemented. A 2D time dependent numerical model was used to simulate such a flow.

The first results obtained at this preliminary stage confirm the prospective to optimize the flow field by body forces and energy sink/sources distributed properly. The MHD interaction is one of the most obvious candidate for such a distributed flow controlling mechanism. The main problem is to provide a significant level of electrical conductivity. In particularly, the load characteristic in Fig.11 demonstrates rather high level of MHD drag force created by one section of MHD system.

3.2 Heat Flux Management. Experimental and Theoretical Studies of MHD Interaction at Cylinder in Hypersonic Flow.

The Section presents the experimental and analytical results of the study of MHD interaction at blunt bodies moving in air with hypersonic velocities (M>6). One of the simplest configurations – the transverse hypersonic flow around a circular cylinder with
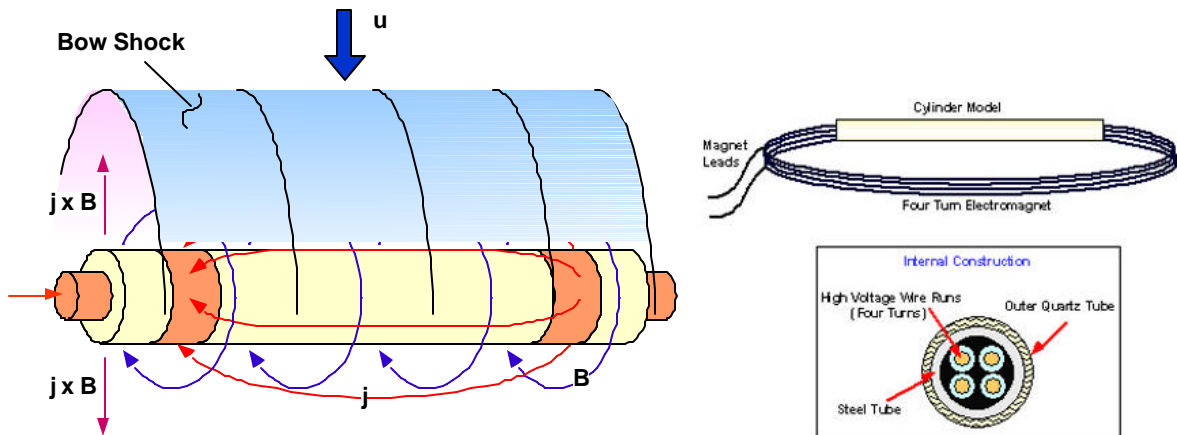
Figure 13 Schematic of MHD flow over the circular cylinder with axial electric current and the model design concept.

axial current inducting an athimutal magnetic field of Teslas level – is considered. The MHD interaction effects are studied at the configuration simulating one of the main features of the on-board MHD flow control systems – non-uniform magnetic field. The goal is to demonstrate the flow field modification; in particular, the strong bow shock stand-off distance change resulting in changing of he peak heat fluxes near the up-stream critical point. The 2D configuration decreases the difficulties in interpretation of the experimental results and numerical simulation of the phenomena. The concept of the experiment and the model design are presented in Fig13.

Experimental Facility

The experimental study discussed in this paper is performed at the TsAGI hypervelocity wind tunnel facility with MHD acceleration (MHD WT) of the airflow. The facility has been described in many details elsewhere [44]. The facility was recently modified in order to meet the new experimental conditions requirements. In the present configuration the MHD WT facility consist of the following main components: the arc pre-heater, the seed injection system, the primary supersonic nozzle; the MHD accelerator equipped with the 2.4 Tesla electromagnet and with the Faraday segmented type of MHD channel of the rectangular cross-section linearly increased from the inlet to the exit; the power supply system providing the independent power feed of each electrode pair; the secondary nozzle accelerating the airflow till Mach number from 8 to 15; the test section of approximately $.5 \times .5 \times .5$ m^3 ; the supersonic diffuser and the vacuum chamber. The general view of the MHD WT facility test section part is presented in Fig.14.

Fig. 14. General view of the MHD WT facility at TsAGI (left) and a Model in the Test Section

In the present configuration air flow at the pressure of 3 atm preheated in the archeater up to 3500K, the airflow is seeded with ~1% NaK and accelerated in the MHD channel that provides parameters of the flow in the test section as following: the airflow cross-section at the secondary nozzle is $.11 \times .11$ m^2, the static pressure is 33Pa, the static temperature is about 600K, the density is about 2.10^{-4} kg/m^3, the velocity is about 6500m/sec (M~12), that corresponds approximately to hypersonic flight at the altitudes between 60 – 80 km. One of the airflow characteristics of most important for the experimental study is the gas composition that differs significantly from the atmospheric air being more (non-equilibrium) exited and dissociated during the intensive energy impute in the MHD channel.
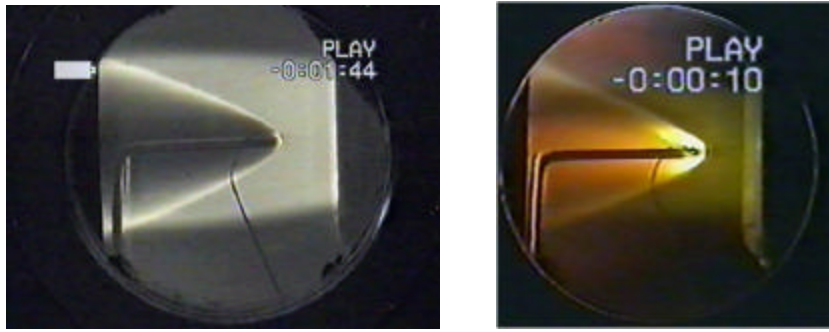
Figure 15. A model in the test section before and during the MHD acceleration

The working cycle of the facility provides approximately 0.5 sec period of the MHD accelerated flow in the test section. The operation mode is confirmed by the static pressure probes along the flow train and the Pitot' tube in the test section. The typical view of a model and airflow in the test section is presented in the Fig.15.

Two main configuration of the model are used. The first one corresponds to the schematic diagram presented in Fig.6, and the second one resulting from the modification made after the first series of experiments with the original configuration. The modification was motivated by the observed deformation and displacement of the model during the magnetic field pulse due to unbalanced electromagnetic forces between different parts of the electromagnet turns. The modification solves such a problem with change of the external electromagnet turns configuration made now symmetrical in respect to the cylinder part, that provides practically full balance of the forces acting on the cylinder part from the different turns. The one of the particular realizations of the modified model is exampled in Fig.16.

Three different orientations are used in the experiments: horizontal, vertical and sloped with proximately 40° to the flow direction. Two first are basically equivalent, and the reason is to provide different visualization direction: along the cylinder axis for horizontal orientation and across the cylinder for the vertical one. The sloped orientation involves the significantly 3D interaction caused by the axial component of the flow velocity with azimuthal magnetic field. Typically, in the case of double oval configuration 8 turns of electromagnet were used.

 Measurements
The main types of diagnostics available in the test section at the model unto now in these experiments are different visualization, electrical potential and currents, spectroscopy.
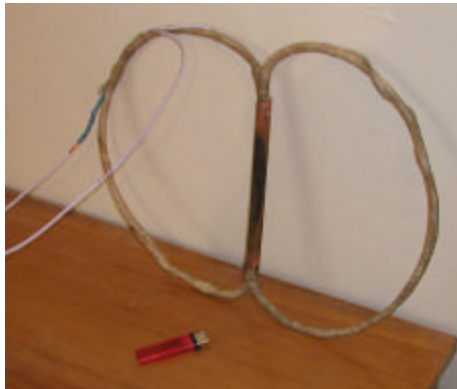
Fig16. The modified Double-Oval model
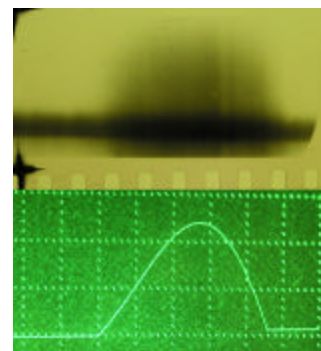
Fig. 17. The streak photography record. The time from left to right 0 .4msec/div, flow

Besides of these the standard measurements of the pressure along the flow train and the Pitot' tube near the model are also applied. The problems of the diagnostics extension connect to the very heavy physical conditions in the test section during the MHD interaction period. First of all, the pulse magnetic field creates a rather strong electromagnetic noise practically avoiding any electronics devices inside the test section. The short duration of the interaction period makes also problematic to measure directly one the main MHD effects studied in this program – the heat flux reduction (or changing) at the leading edge of the model. The fine flow field structure and fast time variation of it require the very high space and time resolution of non-intrusive optical techniques, including spectroscopy and fast speed visualization. The typical metric scale of the flow structure in this experiment is millimeters and the variation time is less than 100 mcsec. The front edge highly sophisticated diagnostics equipment was not available now within this program. Thus, the approach used here is the accumulation of maximum available information even not satisfying the requirements formulated above and the development of the numerical simulation strongly related to the given experimental conditions in order to extract the physical information from the correlation of the numerical and physical models.

One of the main efforts of experimental program was devoted to the fast visualization of the interaction zone behind the bow shock. Three different techniques were used:
1. Streak photography with a photo-electronic multiplier
2. Fast camera visualization with analogous camera KC-2 providing visualization on the conventional photo film with the seed 5000f/s or 10000 f/s;
3. Fast digital camera visualization

As a rule only one technique of the fast visualization is used during particular run.
The visualization of the MHD effect on the bow shock stand-off distance is provided with the streak photography technique. The luminosity from the narrow region of the flow along the up-stream stagnation line is recorded with the high time resolution that characterizes the MHD interaction in the x-t diagram. The streak photography is applied both for vertical and horizontal orientations. With the streak photography one of the most important features of the facility has been revealed – a rather strong interaction upstream of bow shock [45-48]. The example of correlation of the streak record and the Rogovsky' belt signal is presented in Fig.17.
The whole flow field visualization is applied to estimate the MHD interaction effects on
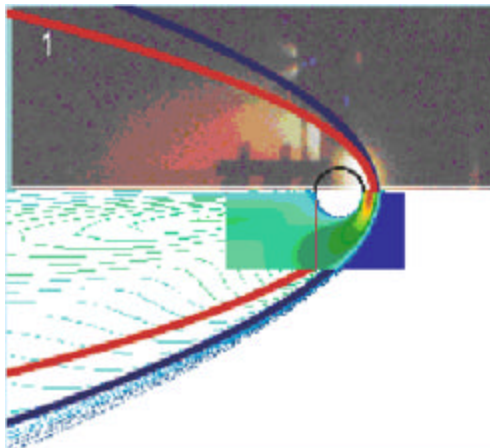
Fig.18. The comparison of the visualization of the flow during MHD interaction (upper) with 2D calculated temperature distribution and Billig' correlation (1 - M=15 and 2 –

Fig.19. Imaging of the flow around clylinder with and without MHD interaction as recorded with Pulnix digital camera. The flow direction is from the right to the left.

the structure of the flow field. . The model orientation is chosen for each particular run depending on the task. Three different orientations were typically used: vertical, horizontal and slanted. For two first orientations the flow direction is perpendicular to the cylinder axis. The difference is only the visualization direction – for the vertical orientation the optical axis crosses the bow shock area from the side view of the cylinder; for the horizontal orientation the imaging of the interaction area summarizes the luminosity along the whole length of the cylinder.

In Fig.18 the correlation of the visualization and calculation is shown. The fast digital
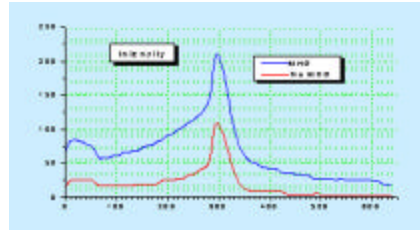
Fig.20. Intensity distribution along the flow direction for non-MHD (lower) and MHD (upper) cases. The maximum intensity is located up-stream of the leading edge of the cylinder. The leading and tailoring edges locations can be recognized from well visible curve broken.

camera Pulnix was also used for flow visualization with vertical orientation of the model. This camera has a rather low speed (~250 f/s) but can be synchronized very precise that provides at least one frame in desirable moment. In Fig.19 the comparison of the flow luminosity with and without magnetic field is presented. The flow is from the right to the left. The cylinder edges are clearly seen. The digitized intensity distribution along the flow direction is plotted in Fig.20.

Numerical Simulation

As it was mentioned above the experimental data analysis is performed with a wide utilization of the numerical simulation. The numerical model used in this analysis is based on the full 2D time-dependent Navier-Stocks equations coupled with 2D electrodynamics equation in the low magnetic Reynolds number approximation and,
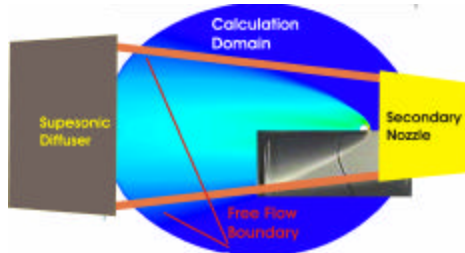
Fig. 21. The calculation domain used in the recent simulations.

optionally, with the finite rate chemical kinetics for standard reduced air kinetics scheme including up to 11 species and 80 chemical reactions. The effects of the NaK seed are described in several different models revealing not important deference. The detailed description of the model can be found in our previous publications [45-49].

The governing equations mathematically expressing the problem under consideration are as follows.

$$\frac{\partial \mathbf{U}}{\partial t} + \frac{\partial \mathbf{F}}{\partial x} + \frac{\partial \mathbf{G}}{\partial y} + \frac{\partial \mathbf{F}_v}{\partial x} + \frac{\partial \mathbf{G}_v}{\partial y} = \mathbf{S}$$

(3.1)

Vector of conservative variables is expressed as:

$$\mathbf{U} = \begin{pmatrix} r \\ rv_x \\ rv_y \\ rE \\ rY_1 \\ \vdots \\ rY_N \end{pmatrix}$$

(3.2)

where r is the density, v_x and v_y are the components of the velocity vector, E is the total specific energy, $\{Y_i\}$ are the mass fractions $Y_i = r_i/r$, $\sum_{i=1}^{N} Y_i \equiv 1$.

Inviscid flux vectors $\mathbf{F}$ and $\mathbf{G}$ read as:

$$\mathbf{F} = \begin{pmatrix} rv_x \\ rv_x^2 + P \\ rv_x v_y \\ v_x rE + v_x P \\ rv_x Y_1 \\ \vdots \\ rv_x Y_N \end{pmatrix}, \quad \mathbf{G} = \begin{pmatrix} rv_y \\ rv_x v_y \\ rv_y^2 + P \\ v_y rE + v_y P \\ rv_y Y_1 \\ \vdots \\ rv_y Y_N \end{pmatrix},$$

(3.3)

where P is the pressure to be defined below.
Viscous flux vectors $\mathbf{F}_v$ and $\mathbf{G}_v$ are as follows:

$$\mathbf{F}_v = \begin{pmatrix} 0 \\ t_{xx} \\ t_{xy} \\ e_x \\ J_{x1} \\ \vdots \\ J_{xN} \end{pmatrix}, \quad \mathbf{G}_v = \begin{pmatrix} 0 \\ t_{xy} \\ t_{yy} \\ e_y \\ J_{y1} \\ \vdots \\ J_{yN} \end{pmatrix}$$

(3.4)

Here, t_{xx}, t_{xy} and t_{yy} are the components of the viscous strain tensor and are expressed as:

$$t_{xx} = -2\mathbf{m}\frac{\partial v_x}{\partial x} - \frac{2}{3}\mathbf{m}\nabla v ,$$

$$t_{xy} = t_{yx} = \mathbf{m}\left(\frac{\partial v_x}{\partial y} + \frac{\partial v_y}{\partial x}\right),$$

(3.5)

$$t_{yy} = 2\mathbf{m}\frac{\partial v_y}{\partial y} - \frac{2}{3}\mathbf{m}\nabla v$$

In these expressions μ is the molecular viscosity, $\nabla V = \frac{\partial v_x}{\partial x} + \frac{\partial v_y}{\partial y}$ is the divergence operator.

In (3.5) the Stokes' hypothesis on the second viscosity coefficient has been used.

The energy fluxes are specified as follows:

$$e_x = -\mathbf{l}\frac{\partial T}{\partial x} + \left(v_x t_{xx} + v_y t_{xy}\right) + \sum_{i=1}^{N} h_i J_{xi} , \qquad e_y = -\mathbf{l}\frac{\partial T}{\partial y} + \left(v_x t_{xy} + v_y t_{yy}\right) + \sum_{i=1}^{N} h_i J_{yi}$$

(3.6)

Here, $\mathbf{l}$ is the heat conductivity, T is the gas temperature. The last terms in (3.6) represent the fluxes of enthalpy in the multi-component mixture. Mass-diffusion fluxes, J_{xi} and J_{yi} are determined according to the Fick's law:

$$J_{xi} = \mathbf{r}D_{im}\frac{\partial Y_i}{\partial x} , J_{yi} = \mathbf{r}D_{im}\frac{\partial Y_i}{\partial y}, \quad i=1,N$$

(3.7)

Transport coefficients, Dim, μ and λ are calculated here from one the model implemented in "PLASMAERO", namely:

$$D_{im} = \frac{1 - x_i}{\sum_{j\neq i} x_i / D_{ij}}$$

(3.8)

where $x_j = Y_j \dfrac{W}{W_j}$ is the mole fraction of j-th species, Wj is the molecular weight of j-th species and W is the molecular weight of the mixture.

$$W = \left(\sum_{i=1}^{N} Y_i / W_i \right)^{-1}.$$

Binary diffusion coefficients Dij are calculated as :

$$D_{ij} = 2.68 \cdot 10^{-7} \cdot$$
$$\frac{T^{3/2} \sqrt{(W_i + W_j)/(2W_i W_j)}}{P \cdot \mathbf{s}_{ij}^2 \cdot \Omega_{ij}^{(1.1)}(T_{ij}^*)} \left[\frac{m^2}{s} \right]$$

(3.9)

where $\mathbf{s}_{ij} = \dfrac{1}{2}(\mathbf{s}_i + \mathbf{s}_j)$ is the effective diameter of the particles, $\mathbf{s}_i$ and $\mathbf{s}_j$ represent the diameter of the particle of sort i and j, respectively. $T_{ij}^* = kT/\mathbf{e}_{ij}$ is so called characteristic temperature in the Lennard-Jones interaction potential model, k is the Boltzman' constant. $\mathbf{e}_{ij} = \sqrt{\mathbf{e}_i \cdot \mathbf{e}_j}$ is the parameter of the Lennard-Jones potential model.

$$\mathbf{m} = \sum_{i=1}^{N} \mathbf{m}_i \left(1 + \sum_{j \neq i} G_{ij} \cdot \frac{x_j}{x_i} \right)^{-1},$$

(3.10)

where $\mathbf{m}_i$ are given as

$$\mathbf{m}_i = 2.6693 \cdot 10^{-6} \frac{T^{3/2} \sqrt{W_i \cdot T}}{\mathbf{s}_i^2 \cdot \Omega_i^{(2.2)}(T_i^*)} \left[\frac{kg}{m \cdot c} \right]$$

(311)

and functions G_{ij} are given as

$$G_{ij} = \frac{\left[1 + \left(\mathbf{m}_i / \mathbf{m}_j \right)^{1/2} \left(W_i / W_j \right)^{1/4} \right]^2}{2^{3/2} \left[1 + W_i / W_j \right]^{1/2}}.$$

Heat conductivity is calculated according to

$$\mathbf{l} = \sum_{i=1}^{N} \mathbf{l}_i' \left(1 + 1.065 \sum_{j \neq i} G_{ij}' \cdot \frac{X_j}{X_i} \right)^{-1},$$

(3.12)

where

$$l_i' = l_i \left(0.115 + 0.354 \cdot c_{pi}/R_i\right),$$

and G_{ij}' are given as

$$G_{ij}' = \frac{\left[1 + \left(l_i/l_j\right)^{1/2}\left(W_i/W_j\right)^{1/4}\right]^2}{2^{3/2}\left[1 + W_i/W_j\right]^{1/2}} .$$

(3.13)

Heat conductivity of species i is

$$l_i = \frac{5}{2} m_i c_{vi} , \quad c_{ni} = \frac{3}{2} \cdot R_i , \quad R_i = R^0/W_i,$$

where c_{pi} is the heat capacity at constant volume, R_i is the gas constant and R^0 is the universal gas constant.

Thermodynamic pressure of mixture is defined as

$$P = rR \cdot T$$

(3.14)

where P is the pressure, T is the temperature and $R = R^0/W$ is the gas constant of the mixture $R = \sum Y_i R_i$.

The specific internal energy is given by the relation

$$e = h - P/r ,$$

(3.15)

where e and h are the mixture internal energy and enthalpy, respectively. The total energy is given as

$$E = e + \frac{1}{2}\left(v_x^2 + v_y^2\right)$$

(3.16)

The enthalpy of the mixture can be expressed in the form:

$$h = \sum_{i=1}^{N} Y_i h_i(T) .$$

(3.17)

The *i*-th species enthalpy is determined as

$$h_i(T) = h_{i,f} + \int_{T_{ref}}^{T} c_{pi}(T)\, dT\,,$$

(3.18)

where $h_{i,f}$ is the formation enthalpy and $c_{pi}(T)$ is the heat capacity at constant pressure. The source-term $\mathbf{S}$ in Equ.(1) is represented in the form:

$$\mathbf{S} = \begin{pmatrix} 0 \\ S_x \\ S_y \\ S_e \\ \dot{w}_1 \\ \vdots \\ \dot{w}_N \end{pmatrix}$$

(3.19)

Here, S_x and S_y are the components of electromagnetic force, S_e is the energy source because of electromagnetic field. They should be computed from the appropriate MHD-models.

The source-term $\dot{w}_i$ represents the production rate of i-th component due to the chemical conversion. They are computed from the chemical kinetics model. Any of the chemical reaction can be represented in the following symbolic form:

$$\sum_{l=1}^{N} \mathbf{n}'_{l,r} X_l \quad \underset{k_{fb}}{\overset{k_{fr}}{\rightleftarrows}} \quad \sum_{l=1}^{N} \mathbf{n}'_{l,r} X_l$$

(3.24)
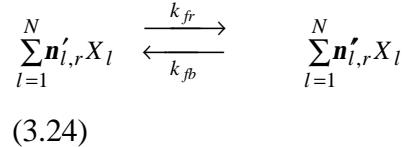
Where $V\mathcal{C}_{l,r}$ and $V^2_{l,r}$ are the stoichiometric coefficients of the reagents and products, respectively. The rate of production of species i, $\dot{w}_i$ is determined according to the low of acting mass:

$$\dot{w}_i = W_i \sum_{r=1}^{N_r} \left[\mathbf{n}''_{i,r} - \mathbf{n}'_{i,r}\right] \cdot \left(k_{fr} \prod_{l=1}^{N} c_l^{\mathbf{n}'_{l,r}} - k_{br} \prod_{l=1}^{N} c_l^{\mathbf{n}'_{l,r}} \right)$$

(3.25)

Here, $c_l = \mathbf{r}_i/W_i$ is the molar concentration of species i, k_{fr} and k_{br} are the rate constants of forward and backward reaction, which are given in the Arrhenius form:

$$k = a \cdot T^b \cdot \exp\left(- E_a/T\right)$$

(3.26)

a, b and E_a are the reaction parameters, E_a is the activation energy.

In general, the electrodynamics of steady-state weekly-ionized gas discharge can be described by Ohm's law:

$$\mathbf{j} + \frac{\boldsymbol{b}}{B}[\mathbf{j} \times \mathbf{B}] = \boldsymbol{s}(\mathbf{E} + [\mathbf{v} \times \mathbf{B}])$$

(3.27)

where $\mathbf{j}$ is the electric current density, E is the electric field strength, $\boldsymbol{s}$ is the electric conductivity, B is the magnetic field induction, and $\boldsymbol{b}$ is the Hall parameter.

The components of electro-magnetic force are defined as

$$S_{x,y} = [\mathbf{J} \times \mathbf{B}]_{x,y}$$

(3.28)

Energy rate of change is

$$S_e = (\mathbf{J} \cdot \mathbf{E}) - Q_{rad}$$

where approximation to the radiative power Q_{rad} is taken in the form:

$$Q_{rad} = \boldsymbol{e} \cdot \boldsymbol{s}_{SB} \cdot T^4 \quad ,$$

(3.29)

where $\boldsymbol{e}$ is the effective absorption coefficient, and σSB is the Stefan-Boltzman constant.

Coupled with the definition of electric potential,

$$\mathbf{E} = -\mathrm{grad}\,\boldsymbol{j} ,$$

(3.30)

and continuity equation for the current density

$$\mathbf{div}\,\mathbf{j} = 0,$$

(3.31)

the equation (3.27) can be reduced to single two-dimensional (three-dimensional in general) elliptical type equation for potential.

The boundary conditions for the potential typically used are specified value of electrical potential at the electrode-type surface, and zero value of the normal component of the current density on insulator-type of bounds:

$$\boldsymbol{j} = \boldsymbol{j}_w,\ j_n = 0.$$

(3.32)

This model in different varieties are used for the simulation of a wide range of magneto-plasma aerodynamics, including MHD interaction studies, gas discharge development in high speed flows, plasma and MHD assisted mixing, ignition, and combustion control [47-49]. The typical approach used in these and many others paper for numerical simulation of the MHD interaction effects at a blunt body in hypersonic flows is based on consideration of upstream region of the flow, where the bow shock could be directly affected by MHD momentum and energy redistribution. It was stressed later [50-52] that wake interaction could be very important as well. For this reason the significantly

extended downstream calculation domain is usually implemented in our recent studies [51-52].

The most recent modification is a remarkable extension of the calculation domain. It was motivated by preceding analysis shown us the potential importance, of first – the MHD interaction in down stream area (wake interaction) and, second, by the intention to check the effect of electrodynamics boundary conditions. The newly constructed calculation domain covers now practically whole flow area inside of the test section. The grid consists of 120×181-mesh points with the finest resolution used for close-up region of the cylinder surface. Inspite the symmetrical nature of the phenomena in the frame of the applied approximation the whole area was considered to suppress randomly appeared numerical instabilities at the symmetry line while it was used as a boundary. The structure of the calculation domain is schematically presented in Fig.18 along with indication of the main hardware elements of the facility potentially affecting the flow field in the test section. In the lower right part of the picture the fragment of the flow visualization (b&w backgrounder) is introduced to specify the free flow configuration in the experiments.

The extended calculation domain reveals a significant advantage in specifying the outlet boundary conditions. Indeed during the MHD interaction a rather large region of subsonic flow could form. Typically used supersonic conditions are no longer valid when subsonic sub-region reaches the outlet border.

All numerical results discussed in this paper are obtained with the simplified version of the model not including the chemical finite rate kinetic. Such a simplification influences, of course, in some cases on the quantitative results, but still provides the qualitative physically correct description of the processes with significantly lower computational resources.

Analysis

The overview of the experimental data collected during this study and simulation results led to to the basic question: *Why the experimental observations of up-stream MHD interaction at the cylinder are significantly over predicted in numerical simulations*?

As a governing mechanism mainly responsible for the significant reduction of the MHD interaction effectiveness, the strong Hall effect has been indicated in our papers [46-49]. The characteristics value of the Hall parameter is estimated as high as 10 that could result in dramatic reduction of the actual MHD interaction. It was also shown that the actual MHD interaction parameter could saturate as a function of magnetic induction value at the level corresponding to the condition of $w_e t_e \sim 1$ if the Hall component of the electric field being nearly shorted. The experimental conditions at the facility seem to promote such a situation. The rather low pressure defines the high values of free path of electron t_e and consequently a large hall parameter; the probably poor electrical insulation along the flow train leads to the significant shorting of the Hall field; the non-equilibrium ionization of airflow in the secondary nozzle due to the strong coupling of the electron and vibrational temperatures could also result in effective Hall current leakage from the MHD accelerator through the test section to the grounded hardware elements of the

facility. For these or probably other reasons the electrical potential of the model in the test section is only ~40V while the several time higher value is expected. The intensive flow luminosity in front of the bow shock during the magnetic field pulse confirms indirectly the significant electrical conductivity in oncoming flow. In the next Sections the explanation of the experimental observations is presented as derived from the comparison of the physical and numerical results.

Bow Shock

The correlation of the bow shock shape and location as from the flow visualization results, numerical simulation and the Billig' formula is presented in Fig.18. The curve 1 of Billig' correlation formula corresponds to Mach 15, and the curve 2 – to Mach 10. The space resolution of the flow visualization (the brightest frame from the series of Fig.14) is not good enough that probable leads to uncertainties in the localization of the experimental bow shock: the upstream part corresponds more likely to the lower Mach number but the downstream part is closer to the high Mach number case. One could also conclude that the perfect gas model used in this simulation is not fully adequate to the physical situation. It was also confirmed in our calculation including the finite rate kinetics. The important result is also that it is hardly possible to derive the bow shock displacement and/or deformation caused by MHD interaction near the stagnation point from flow visualization in this experiment. It should be noted also that the Billig's correlation is hardly valid for M>10 flows.

Wake effects

The Fig.18 shows from the other hand that the downstream effects are much more resolvable. The angle of the downstream part of the bow shock is clearly changed during MHD interaction, and the luminosity distribution in the close wake area is changed remarkably too. In order to prove this conclusion the special configuration of the model support was developed recently to free wake area for visualization (see Fig.19, where the flow direction is from the right to the left).

Fig. 22. The experimental arrangement for wake interaction study.
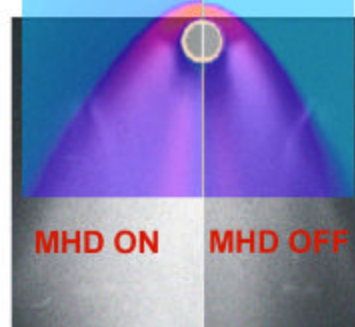
Fig.23. The visualization (b&w) and computation (colored) comparison of the wake area flow field under MHD-off and MHD-on conditions.

The comparison of MHD-off and MHD-on cases both for the experiment and simulation are presented in Fig.23.

The experiment confirms the strong temperature elevation in the near cylinder wake, which was predicted numerically. At the same time it is clearly seen that simulation gives the wider bow shock shape in the upstream portion. Note, that simulation predicts also the weak but still resolvable bow shock stand-off distance increasing. The satisfactory correlation of the experimental and calculated the modification of the shock shape of its downstream part confirms implicitly the adequate inlet boundary conditions used in this simulation. Let us consider the inlet boundary conditions effects in more detailed.

Inlet boundary conditions effects

One of the most important features of the MHD WT facility used in this experimental study is the MHD accelerator that provides the elevation of stagnation pressure of the airflow after the arc heater. Namely MHD accelerator defines the unique characteristics of this WT for hypervelocity steady-state experiments. From the other hand airflow in the test section after fast expansion in the secondary nozzle seems to be very non-equilibrium, the vibrational temperature and dissociation degree of two-atomic molecules, first of all - oxygen, both correspond more likely to the temperature at the MHD accelerator exit rather than to the in-test section temperature. This results in the higher than equilibrium electron temperature and, consequently, in high ionization degree of NaK seed used to provide acceptable electrical conductivity in the MHD channel. Thus, the oncoming airflow in the test section is well electrically conductive. Consequently, the MHD interaction can take place anywhere while the local magnetic induction is high enough. The fact of the intensive MHD interaction is experimentally confirmed by the streak photography (see Fig.17) clearly demonstrated the strong increase of the flow luminosity from the flow far upstream of the cylinder leading edge with no visible displacement of the bow shock. This effect was detailed investigated and described in papers [50-52]. It was recognized recently, however, that the upstream interaction reveals another important mechanism of losses – the overall shorting of the Hall field. Such a shorting occurs in MHD devices with poor insulation of the flow train from the ground.

Hall Field shorting

The Hall component of electric field is originated from the tensor nature of the electrical conductivity of plasma in the presence of magnetic field. The generalized Ohm's law with neglecting of the typically small so-called ion slip effect is given by the expression (3.27)
where s and b stand for scalar electrical conductivity and Hall parameter, correspondingly. The Hall parameter $b = w_e t_e$ with w_e is the cyclotron frequency and t_e is the free path time of electron. The simplified relation between these important values is

$$s = n_e e m_e = n_e e b / B \quad , \text{ with } B = |\mathbf{B}|.$$
(3.33)

It is convenient for this analysis to define the local frame reference $\{e_1, e_2, e_3\}$ in respect to the magnetic induction vector $\mathbf{B}$ as $(\mathbf{Be}_1) = B$, $(\mathbf{Be}_2) = (\mathbf{Be}_2) = 0$. Furthermore, let us decompose the flow velocity vector as

$$\mathbf{u} = \mathbf{u}_\perp + \mathbf{u}_\|, \qquad \text{where } (\mathbf{e}_1 \mathbf{u}_\perp) = 0.$$

By choice of $\mathbf{e}_2$ and $\mathbf{e}_3$ to provide $(\mathbf{e}_3 \mathbf{u}_\perp) = 0$, the generalized Ohm,s law can be rewritten in the form

$$j_1 = \mathbf{s} E_1,$$
$$j_2 = \mathbf{s} E_2 - \mathbf{b} j_3,$$
$$(3.34)$$
$$j_3 = \mathbf{s} (E_3 - uB) + \mathbf{b} j_2.$$

In resolved form this gives

$$j_B = \mathbf{s} E_B,$$
$$j_H = \mathbf{s} E_H - \mathbf{b} j_F,$$
$$(3.35)$$
$$j_F = \mathbf{s}/(1 + \mathbf{b}^2) (E_F - uB + \mathbf{b} E_H),$$

where the new indexes $B, H,$ and F denote now B field direction, Hall field directions, and Faraday field directions, correspondingly, and $u = |\mathbf{u}_\perp|$. With no Hall component of current density $(j_H = 0)$ the Hall field is defined by Faraday component of current density

$$E_H{}^{ideal} = \mathbf{b} j_F/\mathbf{s}. \tag{3.36}$$

It can be easily found that the Hall field is always opposite to flow direction (in the plane normal to the B-field vector) and naturally scaled with the 'ideal' value $E_H{}^{sc} = -\mathbf{b} uB$, which can be attributed to the value of $E_H{}^{ideal}$ at the Faraday short circuit condition $(E_F = 0)$. Substituting the ideal Hall field (36) into (35.3) one can obtain

$$j_F{}^{ideal} = \mathbf{s} (E_F - uB), \tag{3.37}$$

that reveals no Hall effect appearance. From the other hand the case of total Hall field shorting reads

$$j_F{}^{shorted} = \mathbf{s}/(1 + \mathbf{b}^2) (E_F - uB), \tag{3.38}$$

which is $(1 + \mathbf{b}^2)$-times less as compared with ideal value. For $\mathbf{b} >> 1$ typical of the conditions considered here the reduction of the primary importance value – Faraday component current density can be dramatically high. This is why the main rule for any MHD based application is to keep the Hall field value as close as possible to its ideal level. The general way to provide such conditions is to prevent the Hall current leakage.

At the facility used in this experimental studies the upstream and downstream hardware components of he flow train seem to be grounded. At least no Hall voltage was measured between the MHD accelerator entrance and the test section. At the same time it was definitely confirmed a rather high insulation between the model (when made of cupper) and the test section wall. Thus, the model environment can be grounded only through the oncoming flow while the working media in the secondary nozzle and behind the model location near the diffuser is electrically conducting. In order to check this assumption the series of calculation of the MHD interaction was undertaken. The variable parameters of this series are the ionization degree of the oncoming flow and the inlet boundary conditions. The electrodynamics boundary conditions at the outlet of the calculation domain specify for all cases the grounded electrical potential value: $j_{out} = 0$.
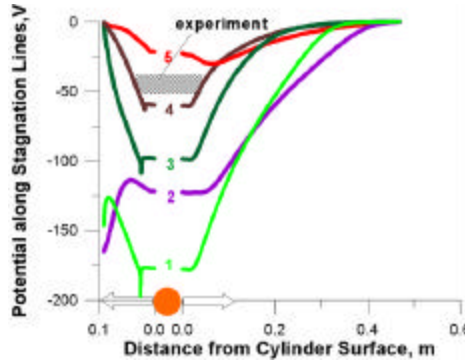
Fig.24.. The stagnation line electrical potential distribution for different ionization degrees in oncoming flow.

$1 - 10^{-4}; 2 - 10^{-2}; 3 - 10^{-4}; 4 - 5.10^{-3}; 5 - 10^{-2}$.

The stagnation line potential distributions for several cases are presented in Fig.24. . In cases *1* and *2* the inlet boundary conditions are $j_n = 0$, and potential grounded conditions $j_{it} = 0$ for cases *3* through *5*. The experimental values of the cylinder potential are localized in the dashed area in the Fig.21. These results demonstrate clearly, first, the importance of the inlet boundary conditions as it follows from comparison of curves *1* and *3* as well as curves *2* and *4*. For each pair the oncoming flow conductivity is the same. Note that the ionization degree value equal to *.01* corresponds to full ionization of seed, and it is most likely maximal available ionization degree under conditions considered here. The second conclusion can be derived from the comparison of calculation and experimental results is that the only non-equilibrium conductivity ahead of the bow shock is not enough to explain the experimental values of the cylinder potential. The satisfactory agreement can be reached if the inlet grounded condition is implemented.

Thus, it can be concluded that the inlet and outlet flow in the test section are effectively grounded, and, secondly, the conductivity of the oncoming flow is non-equilibrium corresponding to ionization degree 70 to 80 percent of seed. The latter agrees with the electron concentration measured by the microwave adsorption technique at the earlier stages of the MHD WT facility utilization for hypervelocity experiments [53].
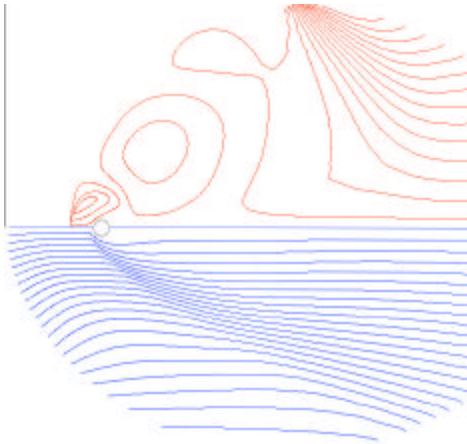
Fig.25. The electrical current stream lines are as for non-shorted (red, upper half) and shorted (blue, bottom half) conditions.
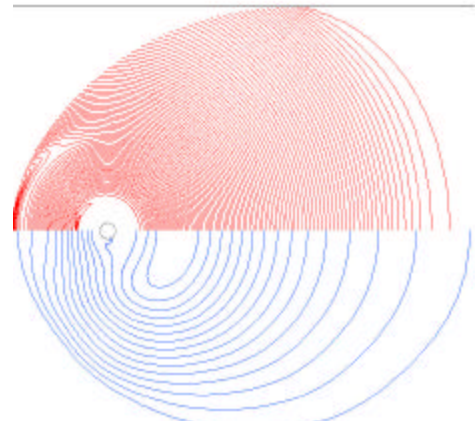
Fig.26. The eqipotential lines are as for non-shorted (red, upper half) and shorted (blue, bottom half) conditions.

To illustrate the difference between shorted and non-shorted conditions the current streamlines are shown in Fig.25. The upper half corresponds to non-shorted conditions (case *1* from Fig.24), and the bottom half – to shorted ones (case 5 from Fig.24). The line intervals are the same for both cases. The equipotential lines structures for the same conditions are presented in Fig.26.

The non-shorted conditions cases demonstrate several features important for understanding of the phenomena studied. The current loops are localized behind the bow shock only. The intensity of the circulating current density is relatively low. (Note the current concentration at the upper boundary is caused by switching of boundary condition type from Neumann' ($j_n = 0$) to Dirichlet' ($\boldsymbol{j} = 0$) and have no physical sense for the experimental considered here.) Three main current loops are clearly recognized: first localized in upstream of cylinder, the second - in near wake region, and the third located at the outlet part of the calculation domain and can be attributed to the particular boundary structure used in this simulation. In the opposite shorted conditions case the current streamlines pattern is totally different. The electrical current goes practically along the flow filed streamlines that agrees well with the analysis of the preceding section.

As for potential distributions for two cases the clearly visible effect is that the totally shorted area if formed in close vicinity of the cylinder even for the non-shorted conditions case in spite the net Hall current is canceled by boundary conditions applied for this case. Thus, the Hall filed shorting phenomenon reveals rather local nature. It will be discussed later in more detailed.

The current streamline pattern effectively visualizes the bow shock locations for both considered cases. As it can be seen from the Fig.25, for example, the predicted bow shock location for non-shorted case is shifted upstream for about two cylinder diameters as compared with still very little shock displacement for the shorted conditions case. It could be attributed to the different body force intensity (MHD interaction intensity, which is the main subject of this study) ahead of the cylinder leading edge. To check this hypothesis let us consider the body force vector distribution at the close-up region of the cylinder shown in Fig.27 for the shorted conditions case. Surprisingly, the body force

vector is directed *downstream* but not upstream as it could be expected in upstream area of the cylinder from rough estimations. Furthermore, the intensity of the body force is
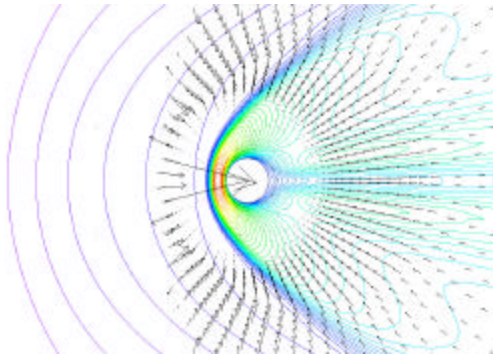
Fig.28. The planar component of the body force vector distribution in close-up cylinder area. The length of the vectors represents relative value of the physical quantity.

negligible small as compared with the value typical of whole interaction area. The qualitatively similar situation occurs for the non-shorted conditions case. Thus, it would be hardly possible to motivate the difference in the bow shock locations by the different MHD interaction in upstream zone.

It is now the time to analyze the electrodynamics and gasdynamics fields' interaction in more detailed.

Gasdynamics and electrodynamics fields

The particular task for this section is to understand the main electrodynamics features found from experimental and calculation data comparison. The summary of the above comparison could be as following:

- The electrical current streamlines coincide generally with flow direction.
- The electrical potential is significantly non-monotonic along the flow direction approaching the minimum level at the cylinder locations.
- The equi-potential lines are similar to the cylinder surface in the vicinity of the cylinder.
- The body force vectors are mostly directed to the cylinder surface especially at the upstream portion of the near cylinder flowfield.

Basing on the analysis started above one can conclude that the configuration considered in this study can be treated as a Hall type MHD generator under nearly short circuit conditions. One of the general features of this configuration is that the Hall component of the electric field is directed opposite to the flow velocity. Considering for simplicity the short circuit condition for the 'Faraday' field component ($E_F = E_z = 0$) that is the practically important case of well conductive cylinder (metallic) material. (It was already mentioned above that the axial component of electric field is practically very close to zero due to reversing sign of the induced e.m.f. $\mathbf{u \times B}$ in upstream and downstream areas even in a case of insulator made cylinder). The main component of body force interested for this analysis is radial directed (in the cylinder center reference frame)

$$f_r = (\mathbf{j} \times \mathbf{B})_r = -j_z B_q. \tag{3.39}$$

For the assumed conditions one can derive from the Ohm's law

$$j_z = s u_r B_q - w_e t_e j_r = (n_e e u_r - j_r) w_e t_e, \tag{3.40}$$

where $j_{,conv} = n_e e u_r$ can be called as a *convective current*. The radial current for the case $E_r = 0$ (the local short circuit condition) is

$$j_r(E_r=0) = s w_e t_e u_r B_q/(1 + w_e t_e^2) \sim j_{conv} \tag{3.41}$$

when $w_e t_e \gg 1$.

The radial current can be also presented in the form

$$j_r = j_{conv}(1 - E_r/E^*_r), \tag{3.42}$$

where

$$E^*_r = -w_e t_e u_r B_q, \tag{3.43}$$

resulting in

$$j_z \sim w_e t_e j_{conv} E_r/E^*_r. \tag{3.44}$$

Thus, the radial body force is defined as

$$f_r = -j_z B_q \sim - j_{conv} B_q w_e t_e E_r/E^*_r = - j_{conv} B_q^2 \, m_e \, k_H \tag{3.45}$$

that reveals the governing role of the 'a local Hall load factor' $k_H = E_r/E^*_r$.

It is useful here to introduce the power extraction/release associated with Hall component of electrical field

$$q_r = j_r E_r \sim - j_{conv} u_r B_q w_e t_e (1 - k_H) k_H. \tag{3.46}$$

The sign of the right hand expression is defined only by the Hall load factor k_H, because of ($j_{conv} u_r B_q$) is always non-negative being proportional to ($u_r B_q$)^2. The power generation mode (power extraction) corresponds to condition $0 < k_H < 1$; the conditions $k_H < 0$ and $k_H > 1$ define the power release mode.

The difference of these two cases becomes clear from comparison of body force direction. The sign of the scalar product $(f_r u_r) \sim - j_{conv} u_r B_q^2 \, m_e \, k_H$ is defined by the sign of k_H. Thus, when the Hall load factor is negative $k_H < 0$ then both $q_r > 0$ and $(f_r u_r) > 0$ that

corresponds to *the MHD acceleration mode* (body force acts along the flow velocity). When, in turn, the Hall load factor k_H is greater than one $(k_H > 1)$ then $q_r > 0$ (power release mode) and $(f_r u_r) < 0$ (body force acts against the flow velocity).

That corresponds to *the MHD break mode*.

Typically of the operation conditions of the circular cylinder in a transverse hypersonic flow the MHD interaction reveals all of three modes simultaneously.

The dominating direction of the electrical streamlines is defined by the closed circuit condition of the 'effective Hall MHD generator'. Generally speaking the induced total voltage of such a generator is positive in respect to flow direction through generation region and, correspondingly, the induced total current is also positive (i.e. the electrical current goes in downstream direction). This feature leads to the non-monotonic character of the potential distribution with a rather deep minimum (see Fig.21) that is defined by the fact that the downstream portion of the 'Hall generator' is significantly more powerful than the upstream one. So, the downstream generator works against the upstream as a load that resulting in reverse electrical filed sign there. And the latter is a key issue to understand why the body force vectors are in opposite direction to be expected one.

In terms of expressions (13) and (14) the local Hall load factor k_H becomes negative in the upstream region that resulting in the MHD accelerating mode: both power and momentum are released in the flowfield. In the upper vicinity of the cylinder where the body force is also mostly directed to the cylinder surface the MHD generation mode takes place because the radial component of flow velocity has changed its sign. The power is extracted from the flow and the flow decelerated by the body force.

The distribution of the power released/extracted from the flow for two cases (shorted and non-shorted conditions) is presented in Fig.29.

In the shorted conditions case the only downstream area works as an MHD generator extracting the power from the flow. This power is released in upstream area in two modes: MHD brake (mostly in wake area behind the cylinder) and MHD accelerator in ahead of the cylinder. In the case of non-shorted Hall field (the upper half of the distribution in Fig.29) the strong MHD generating zone is formed along the bow shock. These distributions agree well with the estimations given above in this subsection.
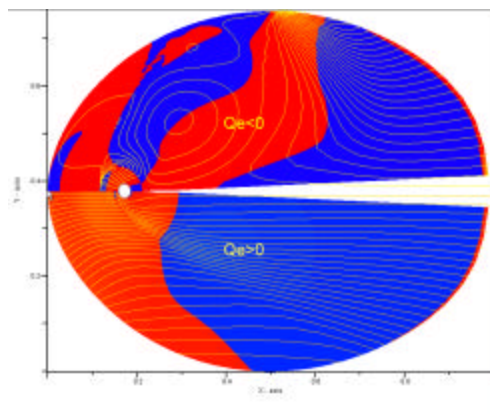
Fig.29. The electrical power released (red) and extracted (blue) from the flow for two cases: the upper – non-shorted conditions, the bottom – shorted conditions.
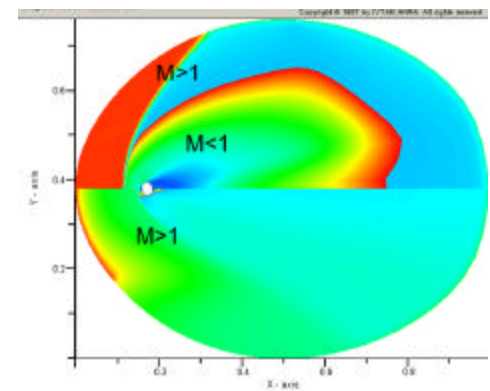
Fig.30. Comparison of the Mach number distributionin two cases. The upper half represents the non-shorted conditions case, the botoom half – the shoretd conditions case.

The structures of the flow field and electrodynamics field are strongly interconnected; therefore the flow field for two different cases considered here are to be different as well. This obvious suggestion is proved by Mach number distributions for corresponding conditions presented in Fig.30.

For clarity the subsonic area is leveled separately. Besides of general difference of flow fields of two cases related to the strong difference of the bow shock locations, an important feature of the non-shorted case is that the extended subsonic zone is formed around the cylinder especially in the wake area. The reason of the formation of such a subsonic zone in the wake can be found in the MHD break mode occurring here. Indeed, the MHD body force is directed counter flow, the high temperature defines a low density, and the flow velocity is originally low due to the friction at the cylinder surface, all of these results in the relatively high MHD interaction parameter for wake region. Thus, it is the most likely that the wake interaction resulting in the significant extension of low velocity region is responsible for the bow shock upstream displacement. The bow shock location along with its shape corresponds for given oncoming flow parameters to an effective body of modified shape. In the shorted conditions case this effect is much weaker pronounced because of the strong reduction of overall interaction. As it was indicated above (see.Fig.20 and corresponding comments) the relatively high wake interaction was observed even in the experiment under conditions close to the totally shorted Hall voltage.

Peak Heat Flux Reduction
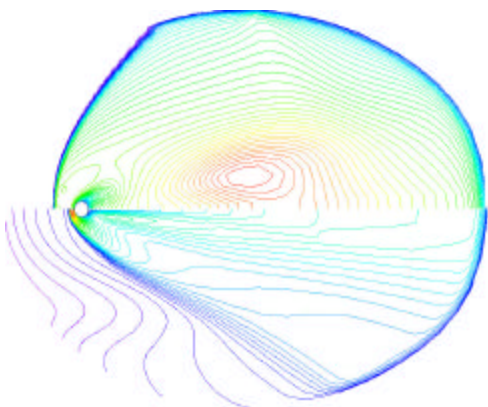
Fig.31. Temperature distributions for the
conditions of Fig.30.
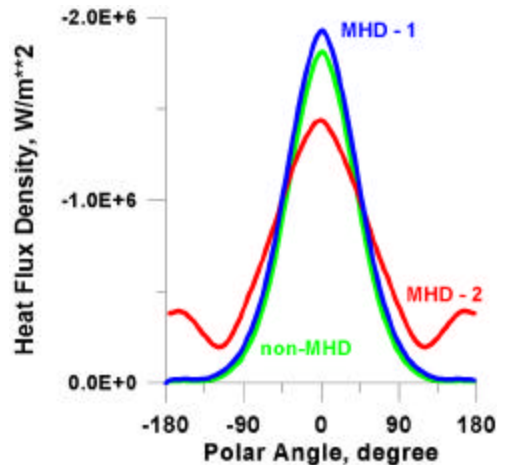
Fig.32. Heat Flux Density vs polar angle
for three cases: non-MHD stands for
reference case of a conventional flow;
MHD-1 presents the result for the shorted
conditions case; and MHD-2 – for the non-
shorted conditions case.

The practical aspect important for potential applications of this study is to limit the peak heat flux at the leading edge of the body in hypersonic flows. Many optimistic predictions based on various numerical simulations of the MHD interaction at a blunt body in hypersonic flows have published recently [54-58]. The prediction of the heat flux

reduction by an order of magnitude was made in papers [45,46] directly related to the experiment discussed here. From results of all cited above papers it be concluded definitely that under given flow conditions there is strong correlation between the peak heat flux density at the stagnation point and the bow shock stand-off distance. It is also in full agreement with the rules of classical hypersonic aerodynamics (see, for example, [59]).

After this short prelude looking at the flow filed calculated for two cases often referred here (exampled in temperature distribution in Fig.31) one could expect a rather significant effect for the non-shorted conditions case and probably poor result for the shorted conditions case. The prove of such suggestion is given in Fig.28, where the distributions of the normal-to-wall heat flux density are plotted. The shorted conditions case with poor MHD interaction and a negligible bow shock displacement reveals as expected a rather low effect in the heat flux distribution. Even more, a some increasing occurs near the stagnation point that could be attributed to the heat addition with the Joule heating taking place along the stagnation line. In turn, a significant (but not dramatic as it was in optimistic predictions) heat flux density reduction is found for the non-shorted conditions case. Some penalty of this 'positive' effect is the increasing of the heat flux density at downstream cylinder surface. And the total effect would be probably equalized. Nevertheless, the primary goal to reduce the peak heat fluxes seems to be available.

A notable comment on this result is that the downstream (wake) interaction provides the desirable effect at upstream part of the cylinder.

3.3 Experimental and Theoretical Studies on MHD Interaction at Wedge in Hypersonic Flow

The analysis of the hypersonic flow around a cylinder with the axial current inducing the azimuthal magnetic field has revealed the several important features of the interaction process detailed described in the previous Section. The most important of these are to be mentioned here:

1. The phenomenon is heavily governed by Hall effect under given experimental conditions (low static pressure, ~one percent ionization degree, magnetic induction level of about 1 Tesla in near body interaction area);

2. The disadvantages of the experimental conditions, which cannot be significantly changed or improved, is practically short circuiting in respect to Hall field induced in the test section. This results in reduction by two-three orders of magnitude of the actual MHD interaction parameter based on the characteristics size of upstream interaction area;

3. On the other hand the rather intensive interaction in downstream region is observed both experimentally and computationally. Such an interaction forms an very extended subsonic region behind the cylinder affecting considerably the upstream supersonic flowfield;

4. The prediction of the peak hear flux reduction caused by MHD interaction of such a type shows that the effect could be very low or even opposite one for Hall field shorted conditions, however under conditions the similar to experimental ones but with blocked Hall current leakage through the test section it could reach very remarkable value of several tens of percents.

Experimental Study of MHD Flow Control at a Wedge

Figure 33.The first version of the model of Type II.
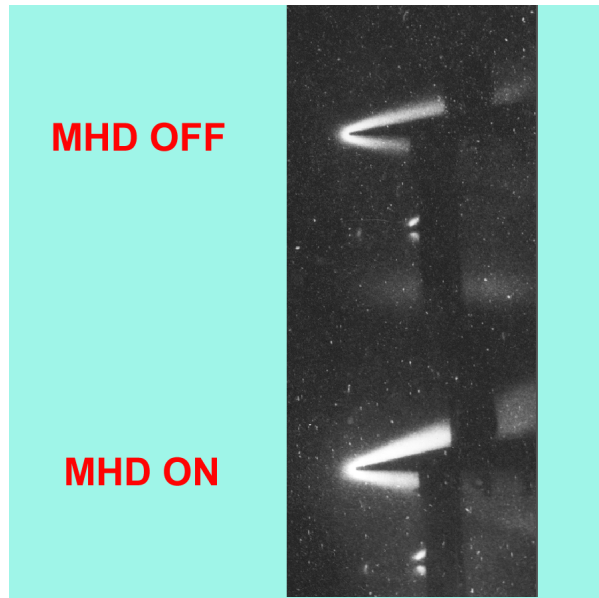
Figure 34. Visualization of flow around the wedge model.
Run 117. 10.05.2002
Flow is from the left to the right. Kodak film. 2000f/sec.

The main goal of the new series experimental and theoretical study is to demonstrate the possibility of MHD interaction to modify hypersonic flow field. The far prototype of the experimental model is an element of an hypersonic vehicle forebody or vertical (horizontal) wing. The potentiality of MHD control flow can be exampled and evaluated on the turning flow by different values of magnetic or/and magnetic field, that could be interested in practice to tune the multishock configuration at in-take while the operation mode being off-design.

The Model II used in the second stage is a wedge equipped with the pulse magnetic system similar to that used in the cylinder study. The general idea of the models of this series can be seen from the Fig.33. The first version of the Model II is very similar to the cylinder Model I. The magnetic field is created by a pulse current in the double-oval coil of total six or eight turns. The magnetic induction at the wedge surface closed to magnetic system is about 1. – 1.5 Tesla. The wedge is made of the copper sheet of ~1.5mm thick. The wedge is fixed at magnetic system. The typical experimental result is presented in Fig.34.

Qualitatively the result is clear: during the MHD interaction the luminosity region expands significantly that is well correlated with the simulation based on the approach verified at stage I of the cylinder study.

MHD OFF

MHD ON

MHD OFF

MHD OFF
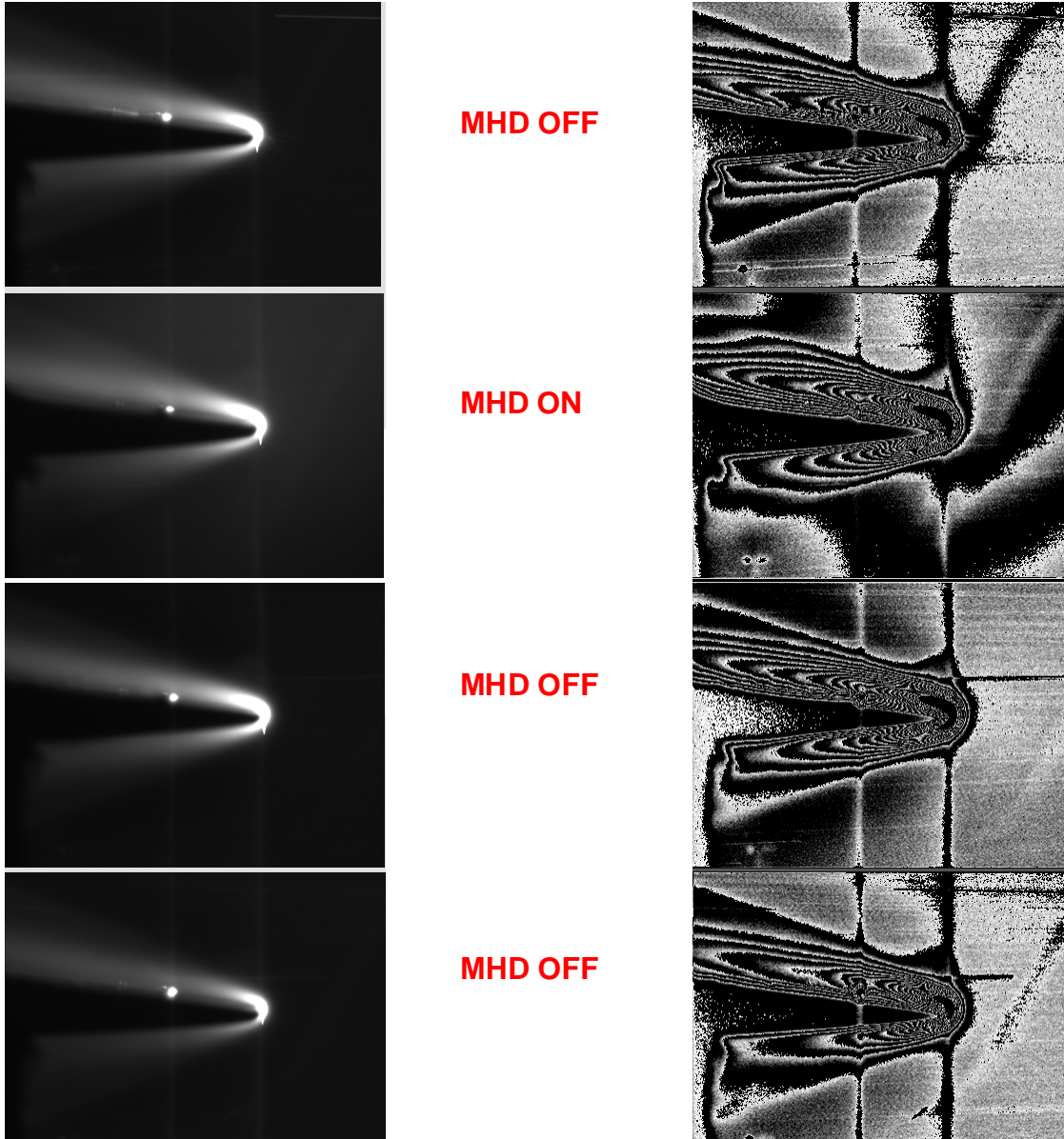
Figure 35. The visualization of flow around the wedge model. Run 131 04.24.2003. Flow from the right to the left. Four consequence frames are presented. Digital camera Pulnix-6710, 250fps, exposure time 30 mks. The left column is original imaging, the right column is the filtered image.

Unfortunately, the model design has revealed many disadvantages, such as the well conducting surface facing flow, weakness of the structure and others. Pulse internal electromagnetic forces inside the magnetic system coil destroyed the model during the run. The new wedge model series is based on the ceramics material. The first model of this series was made of dielectric paste materials mixed with epoxy glue. Flow facing surface was protected with high temperature paste. The two probes were imbedded into the model to provide the electrical potential measurement during the magnetic system pulse. The first experiment conducted on was partial successful: the model had resisted

to the mechanical strength, however the high temperature protection material was significantly eroded that makes impossible to use this
model in further experiment. The flow visualization has failed because of too short exposure time was used.
After the next step modification the wedge model was protected with high temperature BN ceramics. The ceramics plates of ~ 1.5 mm thickness were glued to the flow facing surface with high temperature glue with working temperature $300^{o}C$.

The run with this modified model was performed on 04.28.2003. The run is considered as successful, no significant damage except a small 'hot spot' appeared on the top surface. At the first time the digital camera Pulnix-6710 was used for flow visualization for the Model II type. The results are partially presented in Fig.35. Because of low speed (only 250fps) the only frame corresponding to the magnetic pulse period could be obtained in each experiment. The good advantage of the equipment used is the possibility of the precise synchronization of the camera with power supply of magnetic system. The synchronization is always defined by the second frame and the maximal current of magnetic system.

The MHD effect can be recognized with very careful comparison of the imaging at the moment of magnetic pulse (frame #2) with the other frame of the series. The better results are obtained with the digitally filtered images as it was exampled in the right column in the Fig.35. The qualitative changes are clearly seen however any quantitative conclusions are hardly possible. One of the reasons of this diagnostics found in the analysis is very strong luminosity coming from high temperature stagnation area at the wedge edge screening the flow structure modifications in low temperature regions. The limited range of intensity grads provided with this camera (1:256) results in very low resolution of flow field when the luminosity variation is rather small in scale of the maximal intensity came from the stagnation area.
To solve this problem several techniques were tested: the exposure time variation; the filtering of stagnation region radiation; the spectra filtering. The first method is not effective, two others are rather productive.

Figure 36. The 'double angle' wedge model at the assemblage.

Meanwhile the new model has been also fabricated. The different design more close to the original idea was used. The model configuration is a 'double angle' wedge with two

steps of flow turn both of approximately 10°. The model was constructed from ~5mm thickness BN plates of $100{\times}30$ mm^2.

The magnetic system leads are located in six slots at the bottoming surface of the plates. Eight electrical probes are imbedded into the flow-facing surface to measure the electrical potential distribution along the flow at two lines. Some details of this model are visible in Fig.36.

The visualizations of the flow around the wedge obtained in several runs are presented in figs 37 trough 40.
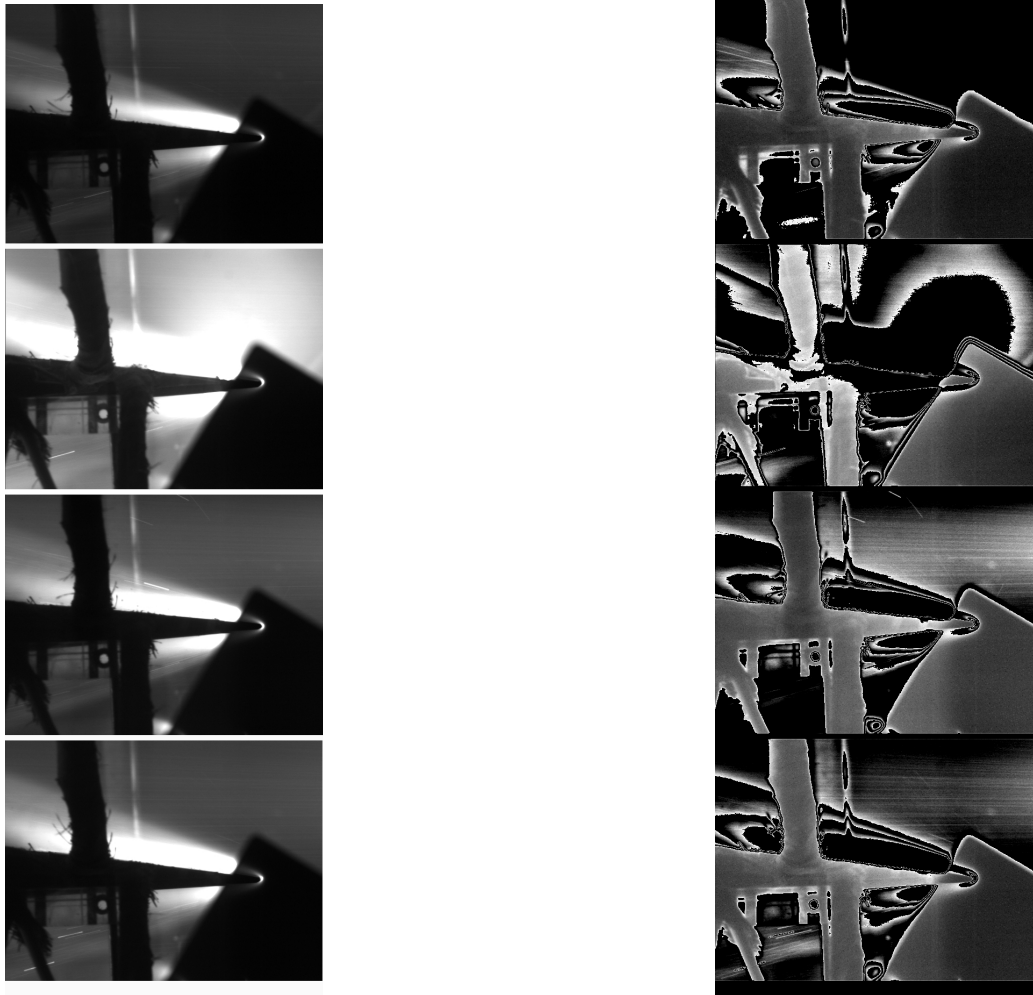
Figure 37. The visualization of flow around the wedge model. Run 132 04.24.2003. Flow from the right to the left. Four consequence frames are presented. Digital camera Pulnix-6710, 250fps, exposure time 30 mks. The left column is original imaging, the right column is the filtered image.

Fig.37 the visualization of flow in Run 132 is presented. Four consequent frames are shown. The second frame corresponds to the maximal magnetic field strength, which was about 2 Teslas at the surface of each of eight leads of magnetic system. In order to resolve the fine structure at the edge the filtering of the edge region was applied as it is
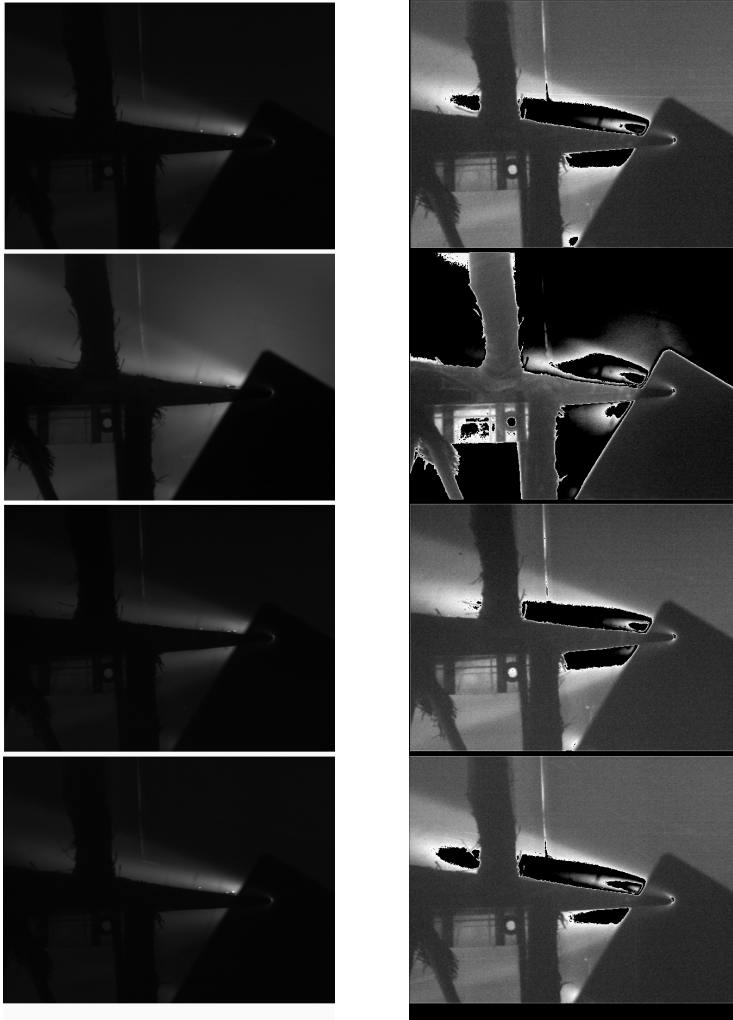
Figure 38. The visualization of flow around the wedge model. Run 133 04.24.2003. Flow from the right to the left. Four consequence frames are presented. Digital camera Pulnix-6710, 250fps, exposure time 30 mks. The left column is original imaging, the right column is the digital filtered image.

clearly seen from the pictures. The reduction degree is 1/100. The edge area is now well resolved however only very small changes caused by magnetic filed could be found. The result is very similar to the previous observation made in the stagnation region of the cylinder in cross-flow. The digital filtering has revealed more details of flow modifications caused by MHD interaction. The strong (temperature) perturbation is clearly seen in upstream area. As it was found earlier the reason of this effect is the rather strong Hall current leakage into the secondary nozzle. The interesting fact is that there is no evident flow structure change in the region of maximal magnetic field strength (at the central part of the wedge just in between the well seen upper and bottom leads). It should be noted that in this run and any others as well the flow structure is practically totally recovered after magnetic field pulse.

It was concluded that the simple filtering is not high effective as it was expected. The new technique proposed by Dr.S.Leonov has been applied in the most recent experiments. The spectra filtering is used. The analysis of spectra obtained earlier in the cylinder study has shown that there is the emitting region near the resonance line of atomic oxygen. The corresponding filter is fortunately available at IVTAN with the wavelength =779nm and the width =15nm.

Two models were tested: the regular wedge and the double angle wedge described above.

Figure 40. Intensity distribution across the flow. The blue curve corresponds to no magnetic field (frame#1 of fig.39), the red curve corresponds to maxim al magnetic field (fram#2 of fig.40

The MHD interaction effects are now well visible. Besides the commonly observed increasing of luminosity from the flow field the well resolved the oblique shock angle increases significantly. The important detail is the also rather well pronounced the area with a strong magnetic field. The information supporting these preliminary conclusions is presented in Fig.41 where the intensity distribution along a vertical line is plotted for two cases with and without magnetic field.

Supporting Numerical Simulation
The wedge experiments were planned with the wide utilization of the numerical model
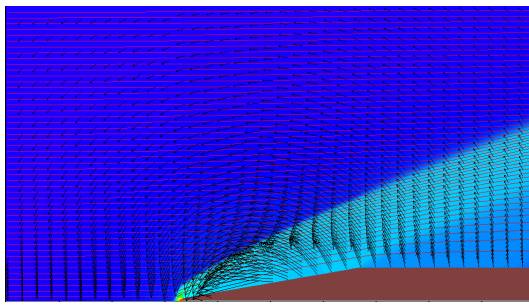
Figure 41. Pressure, flow stream lines and magnetic field vector distribution in the flow around the extended wedge.
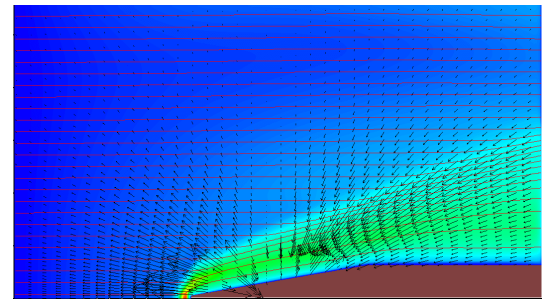
Figure 42. Temperature, flow stream lines and body force vector distribution in the flow around the extended wedge.

developed and validated on the cylinder in cross-flow experiments described above. In Figs.41 and 42 the flow parameters distribution are presented for the experimental conditions. The qualitative correlation of temperature field with the experimental imaging is clearly seen.

3.4. Shock-on-Lip MHD Control

A special model was designed to study the MHD interaction at the configuration simulating the hypersonic inlet. The model consists of two parts: a wedge simulating a forebody and a plate simulating a cowl. The goal is to demonstrate the MHD interaction potentiality to control the inlet flow under off-design operation when the primary oblique shock fails to meet the cowl lip. The experimental Cowl-Wedge Model on the holder is shown in Fig.43.

Figure 43. The Cowl-Wedge Model on the holder. The cowl (blue edge) is located above the active zone of the wedge (red edge). The external leads of magnetic system are turned counterclockwise direction to extend the observation area of the flow near the inlet.

An additional visualization problem has appeared during the preparation of these experiments. It was realized that the focusing procedure is critically important for visualization of such a '2D model'. The rather short focusing distance results in rather large detergency of the observation angle diffusing the flow structure imaging and causing more complexity in the interpretation of the result. Trying to decrease this effect with available lenses two cases were used. In the first case the camera was focused on the wedge edge, in the second it was focused on the some location in between the cowl edge and the wedge surface. Results have shown that for both cases the problem of proper interpretation still exists. More efforts are needed to improve this technique considerably.

The visualizations of the flow field for these cases are presented in Figs.44 and 45 in the similar format as for the previous cases.

Figure 44. Run 137 07.21.2003.The Cowl-Wedge Model, VisualizationWith the spectral filtering.
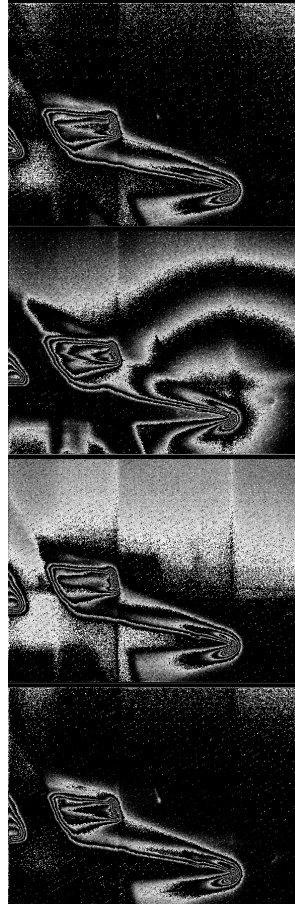
Figure44a . Run 137 07.21.2003.The Cowl-Wedge Model, VisualizationWith the spectral filtering with followeddigital filtering

Figure 45 Run 138 07.21.2003.The Cowl-Wedge Model, VisualizationWith the spectral filtering with followeddigital filtering
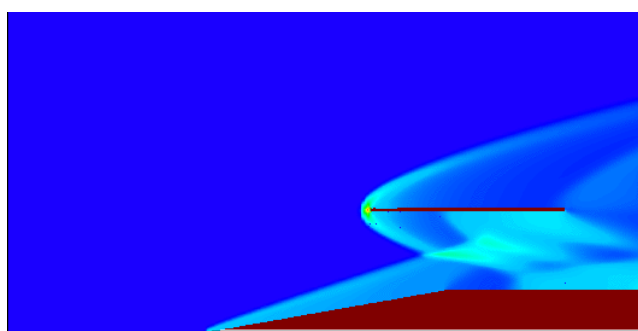
Figure 46. Pressure distribution with no Magnetic field under conditions of the Run 138.

The comparison of two first frame clearly shows that the main oblique shock entering under cowl while the magnetic field absents shifts up to meet the cowl lip as it was designed. Furthermore the secondary oblique shock is formed at the upstream edge of the region of high magnetic field. The focusing problems indicated
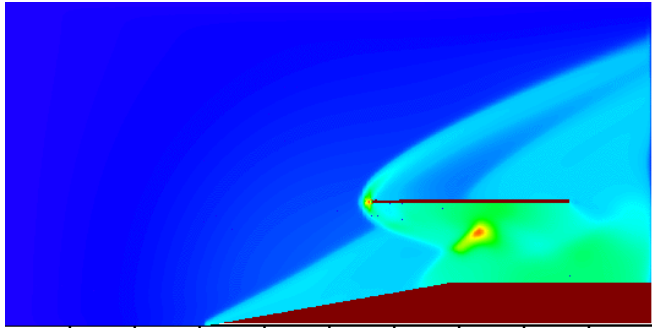
Figure47. Pressure distribution for the conditions of Run 138.
Magnetic field1.75T at the lead surface.

above make it difficult to resolve many other details of the flow structure. The center focusing case presented in Fig.45 shows much more clearly the flow structure in under-cowl lip region where the secondary oblique shock has been created by MHD interaction.

The MHD interaction effect is very well seen from the corresponding numerical simulation. In Fig.46 and 47 the pressure distributions under conditions of Run 138 with the Cowl-Wedge model are presented. The oblique shock displacement from the deep internal region to the cowl lip is observed. However, under the experimental conditions the MHD interaction is not high enough to fit the shock to the cowl lip. It important to note that the MHD interaction saturates at the magnetic field strength much lower as compared with the value reached in the experiments (~2 Tesla at the lead surface). It is in full agreement with the explanations involving the strong Hall effect has been discussed above while considering the experimental results on the cylinder in cross-flow. To illustrate this fact the pressure distribution for the higher magnetic field
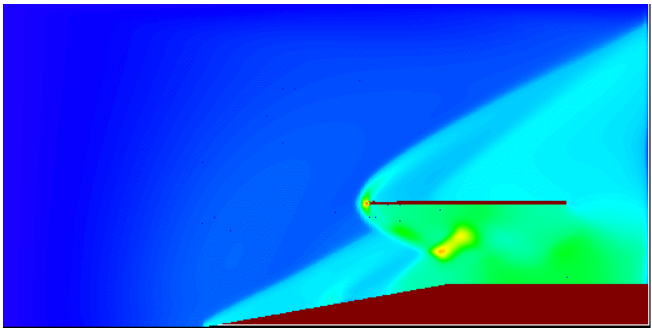
Figure48. Pressure distribution for the conditions of Run 138.
Magnetic field 2.5T at the lead surface.

is presented in Fig.48. The pressure distribution is changed above the cowl but the oblique shock configuration is practically the same.

The discussed result is probably the first direct experimental confirmation of the applicability of the MHD interaction for in-take flow control at least in principle. At the same time the physical phenomena are very complicated and much more studies are needed to meet the practical requirements.

4.Conclusions

During the last decade the significant progress in MHD aerospace applications has been achieved. Besides the topics considered in this paper there are several others very promising MHD applications field: on-board MHD electrical power generation, MHD assisted mixing, ignition and combustion; MHD enhancement of propulsion cycle and others.

The potentiality of the MHD interaction for the hypersonic flow control has been demonstrated experimentally and theoretically.

At the same time it was found that the physical phenomena involved are very complicated and not fully understood.

The low-pressure conditions typical of hypersonic external flows in atmosphere result in a strong Hall effect even under magnetic field strength much lower as compared with the required level.

The Hall effect reduces the effectiveness of MHD interaction. In order to recover the MHD interaction performance new revolutionary ideas for on-board system configurations are urgently needed.

The problem of the electrical conductivity of oncoming airflow is still very serious. The methods proposed up to now are not effective at least under real flight conditions.

The experimental study of MHD interaction in hypersonic flow seems to be very complicated problem because of the great difficulties to provide adequate conditions in on-ground experimental facility. In addition to the well-known problems of 'conventional' hypersonic aerodynamics the serious problem in electrodynamics boundary conditions arises.

The extrapolation of the experimental results obtained at small-scale on-ground experimental facilities with the numerical models developed and validated with such experiments show nevertheless the significant positive effects of MHD interaction applications at hypersonic vehicles.

References

1. Kantrowitz A.R. A Survey of Physical Phenomena Occurring in Flight at Extreme Speeds. -Proceedings of Conf. on High Speed Aeronaut., N.Y., 1955, p.335.
2. Kulikovski A.G., "On the Flow of Conducting Fluid Over the Magnetized Bodies", Doklady of USSR Acagemy of Sciences, 1957, v.17, No.2 (in Russian).
3. Zinober A.B., "Magnetohydrodynamic Flow Around Bodies", Riga, Zinatne, 1970, 291p. (in Russian).
4. Kulikovski A.G., Lyubimov G.A., "Magnetohydrodynamics", M: Fismatgiz, 1962, 246p. (in Russian).
5. Resler E.L., Sears W.R., "The Prospects for Magnetohydrodynamics", JAS, 1958, v.25, No.4, pp.235-245.
6. Bush W.B. "Magnetohydrodynamics – Hypersonic Flow Past a Blunt Body", Journal of the Aero/Space Sciences, v.25, Nov., 1958, pp.685-690.
7. Bush W.B. "Compressible Flat-Plate Boundary Layer Flow with an Applied Magnetic Field", Journal of the Aero/Space Sciences, v.26, Jan., 1960, pp.49-58.

8. Bleviss Z.O. "Magnetohydrodynamics of Hypersonic Couette Flow", Journal of the Aero/Space Sciences, v.25, Oct. 1958, pp.601-615.
9. Bityurin V.A., Potebnja V.G., Alferov V.I. "On MHD Control of Hypersonic Flows. Planning of Experimental Studies of MHD Effects on Bow Shock" In 34th SEAM, 1997, June 18-20, USA, Mississippi, p.4.4.1.
10. Lineberry J.T., Rosa R.J., Bityurin V.A., Bocharov A.N., Potebnja V.G. "Prospects of MHD Flow Control for Hypersonics", 35th Intersociety Energy Conversion Engineering Conference, AIAA 2000-3057, 24-28 July 2000, Las Vegas, NV.
11. Hoffmann K.A., Damevin H.-M., Dietiker J.-F. "Numerical Simulation of Hyprsonic MHD Flow", AIAA Paper 2000-2259, June, 2000.
12. Poggie J., Gaitonde, "Magnetic Control of Hypersonic Blunt Body Flow", AIAA Paper 2000-0452, Jan, 2000.
13. Deb P., Agarwal R. "Numerical Simulation of Compressible Viscous MHD Flow with a Bi-Temperature, Model for Reducing Supersonic Drag of Blunt Bodies and Scramjet Inlets", AIAA Paper 2000-2419, June, 2000.
14. Rosa R.J. MHD Energy Conversion, McCran hill, 1967
15. Sedov L.I., "Similarity and Dimensionality Methods in Mechanics", 10th Edition, M: Nauka, 1987, 432p. (in Russian).
16. Concept of Perspective of Multistage Aero-Spacecraft, Review No 686. ONTI, TsAGI, 1989 (in Russian).
17. Laster M.L., Buslinell D.M. A National Study for Hypersonic Facility Development. ALAA Paper N94-2473, 1994.
18. GOST 4401-81. The Standard Atmosphere. Parameters, Moscow, Standard Publ., 1981
19. Bush W.B. "Compressible Flat-Plate Boundary Layer Flow with an Applied Magnetic Field", Journal of the Aero/Space Sciences, v.26, Jan., 1960, pp.49-58.
20. Mnatsakanian A.Kh., Naidis G.V. On Magnetogasdynamics effects on spacecraft motion in the Earth atmosphere. -Tech.Report 92/11, IVTAN, 26p., 1991 (in Russian).
21. Bityurin V.A., Ivanov V.A. An Alternative Energy Source Utilization with an MHD Generator // Proceedings of the 33rd Symposium on Engineering Aspects of Magnetohydrodynamics, Tennessee, USA, June 13-15, 1995, pp.X.2-
22. Gorelov V.A., Kireev A.Yu, Results of the Calculation of The Flow around a Spacecraft of Conic and Plate Types, Tech.Notes, TsAGI-IVTAN, ,Moscow, 1994, 27p.
23. Bityurin V.A., Ivanov V.A., Botcharov A.N. at cl. *Magnegasdynamics Control of Spacecraft Motion in the Upper Atmosphere*, Tech.Rep. 94/3, IVTAN-ANRA, Moscow, 1994, 37p. (in Russian)
24. Asinovsky E.I., Amirov R.Kh. The Analys of the Development a hypersonic MHD Generator Pre-Ionizer, TR 1255/921 1, IVTAN, Moscow, 1993 (in Russian).
25. Wideman J.K. et.al. Feasibility Analysis of Aircraft MHD, Proc. 26th Symp. on Eng. Aspects of MHD, 1986.
26. V.A.Bityurin, A.P.Likhachev, S.A.Medin, and G.A. Lyubimov, On the Dynamics of a non-Uniform Conducting Flow in an MHD Generator Channel. Magnetohydrodynamics: an International Journal, Vol.2, No. 2~3, pp. 173-184,1989.

27. Macheret S.O., Miles R.B. and Nelson G.L. Feasibility Study of a Hybrid MHD // AIAA Paper 97-2429, Radiatively Driven Facility for Hypersonic Ground Testing, 1997.

28. Brichkin D.I., Kuranov A.L. and Sheikin E.G. MHD-Technology for Scramjet Control. // AIAA Paper 98-1642, 8th International Space Planes and Hypersonic Systems and Technologies Conference, April 27-30, 1998, Norfolk, VA.

29. Kuranov A.L., Sheikin E.G. The Potential of MHD Control for Improving Scramjet Performance // AIAA-99-3535, 30th AIAA Plasmadynamics and Lasers Conferences, June 28 – July 1, Norfolk, VA.

30. V.A.Bityurin and J.T.Lineberry, Aerospace Applications of MHD // Invited Lecture 13th International Conference on MHD Electrical Power Generation and High Temperatures Technologies, October 12-15, 1999, IET AC, Beijing, China.

31. Dertin, John J., «Hvpersonic Aerothermodynamics». AIAA Educational series, 1994

32. G.G.Tcherny, Gasdynamics. 1987. Moscow, (in Russian)

33. V.A.Bityurin and V.A.Ivanov, An Alternative Energy. Source Utilization with an MHD Generator, In: 33rd Symp.on Eng. Aspects of MHD, June 13-15 1995, UTSI. Tullahoma, TN, p.X-2. 1.

34. J.Cole, J.Camphell, and A.Robertson, Rocket-Induced Magnetohydrodynamic Advanced Propulsion Concept, AIAA Paper 95-4079.

35. E.P.Gurjanov and P.T.Harsha, AJAX: New Directions in Hypersonic Technology, AIAA Paper 96-4609.

36. V.A.Bityurin, V.A.Zeigarnik, A.L.Kuranov, On a Perspective of MHD Technology in Aerospace Applications. // AIAA Paper 96-2355, 27th AIAA Plasmadynamics and Lasers Conference, New Orleans, 1996.

37. V.A. Bityurin and J.T. Lineberry, V.G. Potebnia, V.I. Alferov, A.L. Kuranov and E.G. Sheikin, Assessment OF Hypersonic MHD Concepts // AIAA 97-2393, 28th Plasmadynamics and Lasers Conference, June 23-25, 1997, Atlanta, GA

38. K.I.Kovalev, T.A.Markina, Power Facility with an Build-in Multipole MHD Generator, High Temperatures, vol.33, No3, 1995

39. Kovalev L.K., Larionoff A.E., Poltavets V.V., Kovalev K.I. Theoretical and Experimental Studies of Faraday Multipole MHD Generators. In: 11th Int.Conf. on MHD Electrical power Generation, China, 1992.

40. Kovalev L.IC, Kovalev K.L Faradeevskie mnogopolusnye magnitigidrodinamicheskie generatorv postojannogo i peremennogo toka. (in Russian). Electrichestvo, 1990, No.7.

41. E.N.Vasilyev, V.A.Derevyanko, A.F.Latypov and V.V.Ovshinnikov, Conception of Using T-layer MHD Generator in Hypersonic Aircraft Engine. In: Eleventth International Conference on Magnetohydrodynamic Electrical Power Generation, 1992, Beijing, China, October 12-16, vol.IV, p. 1320.

42. B.C.Lin, et al., An Assessment of Unseeded MHD Accelerator Using T-layer Concept, Proc. of 33-rd SEAM, p.V.7-1-10, Tullahoma TN, June, 1995.

43. V.S.Slavin, V.V. Danilov M.V., A.V.Romashko, K.A. Finnikov, U.M.Ermoshkin, Kraev, T-Layer MHD in Aerospace Applications // Workshop "Perspectives of MHD and Plasma technologies in Aerospace Applications", March, 24-25, IVT RAS, Moscow, 1999, p.31-43

44. Alferov V.I. "Current Status and Potentialities of Wind Tunnels with MHD Acceleration", High Temperature, 2000, v.38, No.2, pp.300-313.
45. J.T.Lineberry V.A.Bityurin, A.N.Bocharov, D.S.Baranov A.B.Vatazhin, V.I.Kopchenov, O.B.Gouskov V.I.Alferov, A.S.Boushmin, "Cylinder with Current in Hypersonic Flow", In: 3rd Workshop on Magneto-Plasma Aerodynamics in Aerospace Applications, April 24-26, 2001, pp 15-25.
46. Bityurin V.A., Baranov D.S., Bocharov A.N., Margolin L.Ya.,.Bychkov S.S, Talvirsky A.D., Alferov V.I., Boushmin A.S., Podmasov A.V. Experimental Studies of MHD Interaction at Circular Cylinder in Hypersonic Airflow, In: Proc. of 4th Moscow Workshop on Magneto-Plasma Aerodynamics in Aerospace Applications, IVTAN, Moscow, 9-11 April, 2002
47. V.A. Bityurin, A.N. Bocharov, D.S. Baranov, S.B.Leonov "Numericall Simulation and Experimental Study of MHD-driven Mixing and Combustion", 40th AIAA Aerospace Sciences Meeting & Exhibit, January 14-17, 2002, AIAA Paper 2002-0492, Reno, NV
48. Bocharov A.N.,Baranov D.S., and Bityurin V.A. "Experimental and Theoretical Studiy of MHD Assisted Mixing and Ignition in Co-Flow Streams", 33rd Plasmadynamics and Lasers Conference, Maui, Hawaii, 2002, AIAA Paper 2002-2248.
49. A.Bocharov, S.Leonov, I.Klement'eva, and V.Bityurin, "A Study of MHD AssistedMixing and Combustion", In: 41 st Aerospace Sciences Meeting and Exhibit, Reno, NV, 2003, AIAA Paper 2003-358
50. Bityurin V.A., Bocharov A.N., Baranov D.S., Vatazhin A.B., Kopchenov V.I., Gouskov O.B. Alferov V.I., Boushmin A.S, Lineberry J.T., "Theoretical and Experimental Study of an MHD Interaction Effects at Circular Cylinder in a Transversal Hypersonic Flow", In: 40th AIAA Aerospace Sciences Meeting & Exhibit, January 14-17, 2002, AIAA Paper 2002-0491, Reno, NV.
51. Lineberry J.T., Bityurin V.A., Bocharov A.N., "MHD Flow Control Studies. Analytical Study of MHD Flow Interaction Around a Right Circular Cylinder in Transverse Hypersonic Flow", In: Proc. of 14th Intern. Conf. On MHD Electrical Power Generation and High Temp. Technologies, Maui, Hawaii, May 20-23, 2002, pp. 135-149.
52. Bityurin V.A., Bocharov A.N., Lineberry J.T., Suckomel C."Studies on MHD Interaction in hypervelocity Ionized Air Flow over Aero-Surfaces" 43rd AIAA Aerospace Sciences Meeting & Exhibit, June 23-26, 2003, AIAA Paper 2003-1365, Orlando, FL .
53. Alferov V.I., Private Communications, 2002
54. Damevin H.-M., Hoffman K.A. "Numerical Simulations of Hypersonic Magnetogasdynamics Flows over Blunt Bodies". In: 40th AIAA Aerospace Sciences Meeting & Exhibit, January 14-17, 2002, AIAA Paper 2002-0201, Reno, NV
55. Damevin H.-M., Hoffman K.A. Computation of Hypersonic, "Chemically Reacting Magnetogasdynamic Flows over a Cylinder" In: 40th AIAA Aerospace Sciences Meeting & Exhibit, January 14-17, 2002, AIAA Paper 2002-0648, Reno, NV
56. MacCormack R.W. "Three Dimensional Magneto-Fluid Dynamics Algorithm Development", In: 40th AIAA Aerospace Sciences Meeting & Exhibit, January 14-17, 2002, AIAA Paper 2002-0197.

57. Dietiker   J.-F   ,and   Hoffmann   K.A,.   "Computations   of   Turbulent Magnetohydrodynamic Flows", In: Proc. of 14th Intern. Conf. On MHD Electrical Power Generation and High Temp. Technologies, Maui, Hawaii, May 20-2, 2002, pp. 123-135.
58. Gaitonde D., Poggie J., "Preliminary Analysis of 3-D Scramjet Flowpath with MGD Control", In: Proc. of 14th Intern. Conf. On MHD Electrical Power Generation and High Temp. Technologies, Maui, Hawaii, May 20-2, 2002, pp. 79-96
59. John J.Bertin, "Hypersonic Aerothermodynamics", AIAA Education Series,1994

PLASMA FLOW CONTROL FOR BOUNDARY LAYERS

Roger L. Kimmel[*]

1 Introduction

Viscous phenomena assume a special importance in hypersonic flight. An overriding concern is heat transfer, which is primarily a boundary layer phenomenon. Frictional heating causes the boundary layer thickness to increase as Mach number increases, leading to viscous interaction between the growing boundary layer and the external inviscid flow, altering the vehicle pressure distribution.   The interaction of thick boundary layers with control surfaces may reduce control effectiveness. Although wave drag dominates blunt configurations, skin friction drag becomes important for slender configurations.[1]

The effects of viscous phenomena depend to a great extent on whether the boundary layer is laminar or turbulent. Estimates for the National Aerospace Plane (NASP)[2] showed that the payload-to-gross-weight ratio would nearly double if the vehicle boundary-layer were fully laminar, compared to fully turbulent.

A generic hypersonic transport was considered in Ref. 1 to assess the relative effects of skin friction and heat transfer. The hypersonic transport described in Ref 3 was chosen as a baseline. For this study, the vehicle was sized at 61 m in length, a reasonable value for vehicles designed for sustained hypersonic flight. The longer the vehicle, the greater the wetted area and the greater the contribution of skin friction. The analysis conditions were Mach 8, 10, 12, and 14. The altitude was varied at each Mach number to keep the freestream dynamic pressure constant at 71.8 kPa, which is again a reasonable value for an airbreathing trajectory. These conditions produced Reynolds numbers based on freestream conditions and vehicle length from 131×10^6 (Mach 14) to 247×10^6 (Mach 8). The configuration was analyzed using the Supersonic, Hypersonic, Arbitrary Body Program (SHABP).[4] SHABP calculates skin friction using correlations based on the length Reynolds number along each body panel. The boundary layer was treated as either all laminar or all turbulent to provide upper and lower bounds on skin friction. Calculations were carried out for zero angle of attack. The inlet was treated as flow-through, and no drag was calculated for the internal surfaces. The results here are representative of large, slender vehicles with significant wetted area.

Fig. 1 shows that the for fully laminar or fully turbulent conditions, the percentage of drag due to skin friction varies little over the Mach number range examined. For fully turbulent flow, skin friction contributes over 30% of the overall vehicle drag. For fully laminar flow, the skin friction contribution is about 10%. Given the large length Reynolds numbers, it is quite likely that the bulk of the flow over the vehicle is turbulent, even at the highest Mach number. A similar vehicle analyzed by Finley[5] showed 65% to

[*] Air Force Research Laboratory, United States

1

100% of the vehicle area turbulent at Mach 15, depending on whether a correlating factor of $Re_\theta/M = 300$ or 100 (respectively) was used.

Heat transfer to the vehicle was estimated from the skin friction results, using the Reynolds analogy, $C_H = 1/2 C_f$. The ratio of fully laminar to fully turbulent heat transfer, integrated over the vehicle, is shown in Fig. 2. At Mach 8, turbulent heat transfer is up to eight times laminar heat transfer. Increased heating has a negative impact on vehicle performance. Heating must be managed either through increased thermal protection or active cooling, or by restricting the vehicle trajectory to limit higher velocity flight to high altitude. The first strategy results in increased weight, the second results in reduced range.

The requirement to control boundary layer transition and boundary layer thickness in airbreathing hypersonic engines and inlets has been noted.[6] The presence of the boundary layer has a number of deleterious effects on engine performance.[7] The boundary layer increases flow distortion and reduces mass flux through the inlet. Boundary layer separation, which is a strong function of the state of the boundary layer, laminar or turbulent, exacerbates these effects, and also can lead to unsteadiness and locally increased heating. The study cited in Ref. 6 listed surface discharges for reducing skin friction and controlling transition as a technology worthy of further investigation.

The benefits of being able to control the development of the viscous boundary layer on high-speed vehicles are clear. A number of factors make plasma boundary layer control an attractive option. At high hypersonic Mach numbers where boundary layer ionization is thermal in nature, the highest temperatures and ionization levels downstream of the bow shock will occur within the boundary layer.[8] For control methods involving artificially ionized plasmas, boundary layer control relies on ionization of only the near-body fluid, in contrast to inviscid flow-control schemes involving the ionization of large volumes of plasma. Presumably, since the volume of ionized fluid is less, power requirements would also be lessened. Also, the boundary layer is easier to ionize than the inviscid flow due to its lower density. The sensitivity of boundary-layer transition to the mean boundary-layer state means that even small MHD control inputs may have a large effect on the overall system. Glow-discharges have been used for many years to excite boundary-layer instabilities in supersonic,[9,10] and hypersonic flows.[11] MHD boundary-layer control exploits the fact that fields from on-board magnets will be highest near the vehicle surface. Also, control inputs can be limited to locations where they are most effective to reduce weight.

This paper discusses some aspects and recent advances in the application of plasmas to high-speed boundary layer control. Two control methods, MHD control and Joule heating, will be examined in detail. A number of recent works have examined electrohydrodynamic (EHD) flow control in low-speed boundary layers, but as of yet this technique has not been applied to high-speed flows.

2 MHD Control

MHD boundary-layer control relies on the forces exerted on a conductor (the plasma) flowing through a magnetic field. In the flow shown in Fig. 3, plasma flows over a wall with a magnet embedded in it. Any number of magnetic field arrangements may be

conceived (see Ref. 12 for example), but the scenario shown in Fig. 3 illustrates the basic concept. Assuming a scalar conductivity, a body force **F**, generated on the plasma is given by

$$\mathbf{F} = \sigma\left(\mathbf{E} + \mathbf{u} \times \mathbf{B}\right) \times \mathbf{B}$$

where σ is the fluid conductivity, **u** is its velocity, **B** is the magnetic field, and **E** is the electric field imposed on the plasma by the external circuit. A primary figure of merit for characterizing MHD flows is the interaction parameter, which is the ratio of Lorentz force ($\sigma\mathbf{u} \times \mathbf{B}$) to inertial forces on a fluid element. The interaction parameter is given as

$$Q = \frac{\sigma B^2 L}{\rho u} K$$

where L is the interaction length scale, ρ is the fluid density, and K is the load factor, $K = E/uB$. For the time-being, we will consider a load factor of unity. The Lorentz force will be a retarding force, regardless of whether the magnetic field is oriented into or out of the wall, and will decelerate the boundary layer.

Rossow[13] analyzed the flow of a laminar conducting boundary layer over a flat plate with a magnetic field normal to the plate surface. He considered both the case above, where the magnetic field is fixed relative to the plate, and the case in which the field is fixed to the moving fluid, as would be encountered by a vehicle flying through the earth's magnetic field. Although Rossow's analysis and assumptions are open to some question,[14] the qualitative trends derived from his work are similar to those observed by other investigators. His results show that as the interaction parameter increases, the boundary layer was increasingly decelerated. Skin friction of course decreased, and displacement thickness increased with increasing Q. As noted by Rossow, however, the magnetic-field / fluid interaction that decelerates the fluid also creates a drag on the magnet embedded in the plate, offsetting the decrease in skin friction. In the cases considered by Rossow, the net effect was to increase the overall drag on the plate.

Bush[15] derived a similarity solution for conducting laminar boundary layers in the presence of an applied magnetic field. In the case examined by Bush, the magnetic field was set proportional to $x^{-1/2}$ to obtain a similarity solution. Bush also observed the trend of decreasing skin friction with increasing interaction parameter. Similar effects were predicted by Sastry and correlated with the Hartmann number.[16] The Hartmann number is proportional to the square root of the ratio of MHD to viscous forces per unit fluid volume and is expressed as

$$Ha = KBL\sqrt{\frac{\sigma}{\mu}}$$

where μ is the fluid viscosity. It can be shown that if the same length scale is used,[17] the ratio of the Hartmann number squared is equal to the product of interaction parameter and the Reynolds number.

Borghi et al.[18] calculated the ionized viscous flow over a blunt leading-edge flat plate. Magnetic fields were created by linear current-carrying conductors embedded within the

model, parallel to the leading edge and transverse to the flow. Two cases were considered, one where a magnetic field was imposed at the leading edge, the other where the field was imposed at mid-span. In both cases, the applied magnetic field created a local reduction in skin friction. For the case of the field applied at mid-span, this was accompanied by an increase in surface static pressure. The magnetic field at the stagnation point had little, if any, effect on surface pressure.

Poggie and Gaitonde[19] computed laminar viscous MHD flows in the vicinity of the stagnation region of an axisymmetric, spherically blunt body, and report a thorough literature search on this subject. The magnetic field in their computations was a dipole centered at the sphere and aligned with the body axis. They also showed a reduction in stagnation-point skin friction and heat transfer. These results are in qualitative agreement with the earlier theory of Bush.[20]

Although the density of hypersonic flows is usually relatively low, the combination of high velocities and low conductivity leads to quite low interaction parameters. Compared to liquid metals, for example, the conductivities of typical plasma and electrolyte flows are relatively low. Ref. 14 cites the conductivity of copper at 6×10^7 mho/m, mercury at 10^6 mho/m, and salt water at 25 mho/m. Ionization is insignificant below about Mach 10 for typical trajectories.[21] Non-equilibrium ionization such as electron beams, DC, RF, or microwave discharges may be used to produce plasma at lower Mach numbers. For non-equilibrium ionized air, conductivities are typically on the order of one mho/m.[22,23,24] Measurements reported by Sears[25] suggest that conductivities of 100 mho/m may be attained in thermal plasmas above about Mach 16. This can be augmented by seeding the air with an alkali metal. For a flat plate at M=6 at 30km altitude, assuming $\sigma = 1$ mho/m, $L = 1$ meter, and $B = 1$ Tesla (conditions achievable in the laboratory), the interaction parameter based on freestream conditions is Q=0.03, indicating that the Lorentz force imposed on the fluid is quite small compared to the fluid inertia.

However, the interaction parameter within the boundary layer should be larger than the freestream MHD interaction parameter. The freestream or edge velocity is not a suitable scale for assessing MHD boundary-layer flows, since the boundary-layer velocities are lower than the edge velocity. Analysis of experiments by Henoch and Stace[26] on MHD control of turbulent salt-water, flat plate boundary-layers showed that the friction velocity $u*$, where

$$u* = \sqrt{\frac{\tau_w}{\rho_w}}$$

and τ_w and ρ_w are the skin friction and density evaluated at the wall, was an appropriate velocity scale. The friction velocity is a more appropriate scale for boundary layer phenomena since it is much less than the edge velocity. As noted by Macheret et al., by expressing the skin friction in terms of the skin friction coefficient, c_f,

$$\tau_w = \frac{1}{2} \rho U^2 c_f$$

the interaction parameter based on the friction velocity, $Q*$, for a load factor of one, is related to the interaction parameter based on freestream velocity by

4

$$Q^* = Q\sqrt{\frac{2}{c_f}}$$

Since c_f is typically $O(10^{-3})$[27], the interaction parameter based on friction velocity can be 40 times that based on freestream velocity.

The interaction parameter may also be boosted by imposing an electric field. The necessity of boosting the interaction parameter in low-conductivity MHD flows has been recognized and applied for some time to electrolyte MHD flows.[26,28] The load factor may be larger than one, even in hypervelocity flows. Fields of 10^4 V/m are easily achievable.[22,29,30] Also, by supplying an external power source, the sign of the imposed electric field may be made opposite to the $\mathbf{u} \times \mathbf{B}$ field. If the imposed field is opposite in sign and greater than $\mathbf{u} \times \mathbf{B}$, the flow may be accelerated instead of decelerated. This MHD acceleration of the boundary layer would be expected to produce a fuller, more stable boundary layer profile and create a propulsive force on the vehicle from the magnetic / electric field interaction (at the expense of increased skin friction). Calculations by Jaffe[31] for an incompressible laminar boundary layer demonstrated this trend. It should be noted that as the load factor or current increases, Joule heating also increases.

MHD control of hypersonic boundary-layer transition has been considered since at least the 1950's.[32] There is no doubt that MHD effects may be used to influence mean boundary-layer profiles, which in turn moderate hydrodynamic stability for traveling[32,33,34] and stationary waves.[35] MHD forces can also operate on flow fluctuations as well as the mean flow. For example, if the mean flow is co-planar with the magnetic field and no electric field is imposed, $\mathbf{u} \times \mathbf{B} = 0$ and no Lorentz force is generated due to the mean flow. However, boundary-layer instabilities generate transverse velocity fluctuations, which in turn generate fluctuating Lorentz forces that oppose them. Stuart's[36] calculations for incompressible planar Poiseuille flow of a conducting fluid with a co-planar magnetic field showed that the neutral stability curve shrank with increasing interaction parameter and was completely stabilized with a sufficiently large interaction parameter. Lock's[37] calculations for the same flow with a magnetic field perpendicular to the main flow showed that since this field could operate on the mean flow, it was more effective in stabilizing the flow than the co-planar field.

Limited calculations support the concept of stabilizing the boundary-layer to traveling disturbances using MHD forces. Rossow extended calculations of mean MHD boundary layer profiles to calculate the neutral stability diagrams for incompressible flat plate, MHD flows with magnetic fields co-planar and transverse to the mean flow. These results showed a fixed co-planar magnetic field or a transverse field moving with the flow to be stabilizing. A transverse field fixed to the flat plate (generating a retarding force on the mean flow) was destabilizing.

In general, for 2D flows above about Mach 5, the dominant boundary-layer instability is the second mode.[38] The first work to consider MHD effects on second-mode instability was by Cheng et al.[39,40] This work featured DNS simulation of second-mode instabilities in a flat plate, $M_e = 4.5$ boundary-layer. A uniform conductivity of 100 mho/m was imposed on the fluid. A number of dipole magnet configurations were considered. The

basic results can be illustrated by considering flow over a dipole pair. The first dipole was placed 0.02 m from the leading edge of the plate, with dipole moment in the positive y-direction. The second dipole was located 0.025 m downstream of the leading edge, with dipole moment in the negative y-direction. Two cases were considered, one with a field strength equal to approximately 2.5 T at the wall, the other with a field strength of approximately 1.2 T at the wall. The interaction parameters, based on edge conditions, were 1.0 and 0.26, respectively.

The flow of the conducting fluid through the magnetic field created an adverse pressure gradient upstream and in the immediate vicinity of the dipole. The adverse pressure gradient was sufficient to separate the boundary-layer for the high interaction parameter case. Downstream of the magnet, the flow relaxed through a favorable pressure gradient. A second mode disturbance that was unstable in the non-MHD boundary-layer was introduced at the upstream boundary. The instantaneous wall pressure (Fig. 4) illustrates the instability of the disturbance, as pressure fluctuations increase with increasing x. When the 1.2 T magnetic field was imposed on the same flow, wall-pressures showed that the second mode amplification was slightly increased in the initial adverse pressure gradient. The second mode was stabilized through the rest of the interaction, even in regions of adverse pressure gradient (Fig. 5). Damping was even higher for the 2.5 T field.

Since it is well-known that inflected velocity profiles are generally more unstable than profiles without velocity inflections, the strong damping of instabilities observed in the MHD flows was unexpected. The authors ascribed this effect to the tight tuning of the most unstable second-mode frequency to the boundary-layer thickness. Since the boundary-layer was dramatically thickened through the interaction, the most unstable frequency was tuned away from the forced disturbance to a lower frequency. This behavior was reminiscent of effects seen in models with geometrically-imposed adverse and favorable pressure gradients.[41] Although MHD effects stabilized monochromatic disturbances, it was not clear that transition could be delayed by such a configuration, since the most unstable frequency would just be shifted to a lower value where other environmental disturbances would amplify. Nevertheless, this work constitutes the first result that second-mode growth may be moderated by MHD effects.

Palm et al. measured the effect of MHD forces on a helium channel flow at M=4, in an experimental realization of the flow shown in Fig. 3. In these experiments, a Nd-Fe-B permanent magnet was mounted in the tunnel sidewall, and electrodes in adjacent walls created an imposed electric field. The flow was pre-ionized upstream of the DC electrodes using a radio-frequency discharge. Wall pressure fluctuations were monitored just downstream of the magnet. Wall pressure fluctuations were reduced when a 50 mA current was passed through the DC electrodes, with the bottom DC electrode negative and the top ground. When the electrode polarity was reversed, no effect on pressure fluctuations was observed. When the magnet polarity was reversed, the electrode polarity resulting in pressure fluctuation reductions was also reversed, in this case with the top electrode negative and the bottom ground. The experiment was repeated using unmagnetized, dummy Nd-Fe-B blocks in the tunnel wall. In this case no effect was observed. These observations further bolstered the authors' conclusions that the observed effects were due to MHD forces on the fluid.

Although it was not clear whether the channel flow was laminar or turbulent, results show that a sufficiently high interaction parameter can be obtained in the laboratory to modify weakly ionized MHD boundary-layers. A notable result of the above experiment is that results were achieved at very low interaction parameter, based on edge velocity, Q = 1.5×10^{-4}. The interaction parameter based on estimated friction velocity was approximately 0.15.

A surprising result from these experiments was that an electrode polarity that should have exerted an accelerating force on the fluid had no effect, and a polarity that should have generated a decelerating force reduced pressure fluctuations. Pressure measurements were made downstream of the magnet, in the region of return magnetic field lines. Also, the current paths in the interaction are unknown. Future work on this experiment will focus on a larger, better-characterized flow and improved diagnostics.[42]

A complicating factor of MHD boundary layer control is that Hall effects are likely to be present in the low-density, high-magnetic-field scenarios typical of MHD plasma boundary-layer control applications. The Hall effect arises in low density flows when the period of revolution of an electron about a magnetic field line becomes appreciable compared to the time between electron-neutral collisions. The magnitude of this effect is described by the ratio of these two times, or the Hall parameter, $\beta = \omega\tau$, where ω is the electron cyclotron frequency, and τ is the period between electron-neutral collisions.[43] When the Hall parameter is large, electrons in effect become trapped within the magnetic field. This is manifested in two ways. First, the effective resistance of the fluid perpendicular to magnetic field lines increases. The effective conductivity of the plasma perpendicular to the magnetic field lines is reduced by

$$\sigma_{B \neq 0} = \frac{\sigma_{B=0}}{1 + \beta^2}$$

and the current responsible for the Faraday force, that perpendicular to the magnetic field lines, is correspondingly reduced.

This reduction in the effective conductivity of the fluid perpendicular to magnetic field lines is demonstrated graphically in Fig. 6, from Ref. 29. In this case, a 50 mA DC discharge between two electrodes on a flat plate was created. A magnetic field perpendicular to the flat plate was imposed. The discharge was run in a constant-current mode. As B increases, the voltage required to sustain the 50 mA discharge increases. Based on the equation above, the Hall parameter was estimated to be approximately one at B=0.9T. Similar results were observed in Ref. 42, where the discharge was run in a voltage-stabilized mode, and the current was allowed to vary with B. In this case, a Hall parameter of three was inferred at the maximum field achievable in the experiment, B=1.4 T.

The second effect of a large Hall parameter is the generation of an additional current, the Hall current with its own corresponding **j**x**B** force. The Hall force may be visualized by considering that the drift velocity, v_d, of the charge-carriers becomes appreciable. This gives rise to an additional force on the electrons, $\mathbf{v_d} \times \mathbf{B}$, creating the Hall current, j_H parallel to the velocity vector. The interaction of the Hall current and the magnetic field

produces the Hall Force, $\mathbf{j_H} \times \mathbf{B}$, perpendicular to both the magnetic field and the Faraday force. This creates an inherent three-dimensionality in the MHD forces. For the flow shown in Fig. 3, the Hall force would tend to push the flow against one of the sidewalls. The inevitability of Hall effects in low-density flows has been known for some time, and numerous schemes have been developed for dealing with them.[12,42,43]

It is conceivable that the Hall forces could be exploited in conjunction with the Faraday force to aid in controlling the boundary layer. For the scenario shown in Fig. 3, a boundary-layer crossflow would be created that might be used to negate crossflow instability on a swept wing.

3   Control via Joule Heating

Boundary layers may be manipulated by the application of electrical fields alone, either through Joule heating of the fluid or EHD forces on the plasma. An advantage of this form of boundary layer control over MHD control is that no magnets are required. A number of researchers have exploited EHD forces in subsonic boundary layers on flat plates using glow discharges,[44] and corona discharges.[45,46] Glow discharges have been used to delay separation and enhance lift on airfoils[47,48,49,50] and to trip the boundary layer on 3D airfoils.[51] Wilkinson[52] has explored spanwise-oscillating discharges as a means of reducing Reynolds stress and skin friction in turbulent boundary layers. As of the time of this publication, EHD control has not been applied explicitly to hypersonic boundary layers. Macheret et al. suggest that velocities induced by EHD effects could be appreciable at low density, but also note that Joule heating effects may be hard to separate from EHD effects.

Limited results on Joule heating control have been obtained in supersonic boundary layers. Analysis of surface microwave discharges[53] indicates local heating, with attendant increases in pressure and boundary layer displacement thickness, for these flows. Leonov et al.[54,55,56,57,58] has considered pulsed DC discharges in subsonic, transonic, and low supersonic flows. In these experiments, pulses of up to 10 kW and 60 ms duration are applied to electrodes in the wall. These discharges are created between wall electrode pairs, usually separated transversely relative to the flow. For lower power discharges, the boundary layers were observed to thicken, increasing wall pressure and creating a wave structure above the boundary layer edge. Sufficiently high-power discharges separated the boundary layer and even caused choking in duct flows.

Detailed measurements of the structure of continuous DC boundary-layer discharges on a flat plate have been made in the AFRL Mach 5 Plasma Channel.[59] The plasma channel is a continuous flow facility with a freestream Mach number of 5.3. In all cases presented below, the stagnation pressure was 370 torr and the stagnation temperature was 280K. A photograph of the experimental configuration is shown in Fig. 7, and a schematic is shown in Fig. 8. The plate was constructed of machinable ceramic with copper electrodes. A photograph of the discharge is shown in Fig. 9. In all cases the discharge is 50 mA and the upstream electrode is the cathode.

Pressure measurements were made with MKS Baratron absolute pressure transducers. Surface pressure measurements were made with transducers with a 0 to 2 torr range. The

pitot probe measurements were made with a 0 to 100 torr transducer. The manufacturer's stated accuracy of the transducers is specified as +/-0.5%.

The effect of the DC discharge on surface pressures is shown in Fig. 10. After an initial 20-second period, the discharge was turned on for 40 seconds, then turned off. A sample voltage trace during a discharge is shown in Fig. 11. For all discharges, voltage varied from 1100-1200V. The largest increase in pressure, up to 10% of the undisturbed static pressure, occurs just downstream of the cathode.

The mechanism for the increase in surface pressure is postulated to be the increase in boundary layer displacement thickness due to heating from the discharge. The local flow deflection, θ, due to the growth of the boundary layer is equal to $d\delta^*/dx$. The pressure increase due to this deflection is related to the Mach number through the $\overline{\chi}$ parameter[60] where

$$\overline{\chi} = \frac{M_\infty^3}{\sqrt{\mathrm{Re}}}\sqrt{C} \tag{2}$$

and C is the Chapman-Rubesin parameter, $\rho_w \mu_w / \rho_e \mu_e$. For an adiabatic flat plate in the weak interaction regime,

$$\frac{p}{p_\infty} = 1 + 0.31\overline{\chi} + 0.05\overline{\chi}^2 \tag{3}$$

It is obvious from Eqns. (2) and (3) that the induced surface pressure from changes in boundary layer displacement thickness is a strong function of Mach number. This and the results shown in Fig. 10 indicate a potential for creating forces and moments on hypersonic vehicles through surface plasma discharges. The 10% pressure increase shown in Fig. 10 is equivalent to approximately a 1-degree flow deflection through an oblique shock at Mach 5.

Energy input to the laminar boundary layer will certainly influence its stability. Adverse pressure gradients will certainly trip or otherwise destabilize the boundary layer. Changes in the boundary layer profile, the enthalpy of the boundary layer fluid, and heat transfer to the wall have all been demonstrated to affect stability and transition.[61] These effects are interrelated and quite complex, and it is impossible to predict a-priori the net effect on boundary layer stability.

A Pitot pressure survey through the boundary layer and bow shock is shown in Fig. 12. It is clear from these data that the boundary layer is decelerated and slightly thickened due to the discharge. Above the boundary layer edge, Pitot pressure is slightly increased in the presence of a discharge due to the more efficient compression through the weak oblique shock emanating from the cathode, followed by a normal shock at the Pitot probe at a lower Mach number. These effects on Pitot pressure and the above observed effect on surface pressure are similar to those observed by Leonov et al. for surface DC discharges and predicted by Shibkov et al. for surface microwave discharges. The propagation of the compression wave system from the cathode is demonstrated by streamwise Pitot surveys shown in Fig. 13. The compression wave is manifested as an increase in Pitot pressure when the discharge is on. As the height above the plate

increases, the compression front moves downstream. At more downstream locations, the Pitot tube is engulfed in the growing boundary layer, and Pitot pressure decreases when the discharge is turned on, due to thickening of the boundary layer.

The heating in short-duration discharges is due to Joule heating. For longer discharges the electrodes become hot, and some heating of the fluid may arise from convective heat transfer from the electrodes. This is illustrated in Fig. 14. In this case the discharge was turned on for periods of 40, 20, 10, and five seconds. It is seen that for the 40-second discharge the Pitot pressure drops about 6% immediately after the discharge is turned off. After this, approximately 50 seconds is required for it to decay to its undisturbed value. This slow decay in Pitot pressure indicates that heating of the electrode has occurred during the discharge, and about 50 seconds is required for convective cooling to return it to its original temperature. As the plasma-on time is decreased, the initial Pitot pressure drop when the plasma is turned on increases, and the period of slow-decay decreases. For the five-second discharge, most of the Pitot-pressure decay occurs immediately after the plasma is turned off. In this case, the electrode and plate have had little time to heat during the discharge. It might be expected in this case that the bulk of the observed effect is due to Joule heating. The Pitot pressure recovers quickly after the discharge is extinguished since the Joule heating disappears almost immediately. However, the plate and electrode constitute a complex thermal system. The copper electrode may heat and cool rather quickly. Future work will examine a thermal modeling, electrode temperature measurements, and plasma temperature measurements to help separate convective heating from Joule heating.

4 Conclusions

The boundary layer is shown to be more accessible to plasma flow control than inviscid flow. The boundary layer is more easily ionized. MHD interaction parameters are higher in the boundary layer than the freestream. Also, relatively small changes in the boundary layer may have global effects through viscous interaction and the fluid-dynamic amplification of disturbances in the boundary layer.

There is no doubt that, in principle, boundary layer profiles can be modulated with MHD effects if the interaction parameter is high enough. Obtaining high-enough conductivity for a reasonable interaction parameter is a challenge. The Hall effect places an upper limit on the maximum magnetic field that can be imposed effectively, and creates three-dimensionality. The net payoff of boundary layer control for skin friction and heat transfer remains to be demonstrated. Skin friction and heat transfer reduction from decelerating the boundary layer comes at the cost of reaction drag on the magnet in the vehicle and an unstable velocity profile. Conversely, an accelerated profile that is more stable and produces a propulsive force on the vehicle will increase skin friction and heat transfer. Payoffs in reduced heat transfer and engine operability may offset some of these negatives.

Initial experiments and computations have indicated the potential for controlling boundary layer transition through MHD. Even relatively simple experimental and computational configurations have created surprising results. The boundary layers in MHD flows will be subjected to numerous effects including EHD forces, Joule heating, and three-dimensionality. Extensive and careful computational and experimental work is

required to fully understand the complex physics of these flows and to utilize the potential for MHD control to its fullest. Although MHD boundary layer control is certainly possible in principle, complete systems analyses will be required to evaluate its overall practicality.

Non-MHD electromagnetic flow control for boundary layers, notably Joule heating, has been shown to have a surprisingly large effect on surface pressures. The magnitude of this effect may be expected to increase with Mach number due to scaling of the viscous interaction parameter. A major challenge in using this method of flow control for vehicle maneuvering will be to scale-up the pressures created by the discharges. The practicality of this method remains to be demonstrated also. Initial demonstrations have been in cold gases. The efficacy and practicality of the technique in hot, flight-temperature boundary layers remains to be demonstrated.

5 Acknowledgments

References

[1] Reed, H. L., Kimmel, R. L., Schneider, S., Arnal, D., and Saric, W., "Drag Prediction and Transition in Hypersonic Flow," AGARD Paper C-15, Symposium on Sustained Hypersonic Flight, AGARD Conference on Future Aerospace Technology in the Service of the Alliance, 14-17 April 1997, Ecole Polytechnique, Palaiseau, France.

[2] Whitehead, A., "NASP Aerodynamics," AIAA paper 89-5013, July 1989.

[3] Small, W. J., Kirkham, F. S., and Fetterman, D. E., "Aerodynamic Characteristics of a Hypersonic Transport Configuration at Mach 6.86," NASA Technical Note NASA TN D-5885, June, 1970.

[4] Burns, K. A., Deters, K. J., Haley, C. P., and Khilken, T. A., "Viscous Effects on Complex Configurations," Air Force Wright Laboratory Technical Report WL -TR-3059, August 1995.

[5] Finley, D., "Hypersonic Aerodynamics Considerations and Challenges," AIAA paper AIAA-90-5222, October 1990.

[6] Suchomel, C. F., Van Wie, D. Risha, D. J., "Perspectives on Cataloging Plasma Technologies Applied to Aeronautical Sciences," AIAA Paper 2003-3852, June 2003.

[7] Heiser, W. H., and Pratt, D. T., *Hypersonic Airbreathing Propulsion*, American Institute of Aeronautics and Astronautics, Washington, D.C., 1994, pp 237-239.

[8] Blottner, F. G., "Chemical Nonequilibrium Boundary Layer," *AIAA Journal*, vol. 2, no.2, February 1964, pp. 232-240.

[9] Corke, T. C., Cavalieri, D. A., and Matlis, E., "Boundary-Layer Instability on Sharp Cone at Mach 3.5 with Controlled Input," *AIAA Journal*, vol. 40, no. 5, May 2002, pp. 1015-1018.

[10] Kastell, D. and Shiplyuk, A. N., "Experimental technique for the investigation of artificially generated disturbances in planar laminar hypersonic boundary layers," *Aerospace Science and Technology*, no. 6, 1999, pp. 345-354.

[11] Maslov, A. A., Mironov, S. G., Shiplyuk, A. A., Sidorenko, A. A., Buntin, D. A., and Aniskin, V. M., "Hypersonic Flow Stability Experiments," AIAA Paper 2002-0153, January 2002.

[12] Lineberry, J. T., Rosa, R. J., Bityurin, V. A., Botcharov, A. N., and Potebnya, V. G., "Prospects of MHD Control for Hypersonics," AIAA Paper 2000-3057.

[13] Rossow, V. J., "On Flow of Electrically Conducting Fluids Over a Flat Plate in the Presence of a Transverse Magnetic Field," NACA TN 3971, May 1957.

[14] Ostrach, S., "Laminar Flows with Body Forces," *High Speed Aerodynamics and Jet Propulsion, vol. IV, Theory of Laminar Flows*, Moore, F. K. ed., Princeton University Press, Princeton, NJ, 1964, pp. 691-712.

[15] Bush, W. B., "Compressible Flat-Plate Boundary-layer Flow With an Applied Magnetic Field," *J. of the Aerospace Sciences*, v. 27, no. 1, Jan 1960, pp. 49-58.

[16] Sastry, M. S., "Magneto Hypersonic Boundary-Layer Flow past a Plate," *AIAA Journal*, vol. 5, no. 1, 1967.

[17] Crawford, C. H., and Karniadakis, G. E., "Control of External Flows via Electro-Magnetic Fields," AIAA paper 95-2185, June 1995.

[18] Borghi, C. A., Carraro, M. R., and Cristofoline, A., "Numerical Modeling of MHD Interaction in the Boundary Layer of Hypersonic Flows," IEEE Transactions on Magnetics, Vol. 39, no. 3, May 2003, pp. 1507-1510.

[19] Poggie, J., and Gaitonde, D., V., "Magnetic Control of Hypersonic Blunt Body Flow," AIAA paper 2000-0452, January 2000.

[20] Bush, W. B., "Magnetohydrodynamic–Hypersonic Flow Past a Blunt Body," *J. of the Aerospace Sciences*, v. 25, no. 11, Nov. 1958, pp. 685-690, 728.

[21] Bussing, T. R. A., Eberhardt, S., "Chemistry Associated with Hypersonic Vehicles," AIAA paper 87-1292, June 1987.

[22] Palm, P., Meyer, R., Plönjes, E., Bezant, A., Adamovich, I. V., Rich, J. W., Gogineni, S., "MHD Effect on a Supersonic Weakly Ionized Flow," AIAA paper 2002-2246, May 2002.

[23] Kimmel, R. L., Hayes, J. R., Menart, J., Shang, J., and Henderson, S., "Measurements of a Transverse DC Discharge in a Mach 5 Flow," AIAA paper 2003-3855, June 2003.

[24] Macheret, S. O., Shneider, M. N., and Miles, R. B., "Magnetohydrodynamic and Electrohydrodynamic Control of Hypersonic Flows of Weakly Ionized Plasmas, AIAA paper 2002-2249, May 2002.

[25] Sears, W. R. "Magnetohydrodynamic Effects in Aerodynamic Flows," ARS Journal, vol. 29, no. 6, June 1954, pp. 397-406.

[26] Henoch, C., and Stace, J., "Experimental investigation of a salt water turbulent boundary-layer modified by an applied streamwise magnetohydrodynamic body force," *Physics of Fluids*, vol. 7, no. 6, June 1995, pp. 1371-1383

[27] Van Driest, E. R., "Turbulent Boundary Layer in Compressible Fluids," *Journal of the Aeronautical Sciences*, vol. 18, no. 3, March 1951, pp. 145-160, 216.

[28] Weier, T., Gerbeth, G., Mutschke, G., Platacis, E., Lielausis, O., "Experiments on cylinder wake stabilization in an electrolyte solution by means of electromagnetic forces localized on the cylinder surface," *Experimental Thermal and Fluid Science*, vol. 16, nos. 1&2, January /February 1998, pp. 84-91.

[29] Kimmel, R. L., Hayes, J. R., Menart, J. A., Shang, J., and Henderson, S, "Measurements of a Transverse DC Discharge in a Mach 5 Flow," AIAA 2003-3855, June 2003.

[30] Menart, J. A., Shang, J., Kimmel, R. L., and Hayes, J. R., "Effects of Magnetic Fields on Plasmas Generated in a Mach 5 Wind Tunnel," AIAA 2003-4165, June 2003.

[31] Jaffe, N. A., "Effects of a Transverse Magnetic Field and Spanwise Electric Field on the Boundary-layer of a Conducting Fluid," *AIAA Journal*, vol. 4, no. 10, pp. 1843-1846, Oct. 1966.

[32] Rossow, V. J., "Boundary-Layer Stability Diagrams for Electrically Conducting Fluids in the Presence of a Magnetic Field," NACA TN 4282, August, 1958.

[33] Cheng, F. Zhong, X., Gogineni, S., Kimmel, R. L., "Effect of Applied Magnetic Field on the Instability of Mach 4.5 Boundary-layer over a Flat Plate, AIAA paper 2002-0351, January 2002.

[34] Cheng, F., Zhong, X., Gogineni, S., Kimmel, R. L., "Magnetic-field effects on second-mode instability of a weakly ionized Mach 4.5 boundary layer," *Physics of Fluids,* vol. 15, no. 7, July 2003, pp. 2020-2040.

[35] Chandrasekhar, S., "The stability of viscous flow between rotating cylinders in the presence of a magnetic field," *Proceedings of the Royal Society of London*, series A, vol. 216, February 1953, pp. 293-309

[36] Stuart, J. T., "On the stability of viscous flow between parallel planes in the presence of a co-planar magnetic field," *Proc. Roy. Soc. London*, ser A, vol. 221, no. 1145, 21 Jan 1954.

[37] Lock, R. C., "The stability of the flow of an electrically conducting fluid between parallel planes under a transverse magnetic field," Proc. Roy. Soc. Of London, ser. A, vol. 233, nol. 1192, 6 Dec. 1955, pp. 105-125.

[38] Mack, L. M., "Boundary-Layer Stability Theory," *Special Course on Stability and Transition of Laminar Flow*, edited by R. Michel, AGARD Report No. 709, pp. 3-1 to 3-81, 1984.

[39] Cheng, F. Zhong, X., Gogineni, S., Kimmel, R. L., "Effect of Applied Magnetic Field on the Instability of Mach 4.5 Boundary-layer over a Flat Plate, AIAA paper 2002-0351, January 2002.

[40] Cheng, F., Zhong, X., Gogineni, S., Kimmel, R. L., "Magnetic-field effects on second-mode instability of a weakly ionized Mach 4.5 boundary layer," *Physics of Fluids,* vol. 15, no. 7, July 2003, pp. 2020-2040.

[41] Kimmel, R. L., Poggie, J., and Schmisseur, J. D., "Effect of Pressure Gradients on Axisymmetric Hypersonic Boundary-layer Stability," AIAA-2000-0538, Jan 2000

[42] McEldowney, B., Meyer, R., Chintala, N., and Adamovich, I. V., "Measurements of Electrical Parameters of a Supersonic Nonequilibrium MHD Channel," AIAA Paper 2003-4279, June 2003.

[43] Rosa, R. J., *Magnetohydrodynamic Energy Conversion*, McGraw-Hill Book Company, New York, 1968, pp. 1-24.

[44] Roth, J. R., Sherman, D. M., and Wilkison, S. P., "Electrohydrodynamic Flow Control with a Glow-Discharge Surface Plasma," *AIAA Journal*, vol. 38, no. 7, July 2000, pp. 1166-1172.

[45] Artana, G., D'Adamo, J., Léger, L., Moreau, E., and Touchard, G., "Flow Control with Electrohydrodynamic Actuators," AIAA Paper 2001-0351.

[46] Léger, L., Moreau, E., and Touchard, G., "Electrohydrodynamic airflow control alonga flat plate by a DC surface corona discharge – Velocity profile and wall pressure measurements," AIAA Paper 2002-2833.

[47] Corke, T. C., Jumper, E. J., Post, M. L., Orlov, D., and McLaughlin, T. E., "Application of Weakly-Ionized Plasmas as Wing Flow-Control Devices," AIAA 2002-0350, Jan. 2002.

[48] Post, M. L., Corke, T. C., "Separation Control on High Angle of Attack Airfoil Using Plasma Actuators," AIAA Paper 2003-1024, January 2003.

[49] Hultgren, L. S, and Ashpis, D. E, "Demonstration of Separation Delay with Glow-Discharge Plasma Actuators," AIAA Paper 2003-1025, January 2003.

[50] Roth, J. R., Sin, H., Madhan, R. C. M., and Wilkinson, S. P., "Flow Re-Attachment and Acceleartion by Paraelectric and Peristaltic Electrohydrodynamic (EHD) Effects," AIAA Paper 2003-531, January 2003.

[51] Johnson, G. A., and Scott, S., J., "Plasma-Aerodynamic Boundary Layer Interaction Studies," AIAA Paper 2001-3052.

[52] Wilkinson, S. P., "Investigation of an Oscillating Surface Plasma for Turbulent Drag Reduction," AIAA Paper 2003-1023, January 2003.

[53] Shibkov, V. M., Alexandrov, A. F., Chernikov, A. V., Ershov, A. P., Georgievskiy, P. Yu., Gromov, V. G., Larin, O. B., Levin, V. A., Shibkova, L. V., Timofeev, I. B., Voskanyan, A. V., Zlobin, V. V., "Influence of the Surface Microwave Discharge on the Parameters of Supersonic Airflow Near a Dielectric Body," AIAA Paper, 2003-1192, January 2003.

[54] Leonov, S., Bityurin, V., Savischenko, N., Yuriev, A., and Gromov, V., "Influence of Surface Electric Discharge on Friction of Plate in Subsonic and Transonic Airflow," AIAA paper 2001-0640, January 2001.

[55] Leonov, S., Bityurin, V., Klimov, A., Kolesnichenko, Y., and Yuriev, A., "Influence of Structural Electric Discharges on Parameters of Streamlined Bodies in Airflow," AIAA paper 2001-3057, June 2001.

[56] Leonov, S., Bityurin, V., Savelkin, K., and Yarantsev, D., "Effect of Electrical Discharge on Separation Processes and Shocks Position in Supersonic Airflow," AIAA paper 2002-0355, January 2002.

[57] Leonov, S., Bityurin, V., Savelkin, K., and Yarantsev, D., "Progress in Investigation for Plasma Control of Duct-Driven Flows," AIAA paper 2003-0699, January 2003.

[58] Leonov, S., Bityurin, V., and Yarantsev, D., "The Effect of Plasma Induced Separation," AIAA paper 2003-3853, June 2003.

[59] Shang, J. S., Kimmel, R. L., Hayes, J. R., and Tyler, C., "Performance of a Low-Density Hypersonic Magneto-Aerodynamic Facility," AIAA 03-0329, January 2003.
[60] Hayes, W. F., and Probstein, R. F., *Hypersonic Flow Theory*, Academic Press, New York, 1959.
[61] Kimmel, R. L., "Aspects of Hypersonic Boundary Layer Transition Control," AIAA Paper 2003-0772, January 2003.
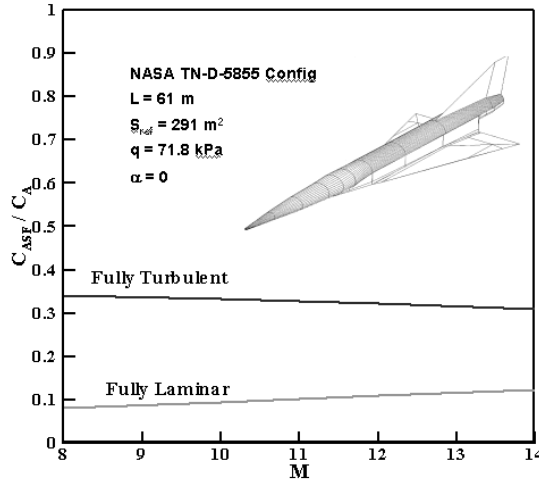
Figure 1 Ratio of axial force due to skin friction to overall axial force for a slender hypersonic configuration.
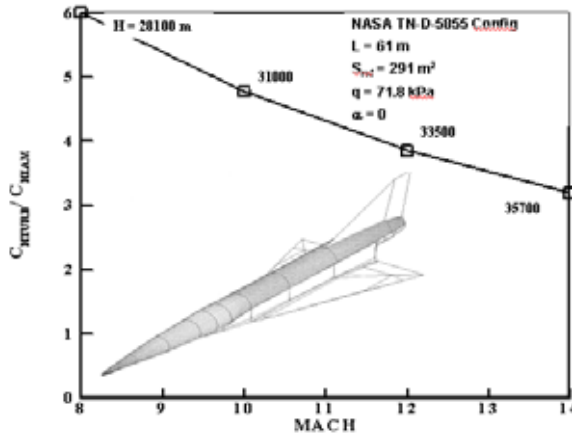
Figure 2 Ratio of integrated laminar to turbulent heat transfer for a hypersonic configuration.
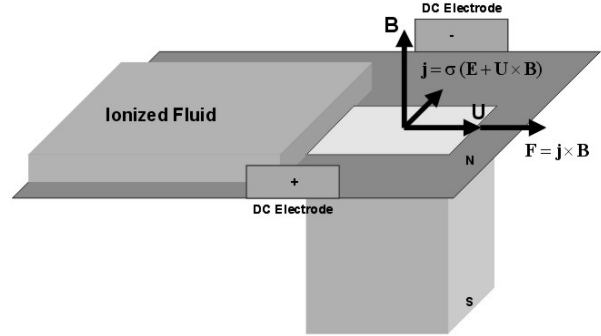
Figure 3 Forces and currents in MHD flow of ionized fluid.
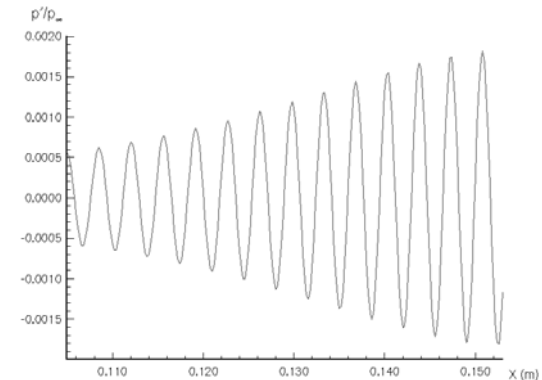
Figure 4 Instantaneous second-mode wall pressure fluctuations in a flat-plate, non-MHD, *M*=4.5 boundary-layer (Ref. 39).
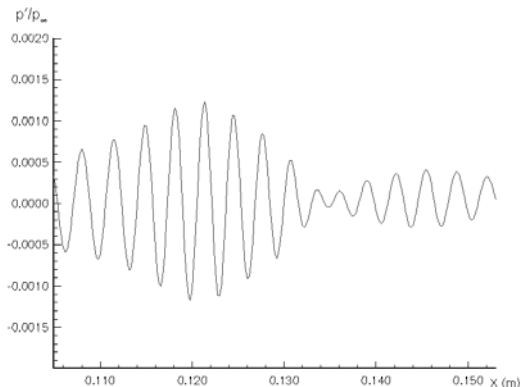
Figure 5 Instantaneous second-mode wall pressure fluctuations in a flat-plate, MHD boundary-layer flow through a 1.2 T field, *M*=4.5 (Ref. 39).
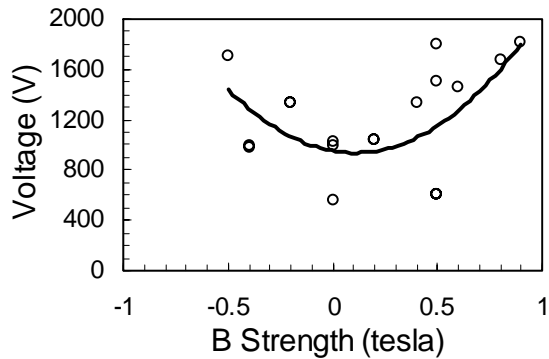
Figure 6 Voltage required to generate a 50 mA discharge as a function of magnetic field strength.
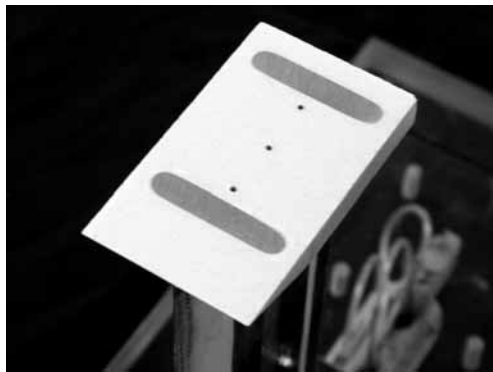
Figure 7 Flat plate model with electrodes and pressure taps
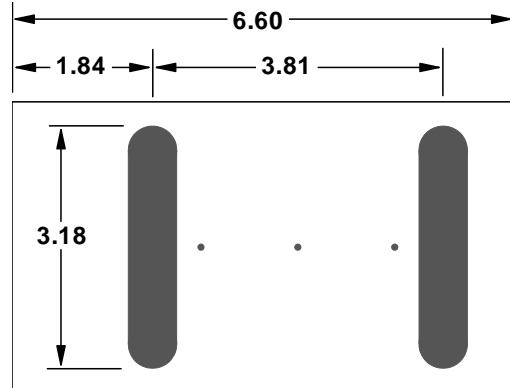
Figure 8 Schematic of flat plate model. All dimensions cm. Electrodes are 0.64 cm wide. Pressure taps are spaced 1.27 cm, starting at *x* = 2.48 cm.

Figure 9 DC surface discharge on flat plate model. Flow is from left-to-right.
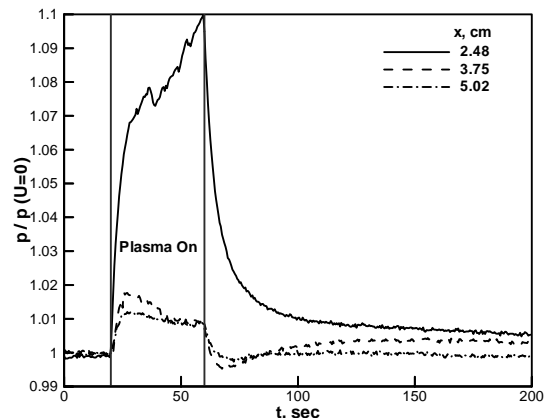
Figure 10 Effect of DC discharge on flat plate surface pressures. Pressures are normalized by undisturbed (U=0) static pressures.
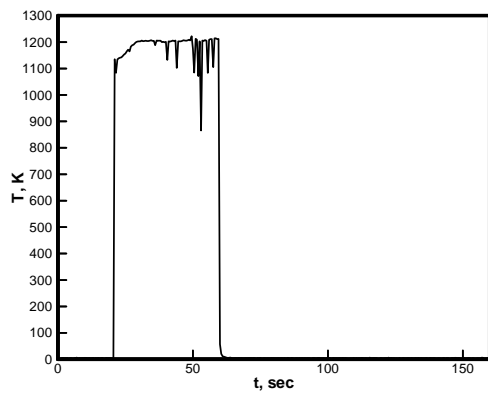
Figure 11 Voltage as function of time during flat plate DC surface discharge.
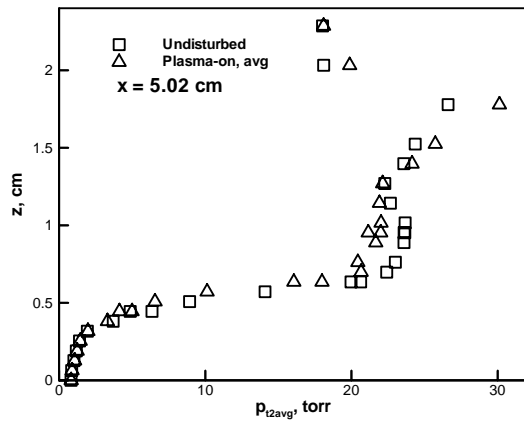
Figure 12 Pitot pressure survey above downstream electrode (anode) on flat plate.
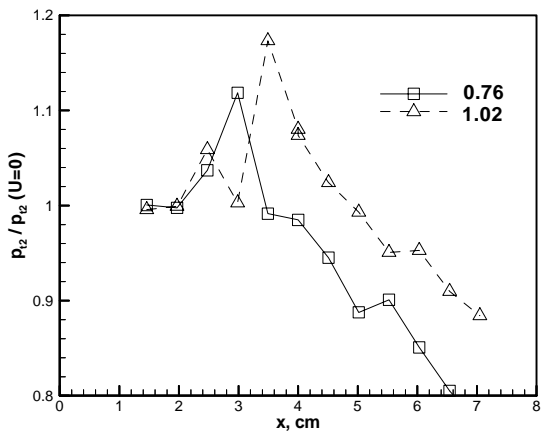
Figure 13 Average Pitot pressure during discharge normalized by undisturbed Pitot pressure as a function of distance along the model for two heights above the plate.
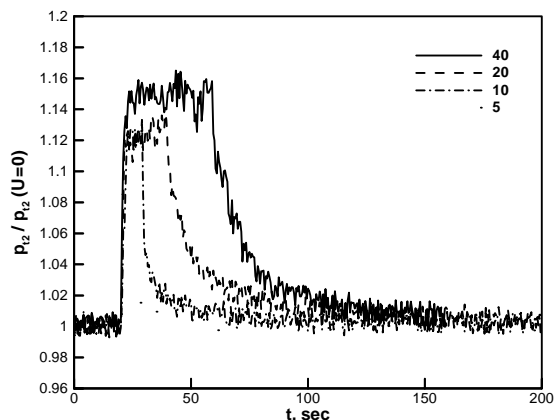
Figure 14 Ratio of average Pitot pressure during discharge to undisturbed Pitot pressure for four different discharge durations.

DESIGN AND IMPLEMENTATION OF A MAGNETOAERODYNAMIC CHANNEL

Roger L. Kimmel[*]
James Menart,[†] **Joseph Shang**[‡]

1 Introduction

Since the beginning of powered flight, the necessity of modulating fluid momentum about flight vehicles has been recognized. This modulation traditionally has taken such forms as flaps or ailerons for attitude control, or suction or blowing to alleviate undesirable momentum changes. Traditionally, fluid momentum modulation has been achieved through mechanical actuators. The application of MHD forces and Joule heating to plasmas has created the possibility of no-moving-parts flow control.

Plasma aerodynamics is a phenomenologically rich field, offering numerous challenges to computation. Among these are the prediction of gas chemistry, transport properties, electrode boundary conditions, and three-dimensionality introduced either through non-uniformities in the plasmas or through Hall effects. In addition, the usual complications of supersonic and hypersonic flight are present. Although great strides have been made in the computation of plasma aerodynamics, numerical simulations will of necessity be subject to physically simplified scenarios. For this reason, experimental research is crucial to the understanding and application of plasma aerodynamics.

Two mechanisms for creating plasmas in hypervelocity flight are aerodynamic heating and applied electromagnetic fields. In hypervelocity flight, thermal plasmas are created either via compression through shock waves or through constant pressure deceleration in boundary layers. Significant heating is required to generate thermal plasmas, so that they are generally not encountered below about Mach 10, typically in reentry trajectories.[1] Because of the high temperatures required to generate thermal plasmas, they typically have been simulated in impulse facilities or arc-jets. These facilities present numerous operational challenges, and are relevant only to reentry-velocity flight scenarios. The use of non-equilibrium plasmas offers the ability to create low translational temperature plasmas and to operate at lower Mach numbers.

Initial experimental work on plasma aerodynamic flows in the Air Force Research Laboratory was undertaken in the existing Mach 6 High-Reynolds Facility.[2] Research in this facility presented a number of operational difficulties. To facilitate plasma generation, the tunnel was exhausted to vacuum in order to run at the lowest stagnation pressure possible (206 kPa).[3] Static pressures above about 2 Torr created constrictions in DC discharges. Electromagnetic noise from RF plasma discharges interfered with the

---

[*] Air Force Research Laboratory, United States
[†] Wright State University, United States
[‡] Wright State University, United States

tunnel stagnation-valve controller, rendering RF plasmas unusable. Also, great care had to be taken to isolate DC electrodes from any unintended ground paths inside the all-metal wind tunnel. A tunnel stagnation temperature of 610 K was required to avoid air liquefaction, which also increased operational problems. These efforts provided an impetus to construct a new device designed for magnetoaerodynamic experiments. Prior publications[4,5,6,7] describe initial shakedown and diagnostic development of the new device, the Mach 5 Plasma Channel. This paper describes the design philosophy, construction, and initial results from the channel.

2 Design Requirements

Based on experience with the Mach 6 High Reynolds Facility, a number of general features were desired for the new Plasma Channel. These included low-density operation, dielectric construction to avoid unintentional ground paths, and overall simplicity of operation. The requirement for simple operation created an upper bound on the Mach number to obviate the need for a heater. The design Mach was thus fixed at five.

Although some Mach 5 windtunnels require heating, these are higher-pressure tunnels than the Mach 5 Plasma Channel. The onset of air liquefaction is a function of pressure. Lower pressure delays the onset of liquefaction to lower temperatures. Since the Mach 5 Plasma Channel operates at sub-atmospheric stagnation pressure, static pressures are low enough to avoid liquefaction,[8] and no heater is required.

To breakdown and sustain the plasma, electrons must be accelerated between collisions to velocities high enough to frequently ionize the collision partner. This immediately implies that low pressures are beneficial in generating a discharge. The minimum in the Paschen curve for air occurs at a value of $pd < 1$ torr-cm.[9] At high pressure, a DC discharge tends to constrict. In practice, in experiments in the Mach 6 wind tunnel, DC discharges began to constrict at pressures above about 2 torr (at the conditions of the Mach 6 tunnel, equivalent to a number density of about 2.4×10^{17} cm^{-3}).[10] With the ratio of stagnation to static density in isentropic flow given by[11]

$$\frac{\rho}{\rho_0} = \left(1 + \frac{\gamma - 1}{2} M^2\right)^{-\gamma/(\gamma-1)}$$

a static number density of less than 2.4×10^{17} cm^{-3} at Mach 5 implies that the channel must operate at stagnation pressures less than atmospheric. This also requires that the test section exhaust to vacuum.

The requirement for sub-atmospheric pressures throughout the channel simplifies material requirements and design. To avoid unintended ground paths, as much of the channel as possible must be constructed of a dielectric. Since the channel would be subjected to no more than one atmosphere of pressure, it could be constructed entirely of acrylic plastic. This construction has the added benefit of providing excellent visual access to the channel.

A number of options are available for plasma generation. These include DC discharges, capacitively-coupled RF discharges, inductively-coupled RF discharges, microwave, and electron-beams, among others. Power sources for DC and RF discharges were available

2

from the previous Mach 6 experiments. These had proved satisfactory in generating diffuse discharges in the Mach 6 experiments. DC discharges have the added advantage of having been well-studied and accessible to analysis. For these reasons, the existing RF and DC sources were considered adequate and retained for initial work, although in the future different ionization sources may be considered.

An overriding concern in magnetoaerodynamic flows, especially in those with non-equilibrium plasmas, is the magnitude of the conductivity. A primary figure of merit for characterizing MHD flows is the interaction parameter, which is the ratio of Lorentz force to inertial forces on a fluid element. For a load factor of unity, the interaction parameter, Q, is given as[12]

$$Q = \frac{\sigma B^2 L}{\rho u}$$

where σ is the fluid conductivity, B is the magnetic field strength, L is the interaction length scale, ρ is the fluid density, and u is the fluid velocity.

The conductivities of typical plasma and electrolyte flows are relatively low. Ref. [13] cites the conductivity of copper at 6×10^7 mho/m, mercury at 10^6 mho/m, and salt water at 25 mho/m. For non-equilibrium ionized air, conductivities are typically on the order of one mho/m.[14,15,16] At a stagnation pressure of 1.0 atmosphere, a magnetic field of one Tesla, and a conductivity of 1 mho/m, the interaction parameter per unit length at Mach 5 is approximately 0.6 m^{-1}. With other parameters fixed, B and L must be maximized. This typically leads to MHD channels with elongated magnets to maximize L, and with walls in close proximity to maximize B. The challenge in designing the plasma channel is to place the sidewalls in close proximity, but still provide adequate space for an inviscid core.

3   Construction of the Channel

The device as constructed is a blow-down, semi-free-jet facility. A rectangular cross-section, conical nozzle with a throat area of 73.7 x 5.08 mm expands to a nozzle exit plane of 73.7 x 177.8 mm. The test section has dimensions of 386.08 x 177.8 x 73.66 mm (length x height x width). Additional relief is provided by plenums on the top and bottom of the test section. The nozzle boundary layer separates from the nozzle lip at the beginning of the test section, forming a free shear layer, and reattaches at the beginning of the diffuser. The separating shear layer generates weak waves in the test section, but the plenums are invaluable for introducing instrumentation and models into the test section. The entire length of the channel is 1555 mm and it is constructed of Plexiglas.™ Two 235 mm diameter quartz windows were mounted on the side walls of the test section. The windows expose the entire test section, including the nozzle exit plane. A sketch of the plasma channel is presented in Figure 1. Dry air is supplied from the existing high-pressure supply through a three-stage pressure-reduction system. The high-pressure supply capability is not required, but is merely a convenient source of dry air. A manual pressure regulator is used to set the channel stagnation pressure to one atmosphere or less. The tunnel exhausts to a 2800 m^3 vacuum sphere. Stagnation temperatures range from 270 K to 280 K depending on ambient conditions and throttling through the pressure reduction system.

The original design goal for the facility was to run at stagnation pressures from 0.1 to 1.0 atmosphere. The minimum back pressure that can be maintained downstream of the diffuser is approximately 6 torr. At this back pressure, the minimum stagnation pressure to sustain supersonic flow in the channel is 0.4 atm. The freestream Mach number of approximately 5.3 is slightly higher than design. The simulated altitude range (based on static density) of the facility extends from approximately 30,000 to 38,000 meters. At the lowest attainable stagnation pressure of 300 torr, stagnation temperature of 280 K, and a freestream Mach of 5.3, the freestream in the test section has a velocity, density, and temperature of 691 m/s, 0.0044 kg/m^3, and 42 K, respectively. Under these conditions the mass-flow rate is less than 0.04 kg/s and the unit Reynolds number in the test section is 1.2×10^6 per meter. The freestream neutral particle number density under these conditions is 10^{17} cm^{-3}. Although designed as a blow-down system, continuous operation can be easily sustained through continuous operation of the vacuum pump system. A photograph of the plasma channel is shown in Fig. 2.

4 Tunnel Calibration

The primary concerns regarding flow quality in the channel were the uniformity of the flow arising from the conical nozzle, and the thickness of the sidewall boundary layers. Extensive Pitot surveys were conducted to assess flow uniformity and the extent of the inviscid core. A three-dimensional traverse mechanism was developed for surveys. The placement of the traverse is controllable within a distance of 0.25 mm. All data were collected with a single pressure transducer, the MKS Baratron model 722 capacitance manometer, which has a stated accuracy of +/- 0.5%.

A first measure of flow uniformity is the Pitot pressure measured along the tunnel centerline, as shown in Fig. 3. The Pitot pressures show some gradients for 2 cm downstream of the nozzle exit, then are uniform to within 4% for the next 8 cm. Assuming isentropic expansion from the stagnation chamber, this Pitot pressure variation corresponds to a Mach number variation of 5.35 to 5.30, or less than 1%. At 10 cm downstream of the nozzle exit, the wave structure from the nozzle lip crosses the centerline, causing the Pitot pressure to increase downstream of this location.

Pitot surveys in the vertical direction on the tunnel centerline at three axial stations are shown in Fig. 4. The weak compression wave from the nozzle lip is evident even at the first survey station at $z = +/- 6$ cm, indicating that the nozzle boundary layer separates slightly upstream of the nozzle lip. The wave propagates deeper into the channel core flow at succeeding x-stations, eroding the area of uniform flow. Beneath the wave from the nozzle lip, the shear layer from the nozzle wall is evident. This shear layer is only about 1 cm thick at the two most upstream measuring stations. At the two most upstream measuring stations, the Pitot pressures are uniform to within 2.5% for $-5 < z < 5$ cm.

Spanwise Pitot surveys were conducted at three axial stations (x=0.0, 5.1, and 10.2 cm), at three vertical locations (z=-2.8, 0.0, 2.8 cm), for a total of nine surveys. These surveys are shown in Figs. 5-7. At each axial station the surveys are very similar at each vertical location, but nonuniform in the spanwise dimension. The sidewall boundary layer is evident and thickens as x increases. The Pitot pressures show an unexpected rise from the centerline to the edge of the shear layer, before they drop off in the shear layer. The source of this rise is unknown and under investigation.

4

In summary, the channel flow is remarkably free from gradients in the streamwise and vertical directions, but suffers from some degree of non-uniformity in the spanwise direction. Future work will address treatments for spanwise uniformity.

5 Diagnostics

5.1 Optical Emission Spectroscopy

A system for rotational and vibrational temperature measurement using emission spectroscopy was acquired from Research Support Instruments, Inc. The system hardware consists of a fiber-optic probe connected to an Ocean Optics PC 2000 spectrometer. A collimating head may be attached to the fiber-optic probe to improve spatial resolution. Software is provided to drive the spectrometer and analyze the spectra. Vibrational temperatures are determined using the well-known Boltzman-plot method.[17] The system measures the spectrum of the second positive group of nitrogen, $N_2(C^3\Pi_u) \rightarrow N_2(B^3\Pi_g)$. The intensity of a vibrational transition is given by

$$I_{v',v''} = DN_{v'}\nu^4_{v',v''}S_{v',v''} \qquad (1)$$

The assumption of a Boltzman distribution relates the upper level population and temperature:

$$N_{v'} = \frac{N}{Q_v(T)}\exp[-G(v')hc/kT] \qquad (2)$$

Substitution of equation (2) into equation (1) provides a straight-line relationship between the normalized intensity of the vibrational transition and the vibrational temperature:

$$\ln\left(\frac{I_{v',v''}}{\nu^4_{v',v''}S_{v',v''}}\right) = -\left(\frac{hcG(v')}{k}\right)\frac{1}{T} + const \quad (3)$$

The intensities of vibrational transitions, as normalized in equation (3) are plotted as a function of the normalized transition energy. A straight line is curve-fitted through these points, and rotational and vibrational temperatures are extracted from the slope of the line. Transitions with intensities less than 5% of full-scale are rejected.

The spectrometer FWHM resolution was measured at 0.167 nm using a mercury lamp and software provided by Ocean Optics. Rotational lines are not fully resolved by the spectrometer, so rotational temperatures are estimated comparing a simulated spectrum to the measured spectrum. Twenty rotational lines are simulated at each of fifteen vibrational transitions. The predicted spectrum is convolved with the slit function of the spectrometer, and the mean square error between the predicted and measured spectrum is computed. This curve-fitting procedure is done in 10K increments, effectively creating a 10K resolution in the measured temperature. Integration times for the spectral measurements described below ranged from 3 msec to 50 sec, depending on the signal strength, but the limiting factor in the data acquisition rate is the time required for curve-fitting rotational temperature measurements. Maximum data acquisition rates were several Hz.

Spectral measurements taken in a nitrogen discharge tube (Edmund Scientific CR30609-11) are compared in Fig. 9 to measurements taken with flow-on within the channel at Mach 5 and a DC discharge between two rod electrodes. The lower temperature of the flow-on case is qualitatively discernible from the spectra. Rotational bands in the flow-on case, compared to the discharge tube spectra, are pushed to longer wavelengths, indicating a relatively higher population in the lower rotational states and a de-population of the higher rotational states. Also, the spectral peaks with flow-on are pushed to slightly longer wavelengths, probably due to the increased intensity from P-branch rotational transitions at wavelengths near the band head. Analysis of the spectra confirm these qualitative observations, indicating a rotational temperature of approximately 60K for the flow-on case, compared to approximately 490K for the discharge tube. Vibrational temperatures for the flow-on case are also lower, approximately 3100K compared to 6700K for the discharge tube.

5.2 Langmuir Probe

The Langmuir probe system used in the current measurements was developed for use in high-speed flows and has been described in detail in prior publications.[18] The probe used was a double probe, consisting of two 0.2mm diameter platinum wires 1.6 mm long with axes parallel to the flow, separated vertically by 0.5mm. Conductivity and number density results presented in this paper are the average of both wires. Probe data were analyzed using a model that includes the collisionless to the collisional domains but does not include the effects of high speed fluid flow.[19] Surveys were made in the vertical direction at three axial stations near the downstream portion of the electrodes.

The electron temperature and ion number density measurements made as part of this work are subject to some uncertainty. A number of factors influence the accuracy of Langmuir probe measurements. Five of these factors are the fluid velocity, contamination of the probe surfaces, temporal variations in the plasma, the lack of electrons sensed by the double probe, and possibly a non- Maxwellian electron distribution.

The fluid velocity of course only affects the flow-on results. At the present time the authors are working on an analysis that includes the effects of fluid flow; however, the results in this paper are all determined with a no-flow analysis. When a Langmuir probe is placed into a hypersonic flow, shock waves are developed and these shock waves distort the plasma in the vicinity of the probe. This complicates data reduction.

The second factor affecting the results is contamination of the probe surfaces. This factor was addressed by cleaning the probe with hydrochloric acid after a number of data sets were taken. After cleaning with hydrochloric acid the probes were placed in a water-filled ultrasonic cleaner. This proved to be an effective technique for cleaning the platinum probes.

Unsteadiness in the plasma discharge may also have had some effect on the results. Although attempts were made to minimize unsteadiness, day-to-day changes and oscillations in the visual appearance of the plasma sometimes occurred. This means that one measurement may be in a slightly different discharge than previous measurements. This could be the cause of noise in some of the Langmuir probe results presented here.

The last two reasons listed above, sensing a small fraction of the electrons and an air plasma not having a Maxwellian electron energy distribution, can have a profound effect on the measured electron temperature. Since the electron temperature is used to calculate the ion number density, these problems can also cause errors in these results. It is fortunate that the ion number densities are a much stronger function of the measured saturation currents than the electron temperature. It should be noted that if the electron temperature distribution is not Maxwellian, an electron temperature can not be defined. However, some representative temperature can be approximated for the energy distribution of electrons sensed by the probes. From the shape of the voltage-current curves measured by the Langmuir probes it seems as if something like a Maxwallian distribution is present for the high energy electrons sensed by the double probe.

6 Measurement of DC Discharge Characteristics

6.1 Plasma Generation

The DC discharge is provided by a group of Universal Voltronics reversible polarity switching power units. One of the units is rated at 8 kW with 10kV output source at a signal impedance of 10^4 Ohms. At the breakdown voltage of 400V, a diffuse discharge was achieved at a plasma current as high as 550 mA. The discharge changes into multiple streamers when the electrical current exceeds 900 mA. Other DC power supply units are also available they are rated at 4 kW with 10kV output source at the same impedance. The maximum current output however is limited to 400 mA. The RF power supply and its automatic matching network are the Dressler CESAR-1350 and VM5000W, respectively. This integrated unit is water-cooled and can deliver up to 5 kW at 13.56 MHz into a 50 Ohm load. In routine operation, the automatic matching network will keep the reflected power to less than two percent.

Initial plasma generation efforts concentrated on the generation of DC plasmas in the freestream as test cases for instrumentation. Numerous electrode configurations were tested. The primary difficulty encountered was that discharges preferred a path through the low-density channel boundary layers, rather than through the freestream. The final configuration developed consisted of two stainless steel "shoes" 6.4 mm wide and 45.7 mm long, suspended in the freestream by insulated rods. A photograph of the electrodes and a discharge is shown in Fig. 8. The electrodes were relieved approximately 5 deg to create a low-density region on adjacent surfaces to help guide the discharge between them. The maximum shoe separation for which a freestream discharge could be achieved between the shoes was 50.8 mm. At larger separations, the discharge path was from one shoe to the channel sidewall boundary layer, and then back through the freestream to the second shoe. The 6.4 mm shoe width was also a maximum, before discharge through the sidewall boundary layers occurred.

6.2 Langmuir Probe Measurements

DC discharges were generated between two flat plates, 45.7 mm in length in the streamwise direction and 6 mm wide in the spanwise direction. A photograph of the electrodes and a discharge is shown in Fig. 8. The electrodes were relieved approximately 5 deg to create a low-density region on adjacent surfaces to help guide the discharge between them. Ion number densities are shown for a 50 mA discharge with flow-off and flow-on in Figs 10 and 11, respectively. Measurement conditions for the

no-flow case were 300K and 7 Torr. Ion number densities generally increase from anode to cathode. This is typical for a standard glow discharge.[20] Number densities for the flow-on case are larger than the flow-off case. For the no-flow case number densities tend to decrease from the center of the electrodes back past their trailing edge. This same trend does not appear for the flow-on case. Several factors may contribute to these differences. First, a non-flow analysis was used to reduce the raw measurements made with the Langmuir probe taken in a Mach 5 flow. Also, there are differences between the flow and nonflow cases that affect the discharge, namely the greatly different fluid velocities and the differences in the static density.

Electron temperatures for the flow-off case are shown in Fig. 12. Electron temperatures are generally uniform in the y-direction except close to the cathode. Temperatures lie between about 4,000K to 9,000K, spiking up to 25,000K near the cathode. Electron temperatures at this y-location drop sharply downstream of the trailing edge of the plate. For the flow-on case, Fig. 13, electron temperatures are generally higher than the flow off case and show a different trend as a function of y. Generally, electron temperatures are distributed around approximately 10,000K, but reach 29,000K just downstream of the trailing edge of the anode.

The electrical conductivity of the plasma is a strong function of the electron number density and a somewhat weaker function of the electron temperature. In addition the gas pressure also affects the results. Figures 14 and 15 show the flow-off and flow-on electrical conductivity values as a function of y and x. Conductivity for the flow-on plasma is larger than the no-flow case, but once again this may be due to the data reduction procedure used. Conductivities tend to be higher near the cathode reflecting the higher ion number densities there.

6.3 Temperature and Pitot Measurements

A detailed survey of the rotational and vibrational temperatures in a DC discharge was undertaken using the collimating head for the fiber-optic probe to improve spatial resolution. Spatial resolution was estimated by projecting a light backwards through the collimating head and measuring the spot diameter at the tunnel centerline. The probe volume diameter at the tunnel centerline was less than 3mm. Surveys were made in the streamwise direction on the centerline between the two plates, and in the vertical direction near the center of the two plates for two discharge currents, 100 and 400 mA. Point measurements were also taken near the center of the discharge for a range of currents.

Rotational temperatures as a function of current are shown in Fig. 16. Rotational temperatures are normalized by the freestream static translational temperature in the absence of the discharge. At a Mach number of 5.3 and stagnation temperature of 280K, the expected static translational temperature in the absence of a discharge is 42K. The error bars represent the +/- 10K increment in curvefits of the rotational spectra. Measured rotational temperatures are approximately twice the static temperature.

Due to the very low density of the Mach 5 plasma channel, any assumption that rotational and translational temperatures are in equilibrium must be examined critically. The rotational relaxation number for nitrogen (the average number of collisions required for the exchange of rotational and translational energy) has been measured to be less than

ten.[21,22,23]   With the collision frequency estimated to be approximately 10^7 sec^{-1}, the characteristic rotational relaxation time is $O(10^{-6})$ sec. With a flow velocity of 670 m/s, the expected distance required for relaxation is less than one millimeter. On the basis of these estimates, the discharge might be assumed to be in rotational / translational equilibrium.

An increase in translational temperature by a factor of two in the discharge would correspond to a decrease in Mach number by 1.4, if velocity remains constant. An upper bound on attainable temperature rise in the discharge is obtained by assuming all power goes into heating the fluid. For a discharge voltage and current of 300V and 400mA, respectively, the power expended is 120W. Constant-area and constant-pressure heating cases were examined.   Constant-area heating is analyzed using the control-volume approach of Heiser and Pratt.[24] Assuming constant γ and Cp, the constant-area heating exit velocity is 608 m/s, and the exit temperature is 182K, giving a Mach number of 2.25. For constant-pressure heating, the exit Mach is 4.42 and the exit temperature is 142K.

Mach number changes this large would be evident in Pitot probe measurements. The measured Pitot pressures, shown in Fig. 17, however, show no change when the discharge is on. This indicates no significant heating of the gas at this location. The conclusion that no significant translational heating occurs is bolstered by schlieren visualization of shock waves about a spherical model shown in Fig. 18. In Fig. 18, a portion of the schlieren image with no plasma (the darker vertical strip) is superimposed on another schlieren taken in the presence of a 150 mA discharge. No discontinuities in the shock location or slope are evident, thus indicating no significant heating.   An indication of the sensitivity of this method is obtained by observing that at Mach 5.2, an eight percent change in Mach number creates a one-degree change in Mach angle.

In summary, it must be concluded that the rotational temperature measurements do not provide an unbiased representation of the plasma translational temperature. This is presumed due to inaccuracy in curve-fitting the rotational spectra, or perhaps spatial non-uniformity across the integration path of the measurement. Rotational non-equilibrium is considered unlikely, but cannot be completely ruled out, given the uncertainty in characteristic times for rotational relaxation. The rotational temperatures may be used, however, to extract qualitative trends.

Additional spatial temperature distributions were obtained for discharges from the same electrodes, but with the support rods on the upstream ends of the plates. Rotational and vibrational temperature distributions in the streamwise direction for 100 and 400 mA discharges are shown in Figs. 19 and 20, respectively.   The error bars in these and subsequent figures denote +/- 1σ deviations in the measurements as an indication of unsteadiness in the discharge. Generally the 400 mA discharge has a larger rms than the 100 mA discharge, quantitatively confirming visual observations of increased unsteadiness. Rotational temperatures for the 100 mA discharge are approximately 80K over most of the streamwise survey. Downstream of the plate, rotational temperatures begin to rise, either due to relaxation or heating from the electrode bow shock. Vibrational temperatures generally decrease in the streamwise direction, perhaps indicating vibrational relaxation.

Rotational temperatures approximately twice freestream static translational temperatures are measured in the most upstream portion of the discharge in the 100 mA case. If energy were being dumped into the rotational mode that quickly, one would expect rotational temperatures to continue rising in the downstream direction through the discharge, but instead they remain relatively constant. The lack of a rotational temperature gradient in the x-direction for the 100 mA discharge is another indicator that little of the discharge energy goes into rotational or translational modes of the gas at these x-locations.

Vibrational temperatures for the 400 mA discharge show a more complicated variation than that observed in the 100 mA discharge. This is probably due to non-uniformity of the discharge, as evidenced by a local bright spot in the 400 mA discharge at $x / x_p = 0.7$. This bright spot has characteristics more akin to an arc than a glow discharge. In an arc local heating is taking place.

Rotational and vibrational temperature distributions in the vertical direction at $x / x_p = 0.7$ are shown in Figs. 21 and 22, respectively. The upper and lower plate surfaces are at $y / y_p = 1.0$ and -1.0, respectively. The upper limit of measurement was restricted to $y / y_p = 0.7$, due to mechanical interference in the probe drive. Rotational temperatures in the 100 mA discharge are generally about 80K and uniform throughout the discharge in the vertical direction (Fig. 21). Rotational temperatures for the 400 mA discharge are slightly higher. The rotational temperature for both discharge currents begins to increase below $y / y_p = -0.6$, probably due to the combined effects of heating from the plate bow shock, viscous heating, and local heating in the cathode layer by constricted current flows. Vibrational temperatures are approximately 5000K over most of the 100 mA discharge in the vertical direction, and 7000K for the 400 mA discharge. Like the rotational temperatures, vibrational temperatures also increase at $y / y_p < -0.6$.

Vibrational temperatures for a range of discharge currents, measured at $y / y_p = 0.0$ and $x / x_p = 0.7$ are shown in Fig. 23. Unsteadiness as measured by the rms is quite high for discharges above 100 mA. Vibrational temperatures range from about 4000K at 50 mA, and increase up to about 200 mA. Above this current, they appear to saturate at about 5000 to 7000 K.

7 Surface Discharges in a Magnetic Field

7.1 Magnet System

The initial concept for the magnet system consisted of a pair of air-core solenoids on opposite sides of the channel. A small solenoid with a pulsed power supply was wound for the Mach 6 experiments, and this system was capable of generating a field of up to 2 tesla. The pulsed air-coil solenoid concept for the Mach 5 channel was abandoned because of the difficulty in achieving a tuned circuit, due to the large impedance and inductance of the coils. The pulsed system presented other disadvantages due to the complexity of the power source and the short duration of the magnet field, which complicated diagnostics. A superconductor magnet was briefly considered. The superconductor offered the potential of high magnetic fields, but this concept was also abandoned due to the cost and complexity of the system. The final choice of magnet was a commercially available, large laboratory electromagnet.

The GMW 3474 electromagnet is a continuous-operation, water cooled model. The coils, when connected in series, have a maximum power rating of 10.6 kW (140 amp, 76 Volts). Pole-spacing is adjustable from 0-160 mm, and pole-cap diameters range from 25 to 250 mm. Field strength is a function of pole gap and pole cap diameter. For a fixed pole cap diameter, field strength diminishes as the pole gap increases. For sufficiently small pole gaps, smaller pole cap diameters create a higher field. As the pole gap approaches the pole cap diameter, field uniformity is adversely affected. With a pole gap of 10mm and a pole diameter of 25 mm, the field strength is as high as 3.5 Tesla. In practice, the magnet for the plasma channel is always operated at the maximum pole spacing and pole-cap diameter to clear the channel sidewalls. Under these conditions, the transverse magnetic field has a magnitude of one tesla and is nearly uniform. The magnet is rail-mounted so that it may be moved downstream to access the test-section. A photograph of the magnet installed around the channel is shown in Fig. 24.

The capability for continuous operation of the electromagnet is a distinct advantage, especially given the ability for continuous tunnel operation. One drawback of the magnet is that it impedes visual access to the channel. Several solutions to this problem exist. Forty-five degree mirrors and windows placed on the top and bottom of the test section can permit optical access for schlieren and other diagnostics.[25] Also, axial holes may be placed in the magnet pole at the cost of some field uniformity.

7.2 Effect of Magnetic Fields on Surface Discharges

The effect of DC discharges on boundary layers is currently under investigation. Preliminary studies examined two electrode configurations on flat plates constructed of phenolic resin and vertically mounted in the plasma channel. One configuration had two electrodes flush-mounted front-and-back in the surface of the plate, with the long-axis of the electrodes perpendicular to the freestream velocity vector, to create a streamwise discharge. Pressure taps, shown in Figure 25, were used to monitor surface pressures. In the other configuration, electrodes were placed at the top and bottom of the plate, with their long axes parallel to the freestream velocity to create a transverse discharge. Further details of these measurements are found in Ref 26.

As shown in Fig. 26 for the crossflow electrodes, pressure downstream of the leading electrode increases about 8% when a 50 mA current is applied, in the absence of a magnetic field. Pressure rise at the downstream tap is negligible. When the magnetic field is imposed on the discharge, pressures at both taps rise to more than 12% above their undisturbed values. When the discharge is turned off, pressures decrease but do not completely relax to their pre-discharge values. The upstream electrode is the cathode, the downstream electrode is the anode. For the data shown in Fig. 26, a small fence was placed beside the downstream pressure tap in an attempt to measure a Lorentz force deflection, but no unambiguous effect of magnet polarity was observed. Additional research in this

Several factors are probably in play to create the pressure rises. First, since pressure rises at the upstream tap even in the absence of a magnetic field, the most likely cause for this effect is heating of the boundary-layer fluid. At the low pressure of these tests (about 0.8 Torr), the viscous interaction between the boundary layer and the inviscid flow is pronounced. Heating the boundary layer fluid increases the displacement thickness,

which in turn increases surface pressure due to flow deflection. In tests where the polarity of the electrodes was reversed, the pressure rise at both taps was greatly reduced. Since most heating comes at the cathode, this also implicates heating as a cause of the pressure rise. The relative roles of dissipative heating in the plasma and convective heat transport from the electrodes will be the subject of future research. Due to the relatively low Reynolds number of these tests, convective heating is expected to be minimal, however, heat transfer from the electrodes to the fluid may be the cause of the increased pressures after the discharge is turned off.

In the presence of a magnetic field, other effects occur which could account for the pressure increases at both taps. The discharge was run in a current-stabilized mode. Figure 27 shows the voltage required to create a 50 mA current in the plasma as a function of applied magnetic field for the streamwise electrode configuration. The required voltage increases as B increases due to the Hall effect. Based on these results, the Hall parameter for this flow at one Tesla is estimated to be approximately one. Since the voltage increases with magnetic field strength, Joule heating in the plasma will also increase. This may give rise to the increased surface pressure in the presence of the magnetic field. Also visual observations show changes in the discharge path in the presence of the magnetic field. This may account for the increase in pressure in the downstream tap in the presence of a magnetic field. Also, both Lorentz and Hall forces are imposed on the fluid that, if large enough, could create measurable pressure gradients. Figs 28 and 29 show clearly that the plasma is vectored up and down, consistent with in changes in the Lorentz force, as the magnetic field changes sign. Quantitative measurements have not yet unambiguously demonstrated a coupling of the plasma motion to the neutrals. Future work will focus on examining the relative magnitude of all these effects.

8 Conclusions

A magneto aerodynamic channel has been designed and constructed. The channel has been shown to generate relatively uniform Mach 5.3 flow, with a useable test core. The device can run continuously. This continuous-run capability, in conjunction with a continuous-current electromagnet and DC discharges, creates a unique capability to study magnetoaerodynamic phenomena in detail. The device was first run in January 2002, and already has produced detailed temperature and conductivity maps of DC discharges, results on surface discharges in magnetic field effects, and the discovery of the magnitude of thermal effects on surface pressure in these discharges. Future work will concentrate on the exploitation of surface discharges for control and their enhancement with magnetic fields, and the exploration of MHD effects in inviscid flows.

9 Acknowledgments

References

[1] Bussing, T. R. A., Eberhardt, S., "Chemistry Associated with Hypersonic Vehicles," AIAA paper 87-1292, June 1987.

[2] Shang, J. S., Ganguly, B., Umstattd, R., Hayes, J., Arman, M., and Bletzinger, P., "Developing a Facility for Magneto-Aerodynamics Experiments, *Journal of Aircraft*, vol. 17, no. 7, Nov.-Dec., 2000, pp. 1065-1072.

[3] Shang, J. S., Hayes, J. R., Miller, J. H., Menart, J. A., "Magneto-Aerodynamic Interactions in Weakly Ionized Hypersonic Flow," AIAA paper 2002-0349, January 2002.

[4] Menart, J. A., Shang, J., Henderson, S., Kurpik, A., Kimmel, R. L., Hayes, J., R., "Survey of Plasmas Generated in a Mach 5 Wind Tunnel," AIAA-2003-1194, January 2003.

[5] Shang, J. S., Kimmel, R. L., Hayes, J. R., and Tyler, C., "Performance of a Low-Density Hypersonic Magneto-Aerodynamic Facility," AIAA 03-0329, January 2003.

[6] Kurpik, A., Menart, J., Shang, J., Kimmel, R. L., and Hayes, J. R., "Technique for Making Microwave Absorption Measurements in a Small Plasma Discharge," AIAA 2003-3748, June 2003.

[7] Kimmel, R. L., Hayes, J. R., Menart, J. A., Shang, J., and Henderson, S, "Measurements of a Transverse DC Discharge in a Mach 5 Flow," AIAA 2003-3855, June 2003.

[8] Dahm, F. J., "Air Condensation in a Hypersonic Wind Tunnel," *AIAA Journal*, vol. 1, no. 5, May 1963, pp. 1043-1046.

[9] Raizer, Yuri P., *Gas Discharge Physics*, Springer-Verlag New York, 1997.

[10] Shang, J. S., Hayes, J. R., Miller, J. H., Menart, J. A., "Blunt Body in Hypersonic Electromagnetic Flow Field," AIAA paper 2001-2803, June 2001.

[11] Ames Research Staff, "Equations, Tables, and Charts for Compressible Flow," NACA Report 1135, National Advisory Committee for Aeronautics, Ames Aeronautical Laboratory, Moffett Field, California, 1953.

[12] Rosa, R. J., *Magnetohydrodynamic Energy Conversion*, McGraw-Hill Book Company, New York, 1968, p. 40.

[13] Ostrach, S., "Laminar Flows with Body Forces," *High Speed Aerodynamics and Jet Propulsion, vol. IV, Theory of Laminar Flows*, Moore, F. K. ed., Princeton University Press, Princeton, NJ, 1964, pp. 691-712.

[14] Palm, P., Meyer, R., Plönjes, E., Bezant, A., Adamovich, I. V., Rich, J. W., Gogineni, S., "MHD Effect on a Supersonic Weakly Ionized Flow," AIAA paper 2002-2246, May 2002.

[15] Kimmel, R. L., Hayes, J. R., Menart, J., Shang, J., and Henderson, S., "Measurements of a Transverse DC Discharge in a Mach 5 Flow," AIAA paper 2003-3855, June 2003.

[16] Macheret, S. O., Shneider, M. N., and Miles, R. B., "Magnetohydrodynamic and Electrohydrodynamic Control of Hypersonic Flows of Weakly Ionized Plasmas, AIAA paper 2002-2249, May 2002.

[17] Howatson, A. M., *An Introduction to Gas Discharges*, Pergamon Press, New York, 1976, p. 183.

[18] Menart, J., Shang, J., and Hayes, J., "Development of a Langmuir Probe for Plasma Diagnostic Work in High Speed Flow," AIAA paper 2001-2804, June 2001.

[19] Menart, J. and Shang, J., "Data Reduction Analysis for Cylindrical, Double Langmuir Probes Operating in Collisionless to Collisional, Quiescent Plasmas," AIAA paper 2003-0136, January, 2003

[20] Raizer, Y. P., *Gas Discharge Physics*, Springer-Verlag, Berlin, 1991.

[21] Greenspan, M., "Rotational Relaxation in Nitrogen, Oxygen, and Air," *The Journal of the Acoustical Society of America*, vol. 31, no. 2, February 1959, pp. 155-160.

[22] Kistemaker, P. G., Tom, A., and De Vries, A. E., "Rotational Relaxation Numbers for the Isotopic Molecules of N_2 and CO," *Physica*, vol. 48, 1970, pp. 414-424.

[23] Andersen, W. H., and Hornig, D. F., "The structure of shock fronts in various gases," *Molecular Physics*, vol. 2, pp. 49-63, 1959.

[24] Heiser, W. H., and Pratt, D. T., *Hypersonic Airbreathing Propulsion*, American Institute of Aeronautics and Astronautics, Washington, D.C., 1994, pp. 66-81.

[25] McEldowney, B., Meyer, R., Chintala, N., and Adamovich, I. V., "Measurements of Electrical Parameters of a Supersonic Nonequilibrium MHD Channel," AIAA Paper 2003-4279, June 2003.

[26] Menart, J. A., Shang, J., Kimmel, R. L., and Hayes, J. R., "Effects of Magnetic Fields on Plasmas Generated in a Mach 5 Wind Tunnel," AIAA 2003-4165, June 2003.
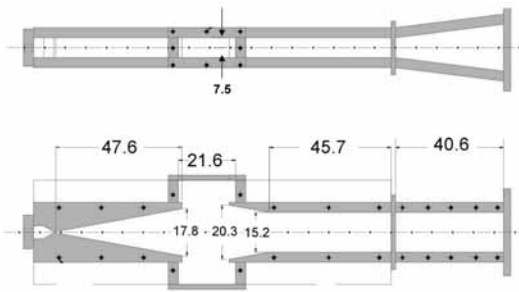
Figure 1 Schematic of the plasma channel. All dimensions centimeters. Flow is from left-to-right
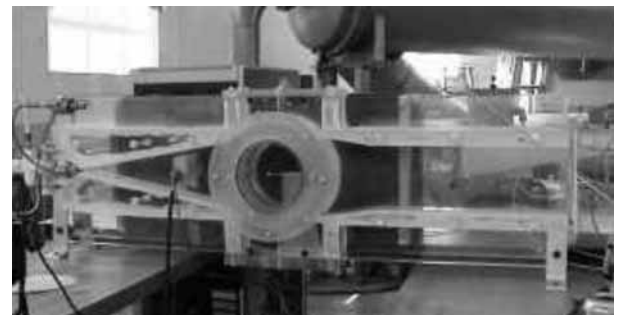
Figure 2 Photograph of the Mach 5 Plasma Channel.
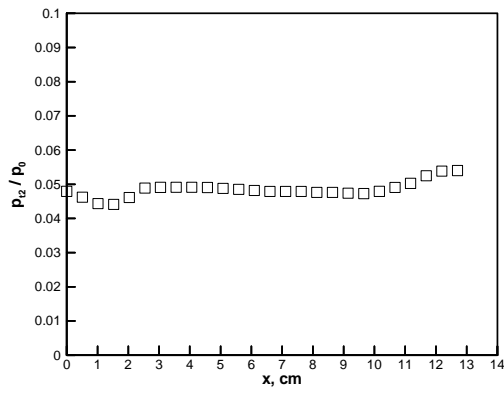
Figure 3   Ratio of Pitot to stagnation pressure along channel centerline. $x = 0$ corresponds to the nozzle exit.
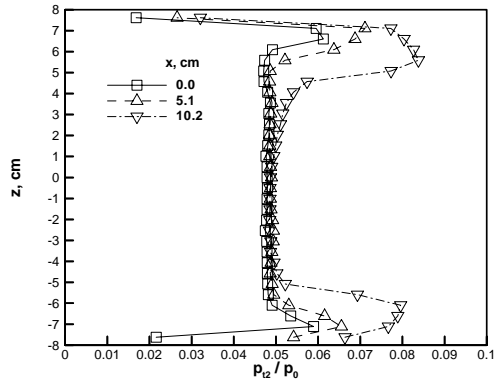
Figure 4   Vertical survey of Pitot pressure, normalized by stagnation pressure, at three axial stations.
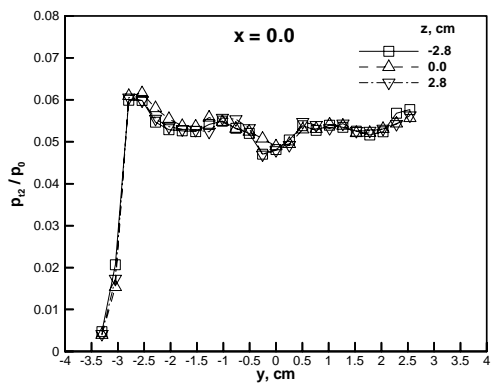
Figure 5   Pitot survey in spanwise direction at three vertical locations, x=0.
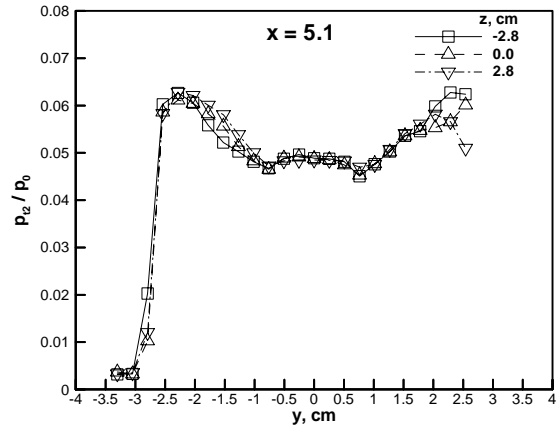
Figure 6   Pitot survey in spanwise direction at three vertical locations, x=5.1 cm.
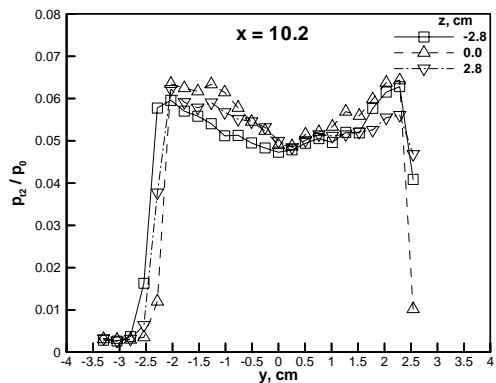
Figure 7   Pitot survey in spanwise direction at three vertical locations, x=5.1 cm.
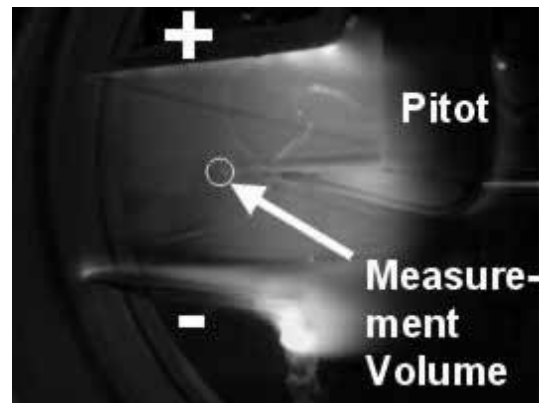
Figure 8 Photograph of discharge with Pitot probe.

15
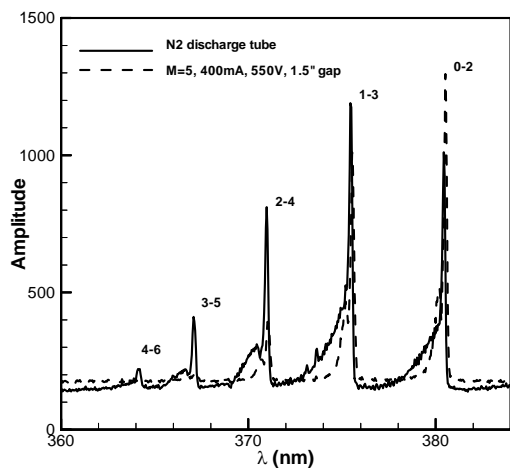
Figure 9 Nitrogen second positive group spectra for static discharge tube and Mach 5 DC glow discharge.

Figure 11 Ion number density in a 50 mA discharge, flow-on.

Figure 10 Ion number density in a 50 mA discharge, no-flow case. In this and next figures, spanwise location is in the center of the electrodes.
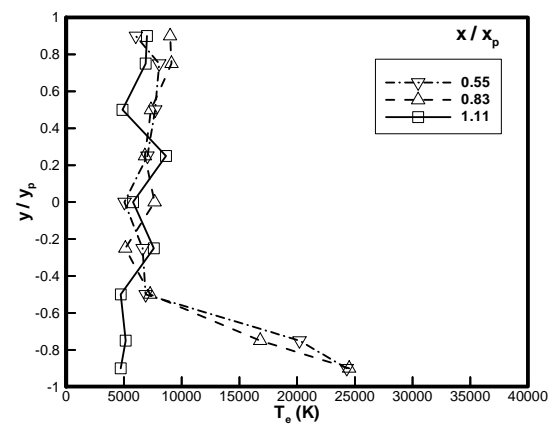
Figure 12 Electron temperature in a 50 mA discharge, no-flow case.
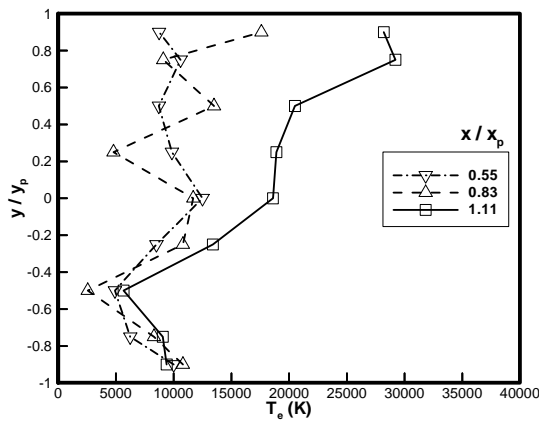
Figure 13 Electron temperatures measured in a 50 mA discharge, flow-on case.
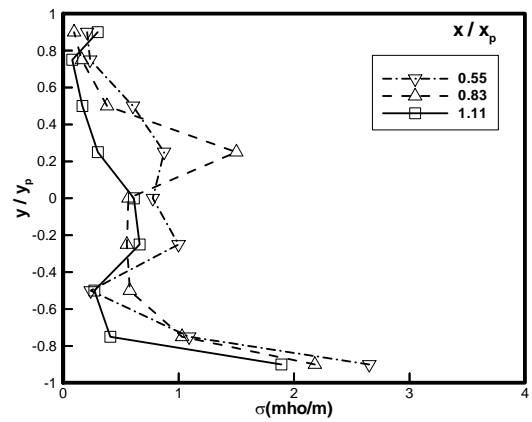
Figure 15 Plasma conductivity measured with the Langmuir probe in a 50 mA discharge, flow-on case.
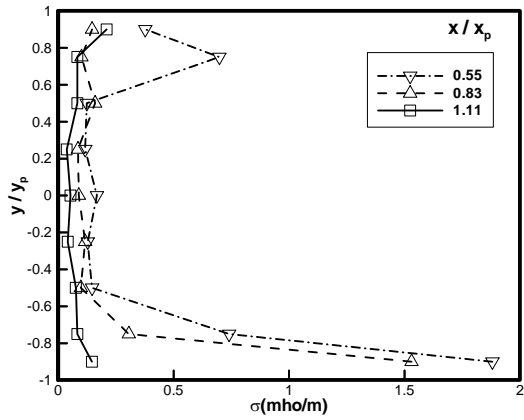
Figure 14 Plasma conductivity in a 50 mA discharge, flow-off case.
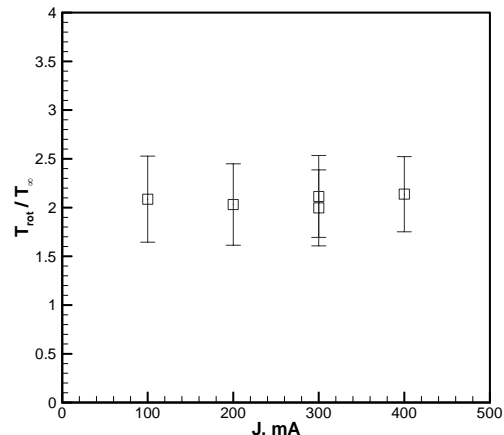
Figure 16 Rotational temperatures measured in discharge as a function of current. Error bars represent + / - 10K uncertainty.
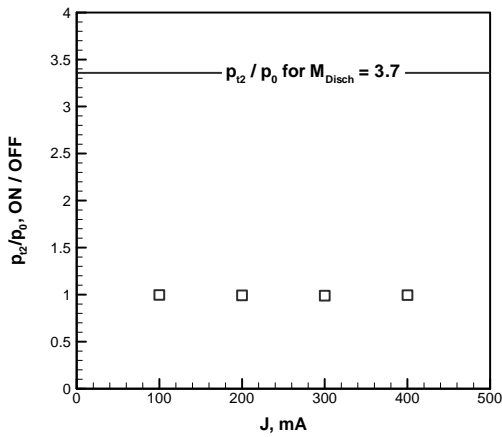
Figure 17 Ratio of current-on Pitot pressure to current-off Pitot pressure
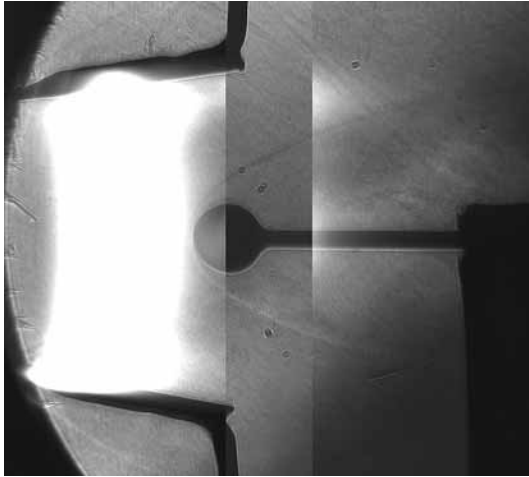
Figure 18 Schlieren image of shock produced by a sphere in the presence of a DC discharge. Luminosity from the discharge is evident between the plate electrodes on the left. The darker vertical strip in the middle is the superimposed schlieren image in the absence of a discharge.
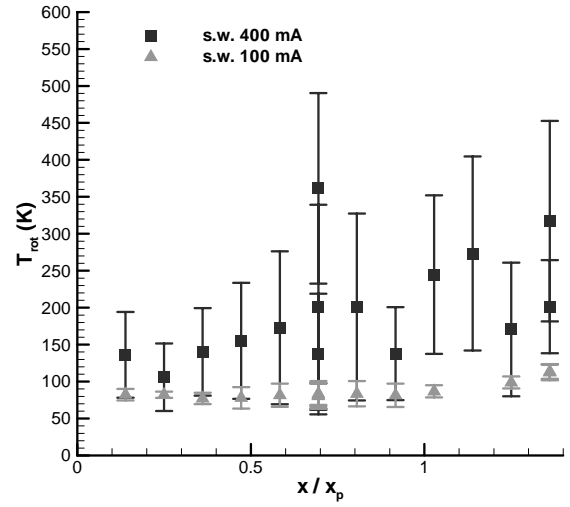
Figure 19 Rotational temperatures for 100 and 400 mA DC discharge between plates, streamwise distribution at $y / y_p = 0.0$.
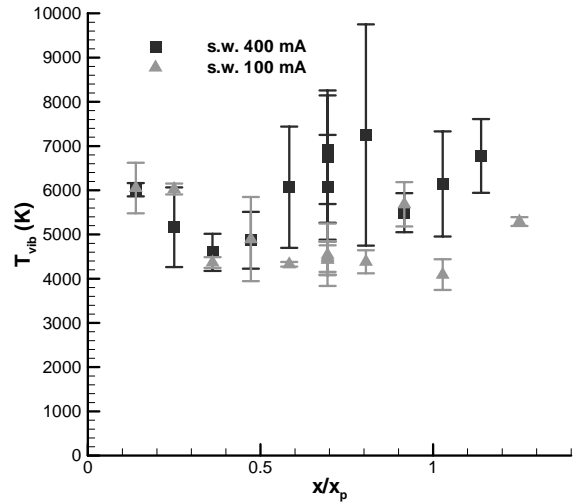
Figure 20 Vibrational temperatures for 100 and 400 mA DC discharge between plates, streamwise distribution at $y / y_p = 0.0$.
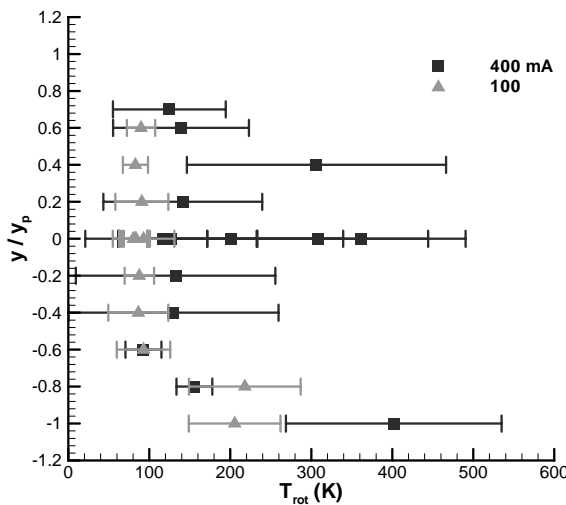
Figure 21 Rotational temperatures for 100 and 400 mA DC discharge between plates, vertical distribution at $x / x_p = 0.7$.

Figure 23 Vibrational temperatures for DC discharges between plates, at $x / x_p = 0.7$, $y / y_p = 0.0$ as a function of discharge current.
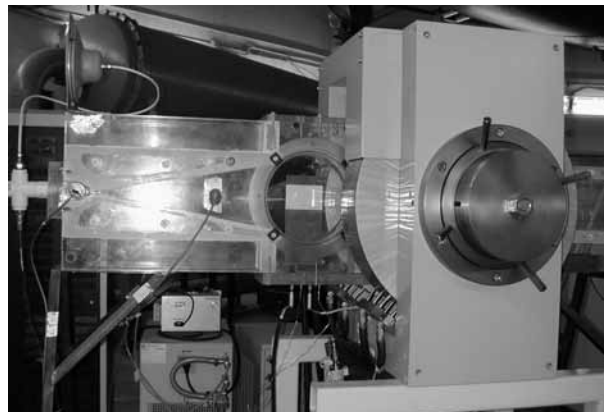
Figure 24 Electromagnet installed around channel.

Figure 22 Vibrational temperatures for 100 and 400 mA DC discharge between plates, vertical distribution at $x / x_p = 0.7$.
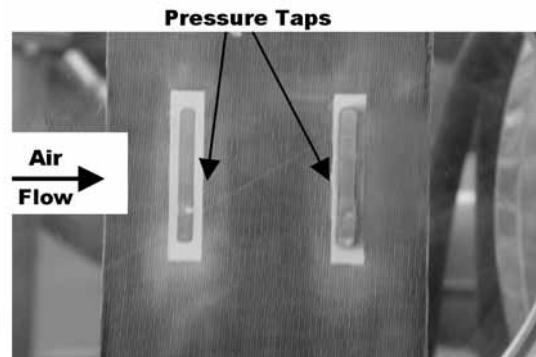
Figure 25 Crossflow-electrode model showing pressure taps.

19
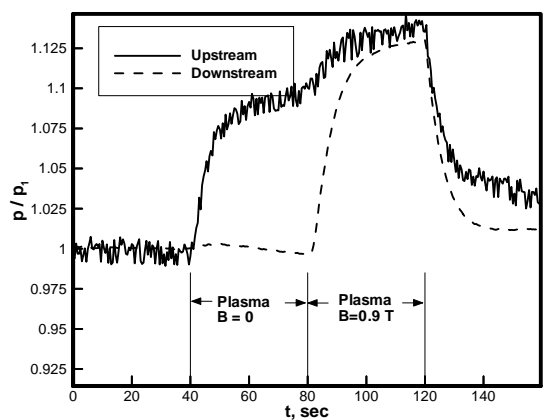
Figure 26   Surface pressures between crossflow electrodes for a 50 mA discharge.

Figure 27   Voltage required to produce 50 mA current in transverse surface discharge as a function of applied magnetic field.

Figure 28   Plasma discharge generated between the cross stream model electrodes, the upstream electrode is the cathode, the current is 50 mA, and the magnetic field strength is 0.34 tesla.
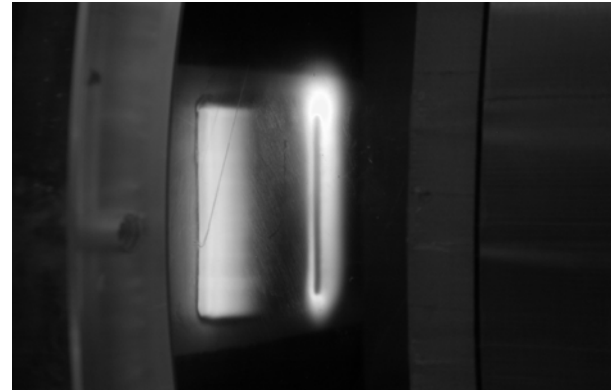
Figure 29   Plasma discharge generated across the cross stream model electrodes, the upstream electrode is the cathode, the current is 50 mA, and the magnetic field strength is –0.35 tesla.

MFD TECHNOLOGIES FOR SPACE PROPULSION APPLICATIONS

Mariano Andrenucci

Professor, Department of Aerospace Engineering, University of Pisa, Italy
Managing Director, Centrospazio, Pisa, Italy

List of symbols

A	correction term in Eq. (35)
b	thrust factor in Eq. (36)
$\boldsymbol{B}$	magnetic induction field
β	Hall parameter
e	electron charge
E	energy
$\boldsymbol{E}$	electric field
$\boldsymbol{F}$	force
Φ_i	ionization potential
γ	flow parameter, Eq. (26)
η	resistivity, efficiency
θ	Hall angle
I_{sp}	specific impulse
$\boldsymbol{j}$	current density
J	total current
k	mass loading parameter
K	Boltzmann constant
m	particle mass
$\dot{m}_i$	ion mass flow rate
$\dot{m}_p$	total mass flow rate
μ_0	vacuum magnetic permeability
n	number density
ν	collision frequency
P	power
$\boldsymbol{P}_{\mathrm{coll}j}$	collision term for species j-th particles with other particles
$\boldsymbol{P}_{ie}=-\boldsymbol{P}_{ei}$	electron-ion collision terms
$\overset{\leftrightarrow}{P}$	pressure tensor
p	scalar pressure
σ	conductivity, ionization cross section
r_i	inner electrode radius
r_e	external electrode radius
ρ	density
t	time
T	temperature, thrust
τ	collision time
v_e	effective exhaust velocity
V	voltage

$\boldsymbol{u}$	average velocity
v_{ac}	Alfvén critical ionization velocity
V	voltage
Z	impedance
ω	Larmor frequency
Ω	flow parameter, Eq. (26)

Subscripts:

a	neutral atom
c	guiding centre
e	electron
ei	electron-ion
ea	electron-neutral
E	guiding centre relative to ion
ε	energy transfer
ϕ	plume divergence
H	Hall
i	ion, ionization
j	species j-th particles
J	total current
l	losses
m	mass
max	maximum value
n	electron relative to ion
p	propellant
P	power
T	thrust
x,y,z	spatial coordinates
v	velocity

Superscripts:

$*$	in coordinates moving with mass average velocity

Symbols:

$\overline{(\ )}$	reference
$\langle\ \rangle$	ensemble average

1. The theoretical bases of plasma propulsion

Electric propulsion is a wide term encompassing a variety of different objects, developed with considerable effort over almost a century[1]. A consolidated classification divides electric thrusters into three main categories: electro-thermal; electrostatic, and electromagnetic[2]. However, although essentially correct, more recently this classification has come to appear too simplistic or schematic to account for the complexity of EP devices. This became more evident with the advent of Hall-effect thrusters on the Western scene. In fact, these devices happened to be classified either as electromagnetic or electrostatic thrusters by equally authoritative sources. This only serves to emphasise the need for a more unitary description of the functioning of these devices. As a matter of fact, such an approach was already used in some of the classic Russian texts[3] and has gained growing recognition in the West in recent years[4]. This unified approach is based on acknowledgement of the fact that, in a very general sense, many types of electric thruster can be described as plasma thrusters. The most important implication of this is to assume that the working fluid employed in the thruster is always an electrically conducting medium which remains quasi-neutral throughout all phases of the process. This means that we can always assume:

$$\left| n_e - n_i \right| << n_e \approx n_i = n \tag{1}$$

The implications of this assumption, as well as a number of other features which are normally associated with the term plasma, are extensively covered in many excellent textbooks[5,6,7,8] and will not be dealt with here. What matters in this context is that this definition leaves out ion thrusters, in that these thrusters inherently involve charge separation as a basic feature of the acceleration process.

As is universally known, the behaviour of an assembly of particles can be thoroughly described through the Boltzmann equation. But as we are interested in the global, collective behaviour of the various components of the working medium, a description in terms of average behaviour is normally sufficient. This is usually done by taking the first three velocity moments of the Boltzmann equation, thus obtaining the mass, momentum, and energy conservation equations for each species. These equations are generally called the fluid equations. When combined with the Maxwell equations and with appropriate constitutive relations, the fluid equations provide a complete description of the collective behaviour of the medium in all its components. Again, all this is treated extensively in classical plasma physics texts.

As we deal with a general problem of thrust generation, what matters particularly for the purpose of the present paper is the momentum equation for each species. We shall accordingly start from this for our analysis. In its general form for the species j this equation takes the form

$$m_j n_j \left[\frac{\partial \boldsymbol{u}_j}{\partial t} + \left(\boldsymbol{u}_j \cdot \nabla \right) \boldsymbol{u}_j \right] = n_j e \left(\boldsymbol{E} + \boldsymbol{u}_j \times \boldsymbol{B} \right) - \nabla \cdot \ddot{P}_j + \boldsymbol{P}_{\mathrm{coll}\, j} \tag{2}$$

where the left hand side will be recognized as proportional to the convective derivative of the average velocity $\boldsymbol{u}_j$. The right side includes the Lorentz force, the divergence of the pressure tensor (describing like–particle collisions) and the exchange of momentum due to collisions with other species in the plasma. For further analysis of the possible accelerating processes, it is useful to limit our attention to a simple case that will permit us to reach some general conclusions without unnecessary complications. We shall therefore consider the following:

- only two fluids: ions and electrons
- as mentioned, $n_e \approx n_i = n$

2

- the collision terms will therefore describe collisions between electrons and ions, being of course:

$$P_{ie} = -P_{ei} = \frac{m_e n_e (u_e - u_i)}{\tau_{ie}} \tag{3}$$

- anisotropic component of the pressure tensor negligible, so that $\nabla \cdot \ddot{P}_j$ reduces to ∇p_j
- ion and electron velocities can be related in terms of current as follows

$$u_e = u_i - \frac{j}{ne} \tag{4}$$

- inertial term on the left side of the electron equation negligible due to the small electron mass
- other minor assumptions should be obvious and will not be mentioned here.

In addition, it is useful to recall the following definitions regarding conductivity, resistivity, and Hall parameter

$$\sigma = \frac{1}{\eta} = \frac{n e^2}{m_e} \tau_{ei} \qquad \beta = \omega_e \tau_e \qquad \omega_e = eB/m_e \tag{5}$$

The momentum conservation equations for the ionic and the electronic components can thus be simply stated as

$$m_i n \left[\frac{\partial u_i}{\partial t} + (u_i \cdot \nabla) u_i \right] = ne(E + u_i \times B) - \nabla p_i - \frac{ne}{\sigma} j$$

$$0 = -ne \left(E + u_i \times B - \frac{1}{ne} j \times B \right) - \nabla p_e + \frac{ne}{\sigma} j \tag{6}$$

Where the dashed boxes have been added to highlight the collisional terms describing the momentum exchange between the two species. Let us first consider the second of Eqs. (6) for the electrons, which we can rewrite as:

$$j = \sigma (E + u_i \times B + \frac{1}{ne} \nabla p_e - \frac{1}{ne} j \times B) \tag{7}$$

or in the equivalent form

$$j = \sigma (E^* - \frac{1}{ne} j \times B) = \sigma E^* - \frac{\beta}{B} j \times B \tag{8}$$

where the term $E^* = E + u_i \times B + \nabla p_e/ne$ represents the electric field in a reference frame in motion with the average heavy particle flow plus the electron pressure gradient contribution. Eq. (8) can be recognized as the generalized Ohm's law, describing the relationship between fields and current in the plasma. The self-consistent E field generated in the plasma by the Hall effect can accordingly be written as

$$E = -u_i \times B + \frac{1}{ne} j \times B - \frac{1}{ne} \nabla p_e + \frac{j}{\sigma} \tag{9}$$

Let us now turn to the first of Eqs. (6) for the ions. This shows that the heavy particles can only be accelerated as a result of one or more of the following:

- the action of the electric field as judged in the moving reference frame, $E*$;
- the pressure gradient contribution, that is, the action resulting from collisions with like particles;
- the action resulting from momentum transfer from the electrons to the ions through collisions.

The ion equation and the electron equation are not connected with each other only by the collisional term ($n\,e\,\boldsymbol{j}\,/\,\sigma$), as the electric field $E*$ is also in common. The pressure term will tend to converge provided that the electron-ion interactions are sufficiently intense to favour the achievement of equilibrium conditions, otherwise the two temperatures and pressures can remain considerably different throughout the acceleration phase.
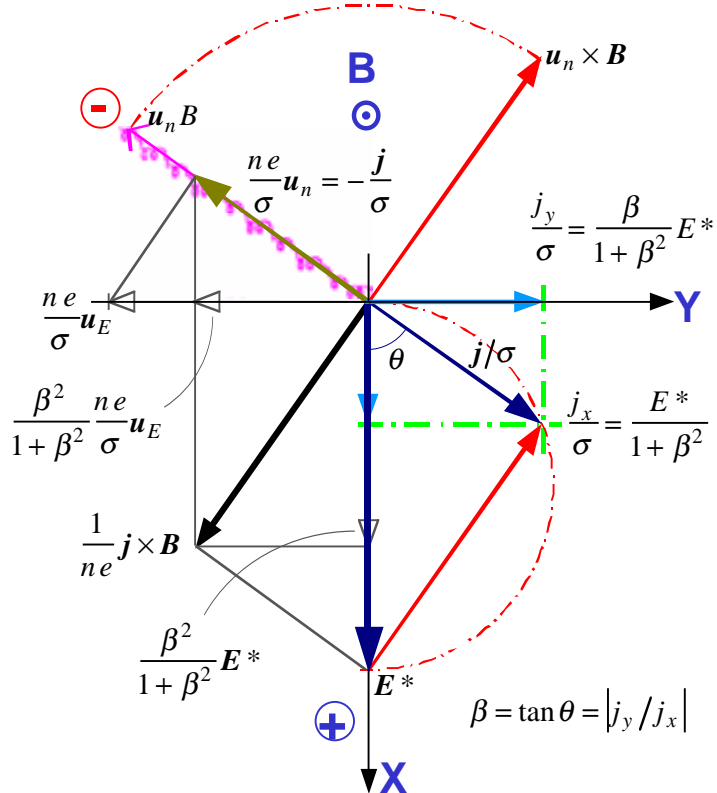
Fig. 1   Vector diagram for fields and currents in plasma thrusters

The situation is summarized in Fig. 1, where we have neglected the pressure terms to make the representation simpler. As can be easily seen, the situation can be summarized in this way: electrons accelerate under the action of the electric field resulting from the sum of the field as viewed by the reference frame in motion with the fluid plus the component associated with the relative velocity of the electron fluid with respect to the average mass. If the inertial term is negligible, all the momentum acquired in this way is transferred to the ion by collision. In addition, the ions also respond to the same electric field directly drawing momentum from this.

By combining the momentum equations for the two species and with the following further definitions

$$\nabla p = \nabla p_e + \nabla p_i \qquad\qquad \rho = m_i\, n \qquad\qquad (10)$$

we finally obtain

$$\rho \frac{d\boldsymbol{u}}{dt} = -\nabla p + \boldsymbol{j} \times \boldsymbol{B} \qquad\qquad (11)$$

where everything finally reduces to the familiar Lorentz force term (apart from the pressure gradient contribution); but we should bear in mind that this results from the combined effects of collisions and of the self-consistent electric field.

It is worth noting that the overall force $j \times B$, so far described as resulting from its components along E^* and $u_n = u_e - u_i$, can also be decomposed along the two directions respectively parallel and perpendicular to E^*, the latter coinciding with the direction of the electron guiding centre drift with respect to the average heavy particle flow $u_E = u_c - u_i$. It can be easily verified that in this case we can write the ion equation in a form which highlights the role of the Hall parameter

$$m_i n \left[\frac{\partial u_i}{\partial t} + (u_i \cdot \nabla) u_i \right] + \nabla p = \frac{\beta^2}{1 + \beta^2} \left[n e E^* + n \frac{m_e}{\tau_{ei}} (u_c - u_i) \right] \tag{12}$$

All types of plasma thrusters - as a matter of fact, essentially all types of thrusters - are based on one or more of the above effects included in this equation. Gasdynamic thrusters and arcjets are totally based on pressure gradients; ion thrusters on an externally generated electrostatic field; MPD thrusters mainly on the collisional contribution from the electron component and Hall thrusters on the self-consistent electric field associated with the Hall effect.

As regards the energy conservation equations for the two species, these can be derived from Eqs. (6) by scalar multiplication by u_i and u_e respectively:

$$u_i \cdot \rho \frac{d u_i}{d t} = -\nabla p_i \cdot u_i + n e E \cdot u_i - \frac{n e}{\sigma} j \cdot u_i$$
$$0 = -\nabla p_e \cdot u_e - n e E \cdot u_e + \frac{n e}{\sigma} j \cdot u_e \tag{13}$$

The last term in the second of Eqs. (13) can be decomposed by use of Eq. (4). With obvious further simplifications we obtain

$$\frac{d}{d t} \left(\rho \frac{u_i^2}{2} \right) = -\nabla p_i \cdot u_i + n e E \cdot u_i \boxed{- \frac{n e}{\sigma} j \cdot u_i}$$
$$0 = -\nabla p_e \cdot u_e - n e E \cdot u_e \boxed{+ \frac{n e}{\sigma} j \cdot u_i} - \frac{j^2}{\sigma} \tag{14}$$

where the dashed boxes now highlight the collisional terms describing the frictional power exchange between electrons and ions, and the j^2/σ term represents the associated Joule heating. Adding up Eqs. (14) and remembering Eq. (4) the collisional terms cancel out, and we are left with

$$\frac{d}{d t} \left(\rho \frac{u_i^2}{2} \right) = -\nabla p_i \cdot u_i - \nabla p_e \cdot u_e + E \cdot j - \frac{j^2}{\sigma} \tag{15}$$

If we want to show explicitly the role of the overall Lorentz force in the energy equation (15), we can go back to Eq. (9), and scalarly multiply with j, thus obtaining

$$E \cdot j = -(u_i \times B) \cdot j - \frac{1}{ne} \nabla p_e \cdot j + \frac{j^2}{\sigma} \tag{16}$$

Considering that it is

$$-\left(\boldsymbol{u}_i \times \boldsymbol{B}\right) \cdot \boldsymbol{j} = \left(\boldsymbol{j} \times \boldsymbol{B}\right) \cdot \boldsymbol{u}_i \tag{17}$$

we can write

$$\boldsymbol{E} \cdot \boldsymbol{j} - \frac{j^2}{\sigma} = \left(\boldsymbol{j} \times \boldsymbol{B}\right) \cdot \boldsymbol{u}_i - \frac{1}{en} \nabla p_e \cdot \boldsymbol{j} = \left(\boldsymbol{j} \times \boldsymbol{B}\right) \cdot \boldsymbol{u}_i - \nabla p_e \cdot \left(\boldsymbol{u}_i - \boldsymbol{u}_e\right) \tag{18}$$

so that Eq. (14) can be finally put in the form

$$\frac{d}{dt}\left(\frac{\rho u^2}{2}\right) = -\nabla p \cdot \boldsymbol{u} + \left(\boldsymbol{j} \times \boldsymbol{B}\right) \cdot \boldsymbol{u} \tag{19}$$

where we have omitted the subscript, as the fluid velocity is $\boldsymbol{u} \approx \boldsymbol{u}_i$. Eq (19) could also have been obtained directly from Eq. (11) by scalar multiplication with $\boldsymbol{u}$. However, as observed for Eq. (11), Eq. (19) fails to highlight the separate roles played by the electrostatic field and by the collisions. Indeed, the above analysis shows that the increase in the ion fluid kinetic energy is either drawn from the energy transferred by the electrons through collisions, or from direct action of the electric field on the ions.

Looking back to Eq. (15) we see that if we neglect again the pressure gradient terms the useful energy transfered to the plasma can utimately be referred to the power delivered by the electric field minus the power dissipated as Ohmic heating. We are thus prompted to define a power transfer efficiency as the ratio of net power transferred to ions to the overall electrical power made available; that is

$$\eta_P = \frac{\boldsymbol{E} \cdot \boldsymbol{j} - \dfrac{j^2}{\sigma}}{\boldsymbol{E} \cdot \boldsymbol{j}} = 1 - \frac{j^2/\sigma}{\boldsymbol{E} \cdot \boldsymbol{j}} \tag{20}$$

Let φ be the angle formed by the local flow velocity $\boldsymbol{u} \approx \boldsymbol{u}_i$ with the current vector $\boldsymbol{j}$, so that the angle between the direction of the $\boldsymbol{j} \times \boldsymbol{B}$ force and the local flow direction is $\psi = \left(\pi/2\right) - \varphi$, Taking into account that $j = \sigma E^* \cos\theta$, with a few passages one can find

$$\eta_P = \frac{\left(uB / E^*\right)\cos\psi}{\cos\theta + \left(uB / E^*\right)\cos\psi} \tag{21}$$

This shows that the local power transfer efficiency is determined by the value and direction of the flow and by the Hall parameter. Rather than in terms of velocity alone, Eq. (21) is parametrized in terms of the ratio between the back EMF term uB and the moving frame electric field E^*. As could be expected, the highest transfer efficiency for a given flow velocity is obtained when the velocity vector is parallel to the direction of the overall Lorentz force, which in turn is determined by the value of the Hall angle. This implies that for high values of the Hall parameter ($\beta \gg 1$) high efficiency conditions require the flow velocity to be aligned with the Electric field E^*, a condition typically found in Hall effect thrusters. A velocity flow direction perpendicular to the electric field, as typically found in self-field MPD thrusters would prove efficient only for very low values of the Hall parameter: $\beta \ll 1$. The latter condition is less easily obtained than the former.

2. Electromagnetic Acceleration Modes

Let us now switch over with the analysis of the more complicated nondissipative and dissipative acceleration modes. For this purpose let us turn back to the equation of moption of ions in the form obtained with Eq. (12), which we rewrite here neglecting all pressure terms for simplicity:

$$m_i \frac{d\boldsymbol{u}_i}{dt} = \frac{\beta^2}{1+\beta^2}\left[e\left(\boldsymbol{E} + \boldsymbol{u}_i \times \boldsymbol{B}\right) + \frac{m_e}{\tau_{ei}}\left(\boldsymbol{u}_c - \boldsymbol{u}_i\right) \right] \tag{22}$$

According to this equation, in response to the combined electric and magnetic fields the velocity of ions undergoes an oscillation asimptotically approaching the electron drift rate $\boldsymbol{u}_c$. To analyse this behaviour in greater detail let us consider a simple geometrical arrangement , with a rectangular accelerator of axis x, with electric field directed along the y axis and magnetic field directed along the z axis. With this choice of coordinates, and remembering that

$$\boldsymbol{u}_c = \frac{\boldsymbol{E} \times \boldsymbol{B}}{B^2}$$

Eq. (22) can translated in the following scalar equations

$$m_i \frac{1+\beta^2}{\beta^2} \frac{du_{ix}}{dt} = e u_{iy} B + \frac{m_e}{\tau_{ei}} \frac{E}{B} - \frac{m_e}{\tau_{ei}} u_{ix}$$

$$m_i \frac{1+\beta^2}{\beta^2} \frac{du_{iy}}{dt} = eE - e u_{ix} B \qquad\qquad - \frac{m_e}{\tau_{ei}} u_{iy} \tag{23}$$

that can be reordered as

$$\frac{du_{ix}}{dt} = \frac{eB}{m_i}\frac{\beta^2}{1+\beta^2} u_{iy} + \frac{\beta^2}{1+\beta^2}\frac{m_e}{m_i \tau_{ei}}\frac{E}{B} - \frac{\beta^2}{1+\beta^2}\frac{m_e}{m_i \tau_{ei}} u_{ix}$$

$$\frac{du_{iy}}{dt} = \frac{eB}{m_i}\frac{\beta^2}{1+\beta^2}\frac{E}{B} - \frac{eB}{m_i}\frac{\beta^2}{1+\beta^2} u_{ix} \qquad\qquad - \frac{\beta^2}{1+\beta^2}\frac{m_e}{m_i \tau_{ei}} u_{iy} \tag{24}$$

Taking into account that

$$\frac{m_e}{m_i \tau_{ei}} = \frac{eB}{m_i \beta} \quad \text{and} \quad \frac{eB}{m_i} = \omega_{ci}$$

Eqs. (24) can be written as

$$\frac{du_{ix}}{dt} = \omega_i \frac{\beta^2}{1+\beta^2} u_{iy} + \frac{\omega_i}{\beta}\frac{\beta^2}{1+\beta^2}\frac{E}{B} - \frac{\omega_i}{\beta}\frac{\beta^2}{1+\beta^2} u_{ix}$$

$$\frac{du_{iy}}{dt} = \omega_i \frac{\beta^2}{1+\beta^2}\frac{E}{B} - \omega_i \frac{\beta^2}{1+\beta^2} u_{ix} \qquad\qquad - \frac{\omega_i}{\beta}\frac{\beta^2}{1+\beta^2} u_{iy} \tag{25}$$

To simplify the writing we can introduce the symbols

$$\Omega = \omega_{ci} \frac{\beta^2}{1+\beta^2} \qquad \gamma = \omega_{ci} \frac{\beta}{1+\beta^2} \tag{26}$$

so that Eqs. (25) can be written as

$$\frac{du_{ix}}{dt} = \qquad \Omega u_{iy} + \gamma \frac{E}{B} - \gamma u_{ix}$$

$$\frac{du_{iy}}{dt} = \Omega \frac{E}{B} - \Omega u_{ix} \qquad - \gamma u_{iy} \tag{27}$$

Note that Ω and γ are related by $\gamma = \Omega / \beta$.

Taking into account the initial conditions

$$u_{ix_0} = u_{iy_0} = x_0 = y_0 = 0 \tag{28}$$

the equation system (27) yields the following solutions

$$u_{ix} = \frac{E}{B} \left(1 - e^{-\gamma t} \cos \Omega t \right)$$

$$u_{iy} = \frac{E}{B} \, e^{-\gamma t} \sin \Omega t \tag{29}$$

which show that the x-component of the ion velocity tends asymptotically to u_{ci}, while the y-component eventually reduces to zero. Let us consider the time τ needed for the velocity to approach the limiting value u_c. Imposing the esponential to be less than, say, 0.05, would imply the exponent to be larger than about 3. In other words, we would have in this case

$$\tau \approx \frac{3}{\gamma} = \frac{3}{\omega_{ci}} \frac{1+\beta^2}{\beta} \tag{30}$$

Representative solutions for different values of β and ω_{ci} are illustrated in Figs. 2 a-b. The three cases shown all correspond to the same value of $\omega_{ci} = 0.2$, and to three values of β: 0.1, 1.0 and 10.0. The markers on the curves correspond to identical time intervals for the three cases and show clearly that the lowest-β solution implies a far smaller acceleration than the other two cases.

As can be seen, depending on the value of the involved parameters, three different plasma acceleration modes are possible:

1. Nondissipative: $\qquad \beta \gg 1;$ $\qquad \tau \gg \dfrac{2\pi}{\omega_{ci}}$

2. Dissipative: $\qquad \beta \approx 1;$ $\qquad \tau \approx \dfrac{2\pi}{\omega_{ci}}$

3. Aperiodic dissipative: $\qquad \beta \ll 1;$ $\qquad \tau \gg \dfrac{2\pi}{\omega_{ci}}$

The last mode, as noted above, is characterized by a very low ion acceleration and requires a long channel length $L \gg r_{ci}$, so that it does not possess practical interest for propulsion applications.
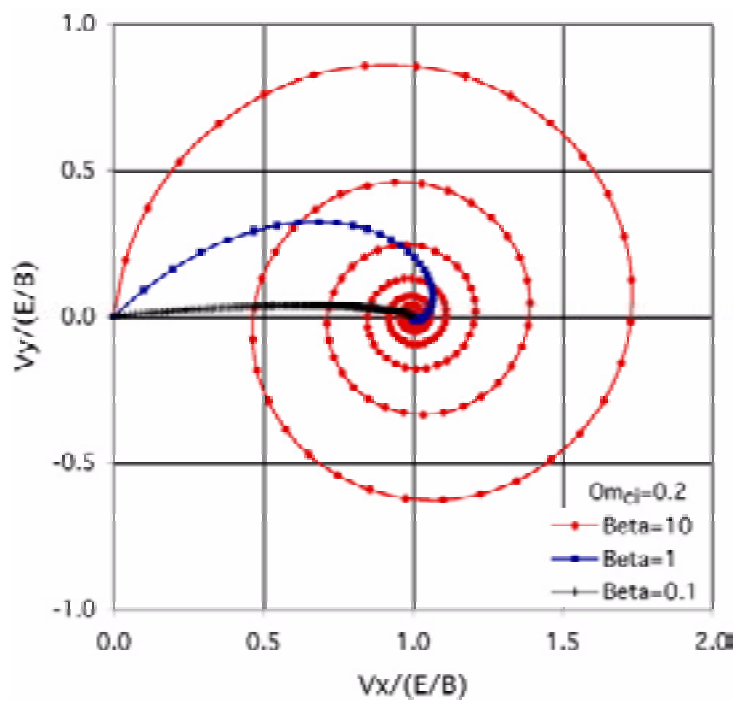
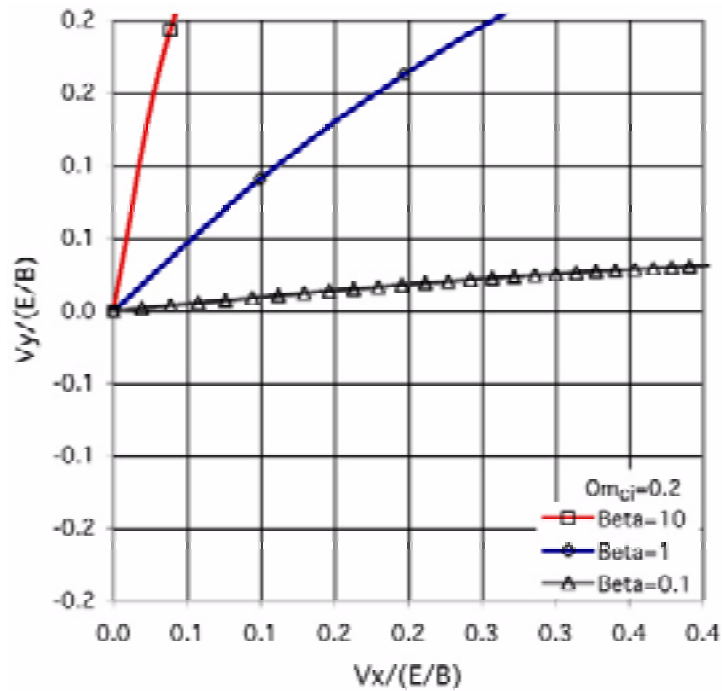Fig. 2a   Representative solutions of electromagnetic equations

Fig. 2b   Initial trends of the above solutions (magnification)

3. Plasma thrusters

We shall now see how all of the above applies to the main categories of plasma thrusters. To the purpose of the present paper, we shall limit our analysis to stationary plasma devices, including self-field and applied-field MPD thrusters, as well as Hall-effect thrusters

3.1 Hall effect thrusters

The operating principle of a Hall effect thruster[9,10] is illustrated in Fig. 3, which also shows how the general scheme of Fig. 1 should be positioned to refer to the specific situation of this type of thruster. The schemes refer specifically to the SPT - or long channel – type of HET thruster, but most of the considerations made below could also apply to an Anode Layer Thruster (TAL)[11]. The latter shall not be considered specifically in the present context.
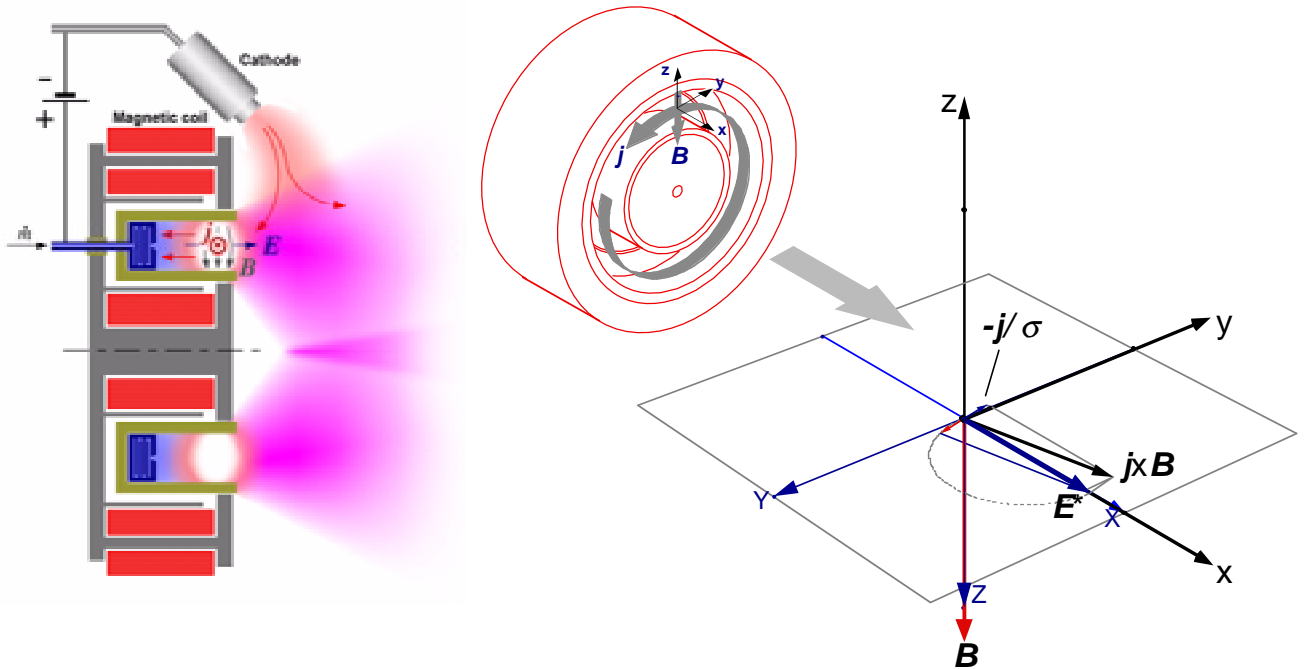
Fig. 3 General scheme of Hall effect thruster

The accelerating principle here is based on a marked increase in electron resistivity at the channel entrance obtained by means of a strong radial magnetic field, which forces the electrons to drift azimuthally while trying to approach the anode. At the density, magnetic induction and electron temperature conditions at which HETs are typically operated (n≈1017÷1018 m-3 , Te≈10÷30 eV , B≈0.02÷0.03 T), the electron Hall parameter is so high that the azimuthal component of the electron current is far larger than its axial component, so that the electron flow can be approximately described as a free azimuthal drift. As a result, the potential profile along the channel axis grows to a far higher value than that to be expected in the absence of the magnetic field, and this in turn forces the ions, which are not significantly magnetized and are therefore free to move along the channel, to accelerate down the potential gradient to high exhaust velocity. This process is triggered by a small fraction of the electron flow leaving the cathode, but most of the electron current is sustained by the electrons produced by ionization of the propellant gas. An equivalent amount of electrons represents the rest of the cathode flow, which performs the ion beam neutralization. In this type of thruster, therefore, the accelerating process is essentially electrostatic, in that the thrust is entirely attributable to the self-consistent electric field generated in the plasma.

To evaluate the overall performance parameters of the thruster, we should integrate the equations over the discharge region, which can only be done with detailed knowledge of the discharge and channel configuration. Fortunately enough, the situation in typical HETs can essentially be described as one in which the magnetic field is purely radial, the electric field is strictly axial and the current is strictly azimuthal, thus implying a purely axial thrust[3]. In this case integration over the discharge volume yields for the exhaust velocity

$$v_e = \left(2e V_A / m_i \right)^{1/2} \tag{31}$$

where V_A is the voltage available for acceleration and other symbols are familiar. Eq. (31) is easily recognized as the usual expression of the exhaust velocity for an ion thruster, which is not surprising as we have seen that the electric field accounts for the largest fraction of the thrust. The connection between V_a and the discharge voltage shall be commented on shortly. Once the exhaust velocity is known, we can derive expressions for the thrust,

$$T = \dot{m}_p \, v_e \tag{32}$$

and the thrust efficiency

$$\eta_T = \frac{T \, v_e}{2 P} = \frac{\dot{m}_p \, v_e^2}{2 P} \tag{33}$$

With respect to this highly idealized representation, several effects exist in real devices which alter the situation and play a crucial role in determining the effectiveness of the acceleration process. The details of the magnetic field configuration have complex and subtle effects on the process. Electron diffusion has been shown to behave quite differently with respect to that suggested by the classical conductivity models. Plasma interaction with the walls and the ensuing secondary electron emission, affect both diffusion and energy losses to the walls, thus implicating the channel geometry in the optimization of the thruster. The ionization process must be effectively completed within a small fraction of the accelerating channel length to ensure proper thruster operation. These and other aspects have been the object of a long process of refinement, mainly carried out in the former Soviet Union, at typical power levels below 1 kW. Over the past decade Hall-effect thrusters have become the object of intense research effort in the Western countries (Fig. 4) and are now entering into routine use for flight applications. This type of thruster is largely considered to be the best electric propuslion option for power levels up to several tens of kWs.
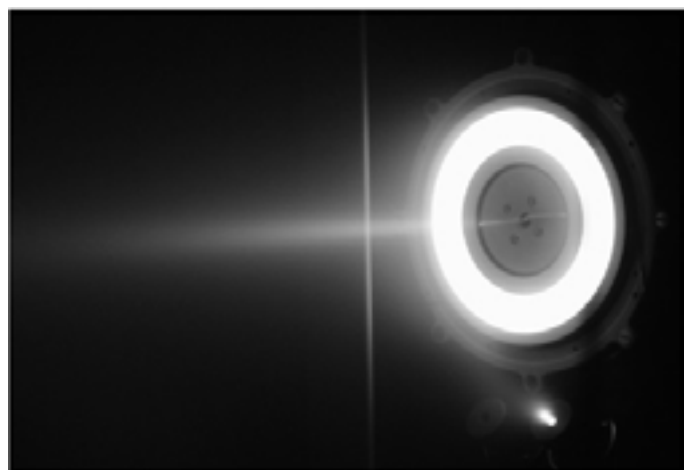

Fig. 4   A Hall-effect thruster under test at Centrospazio-Alta Laboratories

3.2 Self-Field MPD thrusters

The situation is markedly different in self field MPD thrusters[2,12] (Fig. 5). Here the electrically conducting fluid is subjected to the electric field deriving from the voltage applied to the electrodes and the self-induced azimuthal magnetic field associated with the current. The current density j driven by the electric field interacts with the self-induced magnetic field to provide a stream-wise body force $F = j \times B$ that accelerates the fluid along the channel. To better understand the acceleration mechanism let us look at how the general scheme of Fig. 1 is positioned to refer to the specific situation of this type of thruster:
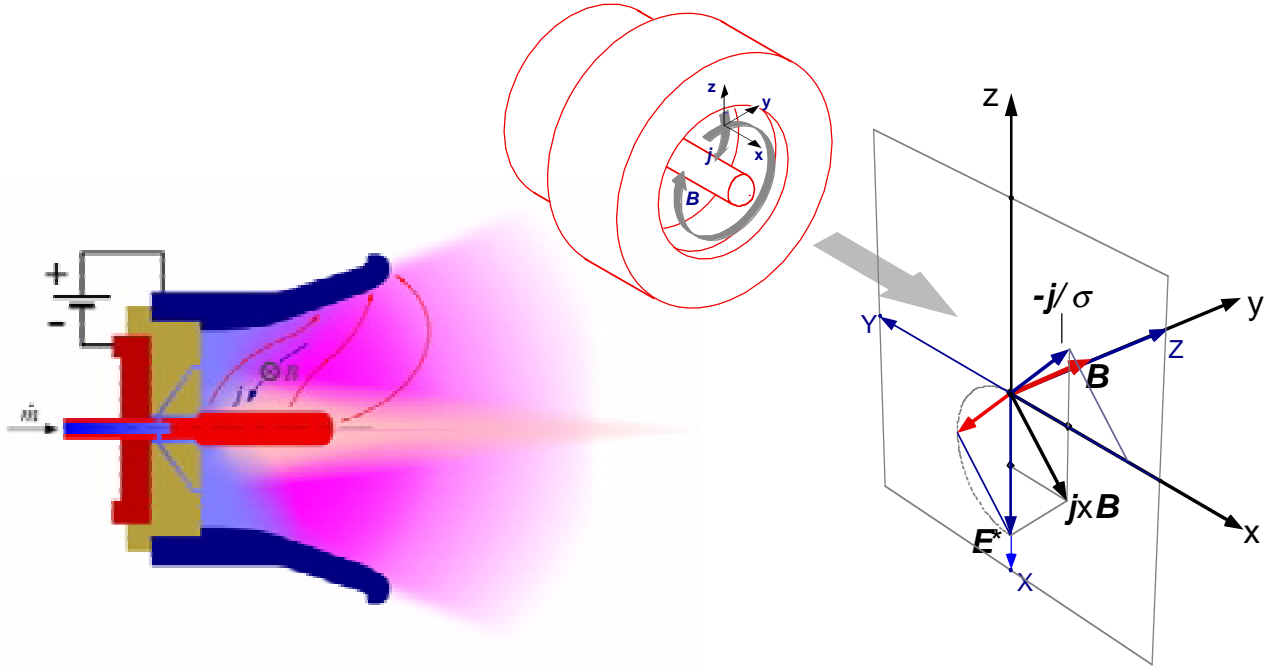
Fig. 5   General scheme of self-field MPD thruster

It can be observed here that the collisional mechanism is mainly responsible for the acceleration process. But the electrostatic contribution may also be significant and in this case tends to compress the flow towards the axis; this may contribute to the thrust but can also entail detrimental effects[13].

The analysis of this operation mode is usually based on a simple 1-dimensional idealization. For a coaxial channel of external radius r_e and internal radius r_i, integration of the distributed Lorentz body-force over the discharge volume leads to the following expression for the thrust:

$$T = \frac{1}{2} L' J^2 = \frac{\mu}{4\pi} ln \frac{r_e}{r_i} J^2 \tag{34}$$

where L' is the channel inductance per unit length. If the channel geometry is more complex, the above expression can be generalized with the inclusion of a corrective term as follows

$$T = \frac{\mu J^2}{4\pi} \ln\left(\frac{r_e}{r_i} + A\right) \tag{35}$$

For instance, in the case of a conical cathode tip involving both a pumping and a blowing contribution one would find $A = 3/4$.

12

In more realistic configurations the relationship between thrust and current squared would depend on the details of electrode geometry and current attachment; but the overall thrust would still follow a law of the type

$$T = b J^2 \qquad (36)$$

where b is factor of a mainly geometrical character; values of b for typical geometries are about $2 \div 3 \times 10^{-7} N / A^2$.

Based on the above analysis, the thrust provided by a given device would appear as determined by the discharge current only, independently from the propellant mass flow rate $\dot{m}$. The effective exhaust velocity u_e would therefore scale with the inverse of $\dot{m}$

$$u_e = \frac{T}{\dot{m}} = b \frac{J^2}{\dot{m}} = b\, k \qquad (37)$$

where we have introduced the characteristic parameter $k = J^2 / \dot{m}$, which is expressive of the electrical power deposited in the channel per unit propellant mass flow-rate.

The useful power associated with the thrust is

$$P_T = \frac{1}{2} \dot{m}\, u_e^{\,2} = \frac{b^2 k}{2} J^2 \qquad (38)$$

so that we can define the dynamic impedance associated with the useful power spent in accelerating the gas as

$$Z_T = \frac{b^2 k}{2} \qquad (39)$$

Finally, we can compare the useful power associated with the thrust with the overall power input

$$P_i = P_T + P_{Losses} \qquad (40)$$

where the power associated with the losses could also be expressed in terms of an equivalent impedance

$$Z_L = \frac{P_{Losses}}{J^2} \qquad (41)$$

We can therefore write a general expression for the thrust efficiency as follows

$$\eta_T = \frac{P_T}{P_T + P_{Losses}} = \frac{Z_T}{Z_T + Z_L} = \frac{\dfrac{b^2 k}{2}}{\dfrac{b^2 k}{2} + Z_L} = \frac{1}{1 + \dfrac{2 Z_L}{b^2 k}} . \qquad (42)$$

An ideal MPD thruster whose thrust scales quadradically with the current will therefore obey the following laws of dependence of power and voltage with the current

$$P_i = \frac{b^2}{2 \dot{m} \eta_T} J^4 \qquad (43)$$

13

$$V = \frac{P_i}{J} = \frac{b^2}{2\dot{m}\eta_T}J^3 \tag{44}$$

In conclusion, the behavioural trends of an ideal MPD thruster can be summarized as follows

$$\begin{cases} T \propto J^2 \\ V \propto J^3 \\ P \propto J^4 \end{cases} \tag{45}$$

Real thruster behaviour has been shown to comply with this idealised model only within a limited range of conditions. Departure from the above scaling trends, at both low current and high current, indicates that the geometrical situation is different from that assumed and the physical situation more complex.

Experimental results indicate that for input power levels insufficient for full ionization of the propellant flow, the exhaust velocity appears to remain constant and the voltage to scale linearly with the current. This has prompted a physical interpretation related to the Critical Ionization Velocity (CIV) phenomenon described by Alfvén,[14] according to which once the ionized part achieves a velocity

$$v_{ac} = \left(2e\Phi_i/m_i\right)^{1/2} \tag{46}$$

(where Φ_i is the ionization potential of the involved species), all of the power fed into the thruster goes into ionizing the the remaining low velocity neutrals rather than further accelerating the ionized fraction. All in all the phenomenon behaves as a sort of latent heat effect, blocking the velocity of the ionized component at the CIV value and implying a 50/50 subdivision of the input power between ionization and kinetic flow energy.

Beyond the full ionization point, thruster behaviour should start to comply with that of a true Lorentz accelerator following the model outlined above. But as soon as the full EM region is entered a variety of disturbing phoenomena (simply known as "onset") affecting the behaviour of the thruster are usually observed with the main result of reduced efficiency.

A number of theories have been put forward to explain this behaviour. Most such theories attribute the efficiency reduction to anode power deposition caused by anode fall potential: a large voltage drop which develops near the anode surface, typically wasting 50 to 70 % of the thruster power. This is in turn related to the Hall effect which can induce propellant mass starvation near the anode region. This drop in plasma density reduces the current density that the plasma can stably conduct away from the anode. The depletion of charge carriers in the near anode region causes large voltage falls in both the sheath and the neutral plasma. In the anode sheath, large space-charge voltages develop to pull electrons into the anode.[15] In the low density neutral plasma near the anode, anomalous resistivity due to current driven instabilities becomes dominant, causing large voltage drops[16]. In addition, the action of the axial current flowing across the azimuthal magnetic field can create large radial electric fields in the neutral plasma near the anode.

Various solutions have been suggested to cope with onset phenomena and anode starvation, including arrangements to reduce Hall current, propellant injection through the anode and the use of other propellants. Alternatively, one could exploit the Hall current through the addition of an axial magnetic field, a solution which is adopted in applied field thrusters (see below).

In conclusion, it would seem that acceptable efficiency levels (above 30%) in self-field MPD thrusters can only be reached at high power (above 100 kW). Therefore, the steady-state version of this type of thruster is regarded as a high-power propulsion option. When operated below 200 kW, the self-induced magnetic field becomes only marginally sufficient to provide the desired body force and external fields are frequently added to enhance performance. On the other hand, in the megawatt range, self-field MPD propulsion seems to offer the unique capability, among all developed electric thrusters, of processing very high power levels in a simple, compact and robust device that can produce very high thrust densities. These features render steady-state MPD propulsion particularly attractive for energetic deep-space missions requiring high thrust levels.
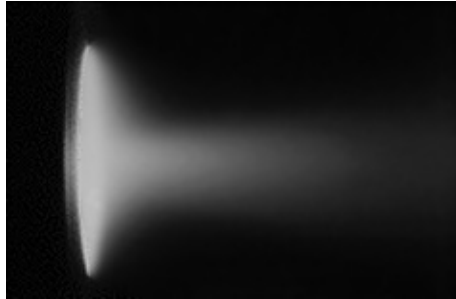
Fig. 6   A Self-field MPD thruster under test at Centrospazio-Alta Laboratories

3.3   Applied-field MPD thrusters

When an externally applied magnetic field is superimposed on an MPD channel the situation changes considerably[17,18] (Fig 7). The thrust fraction generated within the channel is quite small and Lorentz actions mainly result in a swirling effect. The strong axial magnetic field hinders electron flow to the anode forcing them to follow trajectories far downstream of the thruster exit. In the region where current stream lines bend to assume a more marked radial component, the Lorentz actions exhibit an azimuthal component which sustains the swirling and a meridian component which provides a blowing and a pumping contribution, both contributing directly to the thrust. The vector diagram describing this situation is shown in Fig 8-a which only accounts for the applied magnetic field.

In these thrusters the self-induced field is often of the same order of magnitude as the field applied. As a consequence, the magnetic field lines are twisted in a helical fashion and the situation becomes as shown in Fig. 8-b. It can be observed that the effect of the superimposition of the self-field and applied-field components is to increase the axial contribution to the thrust. Typical values of the Hall parameters in this type of thruster are about 3 to 5.[18]
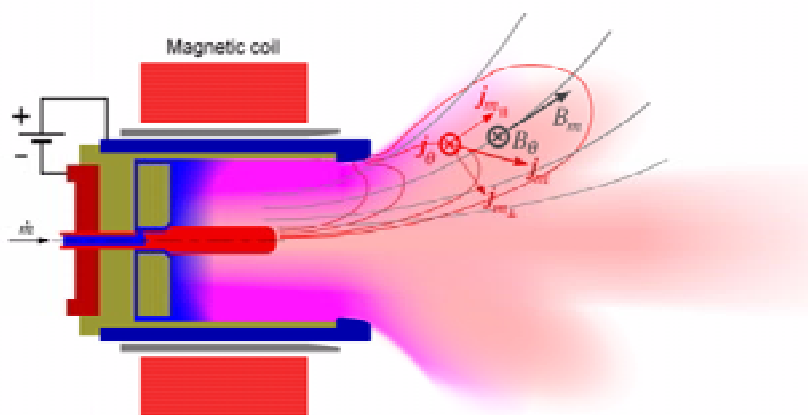

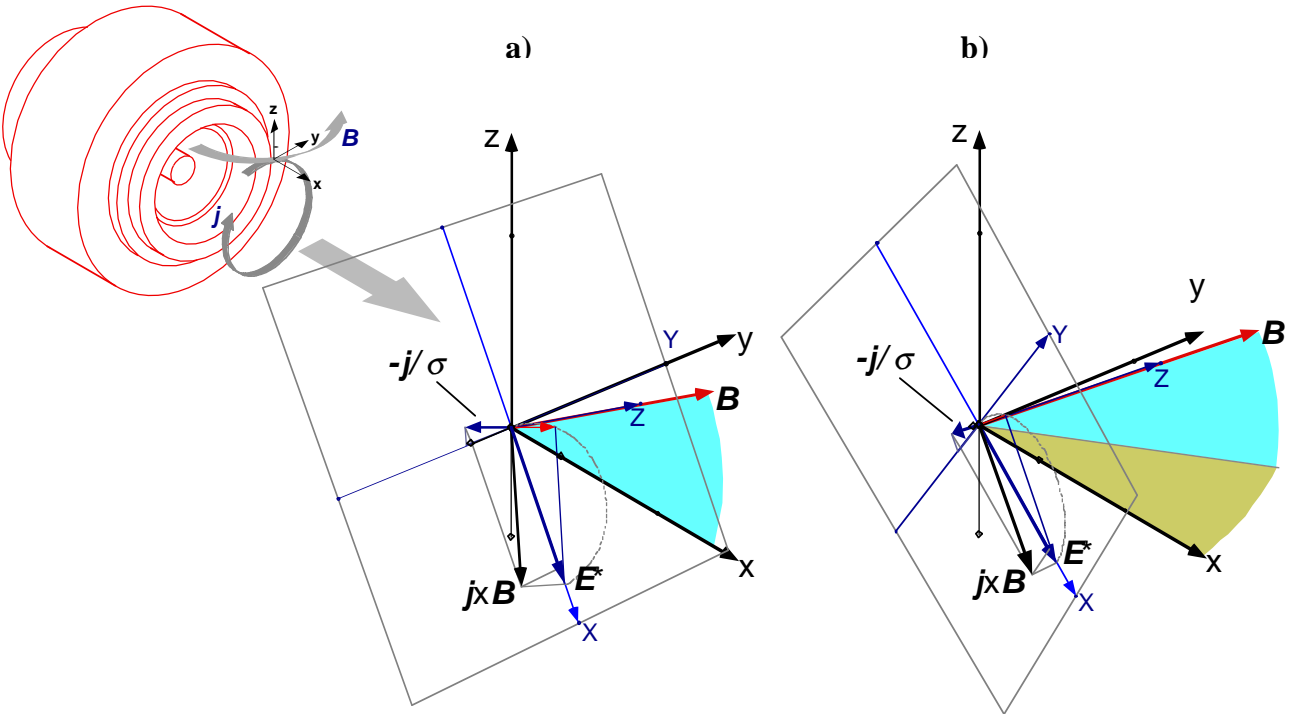**Fig. 7   General scheme of applied-field MPD thruster**

Fig. 8   Vector diagrams for applied-field MPD thruster

The electrostatic contribution to the thrust is therefore larger than the collisional one. The overall result vaguely resembles the situation to be found in a channelless Hall effect thruster in which the electron flow ring is located outside the thruster front. This type of thruster therefore exhibits behaviour which is intermediate with respect to self-field MPD and Hall thrusters and may justify expectations for more efficient operation and less sensitivity to instabilities and erosion compared to the former. On the other hand, the fact that the discharge extends considerably downstream does not favour accurate vacuum chamber testing. Therefore, this type of thruster has yet to be adequately optimised.
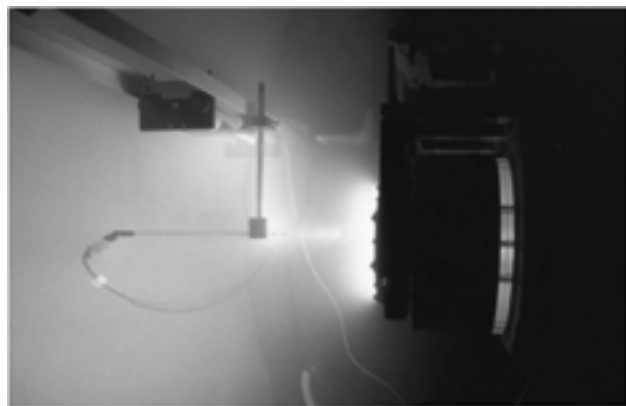
Fig. 9   An HPT applied-field thruster under test at Centrospazio-Alta Laboratories

16

4. Conclusions

It has been shown that the three principal types of plasma thrusters lend themselves to a unitary description in which the accelerating process can always be expressed in terms of Lorentz force, as resulting from the contribution of an electrostatic component and a collisional component (plus a possible contribution of pressure gradients). The paper has highlighted that the differences between the different types of thrusters are mainly due to a different balance of these two components, with Hall effect thrusters almost entirely based on the electrostatic contribution, self-field MPD thrusters mainly based on the collisional effect and applied-field MPD thrusters representing an intermediate solution with comparable Hall and self-field contributions.

References

[1] M. Andrenucci, "The History and Status of Electric Propulsion Technology", *Proc. 8th International Workshop on Combustion and Propulsion*, Pozzuoli, Italy, June 2002.

[2] R. G. Jahn, *Physics of Electric Propulsion,* McGraw-Hill Book Co., New York, NY, 1968.

[3] S. D. Grishin, L. V. Leskov, *Electrical Rocket Engines of Space Vehicles*, Publishing House Mashinostroyeniye, Moscow, 1989.

[4] P. J. Turchi, "Electric Racket Propulsion Systems", in *Space Propulsion Analysis and Design*, eds. R. W. Humble, G. N. Henry, W. J. Larson, McGraw-Hill Book Co., New York, NY, 1995.

[5] F. F. Chen, *Introduction to Plasma Physics and Controlled Fusion: Volume 1,* Plenum Press, New York, 1990.

[6] J. A. Bittencourt, *Fundamentals of Plasma Physics*, Pergamon Press, Oxford, UK, 1986.

[7] M. A. Lierberman and A. J. Lichtenberg, *Principles of Plasma Discharges and Materials Processing,* John Wiley and Sons Inc., New York, NY, 1994.

[8] M. Mitchner and C. H. Kruger, Jr., *Partially Ionized Gases,* John Wiley and Sons Inc., New York, NY, 1992.

[9] Zhurin, V.V., Kaufman, H.R., and Robinson, R.S., "Physics of Closed Drift Thrusters," IEPC 97-191, *25th International Electric Propulsion Conference*, Cleveland, OH, August 1997.

[10] V. Kim, "Main Physical Features and Processes Determining the Performance of Stationary Plasma Thrusters", *J. Propulsion and Power*, vol. 14, no. 5, Sept-Oct 1998.

[11] E. Y. Choueiri, "Fundamental Difference Between the Two Hall Thruster Variants", *Phys. Plasmas*, vol. 8, no. 11, Nov 2001.

[12] E. Y. Choueiri, "Scaling of Thrust in Self-Field Magnetoplasmadynamic Thrusters", *J. Propulsion and Power*, vol. 14, no. 5, Sept-Oct 1998.

[13] A. D. Gallimore, R. G. Jahn, and A. J. Kelly, "Anode Power Deposition in Magnetoplasmadynamic Thrusters", *J. Propulsion and Power*, vol. 9, no. 3, 1993.

[14] Alfvén, H.,"Collision Between a Nonionized Gas and a Magnetized Plasma," *R. of Mod. Physics*, V. 32, pp. 710-713, 1960.

[15] F. G.Bakshat, B. Y. Moizhes and A. B. Rybakov, "Critical Regime of a Plasma Accelerator," *Sov. PhYs. Tech. Phys*, V. 18, no. 12, pp. 1613-1616, June 1974.

[16] E. Y. Choueiri, A. J. Kelly and R. G. Jahn, "Current Driven Plasma Acceleration versus Current Driven Energy dissipation, Part III," AIAA Paper 92-3739, *28th Joint Propulsion Conference*, 1992.

[17] G. Krulle, M. Auweter-Kurtz, and A. Sasoh, "Technology and Application Aspects of Applied Field Magnetoplasmadynamic Propulsion,"*J. Propulsion and Power*, vol. 14, no. 5, Sept-Oct 1998.

[18] M. Auweter-Kurtz, and H. Kurtz, "Arc Devices for Space Propulsion", *ISU/AAAF Short Course Introduction to Space Propulsion*, Versailles, France, May 2002.

RUSSIAN EFFORTS IN MHD AEROSPACE APPLICATIONS

V.A.Bityurin[*]

Institute of High Temperatures of Russian Academy of Sciences,
Moscow, Russia

1. Introduction

The regular study of MHD aerospace applications has been started in Russia in early 90s [1-3]. The first analysis based on our experience of the development of large-scale on-ground MHD systems has shown the principal possibility of effective utilization in flow-flight control for hypersonic vehicle especially during re-entry missions and promising prospective of on-board applications of MHD electrical power generation [4-5]. It was found, for example, that during re-entry the airflow parameters in the viscous shock layer allow to provide the significantly high MHD interaction with a rather low value of magnetic induction (~ 1T), which can be easily created with conventional techniques. From the other hand, the typically used flight velocity at altitudes less than 40-50 km can not provide aerodynamics heating of the airflow sufficient for acceptable electrical conductivity. For this reason MHD interaction in such cases needs the artificially created ionization by some energy deposition (microwave, e-beam, gas discharge and so on) or seeding by low ionization potential material [5, 6]. The necessity to use the additional energy release in airflow for elevation of ionization degree of oncoming air lies in the background of the strong connection of MHD based flow/flight control with the Plasma Aerodynamics approach dealing with the various types of electrical discharges to create plasma formations capable to modify significantly airflow characteristics. The benefit of the externally applied magnetic field was also recognized for Plasma Aerodynamics because of the importance of the magnetic field impact on the discharge development and the appearance of additional channel of influence through the body force **j×B.** This is why the new field – *Magneto-Plasma Aerodynamics* was specified [7-11].

Magneto-plasma aerodynamics (MPA) is formed during the last decade as a new scientific region mostly related to miscellaneous aerospace applications. It is anticipated that the MPA technique widely involving the remote flow control by electric, magnetic and electromagnetic fields generated with on-board systems can significantly improve the characteristics of super- and hypersonic vehicles, propulsion systems, high-speed combustors, on-board electrical generator systems, and so on.

The physical background of MPA is composed mainly but not exclusively of fluid mechanics (super- and hypersonic aerodynamics of real gases, physics of shock wave, magneto hydrodynamics), physics of low temperature plasma (gas discharge, plasma chemistry, chemical and physical kinetics), and power engineering (ram/scramjet, MHD generation/acceleration). This MPA structure is illustrated in diagram of Fig.1.

As one can see from the scheme in Fig.1 the MHD interaction plays the very important role contributing in all three main directions of the potential applications. From the other hand the scientific background of MHD is composed of fundamentals of the fluid mechanics and the low temperature plasma physics.

---

[*] Director of Division, Institute of High Temperatures of Russian Academy of Sciences, President of International Liaison Group on MHD Energy Conversion (ILG MHD)
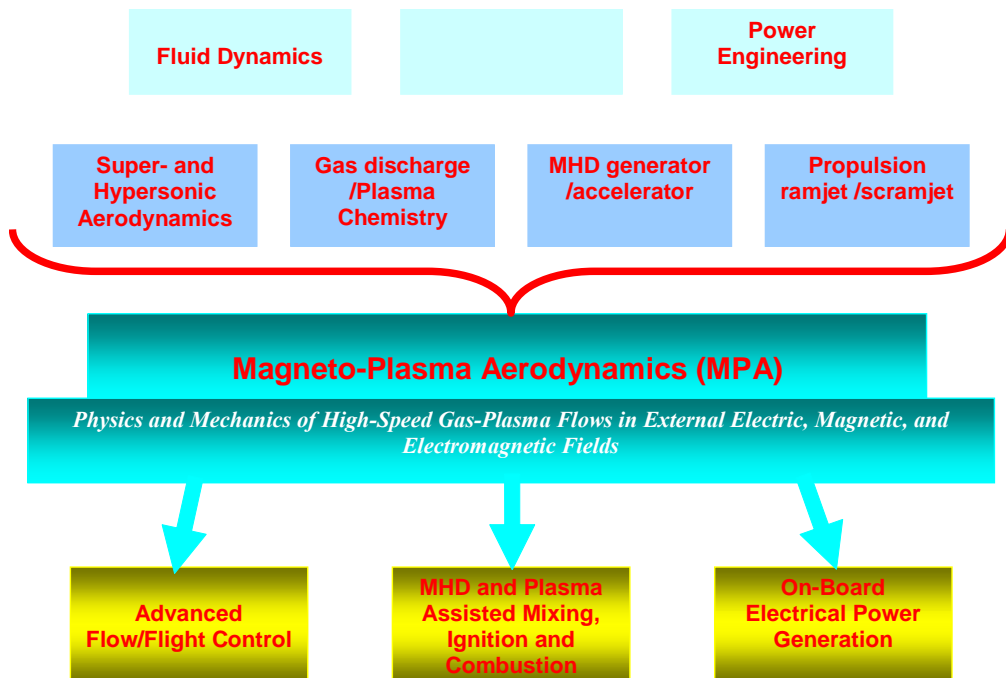
DEFINITION OF MAGNETO-PLASMA AERODYNAMICS

Fluid Dynamics		Power Engineering

Super- and Hypersonic Aerodynamics	Gas discharge /Plasma Chemistry	MHD generator /accelerator	Propulsion ramjet /scramjet

Magneto-Plasma Aerodynamics (MPA)

Physics and Mechanics of High-Speed Gas-Plasma Flows in External Electric, Magnetic, and Electromagnetic Fields

Advanced Flow/Flight Control	MHD and Plasma Assisted Mixing, Ignition and Combustion	On-Board Electrical Power Generation

Figure 1 MPA structure

Russian MHD community is formed and experienced mainly in frame of two large-scale R&D programs initiated in the Soviet Union in late 60th: development of MHD generators driven by combustion products of fossil fuels for base load applications, and pulse power MHD generators working with solid state rocket propellant for special applications. Two others type of MHD electrical power generation: noble (both seeded and unseeded) gas non-equilibrium MHD generators and non-uniform conducting flow MHD generator were studied less intensive mostly to understand the physics of such devices.

The pulse power MHD generators (Pamir, Khibiny, …) in range of electrical power output from several MWe till to more than 500 MWe (Sakhalin - largest MHD generator in the world) are the only type of MHD generators have found real practical applications. The enthalpy extraction was reached at the level above 10 percents (TRI NITI headed cooperation). The experience accumulated in this field could be beneficial for MHD aerospace applications as a high power density MHD energy conversion in supersonic flows.

The natural gas combustion products MHD generator developed for base load electrical power generation has demonstrated the electrical power output about 20MWe in short duration, and from 5 to 10 MWe in long duration test runs both at the IVTAN pilot MHD power plant U-25 of 300 MWth. The enthalpy extraction was demonstrated at the level of several percents (IVTAN was a leading organization). The experience of the long duration operation of segmented electrode MHD channels under moderate Hall effect conditions is the undoubted value in MHD control of internal flows and for on-board MHD electrical power generation.

The study of non-equilibrium MHD generators has resulted in a deep understanding of the physical phenomena including the ionization instability problem that is most important in defining the performance of such an MHD energy conversion. In physical experiments with a shock tube driven noble gas MHD generator the enthalpy extraction was demonstrated at the level above 30 percents. (Kurchatov' institute). Japanese colleagues have demonstrated the

highest level of the enthalpy extraction of about 40 percents in late 80th. The physics of the non-equilibrium ionized non-seeded gases in MHD channels studied in particular in Ioffe Physical-Technical Institute are extremely important for many recently proposed techniques to provide the electrical conductivity of oncoming airflow at hypersonic vehicles. The concept of non-uniform conducting flow MHD generators is especially attractive for various aerospace applications.

Considering the on-board electrical power generation the multi pole external MHD generator was preliminary analyzed that has shown rather promising prospective of MHD energy conversion method to reach the multi-megawatt level of power extraction [12]. The estimation of the MHD interaction for thrust vectoring through the boundary layer control in over-expanding nozzle has revealed also the attracting features of MHD [13].

At that time the desirable experimental program for aerospace MHD study was proposed and analyzed [14]. The program was based on utilization of the unique hypervelocity Wind Tunnel with MHD accelerator constructed in TsAGI in 80s by the team of Prof.V.Alferov [15-19]. It was found from the numerical simulation that the facility parameters are acceptable to demonstrate the principal MHD effects useful for future applications in aerospace development.

An important step in the growth of the interest to the non-traditional methods of super- and hypersonic flows control was the first open publications on AYAX concept of hypersonic vehicle, proposed in 80s by Lininets Company in the USSR [20-22]. This concept is based on a complex utilization of non-traditional approaches including Plasma Aerodynamics methods for drag reduction and shock modification; MHD flow control; MHD electrical power conversion of the kinetic energy of oncoming airflow; MHD acceleration; hydrocarbon fuel reforming and some other techniques. One of the anticipated results is to enhance significantly the scramjet performance. IVTAN in cooperation with NASA and LyTec (USA) has performed pioneering thermodynamic analysis of AYAX concept in respect to the scramjet operation map [23-26] and confirmed that the concept is in principle correct. From the other hand it was found, that the practical realization and especially in the originally proposed scheme is hardly possible due to relatively high role of dissipation typical of the real MHD devices. Nevertheless the stimulating impact of the AJAX concept on the contemporary MHD aerospace applications study is extremely high.

Concluding the review of the preliminary stage of the MHD part of Magneto-Plasma Aerodynamics another interesting branch should be mentioned – MHD assisted mixing, ignition and combustion control in non-premixed co-flow stream. The origination point of this problem is the classical MHD generator study related to the special type of MHD generators with non-uniformly conducting flows. In such of MHD generator proposed in earlier 60s the flow consists of relatively small fraction of electrically conducting fluid separated by large fraction of non-conducting gases expanding in the channel and working against the conducting layers or clots decelerated by magnetic field. The detailed study of the interaction between conducting and non-conducting fraction of the flow has revealed the important role of the turbulence mixing of such a system especially intensive in the presence of non-potential body force $\mathbf{j} \times \mathbf{B}$ [27-30]. Being negative for MHD performance of the considered MHD generator type this mechanism could be useful to intensify mixing of air and fuel streams in high-speed combustors.

Thus, at the preliminary stage of the analysis of MHD potentiality in aerospace applications three main tasks were formulated:

- ❑ MHD flow/flight control to optimize the momentum and energy flux to the vehicle surface;
- ❑ MHD on-board electrical power generation and trust production;
- ❑ MHD assisted mixing, ignition and combustion control.

2. Organization

The current activity in MHD energy conversion is now coordinated by Scientific Council for Direct Energy Conversion (SCDEC) of Russian Academy of Sciences. The chairman of SCDEC is Prof.V.Batenin, director of the Institute of High Temperatures (IVTAN) of Russian Academy of Sciences. There is no special government budget supporting the MHD studies in Russia. However, recently Russian Academy of Sciences has launched several national wide research programs for fundamental studies in different areas. One of then, *Program #20 Studies on Electrical Discharge Effects in High-Speed Gas Flows* includes the most topics of MHD aerospace applications. The scientific co-coordinator of the RAS Program # 20 is academician G.G.Chernyi (Institute of Mechanics of the State University, Moscow). A few small-scale programs on MHD aerospace applications are supported by Ministry of Defense and Ministry of Science and Technology as well.

Since 1999 IVTAN under monitoring of Scientific Council for Direct Energy Conversion (SCDEC), Scientific Council for Fluid Mechanics (SCFM), and Scientific Council for Low Temperature Plasma (SCLTP) all of Russian Academy of Sciences (RAS) and sponsorship of ILG MHD, European Office of Aerospace Research and Development (EOARD), Technical Committee of Plasmadynamics and Lasers Conference of AIAA (PDL TC) organizes the annual International Workshop on Magneto-Plasma Aerodynamics in Aerospace Applications (WSMPA) with about 75-80 papers presented. The next 6th WSMPA-6 is preliminary scheduled for May 2005 in Moscow and will be collocated with 15th International Conference on MHD Energy Conversion (ICMHD-15) organized by ILG MHD.

Besides of these forums the workshop *Thermo Chemical Processes in Plasma Aerodynamics* TCPPA organized by Holding Company Leninets, St.Petersburg plays the important role in forming of MPA and MHD aerospace applications development. The last TCPPA-3 was successfully held on 28 – 31 July 2003. The Russian work is usually wide presented at the winter and summer Aerospace Science Meetings of AIAA and Weakly Ionized Gas Workshops in USA.

Academics, educational and industrial organizations contribute now into the MHD study efforts in Russia with approximately equal portions.

The main participants are:

Academics - Institute of High Temperatures (IVTAN, Moscow), Ioffe Physical-Technical Institute (IPTI, St.Petersburg), Institute of Thermo-physics of Extreme States, Institute of Problems in Mechanics (IPM, Moscow), Institute of Applied Physics (IAP RAS, Nizhny Novgorod) all Russian Academy of Sciences, Institute of Theoretical and Applied Mechanics of Siberian Branch of RAS (ITAM, Novosibirsk);

Educational - Moscow Institute of Physics and Technology (MPTI, Dolgoprudny), Moscow State University (MSU, Moscow), Moscow Aviation Institute (MAI, Moscow), Bauman

Technical University (MTU, Moscow), Krasnoyarsk State Technical University (KSTU, Krasnoyarsk).

Industry - TsAGI, CIAM, TsNIIMash, TRINITI, Leninets.

MHD activity in Russia develops under effective national and international cooperation. The international cooperation involves in particular EOARD/AFOSR, LyTec, the Boeing Co, and Rockwell (USA).

3. MHD Flow Control

3.1 External Flow Field Control / Heat Flux Management (IVTAN, TsAGI, CIAN, TsNIIMash, MPTI)

Starting from 1997 this topic is one the most intensively studied by IVTAN, TsAGI, and CIAM team in co-operation with EOARD and LyTec(USA). The study includes both experiments and numerical simulation. At this stage the study is characterized as a fundamental study with the accent to understand the main MHD interaction mechanisms at a body in hypersonic flows. The simplest classical aerodynamics bodies are used: a circular cylinder and a wedge (see Fig.2).

2D configurations are chosen to simplify and increase the reliability of the adequate numerical simulation. The experiments are performed at MHD WT of TsAGI. The test section and flow cross-section are limited in size. The available model sizes are of 1-2 cm in diameter. Such a small size reduces significantly the MHD interaction parameter defined as the ratio of the integral body force times characteristics length (here it is ~ .01m) to the dynamic pressure that is not higher than 10^4 Pa under given experimental conditions (the
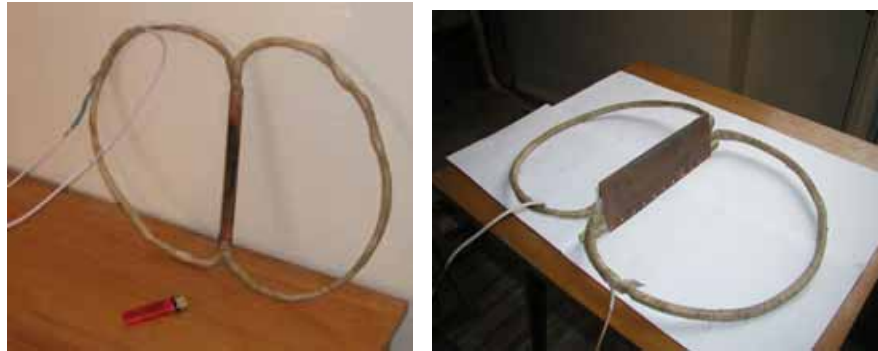
Figure 2 Circular Cylinder (left) and Single Angle Wedge Models used in MHD External Flow Control Experimental and Theoretical Studies (IVTAN-TsAGI-CIAM team

stagnation pressure measured behind the bow shock is about 8000 Pa. The magnetic field in the case of circular cylinder is created by a pulse (2 msec duration) axial current providing the level of 1-2T at the cylinder surface. The prediction made for a perfect gas flow had shown very optimistic results in bow shock stand-off distance increasing and corresponding to that peak heat flux reduction [31] that could not be directly confirmed by experiment [32]. The detailed analysis has revealed a number of 'real' effects, such as finite rate chemistry, non-equilibrium gas flow through the secondary nozzle, the Hall effect dominating role, and the poor electrical insulation along the flow train of the facility [33-34].

At the same time the strong wake interaction effect is observed and properly predicted. Extrapolations to the flight conditions typical of re-entry mission of a body with characteristics size about 1m made with numerical models validated by MHD WT experiment have shown the significant heat flux reduction in the vicinity of upstream critical point of a blunt body [35] Fig.3.

The experimental and theoretical study of the MHD interaction at a wedge in the same flow has been recently started. The first results have shown the significantly stronger MHD interaction that is probably due to larger characteristics length of the interaction region (~ by the order of magnitude) [36]. In Fig.4 the comparison of the experimental results (spectral
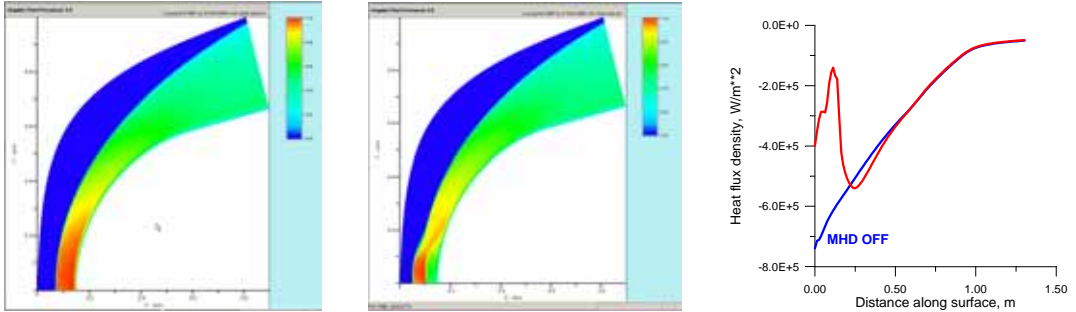
Figure 3 Re-Entry MHD Interaction Evaluation. Temperature Distribution for MHD-off (left) and MHD-on (center) operation; Corresponding Heat Flux Distribution along the Flow (right).

filtered imaging of the flow field) for MHD-off and MHD-on cases is presented.

The third recently tested model composed of a wedge and a plate above it simulates a hypersonic in-take configuration. In this experiment the potentiality of the MHD interaction to provide the in-take flow control to fitting the primary oblique shock to the cowl lip.
 The analysis the MHD interaction effect on the flow over a wedge has been recently conducted by MPTI team [44]. The important peculiarity of this study is the simulation of e-beam ionization of airflow to provide acceptable level of the electrical conductivity of oncoming airflow. The simplified model of e-beam ionization is developed basing on the authors preceding results of the accurate kinetics of e-beam ionization used in MCC [44].
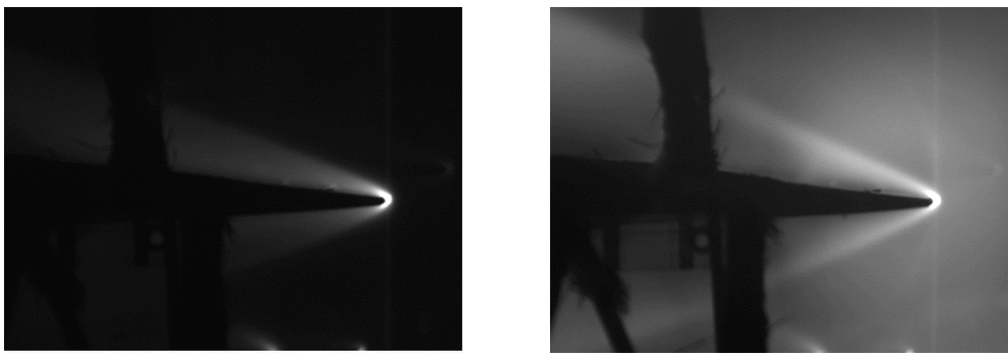

Figure 4 Flow over a wedge. MHD-off (left), MHD-on (right)

One of the important results obtained in paper [44] is that a shock-free MHD flow deceleration has been demonstrated. However, it was found that the stagnation pressure losses are very close to the case of the normal shock losses under similar conditions.
The flow fields calculated for MHD-off and MHD-on cases are compared in Fig.5. The main results are summarized as With an S increase from 0.015 up to 0.05 the oblique bow shock

transforms into two segments with different slope. Further S increase up to 0.2 leads to separation of these two segments, weakness of the bow shock and formation of a severe hanging shock. For these S values, shock-free deceleration of the flow occurs in the MHD interaction region.

The main feature of MHD decelerated flow is the dramatic decrease of the stagnation pressure. For $k=0$, $S\approx0.2$ the stagnation pressure downstream of the MHD interaction region is equal to the stagnation pressure behind the normal shock.

For the same oblique bow shock deviation obtained by different combination of S and k parameter the stagnation pressure downstream of the shock is approximately the same regardless of the S and k combination. The ionized region location does not substantially influence this stagnation pressure as well.
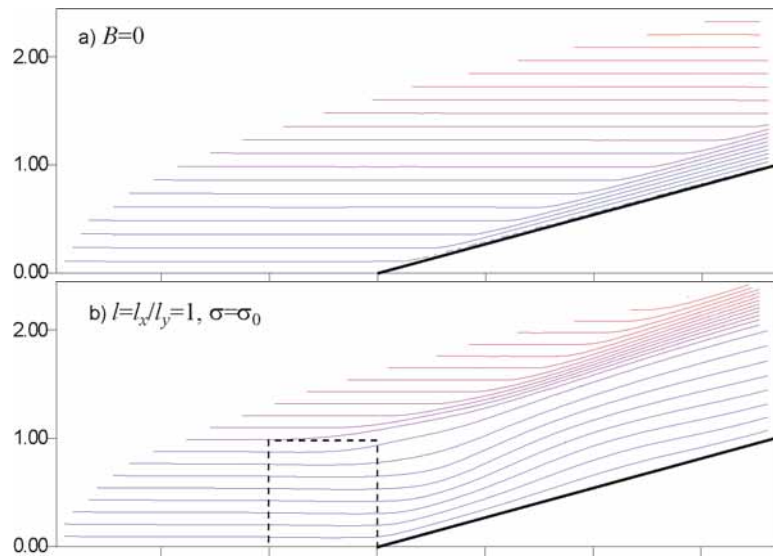
Figure 5 Streamlines for N=0.23 (b) compared to the flow over the wedge without MHD effects (a); σ_0=1.15 S/m.

3.2 Internal Flow Field Control (Ioffe PTI)

Ioffe Physical-Technical Institute RAS works the various aspects of MHD interaction effects for aerospace applications during the last decade [48-89]. Having a great experience in studies of non-equilibrium MHD generators working with non-seeded noble gases IPTI group started the experimental investigation of MHD effects for aerospace applications with noble gas flows driven by shock tubes. Therefore, the main attention is paid to the fundamental aspects of MHD rather then to solving practical problems. The real flight conditions are simulated by MHD interaction parameter, Mach number, Hall parameter.
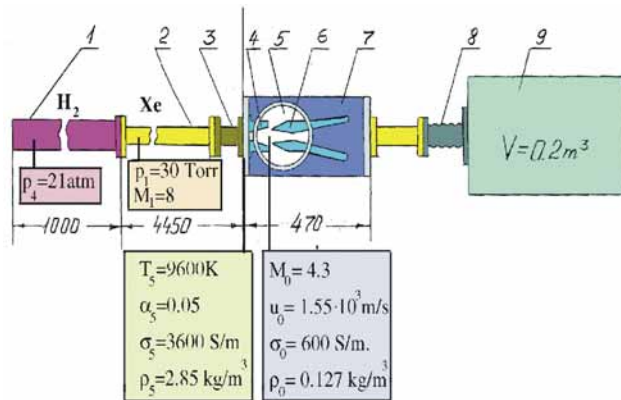
7

Figure 6. Scheme of the experiment at Small Shock Tube: 1 is high-pressure chamber, 2 is low-pressure chamber, 3 is measurement section of a low-pressure chamber, 4 is acceleration nozzle, 5 is optical window, 6 is diffuser model, 7 is vacuum chamber, 8 is Sylphon, 9 is exhaust tank.
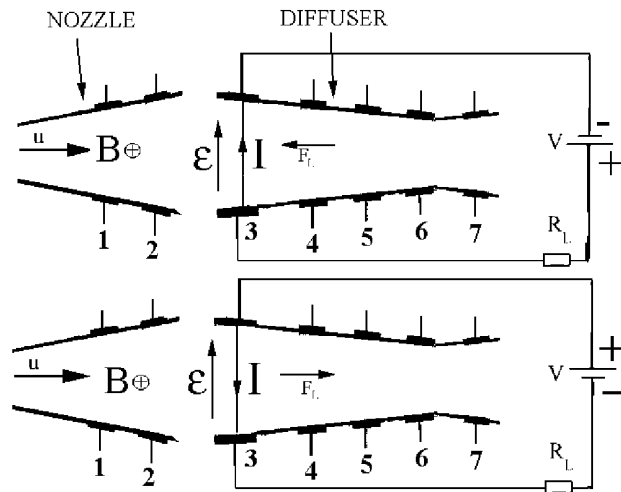

Figure 7. Scheme of current localization.

a) deceleration regime. b) acceleration regime. Figures are numbers of electrodes. The arrows indicate directions of the electric current I, electromotive force ε, and ponderomotive force F_L.

8

The Small Shock Tube facility shown schematically in Fig.6 is used for detailed study of the shock wave structure modification by MHD interaction. The configuration of the MHD
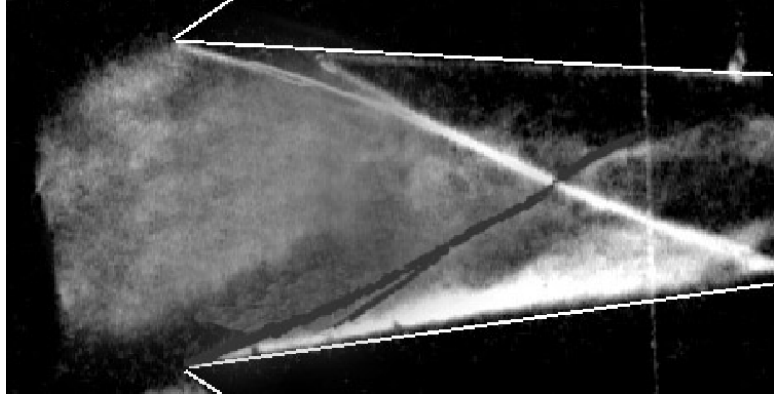
Figure 8. *Examples of changes in shock-wave configurations exposed to electric and magnetic fields.*
a) V=0, B=0;   b) V=120V, B=0;
c) V=125V, B=1.3T - deceleration regimes.
d) V=-150V, B=1.3T - acceleration regime.

interaction section is presented in Fig.7. Due to low level induced voltage the external electrical field was typically applied to provide the desirable current (and correspondingly, MHD interaction) level. The effect of MHD interaction is studied by the modification of the oblique shock wave created at the convergence diffuser. The most sensiotive indicator found is the location of the shock intersection point. The typical result is illustrated in Fig. 9.

Experimental study of the MHD effect on the boundary layer separation at a compressor corner is conducted at Big Shock Tube facility. The MHD interaction level is provided by the external power supply. It was found that such an interaction has strongly influenced on the flow near separation region.

The significant component of these studies is the numerical simulation accompanying the physical experiments. The sophisticated numerical 2D/3D model based on full Navier-Stokes equations, electrodynamics equations for low magnetic Reynolds number, generalized Ohm law with Hall effect included, and electron energy equation has been developed. The numerical simulation provides additional valuable information helping to understand the nature of the observed results. The satisfactory correlation between experiments and simulation is reported.

3.3 MHD Boundary Layer Control (IVTAN, Keldysh' Center, ITES)

The MHD boundary layer control has been considered several years ago [13] for the purposes of the possible trust vectoring. The main idea was to use controllable boundary layer separation process. For the first rough estimation the simplified physical model of MHD induced separation was developed based on the rather conventional gas dynamics approach. The momentum equation is rewritten in form similar to non-MHD interaction. The body force effect could be treated therefore as an effective positive pressure gradient. With such a model several cases of the MHD boundary layer separation have been analyzed. The interesting result was that the very simple model proposed in that study provided acceptable quantitative correlation with experimental data obtained for supersonic pulse power MHD generator flows. Of course, more study is needed to reach a practically useful results.
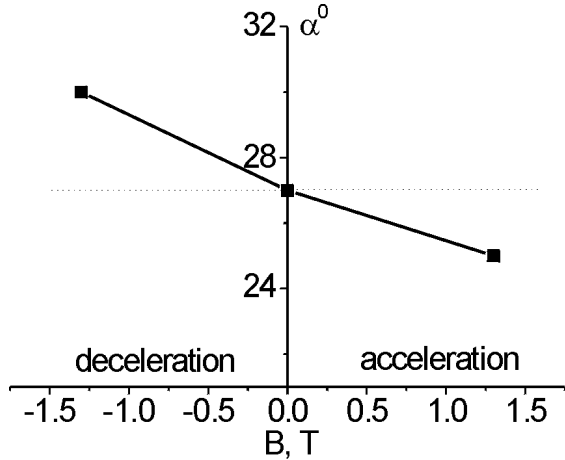
Figure 9. Variation angle α with magnetic field.

4 MHD Assisted Mixing, Ignition and Combustion Control (IVTAN)

This study is supported by EOARD through ISTC during the last three years. The initial period was devoted to the analysis and the development of the adequate numerical models. The problem is that the phenomena are extremely complex involving three disciplines: MHD, diffusive/viscous gasdynamics and multi component chemical kinetics. Again 2D configuration is much more desirable for the analysis. The concept of the process and the preliminary prediction was published in papers [40-41]. The preliminary experimental results are still very scars due to high complexity of the phenomena [42]. The recent efforts in simulation were to develop of the model of the pulse discharge formation at the early stage (0-10 mksec). The process is characterized by strong interaction of chemical kinetics, diffusivity and convection [43]. The comparison of the experimental and analytical results is planned for the next working year starting now.

The process of mixing of gaseous fuel and oxidant is one of fundamental subjects of combustion and propulsion research. It is basically clear that the better (faster) mixing the higher combustion efficiency can be reached under similar conditions. The mixing can be critically important for short residence time combustion systems such as scramjet. One the basic idea used in this study is the Reacting Volume Concept. The reacting volume is formally defined as

$$V_r = \int_{V_o} \sum_i X_{i,O} \cdot \sum_j X_{j,F} dV \; ;$$

where $X_{i,O}$ and $X_{j,F}$ are the mole fraction of i-th oxygen-containing species and the mole fraction of j-th fuel-containing species.

The characteristics of the flow field disturbances created by a body-force $\mathbf{j} \times \mathbf{B}$ is given by the integral vorticity defined as

$$\Omega = \int_{V_o} |\mathbf{rotv}| dV.$$

This parameter represents the integral vorticity of the flow field in the domain that is responsible for the enhancement of the kinematics mixing due to the stretching of a fluid

volume of the media. The mechanism of this process is described in details in our preceding work [27-30].
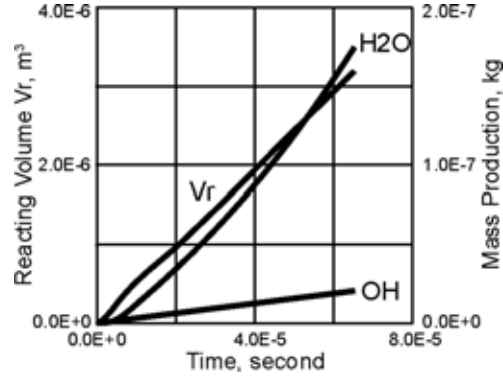

Figure 10. Reacting Volume and Mass production of H₂O and OH vs time

The Fig.10 demonstrates the strong correlation between the reacting volume value and the rate of the combustion products (H_2O and OH) formation. The experimental study of the physical processes involved into the MHD enhanced mixing, ignition, and combustion control is started.
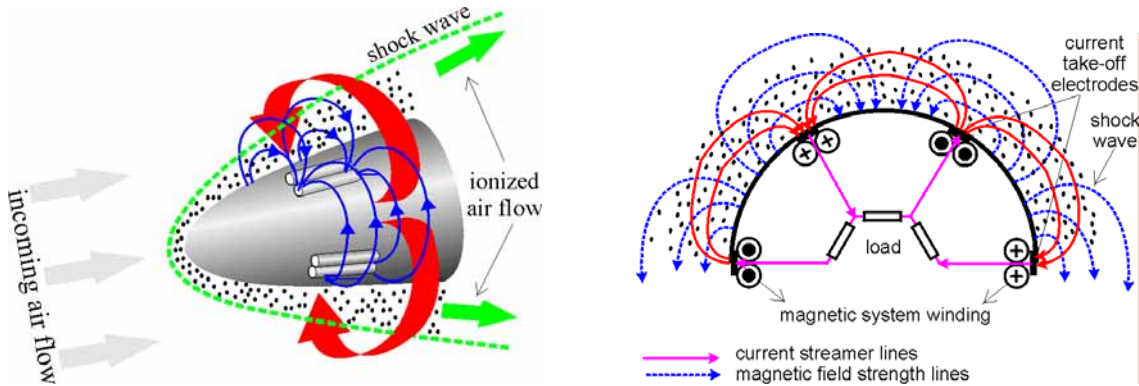

Figure 11. The schematic of the multi-pole magnetic system installed on a hypersonic spacecraft.

5 MHD On-Board Electrical Power Generation

5.1 External MHD Generator -Re-Entry Configuration. (IVTAN)

In the concept considered the magnetic system is assumed to be simulated by one- or two-wind coils zigzag, shaped (see Fig.7). This winding system provides a multi-pole magnetic induction distribution. The depth of the significant magnetic field penetration into the flow in normal-to-surface direction is defined by, the period size of the winding in azimuthal direction

Considering the hypersonic viscous shock layer as the most probable field for MHD influence, one can hypothesize that the most preferable winding configuration is that in which the characteristics thickness of the HVSL is used as the estimation for the half period size. It

is assumed implicitly that the flow direction size of the winding considered is typically much greater than the azimuth period.

Two typical MHD interaction patterns might be considered. The first is when the interaction occurs in the vicinity of a flow directed portion of the winding. (no even/odd difference). (Because of aforementioned remarks on size ratio this case is much more important.) The second pattern is when the flow in the vicinity of an azimuthal portion of the winding. Both are considered in analysis presented in [3,4,6]. It is notable that such a re-entry MHD generator uses first of all the kinetic energy of the moving vehicle mass, and for the velocities above 7 km/sec the potential power stored in the unit mass is much higher than for any fuel.

5.2 Internal MHD Generator - Propulsion Flow Train Configuration. (Leninets, MAI, IVTAN-TsNIIMash-CIAM, Ioffe PTI)

On-board MHD generator imbedded into the rocket engine nozzle
The interesting MHD generator was proposed and studied at Moscow Aviation institute several years ago [45-47]. On-board the electrical power generation with an MHD generator built-in an rocket engine was considered. In the recent paper [47] an electrical power generating system has been proposed and analyzed. The MHD generator proposed is built in the supersonic nozzle of an rocket engine utilizing combustion of the cryogenic fuel — $H_{2,liquid}$ and $O_{2,liquid}$ under the oxygen enrichment equal to 0.8. The total thermal input assumed is to be equal to 2000MWth. The combustion chamber pressure and temperature are 5MPa and 3500K consequently. At the MHD generator inlet flow parameters are T=2600K and p=.37MPa. In order to provide the electrical conductivity need for effective MHD interaction under conditions considered the flow is to be seeded by alkali metal (Cs). It should be noted that seed injection is <u>design</u> to inject seeding material into the MHD interaction region which in the case considered occupied a layer near the wall. The thickness of the layer is approximately equal to intercoil distance in the athimutal direction. In this case the inlet conductivity estimated as high as 15S/m. Magnetic field was provided by 3 or 5 -pair induction coils of racetrack type, located just under the nozzle wall surface. The magnetic induction in middle location on the wall surface was from 1T to 1.5T depending on the number of coil pair used. The length of MHD generation region (equal approximately to cod length) was about 0.6m. The optimization of the magnetic system proposed results in the rather optimistic values of specific parameters of the MHD system. For example, the specific mass being equal to the ration of total MHD generator mass to the electrical power produced has been reported as low as .0036-.002 depending on the magnetic system used. The weight of the magnetic system and nominal electrical power output of the MHD generator proposed are equal consequently. The principal scheme of the proposed MHD generator is presented in Fig.12.
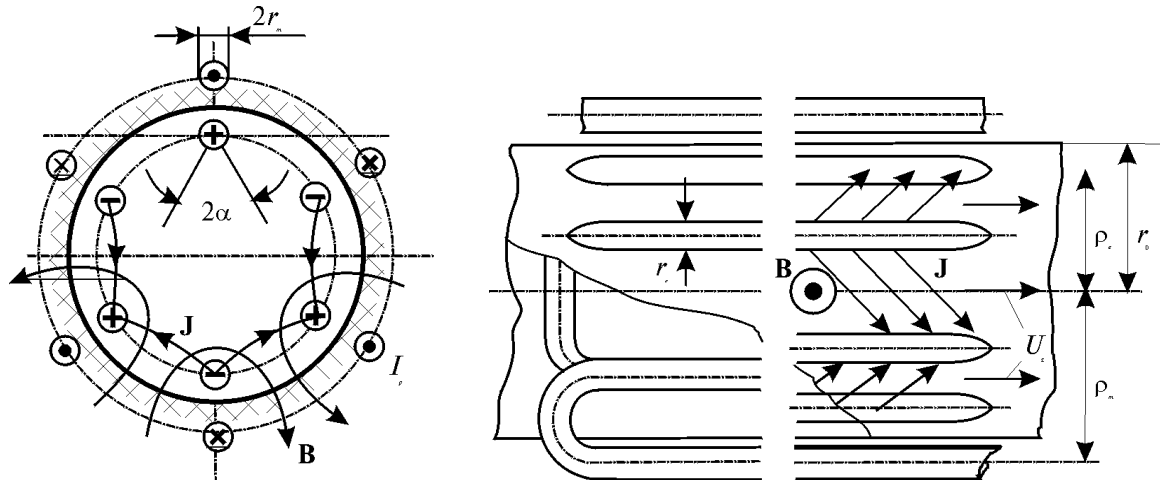
Figure 12. Schematic of Multipole MHD Generator Built-in Rocket Engine - cross-section view (left) and – side view (right)
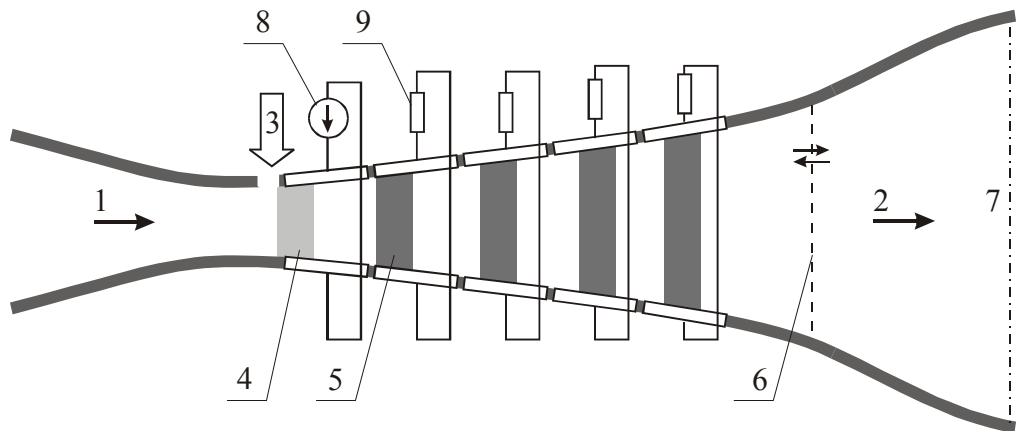

Figure 13. Scheme of MHD generator. 1 – stationary flow of unseeded noble gas; 2 – working medium flow with periodical disturbances; 3 – electron beam; 4 – weakly ionized plasma clot; 5 – recombining plasma layer; 6 – shock wave; 7 – outlet cross section with constant stagnation pressure; 8 – high voltage source; 9 – load.

MHD electrical power generation experiment

The experimental study of the MHD electrical power generation under conditions simulating on some parameters of the conditions of the flow in scramjet flow-train down-*stream* of the combustor is partially supported by the Boeing Co. The experiments are performed on a huge Shock Tube of TsNIIMash . The working media – combustion products of oxygen and hydrogen under the stagnation temperature about 3500K, is generated in the shock tunnel by the ignition of the H2-O2 combustible mixture and expands through the supersonic nozzle into the MHD channel. The MHD channel is a Faraday type segmented MHD channel of .45m length and .025 by .04 m^2 inlet cross-section, see Fig. 13.

Mach number at the inlet is 1.8 increasing to 2.3 at the exit. The seed of water solution of K$_2$CO$_3$ is used. The convectional iron-core electromagnet provides the 1.6 T magnetic

induction in the MHD channel. The first results have successfully demonstrated the MHD electrical power generation. It was found, however, that MHD interaction is lower than the predicted level. The reasons of this are probably the very cool electrode wall and rather strong fluctuations in the channel flow related to multi reflection of the shock waves from the walls of the high pressure vessel [37-39]. The next series with the significant modification of the plasma generation process and with modified elements of MHD generator flow train is planned for the coming fall.

5.3 Stand-alone MHD Generator (TRINITI)

The data on the development of a multi-purpose primary source of high-power electric pulses on the basis of a pulsed (1s - 10s) MHD generator using a solid plasma-generating propellant (SPP) of a new type with a non-liquid superconducting magnet and a dc electric converter is developed. The structural, electrical and functional schemes of such facility are also given. The work was done for the base design of the 10MW MHD generator with a 5s burning time and an interpulse spacing not less than 30 s. There determined optimal parameters of the following basic elements (units): combustor, capsulated charge of SPP, fast overcharge device, supersonic nozzle, cooled Faraday type MHD channel with continuous electrodes, non-liquid superconducting magnet with cryocooler, electric converter (EC) on IGBT-transistors intended for matching an optimal operating mode of the dc MHD generator with an electric energy storage or directly with a load (output voltage - up to 100kV). The external appearance and layout of basic units and MHD facility in general are presented as well as their performance data which are as follows: mass flow rate $\approx$11 kg/s, stagnation pressure $\approx$ 7 MPa, magnetic flux density $\approx$ 3.5 T, current –14 kA, enthalpy extraction $\approx$14%, power density of MHD channel $\approx$400 MW/m^3, specific energy per SPP mass unit $\approx$ 0.9 MJ/kg, MHD facility mass $\approx$1.9 t, length $\approx$ 2.8m, width $\approx$1m, height $\approx$1m, EC mass $\approx$ 2.1 t, specific mass power and energy density from the EC $\approx$2.5MW/t and $\approx$13MJ/t, correspondingly.

5.4 MHD Space Power Plant for Deep Space Mission (KSTU)

It is shown in this study that space conditions form new requirements to MHD generator. The requirements differ qualitatively from those to a ground power plant. Apparently, beginning from the power level of 1 MWe the MHD generator is the preferable type of power plants. Exactly the MHD generators can make manned missions into deep space real. It is carried out the analysis of two types of MHD generator with non-uniform gas-plasma flow supposed to operate in space. The first type utilizing the "frozen ionization" phenomenon in non-equilibrium plasma clots is well combined with sun radiation concentrators. In such devices the level of specific power about 500 W/kg can be achieved. The second type assumes utilization of equilibrium plasma non-uniformities (T-layers). This type of MHD generator is supposed to work with gas-phase nuclear reactor, and in this combination the level of specific power could be of an order of 1500 W/kg

The power plant will consist (see Fig. 14) of the solar concentrator with mirror film which is given parabolic shape by electrostatic forces, the vortical chamber with pseudo-liquefied bed of ceramic balls that consume radiation energy, the MHD generator that converts thermal energy into electricity, the recuperative tubular heat-exchanger, the heat-exchangers for cooling the working body before it is compressed in the compressor stages with diffusing the thermal energy into space (radiative coolers), the three-stage compressor.

The non-stationary process with non-stationary shock waves may be organized in the non-uniform gas-plasma flow where plasma pistons break the flow and at this produce shock waves. Utilization of KF diatomic gas as the working body results in its plasma being equilibrium. In such self-maintaining equilibrium plasma layer the Joule dissipation must be counterbalanced by radiation losses of energy, which determines the temperature of plasma stabilization 10 about $(20-30) \cdot 10^3 K$. The effect of formation of the stabilized equilibrium plasma clots in the MHD processes has been discovered in the middle 1960-s and it is called as T-layer 11. Characteristic peculiarity of the effect is the fact that the electric conductivity of plasma in the layer reaches the value of 10^4-10^5 S/m, which multiply increases efficiency of the MHD interaction. At certain conditions the magnetic Reynolds number Rm defined from the T-layer parameters may exceed 1. This gives an opportunity to organize the inductive connection between the T-layer plasma and the external load circuit.
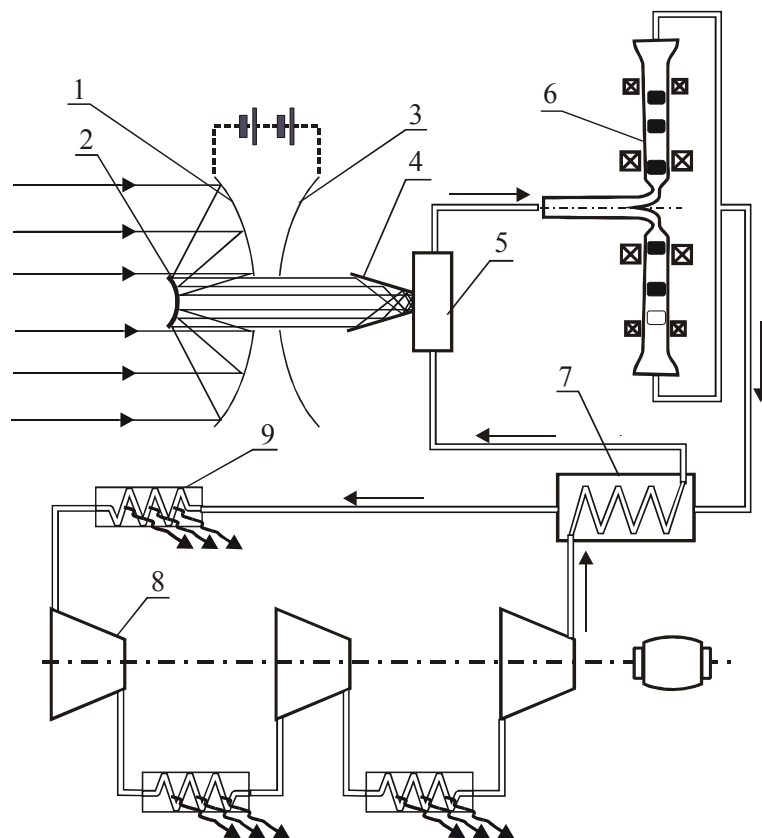

Figure 14. Scheme of power facility. 1, 2 – primary and secondary mirrors, 3 – film with surface electric charge, 4 – funnel of radiarion condensor, 5 - radiation receiver, 6 – MHD generator channel, 7 – recuperative heat exchanger, 8, 9 - compression group with intermediate radiation cooling

The inductive MHD generator arrangement can be represented in accordance with Fig. 15. The generator channel is of a disk shape, and the T-layers form closed current rings in it. The channel is located in the inter-pole cavity of the magnetic circuit. The excitement coil induces the magnetic field. Into a circuit of the excitement coil both the load and the constant EMF source are inserted. From the point of view of electrotechnics the scheme is that of a typical synchronous AC generator; there are just the plasma circuits used instead of the copper coils of rotor.
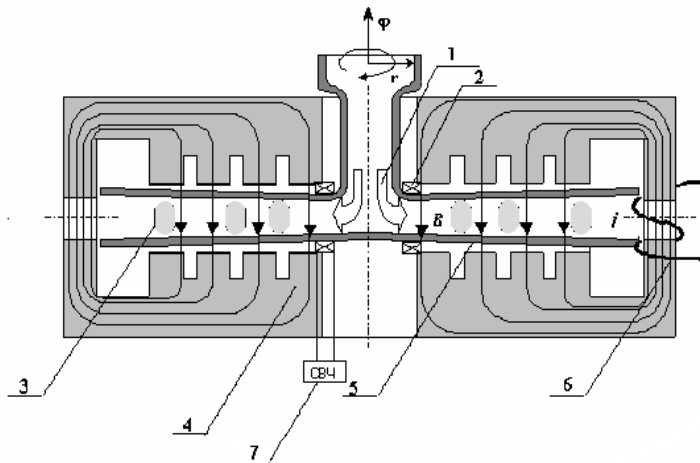
Figure 15. Inductive MHD Generator

6   MHD Enthalpy By-Pass -AYAX Concept (Leninets, IVTAN, ITES)

Nowadays "AYAX" concept is a very popular concept of hypersonic aircrafts development. The analysis of the different aspects of AYAX concept is studied by several groups of Russians researchers. Naturally, that the most significant contribution is provided by Leninets [21,22,95-100]- the original inventor of the concept. The MHD subsystems represent the significant part of the basic technologies [95] included into the concept. It was shown in [96-98] that MHD interaction allows one to increase air mass flow rate at off-design conditions, to increase flow compression in inlet and to increase specific impulse and thrust of scramjet. In order to realize MHD interaction it is necessary to ensure the appreciable electric conductivity of flow. At conditions of hypersonic flight as a rule equilibrium conductivity of a flow is negligible to produce essential MHD interaction in scramjet. Thus it is necessary to put some energy into flow to create nonequilibrium flow conductivity. It is evidently that MHD generator with nonequilibrium conductivity can be realized only in that case, when power spent on flow ionization does not exceed power produced by MHD generator. Such operating mode of system including MHD generator and ionizer we name as a self-sustained mode. Power spent on flow ionization depends on the value of conductivity need to be created, gas-dynamic properties of flow and type of ionizer [97,99]. Power produced by MHD generator depends on the flow conductivity, gas-dynamic properties of flow, MHD parameters and type of MHD generator. Thus conditions at which the self-sustained operational mode can be realized depends upon many factors, such as: location of MHD generator on the vehicle, geometry of scramjet, flight path of the vehicle, MHD parameters, ionizer type and so on.

One of the recent results (Fig. 16) presented in [100] is obtained with the simplified MPCE (Magneto-Plasma-Chemical Engine), schematic shown in Fig.17. The partial optimization and parametric studies allow forming the operational map where the MHD interaction effect in propulsion system is positive, i.e. the specific impulse is higher in compared with reference no-MHD case. As an intermediate important result the statement that the MHD generator placed up-stream of the combustor is more effective in compared with the MHDG located after combustor chamber. The detailed analysis based on the sophisticated 2D viscous
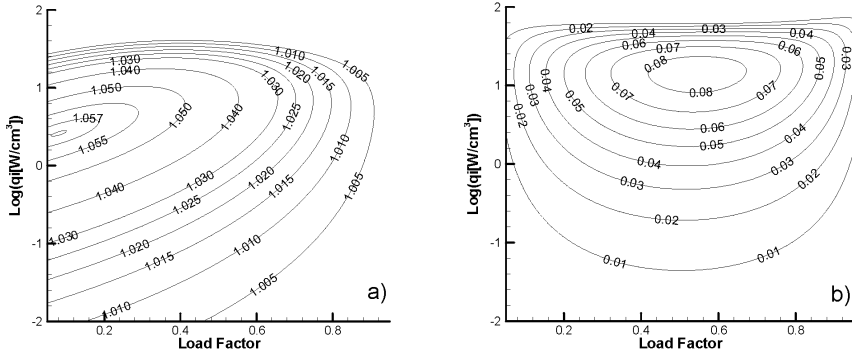
Figure 16. Contours of relative specific impulse (a) and power excess (b) for MPCE with
$\theta_N=15^o$, $M_d=10$, $F_{th}=0.12$. $M_0=6$, $L=2m$, $k_3=1.1$, $B=5T$

calculation of the flow [101] it was demonstrated that in some cases the MHD generator located upstream, of the combustor chamber can provide the highest compression.

At IVTAN the analysis of thermodynamics cycle of the AYAX-type configuration was recently performed. It was found that for thermal equilibrium the MHD devices introduced into the engine flow train could hardly increase the cycle efficiency. As it was indicated by prof.A.Vatazhin [102] (CIAM) the reason is probably the high speed ramjet/scramjet operates in extremely thermal non-equilibrium mode. Therefore, the aim of MHD devices is to provide the conditions suppressing the finite rate kinetics effects. It seems that the more general analysis of the AYAX concept is urgently needed to understand the potentiality of the MHD interaction in improving the propulsion system performance at high Mach numbers.
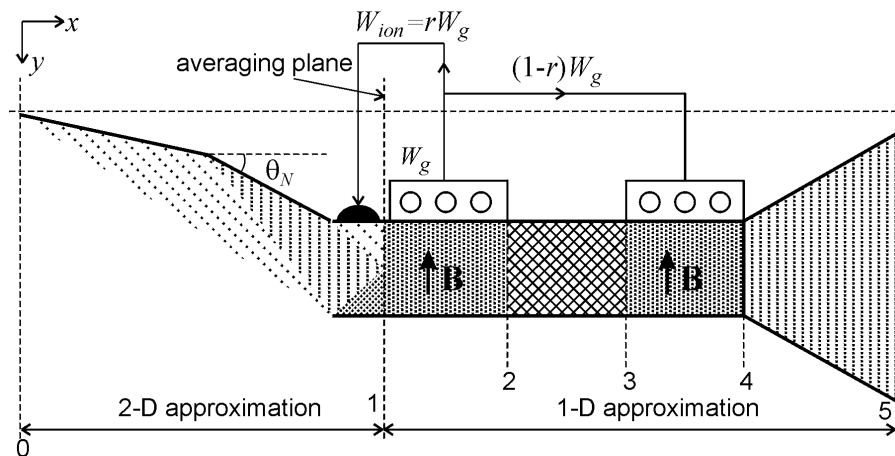

Figure 17 Simplified scheme of MPCE.

7   MHD Acceleration for On-Ground Test Facility (TsAGI)

Experimental Study of Hypersonic Flows

One of the main requirements for experimental study of hypersonic (hypervelocity) flows ($M \geq 12$) on ground test facilities is to provide the similarity of hypersonic velocity and density fields. Another important point in these laboratory studies for hypersonic flow is the real gas effects that become important in high Mach number regimes around complex aerodynamics objects [103].   In Fig.18 the typical stagnation parameters p_{st} and T_{st} needed to reach desirable flow parameters (velocity and density) in the plenum chamber of a hypersonic wind tunnel are plotted.
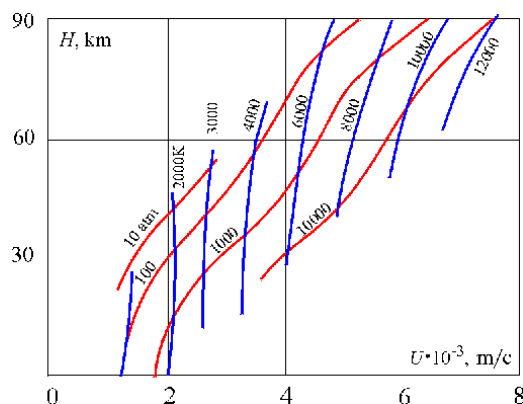

***Figure 18. Inlet wind tunnel parameters needed
for modeling flight conditions and calculated for
adiabatic nozzle expansion***

For extreme test conditions, values of stagnation pressure greater than 1000atm and stagnation temperature greater than 10,000K are necessary. This is a rather great technical problem for realization of a facility capable of simulation of hypersonic flows. Another problem raised in hypersonic experimental studies is the need to simulate the working gas composition in the test section. For these and other reasons, the utilization of an MHD gas accelerator for the experimental study of hypersonic (hypervelocity) flows was proposed many years ago [104-105].

One of the most successful operating MHD hypersonic facilities is located at TsAGI [15-19]. This facility is especially suitable for fundamental experiments to demonstrate MHD flow control. The working media (air) used in the TSAGI facility is seeded with alkali metal and provides elevated conductivity to the air plasma needed to effective achieve an MHD interaction level over a rather wide range of operating parameters.

The TsAGI MHD WT test facility consists of following main elements:

√   source of working (electrically conducting gas with primary supersonic nozzle;

√   tests section with means for locating a tested model in the flow;

√   MHD accelerator with magnetic system;

√   secondary high Mach number nozzle;

√   diagnostics and control system.

A schematic of the TSAGI facility is presented in Fig.19. The electrical power of the facility in the range of operating parameters is p=0.1-2MPa, T=3000K-6000K, with mass flow rate 0.02-0.25kg/s is correspondingly 0.2-2MW. There is capability to provide values of T=5000K and p=20MPa in the source of the hot plasma flow.
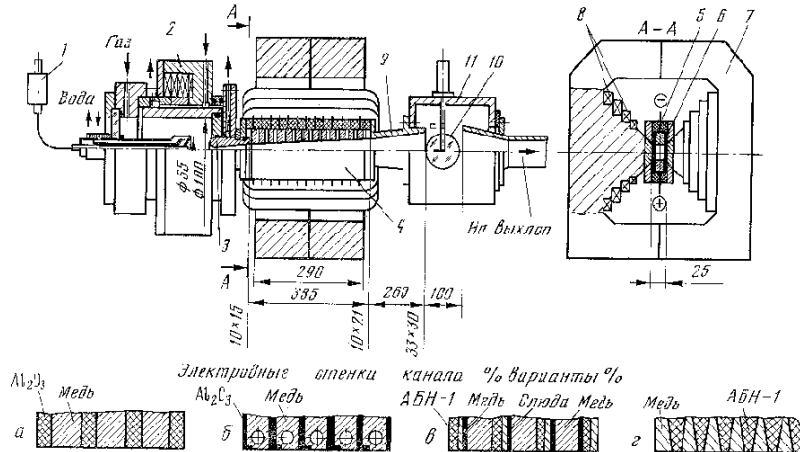

Figure 19. Schematic diagram of the TsAGI MHD WT facility.

The detailed technical and operating, characteristics of this facility are discussed in papers [15-19]. As a rule, experimental runs are carried out with flow of air that is seeded with 1% of K-Na eutectic. The state at the accelerator inlet is T=2700K, u=1900m/s, M=2, static pressure p=0.2-0.5atm depending on air mass flow rate.

Aerodynamic measurements include static pressure distribution in the test section, static pressure at the secondary nozzle exit cross-section, and, the pressure distribution on the model surface in the test section.

Visualization of the hypersonic flow field, shock waves structure and its evolution in time, are also available at MHD facility. One example of the visualization of the flow around a TAV Bor-4 model is presented in Fig. 20.
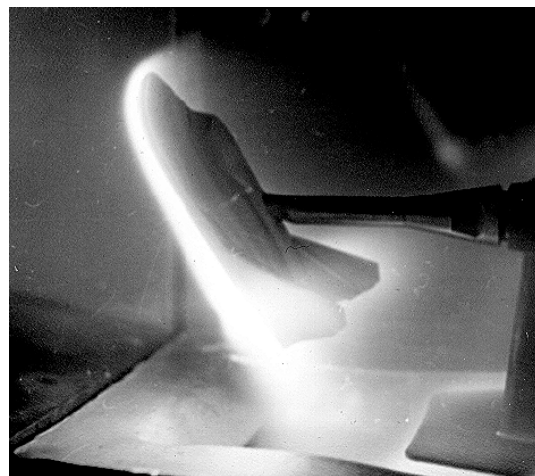

Figure 20. An example of visualization of the hypersonic viscous shock layer- on a TAV model.

At the present time the TsAGI MHD WT facility (Fig.21) is a main experimental tool used for the experimental study of the MHD interaction at the models in hypersonic flows being conducting by IVTAN-TsAGI research team.

***Figure 21. MHD WT Facility in Recent MHD Flow
Control Experiments***

8 Conclusion

The Russian activity in MHD aerospace application research is relatively high.

The complexity of the problem, which is obviously interdisciplinary category, needs more strong and deep coordination or/and more extended budget.

The experimental study in MHD field is relatively expense. There are several facilities available for MHD experimental studies, however the specially designed equipment in urgently needed.

The simulation of the real flight (hypersonic) conditions in on-ground experiments is very serious problem.

The real effects such as finite rate kinetics in airflow, Hall shorting, arcing phenomena on electrodes and many others could be very important and perhaps limiting the MHD utilization.

The experienced accumulated during the preceding on-ground MHD generator studies is rather high value for the MHD aerospace system development.

References

1. A.Kh.Mnatsakanyan, G.V.Naidis, On magnetogasdynamics Effects on Spacecraft Motion in the Earth Atmosphere, - IVTAN Techn.Report #92/11,26 p., Moscow, 1991 (In Russian)

2. E.I.Asinovsky, R.Kh.Amirov, The Analysis of the Development aic MHD Generator Pre-Ionizer, Techn.Report 1255/92, 11,IVTAN, Moscow, 1993 (in Russian)

3. V.A.Bityurin, V.A.Ivanov, A.N.Bocharov et al, Magnetogasdynamics Control of Spacecraft Motion in Upper Atmosphere, Tech,Report IVTAN ANRA #94/3, 37p.,Moscow, 1994 (In Russian)

4. V.A.Bityurin, V.A.Zeigarnik, A.L.Kuranov, On a Perspective of MHD Technology in Aerospace Applications. // AIAA Paper 96-2355, 27th AIAA Plasmadynamics and Lasers Conference, New Orleans, 1996.

5. V.A. Bityurin, J.T. Lineberry, V.G. Potebnia, V.I. Alferov, A.L. Kuranov and E.G. Sheikin, Assessment of Hypersonic MHD Concepts // AIAA 97-2393, 28th Plasmadynamics and Lasers Conference, June 23-25, 1997, Atlanta, GA

6. V.A.Bityurin, A.N.Bocharov, J.T.Lineberry, MHD Aerospace Applications. // International Conference on MHD Power Generation and High Temperature Technologies 1999, Beijing PRC, October 12-15, 1999.

7. Perspectives of MHD and Plasma Technologies in Aerospace Applications, Moscow, March 1999, Institute for High Temperatures, Russian Academy of Sciences V.A.Bityurin (Editor).

8. The Second Workshop on Magneto-Plasma-Aerodynamics in Aerospace Applications, Moscow, April 2000, Institute for High Temperatures, Russian Academy of Sciences

9. The 3rd Workshop on Magneto-Plasma-Aerodynamics in Aerospace Applications, Moscow, April 2001, Institute for High Temperatures, Russian Academy of Sciences V.A.Bityurin (Editor).

10. The Fourth Workshop on Magneto plasma Aerodynamics for Aerospace Applications, Moscow, April 2002, Institute for High Temperatures, Russian Academy of Sciences, V.A.Bityurin (Editor)..

11. The Fifth International Workshop on Magneto- and Plasma Aerodynamics For Aerospace Applications, Moscow, April 2003, Institute for High Temperatures, Russian Academy of Sciences, V.A.Bityurin (Editor)..

12. Lineberry J.T., Rosa R.J., Bityurin V.A., Bocharov A.N., Potebnja V.G. "Prospects of MHD Flow Control for Hypersonics", 35th Intersociety Energy Conversion Engineering Conference, AIAA 2000-3057, 24-28 July 2000, Las Vegas, NV.

13. Bityurin V.A., Gubertov A.M., Ivanov V.A., Kuranov M.L., Okunev V.I. MHD Control Estimation of Supersonic Boundary Layer. // Twelfth International Conference on Magnetohydrodynamic Electrical Power Generation, Yokohama, Japan, October 15-18, 1996, vol.12 p.618.

14. Bityurin V.A., Potebnja V.G., Alferov V.I. On MHD Control of Hypersonic Flows. Planning of Experimental Studies of MHD Effects on Bow Shock. // In 34th SEAM, 1997, June 18-20, USA, Mississippi, p.4.4.1

15. . V.I.Alferov, O.N.Vitkovskaya, V.P.Rukavetz, G.I. Scherbakov, In: Electroarc Gas Heaters, TsAGI Proc, 1978 (Russian)

16. V.I.Alferov, O.N.Vitkovskaya, Yu.S. Ustinov, G.I. Scherbakov, Teplofizika Vysokikh Temperatur, Vol.9, No2, 1971 (see also High Temperatures, 1971).

17. V.I.Alferov, O.N.Vitkovskaya, V.P.Rukavetz, G.I. Scherbakov, Teplofizika Vysokikh Temperatur, Vol.7, No1, 1979 (see also High Temperatures, 1979)

18. V.I.Alferov, O.N.Vitkovskaya, A.P.Rudakova, G.I. Scherbakov, Teplofizika Vysokikh Temperatur, Vol.17, No2, 1979 (see also High Temperatures, 1979)

19. V.I.Alferov, A.P. Labazkin, A.P.Rudakova, G.I. Scherbakov, Application of MHD Accelerators in Hyper-Velocity Experimental Aerodynamics.// Eleventh Intern.Conf. on Magnetohydrodynamics Electrical Power Generation, 1992, Beijing, China, October 12-16, vol.4,p.1308.

20. Novichokv, Niloaly, "Space Wings of Russia and the Ukraine", Echo of the Planet/Aerospace, Moscow, Sept. 1990.

21. E.P. Gurjanov and P.T. Harsha, AJAX: New Directions in Hypersonic Technology, AIAA Paper 96-4609

22. D.I. Brichkin, A.L. Kuranov, E.G. Sheikin, MHD-Technology for Scramjet Control, 8th International Space Planes and Hypersonic Systems and Technologies Conference, April, 1998, Norfolk, VA, AIIAA 98-1642.

23. V.A.Bityurin and J.T.Lineberry, Overview of MHD Applications (MHD Assisted Hypersonic Flight), In: Plasma/ Electromagnetic Advanced Propulsion Workshop, 10-11 Dec., 1997, UTSI, TN

24. J.Cole, J.T.Lineberry, V.A.Bityurin. MHD Augmented Hypersonic Propulsion Systems // Workshop "Perspectives of MHD and Plasma technologies in Aerospace Applications", March, 24-25, IVT RAS, Moscow, 1999, p.22-30

25. V.A.Bityurin, A.I.Klimov, S.B.Leonov, A.N.Bocharov, J.T.Lineberry, Assessment of a Concept of Advanced Flow/Flight Control for Hypersonic Flights in Atmosphere // AIAA 99-4820, 30th Plasmadynamics and Lasers Conference, 28 June – 1 July, 1999/Norfolk,VA.

26. V.A.Bityurin, J.T.Lineberry, R.J.Lichford, J.W.Cole. Thermodynamic Analysis of the AJAX Propulsion Concept (invited) // AIAA 2000-0445, 38th AIAA Aerospace Sciences Meeting, 10-13 January 2000/Reno, Nevada.

27. Bityurin V.A., Potebnia V.G., Tseskis A.L. Evolution of a Current Carrying Plasma Clot in Turbulent Flow. // 33rd SEAM, The University of Tennessee Space Institute, USA, 12-15 June, 1995, p.VI.7-1.

28. Bityurin V.A., Potebnia V.G., Tseskis A.L. On Evolution of Plasma Clot in Media with stochastic Flow Field, // JTP Letter, 1996, т.22, №2, с.80-83.

29. Bityurin V.A., Potebnia V.G., Tseskis A.L. Energy Transfer in Gas-Plasma Flows with Current Carrying Clusters. // Magnrtohydrodynamics, 1997, т.33, №3, с.297-305.

30. V.A.Bityurin, V.G.Potebnia, A.L.Tseskis, Energy Transfer in MHD Flows with Current Carrying Clots. // 17th Symposium on the Efficient Use of Energy and Direct Power Generation, Sapporo, Japan, March 15-17, 1995, p.2.10.

31. J.T.Lineberry, V.A.Bityurin, A.N.Botcharov, D.S.Baranov, A.B.Vatazhin, V.I.Kopchenov, O.B.Gouskov, V.I.Alfyorov, A.S.Boushmin. Cylinder with Current in Hypersonic Flow // The 3rd Workshop on Magneto- and Plasma- Aerodynamics for Aerospace Application, IVTAN, Moscow, 24-26 April, 2001, pp.15-25

32. V.A.Bityurin, D, A.N.Bocharov, A.V.Vatazhin, V.I.Kopchenov, O.B.Gouskov,, V.I.Alferov, A.S.Bouhsmin, J.Lineberry, Theoretical and Experimental Study of MHD Effects at a Circular Cylinder in a Transversal Hypersonic Flow, AIAA Paper 2002-0491, 40th AIASA Aerospace Aciencis Meeting, 14-17 Junuary 2002, Reno, NV.

33. V.A.Bityurin, D.S.Baranov, A.N.Bocharov, S.S.Bychkov, A.Ya.Margolin, A.D.Tal'virsky, V.I.Alferov, A.S.Bouhsmin, A.V.Podmazov, V.S.Tikhonov. Experimental Study of MHD Interaction at a Cylinder in Hypersonic Flow // The 4rd Workshop on Magneto- and Plasma- Aerodynamics for Aerospace Application, IVTAN, Moscow, 9-11 April, 2002

34. Lineberry J.T., Bityurin V.A., Bocharov A.N., MHD Flow Control Studies. Analytical Study of MHD Flow Interaction Around a Right Circular Cylinder in Transverse Hypersonic Flow. In: Proc.of 14th Inter.Conf. on MHD Electrical Power Generation and High temperature Technologies, Maui,Hawaii, May 20-23, 2002, pp135-149.

35. V.A.Bityurin, A.N.Bocharov, A.V.Krasilnikov, A.V.Mikhailov, Experimental Investigation of MHD Electrical Power Generation, AIAA Paper 2003-0377

36. V.A.Bityurin, A.N.Bocharov, J.T.Lineberry, C.Sukhomel, Studies on MHD Interaction in Hypervelocity Ionized Air Flow over Aero-Surface, 34th AIAA Plasmadynamics and Laser Conference, 23-26 June 2003, Orlando, Florida

37. V.A.Bityurin, A.N.Bocharov, A.V.Krasilnikov, A.V.Mikhailov, MHD Electrical Power Generation Driven by Hydrogen/Oxygen Combustion, 5th International Workshop on Magneto-Plasma Aerodynamics in Aerospace Applications, IVTAN,Moscow, 7-10 April 2003

38. A.B.Vatrazhin,O.V.Gouskov,V.I.Kopchenov, V.A.Bityurin, Numerical Investigation of Supersonic Flow Structure in MHD Duct with Wall Irregularities, 5th International Workshop on Magneto-Plasma Aerodynamics in Aerospace Applications, IVTAN,Moscow, 7-10 April 2003

39. V.A.Bityurin, A.N.Bocharov, Advanced MHD Assisted Mixing of Reacting Streams // AIAA 2001-0793, 39th AIAA Aerospace Sciences Meeting and Exibit, 8-11 January 2001, Reno, Nevada.

40. Bocharov A., Bityurin V., Klement'eva I., Leonov S. Experimental and Theoretical Study of MHD Assisted Mixing and Ignition in Co- Flow Streams // Paper AIAA 2002- 2228, 40th AIAA Aerospace Sciences Meeting & Exhibit, 14-17 January 2002/ Reno, NV, P.8

41. A.N.Bocharov, S.B.Leonov, D.S.Baranov, I.B.Klement'eva, V.A.Bityurin. On MHD Enhanced Mixing and Combustion in Co-Flow Streams // The 4rd Workshop on Magneto- and Plasma- Aerodynamics for Aerospace Application, IVTAN, Moscow, 9-11 April, 2002

42. A.N. Bocharov, V.A. Bityurin, I.B. Klement'eva, S.B.Leonov,A Study of MHD Assisted Mixing and Combustion AIAA Paper -2002-5878 Maui,Hawaii, May 20-23, 2002, pp135-149

43. V.A.Bityurin, A. Bocharov, I. Klement'eva, S. Leonov, A Study of MHD Assisted Mixing and Combustion // Paper AIAA-2003-0378, 41st Aerospace Sciences Meeting and Exhibit, Reno, Nevada, 6-9 Jan 2003

44. Soloviev V.R., Krivtsov V.M., Konchakov A.M., MalmuthN.D.,"Modeling of the MHD Effects in 2-D planar Flow over a Wedge", In: Proc. of 14th Intern. Conf. On MHD Electrical Power Generation and High Temp. Technologies, Maui, Hawaii, May 20-2, 2002, pp. 97-112

45. K.I.Kovalev, T.A.Markina, Power Facility with an Build-in Multipole MHD Generator, High Temperatures, vol.33, No3, 1995

46. Kovalev L.K., Larionoff A.E., Poltavets V.V., Kovalev K.I. Theoretical and Experimental Studies of Faraday Multipole MHD Generators. In: 11th Int.Conf. on MHD Electrical power Generation, China, 1992.

47. Kovalev L.IC, Kovalev K.L Faradeevskie mnogopolusnye magnitigidrodinamicheskie generatorv postojannogo i peremennogo toka. (in Russian). Electrichestvo, 1990, No.7.

48. 13. R. V. Vasil'eva, A. V. Erofeev, E. A. D'yakonova, T. A. Lapushkina, and S. A. Poniaev. Ionizational instability in an ionized inert gas flowing in a magnetic field.

49. Phys. Rev. E, V. 63, 036402, 2001.

50. R.V.Vasil'eva, A.V.Erofeev, T.A.Lapushkina, and E.A. D'yakonova. Formation of Shocks at the Interaction of a Supersonic Flow with Magnetic Field. - AIAA Paper, 2000, No 2000-2671.

51. Vasil'eva R.V., Erofeev A.V., Zuev A.D., D'yakonova E.A., Markhotok A.A. Characteristics of Pure Noble Gas Hall MHD Generatore in Environs of Critical Magnetic Field. Proc. of 32nd Symposium on Enginering Aspect of Magnetodynamics, Pittsburgh, USA, 1994. P.10.1-10.5.

52. Vasil'eva R.V., Erofeev A.V., Zuev A.D., Lapushkina T.A., D'yakonova E.A., Marhotok A.A. Parameters of Pure Noble Gas Disk MHD Channel at Developed Ionizational Instability. Proc. of 33rd Symposium on Engineering Aspects of Magnetohydrodinamics. Tullahoma, USA, 1995, P.11.4-1-11.4-5.

53. A.V. Erofeev, R.V.Vasil'eva, A.D.Zuev, T.A.Lapushkina, E.A.D'yakonova and

54. A.A. Markhotok. Experimental Comparative Studies on the Hall and Faraday Channels with Ionizationally Unstable Inert Gas Plasma. Twelfth Internetional Conference on Magnetohydrodynamic Electrical Power Generation. Yokohama, Japan, October 15-18, 1996, Vol.1, p.74-82.

55. . A.V.Erofeev, T.A.Lapushkina, S.A.Poniaev, R.V.Vasil'eva. Experimental Determination of Electrical Parameters of Anisotropically Conducting Medium in MHD Channel. Proc. of the 14th International Conference on MHD Electric Power Generation and High Temperature Technologies, 2002, Maui, Hawaii, May 22-23, p. 381-386.

56. E.A.D'yakonova, A.V.Erofeev, T.A.Lapushkina, R.V.Vasil'eva. On Characteristics of MHD Channel with Ionizationally Unstable Inert Gas Plasma. Proc. of International Conference on MHD Power Generation and High Temperature Technologies 1999, Beijing PRC, October 12-15, 1999, Vol. I, p. 299-307.

57. A.V.Erofeev, R.V.Vasil'eva, T.A.Lapushkina, A.D.Zuev. On Possibility of Pre-Ionized Air Using in an MHD Generator on Aerospace Plane. Proc. of 34th Symposium on Enginering Aspect of Magnetodynamics, Starkville, USA, 1997, P.4.3.1-4.3.12.

58. S.V.Bobashev, E.A.D'yakonova, A.V.Erofeev, T.A.Lapushkina, V.A.Sakharov, R.V.Vasil'eva and David M.Van Wie. MHD Design Features in Supersonic Single-Shock Diffuser. International Conference on MHD Power Generation and High Temperature Technologies 1999, Beijing PRC, October 12-15, Vol. II, p. 581-587.

59. S.V. Bobashev, E.A. D'yakonova, A.V.Erofeev, T.A.Lapushkina, V.G. Maslennikov, S.A.Poniaev, V.A.Sakharov, R.V.Vasil'eva and D. M. Van Wie. Shock-tube facility for MGD supersonic flow control. AIAA Paper, 2000, No 2000-2647.

60. S.V. Bobashev, E.A. D'yakonova, A.V. Erofeev, T.A.Lapushkina, V.G.Maslennikov, S.A.Poniaev, V.A.Sakharov, R.V.Vasil'eva and D.Van Wie. Influence of MHD interaction on shock-wave structures in supersonic diffuser. The 2nd Workshop On Magneto- Plasma- Aerodynamics In Aerospace Applications, 2000, IVTAN, Moscow, April 5-7, pp. 64-68.

61. S.V.Bobashev, A.V.Erofeev, T.A.Lapushkina, S.A.Poniaev, V.A. Sakharov, R.V.Vasil'eva and D.Van Wie. Strong action of magnetic and electrical fields on inlet

shock configuration in diffuser. The 3rd Workshop On Magneto- Plasma- Aerodynamics In Aerospace Applications, IVTAN, Moscow, April 24-26, 2001.

62. С.В.Бобашев, Р.В. Васильева, А.В.Ерофеев, Т.А. Лапушкина, С.А.Поняев,

63. Д.М. Ван Ви. Положение присоединенных скачков в сверзвуковом МГД диффузоре при различных способах локализации тока. Четвертое совещание по магнитоплазменной аэродинамике в аэрокосмических приложениях (аннотации к докладам). Москва, 9-11 Апреля 2002 ИВТ РАН, с.50-51.AIAA-2002-5183.

64. S.V. Bobashev, A.V.Erofeev, T.A.Lapushkina, S.A.Poniaev, R.V.Vasil'eva and D. M. Van Wie. Non-stationary Aspects of Electric and Magnetic Fields Action on Shocks in Diffuser. AIAA Paper, 2002, No 2002-2164.

65. V. Bobashev, A.V.Erofeev, T.A.Lapushkina, S.A.Poniaev, V.A.Sakharov, R.V.Vasil'eva and D. M. Van Wie. Effect of the Wall Layers on the Electric Current in a Model of MHD Diffuser. AIAA Paper, 2001, No 2001-2878.

66. S.V.Bobashov, Yu. P. Golovachov, V.G.Maslennikov et al. Interaction of supersonic flow of xenon with magnetic field// AIAA Paper 2001-2879.

67. Yu. P. Golovachov, S.Yu.Sushchikh, D.M. Van Wie. Numerical simulation of MGD flows in supersonic inlets//AIAA Paper 2000-2666.

68. Yu. P. Golovachov, Yu.A..Kurakin, A.A.Schmidt, D.M. Van Wie.Numerical investigation of non-equilibrium MGD flows in supersonic intakes//AIAA Paper 2001-2883.

69. Yu. P.Golovachov. Yu.A.Kurakin. A.A.Schmidt. D.M.Van Wie. Numerical investigation of MGD interaction in non-equilibrium plasma flows in the models of supersonic intakes// Proc. of the 3rd Workshop on magneto-plasma-aerodynamics in aerospace applications. Moscow. 24-26 April 2001. P. 155-159.

70. R. V. Vasil'eva, A. V. Erofeev, E. A. D'yakonova, T. A. Lapushkina, and S. A. Poniaev. Ionizational instability in an ionized inert gas flowing in a magnetic field. Phys. Rev. E, V. 63, 036402, 2001.

71. R.V.Vasil'eva, A.V.Erofeev, T.A.Lapushkina, and E.A. D'yakonova. Formation of Shocks at the Interaction of a Supersonic Flow with Magnetic Field. - AIAA Paper, 2000, No 2000-2671.

72. Vasil'eva R.V., Erofeev A.V., Zuev A.D., D'yakonova E.A., Markhotok A.A. Characteristics of Pure Noble Gas Hall MHD Generatore in Environs of Critical Magnetic Field. Proc. of 32nd Symposium on Enginering Aspect of Magnetodynamics, Pittsburgh, USA, 1994. P.10.1-10.5.

73. Vasil'eva R.V., Erofeev A.V., Zuev A.D., Lapushkina T.A., D'yakonova E.A., Marhotok A.A. Parameters of Pure Noble Gas Disk MHD Channel at Developed Ionizational Instability. Proc. of 33rd Symposium on Engineering Aspects of Magnetohydrodinamics. Tullahoma, USA, 1995, P.11.4-1-11.4-5.

74. A.V. Erofeev, R.V.Vasil'eva, A.D.Zuev, T.A.Lapushkina, E.A.D'yakonova and A.A. Markhotok. Experimental Comparative Studies on the Hall and Faraday Channels with Ionizationally Unstable Inert Gas Plasma. Twelfth Internetional Conference on Magnetohydrodynamic Electrical Power Generation. Yokohama, Japan, October 15-18, 1996, Vol.1, p.74-82.

75. A.V.Erofeev, T.A.Lapushkina, S.A.Poniaev, R.V.Vasil'eva. Experimental Determination of Electrical Parameters of Anisotropically Conducting Medium in MHD Channel. Proc. of the 14th International Conference on MHD Electric Power Generation and High Temperature Technologies, 2002, Maui, Hawaii, May 22-23, p. 381-386.

76. E.A.D'yakonova, A.V.Erofeev, T.A.Lapushkina, R.V.Vasil'eva. On Characteristics of MHD Channel with Ionizationally Unstable Inert Gas Plasma. Proc. of International

Conference on MHD Power Generation and High Temperature Technologies 1999, Beijing PRC, October 12-15, 1999, Vol. I, p. 299-307.

77. A.V.Erofeev, R.V.Vasil'eva, T.A.Lapushkina, A.D.Zuev. On Possibility of Pre-Ionized Air Using in an MHD Generator on Aerospace Plane. Proc. of 34th Symposium on Enginering Aspect of Magnetodynamics, Starkville, USA, 1997, P.4.3.1-4.3.12.

78. S.V.Bobashev, E.A.D'yakonova, A.V.Erofeev, T.A.Lapushkina, V.A.Sakharov, R.V.Vasil'eva and David M.Van Wie. MHD Design Features in Supersonic Single-Shock Diffuser. International Conference on MHD Power Generation and High Temperature Technologies 1999, Beijing PRC, October 12-15, Vol. II, p. 581-587.

79. S.V. Bobashev, E.A. D'yakonova, A.V.Erofeev, T.A.Lapushkina, V.G. Maslennikov, S.A.Poniaev, V.A.Sakharov, R.V.Vasil'eva and D. M. Van Wie. Shock-tube facility for MGD supersonic flow control. AIAA Paper, 2000, No 2000-2647.

80. S.V. Bobashev, E.A. D'yakonova, A.V. Erofeev, T.A.Lapushkina, V.G.Maslennikov, S.A.Poniaev, V.A.Sakharov, R.V.Vasil'eva and D.Van Wie. Influence of MHD interaction on shock-wave structures in supersonic diffuser. The 2nd Workshop On Magneto- Plasma- Aerodynamics In Aerospace Applications, 2000, IVTAN, Moscow, April 5-7, pp. 64-68.

81. S.V.Bobashev, A.V.Erofeev, T.A.Lapushkina, S.A.Poniaev, V.A. Sakharov, R.V.Vasil'eva and D.Van Wie. Strong action of magnetic and electrical fields on inlet shock configuration in diffuser. The 3rd Workshop On Magneto- Plasma- Aerodynamics In Aerospace Applications, IVTAN, Moscow, April 24-26, 2001.AIAA-2002-5183.

82. S.V. Bobashev, A.V.Erofeev, T.A.Lapushkina, S.A.Poniaev, R.V.Vasil'eva and D. M. Van Wie. Non-stationary Aspects of Electric and Magnetic Fields Action on Shocks in Diffuser. AIAA Paper, 2002, No 2002-2164.

83. S.V. Bobashev, A.V.Erofeev, T.A.Lapushkina, S.A.Poniaev, V.A.Sakharov, R.V.Vasil'eva and D. M. Van Wie. Effect of the Wall Layers on the Electric Current in a Model of MHD Diffuser. AIAA Paper, 2001, No 2001-2878.

84. S.V.Bobashov, Yu. P. Golovachov, V.G.Maslennikov et al. Interaction of supersonic flow of xenon with magnetic field// AIAA Paper 2001-2879.

85. Yu. P. Golovachov, S.Yu.Sushchikh, D.M. Van Wie. Numerical simulation of MGD flows in supersonic inlets//AIAA Paper 2000-2666.

86. . Yu. P. Golovachov, Yu.A..Kurakin, A.A.Schmidt, D.M. Van Wie.Numerical investigation of non-equilibrium MGD flows in supersonic intakes//AIAA Paper 2001-2883.

87. Yu. P.Golovachov. Yu.A.Kurakin. A.A.Schmidt. D.M.Van Wie. Numerical investigation of MGD interaction in non-equilibrium plasma flows in the models of supersonic intakes// Proc. of the 3rd Workshop on magneto-plasma-aerodynamics in aerospace applications. Moscow. 24-26 April 2001. P. 155-159.

88. Yu. P. Golovachov, Yu. A. Kurakin, A.A.Schmidt. Numerical simulation of non-equilibrium MHD flows in supersonic intakes//Russian-Japan International Workshop on Actuel Problems of Computational Mechanics. Abstracts. 5-10 August 2002. St Petersburg, Russia.

89. S.V. Bobashev, Yu.P. Golovachov, D.M. Van Wie. Deceleration of supersonic plasma flow by an applied magnetic field. // AIAA Paper 2002-2247.

90. Slavin V.S., Finikov K.A., Bityurin V.A., Kraev M.V. Onboard MHD generator using the electron beams for the maintenance of the current layers in the supersonic air flow, Proceedings of 3rd Workshop on Magneto-Plasma Aerodynamics in aerospace applications, Moscow 24-26 April 2001, p.182-187

91. Slavin V.S., Danilov V.V., Kuzovatov I.A., Finnikov K.A., Gavrilov A.A., Litvintzev K.U., Milovidova T.A., Power and Transport Systems for Space Application, Utilizing the MHD Method of Energy Conversion. // High Temperature Journal ,Vol. 40, N 5, 2002

92. Slavin V.S., Finnikov K.A., Nonequilibrium Plasma Layer Evolution in a Pure Noble Gas Flow in the MHD Generator Channel. // The 2nd Workshop on Magneto-Plasma-Aerodynamics in Aerospace Applications, Moscow, April, 2000, pp. 246-250

93. Slavin V.S., Milovidova T.A., Finnikov K.A., Closed Cycle MHD Generator with Non-Uniform Flow Carrying Recombining Plasma Layers, // Proc. of 14-th Intern. Conf. on MHD Power Generation and High Temperature Technologies (AIAA-2002-2149), Hawaii, USA, May, 2002.

94. Tikhonov A. N. and other. Non-linear Effect of Formation of a Self-Sustaining High-Temperature Conductive Gas Layer in the Non-Stationary Processes of Magnetic Hydrodynamics. // USSR Science Academy Reports, Vol.173, № 4, 1967, p. 808-811, (in Russ.).

95. Kuranov A.L., Korabelnicov A.V., Kuchinskiy V.V. and Sheikin E.G., Fundamental techniques of the "AJAX" concept. Modern state of research, AIAA paper 2001-1915.

96. Brichkin D.I., Kuranov A.L., Sheikin E.G. MHD-technology for scramjet control, AIAA Paper 98-1642

97. Brichkin D.I., Kuranov A.L., Sheikin E.G. The potentialities of MHD control for improving scramjet performance, AIAA Paper 99-4969.

98. Brichkin D.I., Kuranov A.L., Sheikin E.G., Scramjet with MHD control under "AJAX" concept. Physical Limitations, AIAA paper 2001-0381

99. Kuranov A.L., Kuchinskiy V.V. and Sheikin E.G., Scramjet with MHD control under "AJAX" concept. Requirements for MHD systems, AIAA paper 2001-2881

100. A.L. Kuranov, E.G. Sheikin MHD generator with nonequilibrium conductivity of flow on the hypersonic aircraft under "AJAX" concept, The Fourth Workshop on Magneto plasma Aerodynamics for Aerospace Applications, Moscow, April 2002, Institute for High Temperatures, Russian Academy of Sciences, V.A.Bityurin (Editor).pp135-144.

101. A.B.vatazhin, O.V.Gouskov, M.K.Danilov, V.I.Kopchenov, Some Possibilities of MHD Control of Flow in Hypersonic Inlet, The Fourth Workshop on Magneto plasma Aerodynamics for Aerospace Applications, Moscow, April 2002, Institute for High Temperatures, Russian Academy of Sciences, V.A.Bityurin (Editor).pp152-157

102. A.B.Vatzhin, Private Communication, 2003

103. F.Jaarsma, W.B. de Wolf. AGARD - R-600.

104. G.Wood, A.Carter. ARS-Paper No. 903-59, 1959.

105. G.Wood, A.Carter, In: Ionic. Plasma and Arcjet Rocket Engines, GosAtomlsdat, 1961 (in Russian).

MFD Research in US Toward Aerospace Applications

J.S. Shang, Ph.D.
Department of Mechanical and Materials Engineering
Wright State University
Dayton Ohio, USA

Lecture outline
1. Technology Needs
    1.1 Airframe and propulsion integration across flow regimes
    1.2 Thermal management and protection
    1.3 Inlet efficiency
    1.4 Flow control
    1.5 Combustion stability and ignition
2. Plasma Generation
    2.1 Ionization processes
    2.2 Direct current discharge and radio frequency radiation
    2.3 Pulsed microwave plasmoid
    2.4 Electron beam
3. Experimental Facilities
    3.1 Legacy Installations
    3.2 Miniaturized plasma channel
    3.3 Radiatively driven wind tunnel
4. Computational MFD, CMD
    4.1 Significant progress
    4.2 Drift-Diffusion model for glow discharge
    4.3 Recent focus
5. Electrical Propulsion
    5.1 Energy conversions
    5.2 Research in US Academies
    5.3 Current status
6. Electromagnetic Flow Control
    6.1 Remote energy deposition
    6.2 Plasma actuator
7. MFD Scramjet Bypass
    7.1 Genesis
    7.2 Experiments
    7.3 Computations
8. Fuel Ignition, Microgravity Process and Others

Technology Needs

In aerospace application, the aerodynamic performance of most vehicles has reached a level of sophistication in which any additional improvement must be derived from new physical dimensions beyond traditional fluid dynamics [1,2]. The long-standing technological requirements are well known and some of the aerodynamic challenges are

still unsolved but are only remedied by compromised performance. In some other applications, innovations or radical processes are necessary to meet new technology challenges. A well-known and effective physical mechanism in fluid motion is electromagnetic force. However, this environment requires an electrically conducting medium in which the Lorentz force and Joule heating are present. For most hypersonic flights the air mixture in the shock layer, bounded by the bow shock and the vehicle, attains a weakly ionized state. The trapped plasma is characterized by a finite value of electrical conductivity, which may exceed a value of 100 mho/m dependent on the flight speed and altitude. Therefore, the magneto-fluid-dynamics (MFD) is associated closely with hypersonic flows.

Among other demands for high-speed vehicle design, the serious engineering challenges are the integration of the airframe and the propulsion system across the entire flight regimes, thermal management and thermo protection, as well as the propulsive system limitations imposed by inlet mass capture efficiency, combustion stability, and drag reduction [3]. These technical pacing items can be addressed by effective interactions of magneto-aerodynamics. Therefore, MFD is one of the very few remaining frontiers in the discipline of fluid dynamics [1]. In MFD applications, the expanded capability can be very effective in the major areas of plasma aerodynamic flow control, MFD scramjet flow path enhancement, plasma-assisted ignition and combustion, electric propulsion, as well as microgravity process.

In order to meet these technical needs for aerospace applications, the current research efforts in the US to support this technology development are concentrated in plasma generation, MFD facility development, electric propulsion, electromagnetic flow control, MFD scramjet bypass, plasma-assisted ignition and combustion. Research efforts are also noted in astrophysics and microgravity process.

Plasma Generation

In general, the ionization processes are classified into four major categories as the ionization by thermal collision, chemical reaction, photon-ionization, and electron collision [4,5]. From partition functions of molecular structure, the energy state is additive of translation, rotation, vibration, dissociation, and ionization degrees of freedom. In partially ionized gas, elastic and inelastic processes take place simultaneously. However, the inelastic processes are of particular interest, because they control the number density distribution of ionization, recombination, charge-exchange collision, plasma-wall interaction, secondary emission, and sputtering. The total energy required for ionization is also the net balance of various inelastic and elastic collisions, emission, and absorption of a quantum of radiation energy.

Although the ionizing heats of formation of oxygen and nitrogen atoms are 13.62 and 14.55 EV respectively, and the ionization energy of nitrioxide is merely 9.25 EV (1 EV = 1.6×10^{-19} joule); the net energy requirement for ionization is much greater [4,5]. In essence, the non-equilibrium electron energy distribution function determines the rates of all electron collision processes including the generation and depletion of the ionized population in plasma. Therefore, the energy budget for ionization is far greater than the

theoretical threshold described by the chemical kinetics. There are three major groups of plasma generation processes used in the US. The most widely adopted methods are direct current (DC) glow discharge, radio frequency (RF) discharge including pulsing mode [6-9]. The microwave-induced plasmoids are mostly adopted for supersonic combustion ignition [10]. More recently the electron beam technique also gains popularity [11].

The glow discharge excites mostly electrons in the outer shell of atom, the so-called valency electrons [4]. The excitation of the electron in the inner shell requires much more energy and is rarely considered in gas discharge. When the ambient pressure is rising to approach atmospheric and the resistance of the external circuit is comparatively low, the breakdown is likely to result in an arc or streamer. However, Roth et al [8] is able to develop uniform surface plasma using a RF device that operates on displacement currents, up to one atmospheric pressure. As a glow discharge, the RF radiation operates at the Stoletow point, where ionization in air occurs at the minimum energy level of 81 EV per ion-electron pair [8]. Under the atmospheric condition, the ions and electrons collision frequency is around 7 Ghz and 5.3 Thz respectively.
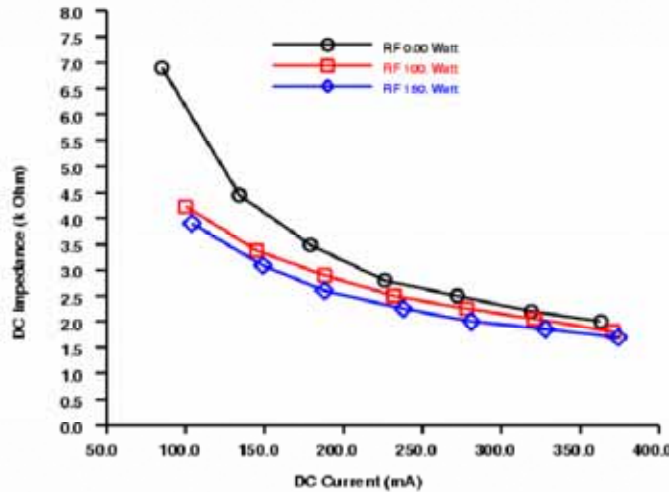

Fig.1 Combined DC and RF plasma generation

The plasma generated either by DC or RF alone has a limited electron number density up to 10^{12}/cc. To overcome this shortcoming, frequently the DC and RF discharge are operated concurrently. The measured impedance of plasma generated by the combination of the DC and RF power supplies in a vacuum chamber is presented in Figure 1. In the joint operation, the impedance of the DC discharge has been reduced by a factor of near two at the breakdown point. These data were collected at an ambient pressure of 7 Torr and the RF power supply was operated at a frequency of 13.56 MHz.

By superposing a DC discharge and electric pulse in parallel, the discharge produces a stable region of elevated electron number density as high as 10^{13}/cc [9]. This experimental observation reaches a good agreement with the calculated results in predicting electron concentration, electron temperature, and cathode fall. In specific, the computational results use a two-temperature chemical kinetic model for plasma including

3

a finite-rate formulation for vibration-electronic energy relaxation and electron translational energy relaxation.

The high-energy electron beam is the most energy efficient process for ionization. The accelerated electrons at a high energy level in the keV range when injecting into the gas medium will dissipate kinetic energy and lead to an ionization cascade. The energy required for plasma generation is as low as 34 EV for air, which is only a few times greater than the ionization energy of air molecules [11]. Recently, some plasmoids generated by pulsed microwave experiments were conducted at NASA Langley Research Center. The volumetric plasma is generated by a pulsed microwave radiation at spectra from 9.5 to 16.5 Ghz (Kμ and X band). Now the research is focused on the phenomenological characterization of the standing wave plasmoids adjacent to interface [10].

In support to the plasma generation research, the traditional plasma diagnostic tools such as the Langmuir probe and microwave absorption technique were further developed for measurements under the high-speed flow condition [12,13]. The overall transport property of the plasma was also augmented by emission spectroscopy [14]. The plasma generated at a relatively low neutral gas temperature, the weakly ionized gas is modeled as multi-component, electrically conducting medium consisting of electron, ion and neutral particles. This electrically conducting medium is considered to be electrically globally neutral. Under these conditions, the drift-diffusion model applies and has extended its applicability to include the plasma sheath with physical-based boundary conditions [15-17]. From this model, the finite-rate ionization fraction, as well as most transport property of the plasma can be computed.

MFD Experimental Facility

In the late 1990's, most MFD experimental facilities were either the legacy installations or modifications of traditional wind tunnels [7,8, 18-21]. For the high-enthalpy ground test facility such as an electric arc shock tube, the enriched electric conductivity is rather straightforwardly achievable by an alkali seed material such as potassium or cesium [19-21]. However, to modify a conventional tunnel for magneto-aerodynamic research is a technical challenge. First, the plasma generator must be isolated from the metal tunnel frame and all instruments using electric induction must be shielded from microwave transmission in the testing section. Second, the perturbation to the inviscid core of the air stream from the plasma generator must be avoided. This need becomes the most challenged issue when the DC and RF discharges were adopted as the plasma generator. Even at the low-density hypersonic testing condition, the pressure level in the shock layer of a blunt body can be two orders of magnitude or more greater than that of the free stream. Invoking Paschen's law to provide a plasma field upstream to a blunt body to compensate the high pressure through an electrode spike is still ineffective to create a sufficient electric conductivity for magneto-aerodynamic experiments.

In Figure 2, a video recording of a spike-tipped blunt body in a Mach 6 weakly ionized air is presented. The free-stream pressure and temperature of the open jet are 2 Torr and 79 K respectively. The transport property was determined to have the maximum electron

density of 2×10^{12} /cm^3, electric conductivity of 2.5 mho/m, electron temperature of about 60,000 K, and the electric field strength up to ±60 V/cm. An external magnetic field was provided by a steady current co-axial solenoid with peak strength of 1.6 Tesla at the pole, but the magneto-aerodynamic interaction parameter $B^2\sigma L/\rho u$ is still negligible.
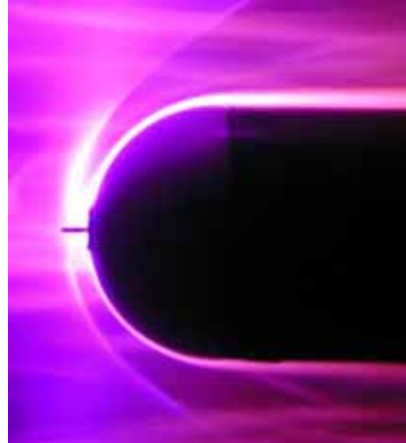

Fig. 2 Spike-tipped blunt body in plasma stream

To overcome the experimental facility shortage, two entirely different approaches were undertaken. One of the approaches adopted an ambitious and innovative concept to break new ground [22-24]; the other approach resorted to miniaturize the experimental facility and to construct the plasma channel with dielectric material [6,25]. These miniaturized facilities with low mass flow rate need smaller amounts of energy for ionization; it also has an intended design advantage in that the small channel dimension allows a small gap between magnetic poles. As the consequence, a strong and uniform magnetic field strength can be maintained. In essence, this type of facility is best suited to a highly focused research objective, however it also has a limited test section size for versatile utilization.

In the later half of 1990, NASA sponsored the magnetohydrodynamics accelerator for research into advanced hypersonics project (MARIAH) [22]. The objective of this project is to evaluate MHD as the pacing technology for hypersonic ground test facilities. A flight simulation environment is designed for a free stream Mach number up to 16; the operation range of temperature and pressure is at least 100 atm and 2,500K respectively or higher. These conditions are difficult to achieve using a conventional arc heater. Unconventional mechanisms and material in the form of ultrahigh pressure gas piston and survivability of electrodes have been evaluated. However, the most innovative concept is the downstream energy addition concept for sustaining a long run time hypersonic test facility.

Miles et al introduced the radiatively driven hypersonic tunnel concept in the mid-1990s [23,24]. In this project, there are concerns regarding the effects of transport phenomena at high pressure, the energy-addition mechanism, and the pertaining chemical kinetics. However, this approach is unique in achieving high enthalpy by using ultrahigh pressure and coupling energy downstream of the nozzle throat. The basic idea is to radiatively add

energy into the expanding air through the nozzle to increase the enthalpy and entropy of the air stream. A final expansion further downstream to a high Mach number brings the flow to the test condition. In this form of energy addition, the thermal management for sustained operation of a high-speed facility is superior to any other approaches. In figure 3, the configuration shows that the electron beam exits from an accelerator and enters the nozzle. The electron beam is guided by magnet and propagates in the opposite direction to the flow. The microwave ionizes and dissipates its energy in the electrical conducting medium.
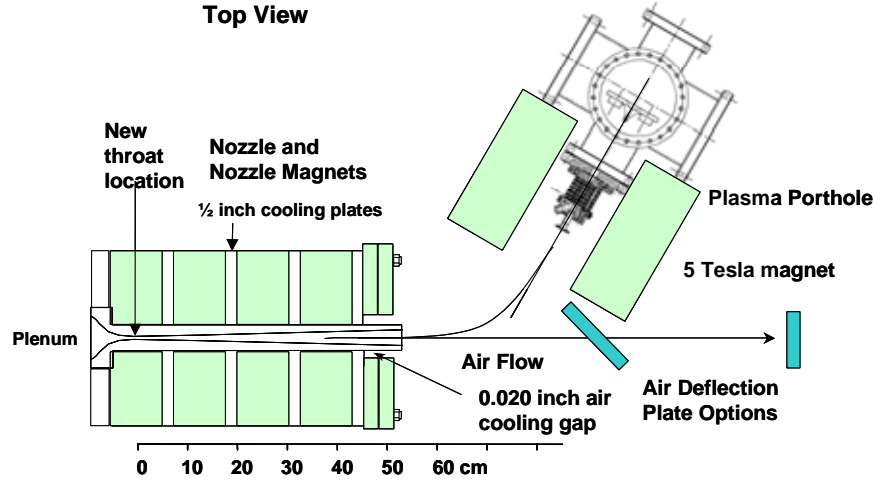
Fig. 3 Electron beam energy source in high-speed tunnel, Courtesy of Miles (Ref. 23)

More recent experimental results were obtained jointly between Princeton University and Sandia National Laboratory as a part of RDHWT/MARIAH program [24]. A major milestone has been reached; the energy delivered by the electron beam has achieved the 1 MW level. The level of microwave power input is more than double the total enthalpy of the flow. Although the technical challenge is formidable for this endeavor, the potential for aerospace application is unfathomable at present.

Computational MFD, CMD

The development of computational magneto-fluid-dynamics (CMD) for aerospace application really started a few years ago [2]. Prior to the late 1990's, CMD were most concentrated on the problem in astrophysics and geophysics. For studying these phenomena, the so-called ideal magnetohydrodynamic (MHD) equation is adequate to describe all pertaining physics [26]. The MHD equations are nonconvex, thus, the wave structure is more complicated than the Euler equations [27]. To simulate wave motion dominant phenomena, the characteristic-based or approximate Riemann algorithm in computational fluid dynamics (CFD), fits perfectly for solving the hyperbolic equation system [28].

MacCormack, Gaitonde, Hoffmann and others have made impressive contributions to the maturation of CMD for aerospace application [29-34]. Especially, MacCormack has

6

modified the Jacobian of the coefficient matrix for the flux splitting formulation of the MHD equations to preserve the homogenous of degree one property [30]. His effort enables the use of characteristic-based schemes that were developed in CFD and in MHD by Powell to solve the inviscid terms of the MFD equations [26]. In addition, MacCormack and Hoffmann et al have led the interdisciplinary CMD development by including the non-equilibrium chemical kinetics in their respective formulations [30,33,34].

Gaitonde, on the other hand, brought the spectral-like, high-resolution numerical procedure to the CMD [31]. His numerical procedure has generated a large group of complicated simulations with incredibly fine details, yet using only comparable computing resources to that of the conventional methods. Furthermore, he leads the progress in modeling the electric conductivity correctly in tensor formulation. By so doing, the Hall current effect in applied magnetic field and ion slip in partially ionized gas can now be analyzed [32].

An international collaboration for glow discharge modeling by Surzhikov and Shang has taken place in 2002 [16,17]. They realized the vast majority of plasma generation processes in experiments are based on the glow discharge and launched a research effort based on the drift-diffusion model by Raizer [15]. For the glow discharge in an externally applied magnetic field, the dominant effects of glow discharge are the Lorentz force and Joule heating. The better description of the plasma transport property is paramount. For the three-component plasma model, the charged particles concentration is computed by the continuity equation for the singly charged ion and electron. The conservation of momentum equations for charged particles have essentially replaced the approximate Ohm's law. In this formulation, the computed current density, electrical field intensity, and magnetic flux density are obtainable after satisfying the charge conservation law ($\partial \rho_e / \partial t + \nabla \cdot \mathbf{J} = 0$) and the external circuit equation ($E = V_n + I_n R_n$). Although additional verification of the computing model is still required, this research result shows promise for practical application.
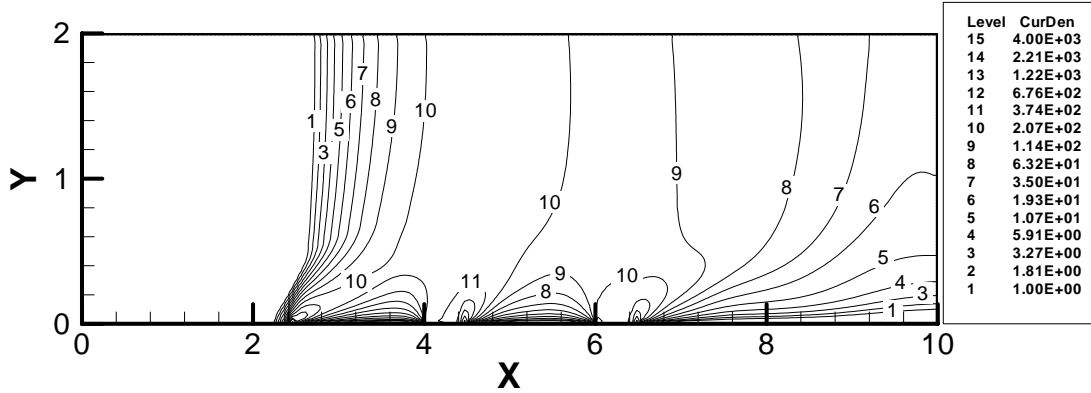

Fig. 4 Computed current density in 2-D discharge channel with segmented electrodes

Figures 4 and 5 exhibit distributions of the electrodynamics and thermodynamic properties of a glow discharge in turbulent flow. The numerical simulations are generated for the channel flow moving at 200m/s and under the influence of an externally applied magnetic field of 0.1 Tesla. The glow discharge computation is modeled for segmented

electrodes by an electric field that is sustained at 5 kV, and all cathodes are located on the lower channel wall. The most important result is that the flow field structure near the cathodes is significantly altered by the applied magnetic field. The electromagnetic force actually produced vortices at each cathode. The computed results reaffirm the fact that the local disturbance to the flow field amplifies readily by the increasing strength of the applied magnetic field.
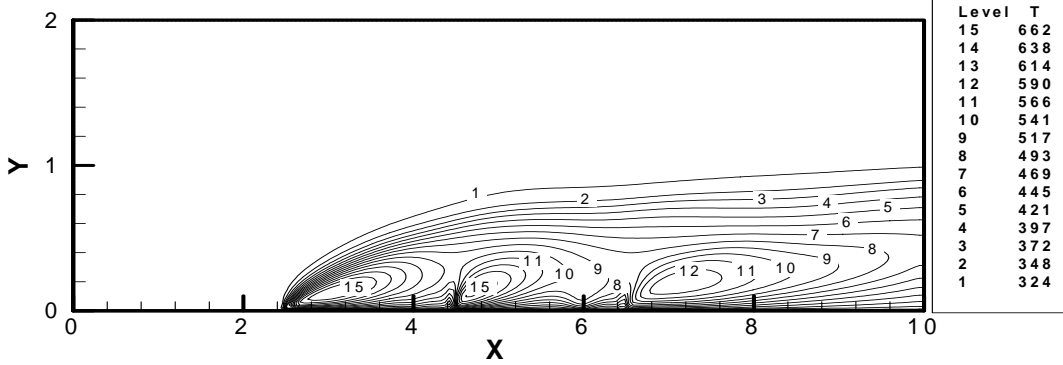

Fig. 5 Temperature distribution in 2-D discharge channel with segmented electrodes

In short, CMD has made impressive progress in the past few years. The predictive capability has advanced to a level for practical aerospace application [32-24]. The most efficient and accurate modeling and simulation procedure is built on the low magnetic Reynolds assumption. Based on this premise, the Lorentz force and Joule heating become source terms and simply append into the Navier-Stokes equations. As the consequence, all developed CFD techniques are equally usable for CMD.

Electrical Propulsion

The MHD energy conversion can be categorized as the electric energy extraction and the kinetic energy converter. In the latter mode, it often uses a closed drift Hall thruster and has been proven to be an attractive electrostatic propulsion device for satellite station keeping or deep space exploration. For this reason, NASA science and technology centers have a vested interest in this area of research. The current KW level hall thrusters can attain a specific impulse in the range from 1,600 to 2,000s at thrust from 10^2 to 10^3 mN, which is far superior to the chemical propulsion system [35]. Most of all, the charged particle acceleration in a Hall thruster is not inhibited by the space charge field for the globally neutral plasma. However, the development of the Hall thruster still faces serious challenge because the interaction of the plasma plumes with the space vehicle is highly nonlinear. This interaction can adversely affect the sensitive subsystems of the spacecraft through backflow or direct impingement.

In US academic institutes, research on electric propulsion spans a wide scope of scientific disciplines. The topics of interest cover the full spectrum from the molecular-scale mechanisms of plasma acceleration to the effect of plasma plume impact on the operational characteristics of large satellite structures. In terms of innovative concepts, the subjects are ranging from micro thruster to magneto plasma sail. A total of fifteen US academies are active in this field of technical endeavor [36]. The typical research emphasis can be highlighted as (1) development of hall thruster simulation tools, (2)

spacecraft and plasma plume interaction, (3) colloid propulsion including the micro emitter arrays, (4) electrodynamic tethers, (5) ion sputtering in ion thruster (6) NASA Glenn evolutionary Xenon thruster (NEXT) ion optics system.

More recently, the complex Hall thruster dynamic is simulated by one-dimensional and two-dimensional calculations using the MFD equations. The computed plasma and neutral density profiles exhibit good agreement with experimental data. The self-consistent calculation displays a direct correlation between the ion and neutral densities. The electron temperature and its general behavior also agree with the experimental observation [37]. As far as the experimental facility is concerned, most of the academic institutes have state-of-the-art facilities to carry out both fundamental and applied research. For the experimental programs relevant to the US interest in future space propulsion applications, both NASA and the US Air Force ground-test facilities have been made available.

Electromagnetic Flow Control

The flow control using electromagnetic force is derived from the magneto-aerodynamic interaction. The electromagnetic field is introduced into the flow by plasma jet injection, homogeneous and heterogeneous plasma discharge, as well as, surface discharge. The distinction between homogeneous and heterogeneous glow discharge is rather artificial, because its operational environment and the electrical circuit load controls the formation of either the diffusive glow or arc (streamer). Nevertheless, the flow control is implemented for shock position control, laminar-turbulent transition, vorticity production, enhanced mixing and combustion ignition [38].

In the present discussion, the electromagnetic flow control included only the energy deposition and plasma actuator [38-42]. In the research area of energy deposition, the techniques for energy deposition include a wide variety of plasma injection, plasma arc, laser pulse, microwave, electron beam, glow discharge etc. The intended applications are equally dispersed to include drag reduction, lift and moment enhancement, improved mixing, shock structure modification, etc [39]. For energy deposition without an externally applied electromagnetic field, the principal mechanisms to alter the flow field structure are through the effects of thermodynamic state and the wake structure of the deposed energy source [40,41].

The total drag reduction by a counter-flow jet issued from a hemispherical blunt body in a Mach 6 stream is depicted in Figure 6. Four different injection stagnation pressures were used to generate the supersonic counter-flow jet. The greatest drag reduction, up to 60% of the unperturbed flow, was obtained for the lowest injection pressure tested. The plasma injection at an estimated stagnation temperature of 4400 K produced 12% further drag reduction. However, the wave drag reduction by the plasma injection is mostly derived from the pure aerodynamic interaction between the jet and the bifurcating bow shock. The greater contribution to drag reduction from the plasma is through added thermal energy content of the weakly ionized gas. The induced magnetic field by the injected plasma is simply too weak to be detected by the existing measuring technique [42].

The idea of an electromagnetic actuator for fluid dynamic application is a more recent innovation [43-49]. A majority of the actuator is operated by the electrostatic force induced by charge separation near electrodes, where the often-neglected electrostatic component of the Lorentz force $\rho_e E$, in plasma becomes significant. Whether the plasma is generated by a RF or DC glow discharge, these electrodes form a dielectric barrier discharge to accentuate the temporal and micro-scale spatial structure of plasma [47]. The most important feature of the dielectric barrier discharge is that the discharge can be maintained up to atmospheric pressure without breakdown to a constricted arc [44-48].

It is also important to realize that this kind of discharge is self-limiting because the discharge terminates on a dielectric surface and the buildup surface charge will shut itself off at an applied voltage. Meanwhile, the interaction of charged particles and the electric field will lead to a collisional exchange between charged and neutral particles to produce a fluid motion. It was also clearly shown that the geometry of the electrodes dictates the orientation of the near-electrode induced fluid motion. A wide range of applications have been demonstrated for flow separation control, lift enhancement, and expansion of the dynamic stall envelope of wing or airfoil at angles of attack [44-48].
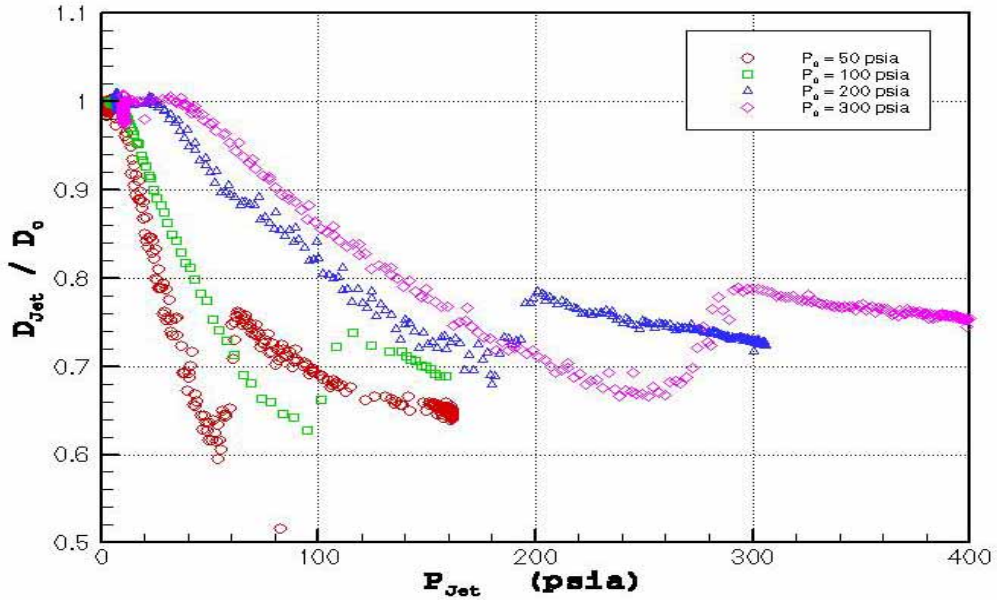

Fig. 6 Wave drag reduction by the counter-flow jet

Probably the most effective application of the electromagnetic actuator is recently demonstrated in hypersonic flow [49]. At the hypersonic condition, the displacement thickness of a boundary layer on the vehicle surface will lead to a strong viscous-inviscid interaction; this aerodynamic phenomenon is referred to as the pressure interaction [50]. Through this unique hypersonic phenomenon, a higher surface pressure on the flight vehicle is produced and proportional to the product of the free-stream Mach number and the slope of the displacement thickness $M_\infty d\delta/dx$. Hayes and Probstein have shown, the increased pressure is dependent to an interaction parameter $\chi = M^3_\infty (C/Rey_\infty)^{1/2}$ [50]. Therefore the most effective means to initiate the aerodynamic interaction is to modify

the boundary layer by a surface discharge. From the viewpoint of fluid dynamic plasma interaction the parameter $\sigma B^2 L/\rho u$ also attains the maximum value, where the fluid inertia is the minimum immediately adjacent to the non-slip velocity surface. Therefore, it is possible to greatly modify the growth rate of the displacement thickness by a minimum surface plasma discharge. The subsequent viscous-inviscid interaction will then further amplify the electromagnetic perturbation.

Figure 7 presents the interaction of a DC discharge by embedded electrodes on a plate in a Mach 5.15 stream. The free stream of the airflow is characterized by a static pressure and temperature of 0.59 Torr and 43 K respectively. To produce the maximum influence of the electromagnetic perturbation, the cathode was placed near the leading edge of the plate where the Joule heating is concentrated [15-17]. At a minute DC discharge energy input of 50 mA at 1 kV, the surface pressure increased by a factor near 16%. Equally important, the increased pressure is near the leading edge of the plate that provides the longest pitch arm for flight control. Additional magneto-aerodynamic interaction is still possible by applying an eternal magnetic field [49].

Fig. 7 Magneto-Aerodynamic interaction in hypersonic stream

This research area has become the most active and is probably the most productive area of MFD research. The knowledge of plasma generation and its implementing technique has opened a vast opportunity for practical application. Meanwhile, the nanotechnology research also offers new possibilities of super magnet development that was the limiter of magneto-aerodynamic interaction in the past. These research results in flow control have a great and realizable potential to impact the full range of the flight corridor of the aerospace vehicle.

MFD Scramjet Bypass

The idea of MFD scramjet bypass is one of the highlights for the AJAX concept vehicle [51-52]. The basic premise is very straightforward in that the electrical energy of the highly compressed, ionized incoming air is removed in the inlet. The lower temperature and slower gas motion in the flow path not only reduced the overriding thermal protection concern, shorten the inlet of the scramjet, but also enhanced the combustion

efficiency. The weight saving alone is very attractive, and the extracted energy from the inlet is put back to the nozzle of the propulsive system as an additional benefit. The idea of using the nozzle as a pump is equally attractive because it is always more efficient to transfer electric energy directly into kinetic energy instead of first degrading it into thermal energy.

The sketch in Figure 8 depicts the essential idea of MHD scramjet bypass. In this sketch, the inlet downstream of the cowl is the electric generator in Faraday configuration with segmented sidewall electrodes, and the MFD or MGD accelerator is located downstream the combustor in the nozzle. Although the rectangular linear configuration is geometrically simple, the electromagnetic field in this MFD device is inherently three-dimensional. The reduced dimension analysis becomes too simple to yield meaningful information. In addition, the gas medium in the operational range strides the regimes between equilibrium and nonequilibrium states of ionization [53]. The performance parameters of the propulsive system are dependent strongly on the flight conditions. If the propulsive efficiency is measured by the specific impulse, the MFD scramjet bypass appears to be much more promising in the equilibrium state of ionization than otherwise [53]. Since most of the energy in seeding ionization is expended to excite the vibrational mode of air molecule, alternative means could be used such as the electron beam to alleviate this limitation [53,54]
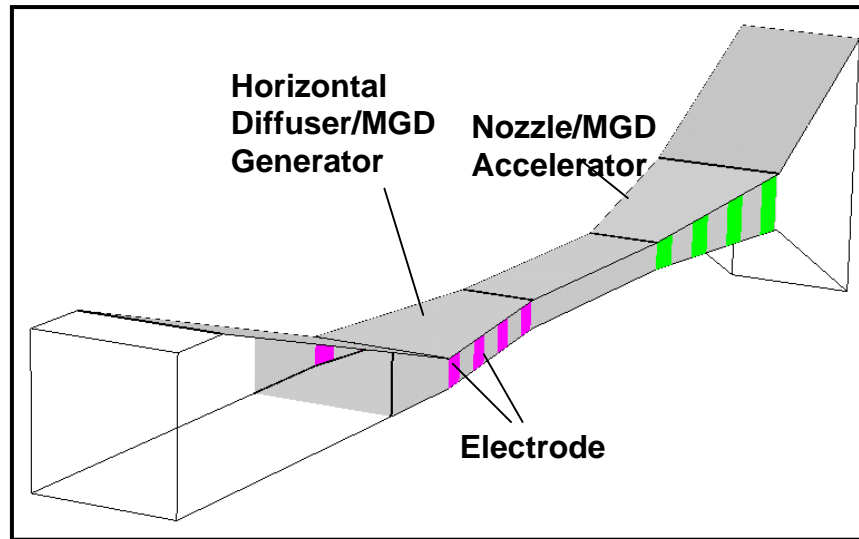

Fig. 8 Sketch of the MFD Scramjet bypass

The most active MFD scramjet bypass experimental research in the US is located in the NASA Centers [55,56], where both Faraday and Hall accelerator configurations are analyzed. According to Litchford, the hall configuration is generally more effective for low-density flows where the Hall parameter is large, while the segmented Faraday configuration yields superior performance for high-density flow [56]. The NASA Ames Research Center is the leading installation in experimental research for MFD scramjet bypass. The contribution to the physical knowledge of the MFD scramjet by Bogdanoff et al [53,55] is significant. The basic facility is an electric arc shock tube. The electric-

arc-driver is supported by a capacitor bank that can store up to 1.24 MJ of energy at 40 kV. The range of gas velocity and the magnetic field in the channel are from 2,000 to 2,900 m/s and approximately 0.92 Tesla respectively. The seeding material is K_2CO_3 and the generated plasma has the range of electric conductivity from 60 to 150 mho/m. The MFD accelerator operates under this condition, yielding the Hall parameter from 0.3 to 1.0, and the load factors vary from 2.1 to 2.3. This range of load factor indicates that roughly 55% of the MFD power is converted to thermal energy by Joule heating, and the rest is used to accelerate the gas medium [55].

This NASA facility can be configured to either the segmented Faraday or the Hall (diagonal) mode to study MFD acceleration. Most importantly, the Ames experimental facility has continuously provided invaluable data for the research in MFD scramjet bypass. A preliminary study was also conducted at the US Air Force Arnold Engineering Development Center (AEDC) for an electron-beam heated hypersonic wind tunnel. This effort is closely coordinated with the RDHWT/MARIAH Research Program discussed previously [24].

In the previous discussion of computational MFD, it has been pointed out the rapid progress in the simulation and modeling technique during the past few years. The integration of three-dimensional, compressible Navier-Stokes and Maxwell equations has been accomplished. Sufficient validation effort has also ensured the physical fidelity in these numerical simulations. In 2003, Gaitonde accomplished a first-ever, three-dimensional computation of the MFD scramjet flow path. Although the Hall effect and ion slip phenomena were included in his formulation, to make the flow field structure tractable all plasma transport properties are prescribed as the input data. The numerical simulation captured all key elements of the MFD scramjet bypass performance characteristics. In addition, his numerical simulation reveals the much more complex vortical structure generated by the side-compression inlet and further accentuated by the Lorentz force. Sustained and refined computational efforts are essential to resolve and to accurately assess the benefit of the MFD scram jet bypass concept.

Fuel Ignition, Microgravity Process, and Others

The most complex subject in MFD for aerospace application is in the area of plasma-assisted combustion for the following reasons. First, this subject area includes a very wide range of topics that use plasma for enhancing ignition, extending flame-holding limits, and increasing mixing and combustion efficiencies [38]. Second, the knowledge base composes not only basic science in quantum physics, chemical kinetics, aerodynamics, electromagnetics but also the microwave, laser, and infrared or optical technology.

In general, the plasma-assisted combustion is categorized into two major groups; the first group is the investigation of the reduced ignition delay time of combustible mixture by vibration and electronic excitations [57,58]. The second group is focused on the laser-based ignition of fuel air mixture [38]. The most recent progress to initiate a combustion shock train using plasma torch is based on DC constricted arc and AC unrestricted arc.

The ignition process is a balance between blockage introduced for ignition and that resulting from the heat released by the combustion. Typical ignition is measured by visible flame, output from pressure or temperature probes, or surface measurements.

The Schlieren images of typical flow patterns generated by a two-anode DC and a constricted arc AC plasma torch are recorded in a quiescent environment [57]. In Figure 9, the accompanying images are not collected at the identical time scale, but both torches reveal that an arc emerges from the torch exit and penetrates into the plasma jet. Since the configurations of these plasma torches are different in the flow rates, injector exit diameters, and voltage-current operational characteristics, the generated flow fields are expected to have distinguished structures. For the DC plasma torch, a narrow, constant jet is produced. The AC plasma torch, which was design to generate an order of magnitude higher flow rate than the DC plasma torch, produces a wide pulsating jet. In spite of the differences, both plasma torches have a thermal efficiency exceeded 90 percent or better.

From a combination of computational and experimental ignition research, the plasma igniters have produced hot pockets of highly excited gas with peak temperatures exceeding 5000k but at low energy supply of 2 kW [57]. As the better understanding is derived from this research, the newly gained capability will enable the design and fabrication of the next generation hydrocarbon-fueled scramjets.
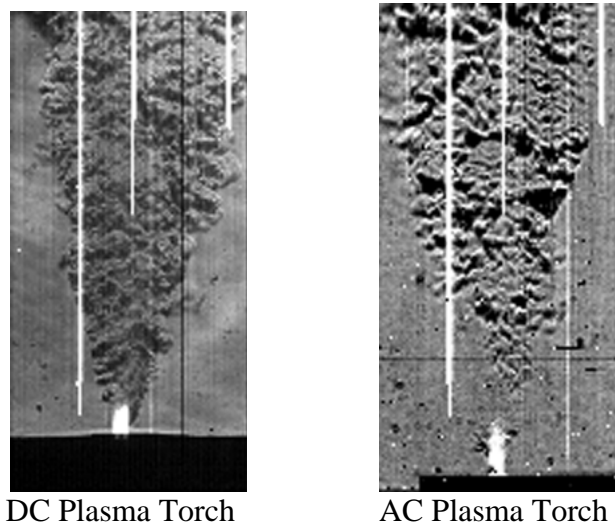

DC Plasma Torch   AC Plasma Torch

Fig. 9 Flow field structure from different plasma torches

The possibility of laser-based ignition is still widely open, in that the laser induced thermal ignition, non-resonant laser induced spark ignition, laser triggered photochemical ignition, and resonant laser induced spark ignition are the most promising. However, in this research area, the fluid dynamics plays a diminishing role in comparison with optics and chemical kinetics.

It is interesting to note that the MFD also has active application in the microgravity manufacturing process, as well as, solar eruptions and flares [59,60]. In the controlled semiconductor crystal growth process, the convective motion produces structural flaws [59]. In electrically conducting semi-conductor melts, the induced Lorentz force can be effectively used to curtail the convective motion. A greater reduction of convective induced motion is possible by exploiting the fluid diamagnetic susceptibility under the influence of an applied magnetic field. Numerical results show that up to 50% convection damping is attributed to the Lorentz force.

On another extreme of application, the dynamic and energetic coronal eruption events cause geomagnetic disturbances, perhaps even the solar cycle. After this eruption, the solar magnetic field must reestablish to reach new equilibrium. The CMD was used to analyze the dynamics and structure of magnetic field lines and their reconnection [60]. Unfortunately, these very interesting phenomena are beyond the scope of the present discussion.

Epilogue

Under the present limited scope and time frame, it is truly impossible to cover all important and excellent magneto-fluid-dynamic research in the US. Please accept my sincere apology for the unavoidable significant omissions and unintentional oversight.

References

1. Resler, E.L., Sears, W.R., The Prospect for Magneto-aerodynamics, J. Aero. Science 1958, Vol. 25, 1958, pp. 235-245 and 258.
2. Shang, J.S., Recent Research in Magneto-Aerodynamics, Progress in Aerospace Sciences, Vol. 31, 2001, pp. 1-20.
3. Covert, E.E., Aeronautical Technologies for the Twenty-First Century, National Research Council, National Academy Press, Washington DC, 1992.
4. Howatson, A.M., An Introduction to Gas Discharges, 2nd Edition, Pergamon Press, Oxford, 1975.
5. Zel'dovich, Ya. B., and Raizer, Yu. P., Physics of Shock Waves and High-Temperature Hydrodynamic Phenomena, Dover Publications, Mineola NY, 2002.
6. Merriman, S., Ploenjes, E., Palm, P., and Adamovich, I., Shock Wave Control by Nonequilibrium Plasma in Cold Supersonic Gas Flows, AIAA J. Vol.39, No.8, 2001, pp.1547-1552.
7. Shang, J.S., Ganguly, B., Umstattd, R., Hayes, J., Arman, M., and Bletzinger, P., Developing a Facility for Magnetoaerodynamic Experiments, J. of Aircraft, Vol. 17 No. 6, Nov-Dec 2000, pp. 1065.
8. Roth, J.R., Sherman, D.M., and Wilkinson, S.P., Electrohydrodynamic Flow Control with a Glow-Discharge Surface Plasma, AIAA J., Vol. 38, No. 7, 2000, pp. 1166-1172.
9. Nagulapally, M., Candler, G.V., Laux, C.O., Yu, L., Packan, D., Kruger, C.H., Stark, R., Schoenbach, K.H., Experimental and Simulations of DC and Pulsed Discharges in Air Plasma, AIAA 2000-2417, Denver, CO, June 2000,
10. Exton, R.J., Balla, J., Herring, G.C., Popovic, S., and Vuskovic, L., Volumetric Near-Field Microwave Plasma Generation, AIAA 2003-4181, June 2003.

11. Macheret, S.O., Sheider, M.N., Miles, R.B., and Lipinski, R.J., Electron Beam Generated Plasmas in Hypersonic Magnetohydrodynamic Channels, AIAA J., Vol.39, No. 6, 2001, pp. 1127-1138.
12. Menart, J., Shang, J.S., and Hayes, J.R., Development of a Langmuir Probe for Plasma Diagnostic Work in High Speed Flow, AIAA 2001-2804, Anaheim CA, June 2001.
13. Kurpik, A., Menart, J., Shang, J.S., Kimmel, R., and Hayes, J., Technique for Making Microwave Absorption Measurements in a Thin Plasma Discharge, AIAA 2003-3748, Orlando FL, June 2003.
14. Kimmel, R., Hayes, J., Menart, J., Shang, J.S., Henderson, S., and Kurpik, A., Measurements of a Transverse DC Discharge in a Mach 5 Flow, AIAA 2003-3855, Orlando FL, June 2003.
15. Raizer, Yu. P., Physics of Gas Discharge, Moscow, Nauka, 1987
16. Surzhikov, S.T. and Shang, J.S., Supersonic Internal Flows with Gas Discharged and External Magnetic Field, AIAA 2003-3625, Orlando FL, June 2003.
17. Surzhikov, S.T. and Shang, J.S., Glow Discharge in Magnetic Field with Heating of Neutral Gas, AIAA 2003-3654, Orlando FL, June 2003.
18. Lowery, H., Stepanek, C., Crosswy, L., Sherrouse, P., Smith, M., Price, L., Ruyten, W., and Felderman, J., Shock Structure of a Spherical Projectile in Weakly Ionized Air, AIAA 99-0600, January 1999.
19. Staats, G.E., Staats, McGregor, W.K., Sprouse, J.A., and Frohlich, J.P., Magnetogasdynamic Experiments Conducted in a Supersonic Plasma Arc Tunnel, AIAA 2000-2566, Denver CO, June 2000.
20. Park, C., Mehta, U.B., and Bogdanoff, D.W., MHD Energy Bypass Ascamjet Performance with Real Gas Effects, J. Propulsion and power, Vol. 19, No.5, 2001, pp1049-1057.
21. Weaver, W.R., Mcfarland, D.R., Carter, A.F., and Wood, G.P., Design and Operational Characteristics of the Langley 20 –Mega watt Plasma Accelerator Facility, 11th Proc. of Symp. On Engineering Aspects of MHD, Calif. Inst. Of Technology, Pasadena CA, 1970, pp. 77-81.
22. Simmons, G.A. and Nelson, G.L., Overview of the NASA Mariah Project and Summary of Technical Results, AIAA 98-2752, Albuquerque NM, June 1998.
23. Miles, R.B., Brown, G.L., Lempert, W.R., Yetter, R., Williams, G.L., Bogdonoff, S.M., Natelson, D., Guest, J.R., Radiatively Driven Hypersonic Wind Tunnel, AIAA J., Vol. 33, No. 8, 1995, 1463-1470.
24. Miles, R.B., Mansfield, D.K., Howard, P.J., Luff, J., Girgis, I., Brown, G., Lipinski, R., Pena, G., Schneider, L., and Howard, R., A 1 MW Radiatively – Driven Hypersonic Wind Tunnel Experiment, AIAA 2003-0090, Reno NV, January 2003.
25. Shang, J.S., Kimmel, R., Hayes, J., and Tyler, C., Performance of a Low-Density Hypersonic Magneto-Aerodynamic Facility", AIAA 2003-0329, 41st Aerospace Science Meeting, Reno NV, 6-9 January 2003.
26. Powell, K. G., Roe, P.L., Linde, T.J., Gombsi, T.I. and De Zeeuv, D.L., A Solution Adaptive Upwind Scheme for Ideal Magnetohydrodynamics, J. Comp. Phys, Vol. 154, 1999, pp. 284-309.

27. Brio M. and Wu, C.C., An upwind Differencing Scheme for the Equations of Ideal Magnetohydrodynamics, J. Comp. Physics, Vol. 75, 1988, 400-422.

28. Shang, J.S., Shared Knowledge in Computational Fluid Dynamics, Electro-magnetics, and Magneto-Aerodynamics, Progress in Aerospace Sciences, Vol. 38, 2002, pp. 449-467.

29. Jones, O.S., Shumlak, U., and Eberhardt, D.S., An Implicit Scheme for Nonideal Magnetohydrodynamics, J. Comp. Physics, Vol. 130, 1997, pp. 231-242.

30. MacCormack, R.W., A Conservative Form Method for Magneto-Fluid Dynamics, AIAA 2001-0195, January 2001.

31. Gaitonde, D., Higher-Order Solution Procedure for Three-dimensional Non-ideal Magnetogasdynamics, AIAA J., Vol. 39, No. 1, 2001, pp. 2111-2120.

32. Gaitonde, D., Three-Dimensional Flow through Scramjet Simulation with MGD Flow Energy-Bypass, AIAA 2003-0172, January 2003.

33. Hoffmann, K.A., Damevin, H-M, and Dietiker, J-F., Numerical Simulation of Hypersonic Magnetohydrodynamic Flow. AIAA 2000-2259, Denver CO, June 2000.

34. Dietiker, J.F. and Hoffmann, K.A., Numerical Simulation of Turbulent Magneto-hydrodynamic Flows, AIAA 2001-2737, June 2001.

35. Morozov, A.I., and Savelyev, In Review of Plasma Physics, Edited by Kadomstev, B.B. and Shafranov, Consultant Bureau, Vol. 21, 2000, p. 203.

36. Blandino, J. et al, Overview of Electric Propulsion Research in US Academia, AIAA 2003-4442, Huntsville AL, 2003.

37. Roy, S. and Pandey, B.P., Numerical Investigation of a Hall thruster Plasma, Physics of Plasmas, Vol. 9, No. 9, 2002, pp. 4052-4060.

38. Suchomel, C.F. and Van Wie, D., and Risha, D.J., Perspectives on Cataloging Plasma Technologies Applied to Aeronautical Sceinces, AIAA 2003-3852, Orlando FL, June 2003.

39. Knight, D., Kuchinskiy, V., Kuranov, A., Sheikin, E., Survey of Aerodynamic Flow Control at High Speed by Energy Deposition. AIAA 2003-0525, Reno NV, January 2003.

40. Riggins, D., Nelson, H.F., and Johnson, E., Blunt-body Wave Drag Reduction Using Focused Energy Depostion, AIAA J., Vol. 37, No. 4, 1999, pp. 460 –467.

41. Shneider, M.N., Macheret, S.O., Zaidi, S.H., Girgis, I.G., Raizer, Yu.P., and Miles, R.B., Steady and Unsteady Supersonic Flow Control with Energy Addition, AIAA 2003-3862, Orlando FL, June 2003.

42. Shang, J.S., Plasma Injection for Hypersonic Blunt-Body Drag Reduction, AIAA J. Vol. 40, No. 6, 2002, pp.1178-1186.

43. Kallio, G. and Stock, D., Interaction of Electrostatics and Fluid Dynamic Fields in Wire-plate Electrostatic precipitators, J. Fluid Mechanics, Vol. 249, 1992, pp. 133-166.

44. Roth, J.R., and Sherman, D.M., Boundary Layer Flow Control with a One Atmosphere Uniform Glow Discharge Surface Plasma, AIAA 98-0328, Reno NV, January 1998.

45. Roth J.R., Sherman, D.M., and Wilkinson, S.P., Electrohydrodynamic Flow Control with a Glow-Discharge Surface Plasma, AIAA J., Vol. 38, No. 7, 2000, pp. 1166-1172.

46. Post, M.L., and Cork, T.C., Separation Control on High Angle of Attack Airfoil Using Plasma Actuators, AIAA 2003-1024, Reno NV, January 2003.

47. Enloe, C.L., McLaughlin, T.E., VanDyken, R.D., Kachner, K.D., Jumper, E.J., Corke, T.C., Mechanisms and Responses of a Single Dielectric Barrier Plasma, AIAA 2003-1021, Reno NV, January 2003.

48. Hultgren L.S., and Ashpis, D.E., Demonstration of Separation Delay with Glow-Discharge Plasma Actuators, AIAA 2003-1025, Reno NV, January 2003.

49. Menart, J., Shang, J.S., Kimmel, R. and Hayes, J., Effects of Magnetic Fields on Plasma Generated in Mach 5 Wind Tunnel, AIAA 2003-4165, Orlando FL, June 2003.

50. Hayes, W.D., and Probstein, R.F., Hypersonic Flow theory, Academy Press, 1959.

51. Gurijanov, E.P. and Harsha, P.T., Ajax: New Direction in Hypersonic Technology, AIAA Preprint 96-4609, Norfolk VA, Nov. 1996.

52. Bityurin, V.A., Zeigarnik, V.A., and Kuranov, A.L., On a Perspective of MHD Technology in Aerospace Applications, AIAA 1996-2355, Norfolk VA, Nov. 1996.

53. Park, C., Bogdanoff, D.W., and Mehta, U.B., Theoretical Performance of a Magnetohydrodynamic-Bypass Scramjet Engine with Nonequilibrium Ionization. J. Propulsion and Power, Vol. 19, No. 4, 2003, pp. 529-537.

54. Macheret, S.O., Shneider, M.N., and Miles, R., Magnetohydrodynamic Control of Hypersonic Flows and Scramjet Inlets Using Electron Beam Ionization, AIAA J., Vol. 40, No.1, 2002, pp. 74-81.

55. Bogdanoff, D.W., and Mehta, U.B., Experimental Demonstration of Magneto-Hydro-Dynamic (MHD) Acceleration, AIAA 2003-4285, Orlando FL, June 2003.

56. Litchford, R.J., Performance Theory of Diagonal Conducting Wall MHD Accelerators, AIAA 2003-4284, Orlando FL, June 2003.

57. Jacobsen, L.S., Carter, C.D. and Jackson, T.A., Toward Plasma-Assisted Ignition in Scamjets, AIAA 2003-0871, Reno NV, January 2003.

58. Williams, S., Arnold, S.T., Bench, P.M., Viggiano, A.A., Dotan, I., Midey, A.J., Morris, T., Morris, R.A., Maurice, L.Q., and Sutton, E.A., Potential Enhancement of Hydrocarbon Fueled Combustor Performance via Ionization, ISABE 99-7236, 1999.

59. Ramachandran, N., Leslie, F.W., Magnetic Susceptibiltiy Effects and Lorentz Force damping in Diamagnetic Fluids, AIAA 2001-0618, Reno NV, January 2001.

60. Oran, E.S., Matchsticks, Scramjets, and Black Holes: Numerical Simulation Faces Reality, AIAA 2002-0001, Reno NV, January 2002.

European Activities
Electromagnetic Fluid Dynamics in ESA

D. Giordano[*]
ESTEC - Aerothermodynamics Section
Keplerlaan 1, 2200 AG Noordwijk, The Netherlands

October 19, 2003

Contents

[*]Domenico.Giordano@esa.int

1   Historical background

Interest about the fluid dynamics of high-temperature gas mixtures in the presence of electromagnetic fields arouse in the ESTEC aerothermodynamics section at the beginning of the year 2000. That interest was triggered by a presentation made by Astrium[1] (Bremen) regarding the influence that electric/magnetic fields can exert on the flow of electrically charged gas mixtures. The effect is illustrated in Fig. 1 [taken from Ref. (1)]. A hypersonic stream flows past a blunted cylinder and becomes ionized across the shock wave. The shock stand-off distance is very small when there is no external magnetic field (Fig. 1.1) but when the experience is repeated in the presence of an external magnetic field (Fig. 1.2) the stand-off distance becomes appreciably greater, a sure indication of drastic changes in the flow pattern. Among those changes, the one of particular interest for spacecraft thermal protection during planetary reentry is the mitigation of the heat-flux distribution imposed on the body invested by the hypersonic stream. According to pioneering investigations (2; 3; 4; 5) on the subject matter, the application of a magnetic field should favour the reduction of the heat flux. A preliminary study (6) on the concept "electrodynamic heatshield" was performed by Astrium and confirmed this potentially beneficial aspect. The study also pointed out weaknesses of the physical models used for numerical simulations and the necessity of flight data to assess the accuracy between theory and real-flight environment.

---

[1]Currently part of EADS.

2   Theoretical studies

As a consequence, a basic-research study (7) was embarked upon, in the ESTEC aerothermodynamics section, to assess from a theoretical point of view the complex physical phenomenology comprising the hypersonic flow field of an ionized gas mixture in the presence of electromagnetic fields, and the corresponding formulation of a consistent set of governing equations. This work has been presented and described in detail in Lecture #3 of this course, to whose nomenclature list the reader is referred to also for notation and symbols appearing in this lecture. The study evidenced two major aspects deserving attention: a) the customary use, adopted by the totality of the CFD community dealing with the problem, of the magnetic-induction equation to characterize the electromagnetic field; b) the tensorial nature of the transport properties.

Concerning aspect a), it is sufficient here to recall that that approach is weak if one does not want to compromise physical and, even, mathematical consistency at the moment of building up a general theory. The recourse to full coupling between fluid-dynamics equations and Maxwell equations[2] is inescapable. Such a choice, in turn, opens a completely new domain of investigation, namely the development of numerical algorithms apt to deal with the full coupling between fluid dynamics and electromagnetism. Efforts in that direction represent the main focus of an ongoing research programme, lead in collaboration with the Dpt of Aeronautical & Space Engineering of the University of Turin (Italy), whose details have been presented in Lectures #5 and #6 of this course.

Aspect b) is of direct relevance to spacecraft thermal protection during atmospheric reentry. This is immediately perceived from the phenomenological relation for the internal-energy diffusive flux

$$\mathbf{J}_\mathrm{U} = \sum_{j=1}^{n} \mathbf{P}_j^\mathrm{u} \cdot \boldsymbol{\nabla} p_j + \mathbf{F}^\mathrm{u} \cdot (\mathbf{E} + \mathbf{v} \times \mathbf{B}) - \lambda_\mathrm{T}^\mathrm{u} \cdot \boldsymbol{\nabla} T$$

provided by linear irreversible thermodynamics. The expression indicates that the component of $\mathbf{J}_\mathrm{U}$ normal to the wall of a reentry body depends not only on the normal gradients of partial pressures and temperature but also on their tangential gradients. With the goal in mind of achieving a controlled mitigation of the internal-energy diffusive flux, this occurrence gives cause for the necessity to produce an accurate assessment of the importance of the off-diagonal terms in the transport tensors. More specifically, a thorough understanding of the anisotropic character of the transport tensors under the influence of the electromagnetic field appears to be a worthwhile target. It represents the task of an ongoing research programme lead in collaboration with teams in the Institute of Inorganic Methodologies and Plasmas of the Italian Research Council, Bari (Italy) and in the Laboratoire "Milieux Hors D'Equilibre" of the Institut Universitaire des Systemes Thermiques Industriels, Marseille (France).

Effects of medium polarization and magnetization were not accounted for in Ref. (7). Discarding them is probably a reasonable assumption to make when dealing with high-temperature environments characteristic of hypersonic flow. Nevertheless the polarization/magnetization phenomenology is an integral part of electromagnetism which describes how matter reacts when subjected to electromagnetic fields. Thus, it is certainly

---

[2]Equations formulated in terms of either the fields $\mathbf{E}, \mathbf{B}$ or the potentials $\phi, \mathbf{A}$.

desirable to be included in a general theory for reasons of completeness and in view of new potential applications. When such an inclusion is attempted, however, one immediately realizes how the level of complexity increases substantially with respect to the one corresponding to the situation of pure electromagnetic field. The inclusion in the Maxwell equations is straightforward. Yet there are conceptual problems still in demand of resolution. Those on the fluid-dynamics side have been briefly mentioned in the introduction of Lecture #3. On the electromagnetism side, the debate on the *correct* definitions of electromagnetic momentum and energy, which can be traced back to the works of Abraham and Minkowski during the first years of the past century, lays still there unresolved. As a consequence, the expression of the electrodynamic-force density required in the matter-momentum balance equation remains undetermined. A research study concerned with these matters and aiming to the formulation of a physically consistent theory of polarizable and magnetizable fluids is in progress internally to the ESTEC aerothermodynamics section.

3   Experimental activities

Experimental investigations are the natural complement of theory and numerical simulations. In this regard, there are two lines of research that can be pursued: ground testing and flight testing. Both lines are being *considered* at the moment in the ESTEC aerothermodynamics section with a view to the possible definition of future activities in collaboration with EADS Bremen and other teams. However, a proposal concerned with a feasibility study of an electrodynamic-heatshield flight experiment has already been channelled through the approval cycle of the ESA technical research programme. The proposal takes advantage of the main findings relative to test cases defined in the Astrium preliminary study (6). Those test cases are relative to two reentry trajectories, one of lower ionization the other of strong ionization, that are thought to represent an envelope defining the domain of potential application for the electrodynamic-heatshield concept. Thus, things are still in an early stage at the moment but preparatory work is in progress and an active phase of activities is foreseen to start in the first quarter of next year.

References

[1] R. Ziemer, Experimental investigation in Magneto-Aerodynamics, Amer. Rocket Soc. J., September, 642–647 (1959).

[2] V. Rossow, On Flow of Electrically Conducting Fluids over a Flat Plate in the Presence of a Transverse Magnetic Field, NACA Technical Report No. 1358, 1958.

[3] E. Resler and W. Sears, The Prospects for Magneto-Aerodynamics, J. Aeron. Sciences **25**, 235–245/258 (1958).

[4] W. Bush, Magnetohydrodynamic-Hypersonic Flow past a Blunt Body, J. Aero/Space Sciences **25**, 685–690/728 (1958).

[5] W. Sears, Magnetohydrodynamic Effects in Aerodynamic Flows, Amer. Rocket Soc. J., June, 397–406 (1959).

[6] D. Konigorski, Electrodynamic heatshield study, ESA GSP contract 14753-00-NL-FM final report, October 2002.

[7] D. Giordano, Hypersonic-Flow Governing Equations with Electromagnetic Fields, in *33rd Plasmadynamics and Lasers Conference*, 20–23 May 2002, Maui HI, (American Institute of Aeronautics and Astronautics). AIAA 2002-2165.
The contents of this work constitute the basis for Lecture #3.

<div style="text-align:center">1.1: External magnetic field off.</div>
<div style="text-align:center">1.2: External magnetic field on.</div>

Figure 1: Influence of an external magnetic field on the hypersonic flow past a blunted cylinder. From Ref. (1).

European Activities - Italian Perspective

C. Borghi[*]

Dpt of Electrical Engineering - University of Bologna

Viale Risorgimento 2, Bologna, Italy

October 13, 2003

Contents

---

[*]`ca.borghi@mail.ing.unibo.it`

1 Activities on MHD Interactions in Plasma Flows

In Italy studies and experimental investigations on MHD interactions in plasma flows and their applications have been carried out since the sixties. In the past most activities aimed to MHD electrical power generation. However the experience and the knowledge acquired have been transferred to other recently investigated MHD technologies. MHD aerodynamics is one of the main activities carried out at present and in the near future plans.

Now the projects on MHD applications are organised in the frame of co-operations among research groups both at Italian and at European levels. Co-operation is essential as MHD is an interdisciplinary field. Its has always been encouraged by the International Liaison Group on Magnetohydrodynamics. This Group originated from the co-operation among the countries active in this field, and its main aim is to stimulate and support the research on MHD.

In order to describe the present activities in Italy and their perspectives, a short description of the main work done in the past is necessary. Afterwards a review of the current projects will be presented.

1.1 The first MHD experiments

1.1.1 The blow down experiment in Frascati

The blow down facility built in the labs of CNEN (now ENEA) in Frascati (Italy) at the end of the sixties, is an experimental facility aimed to demonstrate that it is possible to convert the thermal power of a noble gas into electrical power (see Fig. 1). This was connected to the gas cooled nuclear reactor technology developed at those times.

The experiments were carried out with a caesium seeded helium plasma heated at a temperature of about 1900 K and at a pressure of few bars (1). The plasma, with a thermal power of 2 MW, was injected into a MHD channel of inlet cross section of 5 x 5 cm^2, diverging over a length of 20 cm. The plasma flow was subsonic and the magnetic flux density was 4.5 T. A segmented Faraday channel electrical scheme with 30 electrode pairs was utilised. Pre-ionisation at the channel entrance by means of an electrical discharge was used.

The electrical power extracted, considering the pre-ionisation power expense, was of about 3 kW corresponding to an electrical power density of 18 MW/m^3. In the experiments a Faraday voltage resulted to be equal to the calculated value ($\simeq$ 300 V measured between cathode and anode) and the measured Hall voltage resulted to be 0.6-0.8 times its calculated value. This was ascribed to the bad insulation of the MHD channel.

One of the main results obtained in this experiment, is the importance of the electrical insulation of the channel. When the channel is not insulated, the Hall tension can be shorted and the MHD process can be spoiled with a drastic reduction of the power output delivered by the MHD generator.

Another result is the confirmation of the partial local thermodynamic equilibrium with the electron temperature higher than the gas temperature reached in this mono-atomic plasma as shown in the experiment of Kerrebrok (2). Another aim of the experiments carried out at the beginning of the seventies was to investigate the ionisation instabilities which affect the non-equilibrium MHD plasmas. A new formulation of the quasi-linear

theory for the instability behaviour was developed. That theory leads to a reduction of the Hall parameter to a critical value of it and to an effective electrical conductivity proportionally reduced to the reduction of the Hall parameter. The experimental data were utilised to validate the theory.

In those years several researchers dealt with ionisation instabilities and tried to explain them with linear or quasi-linear theories. The main differences were on the determination of the critical Hall parameter and on the reduction of the electrical conductivity. Later, with the use of sophisticated diagnostics, it was shown that the non-equilibrium noble gas plasma in MHD generators has an highly non-uniform character due to instabilities, with streamers or plasma channels surrounded by cold gas (3; 4).

1.1.2   The MHD shock tunnel facility of the University of Bologna

At the University of Bologna in the end of the seventies and beginning of the eighties, an MHD shock tube facility was constructed and operated (Fig. 2). The aim of this experimental facility was to investigate the possibility to directly convert the thermal energy content of the gas into alternate electrical energy. In order to do this the possibility to use two pulsed shock tubes to operate alternatively was considered.

The shock tube facility of the University of Bologna was a direct shock tube operated with argon as the driven gas. The gas between the shock front and the separation surface was used for the MHD conversion. A segmented Faraday channel of a length of 50 cm and with a constant cross section of 5x5 cm^2 was used. The magnetic flux density on the channel axis was 1.2 T. In order to increase the electrical conductivity of the test gas, K_2CO_3 was used as seed. The pressure and the velocity of argon at the channel inlet were respectively 0.8 bars and about 1000 m/s. During the experiments few amperes was measured.

1.2   T-layer MHD energy conversion

The T-layer MHD generator scheme is shown in Fig. 3. The generator is a traditional segmented Faraday generator. The gas is highly non-uniform with hot plasma vanes separated by cold gas. The expanding gas exerts an accelerating force on the vanes in the direction of the channel divergence. The electrical current flows inside the plasma vanes. Therefore a Lorentz force acting on the vanes, against the gas flow, is originated. The MHD energy conversion is generated by the interaction of the gas expansion force and the Lorenz force. The MHD energy conversion process can be utilised for the electrical power generation. A large number of experimental and theoretical investigations aimed to this in the past. However this process can be utilised in several fields and several technologies as in the case of aerodynamics. The advantage of the T-layer MHD energy conversion is due to the possibility to reduce the gas temperature necessary to obtain a proper electrical conductivity.

A trilateral joint research project was set up to study MHD conversion in highly non-uniform flows in the second half of the nineties. The contributing institutes are the Institute of High Temperatures, Moscow (with the task to co-ordinate the project and to perform the physical modelling), the Eindhoven University of Technology (with the task to perform the experiments) and the University of Bologna (with the task to carry out the

numerical modelling and the numerical simulations). The main goal of the project is to demonstrate the physical feasibility of MHD energy conversion in alternating gas/plasma flows and to analyse the effect on commercial scale installations (5).

The performance of the T-layer MHD generators of commercial size has been studied through numerical simulations based on time dependent one- and two-dimensional models. By means of one-dimensional calculations, enthalpy extractions of 40% have been obtained (6). Two-dimensional time dependant numerical codes have been developed to study optimal conditions to reach high performances in T-layer MHD generators of commercial size electrical power stations (7; 8). The numerical codes consider the fluid-dynamic model, the electrodynamic model and the kinetics of the real gas. The plasma is considered to be constituted by the combustion products leaving the combustor of the power station. Heat losses and turbulence are taken into account. MHD generator of large active lengths (up to 14 m) has been studied.

In Fig. 4, two-dimensional plots of the median channel cross section for the simulation of the T-layer MHD conversion in a commercial size generator, is shown. The plots refer to the temperature, the static pressure, and the x- and z-components of the velocity in the plain containing the gas velocity and the magnetic field, and perpendicular to the T-layers. In this case at the channel inlet a gas temperature outside the T-layer, of 2100 K and a pressure of 7 bars are taken. Here gas velocities between 1000 and 1400 m/s are considered. The magnetic flux density is chosen to be 4 T. The electrical conductivity is taken as a function of pressure and temperature, which fits data obtained in a plasma of natural gas combustion products seeded by means of 1% in weight of potassium carbonate. At optimal conditions an enthalpy extraction larger than 30% has been obtained (9). These results were achieved after a large optimisation work realised through a parametric study. The optimal operating conditions appear to be reached in narrow ranges of parameters such as the gas conditions at the channel inlet, the formation conditions of the plasma layers and the electrical boundary conditions. In Fig. 5, the dependence of the enthalpy extraction and of the isentropic efficiency on the period of formation of the T-layer are shown. At the channel entrance the T-layers are generated with a defined frequency. The time interval between the generation of two consecutive T-layers is cold period of formation.

From the experimental investigation carried on in the shock tube experiment of the Eindhoven University of Technology, utilising combustion gas, the feasibility of the concept has been demonstrated qualitatively. In Fig. 6, a streak picture of a T-layer flowing along the channel is shown (4; 9). In the experiment the observed current response is in agreement with the model calculation.

1.3   Plasma diagnostics

In the lab of Plasma Engineering of the University of Bologna optical plasma diagnostic tools have been developed and operated. They are based on spectroscopic technique and on plasma imaging. The spectroscopic observations are done by means of a Jobin Yvon monochrometer of a focal length of 460 mm and an optical multi-channel analyser with a resolution $\lambda/\Delta\lambda = 900$ (λ is the wave length). The imaging technique is mainly obtained by means of a PCO Sensicam CCD colour fast shutter camera with an exposure time down to 100 ns. The diagnostic systems were built and tested in the discharge chamber

of the lab (Fig. 7).

These diagnostic tools were utilised to study the plasma of the MPD thruster at the Centrospazio-CPR in Pisa (10). The device under operation is shown in Fig. 8. Several operating conditions were investigated. The radiation emission of the plasma in several position of the plasma plume has been analysed (11). Two typical spectra are shown in Fig. 9. Both plots shown in the figure, are taken in a central position of the plasma plume after a time interval from onset of the plasma discharge for which the regime operation is reached. The upper plot refers to the operation obtained without an external magnetic field superimposed to the magnetic field induced by the plasma current. The lower plot refers to the operation with an external magnetic field density of 80 mT. From the Boltzmann plot of the radiation lines of Argon the population density has been obtained. The population temperature derived from the radiation due to the de-excitations of high levels has shown to be of 4-8 eV as the electron temperature measured by means of electrical probs. The population temperature from low levels is much smaller. The plasma appears to be not in partial local equilibrium with a non-Maxwellian electron energy distribution.

Imaging of the plasma plume has been done with the fast shutter CCD camera at an exposure time of few μs (11). In Fig. 10, the image of the plasma plume during its onset is shown. It refers to a test with external magnetic field after 75 μs from discharge starting trigger signal. The image of Fig. 11 refers to the plasma plume during the regime operation. During the plasma onset a clot flowing in the gas direction is observed. The velocity of the clot is 3.3 km/s whereas the estimated gas velocity is 20 km/s. The clot appears to drag plasma filaments which wrap themselves up with a helicoidal structure. During the regime operation the plasma structure appears to be nearly uniform.

1.4   Modelling and Numerical Simulations

Magnetohydrodinamics is a complicated process described by a combination of fluid-dynamics, electrodynamics, and plasma-kinetics. In the momentum conservation equation and the energy conservation equation, that are equations of the traditional fluid-dynamic model, terms determined by electromagnetic quantities are present. These are the Lorenz force term in the momentum equation of the plasma and the Joule heating term in the plasma energy conservation equation. The mean mass velocity, the gradient of the electron pressure and other fluid-dynamic quantities are present in Ohm's law. .Moreover the electromagnetic properties of the plasma and the other transport coefficients depend on the plasma-kinetics. The kinetics of a developing plasma is also dependant on fluid-dynamics and electrodynamics. Therefore each one of the three mentioned models is difficult to separate from the other. However the simultaneous mathematical solution of the fully coupled problem is difficult to obtain.

The fluid-dynamic macroscopic model describes the dynamics of the plasma as a continuum fluid medium characterised by few quantities. These are the result of microscopic phenomena which involve all different species of particles constituting the plasma. This last aspect is described by plasma-kinetics, which takes into account the dynamic of each species constituting the plasma and leads to all transport properties for fluid-dynamic and electrodynamics. The condition for the applicability of the macroscopic model is that the plasma be collision dominated. By this term one means that for all species

the mean free path for particle collisions be much smaller than the characteristic length scale for macroscopic changes and the collision time intervals be much smaller than the characteristic time scale for macroscopic changes. A sufficiently accurate description of magnetohydrodinamics given through the coupling of these three models, can be obtained in several cases even when the collision dominated condition is not satisfied.

The two assumptions of the magnetohydrodynamic approximation are $t_c >> 1/\nu_{eh}$ and $t_c >> \nu_{eh}/\omega_p^2$, where t_c is the characteristic time scale for macroscopic changes, ν_{eh} is the collision frequency between electrons and heavy particles and $\omega_p = (n_e e^2/\epsilon_o m_e)^{1/2}$ is the plasma frequency. The first assumption ($t_c >> 1/\nu_{eh}$) allows to derive the generalised Ohm's law from the momentum conservation equation of the charged species of the plasma. When the second assumption ($t_c >> \nu_{eh}/\omega_p^2$) is made, the displacement current density can be neglected in comparison to the conduction current density, the convection current density can be neglected in comparison to the conduction current density, and the force acting on the fluid due to its net charge can be neglected in comparison to the Lorenz force. Hence the electrodynamic model is given by the following equations:

$$\boldsymbol{j} + \beta_e \boldsymbol{j} \times \mathbf{B} + (\rho_n/\rho)^2 \beta_e \beta_i \mathbf{b} \times (\boldsymbol{j} \times \mathbf{B}) = \sigma \left(\mathbf{E} + \mathbf{u} \times \mathbf{B} + \frac{\boldsymbol{\nabla} p_e}{e n_e} \right)$$

$$\boldsymbol{\nabla} \times \mathbf{B} = \mu_0 \boldsymbol{j}$$

$$\boldsymbol{\nabla} \times \mathbf{E} = -\frac{\partial \mathbf{B}}{\partial t}$$

$$\boldsymbol{\nabla} \cdot \mathbf{B} = 0$$

The first equation expresses the generalised Ohm's law where $\mathbf{b}$ is given by $\mathbf{B}/B$, β_e and β_i are the Hall parameters for electrons and for ions, ρ and ρ_n are the total mass density of the plasma and the mass density of the neutral particles (ρ_n is different from zero for a partially ionised plasma, for full ionisation ρ_n is equal to zero). The other symbols in this equation are standard. The second term in the left hand side of Ohm's equation (Hall term) accounts for the drift velocity of electrons. The third left hand side term accounts for the contribution to the current of ions (ion slip term) and is different from zero only in a partially ionised gas. The last three equations are the Maxwell equations in the MHD approximation.

From the electrodynamic model the dynamic equation for the magnetic flux density $\mathbf{B}$ is derived. The time variation of $\mathbf{B}$ is due to two terms: the first is a diffusion term showing $\mathbf{B}$ to diffuse in space and to decay in time, the second is a convective term with $\mathbf{B}$ convected with the plasma flow. In a stationary plasma with mean mass velocity $\mathbf{u}$ equal to zero the magnetic regime is purely diffusive. In the case of an infinite electrical conductivity in a moving plasma ($\mathbf{u} \neq 0$) the magnetic regime is purely convective. In the last case the MHD interaction does not occur. In the general case (finite conductivity and non stationary plasma) the magnetic flux density will change in time as a result of convection with the fluid and diffusion through the fluid. The ratio between convection and diffusion is characterised by the magnetic Reynolds number R_m. For $R_m << 1$, convection is much smaller than diffusion and the component of $\mathbf{B}$ induced by the plasma electrical current is much smaller than the component of $\mathbf{B}$ obtained by currents external to the plasma (the curl of this component is equal to zero).

For fluid dynamic usually Navies-Stokes equations are utilised. In most models utilised the plasma-kinetics considers the plasma to be in equilibrium ($\dot{n} = 0$) and the continuity equations for each species are used.

Since the end of the eighties one-dimensional and multi-dimensional MHD models and their numerical application were considered in Italy (12; 13). This activity was mainly aimed to design the MHD channel for electrical power stations. The MHD models utilised, considered a purely diffusive magnetic regime. The plasma was obtained from fossil fuel combustion products. A pressure of few bars, a velocity near 1000 m/s and an applied magnetic field of 4-6 T were used. Linear diverging channel of different dimensions were considered. For the optimisation of the design the MHD numerical model based on a quasi-linear approximation, was used for the analysis of the MHD process in an optimisation procedure. For the solution of the synthesis optimisation problem several minimisation techniques were utilised. The most used among them were a gradient minimisation method and the SQP (Sequential Quadratic Programming) method.

Several numerical technique were used for the solution of the multidimensional electrodynamic problem (14; 15). This Finite volume, finite element, and the finite difference method were utilised. In order to ensure the convergence toward a stable solution of the non-symmetrical electrodynamic problem, several discretisation algorithms were developed. One of them is the exponential fitting method that guarantees a robustness of the numerical procedure (15). The problem were considered both for diffusive and for convective-diffusive regimes ($R_m << 1$ and $R_m \simeq 1$ respectively) (14; 15; 16). For the solution of the time dependent multidimensional fluid-dynamics explicit, semi-implicit and implicit methods were utilised (17; 18; 19). The application considered were the MHD channel analysis of MHD generators during transients (20), T-layer plasma vane generators (for which the flow is non-stationary and non-uniform) (21; 22), the non-stationary discharge behaviour in SF6 circuit breakers (23; 24). Recently the problem of hypersonic flows in MHD fields has been studied. In this case the simulation of the flow has been done by means of an up-wind procedure (25; 26; 27).

The characteristic time scale for macroscopic changes of electrodynamics is much shorter than that of fluid-dynamics. Therefore fluid-dynamics is considered a time-dependent problem whereas electrodynamics can be considered a steady problem at each time step of the numerical solution of fluid-dynamics.

1.5   MHD Interaction in Hypersonic Flows

The MHD interaction in hypersonic flows is considered to be utilised in the hypersonic flight at high altitudes in a rarefied atmosphere. In Fig. 12, the main process is shown. At hypersonic velocities, as those occurring during the re-entry of space vehicles, the air between the shock front and the surface of the vehicle reaches a high temperature and becomes ionised. The electrical conductivity realised, can sustain an MHD process affect the aerodynamic drag and the thermal transport toward the wall of the vehicle. The MHD interaction process can be utilised also to control the gas flow at the inlet of a scram jet engine and to accelerate it at the scram jet exit. A further application is the inboard electrical power production in hypersonic vehicles. In the scientific community a great interest on this has arisen in the last years. Many space institutions and the industry of the field consider the possibility to develop a mature technology.

At present in Italy is under realisation a co-operation project on the hypersonic flow-MHD interaction. This project is supported by ASI (Italian Space Agency). Few Italian universities and research institutions take part to the project activities. The University of Bologna is responsible of the project co-ordination. The interaction of a blunt body and of a wedge in a hypersonic flow is investigated both theoretically and experimentally. A numerical simulation of the interaction of a wedge body in a hypersonic flow is presented in Fig. 13. The plots on the left column of the figure show the Mach iso-lines (a), isobars (b) and iso-thermals (c) without MHD interaction. The plots on the right column show the Mach iso-lines (a), isobars (b) and iso-thermals (c) with MHD interaction. In the case considered the MHD interaction appears to affect strongly the dynamics of the fluid. The Hall effect seems to reduce this process. The experimental facility is mounted on the hypersonic wind tunnel of Centrospazio-CPR. A view of the hypersonic wind tunnel of Centrospazio is shown in Fig. 14. A scheme of the hypersonic flow-MHD interaction experiment is shown in Fig. 15. Here the MHD interaction is realised on an oblique surface placed in front of the wind tunnel exit.

2   Future Plans

2.1   MIUR Project on Theoretical Investigation on the MHD Interaction in hypersonic flows

A theoretical project on the hypersonic flow-MHD interaction has been proposed for the support of MIUR (Italian Ministry of the University and the Scientific Research). The project will be realised by the co-operation of the University of Bari, the University of Bologna and the Politecnico of Turin. The aim is to set up and validate a numerical code that can predict the MHD process considering the fluid-dynamics, the electrodynamics and the plasma-kinetics of the gas for a large range of conditions as those realised by a hypersonic vehicle at high altitudes in the atmosphere. The model will analyse diffusive and convective-diffusive magnetic regimes. Different numerical integration schemes between fluid-dynamics, electrodynamics and plasma-kinetics will be set up and their results will be compared.

2.2   ASI Project on the MHD technology in a hypersonic vehicle

A large co-operation project with the participation of several universities, research institutions and industries is proposed to ASI for its financial support. The MHD interaction is studied for the re-entry of a hypersonic vehicle. The main aim is to develop the tools necessary to the design of the nose of USV (Unmanned Space Vehicle). The numerical coding, that will be done by an integration of hypersonic fluid-dynamics, electrodynamics and plasma-kinetics models, will be validated by means of the wind tunnel of Centrospazio and the Scirocco wind tunnel of CIRA.

References

[1] R. Toschi et al., in *5th International Conference on Magnetohydrodynamic Electrical Power Generation*, Munich, April 1971.

[2] J.L. Kerrebrok and M.A. Hoffman, Non-equilibrium ionization due to electron heating: II. Experiments, AIAA Journal, 1080–1086 (1964).

[3] W.M. Hellebrekers, A. Veefkind, and C.A. Borghi., Experiments on the nonuniform discharge structure in noble gas MHD generators, in *Proc. 18th Symposium on Engineering Aspects of Magnetohydrodynamics*, pp. D.2.1-6, Butte (Montana), 1979.

[4] A. Veefkind, Experimental approach to plasma physical aspects of traditional MHD, VKI Lecture Series on "Introduction to Magneto-Fluid-Dynamics for Aerospace Applications", October 2003.

[5] A. Bityurin, C.A. Borghi, A. Veefkind, Trilateral Project on MHD Power Generation with Plasma Nonuniformities - Gas Interacting Flows, in *Proc. 31st Symposium EAM*, pp. IVb.2.1-4, Whitefish (Montana), June 1993.

[6] V.A. Bityurin and A.P. Likhachev, High efficient MHD-generator with space and time dependent current carrying non-uniformities, in *Proc. of the 10th International Conference on MHD Electrical Power Generation*, pp. X.191-197, Tiruchirapalli, India, December 1989.

[7] V.A. Bityurin, C.A. Borghi, P.L. Ribani, High Enthalpy Extraction Numerical Experiment in a Plasma Vane MHD Generator, IEEE Trans. on Plasma Science **23**, no. 5, 844–851 (1995).

[8] C.A.Borghi and P.L.Ribani, Analysis of real gas effects in an MHD generator with STCC non-uniformities, IEEE Trans. on Plasma Science **25**, no. 5, 1136–1143 (1997).

[9] V.A. Bityurin, C.A.Borghi and A. Veefkind, MHD Electrical Power Generation in a T-Layer Plasma Flow, IEEE Transactions on Plasma Sciences **28**, no. 3, 1020–1028 (2000).

[10] M. Andrenucci, MFD technologies for space propulsion applications, VKI Lecture Series on "Introduction to Magneto-Fluid-Dynamics for Aerospace Applications", October 2003.

[11] C.A.Borghi, M.R. Carraro, A. Cristofolini, R. Ghidini, and F. Paganucci, Optical investigation on an Magneto-Plasma-Dynamic thruster, in *AIAA Plasmadynamics and Lasers Conference*, June 2003, Orlando (Florida), (American Institute of Aeronautics and Astronautics). AIAA 2003-4293.

[12] C.A. Borghi, F. Negrini, P.L. Ribani, Constrained Optimal Control Problem for MHD Flows, Magnetohydrodynamics: an International Journal **2**, no. 4, 257–265 (1989).

[13] C.A. Borghi, A. Massarini, G. Mazzanti, P.L. Ribani, One and Two Dimensional Models for a Linear MHD Generator Channel Design, Plasma Devices and Operation **2**, no. 2, 125–139 (1992).

[14] A. Cristofolini and C.A. Borghi, A Difference Method for the Solution of the Electrodynamic Problem in a Magnetohydrodynamic Field, IEEE Transactions on Magnetics **31**, no. 3, 1749–1752 (1995).

[15] C.A. Borghi, A. Cristofolini, G. Minak, Numerical Methods for the Solution of the Electrodynamics in Magnetohydrodynamic Flows, IEEE Transactions on Magnetics **32**, no. 3, 1010–1013 (1996).

[16] C.A. Borghi and A. Cristofolini, Numerical Approach to a Magnetic Convection-Diffusion Problem at High Magnetic Reynolds Numbers, in *Proc. of Int. Conf. on MHD Power Generation and High Temperature Technologies*, Vol. 2, pp. 521-524, Beijing (PRC), October 1999.

[17] A. Massarini and C. A. Borghi, Time Dependent Quasi-Onedimensional Flow Models for Linear MHD Generator Channels, Phys. of Fluids B **4**, no. 9, 2823–2829 (1992).

[18] C.A. Borghi, N. Montevecchi and P.L. Ribani, Pressure Method for the Analysis of a Time Dependent Two-Dimensional non-Uniform Plasma Flow, Magnetohydrodynamics **32**, no. 3, 322–330 (1996).

[19] A. Borghi, A. Cristofolini, N. Montevecchi, and P.L. Ribani, A Time Dependent Two-Dimensional Method for the Solution of the Magneto-Plasma Dynamic Coupled Problem, IEEE Transactions on Magnetics **33**, no. 2, 1722–1725 (1997).

[20] C.A. Borghi, A. Cristofolini and P.L. Ribani, Analysis of Magneto-Plasma Dynamic Transients in a Combustion Gas MHD Generator, Phys. of Plasmas **4**, no. 8, 3082–3090 (1997).

[21] V.A. Bityurin, C.A. Borghi and P.L. Ribani, High Enthalpy Extraction Numerical Experiment in a Plasma Vane MHD Generator, IEEE Transactions on Plasma Science **23**, no. 5, 844–851 (1995).

[22] C.A. Borghi and P.L. Ribani, Analysis of Real Gas Effects in an MHD Generator with STCC non-Uniformities, IEEE Transactions on Plasma Science **25**, no. 5 (1997).

[23] C.A. Borghi, A. Cristofolini, A Fully Implicit Method for the Numerical Solution of the MHD Problem in an SF6 Discharge, in *Proc. 26th IEEE International Conference on Plasma Science*, p. 216, Monterey (California), June 1999.

[24] Carlo A. Borghi, and Andrea Cristofolini, A Hybrid Implicit Numerical Method for the Analysis of the Magneto-Plasmadynamics in a Gas Discharge, IEEE Transactions on Magnetics **37**, no. 5, 3401–3404 (2001).

[25] C.A. Borghi, and A. Cristofolini, Numerical Modeling of MHD Interaction in the Boundary Layer of Hypersonic Flows, IEEE Transactions on Magnetics **319**, no. 3, 1507–1510, (2003).

[26] C.A. Borghi, M.R. Carraro, and A. Cristofolini, An analysis of MHD interaction in the boundary layer of hypersonic blunt body, in *AIAA Plasmadynamics and Lasers Conference*, June 2003, Orlando (Florida), (American Institute of Aeronautics and Astronautics). AIAA 2003-3761.

[27] C.A. Borghi, M.R. Carraro, and A. Cristofolini, Numerical Solution of the Non Linear Electrodynamics in MHD Regimes with Magnetic Reynolds Number near One, in *Compumag 2003*, Saratoga Spring (USA), 2003.
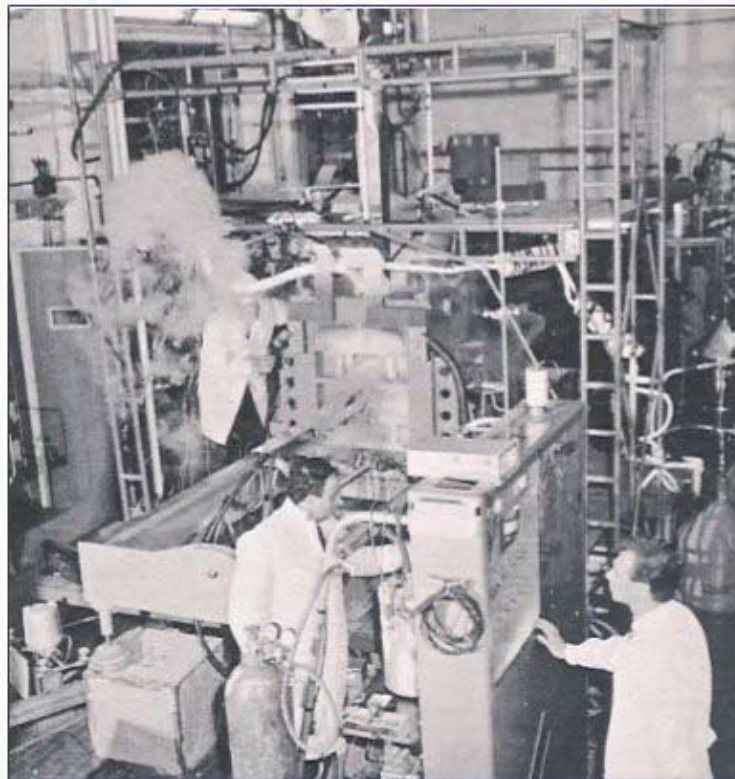
Figure 1: MHD blow-down facility in Frascati.

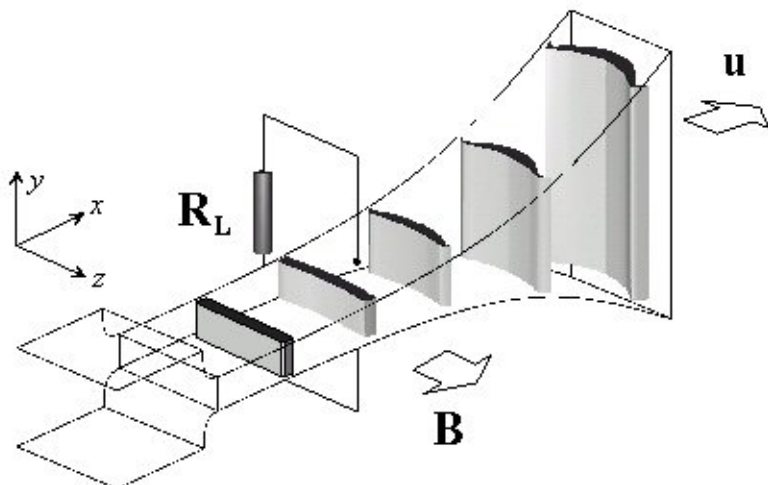Figure 2: MHD shock tunnel at the University of Bologna.
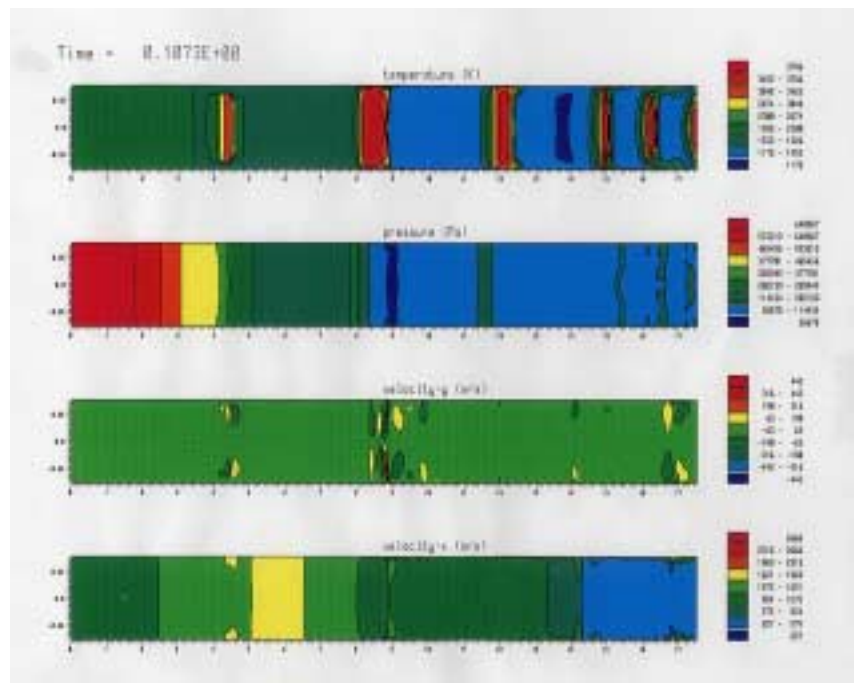
Figure 3: T-layer MHD generator.

Figure 4: Two-dimensional plots of the median channel cross section for the simulation of the T-layer MHD conversion in a commercial size generator. The plots refer to the temperature, the static pressure, and the x- and z-components of the velocity at a time t = 0.1073 s from the initiation of the MHD interaction.
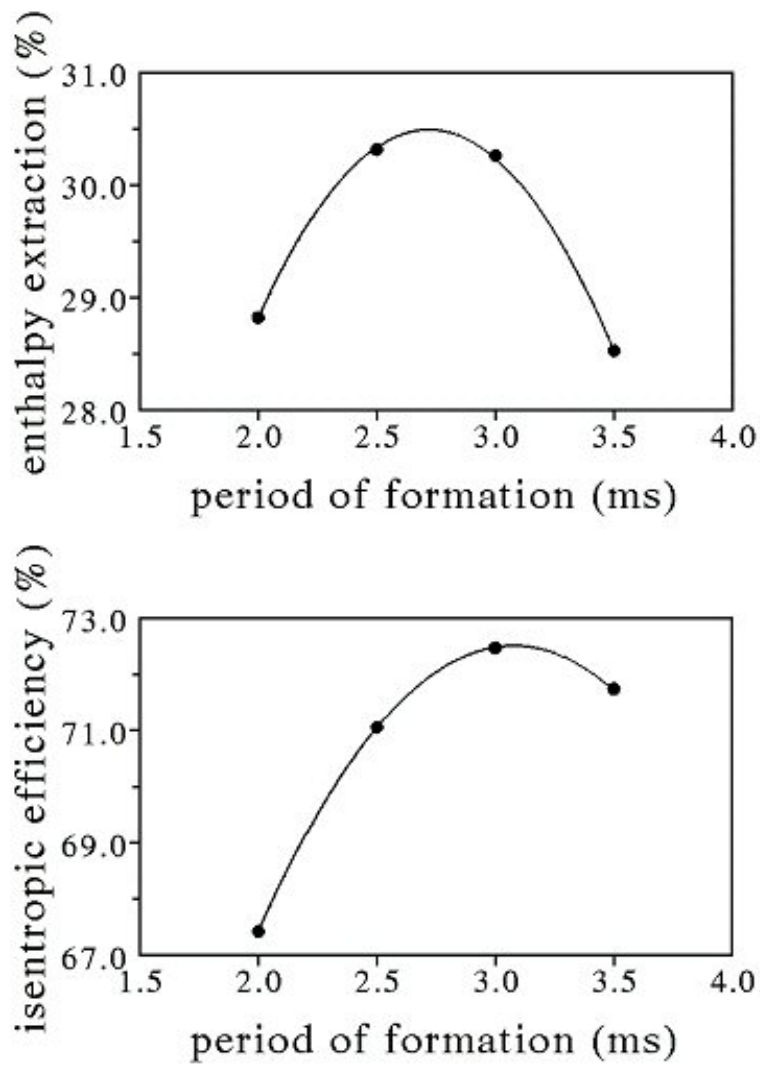
Figure 5: Enthalpy extraction and isentropic efficiency vs. T-layer formation period.
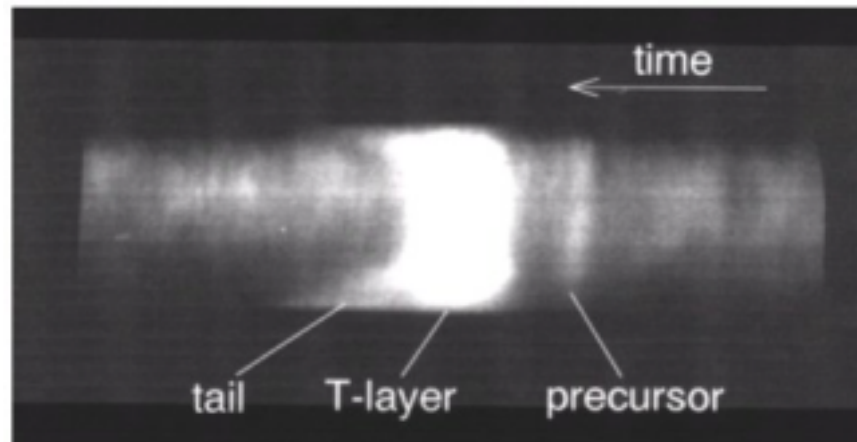
Figure 6: Streak camera picture of a T-layer in the shock tunnel experiment.

Figure 7: Discharge chamber in the laboratory of the University of Bologna.
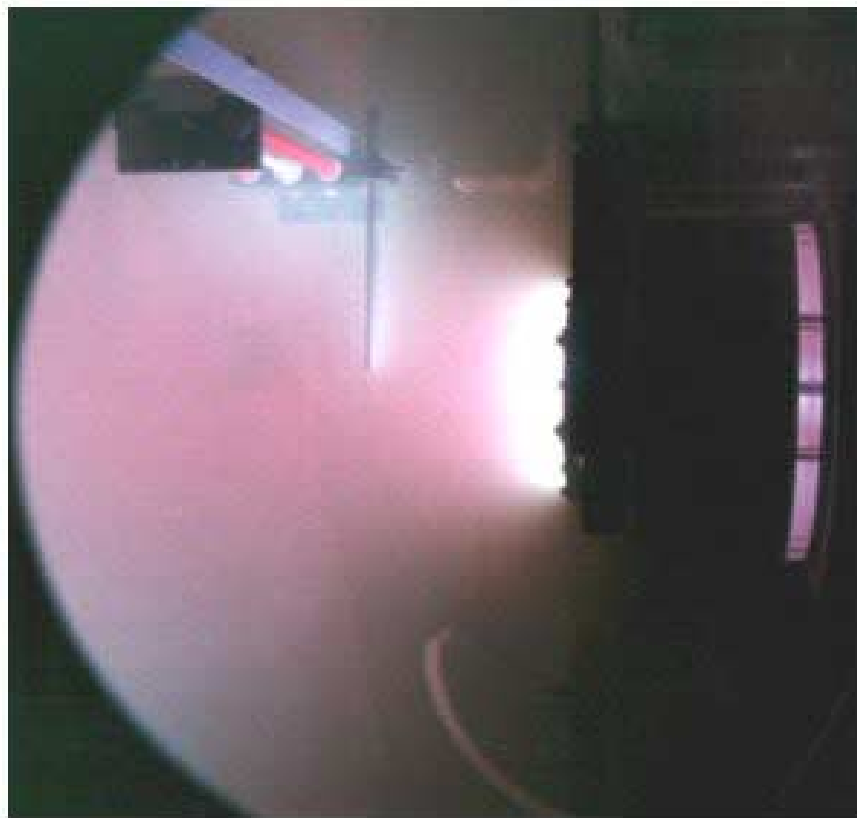
Figure 8: MPD thruster of Centrospazio.
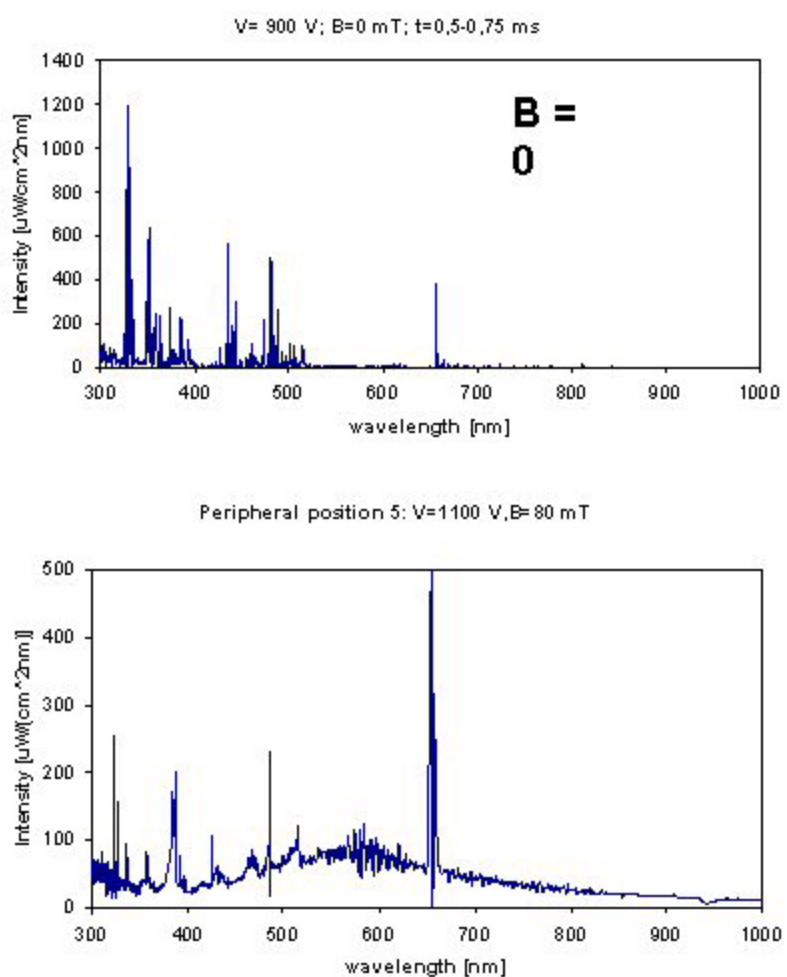
Figure 9: Emission spectra of the plasma of the MPD thruster.
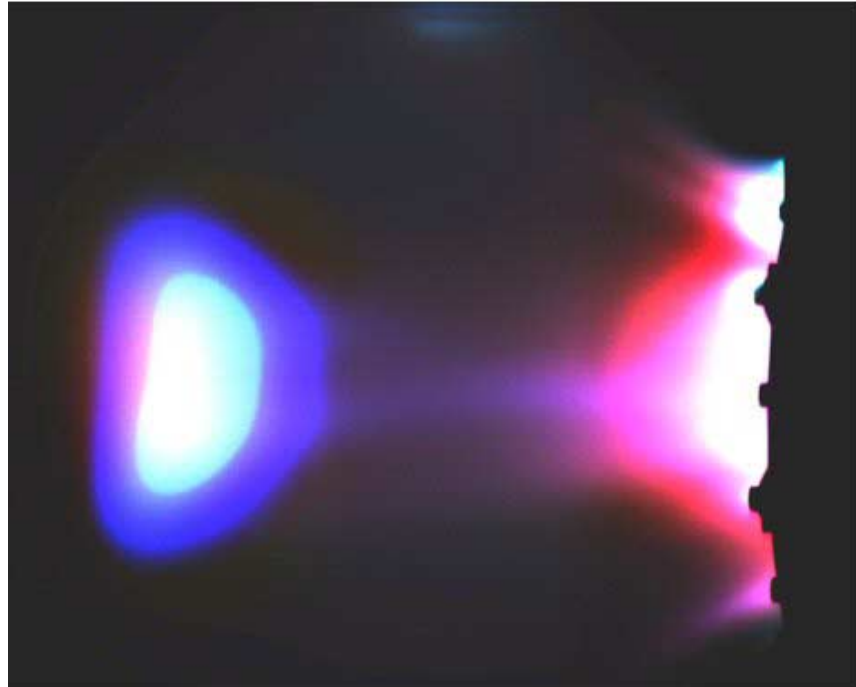
Figure 10: Image of the plasma plume during the start up conditions.
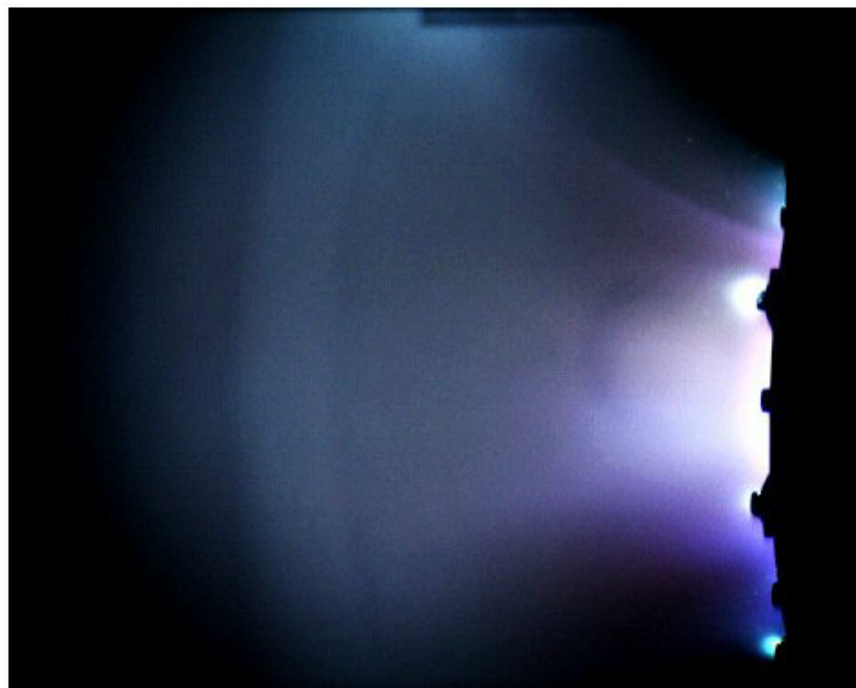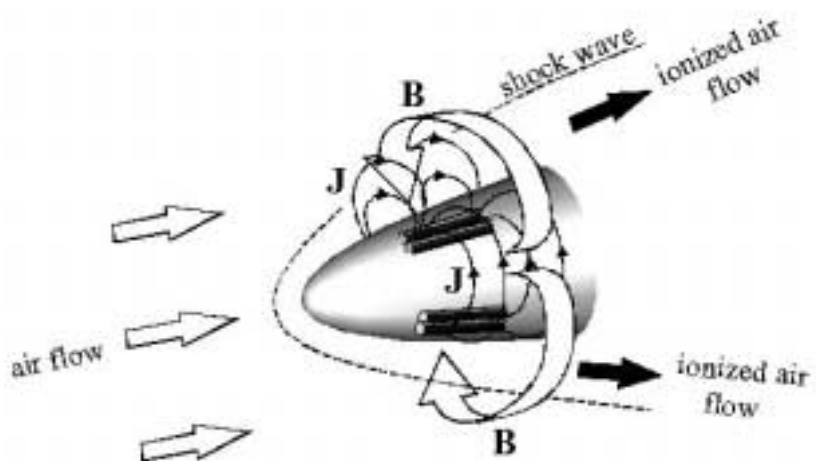

Figure 11: Image of the plasma plume during the regime conditions.

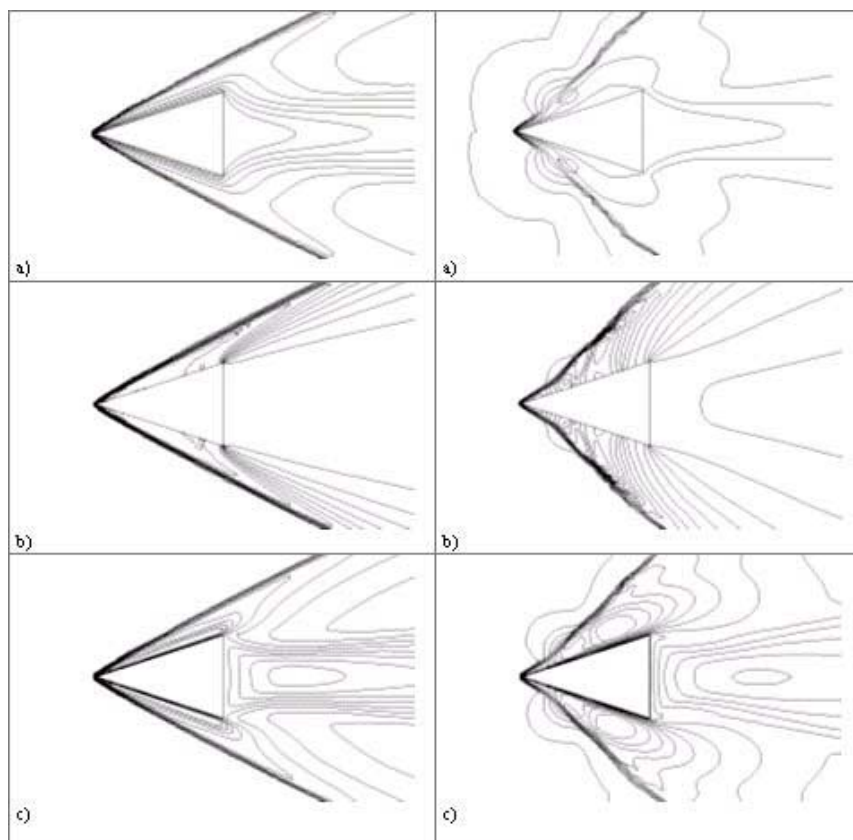Figure 12: Scheme of the MHD interaction on an hypersonic vehicle.

Figure 13: MHD interaction of a wedge body in an hypersonic flow.

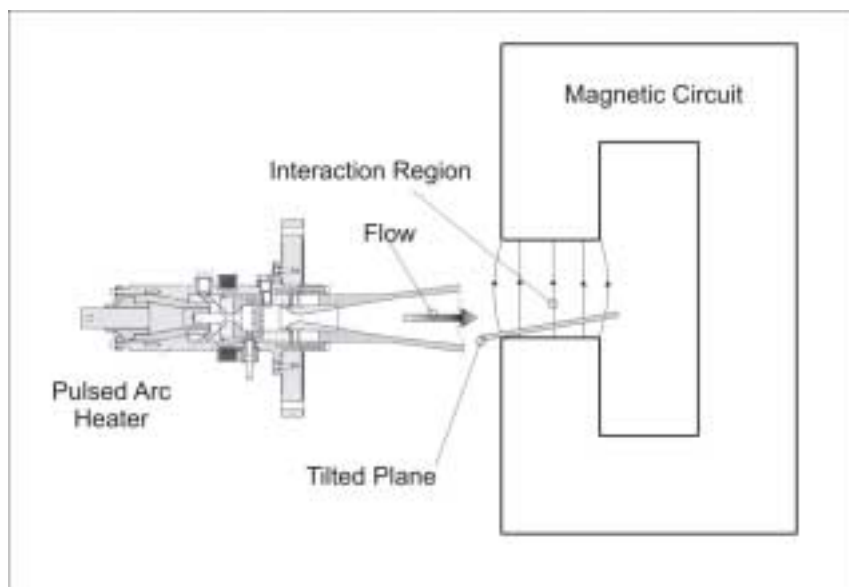Figure 14: Hypersonic wind tunnel of Centrospazio.

Figure 15: Scheme of the hypersonic flow-MHD interaction experiment.

Figure 16: Unmanned space vehicle.